NUREG/CR-2126
EGG-2102

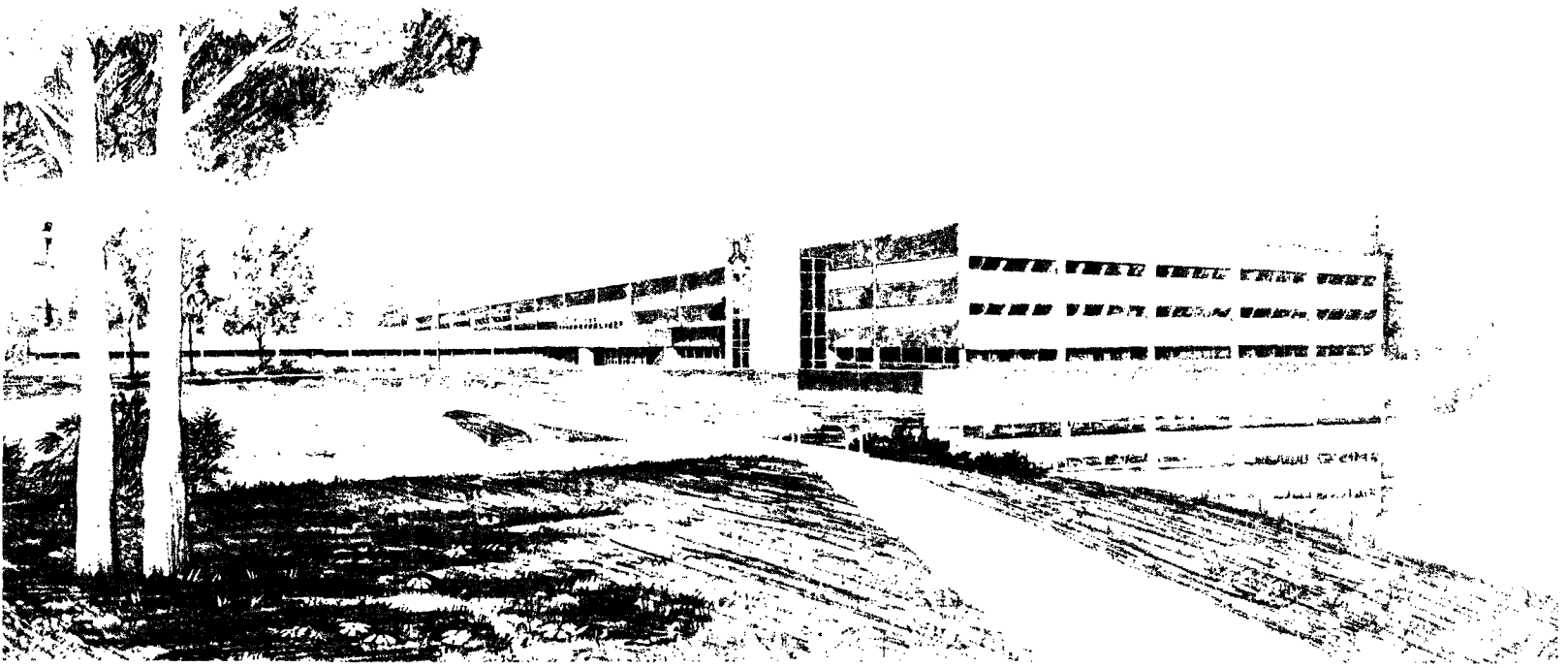

U.S. Department of Energy
Idaho Operations Office • Idaho National Engineering Laboratory

Nuclear Fuel Rod Behavior During Normal and Abnormal Operating Conditions—Results of Test PR-1

Daniel T. Sparks
Richard H. Smith
Richard W. Garner

June 1981

Prepared for the
U.S. Nuclear Regulatory Commission
Under DOE Contract No. DE-AC07-76IDO1570

EG&G Idaho

Available from

GPO Sales Program
Division of Technical Information and Document Control
U.S. Nuclear Regulatory Commission
Washington, D.C. 20555

and

National Technical Information Service
Springfield, Virginia 22161

NUREG/CR-2126
EGG-2102
Distribution Category: R3

NUCLEAR FUEL ROD BEHAVIOR DURING NORMAL AND ABNORMAL OPERATING CONDITIONS—RESULTS OF TEST PR-1

Daniel T. Sparks
Richard H. Smith
Richard W. Garner

Published June 1981

EG&G Idaho, Inc.
Idaho Falls, Idaho 83415

Prepared for the
U.S. Nuclear Regulatory Commission
Washington, D.C. 20555
Under DOE Contract No. DE-AC07-76IDO1570
FIN No. A6041

ABSTRACT

An in-pile experiment to characterize the behavior of boiling-water-reactor-type fuel rods under normal and abnormal operating conditions was performed in the Power Burst Facility. The test, designated PR-1, was performed in February 1979 as part of the Thermal Fuels Behavior Program at EG&G Idaho, Inc.

Results from the experiment were obtained in three primary areas of interest: (a) fuel rod thermal response (gap conductance, fuel stored energy, and fuel effective conductivity) under steady state conditions, (b) thermal-hydraulic conditions at the onset of boiling transition and rod quench during severe power-cooling imbalance operation at pressurized water reactor conditions, and (c) fuel thermal performance during progressively severe power excursions at boiling water reactor hot startup conditions.

SUMMARY

A combination power-cooling-mismatch (PCM) and reactivity initiated accident (RIA) test was performed as part of the Thermal Fuels Behavior Program conducted by EG&G Idaho, Inc., for the U.S. Nuclear Regulatory Commission. The test, designated PR-1, was designed to characterize light-water-reactor-type fuel rods operated under both normal and abnormal environmental conditions. The specific objectives of the experiment were to provide fuel rod thermal response information under steady state and power oscillation conditions, to investigate the conditions at the onset of boiling transition and return to nucleate boiling, and to provide fuel thermal performance data during RIA power excursions.

Test PR-1 was conducted with four unirradiated, boiling water reactor (BWR) type fuel rods, each 0.914 m in length. The rods were contained within individual coolant flow shrouds (hydraulically coupled through common upper and lower plenums) and backfilled to a cold internal pressure of 2.58 MPa with either helium (three rods) or argon (one rod) gas. Fuel densities in the helium filled rods were 92, 95, or 97% of theoretical density to provide a direct evaluation of fuel density on fuel rod thermal response. The nominal pellet-cladding diametral gap (cold) of each test rod was 0.22 mm.

Test PR-1 included three primary test phases; a steady state and power oscillation phase to evaluate fuel rod thermal response, a PCM transient testing phase to evaluate conditions at the onset of boiling transition and return to nucleate boiling, and an RIA power excursion phase to investigate fuel thermal performance and provide information for computer model development during RIA power excursions.

The thermal response data obtained during Test PR-1 complement similar data from the previous Gap Conductance (GC) Test Series experiments. Since the Test PR-1 hardware was originally designed for a GC series experiment, instrumentation on the fuel rods was optimally positioned for thermal response measurements. The effect of fuel density variations in the helium filled test rods was expected to be small on the basis of previous test results. Minor variations were detected in fuel centerline and off-center temperatures between the helium filled rods, but were likely associated with uncertainties in the measurements rather than effects due to fuel density variations. The effect of fill gas composition, however, was pronounced. As expected, fuel temperatures in the argon filled rod were notably higher than the helium filled rods due to the lower thermal conductivity of argon.

Computer code predictions and measurements of fuel temperatures during steady state operation were in fairly good agreement for both the argon and helium filled test rods. The cracked pellet effective fuel conductivity correlation developed from the Gap Conductance Test Series data was in good agreement with measured Test PR-1 data. The correlation provides a method for estimating fuel rod stored energy by adjusting the solid-pellet conductivity model to account for pellet cracking and gas gap redistribution.

A total of 25 power-cooling-mismatch transients were conducted at system pressures between 7 and 15.5 MPa, with test rod peak powers between 36.4 and 56.4 kW/m. Seven flow reduction transients (each at constant test rod power) were conducted at low system pressures, between 7 and 8 MPa, at a coolant inlet temperature of about 544 K. No discernible indications of boiling transition were observed. Either natural circulation was sufficient to preclude boiling transition, or the low temperature excursion associated with a high quality dryout transition was not detectable with the Test PR-1 instrumentation.

Eighteen PCM-type transients were conducted at system pressures between 12.7 and 15.7 MPa. The coolant inlet temperature at each pressure was adjusted to provide an inlet subcooling between 8.4 and 43.3 K. Thirteen of the transients resulted in detectable boiling transition on the rods. Rewet was induced by three methods; (a) increasing flow and decreasing power simultaneously, (b) increasing flow rate at constant power, or (c) decreasing power at constant flow rate. No discernible difference in the conditions at the onset of boiling transition and the conditions at the onset of return to nucleate boiling (quench) was detected. One rod (Rod 524-1) failed, and another (Rod 524-3) very likely failed during the boiling transition cycles. The rods probably failed due to cladding embrittlement following extended high temperature operation.

During the final test phase, progressively severe RIA power excursions were performed at radial average fuel enthalpies (at the peak power elevation) of 107, 144, and 212 cal/g UO_2. Reactor periods to attain these energies were about 42.7, 8.7 and 6.2 ms, respectively. During the two higher energy bursts, measured fuel and cladding temperatures did not increase as rapidly as predicted by pretest calculations. Such behavior is probably associated with the thermocouple response time rather than an inherent delay in temperature increase. Best-estimate corrections were applied to the fuel centerline and cladding temperature measurements to account for the measurement delay time. Film boiling was noted following each power burst. The pressure transducer data from Rod 524-2 indicated rod failure during the final (highest energy) power burst. The cladding displacement measurements on Rods 524-1 and 524-3 indicated separation of these rods during the second (144 cal/g) power burst. The argon filled test rod, Rod 524-4, did not fail during the experiment.

Predictions of fuel thermal response during the RIA testing were generally adequate for fuel temperature magnitude, but cladding temperatures, cladding elongation, and time in high temperature film boiling were overpredicted. The thermal-hydraulic model used for these predictions does not adequately calculate the time of quench for a power excursion, which results in longer times at high temperature and overestimation of fuel rod damage.

ACKNOWLEDGMENTS

The authors thank P. B. Hembree for her postirradiation examination efforts and input to portions of this report, and R. D. McCormick, R. E. Lapointe, and D. H. Schwieder for their data qualification and analytical assistance.

The authors also thank Dr. F. S. Gunnerson, University of Central Florida, for his technical assistance, and Dr. R. VanHouten, United States Nuclear Regulatory Commission, for his recommendations for expanding the experiment objectives and conduct.

CONTENTS

NOTE: All appendices to this report are presented on microfiche attached to the inside of the back cover.

FIGURES

TABLES

NUCLEAR FUEL ROD BEHAVIOR DURING NORMAL AND ABNORMAL OPERATING CONDITIONS—RESULTS OF TEST PR-1

INTRODUCTION

To predict the behavior of light water reactor fuel rods during postulated accident events requires a knowledge of the fuel rod boundary conditions prior to the accident, and an ability to model the phenomena that dominate fuel rod response during the accident scenario. Test PR-1 was an experiment conducted by the Thermal Fuels Behavior Program at EG&G Idaho, Inc., to evaluate both the steady state thermal performance and the transient response of nuclear fuel rods. Data from the experiment provide a basis for evaluation and development of fuel rod computer models under steady state and extreme operating conditions.

The fuel rods used in Test PR-1 were originally designed and instrumented to provide fuel rod thermal response data under steady state and power oscillation conditions for the Gap Conductance Test Series.[1] The primary objectives of the Gap Conductance Test Series were to evaluate fuel rod thermal performance (gap conductance, stored energy, effective fuel conductivity, etc.) under steady state operating conditions, and to evaluate the thermal oscillator technique[1] for determining gap conductance in irradiated fuel rods. The objectives of Test PR-1 were subsequently expanded to include boiling transition and return to nucleate boiling information under power-cooling-mismatch (PCM) conditions, and fuel thermal performance during reactivity initiated accident (RIA) power excursions.

Test PR-1 was performed with four 0.914-m long, boiling water reactor (BWR) type fuel rods (each within a separate coolant flow shroud) symmetrically positioned within the Power Burst Facility in-pile tube (IPT). The test rods were backfilled with either helium (three rods) or argon (one rod) to a cold pressure of 2.58 MPa. The fuel density of the helium filled rods was 92, 95, or 97% of theoretical. With these design variations, the effects of fuel density and fill gas composition on fuel rod thermal response were examined.

The conduct of Test PR-1 consisted of three phases. The first phase included 13.5 h of steady state operation and 12.5 h of power oscillations to obtain fuel rod thermal response data. The second phase consisted of 23 flow reduction and 2 power increase PCM transients. The transients provided boiling transition and return to nucleate boiling information at high pressure conditions (12.7 to 15.7 MPa system pressures). The third phase consisted of three RIA power excursions initiated from BWR hot startup conditions to evaluate fuel thermal performance during RIA power excursions. The power excursions were progressively more severe, with radial average fuel enthalpies of 107, 144 and 212 cal/g UO_2 at the axial peak elevation.

The fuel rod thermal response during Test PR-1 is described, and interpretation of the PCM and boiling transition results are discussed. Results from the RIA power excursions are presented, as is an overview of the posttest condition of the Test PR-1 fuel rods. Finally, results and observations from Test PR-1 are summarized. Detailed descriptions of the test design and conduct; fuel rod characterization and postirradiation examination data; experiment data plots and uncertainties; test rod power determination and uncertainties; measurement correction methods for fuel and cladding thermocouples during RIA power bursts; FRAPCON, FRAP-T5, and RELAP5 models and input; and Test PR-1 documentation and records traceability are contained in the appendices to this report, which are provided on microfiche attached to the inside of the back cover.

FUEL ROD THERMAL RESPONSE DURING TEST PR-1

Thermal response data were obtained from Test PR-1 to complement similar data from previous Gap Conductance (GC) Test Series[1] experiments. The experimental data from the GC series were used as a basis for evaluating the effects of variations in light water reactor (LWR) fuel rod design parameters on (a) fuel rod thermal response (that is, temperature response), (b) effective fuel thermal conductivity, and (c) pellet-to-cladding gap conductance as a function of rod power density. The data were also used to evaluate existing fuel rod response computer codes. The fuel rod design parameters varied were fuel-to-cladding gap width (0.1, 0.22, and 0.35 mm diametral), fill gas composition (helium, xenon, or argon), and fuel density (92, 95, or 97% of theoretical). In all test rods, the fuel centerline temperatures increased much more than did the off-center (pellet surface) temperatures when the initial gap width was increased. This indicates that when the pellets crack, part of the thermal resistance normally associated with the pellet-to-cladding gap is redistributed within the fuel pellet, especially in moderate and large gap rods. This result further illustrates that pellet cracks and the movement of pellet fragments degrade the fuel thermal conductivity while improving the gap conductance. The lower the fill gas conductivity, the higher the fuel temperatures at a given power level. The effect of fuel density on the observed thermal response was small for fuel centerline temperatures, and indistinguishable from normal scatter in the data for fuel off-center temperatures.

Under actual operating conditions, pellet cracking, relocation, and fill gas inclusion significantly alter the thermal conductivity of UO_2 fuel pellets. An analytical procedure was developed for evaluating the "effective fuel thermal conductivity" that takes these effects into account. To be of use in predicting fuel rod effective thermal conductivities, an empirical correlation (K_{eff}) was developed, on the basis of effective thermal conductivities, from Tests GC 2-1, GC 2-2, and GC 2-3. The correlation was obtained for all helium filled test rods in terms of (a) a nominal "hot gap width," (b) the initial cold gap width, and (c) the fuel density. Although fuel density has small effect as an individual parameter, it does serve as a multiplier to fine-tune the relationship for the various helium test rods.

Pellet-to-cladding gap conductance was evaluated as a function of test rod power density by the steady state ($\int kdT$) and power oscillation experimental methods. The steady state values were very consistent between similar rods in the three GC tests. The effect of initial gap width was significant for the helium filled rods between the wide gap and narrow gap rods. Only medium and narrow gap xenon and argon rods were tested, and the effect of gap width was small between the different gap rods for both xenon and argon. The low thermal conductivities of the xenon and argon fill gases significantly decreased the gap conductance of these rods with respect to the relatively high conductivity of helium filled rods. A correlation was developed that provides a simple method for estimating the gap conductance of a particular LWR design fuel rod under a specific set of rod conditions. The correlation accounts for effects of pellet cracking and/or fragmentation and relocation. Since the Test PR-1 hardware was originally designed for a Gap Conductance Test Series experiment (Test GC 2-4), instrumentation were optimally positioned for these measurements. Figure 1 illustrates the positioning of the four rods in the PBF in-pile tube and the rod thermometry locations.

Data were obtained during the power calibration, preconditioning, and power oscillation test segments, from which the fuel rod thermal behavior could be deduced. This section presents the Test PR-1 steady state and power oscillation response data. A comparison with applicable data from previous experiments is also presented. Gap conductance data obtained during the repeated boiling transition transients were complicated by fuel rod dimensional changes, fuel restructuring, and cladding oxidation and, therefore, are not presented.

Fuel Rod Thermal Response During Steady State Operation

The thermal response data from Test PR-1 of primary interest include fuel centerline temperatures, fuel off-center temperatures, and cladding surface temperatures relative to fuel rod local power. The design parameters of interest for Test PR-1 include fuel density (Rods 524-1, 524-2,

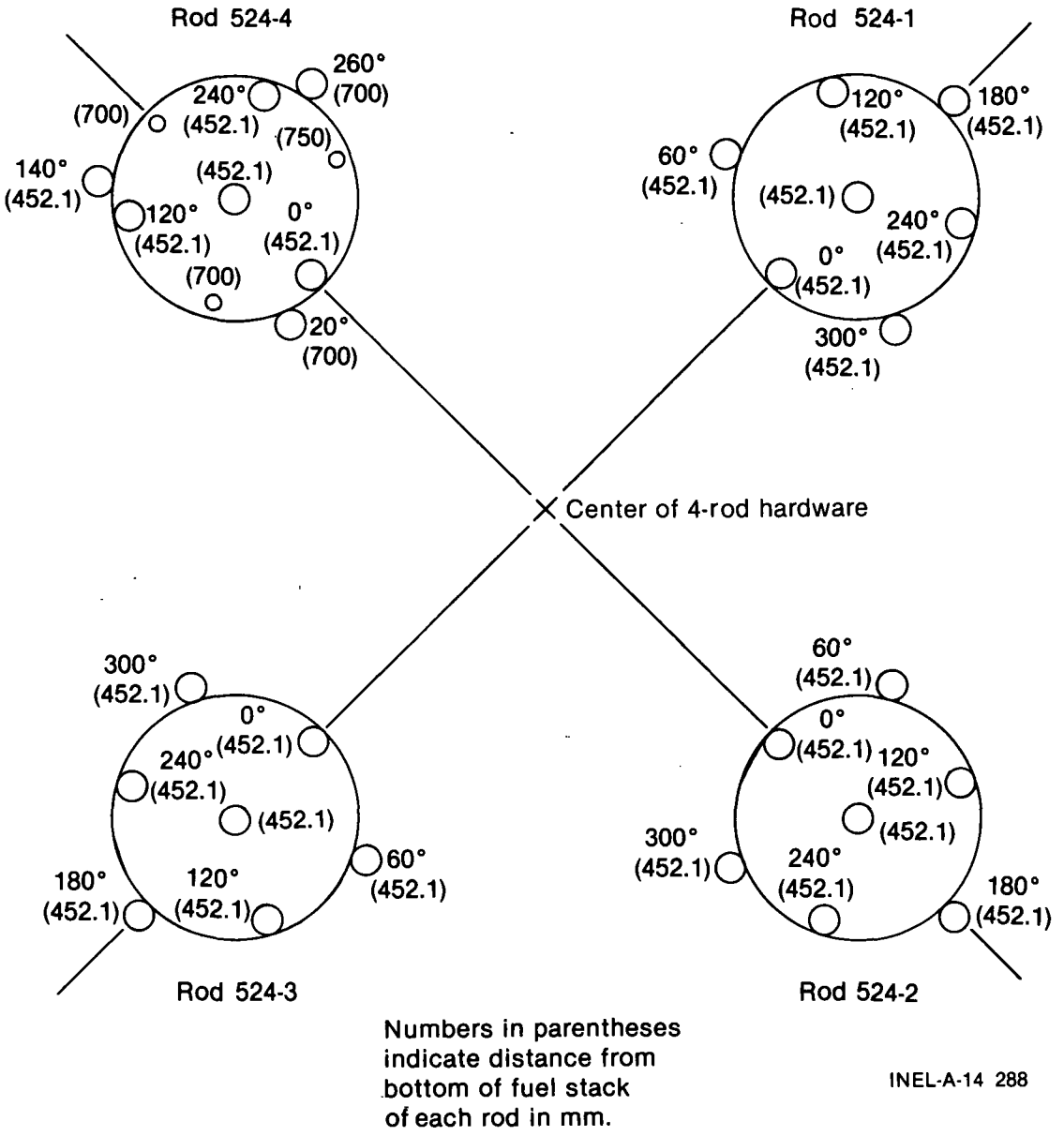

Figure 1. Four-rod orientation and relative fuel rod thermocouple locations for Test PR-1.

and 524-3 were identical, except that the fuel densities were 95, 92, and 97% of theoretical density, respectively) and fill gas composition (Rods 524-3 and 524-4 were identical, except that the fill gas compositions were helium and argon, respectively). Nominal design parameters for the Test PR-1 fuel rods are listed in Table 1.

Test rod local powers were determined from a calorimetric heat balance of each test rod, and an axial power distribution from flux wire activation. The heat balance was accomplished using measured coolant conditions (pressure and inlet temperature), shroud volumetric flow rate, and coolant temperature rise from inlet to outlet through each shroud. Subcooled inlet and outlet conditions were maintained at all power levels to ensure accurate coolant enthalpy determination. The first segment of the power calibration was conducted at a high coolant flow rate to ensure subcooled forced convection heat transfer over the entire test rod. During the second segment of the power calibration, the coolant flow rate was adjusted to preclude saturation at the shroud outlet, but to allow high cladding surface heat transfer at the primary measurement (peak power) axial location.

Table 1. Nominal design parameters of BWR-type fuel rods for Test PR-1

Rod Parameter	Value
Cladding outside diameter (mm)	12.50
Cladding inside diameter (mm)	10.79
Wall thickness (mm)	0.86
Cladding material	Zircaloy-2
Fuel material	UO_2
Fuel density (% theoretical density)	95 (Rod 524-1), 92 (Rod 524-2), 97 (Rod 524-3), 97 (Rod 524-4)
Pellet diameter (mm)	10.57
Initial diametral gap (mm)	0.22[a]
Fill gas composition	Helium (Rods 524-1,-2, and -3), Argon (Rod 524-4)
Cold internal pressure (MPa)	2.58
Pellet enrichment (wt% ^{235}U)	10.0
Pellet shape	Flat ends L/D = 1.0
Pellet length (mm)	10.57
Rod overall length (mm)	990.6
Fuel stack length (mm)	914.4
Plenum length (mm)	55.12
Ratio of plenum volume to fuel volume	0.08
Plenum spring	Coiled carbon steel
Shroud inside diameter (mm)	19.3

a. Corresponds to 2.2% of initial fuel pellet diameter.

The average linear heat generation of each test rod, determined from the energy balance, was adjusted to a local peak power generation by applying a peaking factor of 1.35 (determined from axial flux wires). Differences in measured linear power between the four rods were attributed to measurement uncertainties rather than inherent differences in test rod power generation, and, hence, were averaged to obtain the values used in this analysis. A summary of the conditions attained during the Test PR-1 steady state thermal response testing is presented in Table 2, and graphically shown in Figure 2.

Fuel centerline temperature as a function of test rod peak power is shown in Figure 3 for the three helium filled rods, with variations in fuel density. As was observed in the Gap Conductance Test Series, the effect of fuel density variations between 92 and 97% of theoretical is minimal. The minor variations noted are well within expected uncertainties[a] in the measured centerline temperatures. Similar results were obtained by comparing the measured off-center temperatures for Rods 524-1, 524-2, and 524-3. Azimuthal variations in measured off-center fuel temperatures outweighed any observable difference in temperatures due to fuel density variation.

The effect of fill gas composition on measured temperatures during steady state operation is illustrated in Figure 4. Shown is the measured fuel centerline temperature (as a function of test rod power) for a helium filled rod (524-3) and the argon filled rod (524-4), with all other design features being common to both rods. The low thermal conductivity of the argon gas in Rod 524-4, as compared with the conductivity of helium in Rod 524-3, results in a higher fuel centerline temperature at each power level considered. Fuel centerline temperatures in the argon

a. Uncertainties in fuel temperature measurements range from 3% of reading below 700 K and 4% of reading at 1200 K, to as high as 22% of reading at 2000 K.

Table 2. Summary of steady state thermal response conditions

Reactor Core Power (MW)	Averaged Test Rod Peak Power[a] (kW/m)	Rod 524-1		Rod 524-2		Rod 524-3		Rod 524-4	
		Shroud Coolant Flow Rate (L/s)	Coolant Temperature Rise (K)	Shroud Coolant Flow Rate (L/s)	Coolant Temperature Rise (K)	Shroud Coolant Flow Rate (L/s)	Coolant Temperature Rise (K)	Shroud Coolant Flow Rate (L/s)	Coolant Temperature Rise (K)
Power Calibration[b] (Segment 1)									
4.72	21.29	0.748	5.11	0.758	3.64	0.781	4.52	0.756	4.71
2.32	11.34	0.737	2.75	0.755	1.68	0.774	2.43	0.749	2.31
4.72	21.59	0.735	5.37	0.746	3.64	0.764	4.74	0.747	4.67
7.09	31.98	0.733	7.86	0.749	5.56	0.769	7.01	0.744	7.07
9.52	42.44	0.726	10.70	0.742	7.31	0.760	9.28	0.738	9.21
10.91	48.06	0.731	12.05	0.741	8.31	0.761	10.50	0.743	10.30
9.52	42.62	0.728	10.91	0.743	7.39	0.762	9.37	0.740	9.34
7.20	31.98	0.746	7.86	0.758	5.56	0.780	6.88	0.757	7.03
4.72	21.70	0.744	5.28	0.754	3.64	0.775	4.70	0.757	4.63
3.10	14.66	0.740	3.45	0.749	2.24	0.768	3.13	0.749	3.01
Power Calibration[c] (Segment 2)									
3.11	14.37	0.266	9.56	0.264	6.78	0.270	8.54	0.271	8.25
4.72	21.65	0.310	12.44	0.310	8.92	0.316	11.03	0.315	10.96
6.22	28.40	0.340	15.02	0.340	10.45	0.348	13.17	0.347	13.10
7.91	36.44	0.414	15.85	0.420	11.15	0.431	13.65	0.422	13.93
10.01	45.12	0.532	15.37	0.536	10.71	0.549	12.86	0.541	13.18
6.22	28.45	0.355	14.19	0.361	9.66	0.368	12.12	0.361	12.22
Preconditioning[c]									
3.08	13.88	0.167	14.93	0.164	10.45	0.167	12.38	0.170	12.75
6.19	28.82	0.347	14.67	0.354	10.10	0.360	12.60	0.353	12.57
3.04	13.58	0.167	14.49	0.165	10.19	0.168	12.56	0.171	12.62
6.19	28.02	0.401	12.62	0.407	8.92	0.416	11.07	0.409	10.91
3.00	13.65	0.168	14.49	0.166	10.15	0.169	12.12	0.172	12.48
6.30	27.70	0.384	13.18	0.386	9.05	0.394	11.16	0.391	11.22
3.00	13.47	0.170	14.23	0.166	10.01	0.168	12.12	0.173	12.27

a. Average of (four rods) test rod linear powers at axial peak elevation.

b. Nominal coolant inlet temperature of 538 K and system pressure of 6.5 MPa.

c. Nominal coolant inlet temperature of 540 K and system pressure of 7.2 MPa.

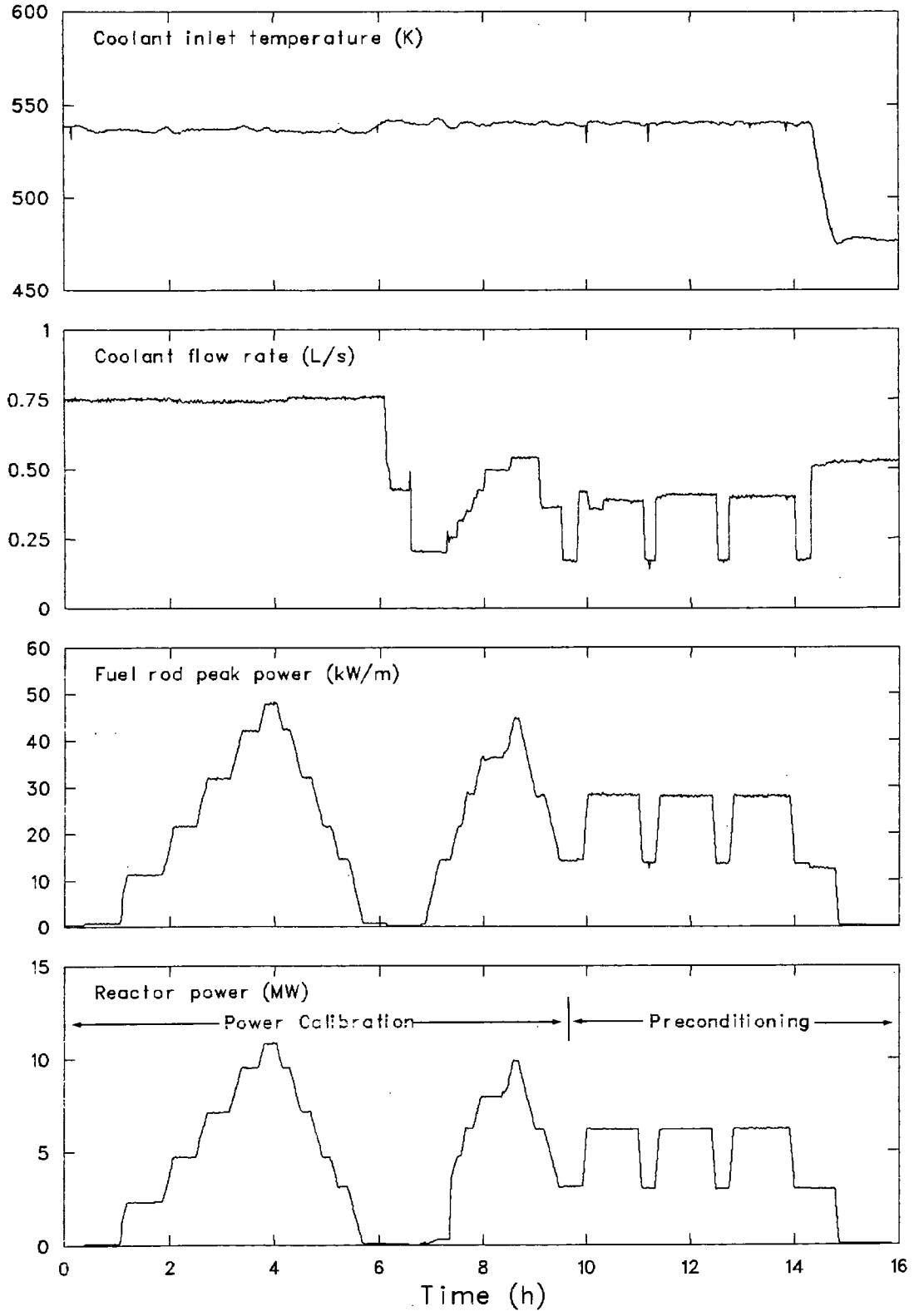

Figure 2. Test rod power, PBF core power, and coolant conditions during Test PR-1 power calibration and preconditioning periods.

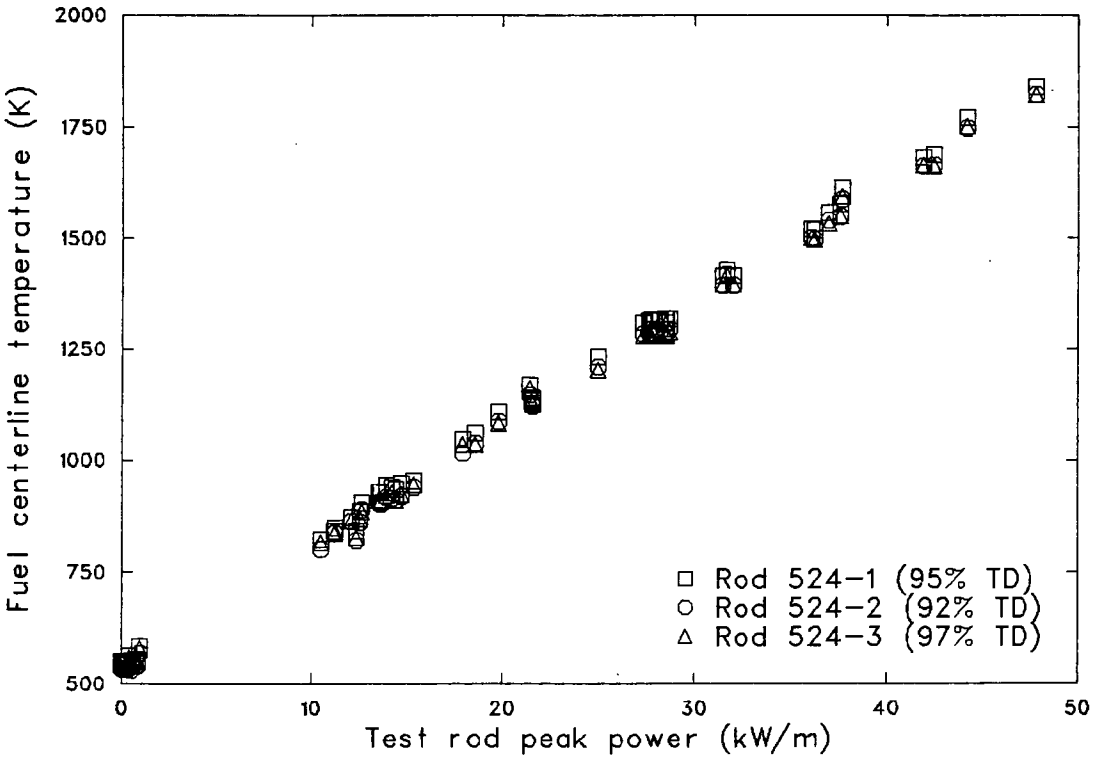

Figure 3. Measured centerline temperatures as a function of rod power for the Test PR-1 helium filled rods with variations in fuel density.

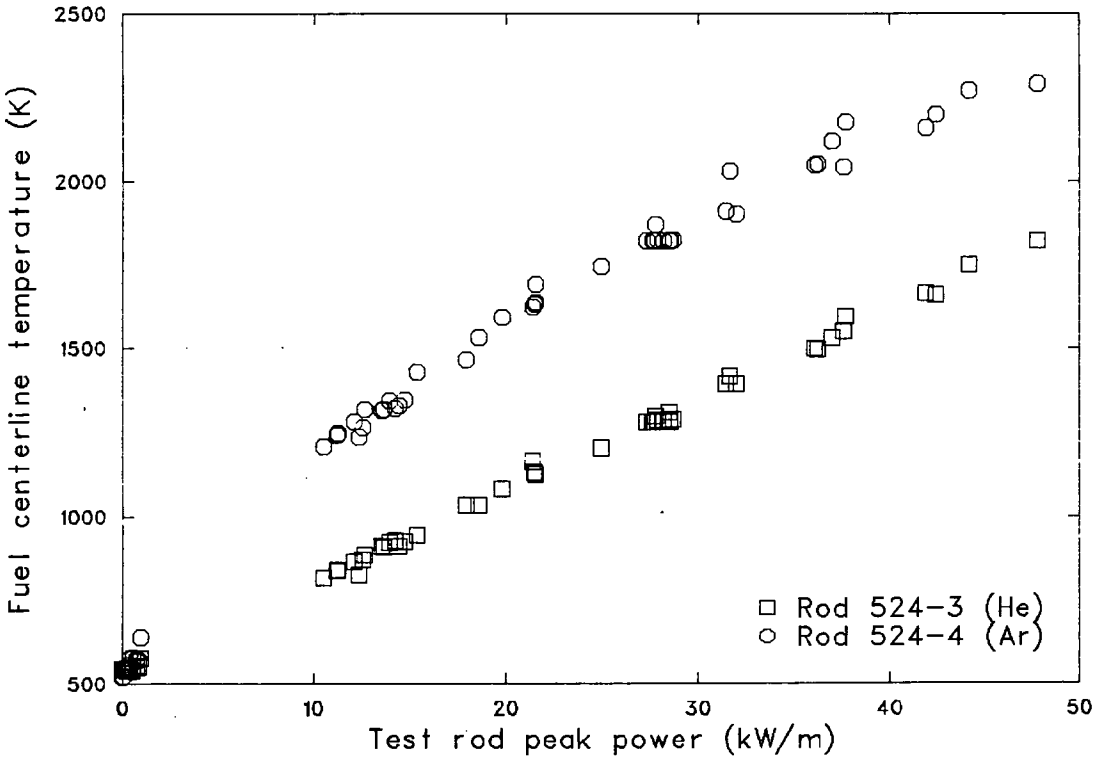

Figure 4. Measured centerline fuel temperatures showing the effects of fill gas composition between helium and argon filled test rods.

filled rod were consistently 400 to 500 K higher than the helium rod at test rod powers above 13 kW/m.

Comparisons between measured and calculated fuel centerline and off-center temperatures are shown in Figure 5. These calculations were made using the FRAPCON[a] computer code[2] for the Test PR-1 helium filled rods. The Ross and Stoute (modified) gap conductance model, in conjunction with the FRACAS-II fuel model, was used. The calculations agree fairly well with the trend and magnitude of the fuel centerline and off-center[b] temperature data in the helium filled test rods.

Similar comparisons between measured and calculated temperatures in the argon filled test rod (Rod 524-4) are shown in Figure 6. The fuel model slightly underpredicts the argon rod fuel centerline temperature. Only measured off-center fuel temperature data from the first power increase are shown for the argon filled test rod due to subsequent deterioration of these measurement devices. The off-center temperature predictions are fairly consistent with the measured temperatures.

a. FRAPCON-2, Idaho National Engineering Laboratory Code Configuration Control Number H019882B.

b. Azimuthal variations in measured fuel off-center temperatures were neglected in this comparison by averaging the off-center temperature measurements.

Fuel Rod Thermal Response During Power Oscillation Operation

The power oscillation or thermal oscillator method[1] relates fuel rod response parameters (cladding temperature, fuel temperature, etc.) to a sinusoidal driving function (rod power) through the phase relationship that is characteristic of the fuel rod design. Inherent in the method is the assumption that the fuel rod response is a linear function of the driving function; i.e., that changes in fuel conductivity, gap conductance, etc., are sufficiently small during the oscillation that

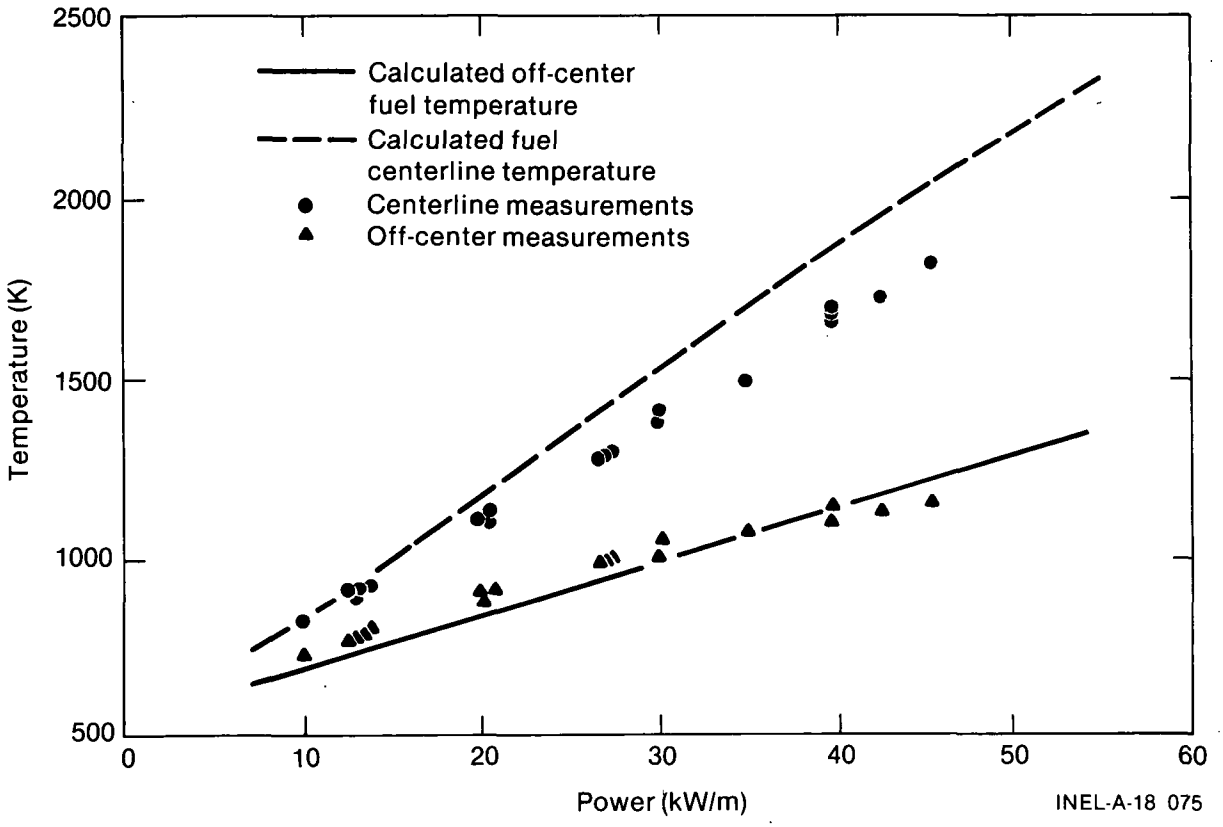

Figure 5. Comparison of measured and calculated centerline and off-center fuel temperatures for Test PR-1 helium filled rods.

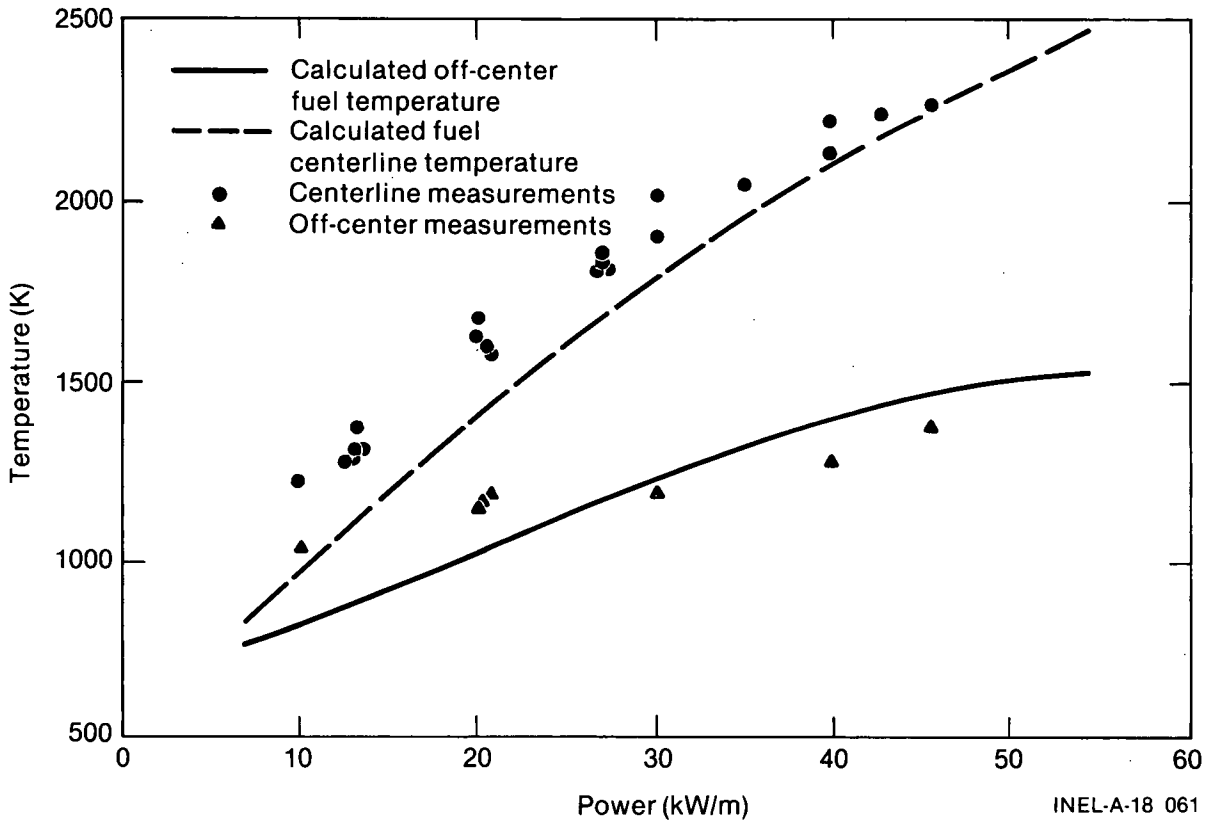

Figure 6. Comparison of measured and calculated centerline and off-center fuel temperatures for the Test PR-1 argon filled test rod.

measured temperatures are proportional to the driving function, with some measurable phase lag between the signals. The primary usefulness of the power oscillation technique (if proven reliable) would be to infer the pellet-to-cladding gap heat transfer coefficient (gap conductance) in irradiated fuel rods from only the external cladding surface temperature response to a driving function. Data were obtained during Test PR-1 to compare with data obtained during the Gap Conductance Test Series and to help evaluate the thermal oscillator method.

The measured phase lags between cladding surface temperature and rod power were used to evaluate gap conductance by the oscillation method during Test PR-1. Data were obtained at four power levels, with repeat data obtained at each level. The nominal oscillation power levels, measured phase angles between power and cladding temperature, and evaluated gap conductance values are shown in Table 3. The data shown in the table are from on-line measurements only. Gap conductance values were deduced from the measured phase angles using a series of curves generated by the HEAT-1[a] computer code. A range of gap conductance values and the specific oscillation conditions were input to the code and the resulting phase angle relationships evaluated. Highly subcooled conditions were maintained at the measurement elevation (0.452 m) during the power oscillations to minimize the perturbation effects on measured cladding temperature due to nucleate boiling. The coolant conditions were: inlet temperature of 478 K, system pressure of 7.17 MPa, and nominal coolant flow rate through each shroud of 0.52 L/s (2700 kg/s•m^2 mass flux).

Also shown in Table 3 are steady state gap conductance values obtained (by the $\int$kdT method) prior to each power oscillation condition. These steady state gap conductance values were calculated using both the MATPRO[3] fuel thermal conductivity correlation and the effective fuel thermal conductivity correlation (K_{eff}) determined from previous GC Test Series data. Comparison of gap conductance values obtained by the

a. HEAT-1, Idaho National Engineering Laboratory Code Configuration Control Number H012582B.

Table 3. On-line power oscillation test results and comparison with steady state gap conductances values

Test Rod[a] Peak Power (kW/m)	Test Rod (orientation)	Measured Phase Angle (degrees)	95% Uncertainty In Measured Phase Angle (± degrees)	Gap Conductance From Measured Phase Angle ($kW/m^2 \cdot K$)	Gap Conductance[b] From ∫kdT Method MATPRO Conductivity ($kW/m^2 \cdot K$)	Gap Conductance[b] From ∫kdT Method K_{eff} Conductivity ($kW/m^2 \cdot K$)	Gap Conductance[b] From ∫kdT Method K_{eff} Lower Conductivity Uncertainty Limit ($kW/m^2 \cdot K$)
11.84	524-1 (300°)	48.68	1.09	5.45	2.20	3.34	5.03
11.84	524-3 (300°)	52.59	0.71	4.17	2.34	3.70	5.79
25.02	524-1 (60°)	45.36	0.31	8.97	2.91	4.38	7.13
25.02	524-4 (140°)	48.98	0.60	5.61	1.26	—[c]	—[c]
37.44	524-1 (60°)	44.04	0.34	10.82	3.97	5.33	8.75
37.44	524-3 (300°)	44.64	0.45	9.68	4.07	5.88	10.05
50.52	524-1 (60°)	40.57	0.46	21.49	5.58	20.75	>100
50.52	524-4 (140°)	35.63	0.33	57.53	3.06	—[c]	—[c]
11.85	524-1 (60°)	47.10	0.46	6.40	2.45	3.34	5.03
11.85	524-4 (140°)	66.56	0.83	1.20	0.76	—[c]	—[c]
24.94	524-1 (60°)	46.65	0.38	7.50	3.15	4.36	7.12
24.94	524-3 (300°)	47.36	0.31	6.83	4.79	4.78	8.09
37.11	524-1 (60°)	43.05	0.33	13.39	4.28	5.29	8.65
37.11	524-4 (140°)	37.74	0.46	68.21	1.70	—[c]	—[c]
51.77	524-1 (60°)	41.09	0.34	17.73	6.50	40.62	>100.
51.77	524-3 (300°)	37.85	0.60	63.45	9.86	79.62	>100.

a. All power oscillations were conducted at ±20% of nominal power level and a period of 20 s/cycle. Coolant conditions were; inlet temperature of 478 K and system pressure of 7.17 MPa.

b. Steady state (∫kdT) gap conductance calculated using appropriate centerline and cladding temperature measurements.

c. K_{eff} conductivity correlation is not applicable to argon filled test rod.

power oscillation method with those obtained by the generally accepted ∫kdT method using the MATPRO fuel conductivity correlation show large discrepancies between the two methods. Gap conductance values calculated using the K_{eff} conductivity correlation are in better agreement with the oscillation method, but are still significantly smaller in most cases. This comparison is presented graphically in Figure 7.

Large differences between gap conductance values obtained by the power oscillation method and the ∫kdT method were also observed during the Gap Conductance Test Series experiments. The exact reasons for the discrepancies have not been determined. Waveform analysis of previous power oscillation data suggest that nonlinearities in the response measurement (cladding temperature) are more pronounced in BWR-design fuel rods than PWR-design rods.[1] The speculated cause of the difference between fuel rod types is enhanced pellet and cladding contact during power oscillations due to the flat-end pellet design in BWR pellets as opposed to the dished-end pellet design in PWR fuel pellets. On the basis of the large amount of thermal oscillator data from the

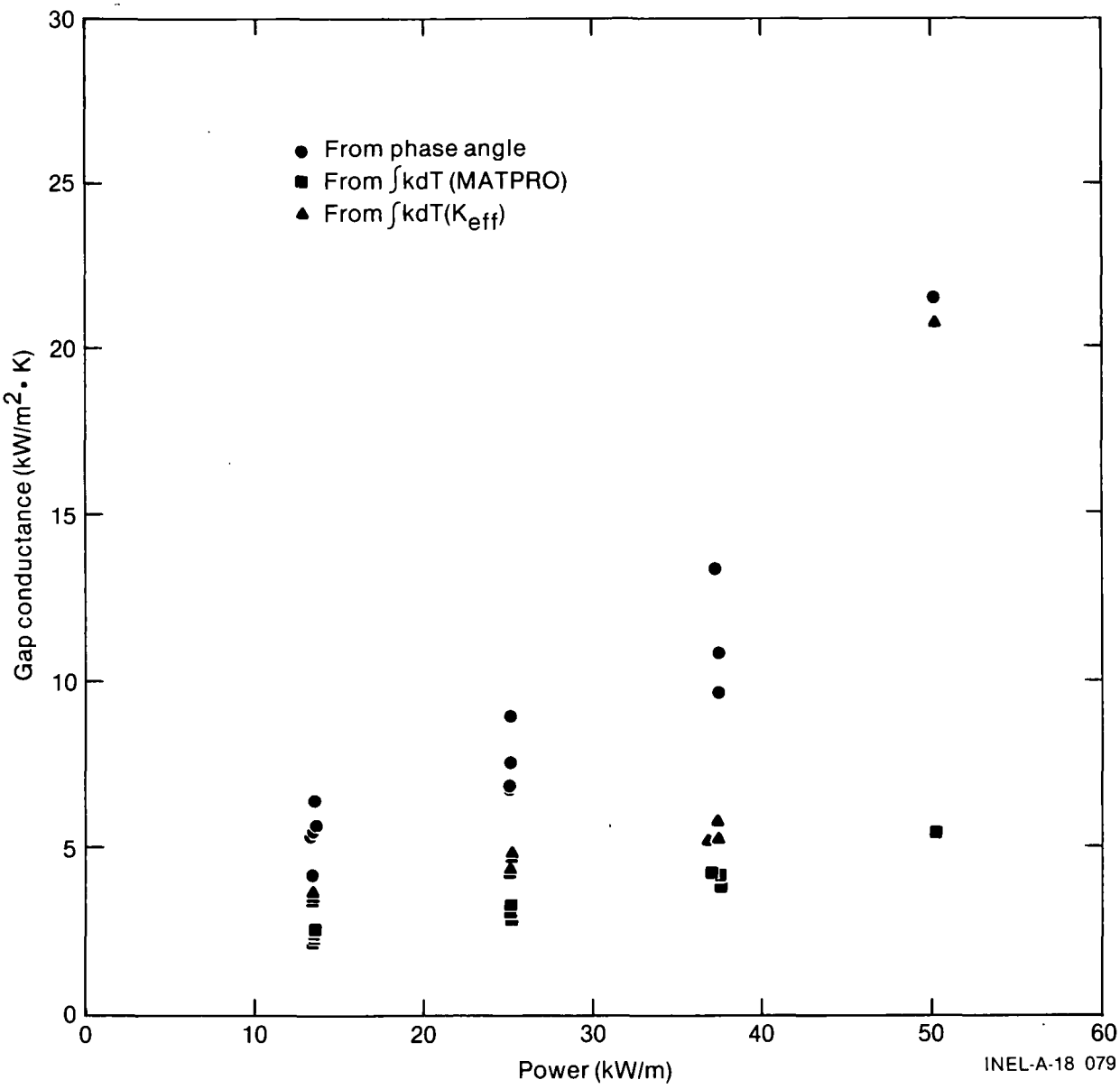

Figure 7. Gap conductance values calculated using power oscillation and ∫kdT methods (Test PR-1 helium rods).

Gap Conductance Test Series and Test PR-1, nonlinearities in fuel parameters (fuel conductivity, pellet-to-cladding gap width, etc.) contribute large uncertainties in gap conductance by the oscillation technique except under specific conditions. The technique is therefore unreliable for determining gap conductance over the range of LWR conditions of interest.

Comparison of Test PR-1 and Gap Conductance Test Series Thermal Response Data

The Test PR-1 steady state thermal response data can be directly compared with data obtained from the Gap Conductance Test Series since the Test PR-1 fuel rods were of similar design and had design parameter variations supporting the GC Test Series matrix. All fuel rods in Test PR-1 had nominal diametral gaps of 0.22 mm (2.2% of initial fuel pellet diameter) to provide direct comparative data. The effect of fill gas composition on measured fuel centerline temperatures is shown in Figure 8. A similar comparison with fuel off-center temperatures is seen in Figure 9. The data from Test PR-1 are in good agreement with steady state results[a] from other testing on common gap width fuel rods.

Each of the helium filled rods in Test PR-1 contained different density fuel pellets. Rod 524-1, with a density of 95% theoretical density, was the same design as Rod GC 503 of the Gap Conductance Test Series, Test GC 2-1. The fuel centerline temperature and fuel off-center temperature measurements for both rods (524-1 and GC 503) are compared in Figures 10 and 11, respectively, and are shown to be in excellent agreement. Some differences do exist, but these are well within the uncertainties in the temperature measurements.

The effect of initial gap width on fuel centerline temperatures for helium and argon filled test rods is shown in Figures 12 and 13. The data from Test PR-1 (2.2% gap) are generally consistent with previous data.[a]

a. The solid lines in Figures 8, 9, 12, and 13 represent the trends of GC Test Series data, and are not mathematical fits or analytical estimates.

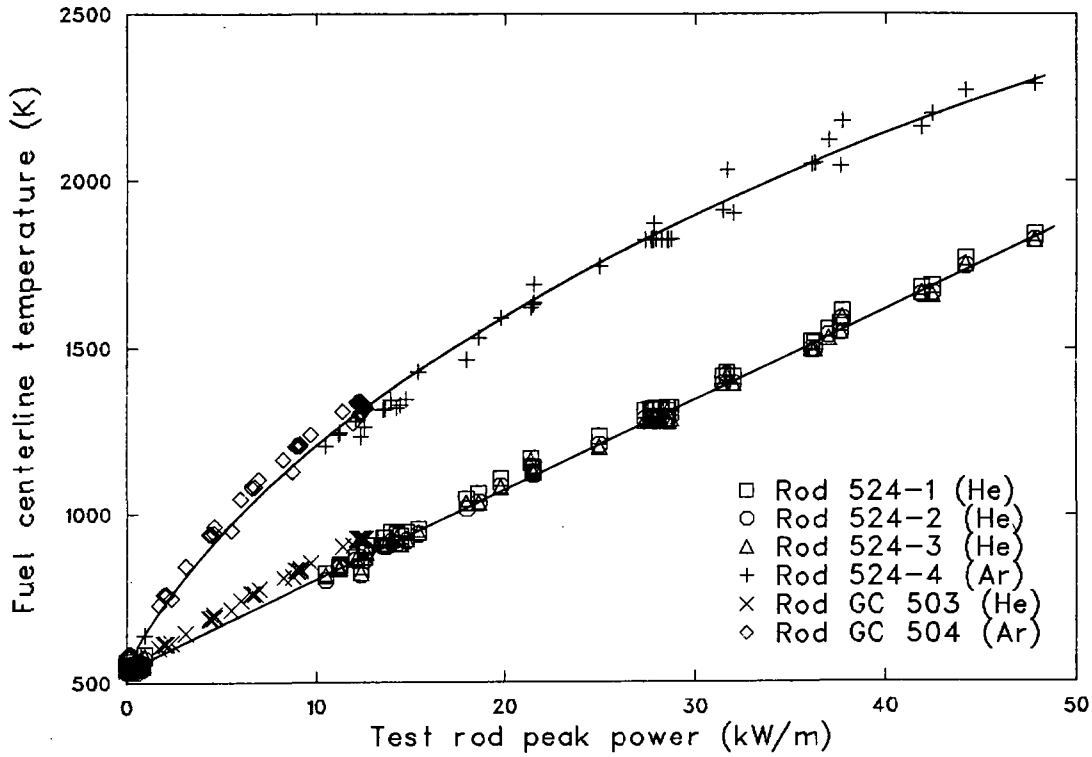

Figure 8. Comparison of Test PR-1 centerline temperature measurements with previous GC experimental data showing the effect of fill gas composition.

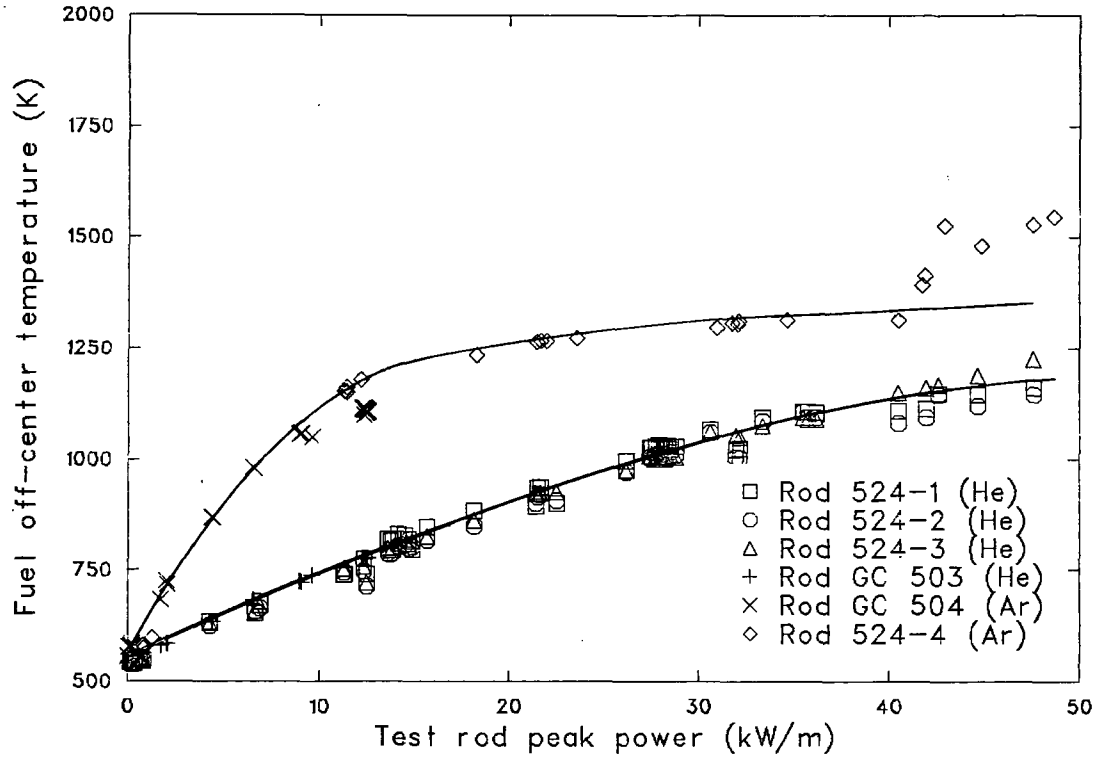

Figure 9. Comparison of Test PR-1 off-center fuel temperature measurements with previous GC experimental data showing the effect of fill gas composition.

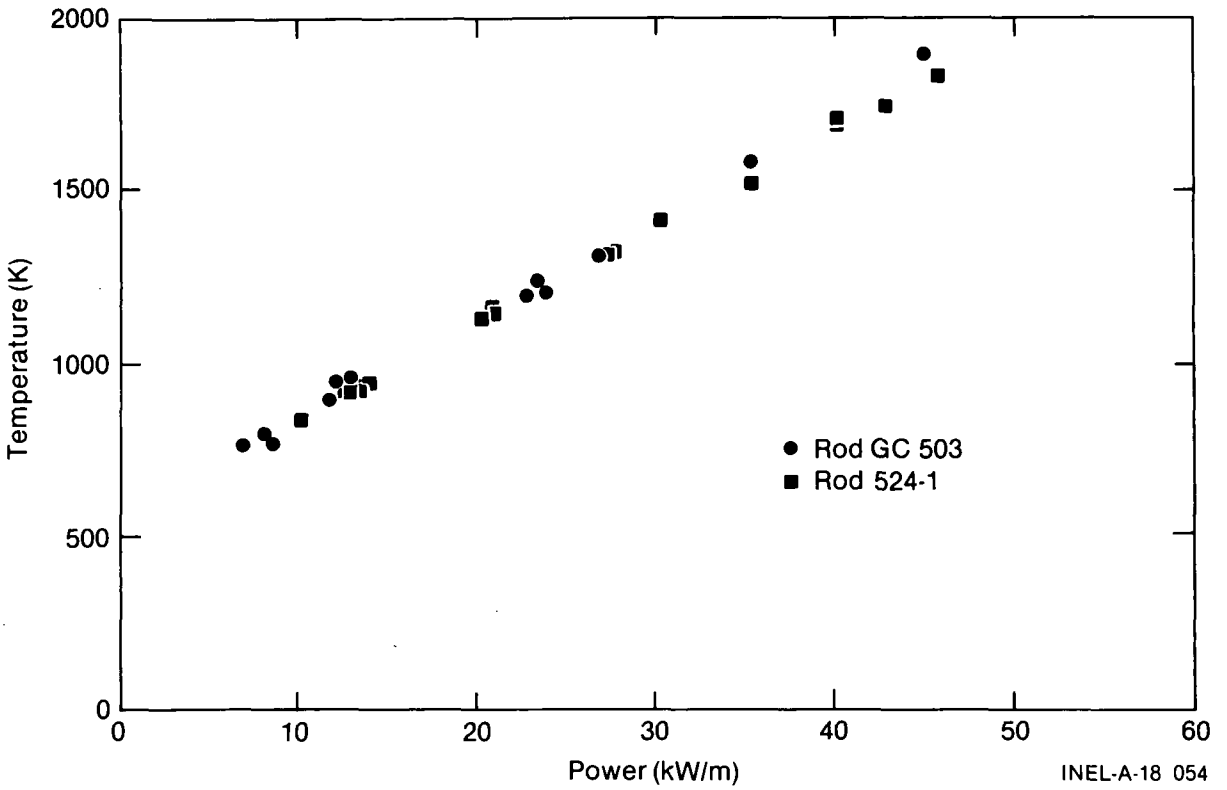

Figure 10. Comparison of fuel rod centerline temperature measurements from Tests PR-1 and GC 2-1.

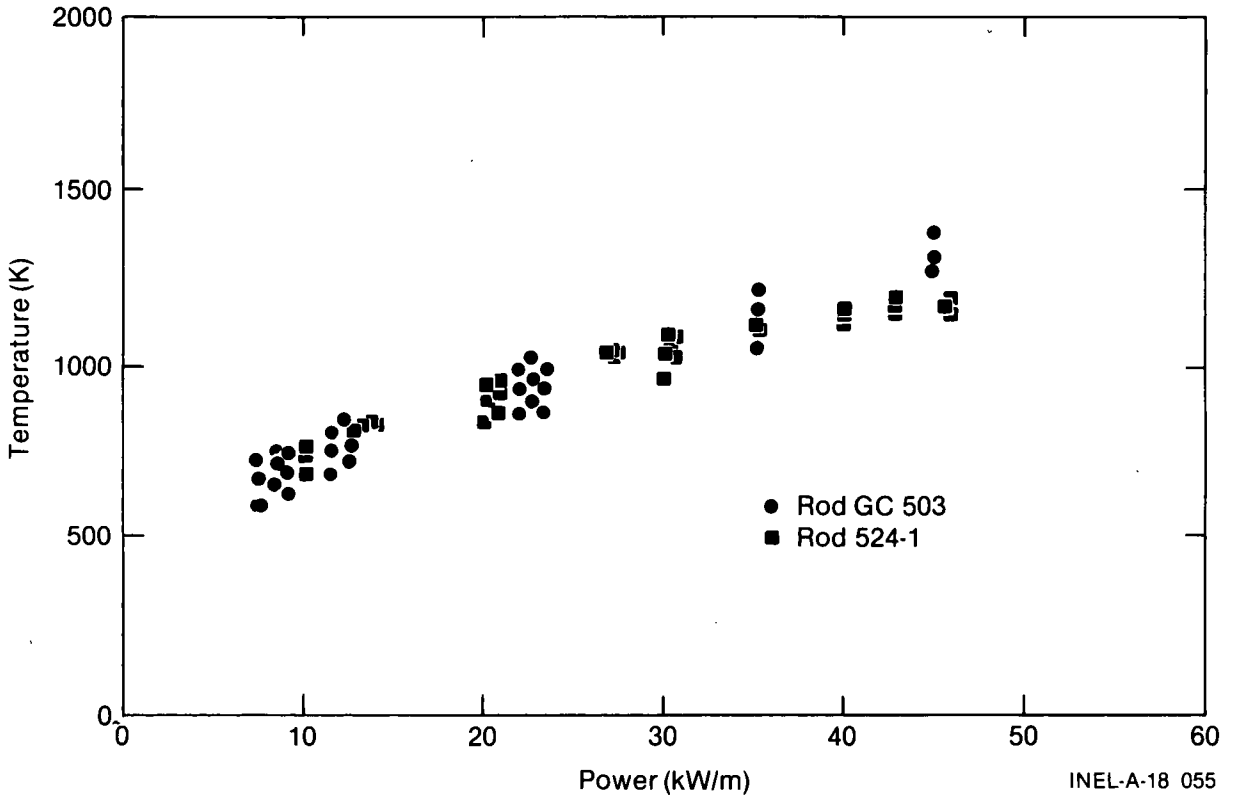

Figure 11. Comparison of fuel rod off-center temperature measurements from Tests PR-1 and GC 2-1.

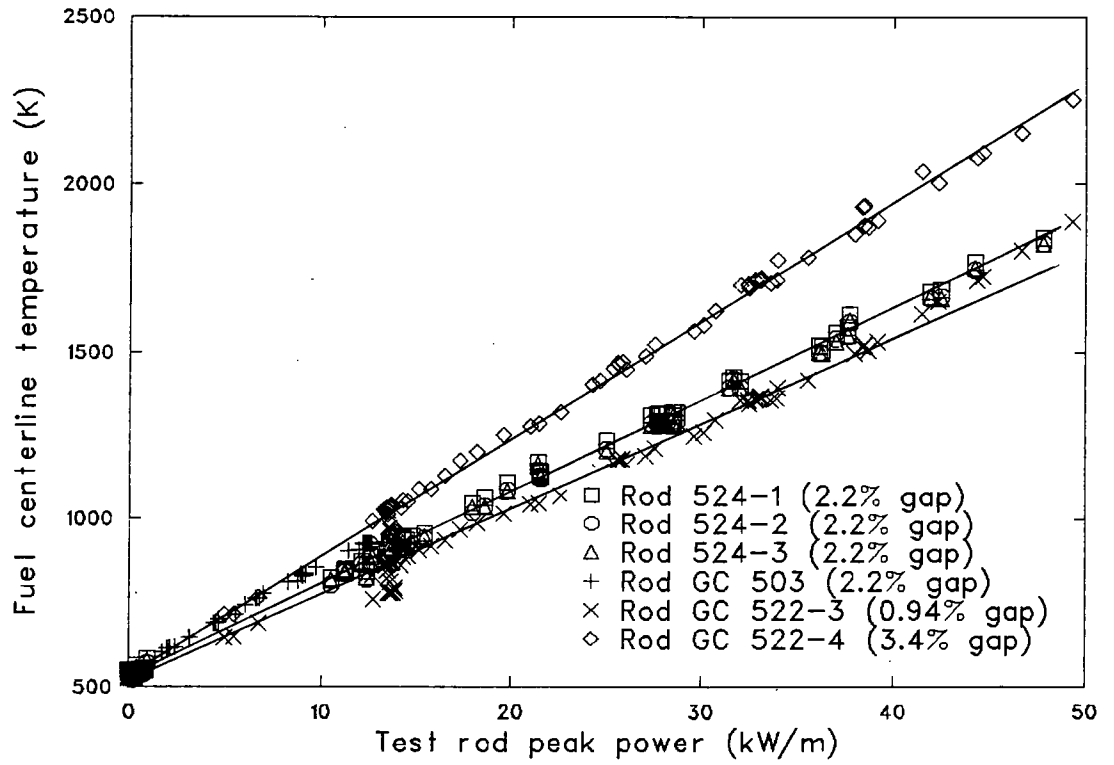

Figure 12. Test PR-1 fuel centerline temperature measurements compared with previous GC experiment results showing the effect of initial gap width in helium filled test rods.

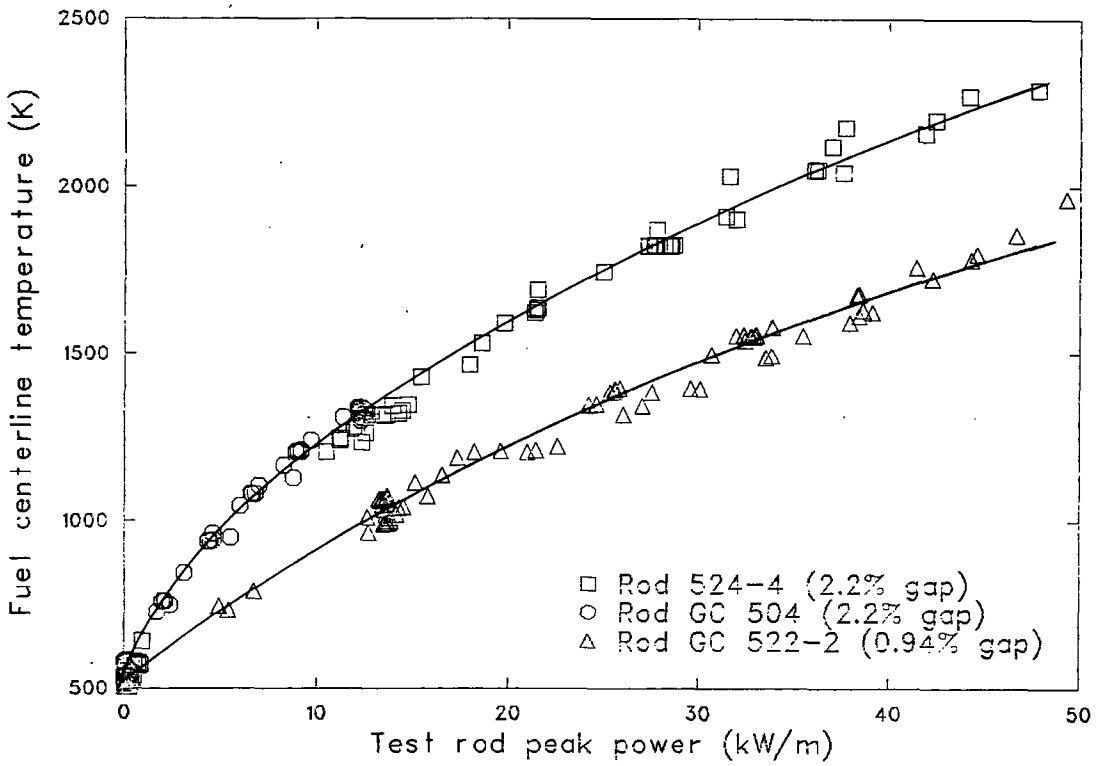

Figure 13. Test PR-1 fuel centerline temperature measurements compared with previous GC experiment results showing the effect of initial gap width in argon filled test rods.

Fuel Thermal Conductivity. As a fuel rod is operated at power, thermal stresses cause the fuel pellets to crack and pieces of the fuel to relocate in such a manner that some of the initial gap area is redistributed toward the center of the pellet. Consequently, pellet cracking and relocation alter both the fuel thermal conductivity and the pellet-to-cladding gap. A change in either the fuel thermal conductance or the pellet-to-cladding gap conductance will alter the radial temperature distribution and, consequently, will affect the amount of stored energy in the fuel rod at any given time. Therefore, evaluation of both the "effective" fuel thermal conductivity and the pellet-to-cladding gap conductance is essential. It is expected that the size and pattern of the fuel cracking will be affected by the initial gap size and the theoretical density of the fuel. This will affect the resulting effective fuel conductivity and fuel-to-cladding gap conductance.

Figure 14 shows the measured fuel off-center temperatures (three azimuthal orientations) in Rod 524-2 as a function of test rod power. Analyses previously made during the GC Test Series indicate that the scatter in the individual off-center temperature measurements, as shown in Figure 14, can be attributed to fuel pellet skewing within the cladding cylinder. If the temperatures were averaged, the resulting value would define a relatively smooth curve (shown in Figure 15), and would be essentially the same temperature that would have resulted had the fuel pellet been located symmetrically within the cladding. In addition, the presence of a thermocouple in the fuel perturbs the local fuel temperature and the measurement must be corrected for this perturbation effect. Figure 16 shows these same averaged off-center temperature measurements after corrections for thermocouple temperature perturbation effects have been made. The methods developed for correcting the fuel off-center temperatures are described in Reference 1.

To evaluate effective fuel thermal conductivities, radial temperature profiles were calculated for the test fuel rods at specific power levels. The UO_2 thermal conductivity relationship used in the calculations was then adjusted and the radial temperature profiles recalculated until the profiles coincided with the measured fuel centerline and off-center temperature (corrected and averaged) measurements. These calculations

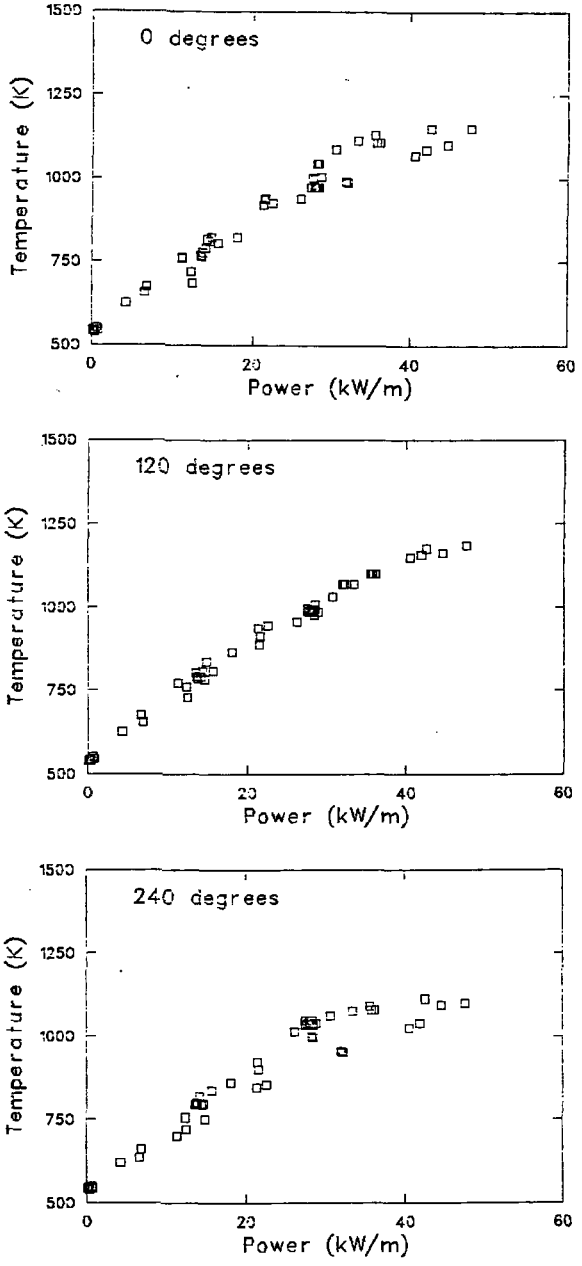

Figure 14. Off-center fuel temperature measurements from Test PR-1, Rod 524-2.

were performed using an ∫kdT computer code called FUELCON,[a] which was developed for this purpose.

The MATPRO fuel thermal conductivity relationship was used in the FUELCON calculations.

a. FUELCON, Idaho National Engineering Laboratory Code Configuration Control Number H003151B.

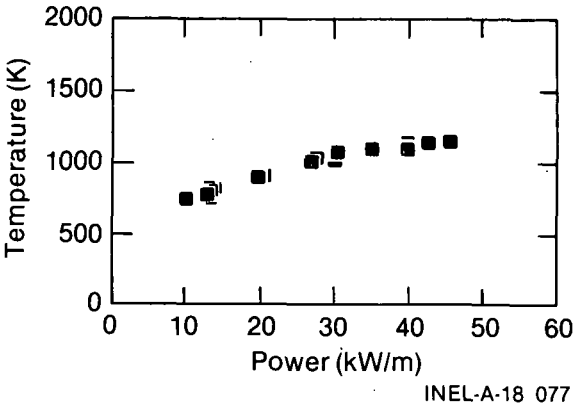

Figure 15. Averaged off-center fuel temperature measurements from Test PR-1, Rod 524-2.

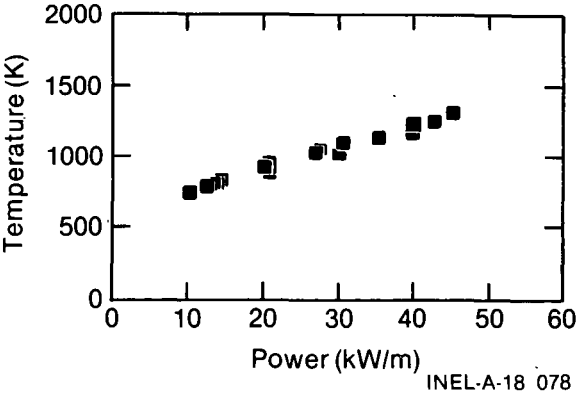

Figure 16. Averaged and corrected off-center fuel temperature measurements from Test PR-1, Rod 524-2.

The MATPRO relationship was developed using experimental data obtained from solid pellets under controlled conditions, during which the pellets generally did not crack. The FUELCON-calculated effective fuel thermal conductivity (K_{eff}) is simply the MATPRO conductivity modified to account for fuel cracking effects, based on experimental data. Figure 17 shows a representative comparison between a radial temperature profile calculated with the MATPRO thermal conductivity relationship and an adjusted thermal conductivity, K_{eff}, as determined by FUELCON. This procedure is described in detail in Reference 1.

The K_{eff} fuel thermal conductivity correlation determined from the Gap Conductance Test Series data is presented below.

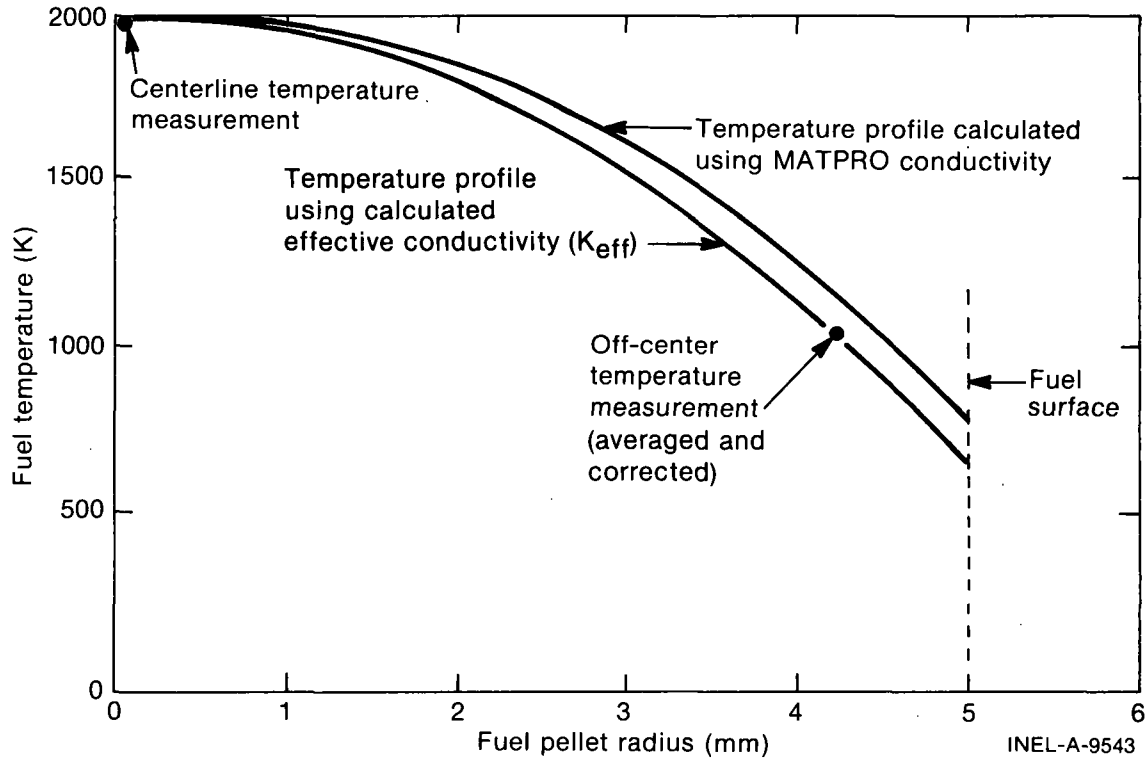

Figure 17. Representative comparison between fuel pellet radial temperature profiles calculated using the MATPRO thermal conductivity correlation and the FUELCON effective thermal conductivity.

$$K_{eff} = K_{MATPRO} - (0.0002189 - 0.050867\chi + 5.678\chi^2) \pm \sigma_{K_{eff}} \quad (1)$$

where

K_{MATPRO} = the temperature-dependent fuel thermal conductivity of a solid pellet

χ = (HG - 0.014 - 0.14 CG) (0.0545/CG)$(TD)^8$

HG = a hot pellet-to-cladding radial gap in millimeters (calculated assuming only radial cracking, thermal expansion, and elastic deflection of an idealized solid pellet and cylindrical cladding)

CG = the initial cold, radial pellet-to-cladding gap in mm

TD = the theoretical density of the fuel in decimal form

$\sigma_{K_{eff}}$ = $0.488169 \times 10^{-3} + 0.134487 \times 10^{-4}$ (POWER) -0.821495×10^{-6} $(POWER)^2 + 0.104021 \times 10^{-7}$ $(POWER)^3$ and is the total uncertainty in K_{eff} as a function of the power in kW/m.

Effective fuel thermal conductivities were calculated for each of the helium filled rods in Test PR-1. Typical examples of the calculated effective fuel thermal conductivity are shown in Figures 18 and 19 for Rods 524-1 and 524-3, respectively, at several test rod power levels. Also shown in the figures are the MATPRO fuel conductivity and the K_{eff} fuel conductivity correlation curves. All effective fuel thermal conductivities calculated from the Test PR-1 data lie well within the error bounds of the K_{eff} correlation.

The comparisons in Figures 18 and 19 show that the effects of pellet cracking and pellet fragment relocation on the fuel thermal conductivity are greatest at low powers and diminish, as would be expected, at high powers and high temperatures, under which conditions pellet thermal

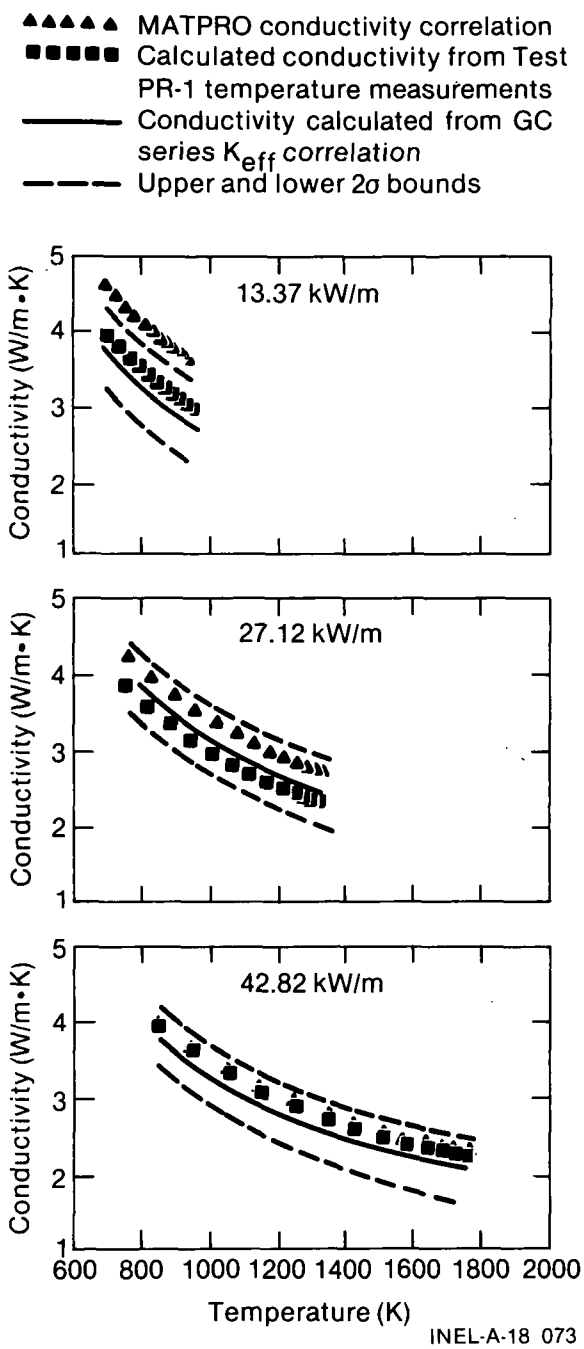

Figure 18. Comparison of MATPRO, K_{eff}, and calculated fuel thermal conductivities as a function of temperature at several power levels. Calculated conductivity is from Test PR-1, Rod 524-1 measurements.

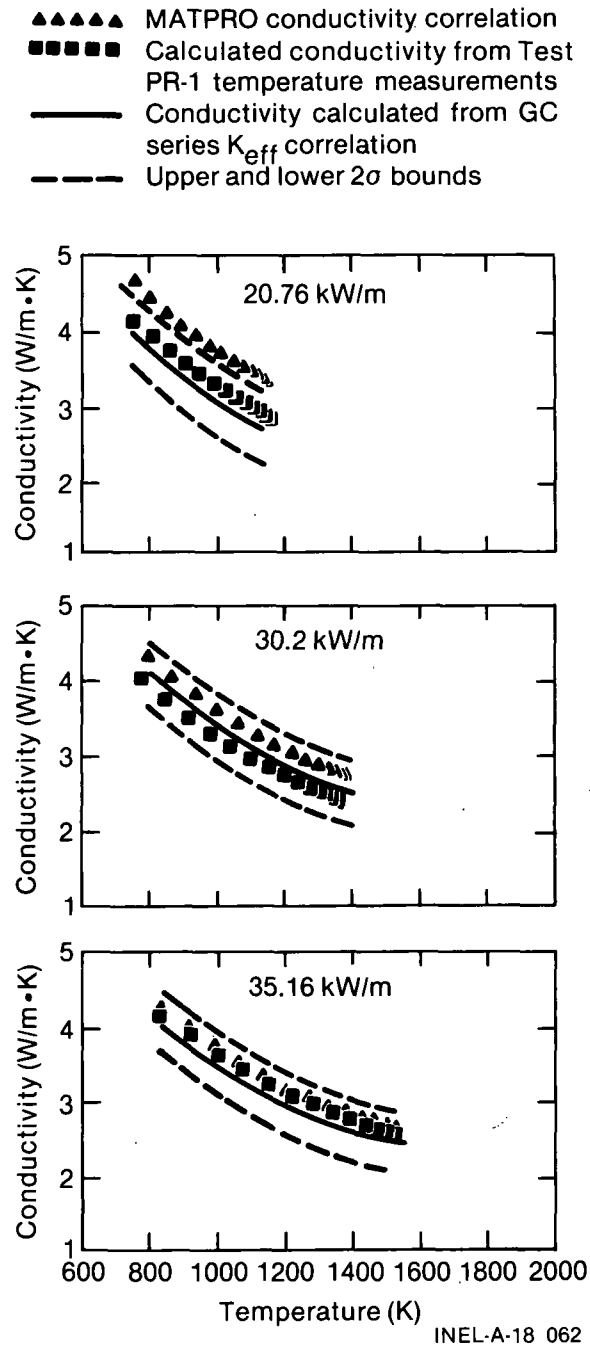

Figure 19. Comparison of MATPRO, K_{eff}, and calculated fuel thermal conductivities as a function of temperature at several power levels. Calculated conductivity is from Test PR-1, Rod 524-3 measurements.

expansion closes the cracks between fragments and the pellet-to-cladding gap. At high power levels, the calculated K_{eff} and MATPRO thermal conductivities are identical.

As expected, the K_{eff} correlation indicates that the initial gap width, hot gap width, and theoretical density have an effect on the in-pile effective fuel thermal conductivity. The density correction in the K_{eff} correlation is significant only at lower fuel pellet temperatures. With the amount of scatter and uncertainty in in-pile temperature measurements it is questionable whether the density correction has any real significance. Fuel thermal conductivities with uncertainty error bounds as a function of temperature were calculated for several UO_2 theoretical densities using the K_{eff} correlation. The effective fuel thermal conductivities determined from temperature measurements for all helium filled test rods were then compared with the K_{eff} correlation fuel conductivities. An example, Figure 20, shows that the effective conductivities of the 92 and 95% theoretical density (TD) fuel rods do not fall within the K_{eff} correlation conductivity error bounds for the 97% TD fuel. Table 4 summarizes the results of these comparisons and indicates which of the fuel rods with theoretical densities of 92, 95 and 97% fall within the error bounds of the K_{eff} calculated fuel thermal conductivities. These results indicate that the density correction in the K_{eff} correlation is probably necessary, but could be improved if a larger data base was available.

The calculated stored energy in each of the helium filled fuel rods, at several steady state power levels, is listed in Table 5. Energies were calculated using the MATPRO fuel conductivity correlation and the fuel conductivity correlation (K_{eff}) developed from the GC Test Series experiments. Because K_{eff} predicts a lower fuel thermal conductivity than MATPRO, the fuel rod stored energy calculated using the K_{eff} correlation is smaller than the energy calculated using the MATPRO correlation.

Gap Conductance. Steady state pellet-to-cladding gap conductance (h_{gap}) values are obtained from the relationship

$$h_{gap} = \frac{Q}{A(T_S - T_C)} \qquad (2)$$

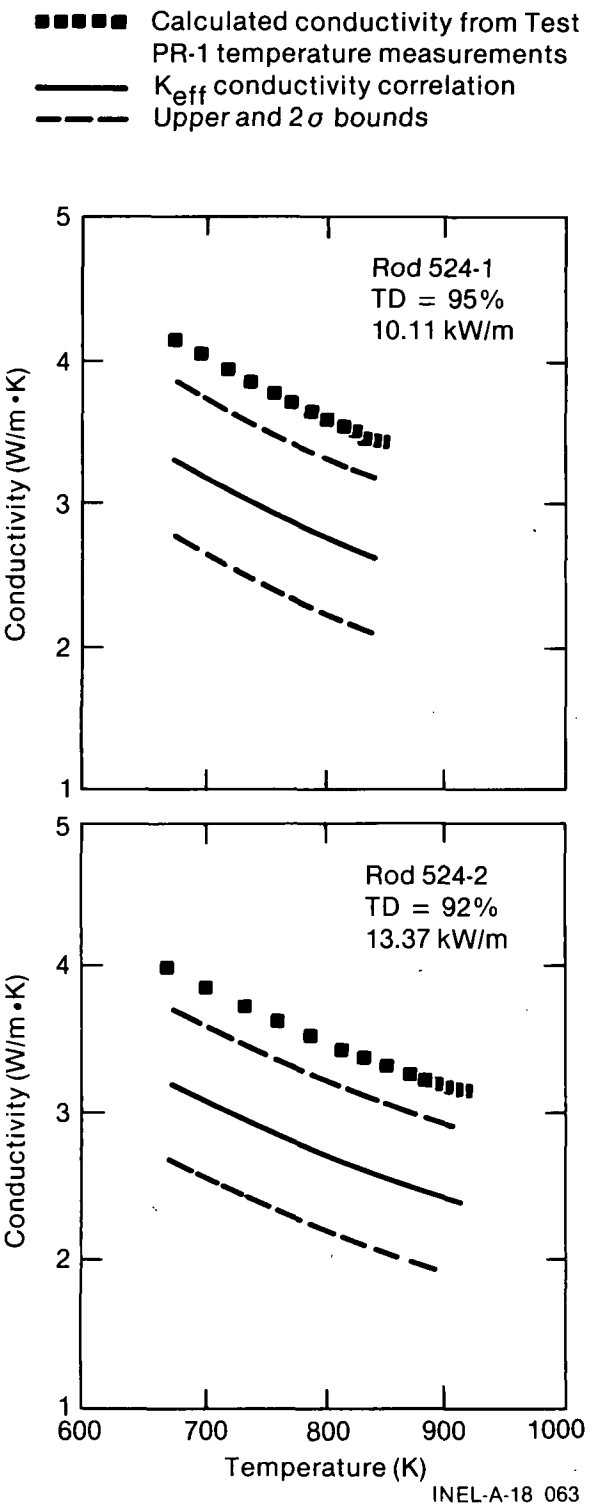

Figure 20. Comparison of calculated conductivities for 92 and 95% theoretical density fuel rods, with K_{eff} conductivity for a fuel theoretical density of 97%.

Table 4. Comparison of K_{eff} conductivities for several theoretical densities with the calculated effective conductivities of the Test PR-1 helium filled rods

Theoretical Density Used in K_{eff} Calculation	Calculated Effective Conductivity of Helium Filled Rods Inside or Outside of K_{eff} Correlation Bounds		
	92% Rod 524-2	95% Rod 524-1	97% Rod 524-3
97%	Outside	Outside	Inside
95%	Outside	Inside	Inside
92%	Inside	Inside	Inside
88%	Inside	Inside	Inside
84%	Inside	Inside	Outside
80%	Outside	Outside	Outside

Table 5. Calculated stored energy in test rod: $\int k dT$ method using both the MATPRO conductivity and the GC Test Series conductivity correlation (K_{eff})

Averaged Test Rod Peak Power (kW/m)	K_{eff} Conductivity (J)			MATPRO Conductivity (J)		
	Rod 524-1	Rod 524-2	Rod 524-3	Rod 524-1	Rod 524-2	Rod 524-3
10.11	1196	1120	1174	1245	1146	1248
13.37	1348	1267	1322	1410	1299	1415
20.76	1683	1583	1660	1757	1623	1766
27.12	1968	1840	1955	2029	1877	2041
30.2	2103	1960	2098	2153	1994	2166
35.16	2311	2143	2319	2347	2175	2360
40.01	2493	2303	2509	2533	2350	2544
42.82	2580	2381	2597	2642	2451	2650
45.66	2645	2444	2659	2753	2556	2759

where

Q = local test rod power (kW)

A = heat transfer area for a solid pellet (m^2)

T_S = pellet surface temperature (K)

T_C = cladding inside surface temperature (K).

In applying this relationship, test rod power densities were evaluated from thermal-hydraulic measurements. The surface area was calculated on the basis of fuel pellet temperature measurements in conjuction with MATPRO fuel expansion estimates at the axial measurement location. The fuel pellet surface temperatures and the cladding inside surface temperatures were calculated from the internal fuel and cladding surface temperature measurements. The pellet surface temperature calculations were made using the K_{eff} fuel thermal conductivity correlation and $\int kdT$ techniques.

The solid curves in Figure 21 represent the calculated gap conductance values for Test PR-1 [with upper and lower 2-sigma (σ] error bounds) as a function of power. Also shown in Figure 21 are the values calculated from the derived GC Test Series correlation. For each of the three Test PR-1 helium filled rods, the gap conductance values determined from the derived correlation lie well within the error bounds of the calculated (steady state) gap conductance values.

The calculated gap conductance values for the three helium filled rods are consistent. The small differences can be attributed to scatter in the data. The correlation derived from the Gap Conductance Test Series data provides a simple method for estimating the gap conductance of a particular LWR design fuel rod under a specific set of rod conditions.

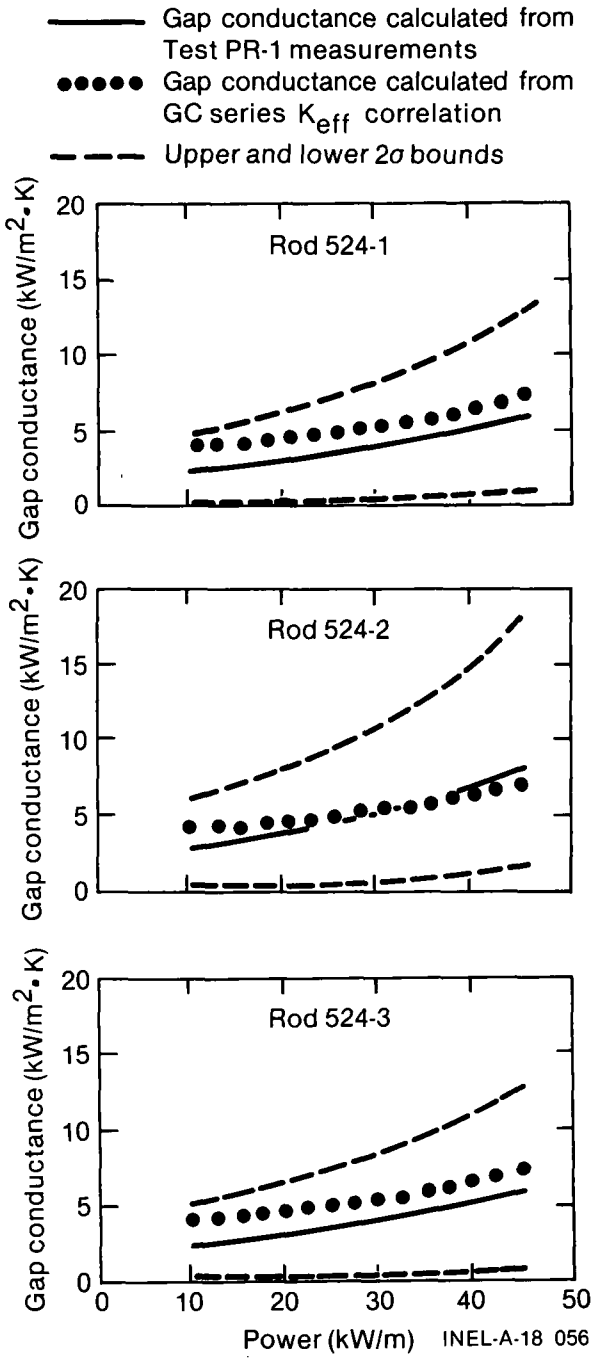

Figure 21. Comparisons of Test PR-1 gap conductances with calculated results from the GC series K_{eff} correlation; Rods 524-1, 524-2, and 524-3.

PCM AND BOILING TRANSITION TEST RESULTS

The specific objectives of Test PR-1 included providing information on boiling transition and return to nucleate boiling during severe power and coolant imbalance conditions. A series of 23 flow reductions (at constant power) and 2 power increase transients (at constant flow) were conducted to attain these objectives. Boiling transition was detected during 13 of the transients, all at the higher system pressures considered (12.7 to 15.7 MPa). Within this section, a comparison between high and low pressure boiling transition, natural circulation considerations as related to Test PR-1, and the fuel rod behavior during the PCM testing are presented. Observations regarding return to nucleate boiling and the relationship to boiling transition are also presented.

General Phenomena Associated With Boiling Transition

The consequences of boiling transition in a light water reactor environment can range from slight to severe, depending on the dominant heat transfer processes and the mitigating actions taken. Test PR-1 was conducted, in part, to provide information on boiling transition and return to nucleate boiling under a variety of coolant conditions representative of the heat transfer modes that might be expected in an LWR under postulated accident conditions. Within this section, an interpretation of the boiling transition phenomenon for the Test PR-1 operating conditions is presented.

Comparison of Boiling Transition Under PWR and BWR Conditions. The phenomenon and consequences of boiling transition in a PWR environment may be significantly different from those experienced in a BWR environment. Such differences can readily be seen by comparing the respective forced convection "boiling curves." A simplified illustration of the forced convection boiling curves considered representative for high (PWR) and low (BWR) pressure conditions is shown in Figure 22. For the high pressure condition (Figure 22, Curve A), more indicative of a PWR-type environment, different heat transfer regimes are progressively encountered as the heat flux increases. As the surface heat flux increases to

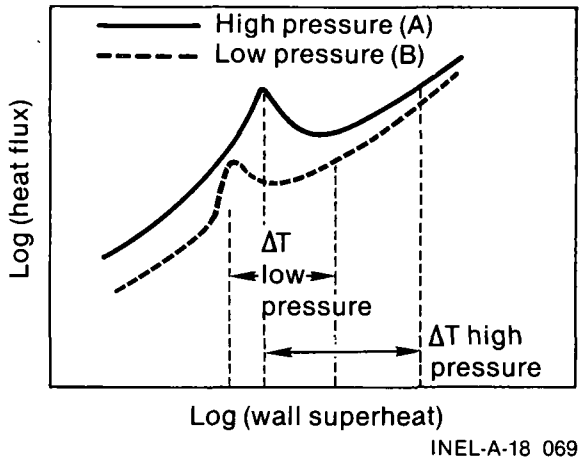

Figure 22. Representative forced convection boiling curves for high and low pressure conditions.

boiling transition,[a] the primary heat transfer mechanism progresses from subcooled forced convection to a partial boiling and subcooled nucleate boiling regime. For a heat flux controlled system, boiling transition results in a large decrease in the heat transfer coefficient (due to establishment of an insulating vapor film) and a corresponding large increase in wall temperature. This transition is commonly referred to as departure from nucleate boiling (DNB) and it results in high temperature, film boiling operation. Most transients in the Power-Cooling-Mismatch (PCM) Test Series and the higher pressure transients of Test PR-1 were conducted under PWR-type conditions, and are generally described by such a boiling transition scenario.

The low pressure (BWR pressures) transients of Test PR-1 are generally described by a forced convection boiling curve, as illustrated in Figure 22, Curve B. At lower heat fluxes, the primary heat transfer regimes include two-phase forced convection and saturated nucleate boiling. Just prior to boiling transition (as the surface heat flux

a. The literature refers to boiling transition by several descriptive terminologies, depending on the reference environment. Some of these include (a) critical heat flux (CHF), (b) departure from nucleate boiling (DNB), (c) boiling crises, (d) dryout,(e) burnout heat flux, and (f) boiling transition. The terminology used within this report is "boiling transition," since the interchange of names becomes confusing over the range of Test PR-1 operating conditions.

increases), an additional mechanism of heat transfer may be encountered for high quality annular flows, such as may occur in BWR technology. In this mode, the vapor velocity and interfacial turbulence level can become so high, and the liquid film so thin, that nucleation is suppressed on the heated surface. This regime, known as forced convective vaporization, results in high heat transfer coefficients; thus, as the heat flux is increased, the wall temperature may decrease. At the boiling transition, the heat transfer decreases and the wall temperature increases. The magnitude of the wall temperature increase is a function of the quality at which boiling transition occurs and, in general, is less than for a subcooled DNB excursion.

The effect of quality on the wall temperature excursion, based on the work of Plummer et al.,[4] is illustrated in Figure 23 for two different coolant mass fluxes. As the equilibrium quality at boiling transition ($<Xe>_c$ on Figure 23) decreases, the boiling transition heat flux and the corresponding wall thermal excursion increases. For the high quality condition ($<Xe>_c = 0.8$), the unstable, negative slope transition boiling region is not evident. This suggests that operation in this region may be accomplished with a minimal wall temperature excursion. The low pressure (~7 MPa) flow reductions of Test PR-1 did not result in readily detectable boiling transitions. Either the rods did not attain boiling transition, or the boiling transition resulted in very low wall temperature excursions, not detectable by the test instrumentation. Using MacBeth's low flow critical heat flux correlation,[5] the expected quality at the onset of boiling transition was near 0.8 at the Test PR-1 low pressure condition, suggesting that the latter explanation for not detecting boiling transition is plausible.

Natural Circulation Considerations During Test PR-1. Several attempts were made during Test PR-1 to reduce flow sufficiently to induce boiling transition under the low pressure (~7 MPa) conditions. Various combinations of inpile tube (IPT) bypass and flow control valve settings (Figure 24) were tried in order to influence the flow reduction capability. With all combinations, the minimum measured flow rate through the individual coolant shrouds was limited (at power) to values between 0.07 and 0.08 L/s. With no test rod power generation, the coolant flow rate could be reduced to nearly 0.03 L/s. Therefore, natural circulation apparently limited the flow reduction. The low flow limitation was observed at all pressure levels and test rod powers between 40 and 53 kW/m. An explanation of the low flow limitation for the Test PR-1 geometry follows.

The coolant within the in-pile bypass region was subcooled during the entire Test PR-1 operation. In contrast, saturated or boiling conditions existed within the individual coolant flow shrouds during power operation. Therefore, during power operation, the coolant density within the in-pile bypass (ρ_{BP}) was greater than the average flow shroud coolant density (ρ_{FS}).

The total volumetric coolant flow rate within an individual coolant flow shroud can be estimated using the following simplifying assumptions:

1. The vapor bubbles formed as a result of boiling within the flow shroud rise with a velocity (V) given by

$$V = V_c + V_B \tag{3}$$

where V_c is the bulk coolant velocity without vapor production, and V_B is the bubble rise velocity resulting from buoyancy effects. Such an assumption is most valid when V_c is small.

2. The liquid-vapor two-phase mixture within the coolant shroud flows at a constant (and equal) velocity (i.e., no interfacial slip).

The average bulk coolant velocity without vapor production is given by the well-known principle

$$V_c = Q_c/A \tag{4}$$

where A is the cross-sectional area for flow ($A \cong 1.698\ cm^2$ for Test PR-1) and Q_c is the volumetric coolant flow rate at zero power ($Q_c \cong 0.03\ L/s = 30\ cm^3/s$). Then, from Equation (4), $V_c \cong 17.7$ cm/s.

The bubble rise velocity resulting from buoyancy effects (V_B) may be estimated by the expression[6]

$$V_B = 1.18 \frac{\sigma g (\rho_l - \rho_v)^{1/4}}{\rho_l^2} \tag{5}$$

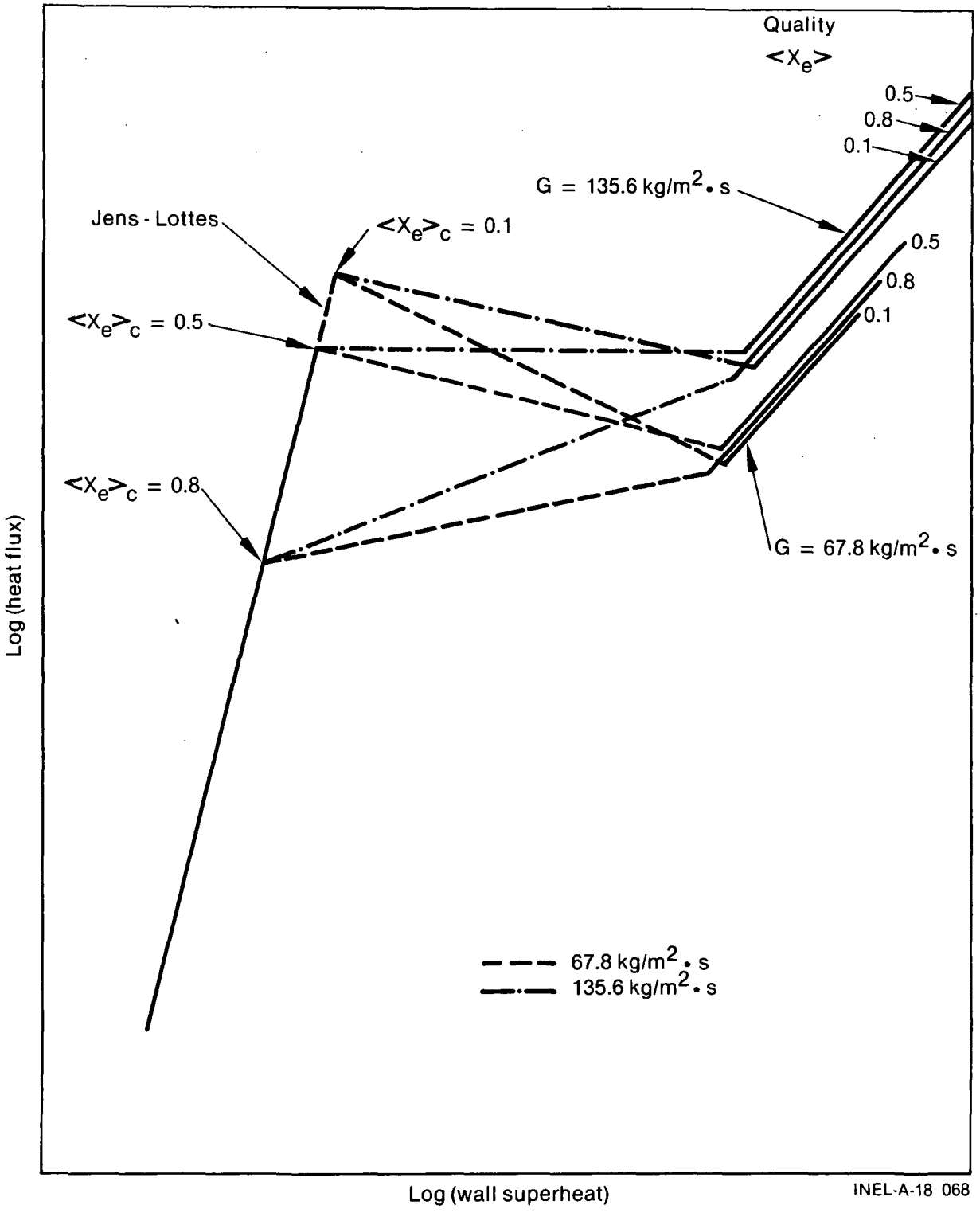

Figure 23. Boiling curves for water showing effect of quality on boiling transition.

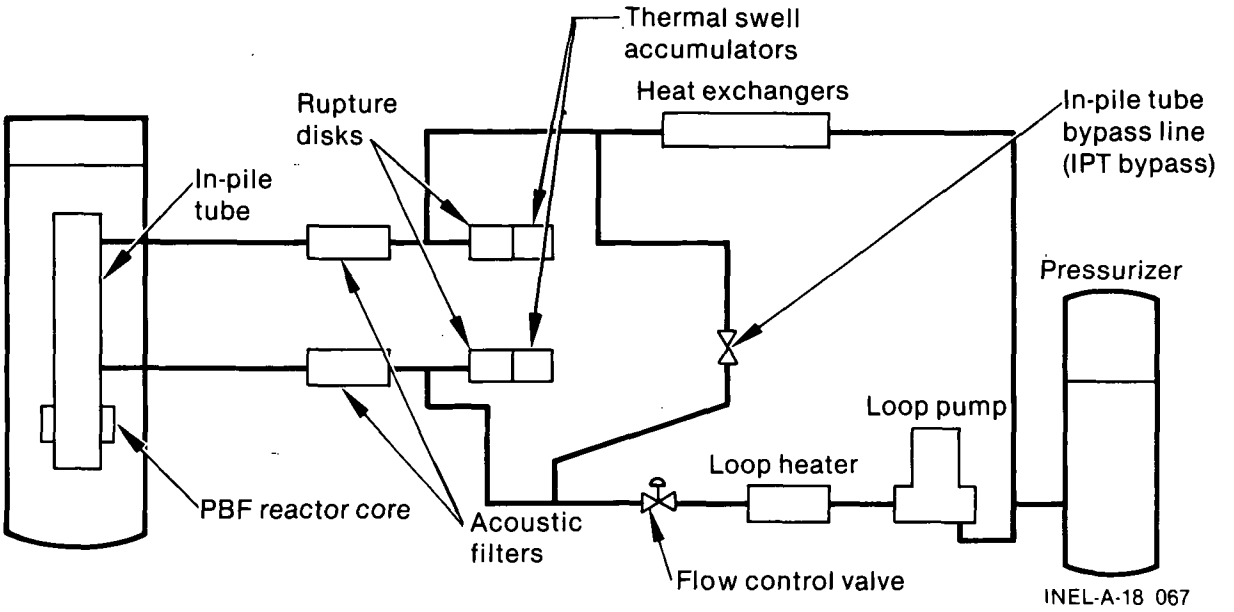

Figure 24. Schematic of PBF test loop and in-pile tube.

where σ is the surface tension of the liquid and ρ_l and ρ_v are the liquid and vapor densities, respectively. Equation (5) is based on experimental observations of bubbles rising in 16 different liquids, and has also been derived analytically.[7] For the Test PR-1 conditions,[a] Equation (5) yields V_B = 20.3 cm/s. From Equation (3) and the calculated results of Equations (4) and (5), the total vapor velocity becomes approximately 38 cm/s. Therefore, from the general form of Equation (4), a total volumetric flow rate of 0.064 L/s is calculated. The calculated volumetric flow rate (0.064 L/s) compares favorably with the minimum measured volumetric flow rate (0.07 to 0.08 L/s).

Onset of Boiling Transition and Return to Nucleate Boiling

The conditions prior to initiating each PCM transient and the method of initiating each cycle are summarized in Table 6. The 13 transients that resulted in detectable boiling transition are evaluated in this section.

Conditions at Onset of Boiling Transition. The primary measurement for detection of boiling transition during Test PR-1 was the cladding displacement sensor [linear variable differential transformer (LVDT)] on each rod. Following boiling transition at high pressures, the temperature excursion on the rods resulted in a change in cladding length due to thermal expansion. During a flow reduction PCM transient, this length change is readily observable. During a power increase transient, the cladding elongation response to boiling transition is somewhat confounded by the general rod elongation during the power increase. The boiling transition can usually be interpreted as a change in slope of the elongation response during a power increase transient, but is not as obvious as the response during a flow decrease. A representative LVDT response (Rod 524-3) during a boiling transition cycle is shown in Figure 25. The rapid increase in cladding displacement at about 210 s corresponds to the onset of boiling transition, and the decrease between 250 and 300 s corresponds to the return to nucleate boiling (quench and rewet) process. The shroud coolant flow rate and test rod peak power are shown for reference in Figure 25. The transient corresponds to PCM Cycle 20 of Tables 6 and 7. Table 7 lists the conditions under which boiling transition was detected during the Test PR-1 PCM transients, based on the cladding displacement responses.

The four Test PR-1 fuel rods were subjected to very similar thermal-hydraulic conditions during the PCM testing, but attained widely varying degrees of fuel rod damage. As seen from Table 7, only PCM Cycle 25 resulted in boiling transition on all four test rods, although the power and

a. Pressure = 15 MPa, T_{sat} = 616 K, ρ_l = 0.597 g/cm^3, ρ_v = 0.0986 g/cm^3, and $\sigma \cong 64$ dyne/cm.

Table 6. Power-cooling-mismatch transient conditions

PCM Cycle	PBF Core Power (MW)	Averaged[a] Test Rod Peak Power (kW/m)	Coolant Inlet Temperature (K)	Nominal System Pressure (MPa)	Method of Transient Initiation/Conclusion
1	10.1	40.39	545	7.2	Flow reduction at constant test rod power; no boiling transition observed.
2	11.4	43.19	543	7.3	Flow reduction at constant test rod power; no boiling transition observed.
3	12.5	47.21	548	7.3	Flow reduction at constant test rod power; no boiling transition observed.
4	12.5	49.18	545	7.2	Flow reduction at constant test rod power; no boiling transition observed.
5	12.5	49.59	547	7.3	Flow reduction at constant test rod power; no boiling transition observed.
6	12.5	47.42	550	7.2	Flow reduction at constant test rod power; no boiling transition observed.
7	12.7	43.71	594	12.7	Flow reduction at constant test rod power; transient concluded by simultaneous flow increase and power reduction.
8	11.8	42.12	607	15.5	Flow reduction at constant test rod power; transient concluded by simultaneous flow increase and power reduction.
9	11.8	42.12	610	15.5	Flow reduction at constant test rod power; transient concluded by simultaneous flow increase and power reduction.
10	11.1	42.12	595	13.4	Flow reduction at constant test rod power; no boiling transition observed.
11	11.1	40.95	594	13.0	Flow reduction at constant test rod power; no boiling transition observed.
12	12.2	45.67	595	13.2	Flow reduction at constant test rod power; no boiling transition observed.
13	12.5	48.86	553	7.3	Flow reduction at constant test rod power; no boiling transition observed.
14	12.5	46.92	593	13.0	Flow reduction at constant test rod power; transient concluded by simultaneous flow increase and power reduction.
15	12.5	44.83	593	13.1	Flow reduction at constant test rod power; transient concluded by increasing flow.
16	11.8	41.63	603	15.5	Flow reduction at constant test rod power; transient concluded by increasing flow.
17	11.8	40.87	604	15.6	Flow reduction at constant test rod power; transient concluded by increasing flow.
18	12.5	45.50	593	12.9	Flow reduction at constant test rod power; no boiling transition observed.
19	12.5	45.50	593	12.9	Flow reduction at constant test rod power; no boiling transition observed.
20	12.5	45.50	593	12.9	Flow reduction at constant test rod power; transient concluded by increasing flow.
21	11.8	42.41	606	15.4	Flow reduction at constant test rod power; transient concluded by increasing flow.
22	12.6	46.53	575	15.0	Flow reduction at constant test rod power; transient concluded by increasing flow.
23	12.6	42.24	605	15.2	Flow reduction at constant test rod power; transient concluded by increasing flow.
24	6 to 12.7	25.00 to 44.94	590	15.6	Power increase at constant flow rate; transient concluded by power decrease.
25	6.5 to 15.3	22.44 to 53.70	590	15.5	Power increase at constant flow rate; transient concluded by power decrease.

a. Rod linear heat generation at peak power elevation; average of four Test PR-1 rods.

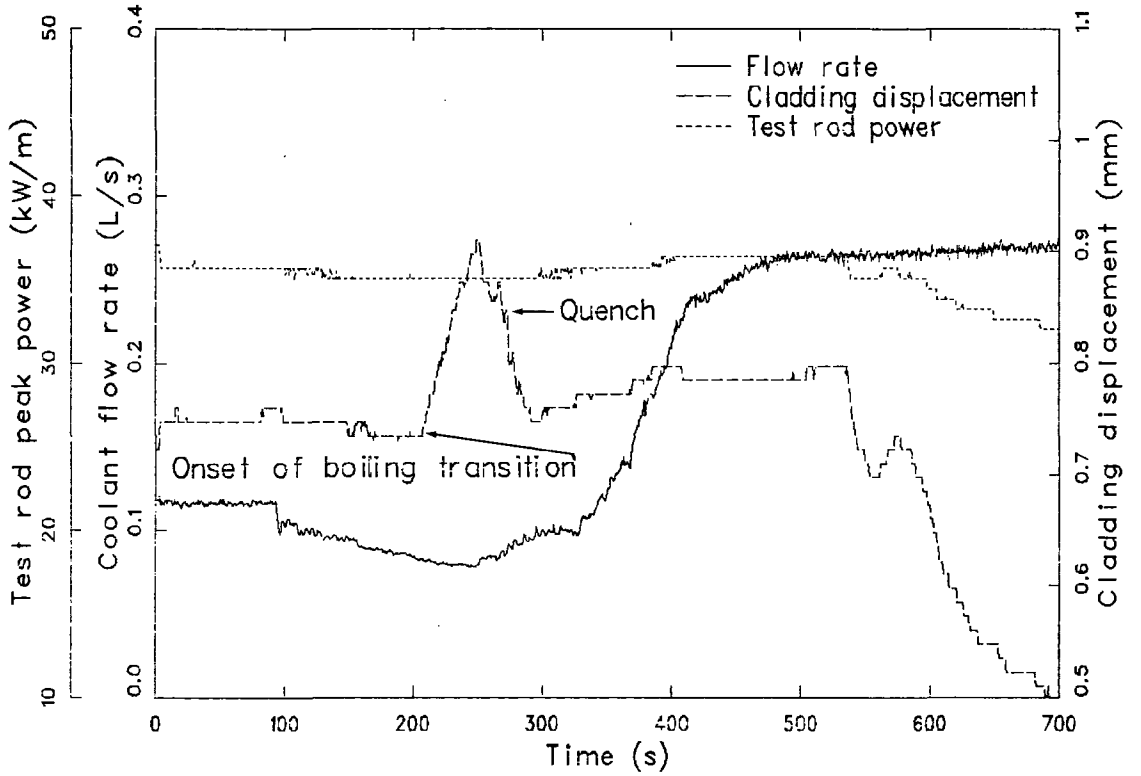

Figure 25. Representative response of LVDT to boiling transition and quench. PCM Cycle 20 (inlet temperature = 593 K, pressure = 12.9 MPa).

coolant flow for each rod were similar during each PCM cycle. Several qualitative explanations for this phenomenon can be postulated. One explanation is simply the stochastic nature of the boiling transition processes. As evidenced by the number and variability of critical heat flux correlations, this explanation appears plausible.

The surface condition of the test rods or rod bowing effects may also explain the observed disparity between rods. As the information in Table 7 suggests, Rods 524-1 and 524-3 consistently attained high temperature boiling transition and, thus, cumulative oxidation of the cladding would be more extensive than for Rods 524-2 and 524-4. This observation is in conflict with the results of Berenson[8,9] on pool boiling, in which higher heat fluxes and surface temperatures were required to attain boiling transition on an oxidized surface compared to an unoxidized surface. In forced convection pool boiling, surface conditions are generally regarded as secondary effects. The surface condition of the rods is, therefore, not likely a dominant factor in the thermal-hydraulic conditions at the onset of boiling transition. Rod bowing, however, cannot be dismissed as a potential contributor to the observed differences.

A third postulated explanation can be visualized by modeling the Test PR-1 four-rod geometry with an electrical analogy. The four test rod coolant anulii represent parallel and nearly equal resistances to the coolant flow. The in-pile bypass region represents a fifth parallel resistance. Since all resistances are coupled through common upper and lower plenums, the potential difference (pressure drop) across each must be equal. If, at the onset of boiling transition on one rod, the two-phase pressure drop within the flow shroud changes, the coolant flow will be redistributed to the five parallel flow paths. Quantitative assessment of the flow distribution is extremely difficult without grossly simplified assumptions or precision local parameter measurements (quality, pressure drop, mass flux, heat flux, etc.). Qualitatively, the dominant cause of some rods attaining boiling transition at conditions others do not is a combination of the inherent hydraulic coupling of the rods in the Test PR-1 geometry, possible rod bowing, and the stochastic nature of the boiling transition process.

During many of the cycles that resulted in boiling transition, instrumentation in the peak power region (0.452 m) of the rod(s) responded to the

Table 7. Boiling transition data summary for Test PR-1

PCM Cycle[a]	Test Rod	Coolant Inlet Temperature[b] (K)	System Pressure[b] (MPa)	Inlet Subcooling[b] (K)	Rod Peak Power at Onset of BT[c] (kW/m)	Coolant Mass Flux at Onset of BT ($kg/s \cdot m^2$)	Approximate Time in BT (s)
7	524-1	593	12.8	9.8	49.8	587	95
	524-3	592	12.7	10.2	49.9	689	103
8	524-1	608	15.4	9.4	44.5	487	51
	524-3	608	15.4	9.4	44.5	560	50
	524-4	609	15.4	8.4	44.5	378	21
9	524-3	609	15.4	8.4	43.7	586	34
14	524-1	593	12.8	9.8	37.7	556	55
	524-3	594	12.8	8.8	37.7	434	25
15	524-1	594	12.9	9.2	36.4	543	78
16	524-1	603	15.3	13.9	42.3	960	60
	524-3	603	15.3	13.9	42.3	880	27
17	524-1	603	15.5	14.7	42.6	898	57
	524-3	603	15.4	14.2	42.7	819	50
	524-4	604	15.4	13.2	43.1	839	21
20	524-1	593	13.1	11.6	38.4	489	337
	524-3	593	12.9	10.4	38.4	458	95
21	524-1	606	15.0	9.3	45.4[d]	1020	232
	524-3	606	15.0	9.3	45.9	763	232
22	524-1	572	15.1	43.8	50.3[d]	1303	>150
23	254-1	604	15.6	14.4	46.6[d]	809	178
	254-3	605	15.5	12.9	46.6[e]	721	153
24	524-1	587	15.7	31.6	40.0[d]	882	>163
25	524-1	588	15.4	29.4	56.4[d]	562	126
	524-2	587	15.4	30.4	50.0	486	80
	524-3	587	15.4	30.4	50.0[e]	468	183
	524-4	590	15.4	27.4	56.4	521	123

a. PCM cycles that are excluded did not result in detectable boiling transition on any test rod.

b. At the first indication of boiling transition (BT) from cladding elongation response.

c. Averaged linear power of four test rods at axial peak power elevation.

d. Data from failed rod.

e. Failure of Rod 524-3 upon quench from PCM Cycle 21 is likely.

high temperature operation. Boiling transition in vertical, forced convection experiments with cosine axial power generation is generally limited to the upper rod regions, except for very high heat flux and low flow rate combinations. Thermal excursions in the peak power region would, therefore, not be anticipated during most of the Test PR-1 transients. Thermocouple shunting in the high temperature region, and possibly large temperature gradients across thermocouple wire inhomogeneities,[10] may have precipitated the observed response. Calculations using the FRAP-T5 computer code and the Babcock & Wilcox-2 CHF correlation indicate that boiling transition at the 0.452-m elevation would occur at a flow 30% of that required for the onset of boiling transition. This condition occurred only once during Test PR-1, during PCM Cycle 23.

Rod 524-4 was instrumented with thermocouples placed in small grooves on the inside cladding surface as well as external cladding surface thermocouples. Both the internal and external thermocouples at the 0.70-m elevation (from the bottom of the fuel stack) responded to the high temperature boiling transition during Cycle 25, providing a comparison of internal and external cladding temperature responses. During this transient, the test rod power was increased to 56.4 kW/m at a constant coolant flow rate (~0.1 L/s). The flow rate was subsequently reduced to about 0.075 L/s. The measured response from the two devices is shown in Figure 26. The internal cladding thermocouple at the 0.70-m elevation consistently indicated higher steady state temperatures (at power) than the external thermocouples, and the magnitude of the difference was consistently greater than the expected temperature drop (~67 K at 52 kW/m) across the cladding thickness. This observation suggests that fuel may have relocated to the proximity of the thermocouple junction, resulting in the higher temperature reading, or the thermocouple may not have been in solid contact with the cladding and was measuring a combination of cladding, fill gas, and fuel temperatures. Although the internal cladding temperature may be biased, the relative temperature increase and the duration of high temperature operation can be compared between the two measurements.

As shown in Figure 26, the internal and external cladding temperatures of Rod 524-4 increased at nearly the same time, but at different rates. The external cladding temperature increased by about 250 K within 6 s. The cladding internal temperature indicated a 210-K increase and peaked between 18 and 25 s after indication of boiling transition. The cladding external temperature measurement also exhibited different quench behavior than the internal thermocouple, apparently quenching within about 12 s of boiling transition, compared to about 50 s for the internal measurement. The different behavior of internal and external cladding temperature responses during quench and rewet has been observed in both in-pile and out-of-pile tests under LOCA blowdown/reflood conditions. In general, external cladding thermocouples have been accredited with inducing earlier quenches at lower temperatures.[11] The difference in quench behavior may be attributed to "fin cooling effects" on the protruding external measurement devices.

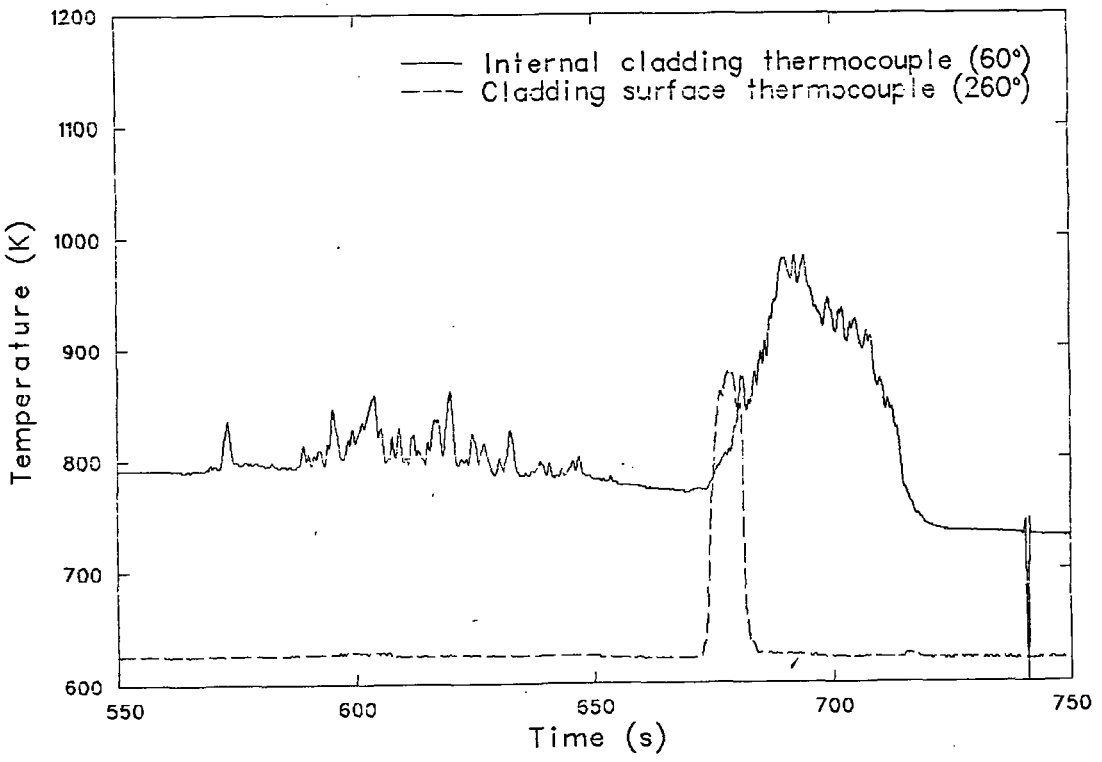

Figure 26. Internal and external cladding temperature response during PCM Cycle 25, Rod 524-4.

Conditions at Return to Nucleate Boiling. Return to nucleate boiling was inferred from the cladding displacement response for each test rod. The coolant conditions, coolant mass flux, and test rod power that resulted in the apparent quench of the rods are listed in Table 8. The data given in Table 8 are internally consistent, with somewhat more spread in the conditions at quench than were observed for the conditions at the onset of boiling transition (Table 7). No significant difference was apparent in the quench behavior of the argon filled rod (524-4) and the helium filled rods.

Comparison of Test PR-1 Data with Previous PCM Test Results

The conditions at the onset of boiling transition are compared in Figure 27 with previously obtained PCM Test Series data on PWR-type test fuel rods. Both the 13- and 15.5-MPa (nominal) pressure data from Test PR-1 are consistent with the trend of the previous data. The data points from Rod 524-1, which lie outside the trend lines of the previous PCM test data, were obtained following rod failure. The data point from the argon filled test rod (Rod 524-4), which lies outside the trend lines, was obtained during PCM Cycle 25. With the exception of this singular data point, inherent differences in the conditions at the onset of boiling transition between the helium filled test rods and the argon filled rod were not observed.

The thermal-hydraulic conditions at the onset of boiling transition (departure from nucleate boiling) during the PBF PCM tests have been empirically correlated. The independent variables selected for the correlation were those readily measured and controlled during testing, including the rod peak power (P_P), inlet coolant mass flux (G), and inlet subcooling (ΔT_{SC}). The purpose of such a correlation is twofold:

1. To provide a "rule of thumb" for quick and simple predictions of the thermal-hydraulic conditions that promote the onset of film boiling during PBF PCM testing

2. To provide a comparison of the conditions at DNB with the conditions at quench.

Using a nonlinear, multivariant, least squares regression analysis of the PBF PCM data, the following correlation was obtained:

$$P_P = 8.24\, G^{0.25}\, \Delta T_{SC}^{0.057} \quad \text{(onset of boiling transition)} \qquad (6)$$

where P_P is the rod linear peak power (kW/m), G is the inlet coolant mass flux (kg/s•m^2), and ΔT_{SC} is the inlet subcooling (K). As illustrated in Figure 28 Equation (6) accurately predicts ($\pm 20\%$) the inlet coolant and power conditions at the onset of boiling transition.

Interestingly, Equation (6) also predicts ($\pm 20\%$) the quench behavior equally well. Figure 29 illustrates the experimentally determined rod peak powers at the onset of boiling transition (open symbols) and quenching (shaded symbols) versus the predicted rod peak powers [Equation (6)] for the PCM Test Series and Test PR-1. As illustrated, the thermal-hydraulic conditions (P_P, G, and ΔT_{SC}) at the onset of film boiling are virtually indistinguishable from those at quenching. The data from Test PR-1 on BWR design test rods are very consistent with data from the PCM Test Series on PWR design test rods for similar pressure conditions.

The onset of boiling transition and quenching behavior described above may also be illustrated on a forced convection boiling curve as shown in Figure 30. At the critical heat flux (Point A), where departure from nucleate boiling occurs, a jump discontinuity in wall temperature (to Point B) occurs. Upon cooldown, however, the system follows the same jump discontinuity and returns to nucleate boiling by way of the critical heat flux. On the basis of the coinciding data trends previously illustrated in Figure 29, little or no hysteresis is expected while traversing Path A-B (Figure 30).

Return to nucleate boiling via the same path as onset of boiling transition has been reported by other investigators. McEwan et al.[12] observed this trend, and no signs of hysteresis, in tests with a heated annulus section using water at 10.3 MPa. Stevens et al.[13] reported similar results using Freon-12 in a uniformly heated tube with upward vertical flow. Sterman et al.[14,15] found, in tests using a 0.25-cm-diameter, 1.39-cm-long, heated

Table 8. Quench data summary for Test PR-1

PCM Cycle[a]	Test Rod	Coolant Inlet Temperature[b] (K)	System Pressure[b] (MPa)	Rod Peak Power at Quench[b] (kW/m)	Coolant Mass Flux at Quench[b] (kg/s•m^2)
7	524-1	596	12.7	39.2[c]	363[c]
	524-3	596	12.7	39.2[c]	376[c]
8	524-1	610	15.3	40.8[c]	363[c]
	524-3	610	15.3	41.0[c]	369[c]
	524-4	610	15.3	41.0[c]	389[c]
9	524-3	609	15.3	41.0[c]	465[c]
14	524-1	593	12.8	36.4[c]	392[c]
	524-3	593	12.8	36.4[c]	411[c]
15	524-1	595	13.1	33.8	369
16	524-1	604	15.3	42.1	458
	524-3	603	15.4	42.1	555
17	524-1	604	15.4	43.1	404
	524-3	604	15.4	43.1	489
	524-4	604	15.4	43.1	477
20	524-1	594	13.1	38.4	352
	524-3	593	13.1	38.4	338
21	524-1	606	15.2	44.6[d]	357
	524-3	606	15.2	44.6	363
22	524-1	~572	15.0	—[e]	—[e]
23	524-1	605	15.3	44.0[d]	362
	524-3	605	15.3	44.0	372
24	524-1	~589	~15.8	—[e]	—[e]
25	524-1	593	15.4	53.6[d]	372
	524-2	588	15.4	52.3	458
	524-3	588	15.4	53.0	452
	524-4	593	15.5	54.3	381

a. PCM cycles that are excluded did not result in detectable boiling transition on any rod.

b. At time of quench as indicated by rapid decrease in cladding elongation (from LVDT).

c. Can only be approximated due to rapidly changing power and mass flux during quench.

d. Data from failed rod.

e. Indeterminate.

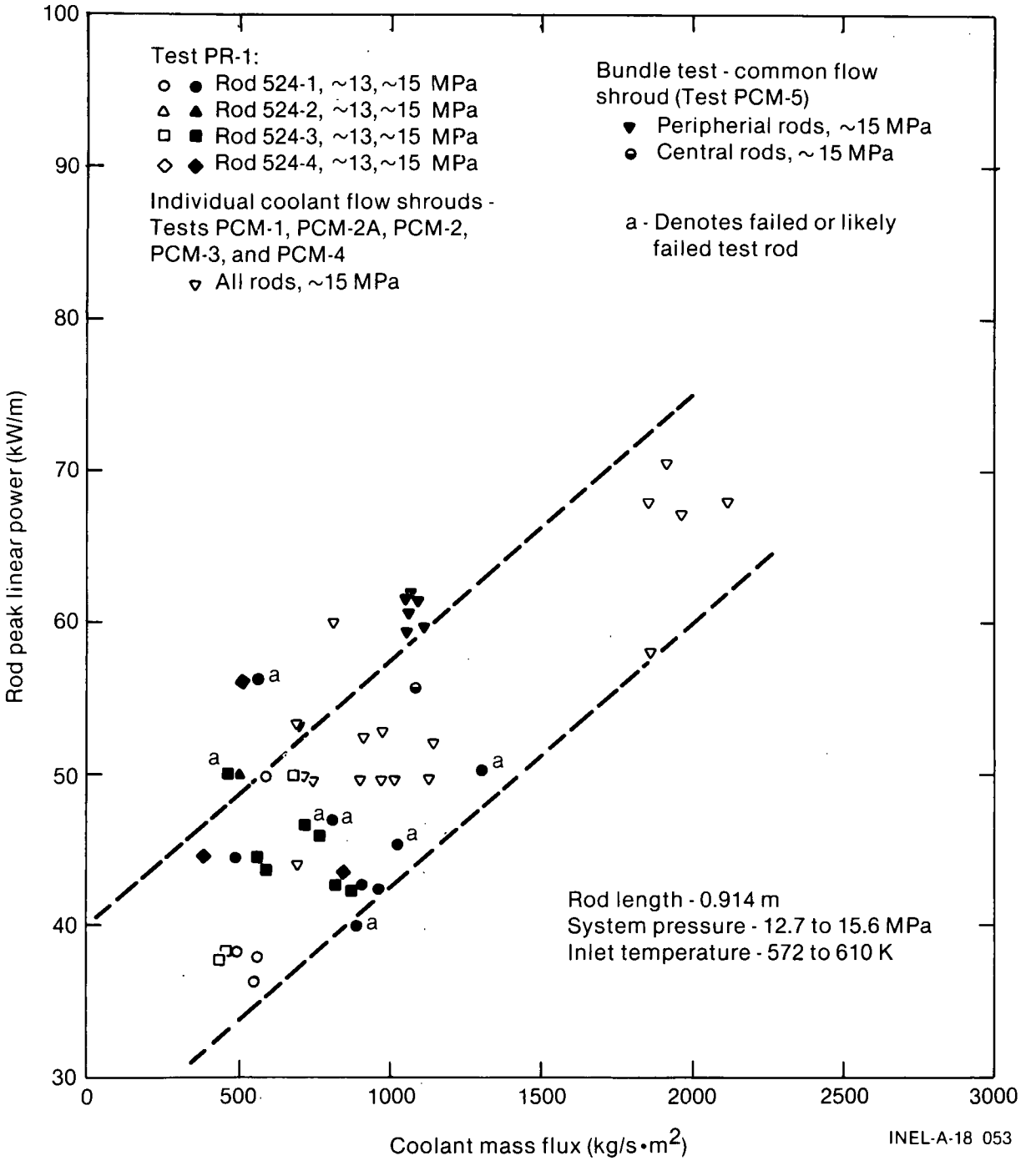

Figure 27. Comparison of conditions at first indication of boiling transition for Test PR-1 and PCM Test Series.

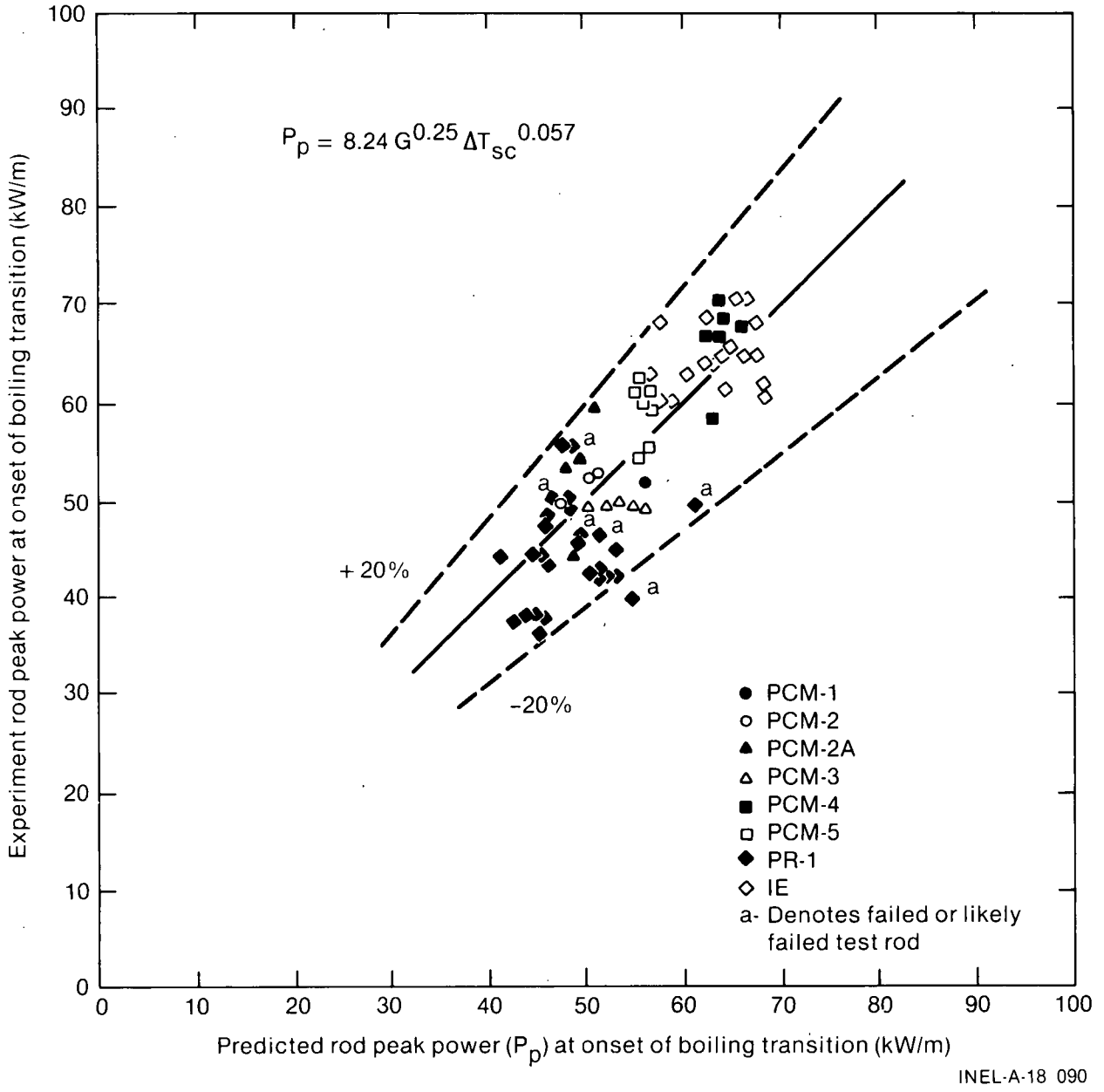

Figure 28. Measured and predicted linear peak rod power at the onset of boiling transition.

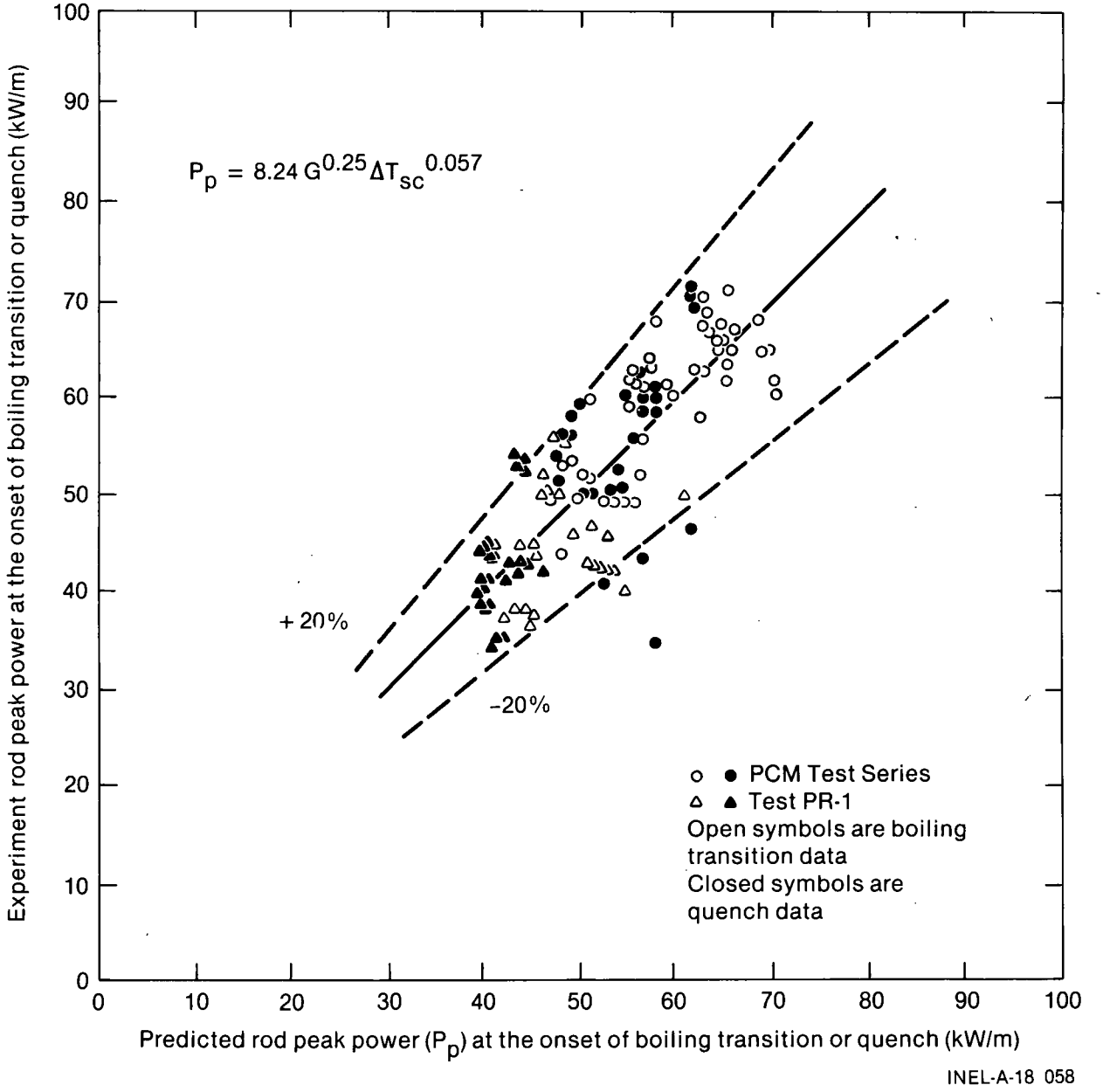

Figure 29. Comparison of conditions at the onset of boiling transition (DNB) and quenching.

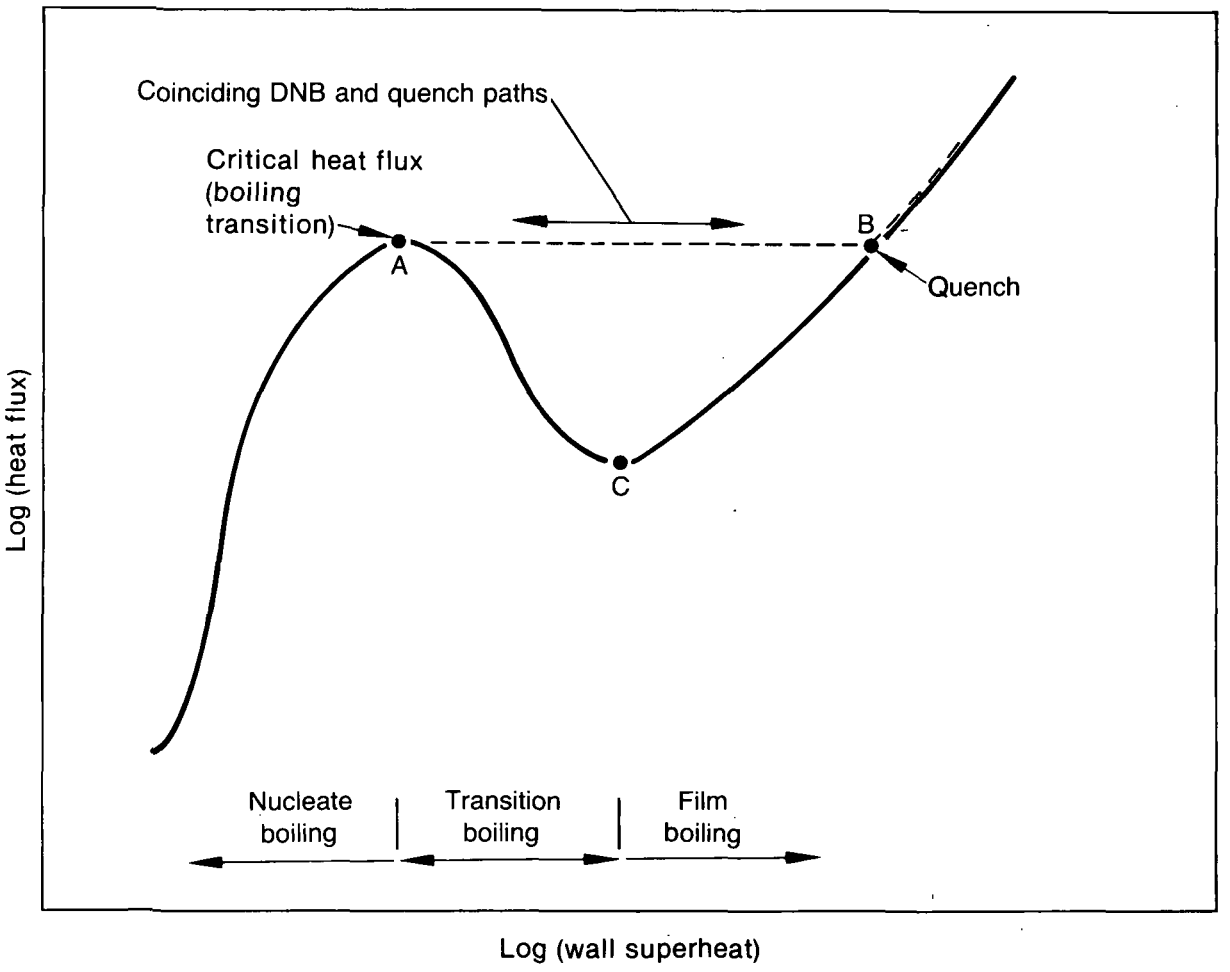

Figure 30. Classical boiling curve illustrating film boiling and quenching paths for high pressure (low critical quality) boiling transition scenario.

tube with water at low pressures (0.20 to 0.71 MPa), that "prolonged film boiling below the burnout flux could not be maintained." MacBeth summarizes this behavior (see Figure 30) by the statement: "Thus, it seems that in a forced-convection system, a region corresponding to BC for pool boiling may or may not be attainable, depending on the system parameters."[16]

Summary of Test PR-1 Fuel Rod Behavior During PCM Testing

As mentioned previously, the four Test PR-1 fuel rods attained widely varying degrees of damage during the PCM test phase. Although cladding thermocouple positioning on the rods was not optimum for temperature measurements in the high temperature film boiling region, the steady state peak temperatures can be estimated by analytical methods. The stabilized cladding peak temperatures at the 0.533-m elevation are shown in a histogram in Figure 31 for those rods that attained boiling transition during the identified PCM cycles. The temperature estimates were calculated assuming steady state film boiling conditions using the Groeneveld 5.9 heat transfer correlation,[17] and the calculated local (0.533-m elevation) power and coolant conditions at the onset of boiling transition. The histogram provides a relative indication of the time-temperature exposure of each test rod, even though the magnitude of the exposure is obviously overestimated.

Noted in Figure 31 is the detected time of failure for Rod 524-1. This rod had attained boiling transition for at least 8 min on eight occasions prior to failure. Figure 32 illustrates the cladding

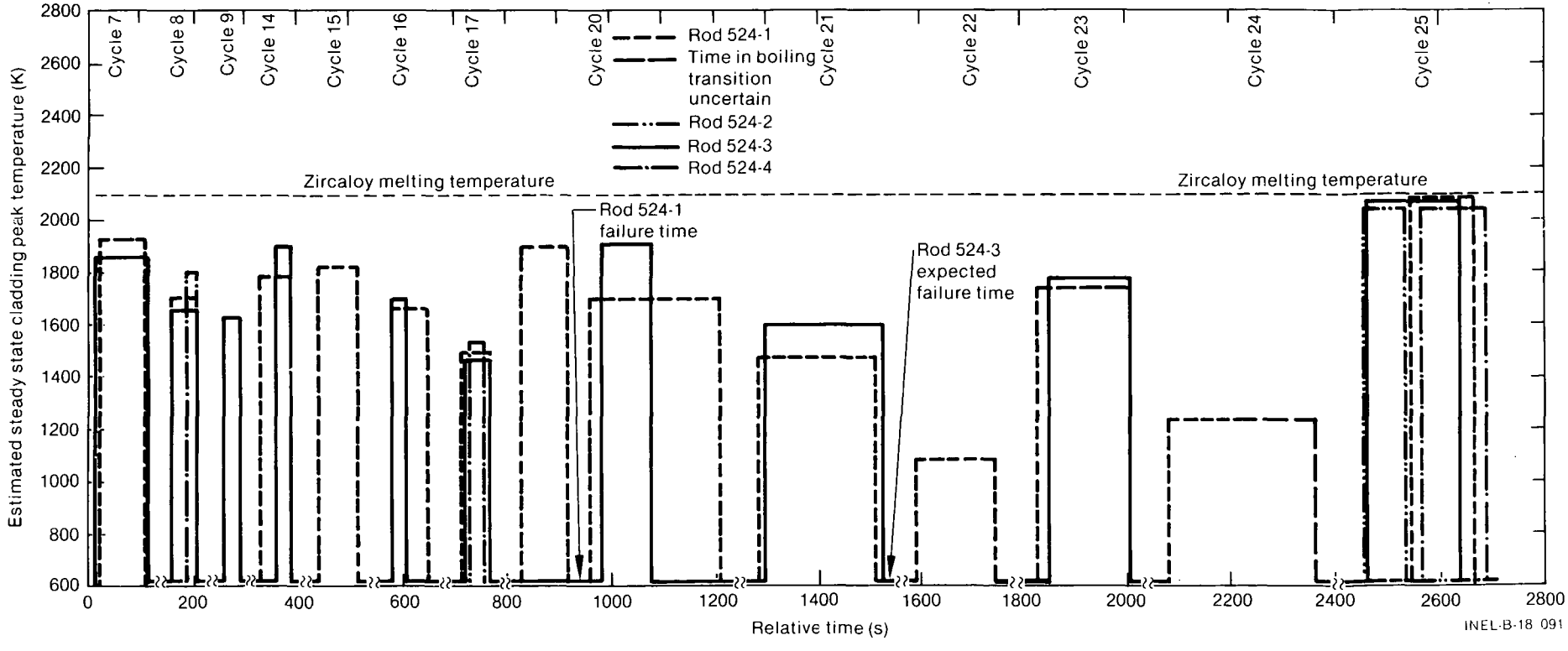

Figure 31. Histogram of estimated steady state cladding peak temperatures at the 0.533-m elevation during Test PR-1 PCM testing.

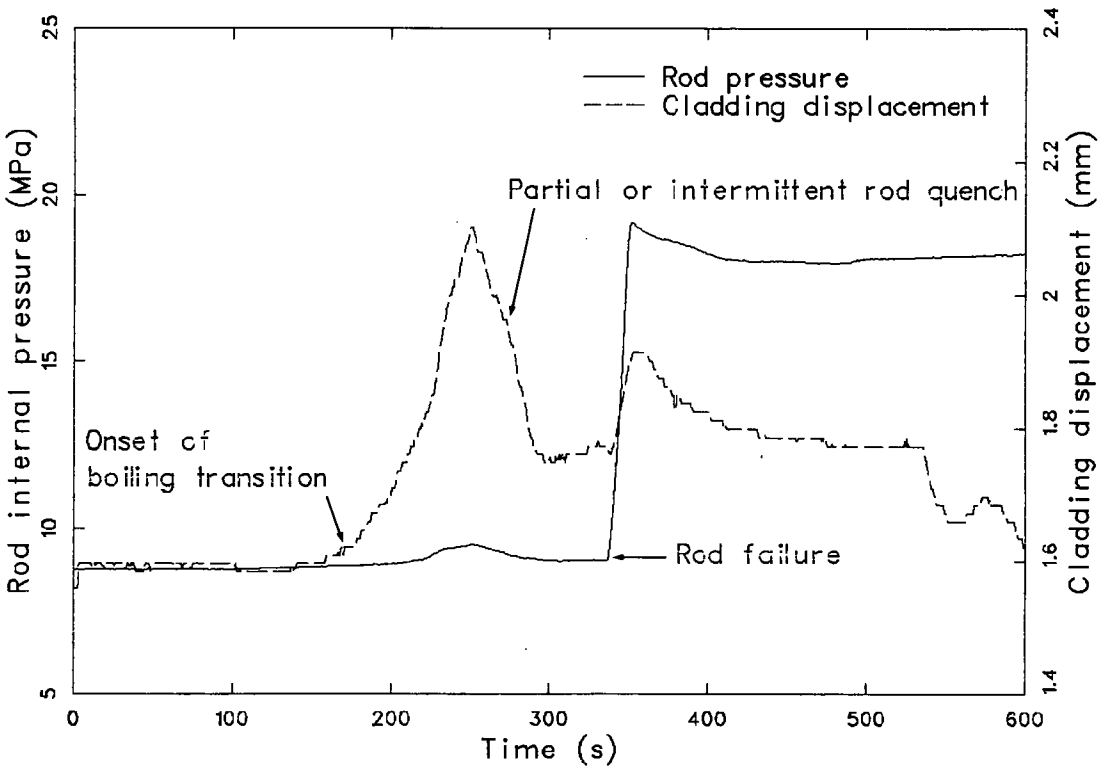

Figure 32. Rod 524-1 cladding elongation and rod internal pressure showing fuel rod failure indication following quench.

elongation response and the rod internal pressure for Rod 524-1 at approximately the time of rod failure. The internal rod pressure increase to system pressure[a] at about 285 s in Figure 32 suggests that the rod failed during the intermittent (or partial) rod quench, due to thermal shock on the highly embrittled cladding. Calculations using the Cathcart oxidation kinetics[3] and the liscensing criterion for embrittlement failure of 17% equivalent cladding reacted (ECR) yields an effective isothermal temperature of 1730 K during the 8.1 min of high temperature film boiling (prior to failure) on Rod 524-1. Following failure, Rod 524-1 was operated under high temperature conditions for at least 18 min.

Using similar criterion as for Rod 524-1, and the relative temperature history (Figure 31) for Rod 524-3, this rod (524-3) would be expected to fail due to extensive oxygen embrittlement upon quenching during PCM Cycle 21 (10.3 min at high temperatures). Since the rod internal pressure instrument for Rod 524-3 was not functioning, failure cannot be verified. It is, however, very likely that Rod 524-3 failed prior to PCM Cycle 25 and the RIA testing. Following PCM Cycle 21, Rod 524-3 was operated in high temperature film boiling for an additional 5.6 min prior to the RIA testing.

As shown in Figure 31, Rods 524-2 and 524-4 experienced very limited times at high temperatures during the PCM testing. Rod 524-2 attained boiling transition only once, during PCM Cycle 25, prior to the RIA testing. The 80 s of high temperature operation for Rod 524-2 likely resulted in some cladding collapse onto the fuel stack, but extensive embrittlement would not be expected. The 165 s of high temperature operation for Rod 524-4 would also suggest cladding collapse onto the fuel stack, but modest cladding oxidation and embrittlement.

a. The system pressure at the detected failure time was about 13 MPa. The rod internal pressure response shown in Figure 32 is offset by about 5.3 MPa.

RESULTS OF TEST PR-1 POWER BURST OPERATION

Three progressively severe RIA power excursions were conducted to conclude Test PR-1. Prior to the bursts, all four test rods had attained various degrees of damage during the PCM testing. Rod 524-1 had extensively oxidized and embrittled cladding, and was waterlogged prior to the first burst. Rod 524-3 was also extensively damaged due to cladding oxidation and embrittlement, and was very likely waterlogged prior to the first power burst. Rods 524-2 and 524-4 were intact prior to the bursts, but likely had oxidized and collapsed (onto the fuel stack) cladding in the high temperature film boiling zones. All four test rods were, therefore, atypical relative to normally operated BWR-6 type fuel rods, and would be expected to require less energy insertion to failure.

An objective of Test PR-1 was to evaluate the thermal response of the test rods during progressively severe power excursions and compare the results with existing fuel rod behavior models. The primary measurements for evaluating thermal response were the fuel thermometry (centerline and off-center thermocouples), cladding surface thermocouples, and the cladding elongation response. All fuel and cladding thermocouples were located at the peak power elevation (0.452 m) except for two cladding surface thermocouples and the internal cladding thermocouples for Rod 524-4. Due to the previous high temperature PCM operation, some of the fuel and cladding thermometry were failed or deemed unreliable. The reactor and test rod energy data for each power burst are summarized in Table 9. The maximum measured values for cladding and fuel temperatures, cladding elongation, and internal rod pressure are listed in Table 10 for each power burst. Specific results for each burst are presented subsequently.

Power Burst 1

Prior to Power Burst 1, operable fuel rod thermometry included the fuel centerline thermocouple, two off-center fuel thermocouples, and two cladding surface thermocouples on each of Rods 524-1 and 524-2; one off-center fuel thermocouple and three cladding surface thermocouples on Rod 524-3; and three cladding surface thermocouples[a] on Rod 524-4. All four LVDTs for measuring cladding elongation were operable.

A radial average fuel enthalpy at the axial peak elevation of 107 cal/g UO_2 (123 cal/g UO_2 peak local fuel enthalpy) was achieved during the first power burst. The maximum cladding surface temperature measured on the four rods was 850 K on Rod 524-2. Film boiling was detected for about 4 s on each test rod. Maximum fuel temperatures of 2140 and 1625 K were measured by the fuel centerline and off-center thermocouples, respectively, on Rod 524-2.

During the power burst, the internal pressure transducer on Rod 524-1 indicated a pressure pulse of 1.2 MPa due to steam formation in this waterlogged fuel rod. A pressure increase of 0.4 MPa was indicated by the system pressure transducers. No indications of additional rod failures were observed. Following the power burst, a steady state heat balance of the assembly was conducted to evaluate fuel loss during the burst. No change in test rod power generation was detected, suggesting minimal fuel loss from the assembly.

a. Only one cladding surface thermocouple on Rod 524-4 was located at the 0.452-m elevation.

Table 9. Test PR-1 power burst energy data

Power Burst	Reactor Period (ms)	Reactor Peak Power (MW)	Reactor Energy Release to Time of Scram (MJ)	Test Fuel Rod Total Energy (cal/g UO_2)	Radial Average, Peak Fuel Enthalpy (cal/g UO_2)	Peak Fuel Enthalpy (cal/g UO_2)
1	42.7	130	110	172	107	123
2	8.7	2650	112	210	144	165
3	6.2	5700	158	294	212	244

Table 10. Maximum measured fuel rod parameters during Test PR-1 power excursions

Power Burst	Test Rod	Maximum Cladding Temperature (K)	Maximum Fuel Centerline Temperature (K)	Maximum Fuel Off-Center Temperature (K)	Maximum Cladding Elongation Change (mm)	Maximum Internal Rod Pressure (MPa)	Comment
1	524-1	795	1120	1425	2.6	1.2 pulse	Rod previously failed during PCM testing.
	524-2	850	2140	1625	2.5	2.6	—
	524-3	760	(X)[a]	1575	2.0	(X)	Rod probably failed during PCM testing.
	524-4	695	(X)	(X)	2.1	1.3	—
2	524-1	1165	1065	1250	Rod separated	5.5 pulse	Rod separation indicated by cladding elongation.
	524-2	1180	2220	(X)	5.8	2.7	—
	524-3	1345	(X)	(X)	Rod separated	(X)	Rod separation indicated by cladding elongation.
	524-4	1180	(X)	(X)	4.5	1.3	—
3	524-1	(X)	(X)	1825	Rod separated	6.7 pulse	Additional rod breakup likely.
	524-2	1615	2750	(X)	8.7	3.35	Rod failed 2.5 s after burst peak power.
	524-3	(X)	(X)	(X)	Rod separated	(X)	Additional rod breakup likely.
	524-4	1290	(X)	(X)	7.8	1.55	No failure observed.

a. (X) indicates failed instrument(s).

Measured thermal response parameters were compared to the FRAP-T5[a] fuel rod behavior code[16] to assist in modeling efforts for the code, and to provide an estimate of the inherent measurement time delay associated with the various thermometry. A comparison between measured and FRAP-T5 predicted fuel centerline temperatures for Rod 524-2 during Power Burst 1 is shown in Figure 33. The centerline and off-center temperature calculations for Burst 1were made using coolant conditions calculated by the RELAP5[b] thermal-hydraulics code.[17] The measured fuel centerline temperature initially increased slighty slower than the predicted temperature. Calculations indicate that the response of the thermocouple system is fast enough to follow the fuel temperature changes during Burst 1. The measured centerline peak temperature was about 90 K higher than predicted. A comparison between the measured and predicted off-center fuel temperatures for Rod 524-2 is shown in Figure 34. This temperature response is typical of the responses of all the operable off-center thermocouples. The measured and predicted off-center temperature rise times are nearly identical. The measured and predicted off-center peak temperatures are almost equal. FRAP-T5 underpredicts the fuel centerline peak temperature, but predicts the off-center temperature quite accurately. This implies that the fuel thermal conductivity calculated by the FRAP model is too high.

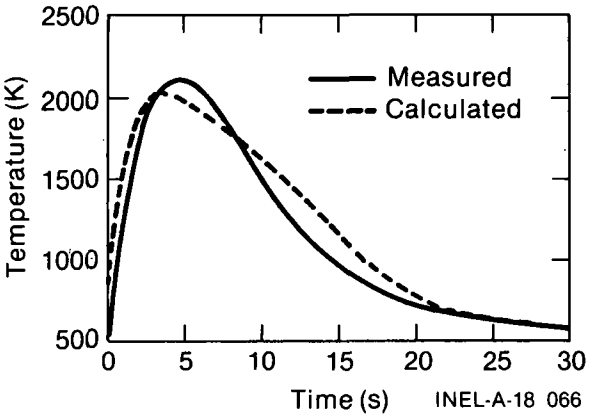

Figure 33. Calculated and measured fuel centerline temperature, Rod 524-2, Burst 1.

a. FRAP-T5, Idaho National Engineering Laboratory Code Configuration Control Number H017582B.

b. RELAP5/MOD1/001, Idaho National Engineering Laboratory, Configuration Control Number F00021.

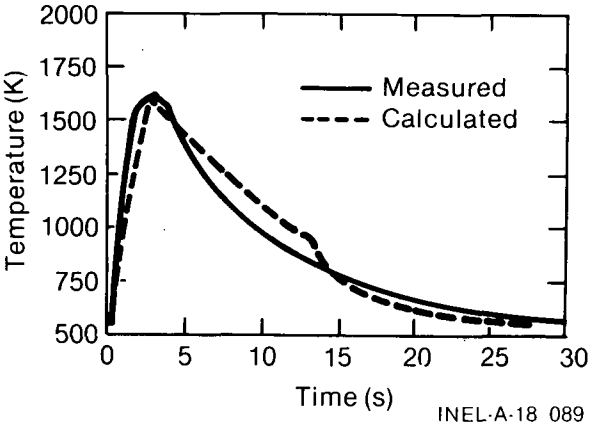

Figure 34. Calculated and measured fuel off-center temperature, Rod 524-2 (180-degree orientation), Burst 1.

There is a small difference between the measured and predicted fuel temperature response as the rod is cooled. The FRAP-T5/RELAP5 models overpredict the temperature by a small amount for a short time just after the peak temperature occurs. This is attributed to the heat transfer coefficients calculated by RELAP5. Both fuel temperature measurements and predictions indicate nearly pretransient temperatures in the time frame shown in Figure 34 (30 s).

Figure 35 presents a comparison of the measured (corrected[c] and uncorrected) and predicted cladding surface temperature responses for Rod

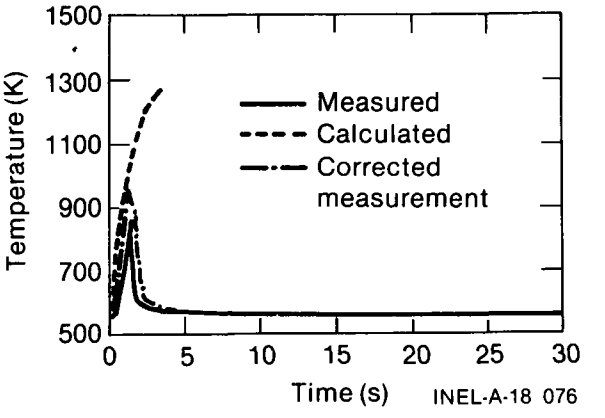

Figure 35. Calculated and measured cladding surface temperature, including corrected temperature measurement, Rod 524-2 (180-degree orientation), Burst 1.

c. The methodology for correcting the measured cladding temperatures for response time is presented in Appendix E of this report.

524-2 during the power burst. The FRAP-T5 code was used for this comparison. The thermal-hydraulic conditions calculated by RELAP5 were not used for the Burst 1 cladding temperature estimates, since the time at the onset of film boiling was overestimated. Cladding elongation estimates were made using FRAP-T5 in conjunction with the RELAP5 calculated thermal-hydraulics.

Figure 36 compares the measured and predicted cladding axial displacement. The calculated time at the onset of film boiling was adjusted to the measured time for these comparisons. The measured cladding displacement indicates film boiling occurred for approximately 4 s. The film boiling time indicated by the cladding surface temperature measurement (Figure 35) is only about 2 s. This is probably due to "fin cooling" of the surface mounted thermocouple. The predicted cladding axial displacement is not in agreement with the measured displacement. Since both time in film boiling and cladding temperature attained are overpredicted, the cladding displacement would be expected to also be overpredicted. However, the calculated permanent rod elongation would not be expected.

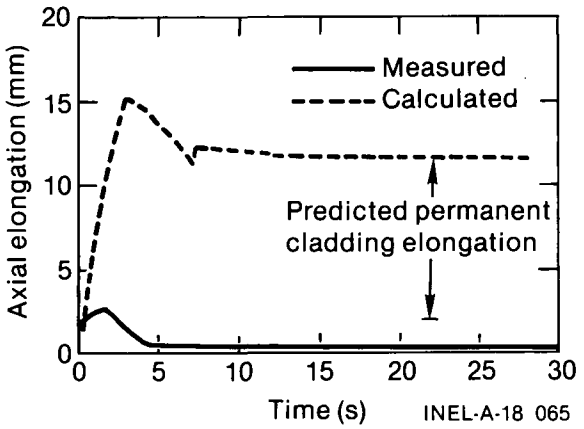

Figure 36. Calculated and measured cladding axial elongation, Rod 524-2, Burst 1.

Power Burst 2

The centerline and one off-center thermocouple on Rod 524-1, and the centerline thermocouple on Rod 524-2 were operable during Power Burst 2. At least one cladding surface thermocouple was operable on each rod prior to the transient. A radial average fuel enthalpy at the axial peak of 144 cal/g UO_2 (165 cal/g UO_2 peak local fuel enthalpy near the pellet surface) was reached in the second power burst. The maximum measured cladding surface temperature was 1345 K on Rod 524-3. The maximum time in film boiling was about 7 s on Rod 524-3. The internal pressure transducer on Rod 524-1 indicated a 5.5-MPa pressure pulse due to steam formation in this rod during the burst. A loop pressure increase of about 0.6 MPa was measured by the system coolant pressure transducers.

The LVDT for Rod 524-3 indicated that this rod fractured and separated during the second power burst. The internal pressure transducer for this rod had been inoperable since the beginning of the test; therefore, the rod failure time could not be determined. The LVDT for Rod 524-1 also indicated that this rod separated during the burst. No significant fuel loss was detected for any of the four fuel rods during the posttransient steady state operation.

The measured and FRAP-T5 predicted fuel centerline temperatures during the second power burst are shown in Figure 37 for Rod 524-2. All FRAP-T5 calculations for Burst 2 were made using coolant conditions calculated by the RELAP5[a] thermal-hydraulics code.[17] As seen in Figure 37, the predicted temperature increase is faster than the measured increase due to the inherent delay time in the centerline thermocouple response. The measured peak temperature of about 2210 K agrees fairly well with the predicted maximum of 2140 K. As was observed during Burst 1, the measured centerline cooling rate was slightly faster than predicted over the time range

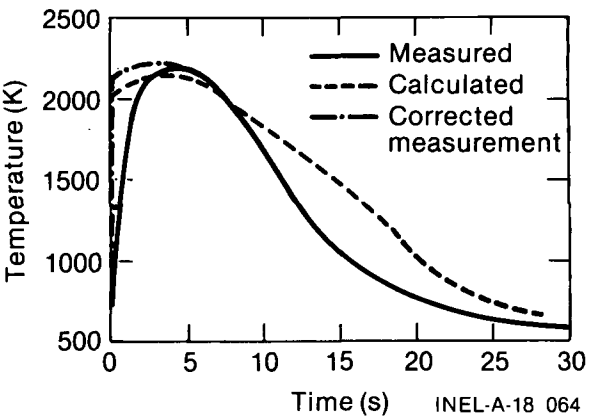

Figure 37. Calculated and measured fuel centerline temperature, including corrected temperature measurement, Rod 524-2, Burst 2.

a. RELAP5/MOD1/001, Idaho National Engineering Laboratory, Configuration Control Number F00021.

of the calculation (30 s). Also shown in Figure 37 is the fuel centerline temperature response corrected for thermocouple response time. The corrected peak temperature is only 10 K higher than measured, but the corrected fuel temperature rise time is much faster. The methodology used to make fuel (and cladding) thermocouple temperature measurement corrections is presented in Appendix E.

The Rod 524-2 cladding displacement indicated that film boiling occurred for about 5 to 6 s. The cladding surface temperature measurements indicate that film boiling occurred for a maximum of 4 s (see Figure 38). This difference in film boiling time can again be attributed to the fin cooling effect of the cladding surface thermocouple. The predicted film boiling duration was not in good agreement with the measured values. Also shown in Figure 38 is the corrected cladding surface temperature response. The maximum temperature is in better agreement with the calculated temperature, and the duration of film boiling is in good agreement with that indicated by the cladding displacement.

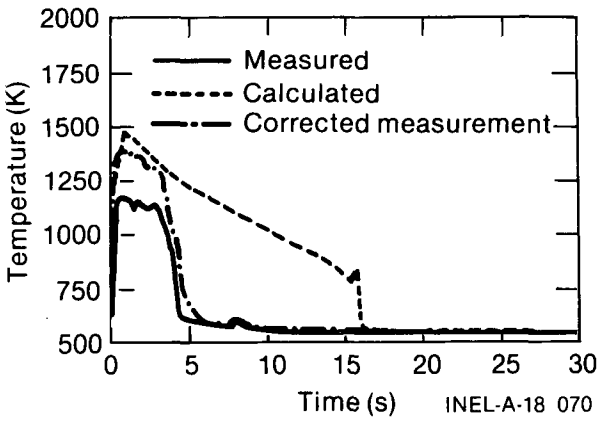

Figure 38. Calculated and measured cladding surface temperature, including corrected temperature measurement, Rod 524-2 (180-degree orientation), Burst 2.

Power Burst 3

The fuel centerline thermocouple of Rod 524-2 and one off-center fuel thermocouple of Rod 524-1 were operable prior to power Burst 3; both failed during the transient. At least one cladding surface thermocouple on each test rod was operable prior to the transient. A radial average fuel enthalpy at the axial peak of 212 cal/g UO_2 (244 cal/g UO_2 peak local fuel enthalpy near the pellet surface) was reached in the third power burst. The maximum indicated cladding surface temperatures on Rods 524-1 and 524-3 (both failed rods) were above the thermocouple melting point (~1640 K). Maximum fuel temperatures of 2750 and 1825 K were measured by the fuel centerline and off-center fuel thermocouples for Rods 524-2 and 524-1, respectively.

The internal pressure transducer of Rod 524-1 indicated a 6.7-MPa pressure pulse due to steam formation in this rod. A loop pressure increase of about 0.9 MPa was measured by the system coolant pressure transducers. The flowmeter for Rod 524-1 indicated zero shroud flow after the power burst, indicating blockage of the annular flow area due to fuel swelling and/or relocation within the shroud.

The internal pressure transducer for Rod 524-2 indicated that this rod failed about 2.5 s after the time of peak power. The measured fuel centerline temperature for Rod 524-2 is shown compared to the FRAP-T5 prediction in Figure 39. The FRAP-T5 calculations for Burst 3 were made using coolant conditions calculated by the RELAP5 code. As seen in Figure 39, the predicted centerline temperature increases faster than the measured temperature during the initial temperature rise. The centerline thermocouple materials melt at ~2500 K. When melting occurs, a junction can be formed above the original junction at an elevation where melting last occurs. This effect is shown in Figure 39. The temperatures measured between about 2 s and 14 s are at the melting front of the thermocouple wires. The measurements after about 14 s are at the axial elevation where a new thermocouple junction was formed when the wires were melted together. A

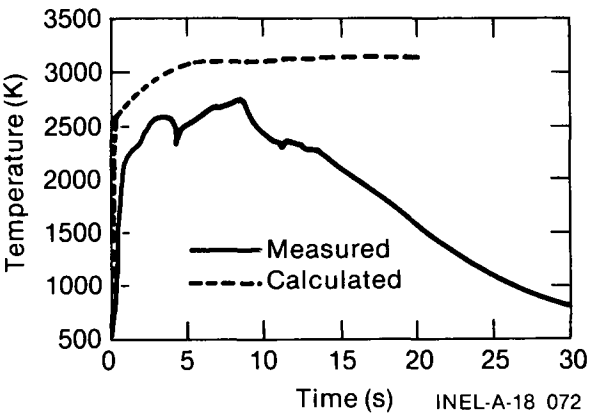

Figure 39. Calculated and measured fuel centerline temperature, Rod 524-2, Burst 3.

correction to the fuel centerline temperature response could not be made due to failure of the centerline thermocouple.

Failure of test Rod 524-2 was predicted by FRAP-T for Power Burst 3, due to cladding strain rate, at about 70 ms following peak power. As noted previously, an indication of failure on Rod 524-2 was observed at about 2.5 s after peak power.

A comparison of the calculated and measured cladding surface temperature for Rod 524-2 is presented in Figure 40. FRAP-T5/RELAP5 calculations do not predict the rod to quench during the time range of the calculation. Due to the fin effects of the surface mounted thermocouple, a direct comparison of the predicted and measured cladding temperature response should not be made. The corrected cladding surface temperature measurement is also shown in Figure 40 and is in relatively good agreement with the maximum calculated cladding temperatures.

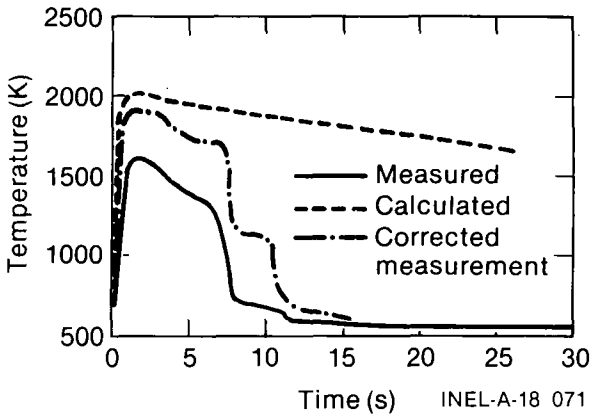

Figure 40. Calculated and measured cladding surface temperature, including corrected temperature measurement, Rod 524-2 (180-degree orientation), Burst 3.

Power Burst Summary

Rod 524-2 failed during the power burst testing at a radial average peak fuel enthalpy of 212 cal/g UO_2. Rod 524-2 had experienced only a short duration (~60 s) of high temperature operation during the PCM test phase. Rod 524-4 was the only rod backfilled with argon and it did not fail during the power burst testing. During the lowest energy burst, measured cladding temperatures on Rod 524-4 were between 120 and 235 K higher than the helium filled test rod temperatures. The measured cladding peak temperature on the argon filled test rod was about 1290 K during Power Burst 3, whereas cladding temperatures above the melting point of the thermoelements (~1640 K) were likely on the helium filled test rods during Burst 3.

Rapid steam formation in previously failed Rod 524-1 (and probably Rod 524-3) produced very sharp pressure pulses during each power burst. This is the first known power burst testing of a waterlogged fuel rod at typical operating temperatures and pressures. During Burst 3, the source pressure pulse was attenuated to about 0.9 MPa at the location of the system coolant pressure transducers (above the shroud outlets). As evidenced by the power calibration checks made after Bursts 1 and 2, no significant amount of fuel was expelled from the Rods 524-1 or 524-3 flow shrouds. This indicates that the fuel pellets in the waterlogged rod(s) did not fragment into small particles during the first two power bursts.

The centerline temperature measurement for Rod 524-2 during Burst 2 was corrected for thermocouple response delay. The measured (uncorrected) peak temperature was only 10 K low, but the response time during the initial fuel temperature rise was much too slow. Corrections were also made to the Rod 524-2 cladding thermocouple temperature response during Bursts 2 and 3. These corrections, required because of fin cooling effects, show that the FRAP-T5 calculated maximum cladding temperatures are quite good; however, the duration of film boiling was generally overpredicted. A comparison of the calculated quench times and the quench times determined from the cladding temperature measurements (uncorrected) should not be made due to fin effects of the cladding thermocouples.

POSTTEST FUEL ROD CONDITION

The Test PR-1 fuel rods encountered conditions ranging from normal operation to extreme power and coolant imbalance. Although the power and coolant conditions for each rod were very similar, the individual rods exhibited different degrees of fuel rod damage upon posttest examination. This section summarizes the posttest condition of each fuel rod and presents an interpretation of the damage of each fuel rod during Test PR-1.

Rod 524-1

During the PCM cycles of Test PR-1, Rod 524-1 was operated in high temperature film boiling for at least 8 min prior to rod failure. Rod failure at high temperature[18] under PCM conditions has been observed in previous PBF testing when the cladding wall thickness was completely converted to oxide and oxygen-stabilized alpha zircaloy. Failure due to thermal stresses on highly embrittled cladding (such as during rewet from high temperature operation) have been observed for lesser amounts of cladding oxidation.[19] Analytical temperature estimates using a modified version of the BUILD5 computer code[20] indicate effective isothermal temperatures of about 1730 K would result in embrittlement failure of Rod 524-1 at the observed failure time.

Following cladding rupture, Rod 524-1 was operated in high temperature film boiling for at least an additional 18 min, during which time both internal and external cladding wall oxidation occurred. The additional high temperature operation resulted in additional cladding oxidation and embrittlement over a large axial extent of the fuel rod.

An overall posttest view of Rod 524-1 is shown in Figure 41. The fuel rod coolant flow shroud was split during the posttest examination to facilitate visual examination of the bottom portion (0 to 54.5 cm from the bottom of the fuel rod end cap) of the rod. The split shroud is also shown in Figure 41. The rod exhibits extensive damage in the central region in the form of fuel and cladding loss, cladding oxidation, and fuel fragmentation.

The upper intact section of the fuel rod (above 58 cm) exhibits severe cladding oxidation, some fuel loss, and a split in the cladding which extends from 58 to about 71 cm. The primary oxidation in this region was likely due to the extended time in high temperature film boiling at this elevation. The observed failure of Rod 524-1 during the high temperature operation of PCM Cycle 20 likely occurred in this region due to extensive cladding oxidation. The cladding split up to the 71-cm elevation was probably a result of steam pressure buildup during the power burst operation on the highly embrittled, waterlogged fuel rod.

The middle section of Rod 524-1 (from about 29 to 58 cm) was the most severely damaged region of the four rods tested. Extensive fuel and cladding loss, fuel fragmentation, and cladding oxidation occurred over most of the region. Although cladding integrity was lost during PCM Cycle 20, based on on-line cladding elongation measurements, the rod geometry was maintained through the first power burst. During the second power burst (144 cal/g), the waterlogged rod separated, probably in the middle section of the rod, and some fuel was likely washed out due to the steam pressure buildup in the rod. The majority of the fuel fragmentation and rod breakup probably occurred during quench from the final power burst (212 cal/g). Blockage of the coolant flow channel due to fuel swelling and/or fragment relocation occurred during the third power burst.

Only limited damage in the form of cladding oxidation was observed in the lower section of Rod 524-1 (see Figure 41). Oxidation in this region likely occurred during the second and third power bursts due to high temperature film boiling operation.

Rod 524-2

High temperature film boiling operation on Rod 524-2 was detected only once prior to the power bursts for a brief (80 s) period (PCM Cycle 25). Extensive cladding damage due to oxidation was, therefore, not anticipated. A posttest overall view of Rod 524-2 is shown in Figure 42. As expected, extensive oxidation in the upper portion of the rod (60 to 75 cm) was not apparent. The overall mottled appearance of the rod is typical of the cladding oxidation previously observed as a result of low energy deposition power bursts.[21]

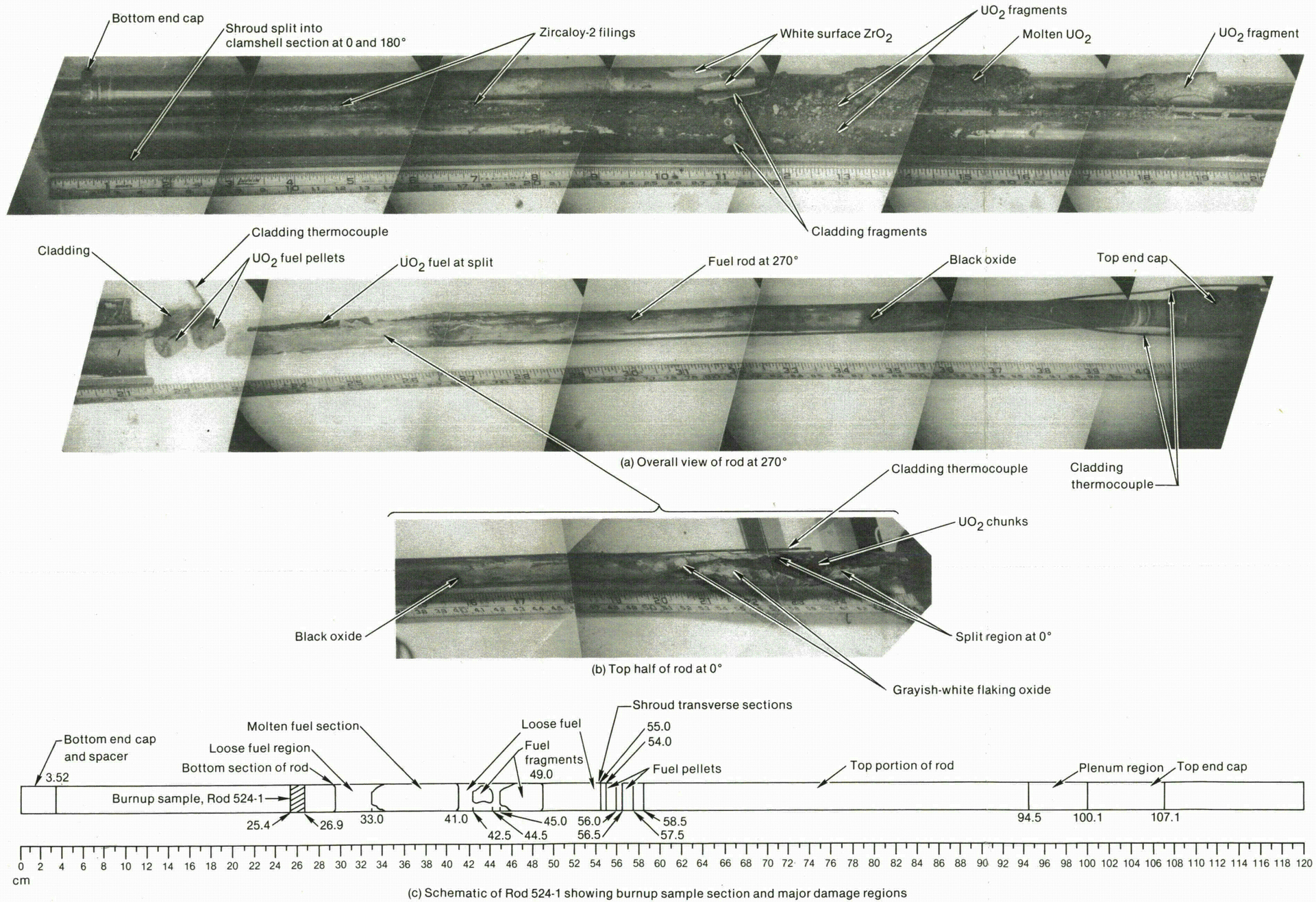

Figure 41. Overall posttest condition of Rod 524-1 following Test PR-1.

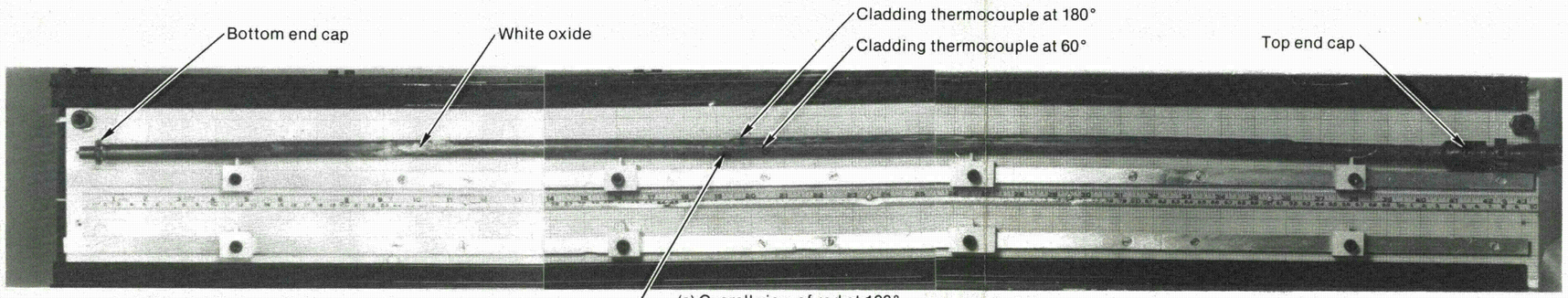

(a) Overall view of rod at 120°

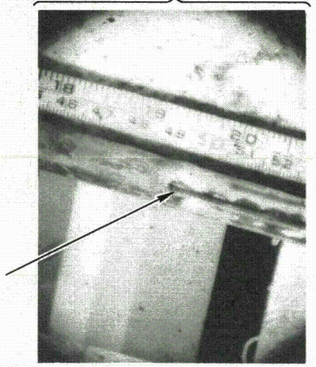

(b) Cladding thermocouple at 180°, 49 cm

(c) Hole in cladding located near end of 0° internal fuel thermocouple

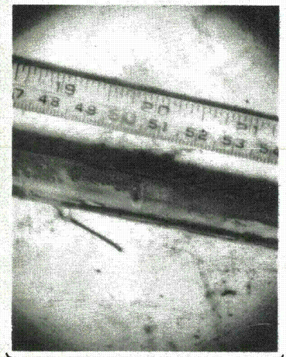

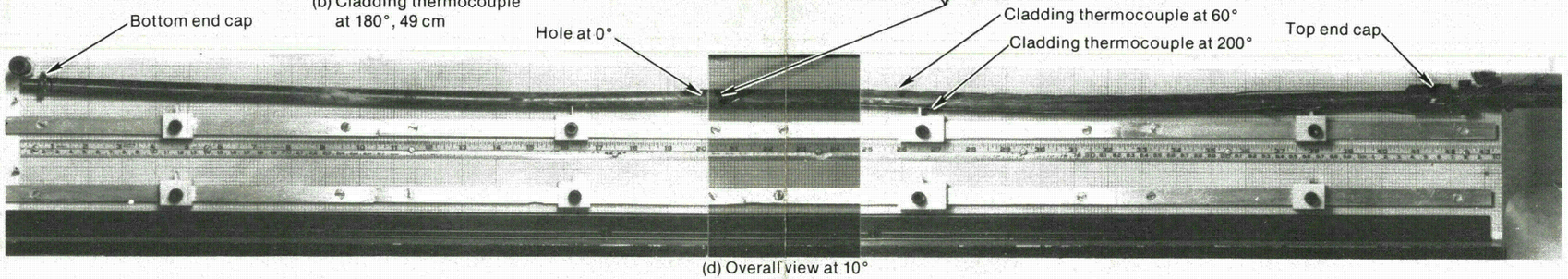

(d) Overall view at 10°

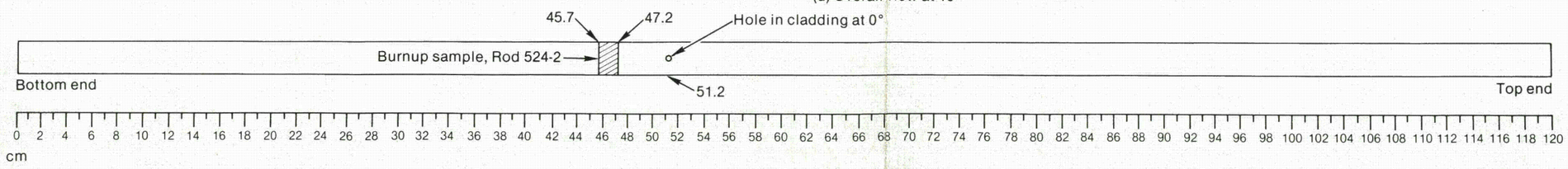

(e) Schematic of Rod 524-2 showing burnup sample section and region of damage

Figure 42. Overall posttest condition of Rod 524-2 following Test PR-1.

Rod 524-2 failed during the final (highest energy) power burst. The failure location can be seen on Figure 42 at the 50.5-cm elevation, which corresponds to the peak power elevation on the rod. The oval cladding breach was likely the result of high local cladding stresses from relocated fuel, or possibly cladding melt-through by high temperature (or molten) fuel. No other locations of cladding integrity loss were apparent from the visual examination.

Rod 524-3

Rod 524-3 was operated in high temperature film boiling for a total of about 15 min during the Test PR-1 PCM testing. Estimates of the cladding time-temperature history suggest that failure of the rod prior to the RIA testing was very likely. Cladding temperatures during the RIA testing apparently exceeded the melting point of the surface thermocouple thermoelements (~1640 K).

The overall posttest appearance of Rod 524-3 is shown in Figure 43. From the photographs, two regions of severe cladding damage are apparent. In the upper region, from 66 to 77 cm, a split in the cladding and extensive white oxide can be seen. Cladding oxidation in this region is predominately due to high temperature film boiling operation during the nine detected high temperature transients on Rod 524-3. Cladding breakup in the upper damaged section is typical of cladding embrittlement failure due to high stress or thermal shock. Initial cladding failure in this region probably occurred during the PCM testing.

The most severely damaged segment of Rod 524-3, from about 31 to 44 cm on Figure 43, exhibits severe cladding oxidation and fracturing, fuel fragmentation, and complete separation of the fuel rod. The cladding elongation measurement on this rod indicated rod separation during Burst 2 (144 cal/g). The third power burst (212 cal/g) likely precipitated most of the damage seen in this region due to the high energy of the pulse and the waterlogged condition of the fuel rod.

Rod 524-4

Rod 524-4 was the only Test PR-1 fuel rod with argon fill gas. The rod did not fail during the entire test operation. The rod experienced brief, high temperature film boiling operation during only three of the PCM cycles (cumulative time about 2.7 min), and therefore the cladding was not extensively oxidized or embrittled prior to the power burst operation. The short exposure to high temperatures prior to the power bursts, and the low conductivity (relative to helium) of the argon fill gas, probably attributed to the minimal damage (and non-failure) of Rod 524-4 during Test PR-1. The posttest appearance of the rod is shown in Figure 44. The overall mottled appearance of the rod is very similar to that observed on Rod 524-2, and is typical of high temperature oxidation during low energy RIA power bursts.

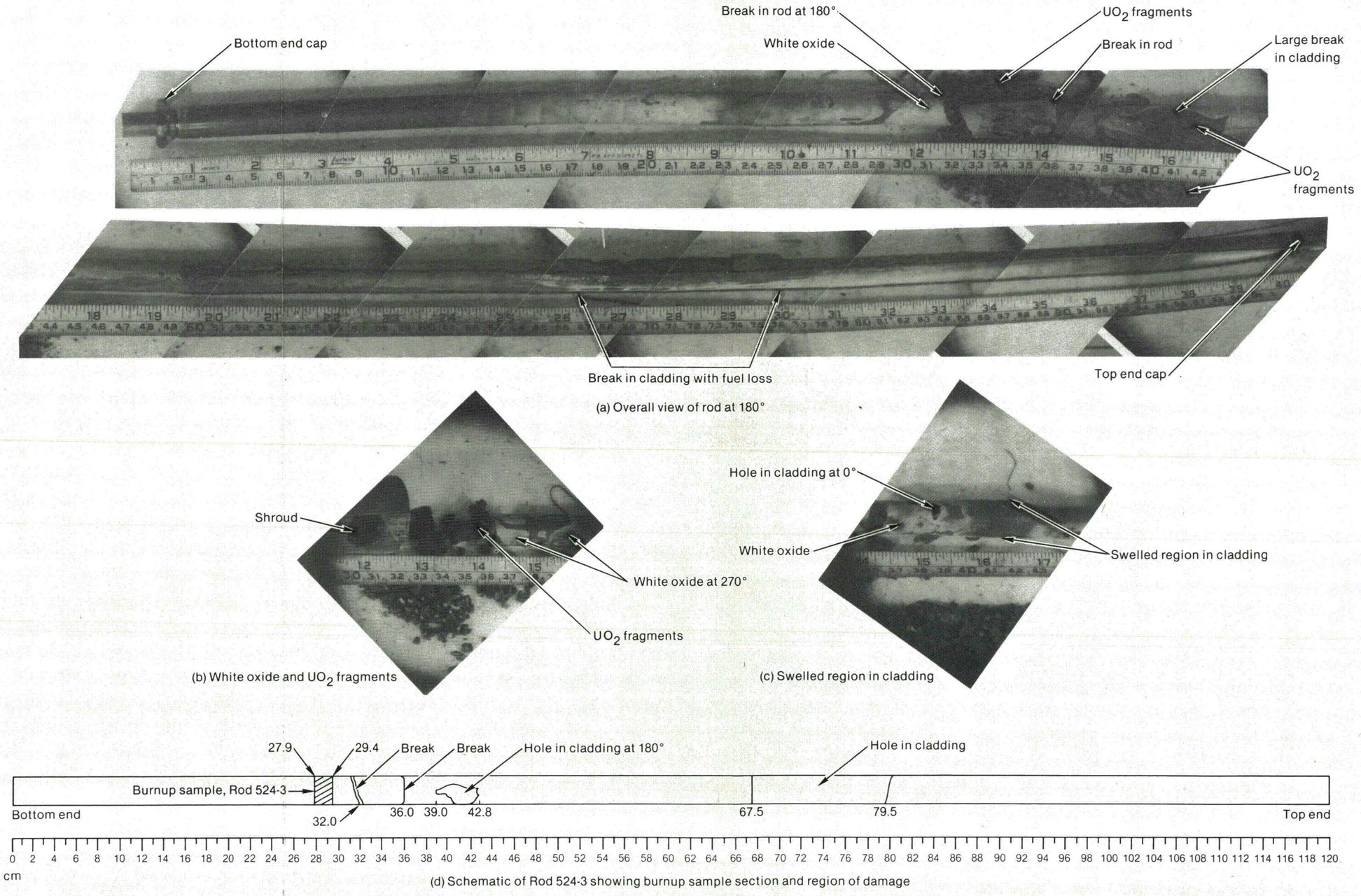

Figure 43. Overall posttest condition of Rod 524-3 following Test PR-1.

UNITED STATES
NUCLEAR REGULATORY COMMISSION
WASHINGTON, D. C. 20555

October 19, 1981

ERRATA SHEET

for

NUREG/CR-2126

NUCLEAR FUEL ROD BEHAVIOR DURING NORMAL AND ABNORMAL OPERATING CONDITIONS-RESULTS OF TEST PR-1

Performed by

EG&G Idaho, Inc.

for the

U.S. Nuclear Regulatory Commission

It has been discovered that pages 47 and 48 are missing in some copies of NUREG/CR-2126 (EGG-2102). If these pages are missing in the copy you received, you can obtain the missing page by writing to R.W. Garner, EG&G Idaho, P.O. Box 1625, Idaho Falls, ID 83415.

DIVISION OF TECHNICAL INFORMATION

AND

DOCUMENT CONTROL

Chief
Fuel Behavior Research Branch
Nuclear Regulatory Commission
Washington, D.C. 20555

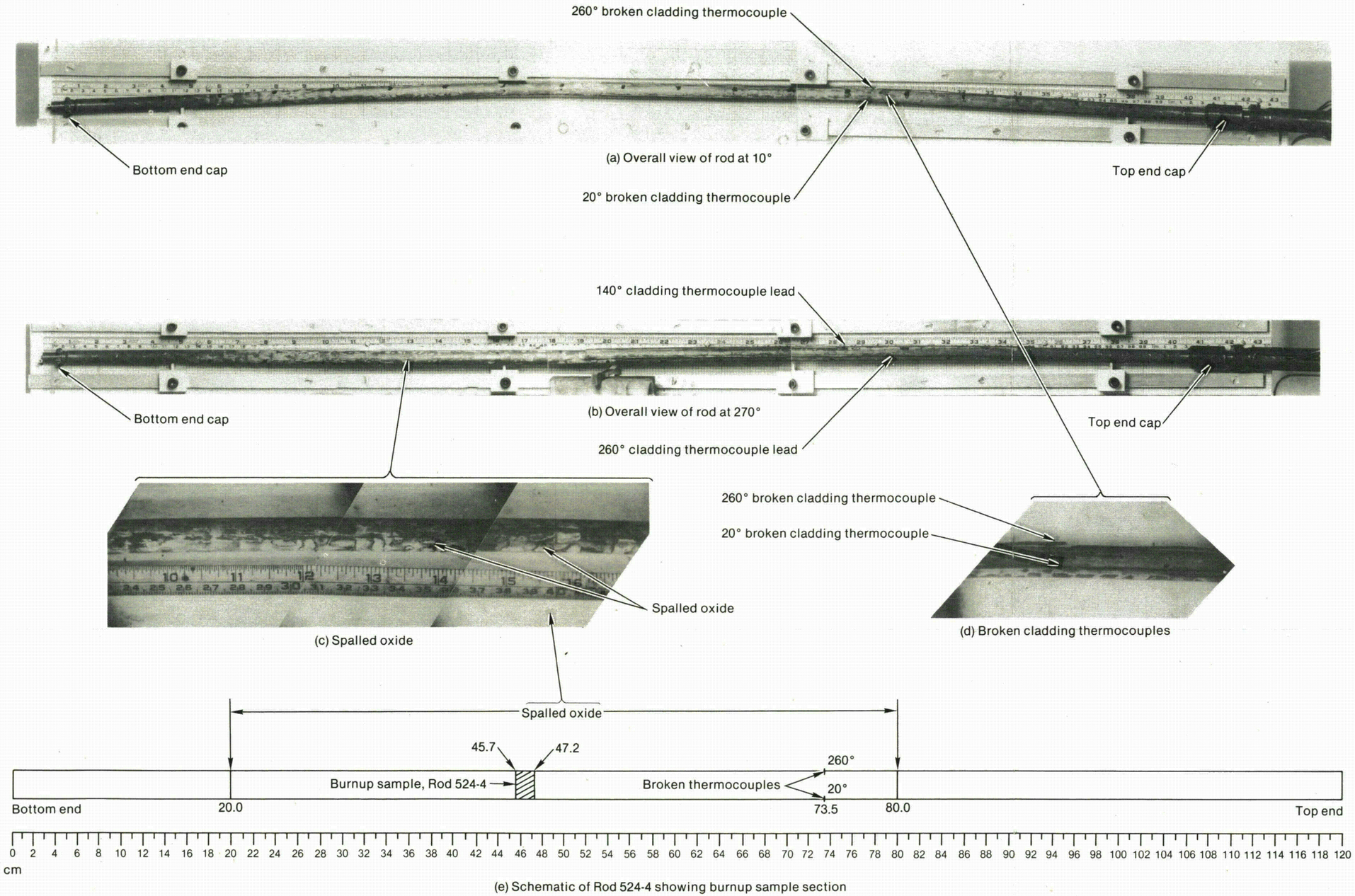

Figure 44. Overall posttest condition of Rod 524-4 following Test PR-1.

SUMMARY OF RESULTS AND CONCLUSIONS

Test PR-1 was conducted to evaluate both the steady state and transient thermal performance of nuclear fuel rods. Specific objectives included obtaining fuel rod thermal response data under steady state and power oscillation conditions, evaluating the conditions at the onset of boiling transition and return to nucleate boiling, and providing data on fuel thermal performance during RIA power excursions. Data from the experiment provide a basis for evaluation and development of fuel rod computer models under steady state and extreme operating conditions. The following results and conclusions are based on evaluation of the Test PR-1 data.

1. Fuel rod thermal response data obtained during the Test PR-1 steady state operation were consistent with results from the Gap Conductance Test Series, which employed similar design fuel rods. The effect of fuel density on centerline and off-center fuel temperatures was minimal; the effect of fill gas composition on the centerline and off-center fuel temperatures was significant. Fuel rods containing relatively low conductivity fill gas attain higher fuel temperatures than rods containing relatively high conductivity fill gas.

2. The measured fuel temperatures (centerline and off-center) for both the helium and argon filled test rods agreed fairly well with FRAPCON 2 code predictions during steady state operation.

3. Calculated effective UO_2 conductivities for the Test PR-1 helium filled fuel rods were in very good agreement with the cracked fuel pellet conductivity correlation (K_{eff}) developed from the Gap Conductance Test Series data. Based on the GC series and Test PR-1 data, correction to the solid pellet (MATPRO) fuel conductivity model to account for pellet cracking and relocation is required to properly estimate the fuel rod stored energy.

4. Large differences were observed between gap conductance values obtained by the power oscillation and steady state ($\int kdT$) methods. Test PR-1 and previous GC series data have shown that the thermal oscillator technique for determining gap conductance is unreliable except for a narrow range of operating parameters.

5. The conditions at the onset of boiling transition and return to nucleate boiling were evaluated at coolant pressures between 13 and 15.5 MPa. The boiling transition and quench data were consistent with trends obtained from previous PCM tests (on PWR rods) at similar pressures. Boiling transition was not observed at BWR pressures. Natural circulation apparently limited the minimum flow rate that could be achieved in the Test PR-1 geometry. A low temperature excursion associated with high quality boiling transition may have occurred, but was not detectable.

6. No discernible difference in the conditions at the onset of boiling transition and the conditions at return to nucleate boiling was apparent.

7. Rod 524-1 failed following about 8 min of intermittent high temperature operation. The estimated temperature history for Rod 524-3 also suggests a high probability of failure of this rod during the PCM testing. The likely cause of failure in each case was extensive embrittlement. In contrast, a positive indication of boiling transition on Rod 524-2 was observed only once during the PCM testing (~80 s in duration). Measured coolant conditions for each test rod were very similar, suggesting the possibility of interactive hydraulic coupling of the rods through the common upper and lower plenums.

8. RIA power bursts were conducted, resulting in radial averaged fuel enthalpies (at the axial peak location) of 107, 144, and 212 cal/g UO_2. Cladding elongation measurements on Rods 524-1 and 524-3 indicated that these rods separated during the second (144 cal/g UO_2) power burst. Both Rods 524-1 and 524-3 were likely waterlogged during the power burst operation. Rod 524-2 failed during the third

(212 cal/g UO_2) power burst, about 2.5 s after peak power. Rod 524-4, the only argon filled test rod, experienced maximum cladding temperatures that were less than the helium filled rods, and did not fail during the Test PR-1 operation.

9. Rod 524-1 was waterlogged during the burst testing since it had failed during the previous PCM transient test phase. The internal pressure transducer for this rod indicated pressure pulses of 1.2, 5.5, and 6.7 MPa during the three progressively severe power excursions. The pressure pulses were attenuated rapidly and resulted in system pressure increases (measured near the shroud outlets) of 0.4, 0.6, and 0.9 MPa, respectively. The contribution to the system pressure increases from Rod 524-3, which was very likely waterlogged, could not be determined.

10. Predictions of fuel centerline and off-center temperatures were made using the FRAP-T5 computer code in conjunction with thermal-hydraulic estimates from RELAP5. In general, fairly good agreement between measured and predicted temperatures was attained for the three RIA power bursts. Corrections to the fuel temperature measurements were required for Bursts 2 and 3 due to the inherent thermocouple response time lag. The duration of high temperature film boiling was overestimated by the RELAP5 calculations, resulting in overpredicted cladding axial elongation and cladding damage.

REFERENCES

1. R. W. Garner et al., *Gap Conductance Test Series-2, Test Results Report for Tests GC 2-1, GC 2-2, and GC 2-3*, NUREG/CR-0300, TREE-1268, November 1978.

2. G. A. Berna et al., *FRAPCON-2: A Computer Code for the Calculation of Steady State Thermal-Mechanical Behavior of Oxide Fuel Rods*, NUREG/CR-1845,December 1980.

3. D. L. Hagrman and G. A. Reymann (eds.); *MATPRO-Version 11, A Handbook of Materials Properties for Use in the Analysis of Light Water Reactor Fuel Rod Behavior*, NUREG/CR-0497, TREE-1280, February 1979.

4. D. N. Plummer et al., *Post Critical Heat Transfer to Flowing Liquid in a Vertical Tube*, MIT Report 72718-91, Massachusetts Institute of Technology, 1974.

5. J. G. Collier, *Convective Boiling and Condensation*, United Kingdom: McGraw-Hill Book Company, Limited, 1972, pp. 250-257.

6. F. N. Peebles and H. J. Garber, "Studies on the Motion of Gas Bubbles in Liquids," *Chemical Engineering Progress, 49*, 2, 1953, pp. 88-97.

7. S. S. Kutateladze and M. A. Styrtkovich, *Hydraulics of Liquid-Air Systems*, Gosenereoizdat, Moscow, 1958.

8. P. J. Berenson, *Transition Boiling Heat Transfer from a Horizontal Surface*, MIT Technical Report No. 17, March 1960.

9. P. J. Berenson, "Film Boiling Heat Transfer from a Horizontal Surface," *Journal of Heat Transfer, 83*, August 1961.

10. R. J. Moffat, *Experimental Methods in the Thermosciences*, Department of Mechanical Engineering, Stanford University, 1978.

11. F. S. Gunnerson and P. S. Dunphy, *A Study of Film Boiling, Quench, and Rewet Phenomena During High Pressure Power-Cooling-Mismatch Testing*, NUREG/CR-1623, EGG-2052, October 1980.

12. L. H. McEwen et al., *Heat Transfer Beyond Burnout for Forced Convective Bulk Boiling*, ASME 57-SA-49, 1957.

13. G. F. Stevens, D. F. Elliott, R. W. Wood, *An Experimental Investigation into Forced Convection Burnout in Freon, with Reference to Burnout in Water*, AEEW-R 321, 1964.

14. L. S. Sterman and N. G. Stiushin, "An Investigation into the Influence of Speed of Circulation on the Values of Critical Heat Flows for Liquid Boiling in Tubes," *Journal of Technical Physics, 22*, (USSR) 1952, p. 446.

15. L. S. Sterman, N. G. Stiushin, V. G. Morozon, "An Investigation of the Dependence of Critical Heat Flux on the Rate of Circulation," *Journal of Technical Physics, 1*, (USSR) 1956, p. 2250.

16. R. V. MacBeth, "The Burn-Out Phenomena in Forced-Convective Boiling," *Advances in Chemical Engineering Progress Symposium Series, 48*, 1968.

17. L. J. Siefken et al., *FRAP-T5: A Computer Code for the Transient Analysis of Oxide Fuel Rods*, NUREG/CR-0840, TREE-1281, June 1979.

18. D. T. Sparks and C. J. Stanley, *Power-Cooling-Mismatch Test Series, Test PCM-1 Fuel Rod Behavior Report*, NUREG/CR-0907, TREE-1374, August 1979.

19. D. K. Kerwin, *Test PCM-5 Fuel Rod Materials Behavior*, NUREG/CR-1430, EGG-2033, May 1980.

20. S. L. Seiffert and T. F. Cook, *Power-Cooling-Mismatch Test Series, Test PCM-4 Postirradiation Examination*, NUREG/CR-0238, TREE-1230, July 1978.

21. R. S. Semken et al., *Reactivity Initiated Accident Test Series, RIA Scoping Tests Fuel Behavior Report*, NUREG/CR 1360, EGG-2024, April 1980.

120555063566 1 ANR3
US NRC
RES
CHIEF
EXP ADV SAFETY TECH BRANCH
WASHINGTON DC 20555

EG&G Idaho, Inc.
P.O. Box 1625
Idaho Falls, Idaho 83415

BLOWBACK OF MICROFICHE ATTACHED TO REPORT NUREG/CR-2126

NUREG/CR-2126 FUEL ROD BEHAVIOR DURING TEST PR-1
EGG-2102 D.T. SPARKS et al; EG&G IDAHO INC.
UNCLASSIFIED JUNE 1981

1 OF 2

NUREG CR
2126
EGG 2102
6 81

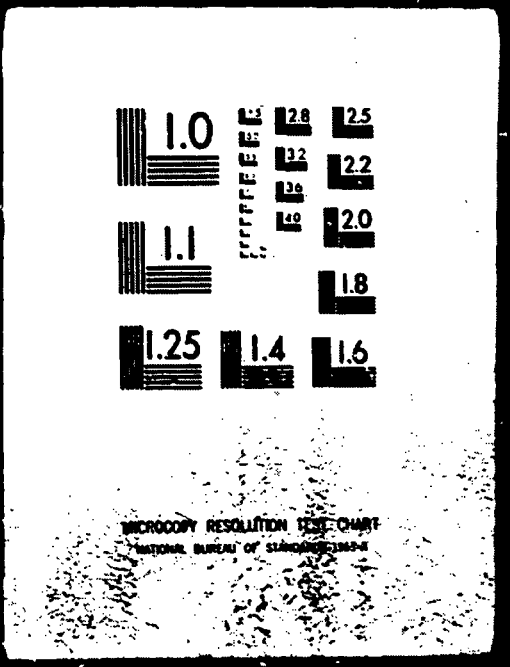

A 2

A

APPENDIX A

EXPERIMENT DESIGN AND CONDUCT

BLANK

PAGE

APPENDIX A

EXPERIMENT DESIGN AND CONDUCT

Test PR-1 was conducted to provide fuel rod thermal response data under steady state and transient conditions, to obtain information on conditions at the onset of boiling transition and return to nucleate boiling, and to evaluate fuel thermal performance and failure thresholds under reactivity initiated accident (RIA) power burst conditions. A description of the experiment design and an account of the experiment conduct are presented in this appendix.

EXPERIMENT DESIGN

The Test PR-1 hardware was originally designed for the Gap Conductance[A-1] Test Series (Test GC 2-4), with the objective of obtaining steady state and transient fuel rod thermal response information. The objectives of the test were subsequently expanded to include boiling transition and quench data during power-cooling-mismatch transients, and fuel temperature distributions during a series of reactivity initiated accident power excursions.

Fuel Rods and Flow Shrouds

Test PR-1 was conducted with four boiling water reactor (BWR) type test fuel rods identified as Rods 524-1, 524-2, 524-3, and 524-4. The active fuel length of each rod was 0.914 m, and the plenum volume was sized in proportion to the active fuel volume to be similar to the plenum/fuel volume ratio in full-size BWR fuel rods. Rods 524-1, 524-2, and 524-3 were backfilled with helium, and Rod 524-4 was backfilled with argon to allow comparisons of the effect of fill gas composition on fuel rod thermal response. The fuel density of the four test rods was also varied to provide comparative data for determining the effect of fuel density during each phase of the test. The individual fuel rod design characteristics are listed in Table A-1.

TABLE A-1. NOMINAL DESIGN PARAMETERS OF BWR-TYPE FUEL RODS FOR TEST PR-1

Rod Parameter	Value
Cladding outside diameter (mm)	12.50
Cladding inside diameter (mm)	10.79
Wall thickness (mm)	0.86
Cladding material	Zircaloy-2
Fuel material	UO_2
Fuel density (% theoretical density)	95 (Rod 524-1), 92 (Rod 524-2), 97 (Rod 524-3), 97 (Rod 524-4)
Pellet diameter (mm)	10.57
Initial diametral gap (mm)	0.22[a]
Fill gas composition	Helium (Rods 524-1,-2, and -3), Argon (Rod 524-4)
Cold internal pressure (MPa)	2.58
Pellet enrichment (wt% ^{235}U)	10.0
Pellet shape	Flat ends L/D = 1.0
Pellet length (mm)	10.57
Rod overall length (mm)	990.6
Fuel stack length (mm)	914.4
Plenum length (mm)	55.12
Plenum volume/fuel volume ratio	0.08
Plenum spring	Coiled Carbon Steel
Shroud inside diameter (mm)	19.3

a. Corresponds to 2.2% of initial fuel pellet diameter.

Each test rod was instrumented with thermocouples to measure cladding surface (external) temperatures, fuel pellet centerline temperature, and off-center fuel temperatures. Since the fuel rods were initially designed and instrumented to be used for gap conductance testing, the axial position of all fuel and all but four cladding thermocouples had been optimized for obtaining gap conductance information. Consequently, the thermocouple positions were not optimal for obtaining power-cooling-mismatch information (departure from nucleate boiling and return to nucleate boiling). Rod 524-4 was also instrumented with cladding internal thermocouples to provide information on rewetting from film boiling conditions. The internal pressure in the upper plenum of each rod was measured by a pressure transducer. Orientation of the test rods in the four-rod hardware, and the relative azimuthal and axial locations of the fuel rod thermocouples are shown in Figure A-1.

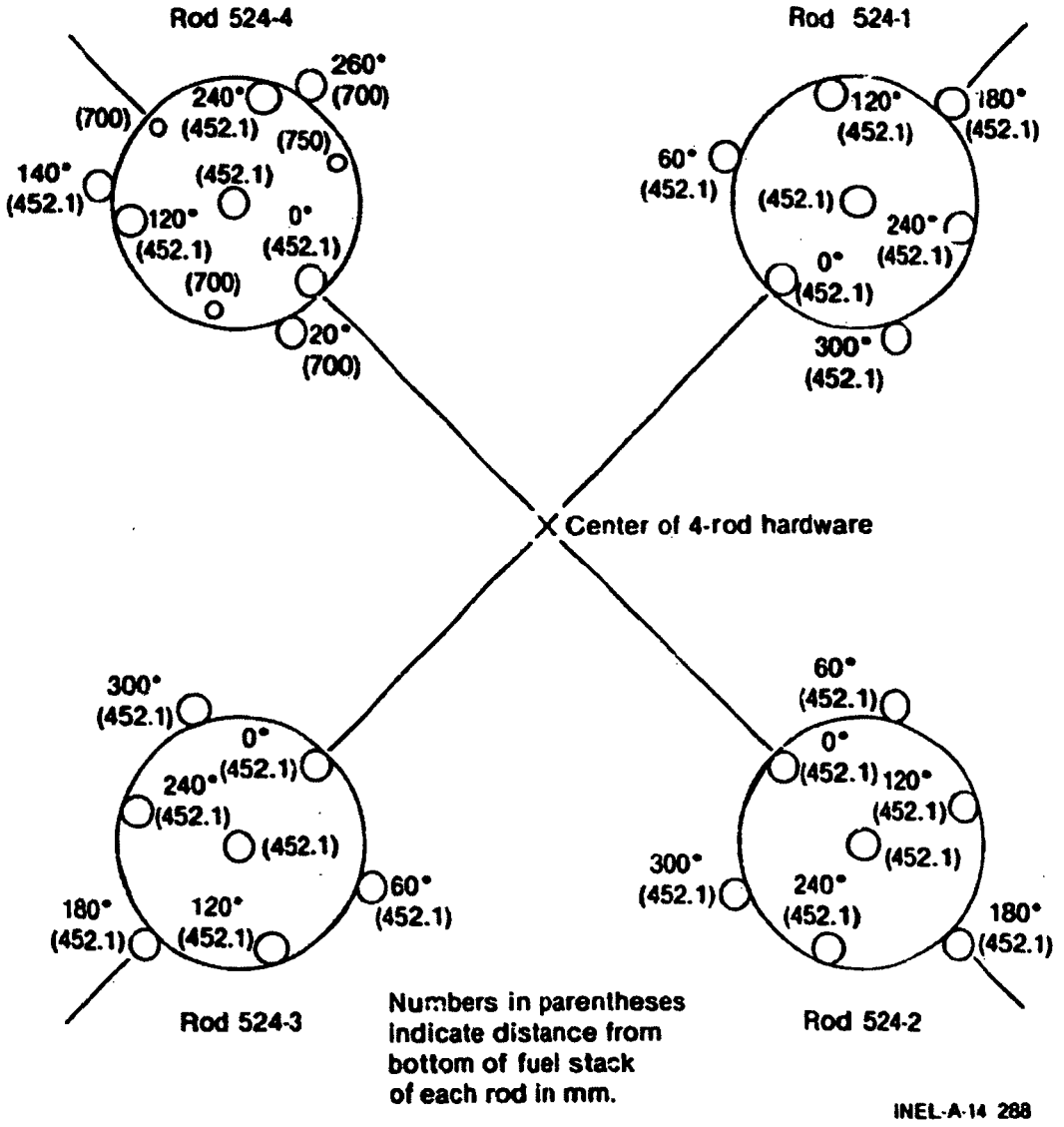

Figure A-1. Four-rod orientation and relative fuel rod thermocouple locations for Test PR-1.

The rods were positioned symmetrically within the Power Burst Facility (PBF) in-pile tube, and were within individual coolant flow shrouds to thermally isolate the rods within the test train. Each shroud was constructed of zircaloy with a 19.3-mm inside diameter. The instrumentation associated with each fuel rod flow shroud consisted of an inlet turbine flowmeter located in each lower shroud extension to measure the coolant volumetric flow rate, differential thermocouples mounted at each shroud

inlet and outlet to measure the coolant temperature increase through the flow shroud, thermocouples located at the inlet and outlet of each flow shroud to measure coolant inlet and outlet temperature, and a differential pressure transducer attached to the top and bottom of the flow shrouds on Rods 524-3 and 524-4 to measure pressure drop across the rod heated length. The recorded data from these instruments were used to calculate fuel rod power and to monitor coolant environmental parameters. A linear variable differential transformer (LVDT) to measure fuel rod cladding elongation was attached to the lower end of each flow shroud. Flux wires to measure the relative axial and azimuthal power profiles were attached to each flow shroud.

Test Train

The test train supported the four fuel rods symmetrically about the central axis of the in-pile tube (IPT). The center hanger rod and lower support plate provided the principal structural support for the assembly.

The coolant entered the IPT at the inlet and was directed through the downcomer to the lower plenum. The flow was subsequently directed upward through the catch basket, through the test rod flow shrouds, and into the upper plenum. Some lower plenum flow bypassed the lower support and entered the bypass region outside the individual flow shrouds. The coolant exited the IPT at the outlet. Details of the test train geometry are contained in Reference A-1.

The instrumentation associated with the test train consisted of pressure transducers mounted near the shroud outlets to measure coolant pressure, and self-powered neutron detectors mounted on supports outside the flow shrouds to measure relative thermal neutron flux.

Plant System

The PBF primary loop, shown in Figure A-2, consists of a pressurizer, coolant pump, coolant heater, heat exchanger, bypass line, and in-pile tube. The loop coolant system provides the capability to monitor and control environmental coolant conditions and flow rate during test conduct.

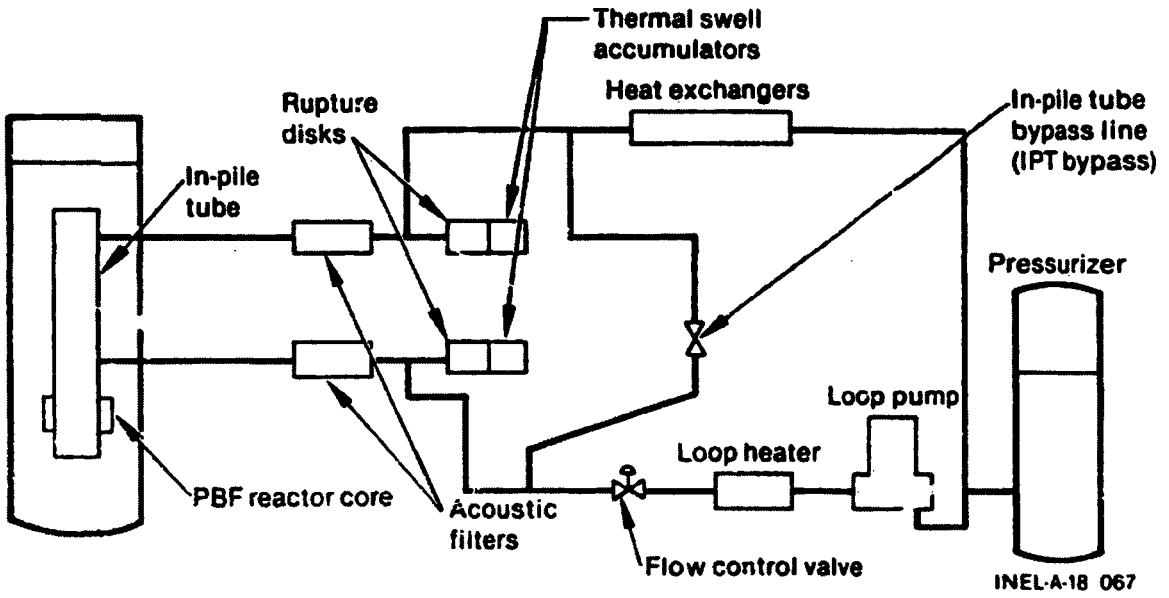

Figure A-2. Schematic of PBF test loop and in-pile tube.

Plant instrumentation to monitor coolant parameters during the test consisted of a differential pressure transducer to measure pressure changes across the in-pile tube, an Ashcroft (Heise) loop pressure gauge, six pressure transducers located at various positions within the loop, and a Venturi loop flowmeter to measure the total loop flow rate. Nine ionization-type flux chambers located in the PBF core region were used to measure reactor power. Flux wires were installed in both the reflector and fuel regions of the reactor core to determine the axial power profile.

EXPERIMENT CONDUCT

Test PR-1 was conducted to assess fuel rod response during various steady state and transient operating conditions. These conditions included (a) operation under steady state and power oscillation conditions to evaluate fuel rod thermal response, (b) power and cooling mismatch transients to evaluate boiling transition (BT) and return to nucleate boiling (RNB), and (c) RIA power excursions to measure fuel thermal performance, and to provide data for development and evaluation of fuel rod computer models. The fuel rod thermal response operation consisted of a two-part fuel rod power calibration, a preconditioning period, and a series of power oscillations. The boiling transition and RNB phases consisted of 23 coolant flow reductions

and 2 power-increase PCM transients. The RIA test phase included three power bursts at increasingly severe energy depositions. Details of each phase of nuclear operation are described below.

Steady State and Power Oscillation Operation

The first segment of reactor power operation consisted of a series of rod power calibration steps to provide data to intercalibrate the test rod power with reactor power and thermal neutron flux. A heat balance of the system using the measured coolant flow rates, coolant temperature rise through the individual flow shrouds, coolant inlet temperature, and system pressure, was used to calculate total rod powers. Local rod powers were determined using the total rod powers and the axial power profile derived from flux wires. The relationship between test rod power and neutron flux provided a method for determining test rod power when two-phase exit conditions, such as existed during the PCM transients, made an energy balance impractical. Data were also obtained to relate control rod position with test rod power to assist in determining control rod positioning for the RIA power excursions.

A rod power calibration was performed at each steady state power level attained. An averaged test rod peak power of 48 kW/m was reached. The power calibration was performed in two segments; the first segment at coolant conditions corresponding to the conditions to be used during the RIA power burst portion of the test, and the second segment at coolant conditions corresponding to the conditions used in the Gap Conductance Test Series[A-1] to provide a common basis for data comparison. Nominal coolant conditions during the first segment of the power calibration were 6.45 MPa system pressure, 538 K inlet temperature, and 0.76 L/s volumetric flow rate through each flow shroud. Nominal coolant conditions during the second segment of the power calibration were 7.20 MPa system pressure, 540 K inlet temperature, and a shroud coolant flow rate adjusted between 0.20 and 0.60 L/s. Steady state fuel and cladding temperature measurement data were used to evaluate fuel rod thermal response and fuel pellet-to-cladding gap conductance (heat transfer coefficient across the gap) as a function of test rod power level.

A fuel rod preconditioning phase followed the second segment of power calibration. The purpose of the preconditioning period was to allow fuel pellet cracking and restructuring similar to that which would occur in an operating power reactor. Steady state fuel rod thermal response data were obtained during the preconditioning phase to evaluate the effects of pellet cracking and fuel relocation on the fuel rod thermal response and pellet-to-cladding gap conductance.

Nominal coolant conditions during the preconditioning were 540 K coolant inlet temperature, 7.17 MPa system pressure, and shroud coolant flow rates of about 0.20 and 0.40 L/s at averaged test rod peak powers of 13 and 28 kW/m, respectively. The axial peak power (averaged), volumetric flow rate through each flow shroud, and coolant temperature rise at each power level of the power calibration and preconditioning phases are provided in Table A-2. Figure A-3 illustrates the power and coolant history during the power calibration and preconditioning phases.

Following the preconditioning period, a series of power oscillations was performed to evaluate the fuel-to-cladding gap conductance by the power oscillation method. Thermal response information was obtained by sinusoidally oscillating core power ±20% at eight nominal power levels, and recording the relative phase lag between power and measured cladding surface temperature. At each power level, the reactor was operated at steady state to assure equilibrium conditions prior to the oscillations, and to obtain steady state thermal response data. At each oscillation condition, the power was oscillated for approximately 40 cycles to obtain sufficient data to reduce statistical uncertainties. Coolant conditions during the power oscillation portion of the test were 478 K inlet temperature, 7.17 MPa system pressure, and about 0.52 L/s coolant volumetric flow rate through each shroud. Table A-3 lists the specific conditions at which power oscillations were performed.

PCM and Boiling Transition Transients

Twenty-three flow reduction and two power-increase PCM transients were completed as part of the boiling transition and return to nucleate boiling

TABLE A-2. SUMMARY OF STEADY STATE THERMAL RESPONSE CONDITIONS

Reactor Core Power (MW)	Average Test Rod Peak Power[a] (kW/m)	Rod 524-1 Shroud Coolant Flow Rate (L/s)	Rod 524-1 Coolant Temperature Rise (K)	Rod 524-2 Shroud Coolant Flow Rate (L/s)	Rod 524-2 Coolant Temperature Rise (K)	Rod 524-3 Shroud Coolant Flow Rate (L/s)	Rod 524-3 Coolant Temperature Rise (K)	Rod 524-4 Shroud Coolant Flow Rate (L/s)	Rod 524-4 Coolant Temperature Rise (K)
Power Calibration[b] (Segment 1)									
4.72	21.29	0.748	5.11	0.758	3.64	0.781	4.52	0.756	4.71
2.32	11.34	0.737	2.75	0.755	1.68	0.774	2.43	0.749	2.31
4.72	21.59	0.735	5.37	0.746	3.64	0.764	4.74	0.747	4.67
7.09	31.98	0.733	7.86	0.749	5.56	0.769	7.01	0.744	7.07
9.52	42.44	0.726	10.70	0.742	7.31	0.760	9.28	0.738	9.21
10.91	48.06	0.731	12.05	0.741	8.31	0.761	10.50	0.743	10.30
9.52	42.62	0.728	10.91	0.743	7.39	0.762	9.37	0.740	9.34
7.20	31.98	0.746	7.86	0.758	5.56	0.780	6.88	0.757	7.03
4.72	21.70	0.744	5.28	0.754	3.64	0.775	4.70	0.757	4.63
3.10	14.66	0.740	3.45	0.749	2.24	0.768	3.13	0.749	3.01
Power Calibration[c] (Segment 2)									
3.11	14.37	0.266	9.56	0.264	6.78	0.270	8.54	0.271	8.25
4.72	21.65	0.310	12.44	0.310	8.92	0.316	11.03	0.315	10.96
6.22	28.40	0.340	15.02	0.340	10.45	0.348	13.17	0.347	13.10
7.91	36.44	0.414	15.85	0.420	11.15	0.431	13.65	0.422	13.93
10.01	45.12	0.532	15.37	0.536	10.71	0.549	12.86	0.541	13.18
6.22	28.45	0.355	14.19	0.361	9.66	0.368	12.12	0.361	12.22
Preconditioning[c]									
3.08	13.88	0.167	14.93	0.164	10.45	0.167	12.38	0.170	12.75
6.19	28.82	0.347	14.67	0.354	10.10	0.360	12.60	0.353	12.57
3.04	13.58	0.167	14.49	0.165	10.19	0.168	12.56	0.171	12.62
6.19	28.02	0.401	12.62	0.407	8.92	0.416	11.07	0.409	10.91
3.00	13.65	0.168	14.49	0.166	10.15	0.169	12.12	0.172	12.48
6.30	27.70	0.384	13.18	0.386	9.05	0.394	11.16	0.391	11.22
3.00	13.47	0.170	14.23	0.166	10.01	0.168	12.12	0.173	12.27

a. Average of (four rods) test rod linear powers at axial peak elevation.

b. Nominal coolant inlet temperature of 538 K and system pressure of 6.5 MPa.

c. Nominal coolant inlet temperature of 540 K and system pressure of 7.2 MPa.

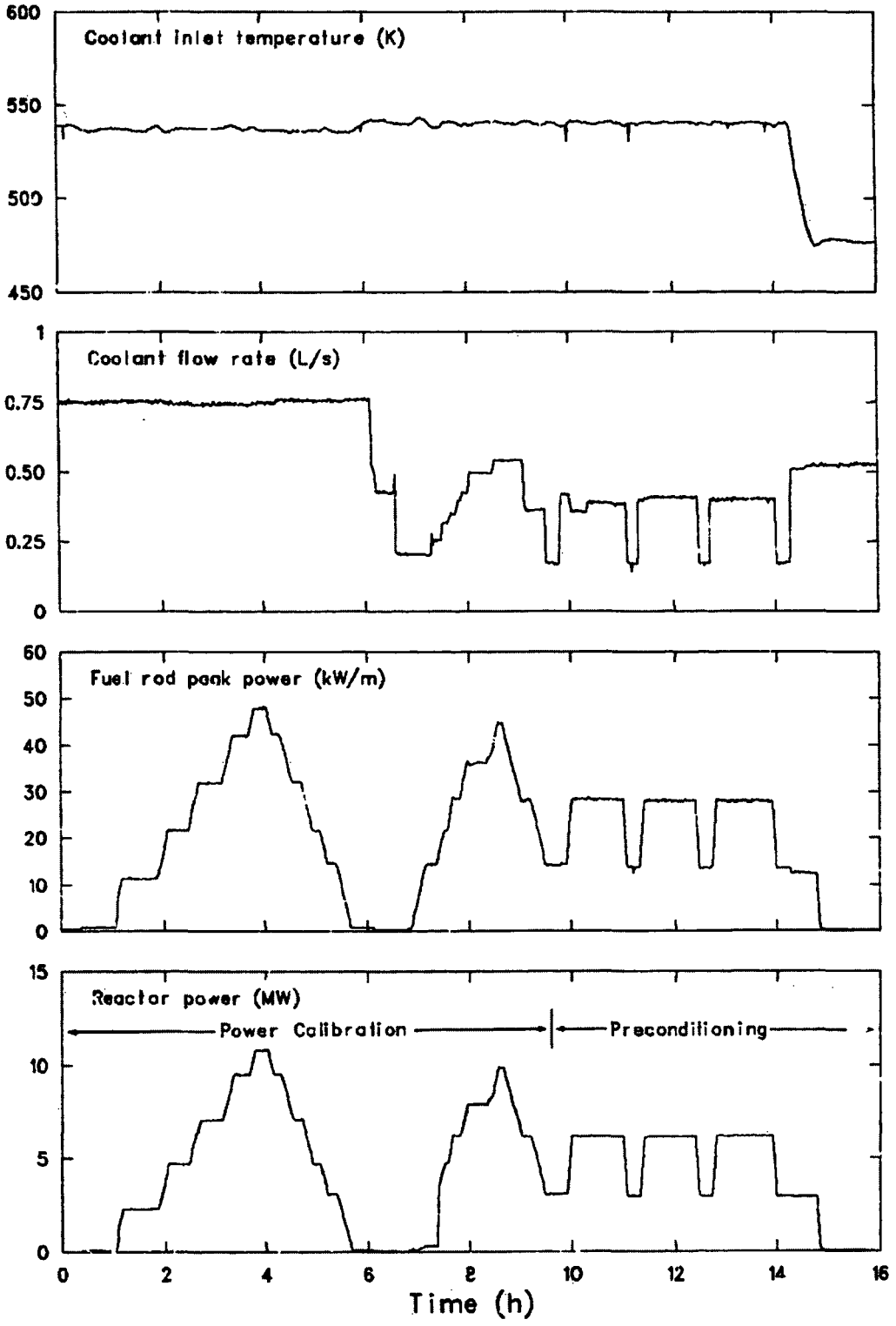

Figure A-3. Test rod power, PBF core power, and coolant conditions during Test PR-1 power calibration and preconditioning periods.

TABLE A-3. SUMMARY OF POWER OSCILLATION CONDITIONS DURING TEST PR-1

Averaged Test Rod Peak Power (kW/m)	Oscillation Amplitude (±%)	Oscillation Period (s)	Rod Number to FRA[a] Input (Orientation)
11.84	20	20	524-1 (300°)
	20	20	524-3 (300°)
25.02	20	20	524-1 (60°)
	20	20	524-4 (140°)
37.44	20	20	524-1 (60°)
	20	20	524-3 (300°)
50.52	20	20	524-1 (60°)
	20	20	524-4 (140°)
Repeats:			
11.84	20	20	524-1 (60°)
	20	20	524-4 (140°)
24.94	20	20	524-1 (60°)
	20	20	524-3 (300°)
37.11	20	20	524-1 (60°)
	20	20	524-4 (140°)
51.77	20	20	524-1 (60°)
	20	20	524-3 (300°)

a. The FRA is a frequency response analyzer that computes the phase lag between the driving signal (power) and response signal (cladding surface temperature measurement). The rod number and orientation refer to a cladding thermocouple orientation on the specified test rod (all at the 0.452-m elevation).

test phase. The objectives of performing these PCM transients were to evaluate the thermal-hydraulic conditions at the onset of boiling transition, and to evaluate the conditions at which return to nucleate boiling occurs.

Prior to the first PCM transient, a period of fuel rod aging was performed. Aging was accomplished by reducing the coolant flow rate at constant power until the upper half of the test rod attained nucleate boiling

conditions. The rod was maintained in nucleate boiling for about 1 h. This procedure was used to remove trapped gases from the surface of the fuel rods and thereby prevent premature boiling transition. The power-cooling-mismatch transients were initiated at nominal system pressures of 7, 13, and 15.5 MPa. The coolant inlet temperature and flow rate were adjusted to provide inlet subcoolings between 8.4 and 43.8 K.

Seven flow reduction transients were conducted at pressures between 7 and 8 MPa. The coolant inlet temperature was approximately 544 K for each transient. Eighteen PCM-type transients were conducted at system pressures between 12.7 and 15.7 MPa. Sixteen of the eighteen higher pressure transients were initiated by flow reduction at constant power, and two were initiated by increasing power at a constant coolant flow rate.

To evaluate the conditions at which return to nucleate boiling occurred, various methods of inducing rewet were used. These methods included (a) increasing flow and decreasing power simultaneously, (b) increasing flow rate at constant power, and (c) decreasing power at a constant flow rate. For each transient, the PBF core power, test rod peak power, coolant inlet temperature, system pressure, and method of transient initiation are listed in Table A-4.

Power Burst Test Conduct

The power burst phase of Test PR-1 consisted of three power excursions. A brief steady state power calibration preceded each power burst to ensure that the figure-of-merit (ratio of test rod power to reactor power) had not significantly changed as a result of the previous testing. New, 100% cobalt flux wires were installed in the reactor prior to each power burst. The coolant conditions for each power burst were nominally 538 K inlet temperature, 6.45 MPa system pressure, and 0.109 L/s coolant volumetric flow rate, which are representative of BWR hot-startup conditions. The procedure to initiate each burst was:

1. The control rods were withdrawn from their scram positions until a reactor transient period of about 10 s was achieved. The reactor power was then increased until two reactor console panel

TABLE A-4. POWER-COOLING-MISMATCH TRANSIENT CONDITIONS

	PBF Core Power (PCM Cycle)	Averaged[a] Test Rod Peak Power (kW/m)	Coolant Inlet Temperature (K)	Nominal System Pressure (MPa)	Method of Transient Initiation
(1.)	10.1	40.39	545	7.2	Flow reduction at constant test rod power; no boiling transition observed.
(2.)	11.4	43.19	543	7.3	Flow reduction at constant test rod power; no boiling transition observed.
(3.)	12.5	47.21	548	7.3	Flow reduction at constant test rod power; no boiling transition observed.
(4.)	12.5	49.18	545	7.2	Flow reduction at constant test rod power; no boiling transition observed.
(5.)	12.5	49.59	547	7.3	Flow reduction at constant test rod power; no boiling transition observed.
(6.)	12.5	47.42	550	7.2	Flow reduction at constant test rod power; no boiling transition observed.
(7.)	12.7	43.71	594	12.7	Flow reduction at constant test rod power; transient concluded by simultaneous flow increase and power reduction.
(8.)	11.8	42.12	607	15.5	Flow reduction at constant test rod power; transient concluded by simultaneous flow increase and power reduction.
(9.)	11.8	42.12	610	15.5	Flow reduction at constant test rod power; transient concluded by simultaneous flow increase and power reduction.

TABLE A-4. (continued)

PBF Core Power (PCM Cycle)	Averaged[a] Test Rod Peak Power (kW/m)	Coolant Inlet Temperature (K)	Nominal System Pressure (MPa)	Method of Transient Initiation
(10.) 11.1	42.12	595	13.4	Flow reduction at constant test rod power; no boiling transition observed.
(11.) 11.1	40.95	594	13.0	Flow reduction at constant test rod power; no boiling transition observed.
(12.) 12.2	45.67	595	13.2	Flow reduction at constant test rod power; no boiling transition observed.
(13.) 12.5	48.86	553	7.3	Flow reduction at constant test rod power; no boiling transition observed.
(14.) 12.5	46.92	593	13.0	Flow reduction at constant test rod power; transient concluded by simultaneous flow increase and power reduction.
(15.) 12.5	44.83	593	13.1	Flow reduction at constant test rod power; transient concluded by increasing flow.
(16.) 11.8	41.63	603	15.5	Flow reduction at constant test rod power; transient concluded by increasing flow.
(17.) 11.8	40.87	604	15.6	Flow reduction at constant test rod power; transient concluded by increasing flow.
(18.) 12.5	45.50	593	12.9	Flow reduction at constant test rod power; no boiling transition observed.
(19.) 12.5	45.50	593	12.9	Flow reduction at constant test rod power; no boiling transition observed.

TABLE A-4. (continued)

PBF Core Power (PCM Cycle)	Averaged[a] Test Rod Peak Power (kW/m)	Coolant Inlet Temperature (K)	Nominal System Pressure (MPa)	Method of Transient Initiation
(20.) 12.5	45.50	593	12.9	Flow reduction at constant test rod power; transient concluded by increasing flow.
(21.) 11.8	42.41	606	15.4	Flow reduction at constant test rod power; transient concluded by increasing flow.
(22.) 12.6	46.53	575	15.0	Flow reduction at constant test rod power; transient concluded by increasing flow.
(23.) 12.6	42.24	605	15.2	Flow reduction at constant test rod power; transient concluded by increasing flow.
(24.) 6 to 12.7	25.00 to 44.94	590	15.6	Power increase at constant flow rate; transient concluded by power decrease.
(25.) 6.5 to 15.3	22.44 to 53.70	590	15.5	Power increase at constant flow rate; transient concluded by power decrease.

a. Rod linear heat generation at peak power elevation; average of four Test PR-1 rods.

lights indicated the plant protection system was operating correctly. Immediately following verification that the plant protection system was operating, the control rods were inserted until the reactor was subcritical.

2. The control rods were then slowly withdrawn until criticality was achieved at a power of about 100 W, and the low power critical position of the control rods determined.

3. The transient rods were inserted into the core to a position (calculated) worth a negative reactivity equivalent to the reactivity insertion required for each power burst.

4. The control rods were then adjusted to the withdrawal position corresponding to the calculated increment for the desired reactivity insertion. The control rod withdrawal increment was checked with the transient rod insertion increment to ensure that a gross error in the control rod increment had not been made.

5. The transient rods were fully inserted into the core, leaving the control rods in a position corresponding to a calculated reactivity increment (above low-power critical) that was equivalent to the reactivity insertion desired.

6. The power burst was initiated by ejecting the four transient rods at a velocity of about 9.5 m/s. The burst was self-terminating because of the inherent Doppler reactivity feedback in the PBF. The feedback is capable of terminating power bursts without primary dependence on mechanical systems.

7. All eight control rods were then completely inserted into the driver core to provide mechanical shutdown of the reactor.

REFERENCE

A-1. R. W. Garner et al., Gap Conductance Test Series 2, Test Results Report for Tests GC 2-1, GC 2-2, and GC 2-3, NUREG/CR-0300, TREE-1268, November 1978.

B

APPENDIX B

FUEL ROD CHARACTERIZATION AND POSTIRRADIATION EXAMINATION DATA

BLANK

PAGE

APPENDIX B

FUEL ROD CHARACTERIZATION AND POSTIRRADIATION EXAMINATION DATA

PRETEST FUEL ROD CHARACTERIZATION

Physical characterization of the Test PR-1 fuel rods was conducted for use in evaluating and verifying fuel rod performance models. Pretest characterization provides the as-built referential information for input to analytical models and for comparison with posttest measurements. Nominal characterization data for the BWR-type rods used in Test PR-1 are presented in Table B-1. Specific physical characteristics for the individual fuel rods are presented in Tables B-2 through B-5, for Rods 524-1 through 524-4, respectively. Selected parameters from Tables B-2 through B-5 are presented graphically in Figures B-1 through B-4. The accuracy of the fuel diameter and length measurements is 5 μm. The cladding measurements are accurate to 3 μm.

FLUX WIRE ACTIVATION ANALYSIS

Rods 524-1 and 524-4 each had one flux wire (0.51% cobalt, 99.49% aluminum) for measuring axial variation in test rod power. The wires were mounted on the outer surface of the flow shrouds and located at azimuthal orientations of 90 (Rod 524-1) and 270 degrees (Rod 524-4). Following the test, the flux wires were removed and the gamma intensity measured in 7.6-mm increments (at 60-s time intervals) along the length of the wire beginning at the bottom.

The flow shrouds for Rods 524-2 and 524-3 had flux wires attached circumferentially around the outer surface for measuring azimuthal variation in test rod power. Each circumferential flux wires (0.51% cobalt) were axially positioned at 10-cm intervals over the active fuel region on each shroud. Each circumferential monitor was bent 360 degrees around the shroud, as shown in Figure B-5(d). The monitor cap end of the flux wire

TABLE B-1. NOMINAL DESIGN PARAMETERS OF BWR-TYPE FUEL RODS FOR TEST PR-1

Rod Parameter	Value			
	524-1	524-2	524-3	524-4
Cladding material	Zircaloy-2	Zircaloy-2	Zircaloy-2	Zircaloy-2
Cladding tube length (mm)	987.63	987.45	987.45	987.45
Cladding outside diameter (mm)	12.50	12.50	12.50	12.50
Cladding inside diameter (mm)	10.79	10.79	10.79	10.79
Wall thickness (mm)	0.86	0.86	0.86	0.86
Fuel material	UO_2	UO_2	UO_2	UO_2
Fuel density (%TD)	95	92	97	97
Pellet diameter (mm)	10.64	10.57	10.58	10.58
Pellet length (mm)	10.58	10.65	10.53	10.45
Number of pellets	86	86	87	87
Pellet enrichment (wt% ^{235}U)	10	10	10	10
Pellet shape (flat ends)	L/D = 1.0	L/D = 1.0	L/D = 1.0	L/D = 1.0
Nominal cold diametral gap (mm)	0.22	0.22	0.22	0.22
Fuel stack length[a] (mm)	910.21	916.25	912.98	915.01
Rod overall length (mm)	1070.1	1069.7	1070.2	1070.4
Shroud inside diameter (mm)	19.3	19.3	19.3	19.3
Plenum length (cm)	55.12	55.12	55.12	55.12
Plenum volume/fuel volume ratio	0.08	0.08	0.08	0.08
Plenum spring	Coiled carbon steel	Coiled carbon steel	Coiled carbon steel	Coiled carbon steel
Plenum spring free length (mm)	60.32	60.32	60.32	60.32
Void volume cm^3	13.2593	14.1475	14.1669	14.2688
Fill gas composition	Helium	Helium	Helium	Argon
Internal pressure (MPa)	2.58	2.58	2.58	2.58

a. Fuel stack is 35.2 mm from bottom of rod end cap.

TABLE B-2. TEST PR-1 FUEL ROD 524-1 CHARACTERIZATION DATA

Distance from Bottom of Tube[a] (mm)	Cladding Dimensions: Inside Diameter (mm) 0°	Inside Diameter (mm) 90°	Outside Diameter (mm) 0°	Outside Diameter (mm) 90°	Wall Thickness (mm) 0°	Wall Thickness (mm) 90°	Pellet Diameter (mm)	Radial gap (mm)	Fuel Density (g/cm^3)	Pellet Length (mm)	Pellet Number
25.4	10.827	10.829	12.503	12.499	0.838	0.835	10.5873	0.1204	10.4251	10.5538	1
50.8	10.824	10.831	12.504	12.498	0.840	0.834					
76.2	10.827	10.832	12.504	12.498	0.839	0.833	10.5810	0.1245	10.1386	10.2437	6
101.6	10.827	10.832	12.503	12.498	0.838	0.833					
127.0	10.826	10.830	12.503	12.498	0.839	0.834					
152.4	10.826	10.829	12.503	12.498	0.839	0.835					
177.8	10.827	10.830	12.503	12.498	0.838	0.834	10.5747	0.1272	10.1657	10.7791	16
203.2	10.827	10.831	12.503	12.498	0.838	0.834					
228.6	10.823	10.829	12.503	12.498	0.840	0.835					
254.0	10.827	10.832	12.503	12.498	0.838	0.833					
279.4	10.827	10.832	12.503	12.498	0.838	0.833	10.5896	0.1202	10.1716	10.6408	26
304.8	10.827	10.831	12.503	12.498	0.838	0.834					
330.2	10.824	10.832	12.503	12.498	0.840	0.833					
355.6	10.826	10.831	12.503	12.498	0.839	0.834					
381.0	10.827	10.831	12.504	12.498	0.839	0.834					
406.4	10.830	10.826	12.504	12.498	0.837	0.836	10.5833	0.1224	10.1788	10.6484	36
431.8	10.834	10.824	12.504	12.498	0.835	0.837					
457.2	10.832	10.828	12.504	12.498	0.836	0.835					
482.6	10.832	10.824	12.504	12.497	0.836	0.837					
508.0	10.831	10.822	12.504	12.497	0.837	0.838	10.7036	0.0615	10.7399	10.6093	47
533.4	10.835	10.812	12.504	12.497	0.835	0.843					
558.8	10.836	10.822	12.504	12.497	0.834	0.838					
584.2	10.832	10.824	12.504	12.497	0.836	0.837					

TABLE B-2. (continued)

Distance from Bottom of Tube[a] (mm)	Cladding Dimensions: Inside Diameter (mm) 0°	Inside Diameter (mm) 90°	Outside Diameter (mm) 0°	Outside Diameter (mm) 90°	Wall Thickness (mm) 0°	Wall Thickness (mm) 90°	Pellet Diameter (mm)	Radial gap (mm)	Fuel Density (g/cm^3)	Pellet Length (mm)	Pellet Number
609.6	10.832	10.822	12.503	12.497	0.836	0.838	10.7080	0.0595	10.7377	10.5729	56
635.0	10.831	10.825	12.504	12.497	0.837	0.836					
660.4	10.833	10.825	12.503	12.497	0.835	0.836					
685.8	10.833	10.824	12.503	12.497	0.835	0.837					
711.2	10.832	10.823	12.503	12.497	0.836	0.837	10.6316	0.0980	10.7129	10.5510	66
736.6	10.836	10.824	12.503	12.497	0.834	0.837					
762.0	10.835	10.820	12.503	12.497	0.834	0.839					
787.4	10.836	10.818	12.503	12.497	0.834	0.840					
812.8	10.837	10.818	12.503	12.497	0.833	0.840	10.7068	0.0604	10.7260	10.4959	76
838.2	10.837	10.820	12.504	12.496	0.834	0.838					
863.6	10.936	10.821	12.503	12.496	0.834	0.838					
889.0	10.833	10.821	12.502	12.496	0.835	0.838					
914.4	10.834	10.823	12.502	12.495	0.834	0.836	10.7053	0.0616	10.6896	10.6578	86
939.8	10.834	10.824	12.502	12.496	0.835	0.836					
965.2	10.832	10.826	--	--	--	--					
Average							10.6371			10.5753	

a. The total tube length for Rod 524-1 was 98.763 ± 0.005 cm. The bottom of the fuel stack was 35.2 mm above the bottom of the cladding tube.

TABLE B-3. TEST PR-1 FUEL ROD 524-2 CHARACTERIZATION DATA

Distance from Bottom of Tube[a] (mm)	Cladding Dimensions: Inside Diameter (mm) 0°	Inside Diameter (mm) 90°	Outside Diameter (mm) 0°	Outside Diameter (mm) 90°	Wall Thickness (mm) 0°	Wall Thickness (mm) 90°	Pellet Diameter (mm)	Radial gap (mm)	Fuel Density (g/cm^3)	Pellet Length (mm)	Pellet Number
25.4	10.819	10.833	12.514	12.515	0.848	0.841	10.5683	0.1289	9.4805	10.6561	1
50.8	10.823	10.832	12.509	12.517	0.843	0.843					
76.2	10.828	10.834	12.512	12.515	0.842	0.841	10.5602	0.1354	9.4585	10.7459	6
101.6	10.829	10.834	12.512	12.513	0.842	0.840					
127.0	10.829	10.834	12.513	12.513	0.842	0.840					
152.4	10.825	10.836	12.511	12.512	0.843	0.838					
177.8	10.825	10.825	12.511	12.513	0.843	0.839	10.5420	0.1440	9.5346	10.7225	16
203.2	10.825	10.831	12.511	12.512	0.843	0.841					
228.6	10.829	10.831	12.511	12.514	0.841	0.842					
254.0	10.830	10.831	12.511	12.514	0.841	0.842					
279.4	10.830	10.835	12.512	12.511	0.841	0.838	10.5708	0.1311	9.5034	10.5344	26
304.8	10.830	10.835	12.513	12.511	0.842	0.838					
330.2	10.829	10.836	12.513	12.511	0.842	0.838					
355.6	10.827	10.832	12.511	12.512	0.842	0.840					
381.0	10.826	10.832	12.511	12.513	0.843	0.841					
406.4	10.827	10.828	12.510	12.511	0.842	0.842	10.5606	0.1337	9.5410	10.6643	36
431.8	10.834	10.831	12.512	12.512	0.839	0.841					
457.2	10.835	10.832	12.512	12.512	0.839	0.840					
482.6	10.831	10.831	12.512	12.512	0.841	0.841					
508.0	10.827	10.835	12.511	12.510	0.842	0.838	10.5878	0.1216	9.6618	10.6341	47
533.4	10.826	10.834	12.512	12.510	0.843	0.838					
558.8	10.830	10.834	12.511	12.510	0.841	0.838					
584.2	10.828	10.829	12.509	12.512	0.841	0.842					

TABLE B-3. (continued)

Distance from Bottom of Tube[a] (mm)	Cladding Dimensions: Inside Diameter (mm) 0°	Inside Diameter (mm) 90°	Outside Diameter (mm) 0°	Outside Diameter (mm) 90°	Wall Thickness (mm) 0°	Wall Thickness (mm) 90°	Pellet Diameter (mm)	Radial gap (mm)	Fuel Density (g/cm^3)	Pellet length (mm)	Pellet Number
609.6	10.831	10.829	12.510	12.512	0.840	0.842	10.5897	0.1202	9.7004	10.6488	56
635.0	10.830	10.830	12.510	12.511	0.840	0.841					
660.4	10.834	10.832	12.512	12.509	0.839	0.839					
685.8	10.832	10.833	12.511	12.509	0.840	0.838					
711.2	10.832	10.834	12.511	12.509	0.840	0.838	10.5771	0.1280	9.6525	10.5583	66
736.6	10.828	10.834	12.509	12.510	0.841	0.838					
762.0	10.828	10.834	12.509	12.509	0.841	0.838					
787.4	10.828	10.833	12.509	12.509	0.841	0.838					
812.8	10.834	10.830	12.510	12.510	0.838	0.840	10.5849	0.1236	9.5958	10.6683	76
838.2	10.833	10.831	12.510	12.510	0.839	0.840					
863.6	10.834	10.834	12.510	12.509	0.838	0.838					
889.6	10.831	10.833	12.510	12.508	0.840	0.838					
914.4	10.834	10.832	12.510	12.508	0.838	0.838	10.5871	0.1230	9.8608	10.6945	86
939.8	10.830	10.834	12.509	12.509	0.840	0.838					
965.2	10.831	10.834	12.509	--	0.839	--					
Average							10.5729			10.6527	

a. The total tube length for Rod 524-2 was 98.745 ± 0.005 cm. The bottom of the fuel stack was 35.2 mm above the bottom of the cladding tube.

TABLE B-4. TEST PR-1 FUEL ROD 524-3 CHARACTERIZATION DATA

Distance from Bottom of Tube[a] (mm)	Cladding Dimensions: Inside Diameter (mm) 0°	Inside Diameter (mm) 90°	Outside Diameter (mm) 0°	Outside Diameter (mm) 90°	Wall Thickness (mm) 0°	Wall Thickness (mm) 90°	Pellet Diameter (mm)	Radial gap (mm)	Fuel Density (g/cm^3)	Pellet Length (mm)	Pellet Number
25.4	10.830	10.821	12.514	12.515	0.842	0.847	10.5736	0.1260	10.5757	10.4972	1
50.8	10.829	10.830	12.511	12.514	0.841	0.842					
76.2	10.833	10.830	12.512	12.516	0.840	0.843	10.5728	0.1296	10.4831	10.6985	7
101 6	10.834	10.828	12.512	12.516	0.839	0.844					
127.0	10.834	10.828	12.513	12.516	0.840	0.844					
152.4	10.830	10.829	12.514	12.514	0.842	0.843					
177.8	10.829	10.832	12.515	12.514	0.843	0.841	10.5808	0.1251	10.5158	10.5410	17
203.2	10.829	10.833	12.515	12.514	0.843	0.841					
228.6	10.829	10.833	12.514	12.517	0.843	0.842					
254.0	10.829	10.834	12.513	12.517	0.842	0.842					
279.4	10.831	10.828	12.512	12.516	0.841	0.844	10.5788	0.1261	10.4610	10.5029	27
304.8	10.834	10.828	12.513	12.517	0.840	0.845					
330.2	10.833	10.832	12.515	12.517	0.841	0.843					
355.6	10.832	10.832	12.515	12.516	0.842	0.842					
381.0	10.827	10.834	12.515	12.515	0.844	0.841					
406.4	10.824	10.833	12.513	12.516	0.845	0.842	10.5746	0.1270	10.4598	10.5347	37
431.8	10.824	10.835	12.513	12.518	0.845	0.842					
457.2	10.828	10.833	12.512	12.518	0.842	0.843					
482.5	10.830	10.829	12.512	12.518	0.841	0.845					
508.0	10.831	10.830	12.513	12.515	0.841	0.843	10.5761	0.1275	10.6102	10.4938	47
533.4	10.831	10.831	12.512	12.515	0.841	0.842					
558.8	10.833	10.835	12.514	12.515	0.841	0.840					
584.2	10.831	10.834	12.513	12.516	0.841	0.841					

TABLE B-4. (continued)

Distance from Bottom of Tube[a] (mm)	Cladding Dimensions: Inside Diameter (mm) 0°	Inside Diameter (mm) 90°	Outside Diameter (mm) 0°	Outside Diameter (mm) 90°	Wall Thickness (mm) 0°	Wall Thickness (mm) 90°	Pellet Diameter (mm)	Radial gap (mm)	Fuel Density (g/cm^3)	Pellet Length (mm)	Pellet Number
609.6	10.828	10.834	12.514	12.517	0.843	0.842	10.5769	0.1266	10.6067	10.5010	57
635.0	10.829	10.831	12.511	12.517	0.841	0.843					
660.4	10.833	10.828	12.512	12.517	0.840	0.845					
685.8	10.833	10.831	12.512	12.517	0.840	0.843					
711.2	10.833	10.827	12.514	12.516	0.841	0.845	10.5887	0.1202	10.6118	10.4995	67
736.6	10.829	10.829	12.514	12.514	0.843	0.844					
762.0	10.829	10.829	12.514	12.514	0.843	0.844					
787.4	10.827	10.833	12.512	12.515	0.843	0.841					
812.8	10.830	10.833	12.512	12.517	0.841	0.842	10.5821	0.1245	10.6119	10.4546	77
838.2	10.830	10.831	12.512	12.517	0.841	0.843					
863.6	10.831	10.826	12.512	12.518	0.841	0.846					
889.0	10.833	10.825	12.511	12.515	0.841	0.845					
914.4	10.833	10.828	12.513	12.515	0.840	0.844	10.5767	0.1292	10.6073	10.5598	87
939.8	10.839	10.831	12.513	12.516	0.837	0.843					
965.2	--	10.829	--	--	--	--					
Average							10.5283			10.5544	

a. The total tube length for Rod 524-3 was 98.745 ± 0.005 cm. The bottom of the fuel stack was 35.2 mm above the bottom of the cladding tube.

TABLE B-5. TEST PR-1 FUEL ROD 524-4 CHARACTERIZATION DATA

Distance from Bottom of Tube[a] (mm)	Cladding Dimensions						Pellet Diameter (mm)	Radial gap (mm)	Fuel Density (g/cm^3)	Pellet Length (mm)	Pellet Number
	Inside Diameter (mm)		Outside Diameter (mm)		Wall Thickness (mm)						
	0°	90°	0°	90°	0°	90°					
25.4	10.829	10.832	12.513	12.513	0.842	0.841	10.5828	0.1241	10.3612	10.4375	1
50.8	10.830	10.832	12.510	12.516	0.840	0.842					
76.2	10.828	10.833	12.511	12.515	0.841	0.841	10.5763	0.1274	10.4216	10.2761	7
101.6	10.830	10.833	12.511	12.514	0.841	0.840					
127.0	10.830	10.831	12.512	12.514	0.841	0.842					
152.4	10.834	10.831	12.511	12.515	0.839	0.842					
177.8	10.833	10.831	12.512	12.516	0.839	0.843	10.5747	0.1282	10.4576	10.4619	17
203.2	10.834	10.828	12.510	12.515	0.838	0.844					
228.6	10.828	10.828	12.509	12.515	0.841	0.843					
254.0	10.828	10.828	12.510	12.513	0.841	0.843					
279.4	10.827	10.833	12.512	12.512	0.842	0.840	10.5801	0.1265	10.5167	10.4991	27
304.8	10.833	10.833	12.512	12.513	0.839	0.840					
330.2	10.835	10.829	12.512	12.513	0.838	0.842					
335.6	10.834	10.827	12.511	12.513	0.838	0.843					
381.0	10.832	10.827	12.510	12.512	0.839	0.843					
406.4	10.832	10.830	12.510	12.513	0.839	0.842	10.5729	0.1291	10.5168	10.5444	37
431.8	10.831	10.830	12.510	12.513	0.839	0.842					
457.2	10.830	10.831	12.510	12.512	0.840	0.841					
482.6	10.830	10.831	12.510	12.511	0.840	0.840					
508.0	10.831	10.832	12.511	12.510	0.840	0.839	10.5746	0.1287	10.6119	10.4201	47
533.4	10.835	10.830	12.511	12.510	0.838	0.840					
558.8	10.835	10.827	12.510	12.511	0.839	0.842					
584.2	10.832	10.824	12.509	12.511	0.839	0.844					

TABLE B-5. (continued)

Distance from Bottom of Tube[a] (mm)	Cladding Dimensions: Inside Diameter (mm) 0°	Inside Diameter (mm) 90°	Outside Diameter (mm) 0°	Outside Diameter (mm) 90°	Wall Thickness (mm) 0°	Wall Thickness (mm) 90°	Pellet Diameter (mm)	Radial gap (mm)	Fuel Density (g/cm^3)	Pellet Length (mm)	Pellet Number
609.6	10.829	10.826	12.508	12.511	0.839	0.843	10.5931	0.1195	10.6153	10.4191	57
635.0	10.831	10.832	12.508	12.511	0.838	0.839					
660.4	10.833	10.830	12.508	12.510	0.836	0.840					
685.8	10.836	10.829	12.508	12.509	0.835	0.840					
711.2	10.834	10.825	12.508	12.509	0.837	0.842	10.5777	0.1259	10.6198	10.4785	67
736.6	10.834	10.825	12.509	12.508	0.837	0.842					
762.0	10.835	10.823	12.509	12.509	0.837	0.843					
787.4	10.834	10.825	12.509	12.509	0.837	0.842					
812.8	10.832	10.827	12.507	12.508	0.838	0.841	10.5802	0.1242	10.6179	10.4299	77
838.2	10.832	10.825	12.507	12.507	0.837	0.841					
863.6	10.832	10.829	12.507	12.508	0.838	0.839					
889.0	10.837	10.829	12.507	12.507	0.835	0.839					
914.4	10.837	10.823	12.507	12.508	0.835	0.842	10.5815	0.1243	10.6207	10.5090	87
939.8	10.837	10.823	12.505	12.508	0.834	0.842					
965.2	--	10.823	--	12.509	--	0.843					
Average							10.5794			10.4476	

a. The total tube length for Rod 524-4 was 98.746 ± 0.005 cm. The bottom of the fuel stack was 35.2 mm above the bottom of the cladding tube.

BLANK PAGE

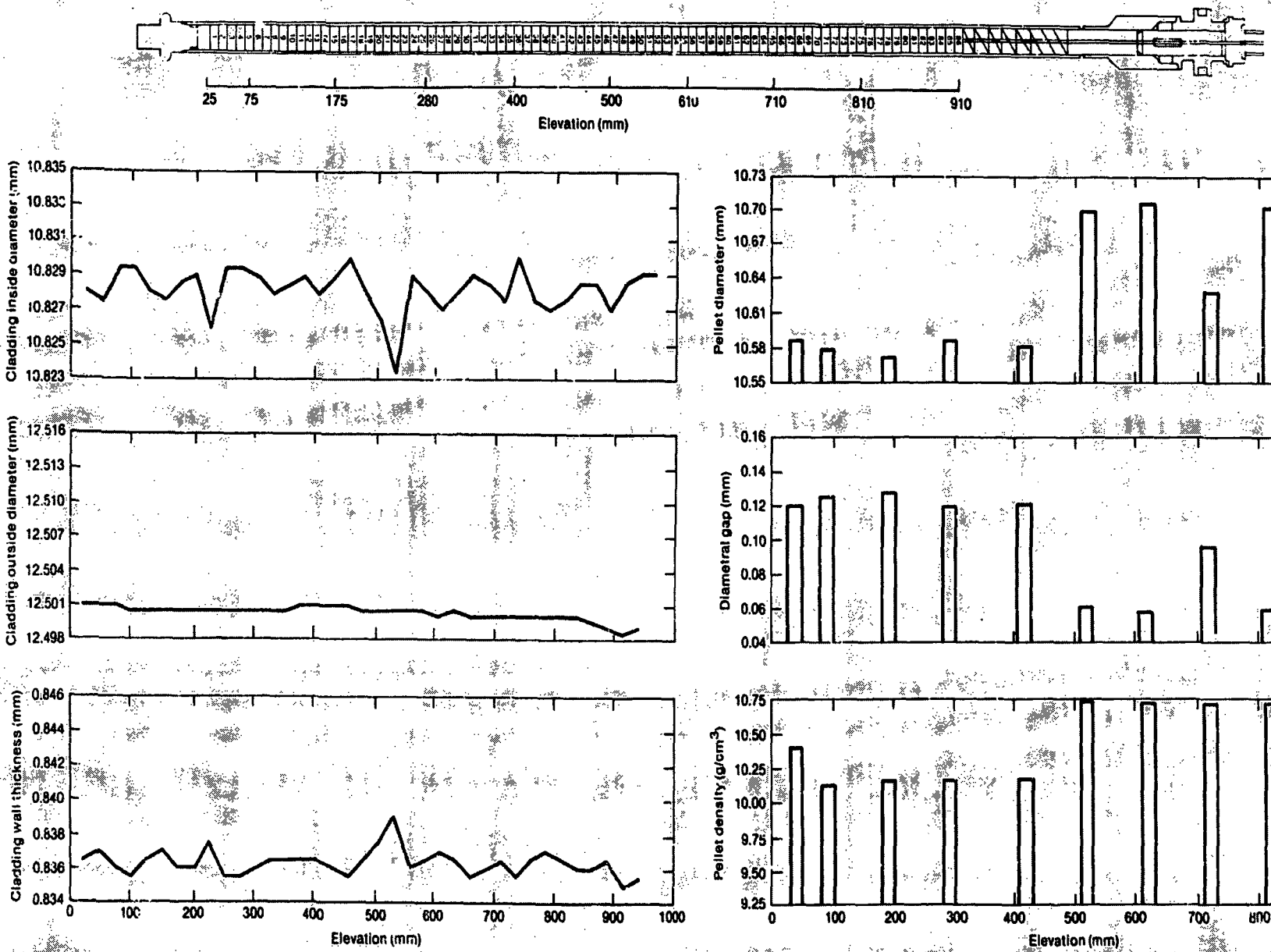

Figure B-1. Physical characteristics of Rod 524-1.

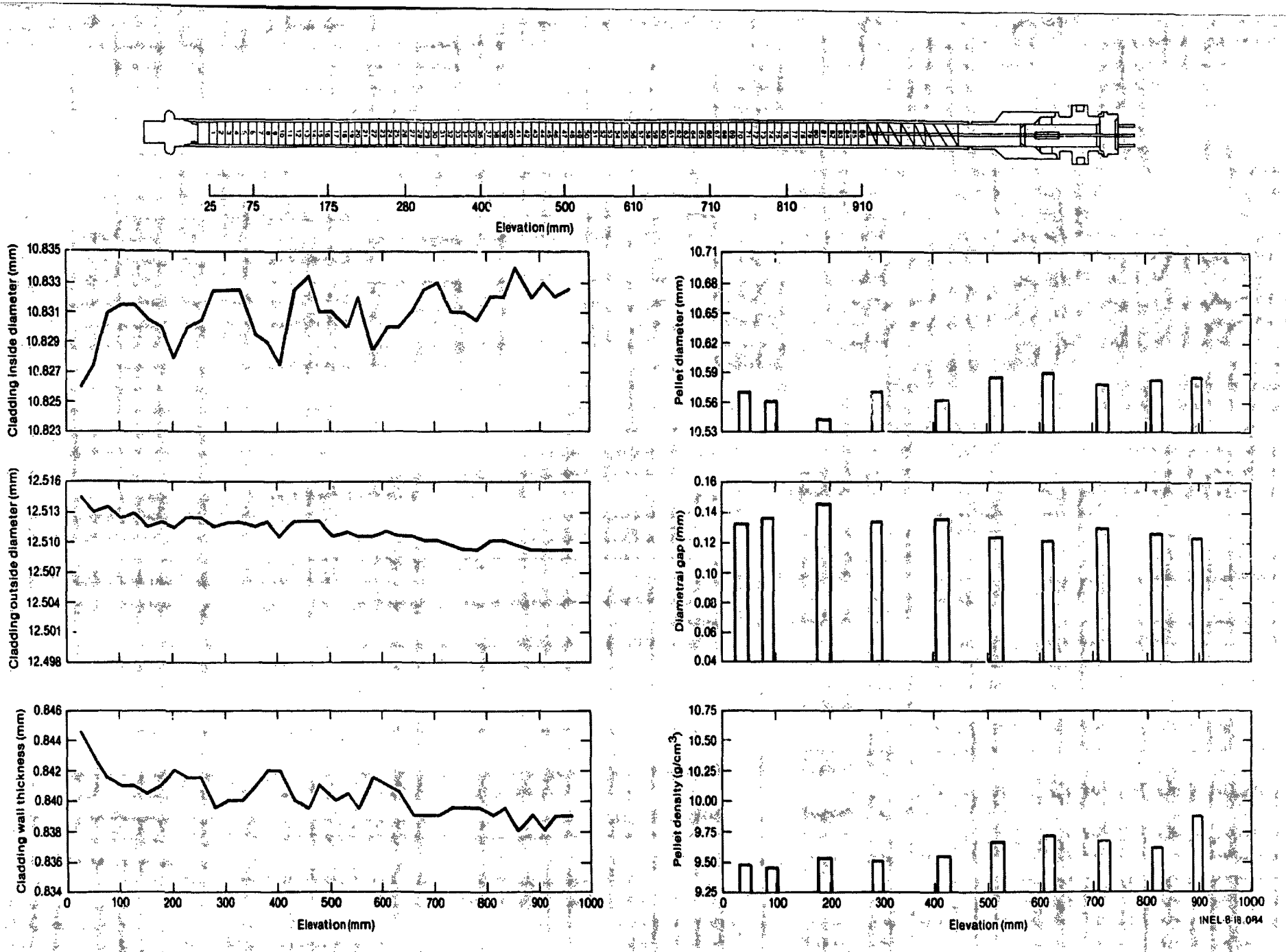

Figure B-2. Physical characteristics of Rod 524-2.

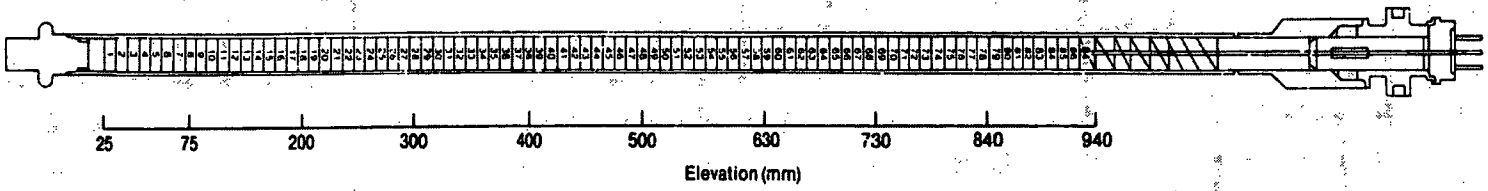

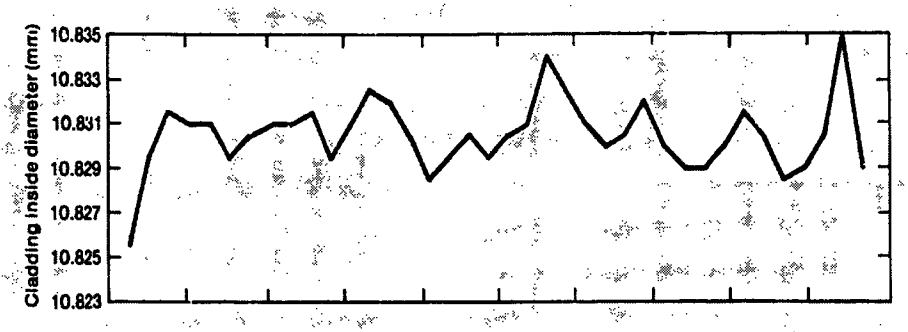

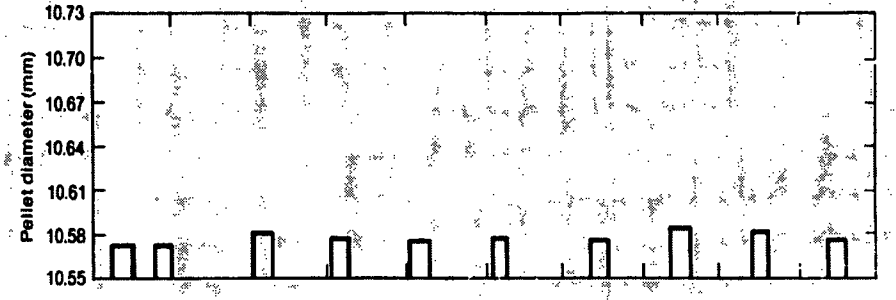

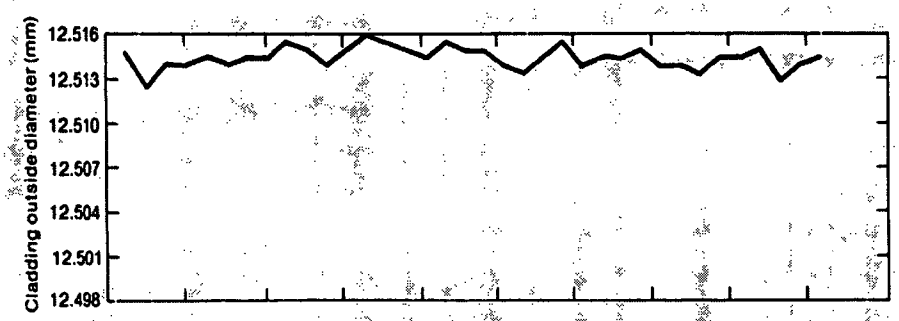

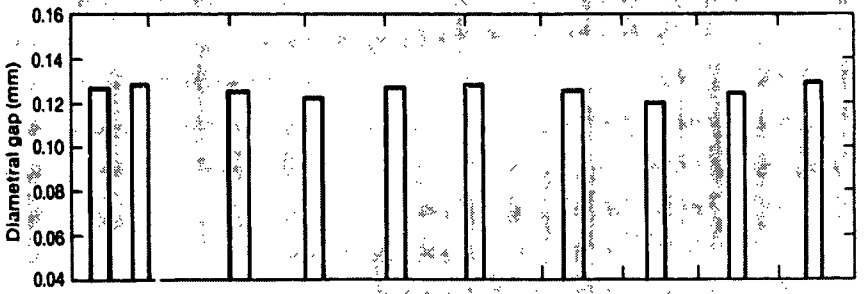

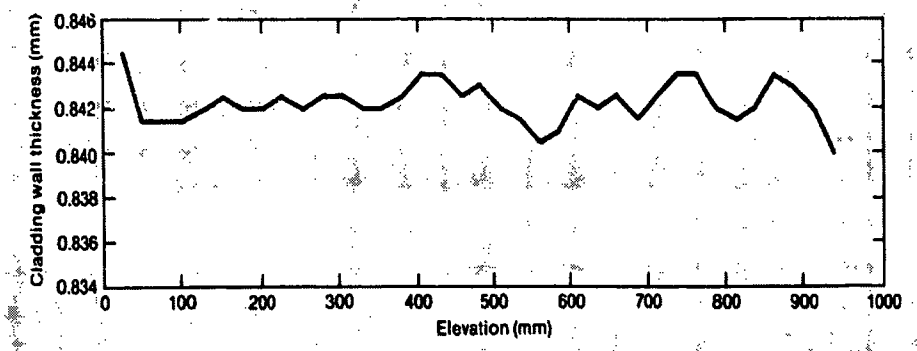

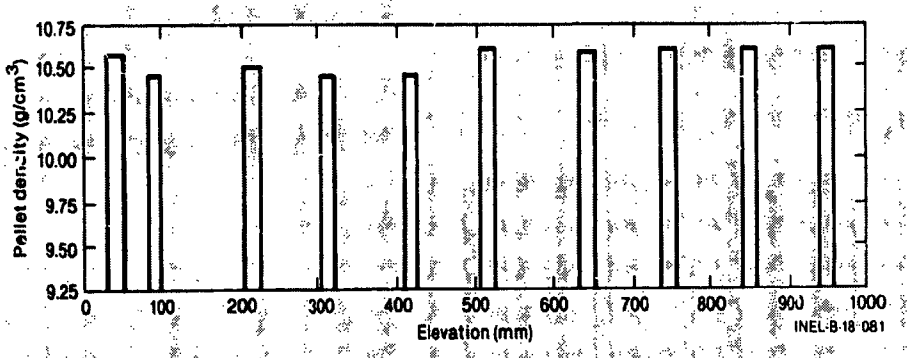

Figure B-3. Physical characteristics of Rod 524-3.

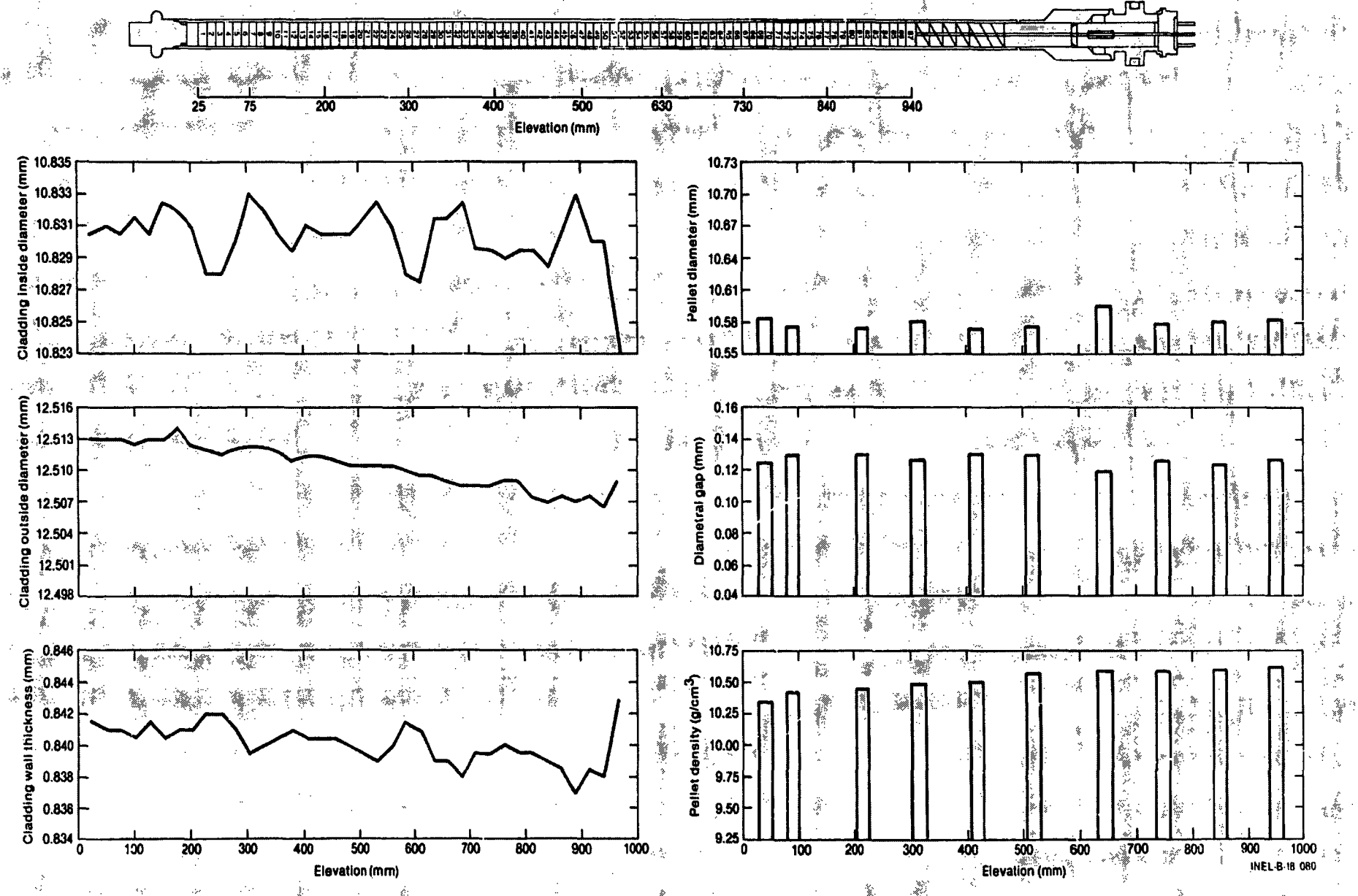

Figure B-4. Physical characteristics of Rod 524-4.

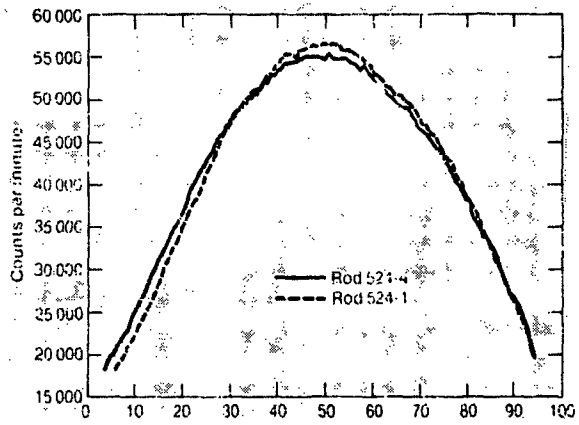

(a) Axial flux wire profile for Rods 524-1 and 524-4

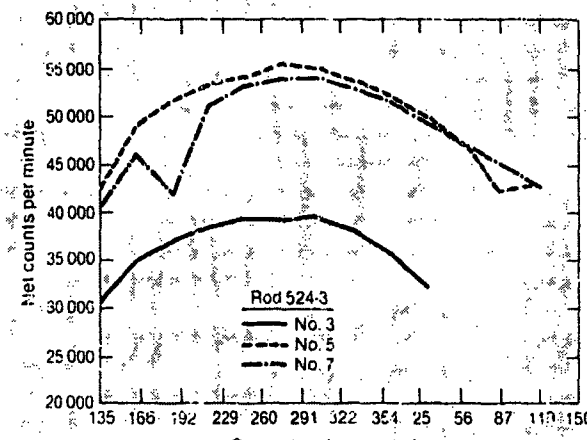

(b) Circumferential flux wire profile for Rod 524-2

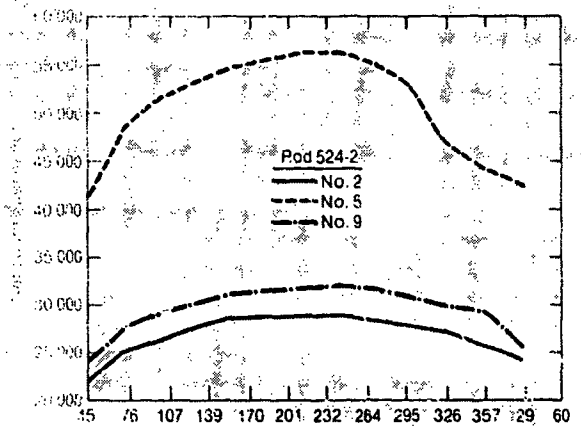

(c) Circumferential flux wire profile for Rod 524-3

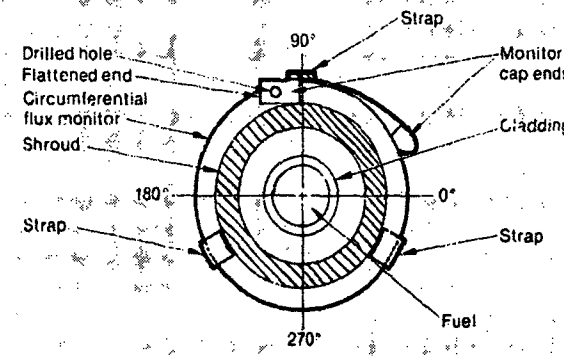

(d) Schematic of circumferential flux monitor

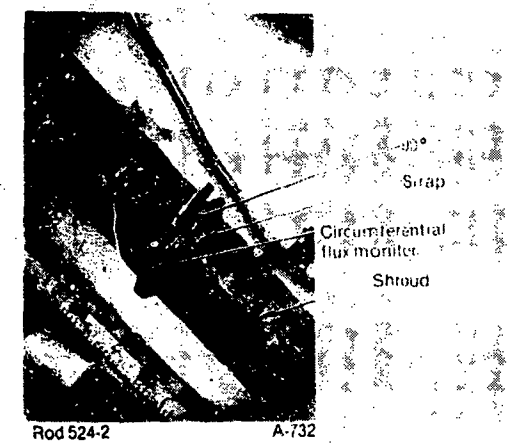

(e) Circumferential flux wire attached to the shroud

Figure B-5. Axial power profile determined from cobalt flux wire activation, and schematic of circumferential flux monitor.

was located at zero degrees on the shroud, such that the flattened end of the wire was bent toward 90 degrees. Tables B-6 through B-8 list the flux wire scan data. The data are graphically presented in Figure B-5. The "K_n factor" given in Tables B-6 through B-8 is the ratio of thermal neutron fluence (Nvt) to the measured counts per minute at common elevations.

Thermal neutron flux is proportional to the induced radioactivity of the flux wires. Time-integrated neutron flux, which is neutron fluence, is determined by measuring the Co-60 activity resulting from Co-59 neutron absorption. The increase in Co-60 activity during irradiation is given by

$$N = N_0 \sigma \Phi \Delta t = N_0 \sigma F \qquad \text{(B-1)}$$

where

N = number of Co-60 atoms per unit volume after irradiation

N_0 = number of original Co-59 atoms per unit volume

σ = absorption cross section of Co-59 ($37.3 \times 10^{24} cm^2$)

Φ = thermal neutron flux [$n/cm^2 \cdot s$)]

Δt = incremental time(s)

F = thermal neutron fluence (n/cm^2).

The thermal neutron fluence was determined for one data point of each flux wire to establish a conversion factor K_n. The factor K_n is the ratio of the thermal neutron fluence (F) to the measured counts per minute (R) at the same elevation, and is assumed constant over each flux wire. The K_n factors for the two axial flux wires are given in Tables B-6 and B-7. The K_n factor for each of the circumferential flux wires is given in Table B-8. To obtain thermal neutron fluence (F) at any axial elevation, multiply the K_n factor by R.

TABLE B-6. AXIAL FLUX WIRE GAMMA SCAN DATA FROM ROD 524-1

Location from Bottom of Fuel Stack (cm)	Counts Per Minute (10^4)	Location from Bottom of Fuel Stack (cm)	Counts Per Minute (10^4)	Location from Bottom of Fuel Stack (cm)	Counts Per Minute (10^4)
5.73	18040	35.45	51368	65.17	50446
6.49	18982	36.21	51297	65.93	50525
7.25	19376	36.97	52058	66.69	49882
8.02	20230	37.73	53112	67.45	49574
8.78	21102	38.50	52799	68.21	49112
9.54	21844	39.26	53638	68.98	48544
10.30	22783	40.02	54276	69.74	47840
11.06	23845	40.78	54652	70.50	46881
11.83	24584	41.54	55219	71.26	47138
12.59	25604	42.31	55274	72.02	46026
13.35	26552	43.07	55381	72.79	45678
14.11	27681	43.83	54951	73.55	45172
14.87	28404	44.59	55805	74.31	44206
15.64	29737	45.35	55980	75.07	43409
16.40	30656	46.12	56095	75.83	42782
17.16	31283	46.88	56322	76.60	42507
17.92	32485	47.64	56173	77.36	41360
18.68	32998	48.40	56116	78.12	40518
19.45	33846	49.16	56580	78.88	39982
20.21	34839	49.93	56479	79.64	38785
20.97	36016	50.69	56554	80.41	38434
21.73	37060	51.45[a]	56508	81.17	37116
22.49	37924	52.21	56550	81.93	36673
23.26	38419	52.97	56424	82.69	35555
24.02	39709	53.74	55807	83.45	34690
24.78	40977	54.50	55851	84.22	33668
25.54	41929	55.26	55894	87.26	32913
26.30	42776	56.02	55551	85.74	31966
27.07	43866	56.78	55142	86.50	31038
27.83	44803	57.55	55235	87.26	29912
28.59	45639	58.31	54665	88.03	29009
29.35	46345	59.07	54075	88.25	28057
30.11	46957	59.83	54022	89.55	27321
30.88	47620	60.59	52827	90.31	26190
31.64	48589	61.36	52788	91.07	25661
32.40	48823	62.12	52424	91.84	24396
33.16	49275	62.88	51658	92.60	23354
33.92	50088	63.64	51498	93.36	22014
34.69	50191	64.40	51191	94.12	20607

K_n = 7.193 E14 (Nvt)/counts per minute

a. Elevation where the thermal neutron fluence was determined.

TABLE B-7. AXIAL FLUX WIRE GAMMA SCAN DATA FROM ROD 524-4

Location from Bottom of Fuel Stack (cm)	Counts Per Minute (10^4)	Location from Bottom of Fuel Stack (cm)	Counts Per Minute (10^4)	Location from Bottom of Fuel Stack (cm)	Counts Per Minute (10^4)
3.47	18168	35.47	50913	65.19	49520
4.23	19198	36.24	50993	65.95	49122
4.99	20016	37.00	52164	66.72	48843
5.76	20379	37.76	51761	67.48	48937
6.52	21233	38.52	52938	68.24	48088
7.28	22065	39.28	52643	69.00	47460
8.04	22685	40.05	53474	69.76	46521
8.80	23255	40.81	53516	70.53	46122
9.57	24748	41.57	54128	71.29	45844
10.33	25322	42.33	54315	72.05	45349
11.09	26450	43.09	54290	72.81	44768
11.85	27022	43.86	54335	73.57	44043
12.61	28119	44.62	54452	74.34	43393
13.38	29303	45.38	54746	75.10	42912
14.14	29953	46.14	55067	75.86	42057
14.90	31153	46.90	54958	76.62	41142
15.66	31992	47.67	54934	77.38	40270
16.42	32859	49.95	54638	78.15	39750
18.71	33506	48.43	54890	80.43	37928
17.19	34426	49.19	54878	78.91	38801
17.95	35122	50.71	55394	79.67	37848
19.47	35898	51.48	54748	81.19	36309
20.23	36727	52.24	54871	81.96	35528
21.00	37661	53.00[a]	54825	82.72	34902
21.76	39155	53.76	54823	83.48	33675
22.52	40162	54.52	54871	84.24	33529
23.28	40800	55.29	54401	85.00	32399
24.04	41815	56.05	54087	85.77	30958
24.81	42663	56.81	54073	86.53	30238
25.57	43493	57.57	53236	87.29	29637
26.33	43806	58.33	53817	88.05	28514
27.09	44981	59.10	53237	88.81	27392
27.85	45779	59.86	52792	89.58	26222
28.62	45793	60.62	52161	90.34	25274
29.38	46888	61.38	51568	91.10	24504
30.14	47156	62.14	51492	91.86	23538
33.19	49454	62.91	50937	92.62	22670
33.95	50127	63.67	50412	93.39	20928
34.71	50998	64.43	50093	94.15	19244

K_n = 7.383 E14 (Nvt)/counts per minute

a. Elevation where the thermal neutron fluence was determined.

TABLE B-8. CIRCUMFERENTIAL FLUX WIRE GAMMA SCAN DATA FROM RODS 524-2 AND 524-3

Rod	Azimuthal Orientation[a] (degrees)	Location from End of Wire (cm)	Axial Elevation From Bottom of Fuel Stack: 13.57 cm (counts per minute x 10^4)	54.22 cm (counts per minute x 10^4)	84.70 cm (counts per minute x 10^4)
524-2	135	0	23959	40826	21989
	166	0.762	27615	48318	25073
	197	1.524	29125	51449	26252
	229	2.286	30061	53165	27564
	260	3.048	31120	54657	28536
	291	3.810	31478	55460	28699
	322	4.572	31706	56326	28836
	354	5.334	31906	56226	28852
	25	6.096	31533	55113	28267
	56	6.858	30620	52674	27571
	87	7.620	29583	46412	26969
	119	8.382	29094	44004	25503
	150	9.144	25477	42277	24253
		K_n factors	7.880E13	7.871E13	7.887E13
524-3	315	0	40486	42656	30736
	346	0.762	46103	49157	34806
	17	1.524	41935	51865	36938
	49	2.286	51153	53555	38398
	80	3.048	53339	54236	39413
	111	3.810	54073	55553	39217
	142	4.572	54122	55145	39627
	174	5.334	52934	53788	38018
	205	6.096	51569	52118	35575

TABLE B-8. (continued)

Rod	Azimuthal Orientation[a] (degrees)	Location from End of Wire (cm)	Axial Elevation From Bottom of Fuel Stack: 13.57 cm (counts per minute x 10^4)	54.22 cm (counts per minute x 10^4)	84.70 cm (counts per minute x 10^4)
524-3 (continued)	236	6.858	49517	49956	32268
	267	7.620	47063	47177	
	299	8.382	44974	42128	
	330	9.144	42707	42966	
		K_n factors	7.822E13,	7.915E13	8.045E13

a. Orientation is relative to center of the test train assembly.

RADIOCHEMICAL BURNUP ANALYSIS

One fuel burnup sample was cut from each of the Test PR-1 fuel rods for radiochemical burnup analysis. The specific locations from which the samples were removed are listed in Table B-9. Each rod was sectioned separately to avoid cross contamination of the samples. The fuel rods were sectioned using a "cono" saw with a diamond impregnated blade, regulated by a variac to control the cutting speed. The diamond impregnated blade was lubricated during cutting with water. Sections of the fuel rods identified for analytical burnup analysis were transferred to the Idaho Chemical Processing Plant, a facility operated by EXXON Nuclear Idaho Company, Inc. The radiochemical burnup analysis results are presented in Table B-10. The fissions per gram of total uranium, based on the ^{95}Zr isotope, are converted in the table to burnup in megawatt days per metric ton of uranium (MWd/t).

TABLE B-9. FUEL ROD BURNUP SECTIONING FOR TEST PR-1

Rod	Sample Location
524-1	Cut section 21.88 to 23.38 cm from bottom of fuel stack.
524-2	Cut section 42.18 to 43.68 cm from bottom of fuel stack.
524-3	Cut section 24.38 to 25.88 cm from bottom of fuel stack.
524-4	Cut section 42.18 to 43.68 cm from bottom of fuel stack.

Two comments can be made concerning the sample taken from Rod 524-1. First, the low burnup values measured via ^{137}Cs and ^{140}Ba may be due to the high solubility of cesium and barium in water. Since this rod failed during the nuclear operation of Test PR-1, the burnup results from these isotopes are probably unreliable. Second, the fuel and zircaloy cladding of the sample had combined, and it was necessary to dissolve both components together. Thus, a portion of the ^{95}Zr atoms observed in the dissolver solution may have been produced via neutron capture of the cladding rather than produced from the neutron-induced fission of ^{235}U. Therefore, the burnup value calculated from the ^{95}Zr concentration is likely biased.

TABLE B-10. TEST PR-1 RADIOCHEMICAL ANALYSIS RESULTS

Rod	Sample Location from Bottom of Fuel Stack (cm)	Isotopic Composition (wt%)				Fissions/g Total U ($\times 10^{17}$) (via ^{95}Zr)[a]	Radiochemical Burnup (MWd/t)
		^{234}U	^{235}U	^{236}U	^{238}U		
524-1	21.88 to 23.38	0.07	10.09	0.11	89.73	2.09 ± 0.09[b]	98.32[b]
524-2	42.18 to 43.68	0.06	10.03	0.11	89.80	3.14 ± 0.13	109.51
524-3	24.38 to 25.88	0.05	10.04	0.11	89.80	2.59 ± 0.11	114.03
524-4	42.18 to 43.68	0.05	10.06	0.11	89.78	3.08 ± 0.13	107.41

a. Calculated from the radionuclide concentration.

b. The Rod 524-1 sample was melted and exposed to water during the test; thus, the burnup values are suspect.

VISUAL AND PHOTOGRAPHIC INSPECTION OF THE TEST PR-1 FUEL RODS

The separate shroud assemblies were visually examined through the hot cell window for evidence of damage. After disassembly and removal of each tested fuel rod from its shroud, the rods were visually inspected for gross damage. Each rod was then mounted on a display board (if intact) and oriented for additional visual examination and photographic documentation. The fuel rods were oriented with respect to a reference scribe mark of 0 degrees located on the bottom end cap. Composite appearances of the four fuel rods are shown in Figures B-6 through B-9. Posttest observations regarding each fuel rod are discussed in this section.

Rod 524-1

Rod 524-1 was waterlogged during the power burst testing because it had failed during the previous PCM transient test phase. This is the first known power burst testing of a waterlogged fuel rod at typical operating temperatures and pressures. When the rod was removed from the shroud, only the upper 42 cm could be removed intact. The shroud had to be split from 0 to 54.5 cm and opened in a clamshell section to remove the remainder of the rod. An overall posttest view of Rod 524-1 is shown in Figure B-6. The lower portion of the fuel rod (0 to 54.5 cm) is shown within the split flow shroud.

As shown in Figure B-6, the fuel rod exhibits extensive damage in the central region in the form of fuel and cladding loss, cladding oxidation, and fuel fragmentation.

The upper intact section of the rod (above 58 cm) exhibits severe cladding oxidation, some fuel loss, and a split in the cladding that extends from 58 to about 71 cm. The primary oxidation in this region was likely due to the extended time in high temperature film boiling at this elevation. The observed failure of Rod 524-1 during the high temperature operation of PCM Cycle 20 likely occurred in this region due to extensive cladding

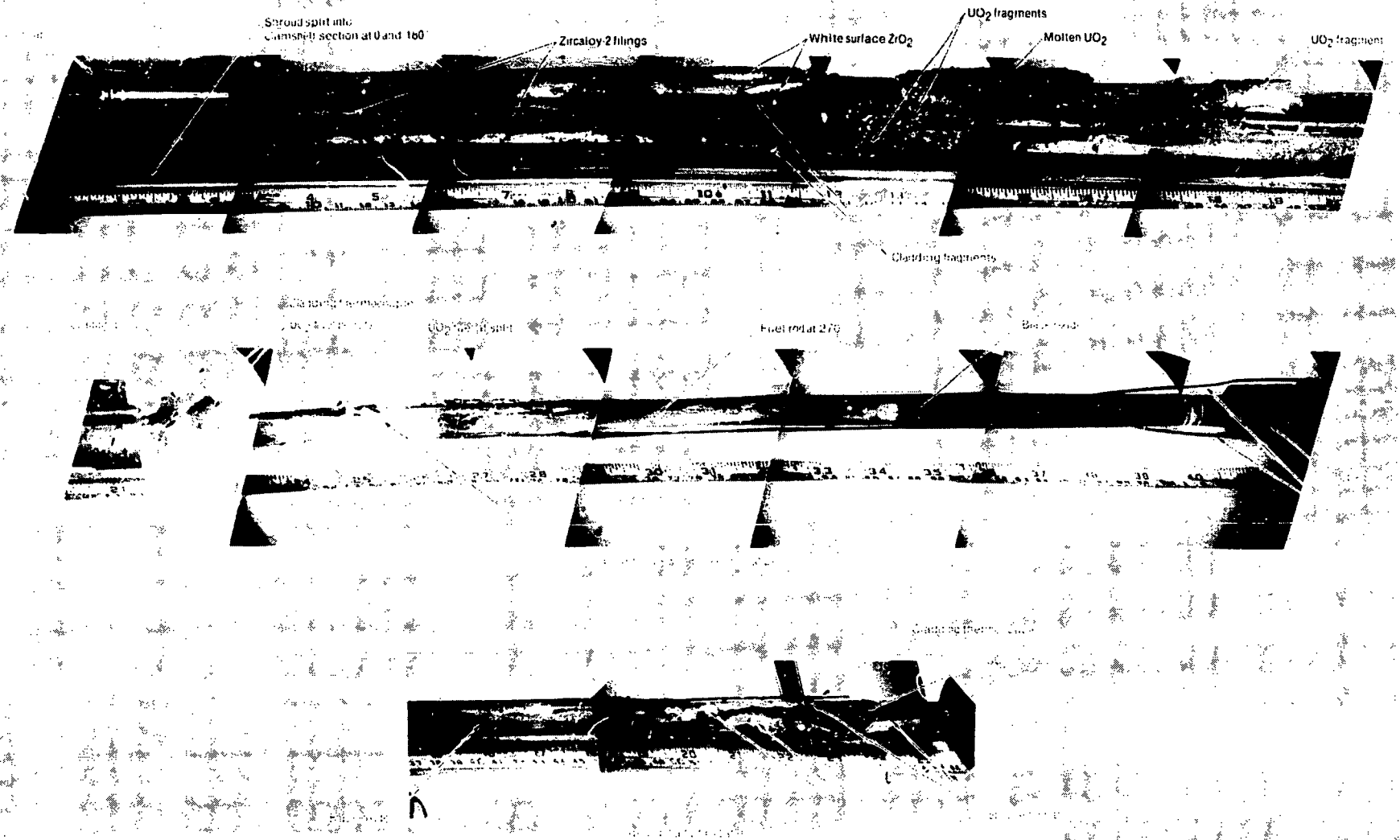
Shroud split into clamshell section at 0 and 180°
Zircaloy-2 filings
White surface ZrO_2
UO_2 fragments
Molten UO_2
UO_2 fragment
Cladding fragments
UO_2 pellet split
Fuel rod at 270°

(a) Overall view of rod at 120

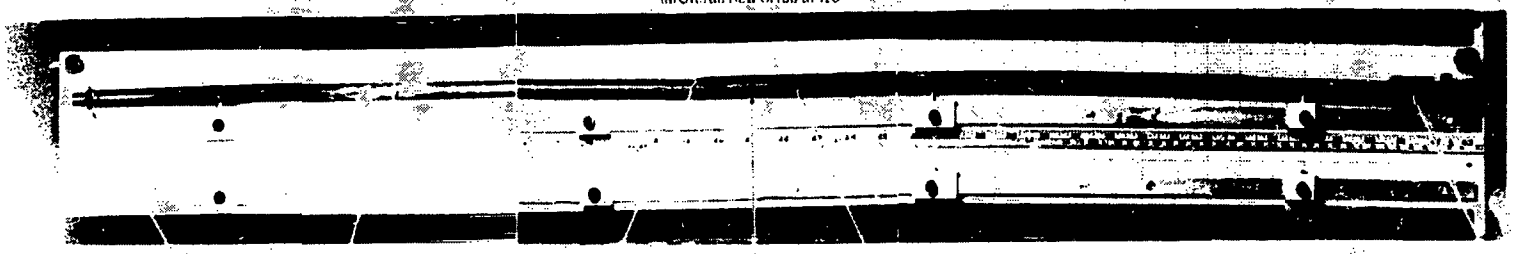

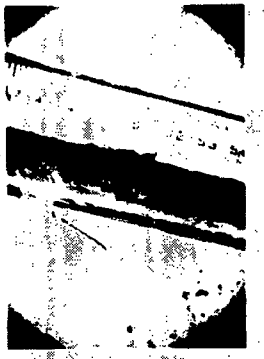

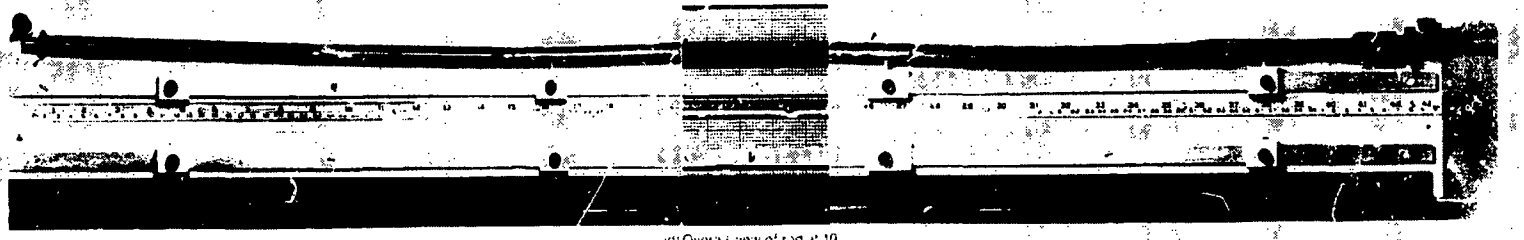

(d) Overall view of rod at 10

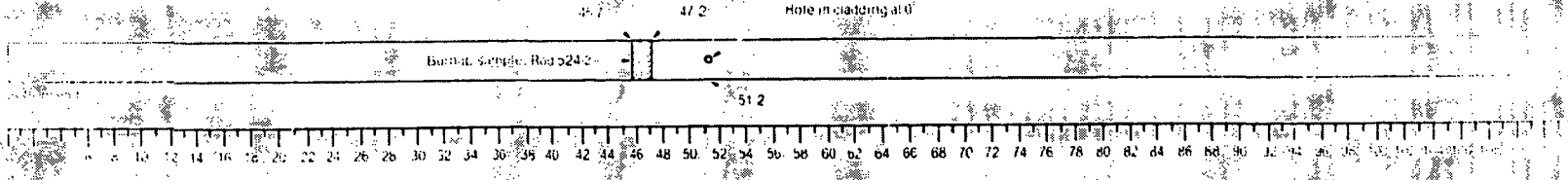

(e) Schematic of Rod 524-2 showing burnup sample section and region of damage

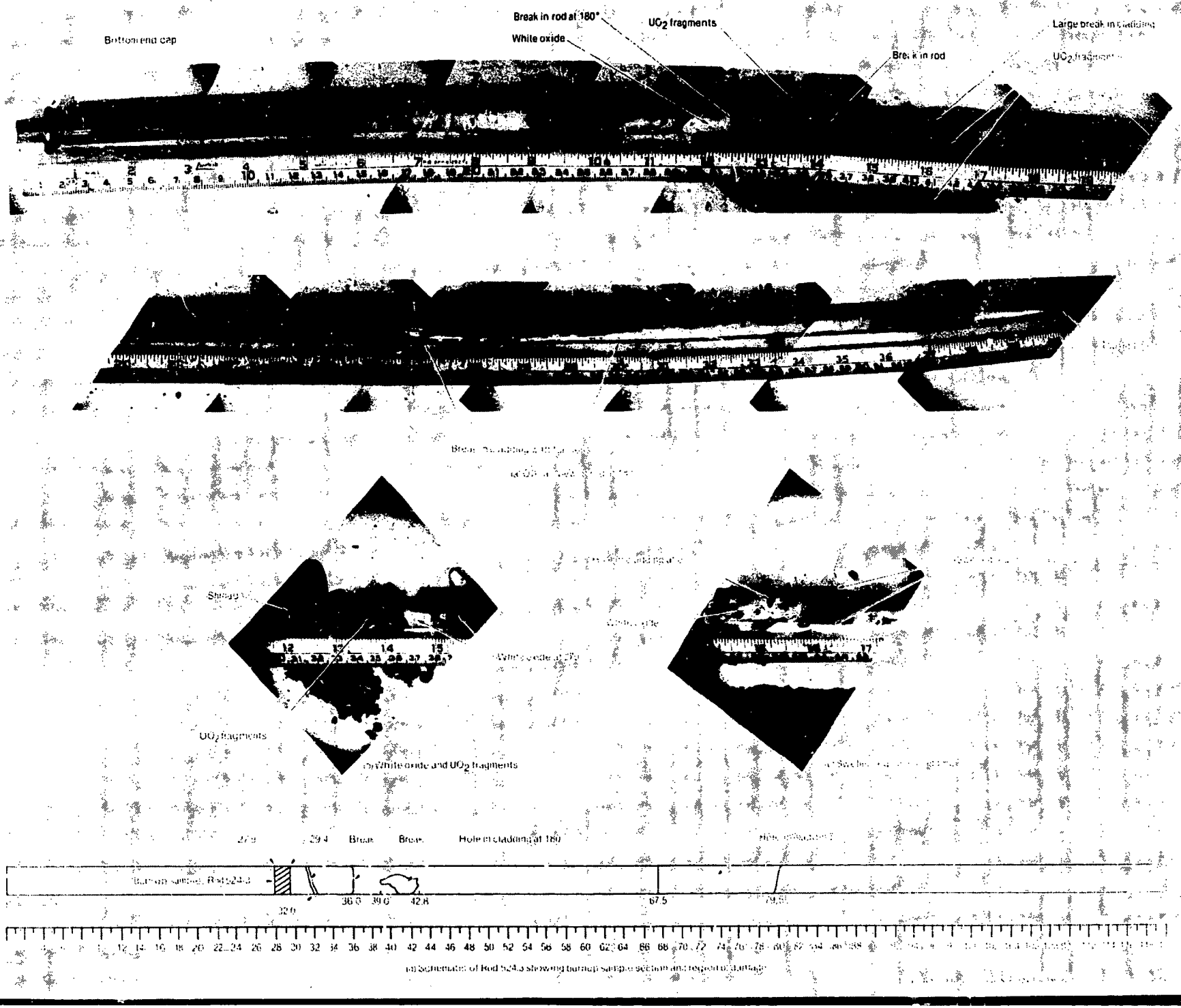
Bottom end cap
Break in rod at 180°
White oxide
UO_2 fragments
Break in rod
Large break in cladding
UO_2 fragments
Sheath
UO_2 fragments
White oxide and UO_2 fragments
Hole in cladding at 180°
36.0
39.0
42.8
67.5

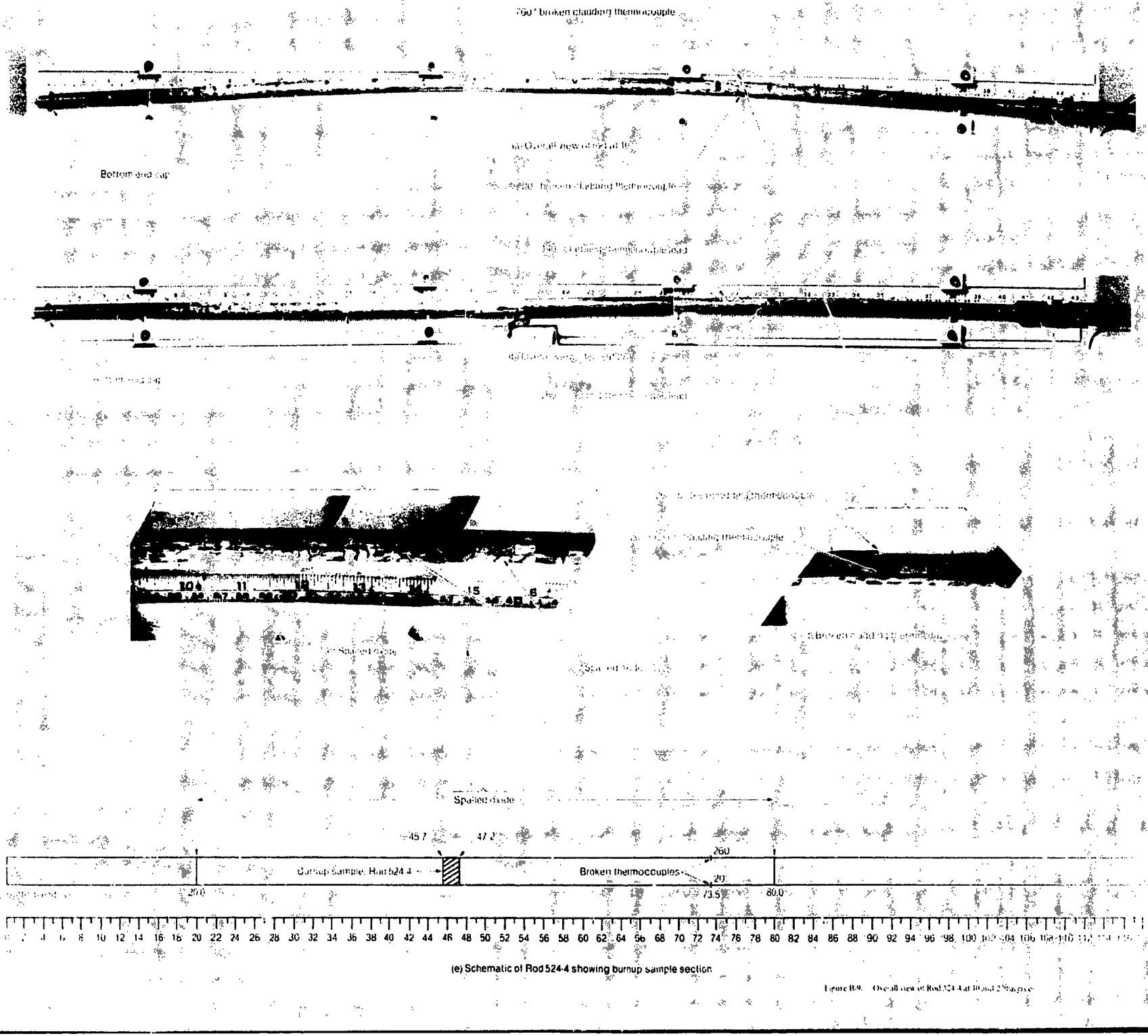

(e) Schematic of Rod 524-4 showing burnup sample section

Figure B9. Overall view of Rod 524-4 at 10 and 2 o'clock

oxidation. The cladding split from 58 to 71 cm was probably a result of the internal rod pressure increase during power burst operation on the highly embrittled, waterlogged fuel rod.

The middle section of Rod 524-1 (from about 29 to 58 cm) was the most severly damaged region of the four rods tested. Extensive fuel and cladding loss, fuel fragmentation, and cladding oxidation occurred over most of the region. Although cladding integrity was lost during PCM Cycle 20, based on on-line cladding elongation measurements, the rod geometry was maintained through the first power burst. During the second power burst (144 cal/g) the waterlogged rod separated, probably in the middle section, and some fuel was likely washed out due to the steam pressure buildup within the rod. The majority of the fuel fragmentation and rod breakup probably occurred during quench from the final power burst (212 cal/g). Blockage of the coolant flow channel due to fuel swelling and/or relocation occurred during the third power burst.

Only limited damage, in the form of cladding oxidation, was observed in the lower section of Rod 524-1. Oxidation in this region occurred during the second and third power bursts due to high temperature film boiling operation.

During the PCM cycles of Test PR-1, Rod 524-1 was operated in high temperature film boiling for about 8 min prior to rod failure. Rod failure at high temperature under PCM conditions has been observed in previous PBF testing when the cladding wall thickness is completely converted to oxide and oxygen-stabilized alpha zircaloy. Failure due to thermal stresses on highly embrittled cladding (such as during rewet from high temperature operation) have been observed for lesser amounts of cladding oxidation.

Following cladding rupture, Rod 524-1 was operated in high temperature film boiling for at least 18 min, during which time both internal and external cladding wall oxidation occurred. The additional high temperature (PCM) operation likely resulted in additional cladding oxidation and embrittlement over a large axial extent of the fuel rod.

Rod 524-2

High temperature film boiling operation was detected on Rod 524-2 only once prior to the power bursts for a brief (80 s) period (PCM Cycle 25). Extensive cladding damage due to oxidation was, therefore, not anticipated. A posttest overall view (excluding the upper and lower extremities) of Rod 524-2 is shown in Figure B-7. As expected, extensive oxidation in the upper portion of the rod (60 to 75 cm) was not apparent. The overall mottled appearance of the rod is typical of the cladding oxidation previously observed as a result of low energy deposition power bursts.

Rod 524-2 failed during the final (highest energy) power burst. The failure location can be seen in Figure B-7 at the 50.5-cm elevation, which corresponds to the peak power elevation on the rod. The hole is 1 x 3 mm in dimension and located at the 0-degree azimuthal orientation on the rod. The oval cladding breach was likely the result of high cladding local stresses from relocated fuel, or possibly cladding melt-through by high temperature (or molten) fuel. No other locations of cladding integrity loss were apparent from the visual examination.

Rod 524-3

The overall posttest appearance of Rod 524-3 is shown in Figure B-8. From the figure, two regions of severe cladding damage are apparent. In the upper region, from 66 to 77 cm, a split in the cladding and extensive white oxide can be seen. Cladding oxidation in this region is predominately due to high temperature film boiling operation for about 15 min during the nine detected high temperature transients on the rod. Cladding breakup in the upper damaged section is typical of cladding embrittlement failure due to high stress or thermal shock. Cladding failure in this region probably occurred during the PCM testing. No indication of Rod 524-3 failure prior to the power bursts was observed, but from the estimated temperature history, the rod likely failed during the PCM transients.

The most severely damaged segment of Rod 524-3, from about 31 to 44 cm in Figure B-8, exhibits severe cladding oxidation and fracturing, fuel fragmentation, and complete separation of the fuel rod. The cladding elongation

measurement on this rod indicated rod separation during Power Burst 2 (144 cal/g). The third power burst (212 cal/g) likely precipitated most of the damage seen in this region due to the high energy of the pulse and the waterlogged condition of the rod.

Rod 524-4

Rod 524-4 was the only Test PR-1 fuel rod with argon fill gas. The rod did not fail during the entire test operation. The posttest appearance is shown in Figure B-9. The overall mottled appearance of the rod is very similar to that observed on Rod 524-2, and is typical of high temperature oxidation during low energy RIA power bursts. The rod experienced brief, high temperature film boiling operation during only three of the PCM cycles (cumulative time of about 2.7 min) and, therefore, the cladding was not extensively oxidized or embrittled prior to the power burst operation. The short exposure to high temperatures prior to the power bursts, and possibly the low conductivity (relative to helium) of the argon fill gas, probably contributed to the minimal damage (and nonfailure) of Rod 524-4 during Test PR-1.

POSTTEST CLADDING DIAMETRAL MEASUREMENTS

Posttest diametral measurements of the test rod cladding were obtained for comparison with pretest measurements. Measurements were taken remotely in a hot cell using a micrometer. Diametral data obtained for the four test rods at various axial elevations are detailed in Table B-11, and plotted in Figure B-10. The measurement elevations are referenced to the bottom of the fuel stack, which is 35.2 mm from the bottom of the fuel rod.

Comparison of the posttest cladding diameters (Table B-11) with the respective pretest dimensions (Tables B-2, B-3, B-4, or B-5) indicates a general increase in diameter following the test. The slight (0.1 to 0.3 mm) increase in diameter of the upper and lower rod extremities is generally associated with the cladding oxygen uptake during the oxidation process. The larger diameter increase (up to 3.6 mm on Rod 524-1 at the 59.98-cm elevation) in the middle portion of each rod is likely a combination of

TABLE B-11. TEST PR-1 ROD CLADDING OUTSIDE DIAMETER DATA

Rod 524-1			Rod 524-2			Rod 524-3			Rod 524-4		
Location From Bottom of Fuel Stack (cm)	Diameter[a] (mm) 0°	90°	Location From Bottom of Fuel Stack (cm)	Diameter[a] (mm) 0°	90°	Location From Bottom of Fuel Stack (cm)	Diameter[a] (mm) 0°	90°	Location From Bottom of Fuel Stack (cm)	Diameter[a] (mm) 0°	90°
1.56	12.65	12.70	1.56	12.50	12.50	1.56	12.62	12.62	1.56	12.52	12.52
6.64	12.70	12.70	6.64	12.47	12.50	6.64	12.70	12.70	6.64	12.57	12.55
11.72	13.97	13.97	11.72	12.52	12.52	11.72	12.85	12.85	11.72	12.55	12.57
14.26	12.93	12.95	16.80	12.62	12.55	14.26	12.90	12.88	16.80	12.60	12.62
16.80	13.11	13.05	21.88	12.62	12.65	16.80	12.93	13.00	21.88	12.67	12.70
19.34	13.11	13.11	26.96	12.75	12.67	19.34	13.00	13.08	24.42	12.72	12.65
21.88	13.16	13.16	29.50	12.70	12.70	21.88	13.21	13.31	26.96	12.80	12.62
24.47	13.28	13.16	32.04	12.78	12.72	24.42	13.33	13.39	29.50	12.72	12.57
57.44	--	14.73	34.58	12.80	12.72	26.96	13.16	13.36	32.04	12.85	12.65
59.98	--	16.10	37.12	12.70	12.78	34.56	13.36	13.97	34.58	12.78	12.70
62.52	--	15.01	39.66	12.80	12.75	37.12	12.52	11.81	37.12	12.75	12.78
65.06	--	15.24	42.20	12.70	12.75	39.66	13.31	13.21	39.66	12.85	12.70
67.60	14.06	13.51	44.74	12.62	12.70	42.20	13.18	13.21	42.20	12.78	12.70
70.14	13.89	13.54	47.28	12.90	--	47.28	13.21	13.11	44.74	12.70	12.70
72.68	13.99	12.95	49.82	13.08	--	49.82	13.23	13.11	47.28	12.72	13.56
75.22	13.87	12.80	52.36	12.98	--	52.36	13.66	12.91	49.82	12.75	13.51
77.76	13.87	12.90	54.90	13.06	--	54.90	13.66	13.03	52.36	12.80	13.51
80.30	13.87	12.93	57.44	13.26	13.79	57.44	13.16	12.95	54.90	12.80	13.51
82.84	13.87	12.80	59.98	13.41	--	59.98	13.18	13.08	57.44	12.75	13.64
85.36	13.36	12.93	62.52	13.16	13.87	62.52	13.69	14.66	59.98	12.65	13.36
87.92	13.31	12.83	65.06	12.93	--	65.06	13.51	14.10	62.52	12.62	13.46
90.46	13.33	12.55	67.60	13.08	13.92	67.60	13.61	14.66	65.06	12.62	13.61
93.00	12.52	12.70	70.14	12.90	--	70.14	15.42	13.84	67.60	12.60	14.22
			72.68	13.16	13.97	72.68	13.69	13.99	70.14	12.60	13.59

TABLE B-11. (continued)

Rod 524-1			Rod 524-2			Rod 524-3			Rod 524-4		
Location From Bottom of Fuel Stack (cm)	Diameter[a] (mm) 0°	90°	Location From Bottom of Fuel Stack (cm)	Diameter[a] (mm) 0°	90°	Location From Bottom of Fuel Stack (cm)	Diameter[a] (mm) 0°	90°	Location From Bottom of Fuel Stack (cm)	Diameter[a] (mm) 0°	90°
			75.22	13.03	--	75.22	13.06	13.44	72.68	12.60	13.51
			77.76	13.21	14.10	77.76	13.00	12.93	75.22	12.55	13.54
			80.30	13.26	--	80.30	13.08	13.00	77.76	12.52	13.33
			82.84	13.11	13.54	82.84	13.18	13.59	80.30	12.50	13.46
			85.38	13.21	--	85.38	12.95	13.49	82.84	12.50	13.59
			87.92	12.75	13.39	87.92	13.31	12.52	85.38	12.83	13.49
			90.46	12.57	--	90.46	12.72	12.52	87.92	12.47	13.33
			93.00	12.70	12.65	93.00	12.52	12.52	90.46	12.45	12.52
			95.54	12.57	--	95.54	12.52	12.62	93.00	12.62	12.52

a. Diametral measurement accuracy is 0.[illegible] mm.

BLANK

PAGE

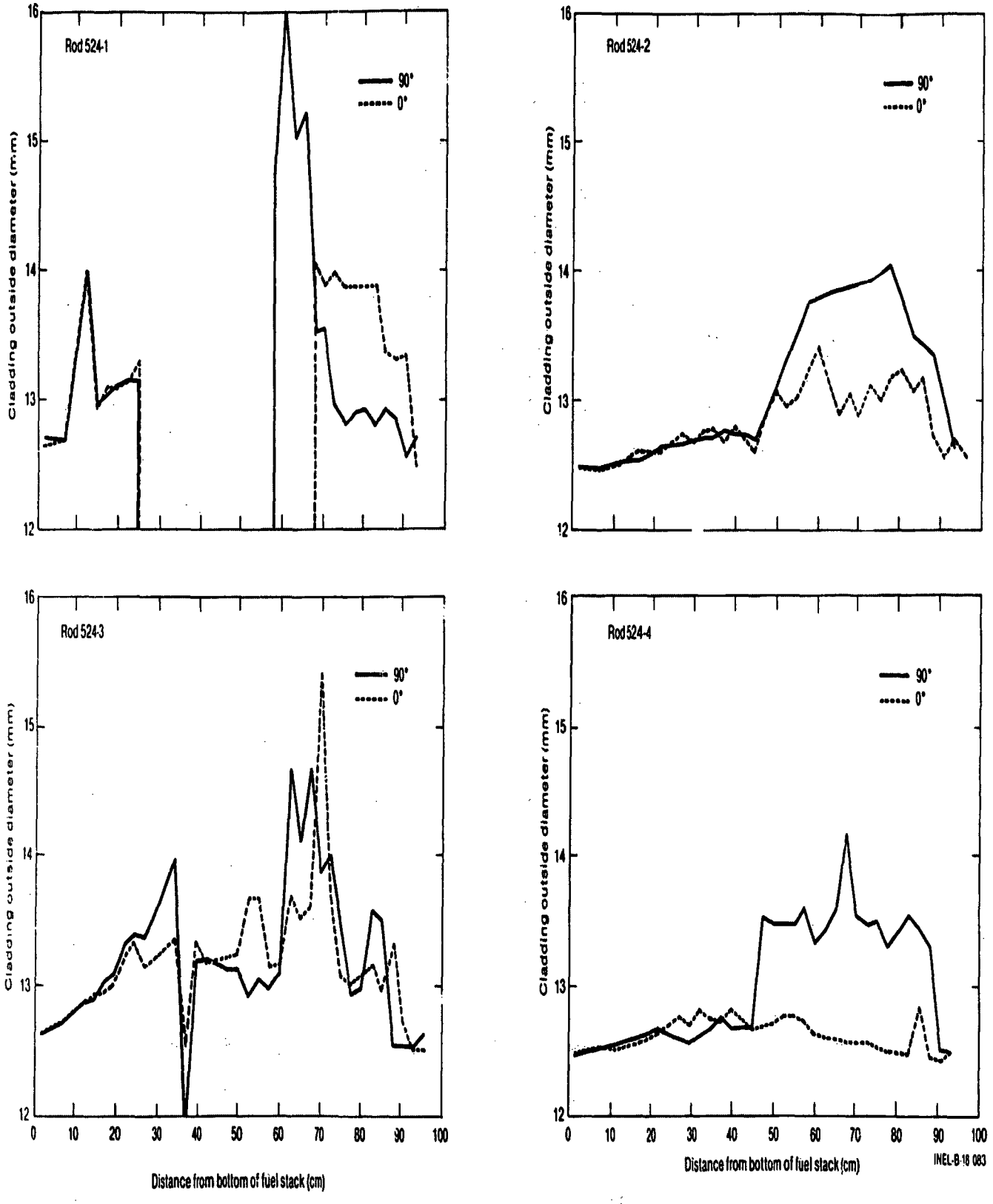

Figure B-10. Test PR-1 cladding outside diameter measurements.

oxygen uptake and cladding swelling due to fuel expansion during the RIA power bursts. The largest diametral increases were observed for the two rods that were waterlogged for the final power burst, Rods 524-1 and 524-3. Steam pressure buildup during the power burst(s) on the waterlogged fuel rods likely contributed to tne cladding diameter increases.

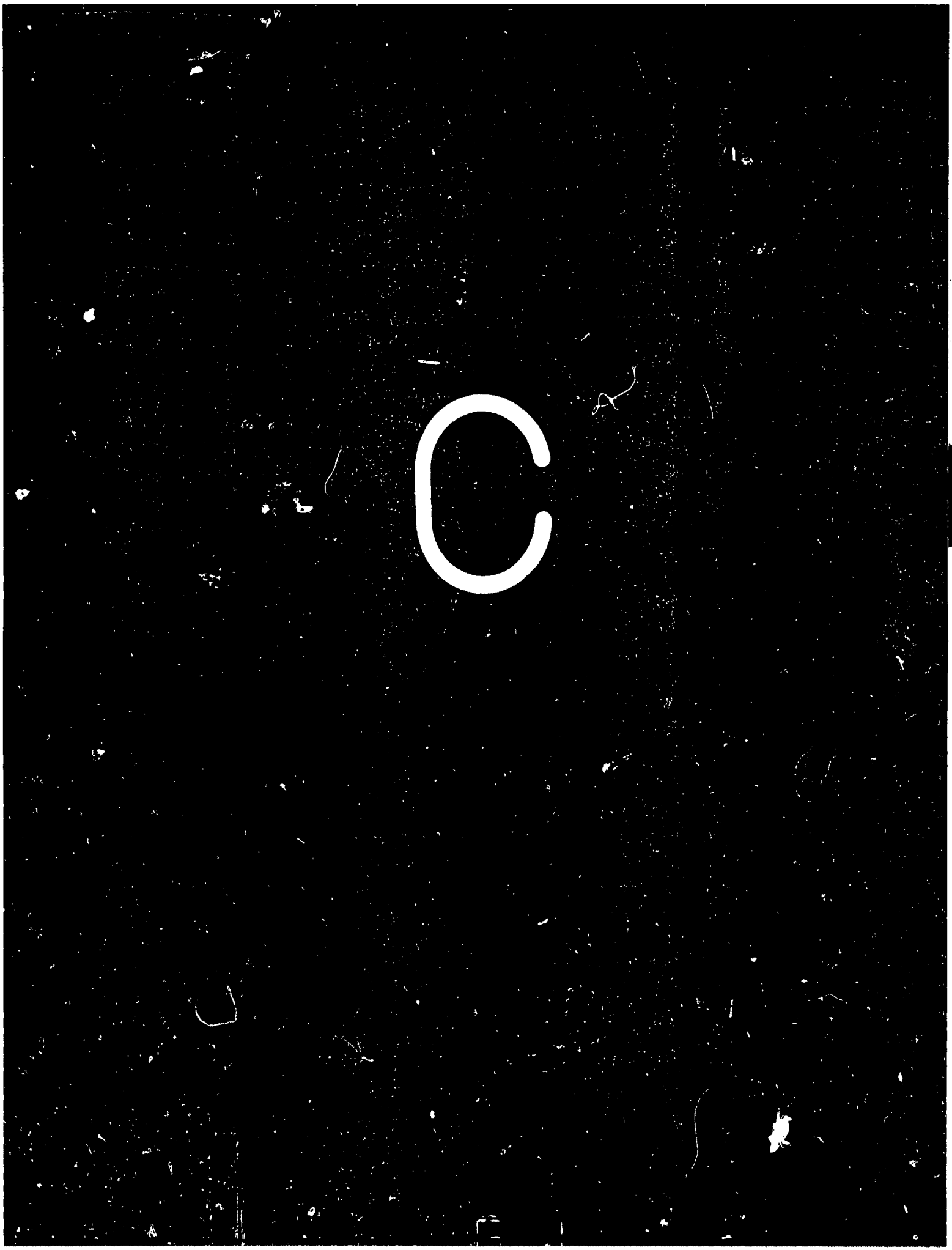

APPENDIX C

TEST PR-1 DATA QUALIFICATION, UNCERTAINTIES, AND DATA PLOTS

BLANK

PAGE

APPENDIX C

TEST PR-1 DATA QUALIFICATION, UNCERTAINTIES, AND DATA PLOTS

This appendix describes the Test PR-1 data qualification procedures, the methods for evaluating uncertainties, and detailed plots of the qualified data.

DATA QUALIFICATION PROCEDURES AND CATEGORIES

The data qualification procedures for Test PR-1 are outlined in this section. The procedures consist of specific actions taken before, during, and after the test, resulting in the categorization of the data as qualified or failed. The plots are presented on microfiche cards titled "Test PR-1 Qualified Data Plots."

The following procedures are listed in order of performance:

1. Data Acquisition Specification (DAS) (part of test setup).

   Transducer calibration coefficients were developed and checked for use in the Data Acquisition and Reduction System (DARS) directory. For those instruments that were not calibrated, coefficients were determined on the basis of laboratory calibration data. Some of the coefficients were adjusted as a result of in-place calibration or special experiment requirements. All such adjustments were either directed or approved by the Data Integrity Review Committee (DIRC).

2. PBF/DARS Precalibration.

   Each DARS channel was calibrated prior to the beginning of the test by voltage insertion at the electronic input. The input magnitude, frequency, polarity or wave form of the test signal was representative of the transducer output for that channel.

The experiment test data were corrected by adjusting the DARS coefficients for zero offset or gain error introduced by the electronics on the basis of this pretest calibration.

3. System Checkout.

After the installation of the test train and interconnections to the PBF/DARS were completed, the following data were taken on each applicable channel;

3.1 Millivolt readings from sensor.

3.2 The sensor was connected to the input patch panel with the same millivolt output as in Step 3.1, and readings taken on:

3.2.1 Low-level amplifier output in millivolts

3.2.2 Processed output in counts

3.2.3 Engineering unit value indicated on DARS terminal or printout.

3.3 The various readings were compared against the calculated outputs for the same input values. If discrepancies were found, appropriate corrective action was taken.

4. Cold Hydrostatic Pressure Verification.

This test verified pressure instrumentation operation by increasing the pressure from ambient (0.62 MPa) to 15.6 MPa in about 10 steps, and then decreasing the pressure back to ambient, taking readings at the same pressure values. The data from the various pressure sensors were checked against a reference gauge to determine that they were functional, and also to determine any systematic errors, hysteresis, drift, etc.

5. Autocalibration.

The instrument channels were calibrated with the automatic system, which makes corrections to the DARS engineering unit coefficients for about 80% of the channels.

6. Heatup.

The PBF operating pressure and temperature were increased from ambient to prenuclear test operating conditions. Instrument readings taken during heatup were used to verify fuel rod and test train instrument readings and determine temperature effects. When the temperature had stabilized at about 540 K, a printout of the test train instrument readings was made. All test train thermocouples were aligned to the mean by adjusting the DARS engineering unit coefficients. The pressure transducers were also corrected at this time against the standard Ashcroft gauge.

Other instruments were also checked for temperature effects, but corrections were considered unnecessary or inappropriate due to other factors.

7. Power Calibration.

During this test phase, intercalibration of fuel rod power with signals from self-powered neutron detectors, self-powered gamma detectors, and ion chambers was accomplished. The nuclear instrumentation was verified during this test phase. Also, nuclear effects on other instrumentation were sometimes noted when comparing sensor outputs during heated, nonnuclear operation with those of nuclear operation. The data were classified in accordance with the DIRC classification for Engineering Unit Data for steady state operation during the test period from power calibration to just prior to the transient test phase.

8. Preconditioning.

This test phase allowed for fuel cracking to simulate normal reactor fuel. Normal steady state response of the instruments applied. This test phase was performed in conjunction with the power calibration.

9. Transient.

This phase of the test included the power oscillations, PCM transients, and RIA power burst operating conditions. Plots of the transducer response of each channel were examined to determine whether the transient signal represented the expected, predicted, and required response. The response of all similar instrumentation channels were compared as a secondary check. The data were later classified in accordance with the DIRC classification system for Engineering Unit Data.

10. Cooldown.

No specific request was made for qualified data during the cooldown phase.

11. PBF/DARS Postcalibration.

Each DARS channel was calibrated at the completion of the cooldown phase in the same manner as was done for the precalibration. Pre- and posttest electronics calibrations were compared to determine electronic drift or offsets. The data were then corrected for any electronics errors where necessary.

12. Data qualification was performed by the Data Qualification and System Engineering Group, and the corrections were applied by the Data Applications Group.

Categories

The classification of engineering unit data is made by assignment of data to defined categories during particular test intervals. The assignment is based on measurement-by-measurement examination of single-channel test data in engineering units. The examination process determines whether the measurement channel output represented the expected, predicted, and required response. As a result of examination, one or more of the categories defined below is assigned to each measurement, for each time interval.

1. Qualified Engineering Unit Data (QEUD)

2. Failed Data (F)

3. Unqualified Data (UD)

4. Not Reviewed Data (NRD).

Qualified Data. Data are qualified with DIRC approval and must meet all the following criteria:

1. Engineering unit conversion equations have been applied.

2. Data acquisition system calibrations have been applied.

3. All identifiable and verifiable systematic errors have been removed.

4. Uncertainty limits have been established for the 95% confidence level, including

    a. Calibration uncertainties

    b. Systematic and random uncertainties due to effects on perturbations of the phenomena

c. Uncertainties due to the application of any models

d. Uncertainties in the measurement channels and DARS.

5. Useful information is contained in the data.

Failed Data. Data are considered failed for one or more of the following reasons:

1. Data do not meet the requirements of any other data classification categories.

2. Useful information is irretrievable from the data.

3. There was a component failure in the measurement channel or in the data acquisition system.

4. Inadequate rejection of extraneous noise, transients, or frequencies.

5. Loss of time synchronization, data channel continuity, etc.

6. Enigmas in the data.

Unqualified Data. Unqualified data have been minimally processed and do not meet other qualification standards because

1. Data are not necessary to support test objectives.

2. Data are redundant and do not provide any information other than for internal or verification purposes.

Not Reviewed Data. Data which have not been reviewed by DIRC. This definition is for internal recordkeeping only.

DATA QUALIFICATION AND UNCERTAINTY

Test parameters within the Power Burst Facility in-pile tube and pressurized water loop are monitored by instrumentation consisting of many measurement channels. A transducer and associated signal conditioning electronics introduce uncertainty into the measurement of a specific parameter. To establish the validity of the experiments performed and their correlation to the analytical models, performance and accuracy of the test instrumentation and data recording system must be demonstrated. Uncertainties in instrument accuracy propagate through the experimental data to the evaluation of the analytical models and overall program results. The test measurement uncertainty analysis results are presented in this section for each measurement channel.

Uncertainty Evaluation Methods

A measurement channel includes the transducer, signal conditioning, and data acquisition and reduction system (DARS). The form of uncertainty presentation may be either tabular, presenting the uncertainty values for a particular operating condition, or graphical, with uncertainty versus input signal from which the user can determine the uncertainty for any value within the useful range of the transducer. The uncertainty values in either engineering units or percent of reading, are determined from the equation

$$U = B + t_{95} S \qquad \text{(C-1)}$$

where

U = uncertainty

B = total channel systematic error (bias)

S = total channel random error (precision index)

t_{95} = two-tailed student "t" factor for 95% confidence level.

The t_{95} factor is determined from a student "t" table and the degrees of freedom associated with random error measurement. The bias, B, is the root-sum-square (RSS) of all the elemental biases in the measurement channel. Likewise, the precision index is the RSS of all the elemental precision indices in the measurement channel. The uncertainty, U, is presented for each measurement channel. The values for bias, precision index, and degrees of freedom are given as backup and for use in propagating errors for any calculated parameters based on these measurements.

Test-independent uncertainty analyses of PBF measurement systems have been performed. The methodology used in the analysis of the uncertainties is based on standard statistical practices, which are applied in evaluating the constant and variable portions of both the bias and random error components of each measurement channel. The individual error components are then combined to produce a total measurement channel uncertainty.

When a measurement channel is analyzed for test-independent measurement uncertainty, that uncertainty applies to a representative assembly of specific types of channel components rather than a specific component. If an individual component is replaced by a component of the same type, the uncertainty of the measurement channel remains unchanged.

The data qualification procedure, performed by the PBF Data Integrity Review Committee (DIRC), serves to identify significant test-dependent uncertainties introduced in specific tests, such as instrument mounting effects, two-phase flow regimes, and transient measurements. In some cases, additional or special calibrations, multiple instrumentation, and additional engineering calculation can result in significantly lower uncertainty estimates than those found in the uncertainty analyses. These test-dependent considerations have been factored into the total uncertainty values presented for each measurement.

Qualification and Uncertainty Values

This section presents the qualification category and uncertainty values for the Test PR-1 data. The uncertainties are total uncertainties composed

of test-dependent and test-independent values. In some cases, the uncertainties are complete estimates; in other cases, the uncertainties are a combination of values compiled from uncertainty analyses and estimates. Generally speaking, the test-dependent uncertainties are estimates, and the test-independent uncertainties were obtained by analysis.

Table C-1 presents the Test PR-1 instruments, identifiers, and measurement locations. A brief description of each instrument is also contained in the table. Table C-2 presents the data qualification and the uncertainty values for Test PR-1. The uncertainties are listed as the random component, "S"; the bias component, "B"; the degrees of freedom, "dF"; and the total measurement uncertainty "U." The numbers are engineering unit uncertainties or percentages of uncertainty.

During the RIA burst phase of the test, the total uncertainty in the instrument measurements had to be estimated. Therefore, only a total uncertainty (U) is shown in Table C-2, and the random (S) and bias (B) component columns are left blank.

The numbers listed under "Notes" correspond to particular notes listed after the tables. The "Qualification" column indicates that the data were either qualified engineering unit data, "Q," or failed data, "F." The time period column lists the IRIG times for which the qualification applies. The RIA bursts are listed separately. Table C-3 gives the IRIG times corresponding to the major points in test history, plus the time that individual segments of the test start.

DATA PLOTS

Plots of the qualified data from Test PR-1 are presented on microfiche cards following the appendixes to this report. Table C-4 presents the general grouping of the plots for the various test phases.

TABLE C-1. INSTRUMENTATION FOR TEST PR-1

Measurement	Instrument	Instrument Location[a]	Fuel Rods Instrumented	Identifier	Description
Coolant pressure	Pressure transducer	Near outlet of IPT flow tube		SYS PRES 70 OUT TT	EG&G Idaho strain gage type transducer.
Coolant pressure	Pressure transducer	Near outlet of IPT flow tube		SYS PRES 17 OUT TT	EG&G Idaho strain gage type transducer.
Coolant flow	Turbine flowmeter	Inlet of each flow shroud		FLOWRATE 01, 02, 03, 04	Flow Technology turbine type full-flow meter.
Coolant inlet temperature	Thermocouple	Two thermocouples near inlet of flow shroud		IN TEMP 01 IN TEMP 02	Stainless steel sheathed, Type K thermocouple.
Coolant outlet temperature	Thermocouple	Outlet of each flow shroud		OUT TEMP 01, 02, 03, 04	Stainless steel sheathed, Type K thermocouple.
Coolant differential temperature	Thermocouple pairs	Inlet and outlet of each flow shroud		DEL TEMP 01, 02, 03, 04	Copper constantan thermocouples connected differentially.
Relative neutron flux	SPNDs	Two vertical columns; five detectors in one column and two in the other; located 180° apart		NEUT FLX 03, 05, 06, 07, 08, 09, 10	Cobalt self-powered neutron detectors.
Integrated neutron flux (axial)	(0.51% Co-Al) for 2 rods	Outer surface of flow shrouds		--	Cobalt-aluminum flux wires.
Integrated neutron flux (circumferential)	(0.51% Co-Al) for 2 rods	Outer surface of flow shroud (ten equally spaced axial elevations)		--	Cobalt-aluminum flux wires.
Cladding elongation	LVDT	Lower end of each rod		CLAD DSP 01, 02, 03, 04	EG&G Idaho type linear variable differential transformer.
Flow shroud change in pressure	ΔP	Shrouds of rods 524-3 and 524-4		SHRD DEL PRESS 03, 04	Sensotec Inc., differential pressure transducer.
Core power	Ion chambers	PBF core		REAC POW NMS3, PPS1, PPS2, PPS3, PPS4	N_2 filled ion chambers.
Transient power	Ion chambers	PBF core		REAC POW TR1, TR2, EV1, EV2	TR is N_2 filled, EV is evacuated. Transient ion chambers.

TABLE C-1. (continued)

Measurement	Instrument	Instrument Location[a]	Fuel Rods Instrumented	Identifier	Description
IPT ΔP	ΔP	Across IPT		IPT DELP PT	Variable inductance type transducer.
Loop pressure	Ashcroft (Heise)	Loop		SYS PRES PT	Ashcroft Type 778 with digital readout.
Fuel centerline temperature	Thermocouple (1)	452.1 mm	524-1 524-2 524-3	FUEL TMP CL 01 FUEL TMP CL 02 FUEL TMP CL 03	Mo-Re sheathed, W5%Re -W26%Re thermocouples, 1.57-mm outside diameter.
Fuel centerline temperature	Thermocouple (1)	452.1 mm	524-4	FUEL TMP CL 04	Mo-Re sheathed, W5%Re -W26%Re thermocouples, 1.57-mm outside diameter.
Fuel off-center temperature	Thermocouple (3)	452.1 mm (0, 120, 240° azimuthal orientations)	524-1 524-2 524-3	OFF TMP -0,-120,-240,01 OFF TMP -0,-120,-240,02 OFF TMP -0,-120,-240,03	Inconel sheathed, Type K thermocouples, 1.0-mm outside diameter.
Fuel off-center temperature	Thermocouple (3)	452.1 mm (0, 120, 240° azimuthal orientations)	524-4	OFF TMP -0,-120,-240,04	Mo-Re sheathed, W5%Re -W26%Re thermocouples, 1.0-mm outside diameter.
Cladding surface temperature	Thermocouple (3)	452.1 mm (60, 180, 300° azimuthal orientations)	524-1 524-2 524-3	CLAD TMP -60,-180,-300,01 CLAD TMP -60,-180,-300,02 CLAD TMP -60,-180,-300,03	Ti sheathed, Type K thermocouples, 1.17-mm outside diameter.
Cladding surface temperature	Thermocouple (3)	Two at 700 mm (20 and 260° azimuthal orientations) and one at 452.1 mm (140° orientation)	524-4	CLAD TMP 70-20, 70-260, 75-140, 04	Ti sheathed, Type K thermocouples, 1.17-mm outside diameter.
Rod internal pressure	Pressure transducer (1)	Upper plenum of rod	All	ROD PRES 01 ROD PRES 02 ROD PRES 03 ROD PRES 04	Kaman eddy current type.
Cladding internal temperature	Thermocouple (3)	One at 700 mm, one at 750 mm	524-4	CLDINTTMP 70-60, 75-180, 04	Inconel sheathed, Type K thermocouples, 0.25-mm outside diameter.

a. Elevations are measured from the bottom of the fuel stack.

NUREG/CR-2126 FUEL ROD BEHAVIOR DURING TEST PR-1
EGG-2102 D.T. SPARKS et al; EG&G IDAHO INC.
UNCLASSIFIED JUNE 1981

2 OF 2

NUREG CR
2126
EGG 2102
6 81

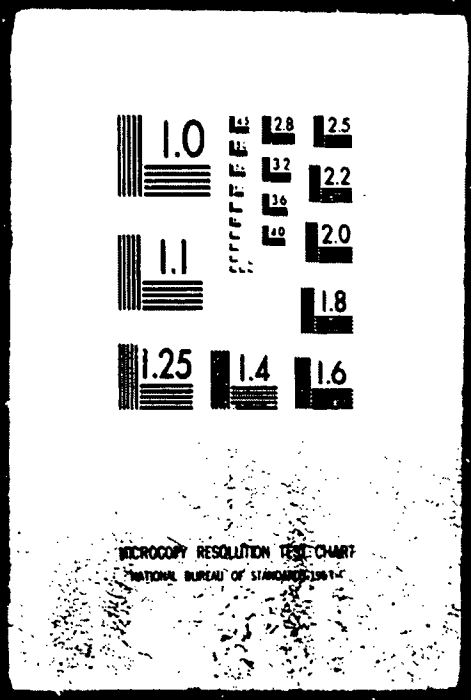

TABLE C-2. PR-1 DATA QUALIFICATION AND UNCERTAINTY VALUES

Measurement Identifier	Parameter Number	Time Period	Qualification	Note[a]	Uncertainty[b]			
					S	dF	B	U
FUEL TMP CL 01	84	Up to 45:07:25:00	Q	12	0.2 K + 1.35% (RDG - 255)	>30	11.73K + 25% (RDG - 1200)	12.13 K + 2.7% (RU - 225) + 25% (RD - 1200) (see note 12)
FUEL TMP CL 02	85	All except bursts	Q		0.2 K + 1.35% (RDG - 255)	>30	11.73K + 25% (RDG - 1200)	12.13 K + 27% (RDG - 225) + 25% (RDG - 1200) (see note 12)
FUEL TMP CL 03	86	Up to 39:00:00:00	Q	1	0.2 K + 1.35% (RDG - 255)	>30	11.73 K + 25% (RDG - 1200)	12.13 K + 2.7% (RDG - 225) + 25% (RDG - 1200) (see Note 12)
FUEL TMP CL 04	97	Up to 51:22:45:00	Q		0.2 K + 1.35% (RDG - 255)	>30	11.73 K + 25% (RDG -1200)	12.13 K + 2.7% (RDG - 225) + 25% (RDG - 1200) (see Note 12)
OFF TEMP O 01	98	All except bursts	Q		1.12 K + 0.38% (RDG - 255)	>30	5.1 K	7.34 K + 0.76% (RDG - 255)
OFF TEMP 120 01	99	Up to 52:10:12:50	Q		1.12 K + 0.38% (RDG - 255)	>30	5.1 K	7.34 K + 0.76% (RDG - 255)
OFF TEMP 240 01	100	Up to 45:07:25:00	Q		1.12 K + 0.38% (RDG - 255)	>30	5.1 K	7.34 K + 0.76% (RDG - 255)
OFF TEMP O 02	101	Up to 52:10:12:50	Q		1.12 K + 0.38% (RDG - 255)	>30	5.1 K	7.34 K + 0.76% (RDG - 255)
OFF TEMP 120 02	102	Up to 53:01:35:50	Q		1.12 K + 0.38% (RDG - 255)	>30	5.1 K	7.34 K + 0.76% (RDG - 255)
OFF TEMP 240 02	103	Up to 53:01:35:50	Q		1.12 K + 0.38% (RDG - 255)	>30	5.1 K	7.34 K + 0.76% (RDG - 255)

TABLE C-2. (continued)

Measurement Identifier	Parameter Number	Time Period	Qualification	Note[a]	Uncertainty[b] S	dF	B	U
OFF TEMP 0 03	104	Up to 52:10:12:50	Q		1.12 K + 0.38% (RDG - 255)	>30	5.1 K	7.34 K + 0.76% (RDG - 255)
OFF TEMP 120 03	105	Up to 42:09:46:00	Q	2	1.12 K + 0.38% (RDG - 255)	>30	5.1 K	7.34 K + 0.76% (RDG - 255)
OFF TEMP 240 03	119	Up to 52:10:12:50	Q		1.12 K + 0.38% (RDG - 255)	>30	5.1 K	7.34 K + 0.76% (RDG - 255)
OFF TEMP 0 04	117	All	F					
OFF TEMP 120 04	118	All	F					
OFF TEMP 240 04	9	All	F					
CLAD TMP 60 01	10	All except bursts	Q		1.12 K + 0.38% (RDG - 255)	>30	5.1 K	7.34 K + 0.76% (RDG - 255)
CLAD TMP 180 01	11	All	F	3				
CLAD TMP 300 01	59	All except bursts	Q		1.12 K + 0.38% (RDG - 255)	>30	5.1 K	7.34 K + 0.76% (RDG - 255)
CLAD TMP 60 02	62	Up to 53:01:35:50	Q		1.12 K + 0.38% (RDG - 255)	>30	5.1 K	7.34 K + 0.76% (RDG - 255)
CLAD TMP 180 02	239	All except bursts	Q		1.12 K + 0.38% (RDG - 255)	>30	5.1 K	7.34 K + 0.76% (RDG - 255)
CLAD TMP 300 02	240	All except bursts	Q		1.12 K + 0.38% (RDG - 255)	>30	5.1 K	7.34 K + 0.76% (RDG - 255)
CLAD TMP 60 03	241	All except bursts	Q		1.12 K + 0.38% (RDG - 255)	>30	5.1 K	7.34 K + 0.76% (RDG - 255)
CLAD TMP 180 03	242	All except bursts	Q		1.12 K + 0.38% (RDG - 255)	>30	5.1 K	7.34 K + 0.76% (RDG - 255)

TABLE C-2. (continued)

Measurement Identifier	Parameter Number	Time Period	Qualification	Note[a]	Uncertainty[b] S	dF	B	U
FUEL TMP CL 02	85	Bursts only	Q	16/12				13.0 K + 4% (RDG - 225) + 27% (RDG - 1200)
OFF TEMP 0 01	98	Bursts only	Q	16				11 K + 4% (RDG - 255)
OFF TEMP 120 02	102	Burst 1 only	Q	16				11 K + 4% (RDG - 255)
OFF TEMP 240 02	103	Burst 1 only	Q	16				11 K + 4% (RDG - 255)
CLAD TMP 60 01	10	Bursts only	Q	16				10 K + 3% (RDG - 255)
CLAD TMP 300 01	59	Bursts only	Q	16				10 K + 3% (RDG - 255)
CLAD TMP 60 02	62	Burst 1 only	Q	16				10 K + 3% (RDG - 255)
CLAD TMP 180 02	239	Bursts only	Q	16				10 K + 3% (RDG - 255)
CLAD TMP 300 02	240	Bursts only	Q	16				10 K + 3% (RDG - 255)
CLAD TMP 60 03	241	Bursts only	Q	16				10 K + 3% (RDG - 255)
CLAD TMP 180 03	242	Bursts only	Q	16				10 K + 3% (RDG - 255)
CLAD TMP 300 03	243	All except bursts	Q		1.12 K + 0.38% (RDG - 250)	>30	5.1 K	7.34 K + 0.76% (RDG - 255)

TABLE C-2. (continued)

Measurement Identifier	Parameter Number	Time Period	Qualification	Note[a]	Uncertainty[b] S	dF	B	U
CLAD TMP 70-20 04	244	Up to 53:01:35:50	Q		1.12 K + 0.38% (RDG - 255)	>30	5.1 K	7.34 K + 0.76% (RDG - 255)
CLAD TMP 75-140 04	245	All except bursts	Q		1.12 K + 0.38% (RDG - 255)	>30	5.1 K	7.34 K + 0.76% (RDG - 255)
CLAD TMP 70-260 04	246	All except bursts	Q		1.12 K + 0.38% (RDG - 255)	>30	5.1 K	7.34 K + 0.76% (RDG - 255)
ROD PRES 01	1	All except bursts	Q		190 kPa + 0.1% RDG	>30	165.2 kPa	545 kPa + 0.2% RDG
ROD PRES 02	2	All except bursts	Q		190 kPa + 0.1% RDG	>30	165.2 kPa	545 kPa + 0.2% RDG
ROD PRES 03	3	All	F	4				
ROD PRES 04	4	All except bursts	Q		190 kPa + 0.1% RDG	>30	165.2 kPa	545 kPa + 0.2% RDG
CLDINTMP 70-60 04	145	All except bursts	Q		1.12 K + 0.38% (RDG - 255)	>30	5.1 K	7.34 K + 0.76% (RDG - 255)
CLDINTMP 75-180 04	146	All	F	13				
FLOW RATE 01	157	All except bursts	Q	5	5.16×10^{-3} + 0.1% RDG	>30	4.1×10^{-3}	14.4×10^{-3} + 0.2% RDG
FLOW RATE 02	158	All except bursts	Q	5 6	5.16×10^{-3} + 0.1% RDG	>30	4.1×10^{-3}	14.4×10^{-3} + 0.2% RDG
FLOW RATE 03	159	All except bursts	Q	5	5.16×10^{-3} + 0.1% RDG	>30	4.1×10^{-3}	14.4×10^{-3} + 0.2% RDG
FLOW RATE 04	160	All except bursts	Q	5	5.16×10^{-3} + 0.1% RDG	>30	4.1×10^{-3}	14.4×10^{-3} + 0.2% RDG

TABLE C-2. (continued)

Measurement Identifier	Parameter Number	Time Period	Qualification	Note[a]	Uncertainty[b] S	dF	B	U
IN TEMP 01	161	All except bursts	Q		1.12 K + 0.38% (RDG - 255)	>30	5.1 K	7.34 K + 0.76% (RDG - 255)
IN TEMP 02	162	All except bursts	Q		1.12 K + 0.38% (RDG - 255)	>30	5.1 K	7.34 K + 0.76% (RDG - 255)
OUT TEMP 01	200	All except bursts	Q		1.12 K + 0.38% (RDG - 255)	>30	5.1 K	7.34 K + 0.76% (RDG - 255)
OUT TEMP 02	201	All except bursts	Q		1.12 K + 0.38% (RDG - 255)	>30	5.1 K	7.34 K + 0.76% (RDG - 255)
OUT TEMP 03	202	All except bursts	Q		1.12 K + 0.38% (RDG - 255)	>30	5.1 K	7.34 K + 0.76% (RDG - 255)
OUT TEMP 04	166	All	F	7				
CLAD TMP 300 03	243	Bursts only	Q	16				10 K + 3% (RDG - 255)
CLAD TMP 70-20 04	244	Burst 1 only	Q	16				10 K + 3% (RDG - 255)
CLAD TMP 75-140 04	245	Bursts only	Q	16				10 K + 3% (RDG - 255)
CLAD TMP 70-260 04	246	Bursts only	Q	16				10 K + 3% (RDG - 255)
ROD PRES 01	1	Bursts only	Q	16				30% RDG
ROD PRES 02	2	Bursts only	Q	16				30% RDG
ROD PRES 03	3	All	F	4				
ROD PRES 04	4	Bursts only	Q	16				30% RDG

TABLE C-2. (continued)

Measurement Identifier	Parameter Number	Time Period	Qualification	Note[a]	Uncertainty[b] S	dF	B	U
CLDINTMP 70-60 04	145	Bursts only	Q	16				10 K +·3% (RDG - 255)
CLDINTMP 75-180 04	146	All	F	13				
FLOW RATE 01	157	Bursts only	Q	16				50% RDG
FLOW RATE 02	158	Bursts only	Q	6				50% RDG
FLOW RATE 03	159	Bursts only	Q	16				50% RDG
FLOW RATE 04	160	Bursts only	Q	16				50% RDG
IN TEMP 01	161	Bursts only	Q	16				7.34 K + 2%
IN TEMP 02	162	Bursts only	Q	16				7.34 K + 2% (RDG - 255)
OUT TEMP 01	200	Bursts only	Q	16				7.34 K + 2% (RDG - 255)
OUT TEMP 02	201	Bursts only	Q	16				7.34 K + 2% (RDG - 255)
OUT TEMP 03	202	Bursts only	Q	16				7.34 K + 2% (RDG - 255)
DEL TEMP 01	123	All except bursts	Q		0.5 K	>30	0.04 K	1.04 K
DEL TEMP 02	124	All except bursts	Q		0.5 K	>30	0.04 K	1.04 K

TABLE C-2. (continued)

Measurement Identifier	Parameter Number	Time Period	Qualification	Note[a]	Uncertainty[b] S	dF	B	U
DEL TEMP 03	125	All except bursts	Q		0.5 K	>30	0.04 K	1.04 K
DEL TEMP 04	126	All except bursts	Q		0.5 K	>30	0.04 K	1.04 K
CLAD DISP 01	26	All except bursts	Q	15	0.65 mm	>30	0.06 mm	1.36 mm
CLAD DISP 02	27	All except bursts	Q	15	0.65 mm	>30	0.06 mm	1.36 mm
CLAD DISP 03	28	All except bursts	Q	15	0.65 mm	>30	0.06 mm	1.36 mm
CLAD DISP 04	8	All except bursts	Q	15	0.65 mm	>30	0.06 mm	1.36 mm
SHRD DEL PRESS 03	13	All except bursts	Q	15	0.36 kPa + 0.1% RDG	>30	0.	0.72 kPa + 0.2% RDG
SHRD DEL PRESS 04	14	All except bursts	Q	15	0.36 kPa + 0.1% RDG	>30	0.	0.72 kPa + 0.2% RDG
NEUT FLX 47-90	5	All	F	8				
NEUT FLX 78-90	20	All except bursts	Q	14	3.75% RDG	>30	0.	7.5% RDG
NEUT FLX 15-270	21	All except bursts	Q	14	8.99% RDG	>30	0.	17.98% RDG
NEUT FLX 31-270	22	All except bursts	Q	14	5.03% RDG	>30	0.	10.06% RDG
NEUT FLX 47-270	23	All except bursts	Q	14	5.5% RDG	>30	0.	11.0% RDG

TABLE C-2. (continued)

Measurement Identifier	Parameter Number	Time Period	Qualification	Note[a]	Uncertainty[b]			
					S	dF	B	U
NEUT FLX 63-270	24	All except bursts	Q	14	5.22% RDG	>30	0.	10.44% RDG
NEUT FLX 78-270	25	All except bursts	Q	14	5.58% RDG	>30	0.	11.16% RDG
SYS PRES 70 TT	6	All	F	9				
SYS PRES 17 TT	7	All except bursts	Q		3.0 MPa	>30	425 kPa	3.4 MPa
REAC POW 30NMS3	57	All except bursts	Q	10 11				8% RDG
REAC POW 50PPS1	58	All except bursts	Q	10 11				8% RDG
REAC POW 50PPS2	60	All except bursts	Q	10 11				8% RDG
DEL TEMP 01	123	Bursts only	Q	16				25% RDG
DEL TEMP 02	124	Bursts only	Q	16				25% RDG
DEL TEMP 03	125	Bursts only	Q	16				35% RDG
DEL TEMP 04	126	Bursts only	Q	16				25% RDG
CLAD DISP 01	26	Bursts only	Q	16				3 mm
CLAD DISP 02	27	Bursts only	Q	16				3 mm

TABLE C-2. (continued)

Measurement Identifier	Parameter Number	Time Period	Qualification	Note[a]	Uncertainty[b] S	dF	B	U
CLAD DISP 03	28	Bursts only	Q	16				3 mm
CLAD DISP 04	8	Bursts only	Q	16				3 mm
SHRD DEL PRESS 03	13	Bursts only	Q	16				2 kPa + 0.6% RDG
SHRD DEL PRESS 04	14	Bursts only	Q	16				2 kPa + 0.6% RDG
NEUT FLX 47-90	5	All	F	8				
NEUT FLX 78-90	20	Bursts only	Q		4.22% RDG	>30	0	8.43% RDG
NEUT FLX 15-270	21	Bursts only	Q		10.46% RDG	>30	0	20.92% RDG
NEUT FLX 31-270	22	Bursts only	Q		5.84% RDG	>30	0	11.68% RDG
NEUT FLX 47-270	23	Bursts only	Q		8.89% RDG	>30	0	17.78% RDG
NEUT FLX 63-270	24	Bursts only	Q		7.56% RDG	>30	0	15.12% RDG
NEUT FLX 78-270	25	Bursts only	Q		8.64% RDG	>30	0	17.28% RDG
SYS PRES 70 TT		All	F					
SYS PRES 17 TT	7	Bursts only	Q					3 MPa + 0.3% RDG
REAC POW 30NMS3	57	Bursts only	Q	10 11				10% RDG

TABLE C-2. (continued)

Measurement Identifier	Parameter Number	Time Period	Qualification	Note[a]	Uncertainty[b] S	dF	B	U
REAC POW 50PPS1	58	Bursts only	Q	10 11				10% RDG
REAC POW 50PPS2	60	Bursts only	Q	10 11				10% RDG
REAC POW 30PPS3	61	All except bursts	Q	10 11				8% RDG
REAC POW 30PPS4	63	All except bursts	Q	10 11				8% RDG
REAC POW 20MPS2	137	All except bursts	Q	10 11				8% RDG
REAC POW 20MTR1	177	All except bursts	Q	10 11				8% RDG
REAC POW 20MTR2	178	All except bursts	Q	10 11				8% RDG
REAC POW 20MEV1	180	All except bursts	Q	10 11				8% RDG
REAC POW 20MEV2	197	All except bursts	Q	10 11				8% RDG
REAC POW 30NMS4	199	All except bursts	Q	10 11				8% RDG
REAC POW 50TR1	219	All except bursts	Q	10 11				8% RDG
REAC POW 50TR2	220	All except bursts	Q	10 11				8% RDG
REAC POW 50EV1	225	All except bursts	Q	10 11				8% RDG

TABLE C-2. (continued)

Measurement Identifier	Parameter Number	Time Period	Qualification	Note[a]	Uncertainty[b] S	dF	B	U
REAC POW 50EV2	226	All except bursts	Q	10 11				8% RDG
LOOPPRES 5-20	163	All except bursts	Q	16	181 kPa + 0.1% RDG	>30	553 kPa	915 kPa + 0.2% RDG
LOOPPRES 5-23	164	All except bursts	Q	16	181 kPa + 0.1% RDG	>30	553 kPa	915 kPa + 0.2% RDG
LOOPPRES 5-24	165	All except bursts	Q	16	181 kPa + 0.1% RDG	>30	553 kPa	915 kPa + 0.2% RDG
LOOPPRES 5-25	203	All except bursts	Q	16	181 kPa + 0.1% RDG	>30	553 kPa	915 kPa + 0.2% RDG
LOOPPRES 5-34	204	All except bursts	Q	16	181 kPa + 0.1% RDG	>30	553 kPa	915 kPa + 0.2% RDG
LOOPPRES 5-35	205	All except bursts	Q	16	181 kPa + 0.1% RDG	>30	553 kPa	915 kPa + 0.2% RDG
REAC POW 30PPS3	61	Bursts only	Q	10 11				10% RDG
REAC POW 30PPS4	63	Bursts only	Q	10 11				10% RDG
SYS PRES PT	65	All	Q					2% RDG
IPT DELP PT	66	All	Q					10% RDG
LOOP FLOW PT	77	All	Q					3% RDG
REAC POW 20MPS2	137	Bursts only	Q	10 11				10% RDG
REAC POW 20MTR1	177	Bursts only	Q	10 11				10% RDG

TABLE C-2. (continued)

Measurement Identifier	Parameter Number	Time Period	Qualification	Note[a]	Uncertainty[b] S	dF	B	U
REAC POW 20MTR2	178	Bursts only	Q	10 11				10% RDG
REAC POW 20MEV1	180	Bursts only	Q	10 11				10% RDG
REAC POW 20MEV2	197	Bursts only	Q	10 11				10% RDG
REAC POW 30NMS4	199	Bursts only	Q	10 11				10% RDG
REAC POW 50TR1	219	Bursts only	Q	10 11				10% RDG
REAC POW 50TR2	220	Bursts only	Q	10 11				10% RDG
REAC POW 50EV1	225	Bursts only	Q	10 11				10% RDG
REAC POW 50EV2	226	Bursts only	Q	10 11				10% RDG
LOOPPRES 5-20	163	Bursts only	Q	16				1.2 MPa + 0.4% RDG
LOOPPRES 5-23	164	Bursts only	Q	16				1.2 MPa + 0.4% RDG
LOOPPRES 5-24	165	Bursts only	Q	16				1.2 MPa + 0.4% RDG
LOOPRRES 5-25	203	Bursts only	Q	16				1.2 MPa + 0.4% RDG
LOOPPRES 5-34	204	Bursts only	Q	16				1.2 MPa + 0.4% RDG

TABLE C-2. (continued)

Measurement Identifier	Parameter Number	Time Period	Qualification	Note[a]	Uncertainty[b] S	df	B	U
LOOPPRES 5-35	205	Bursts only	Q	16				1.2 MPa + 0.4% RDG
OUT TEMP 03	W-13	All except bursts	Q		2.24 K + 0.76% (RDG - 255)	>50	6.16 K	8.4 K + 0.76% (RDG - 255)
REAC POW 30MPS3	W-1	All except bursts	Q	10 11				8% RDG
REAC POW 30MPS4	W-2	All except bursts	Q	10 11				8% RDG
REAC POW 20MPS2	W-47	All except bursts	Q	10 11				8% RDG
REAC POW 20MTR1	W-52	All except bursts	Q	10 11				8% RDG
REAC POW 20MTR2	W-50	All except bursts	Q	10 11				8% RDG
REAC POW 20MEV1	W-48	All except bursts	Q	10 11				8% RDG
REAC POW 20MEV2	W-51	All except bursts	Q	10 11				8% RDG
REAC POW 30NMS4	W-7	All except bursts	Q	10 11				8% RDG
REAC POW 50TR1	W-3	All except bursts	Q	10 11				8% RDG
REAC POW 50TR2	W-4	All except bursts	Q	10 11				8% RDG
REAC POW 50EV1	W-5	All except bursts	Q	10 11				8% RDG

TABLE C-2. (continued)

Measurement Identifier	Parameter Number	Time Period	Qualification	Note[a]	Uncertainty[b] S	dF	B	U
REAC POW 50EV2	W-6	All except bursts	Q	10 11				8% RDG
REAC POW 20MPS1	W-33	All except bursts	Q	10 11				8% RDG
LOOPPRES 5-20	W-37	All except bursts	Q		362 kPa + 0.2% RDG	>30	553 kPa	915 kPa + 0.2% RDG
LOOPPRES 5-23	W-38	All except bursts	Q		362 kPa + 0.2% RDG	>30	553 kPa	915 kPa + 0.2% RDG
LOOPPRES 5-24	W-39	All except bursts	Q		362 kPa + 0.2% RDG	>30	553 kPa	915 kPa + 0.2% RDG
LOOPRRES 5-25	W-53	All except bursts	Q		362 kPa + 0.2% RDG	>30	553 kPa	915 kPa + 0.2% RDG
LOOPPRES 5-34	W-54	All except bursts	Q		362 kPa + 0.2% RDG	>30	553 kPa	915 kPa + 0.2% RDG
LOOPPRES 5-35	W-56	All except bursts	Q		362 kPa + 0.2% RDG	>30	553 kPa	915 kPa + 0.2% RDG
FP GAMMA No1 PT	221	All	Q	16				10% RDG
FP GAMMA No2 PT	222	All	Q	16				10% RDG
FP GAMMA No3 PT	223	All	Q	16				10% RDG
FP NEVT 01	224	All	Q	16				10% RDG
OUT TEMP 03	W-13	Bursts only	Q	16				8.4 K + 2% (RDG - 255)
REAC POW 30MPS3	W-1	Bursts only	Q	16				10% RDG

TABLE C-2. (continued)

Measurement Identifier	Parameter Number	Time Period	Qualification	Note[a]	Uncertainty[b] S	dF	B	U
REAC POW 30MPS4	W-2	Bursts only	Q	16				10% RDG
REAC POW 20MPS2	W-47	Bursts only	Q	16				10% RDG
REAC POW 20MTR1	W-52	Bursts only	Q	16				10% RDG
REAC POW 20MTR2	W-50	Bursts only	Q	16				10% RDG
REAC POW 20MEV1	W-48	Bursts only	Q	16				10% RDG
REAC POW 20MEV2	W-51	Bursts only	Q	16				10% RDG
REAC POW 30NMS4	W-7	Bursts only	Q	16				10% RDG
REAC POW 50TR1	W-3	Bursts only	Q	16				10% RDG
REAC POW 50TR2	W-4	Bursts only	Q	16				10% RDG
REAC POW 50EV1	W-5	Bursts only	Q	16				10% RDG
REAC POW 50EV2	W-6	Bursts only	Q	16				10% RDG
REAC POW 20MPS1	W-33	Bursts only	Q	16				
LOOPPRES 5-20	W-37	Bursts only	Q	16				1.2 MPa + 0.4% RDG

TABLE C-2. (continued)

Measurement identifier	Parameter Number	Time Period	Qualification	Note[a]	Uncertainty[b] S	dF	B	U
LOOPPRES 5-23	W-38	Bursts only	Q	16				1.4 MPa + 0.4% RDG
LOOPPRES 5-24	W-39	Bursts only	Q	16				1.2 MPa + 0.4% RDG
LOOPRRES 5-25	W-53	Bursts only	Q	16				1.2 MPa + 0.4% RDG
LOOPPRES 5-34	W-54	Bursts only	Q	16				1.2 MPa + 0.4% RDG
LOOPPRES 5-35	W-56	Bursts only	Q	16				1.2 MPa + 0.4% RDG
CLAD DSP 01	W-15	All except bursts	Q		2.6 mm + 0.4% RDG	>30	0.06 mm	2.66 mm + 0.4% RDG
CLAD DSP 02	W-16	All except bursts	Q		2.6 mm + 0.4% RDG	>30	0.06 mm	2.66 mm + 0.4% RDG
CLAD DSP 03	W-9	All except bursts	Q		2.6 mm + 0.4% RDG	>30	0.06 mm	2.66 mm + 0.4% RDG
CLAD DSP 04	W-10	All except bursts	Q		2.6 mm + 0.4% RDG	>30	0.06 mm	2.66 mm + 0.4% RDG
NEUT FLX 47-90	W-11	All	F	8				
NEUT FLX 78-90	W-12	All except bursts	Q		3.75% RDG	>30	0	7.5% RDG
NEUT FLX 15-270	W-25	All except bursts	Q		8.99% RDG	>30	0	17.98% RDG
NEUT FLX 31-270	W-26	All except bursts	Q		5.03% RDG	>30	0	10.06% RDG

TABLE C-2. (continued)

Measurement Identifier	Parameter Number	Time Period	Qualification	Note[a]	Uncertainty[b] S	dF	B	U
NEUT FLX 47-270	W-27	All except bursts	Q		5.5% RDG	>30	0	11.0% RDG
NEUT FLX 63-270	W-28	All except bursts	Q		5.22% RDG	>30	0	10.44% RDG
NEUT FLX 78-270	W-41	All except bursts	Q		5.58% RDG	>30	0	11.16% RDG
SYS PRES 70TT	W-42	All	F	9				
SYS PRES 17TT	W-43	All except bursts	Q		3.0 MPa	>30	429 kPa	3.4 MPa
REAC POW 30NMS3	W-8	All except bursts	Q	10 11				8% RDG
REAC POW 50PPS1	W-44	All except bursts	Q	10 11				8% RDG
REAC POW 50PPS2	W-14	All except bursts	Q	10 11				8% RDG
CLAD DSP 01	W-15	Bursts only	Q	16				3 mm
CLAD DSP 02	W-16	Bursts only	Q	16				3 mm
CLAD DSP 03	W-19	Bursts only	Q	16				3 mm
CLAD DSP 04	W-10	Bursts only	Q	16				3 mm
NEUT FLX 47-90		All	F					

TABLE C-2. (continued)

Measurement Identifier	Parameter Number	Time Period	Qualification	Note[a]	Uncertainty[b] S	dF	B	U
NEUT FLX 76-90	W-12	Bursts only	Q		4.22% RDG	>30	0	8.43% RDG
NEUT FLX 15-270	W-25	Bursts only	Q		10.46% RDG	>30	0	20.92% RDG
NEUT FLX 31-270	W-26	Bursts only	Q		5.84% RDG	>30	0	11.68% RDG
NEUT FLX 47-270	W-27	Bursts only	Q		8.89% RDG	>30	0	17.78% RDG
NEUT FLX 63-270	W-28	Bursts only	Q		7.56% RDG	>30	0	15.12% RDG
NEUT FLX 78-270	W-41	Bursts only	Q		8.64% RDG	>30	0	17.28% RDG
SYS PRES 70TT		All	F					
SYS PRES 17TT	W-43	Bursts only	Q					3 MPa + 0.3% RDG
REAC POW 30NM53	W-8	Bursts only	Q	10 11				10% RDG
REAC POW 50PP51	W-44	Bursts only	Q	10 11				10% RDG
REAC POW 50PP52	W-14	Bursts only	Q	10 11				10% RDG

a. Notes are given after table.

b. S = random component; dF = degrees of freedom; B = bias component; U = total measurement uncertainty.

TABLE C-2. (continued)

NOTES FOR TABLE C-2

1. Thermocouple failed after oscillation portion of the test. The thermocouple would respond but was not reading correctly at temperatures >800 K.

2. This instrument failed ~42:09:46:40:00. The thermocouple gave some sporadic readings after this time, but the data are very questionable and the instrument is considered failed.

3. Failed before test started.

4. Failed before test started.

5. For indicated flow rates less than 0.2 L/s, the measurement uncertainty increases to ±0.1 L/s.

6. This turbine flowmeter would (occasionally) stop when the flow dropped below 0.1 L/s. An increase in flow would restart the flowmeter. Data below 0.1 L/s for this instrument are very questionable.

7. Failed before test started.

8. Failed before test started.

9. Failed before test started.

10. The reactor power parameter identifiers were changed for the RIA portion of the test. The following table should be used to correlate the identifiers.

Parameter Number	Calibrations	Burst 1	Burst 2	Burst 3
N-57, W-8	30NMS3 PT	30NMS3 PT	30NMS3 PT	30NMS3 PT
N-58, W-44	0.2KPS1 PT	0.2KPS1 PT	5GPS1 PT	5GPS1 PT
N-60, W-14	0.2KPS2 PT	0.2KPS2 PT	5GPS2 PT	5GPS2 PT
N-61, W-1	30MPS3 PT	482PS3 PT	8.GPS3 PT	10GPS3 PT
N-63, W-2	30MPS4 PT	482PS4 PT	8.GPS4 PT	10GPS4 PT
N-137, W-47	20MPS2 PT	20MPS2 PT	0.5GPS2 PT	0.5GPS2 PT
N-177, W-52	20MTR1 PT	20MTR1 PT	0.5GTR1 PT	1GWTR1 PT
N-178, W-50	20MTR2 PT	20MTR2 PT	0.5GTR2 PT	1GWTR2 PT
N-180, W-48	20MEV1 PT	20MEV1 PT	0.5GEV1 PT	1GWEV1 PT
N-197, W-51	20MEV2 PT	20MEV2 PT	0.5GEV2 PT	1GEV2 PT
N-199, W-7	30NMS4 PT	30NMS4 PT	30NMS4 PT	30NMS4 PT
N-219, W-3	0.2KTR1 PT	0.2KTR1 PT	5GTR1 PT	10GTR1 PT

TABLE C-2. (continued)

10. (continued)

Parameter Number	Calibrations	Burst 1	Burst 2	Burst 3
N-220, W-4	0.2KTR2 PT	0.2KTR2 PT	5GTR2 PT	10GTR2 PT
N-225, W-5	0.2KEV1 PT	0.2KEV1 PT	5GEV1 PT	10GEV1 PT
N-226, W-6	0.2KEV2 PT	0.2KEV2 PT	5GEV2 PT	10GEV2 PT

11. The last term of the uncertainty, 25% (RDG-1200), applies only at temperatures above 1200 K.

12. This thermocouple was responding, but was following fuel temperature not internal cladding termperature; therefore, the instrument is considered failed. However, the data could be used for trend information.

13. The SPNDs were corrected to the flux wire profile.

14. A relative uncertainty has been given to the LVDTs and differential pressures.

15. Not all of the power chambers responded properly for each RIA power calibration and burst. Listed below are the failed parameters and the phase of the test during which they failed.

First RIA Power Calibration	First RIA Power Burst	Second RIA Power Burst	Third RIA Power Calibration	Third RIA Power Burst
Wideband	Wideband	Narrowband	Good data were not recorded for the third power calibration. All power chamber data from 53:03:00:00 to 53:05:00:00 are considered failed.	Narrowband
20MPS1 PAR #47	482PS3 PAR #1	8.6PS4 PAR #63		5GPPS1 PAR #58
20MPS2 PAR #33	482PS4 PAR #2	8.6PS3 PAR #61		5GPPS2 PAR #60
	20MPS1 PAR #47			10GPS3 PAR #61
	20MPS2 PAR #33	Wideband		10GPS4 PAR #63
		8.6PS3 PAR #1		Wideband
		8.6PS4 PAR #2		
		0.5GTR1 PAR #52		10GPS3 PAR #1
		0.5GEV2 PAR #51		10GPS4 PAR #2
		0.5GEV1 PAR #48		0.2KPS2 PAR #14
		0.5GTR2 PAR #50		20MTR1 PAR #52
				20MTR2 PAR #50
				20MEV2 PAR #51
				0.2KPS1 PAR #44
				20MPS2 PAR #47

16. The total uncertainty was estimated for this test phase. No corresponding B, S, and df exist.

TABLE C-3. IRIG TIMES FOR TEST PHASES

This table lists approximate IRIG times for the start and end of the various portions of the test.

Start power calibration	37:16:30:00
End power calibration	38:08:00:00
Start oscillation	38:14:36:00
End oscillation	38:23:56:00
Start DNB	39:08:40:00
End DNB	45:07:45:00
Start Calibration B1	51:22:45:00
End Calibration B1	51:23:25:00
Start Burst 1	52:10:12:50
End Burst 1	52:10:14:30
Start Calibration B2	52:14:46:00
End Calibration B2	52:15:15:00
Start Burst 2	53:01:35:50
End Burst 2	53:01:37:30
Start Calibration B3	53:04:27:00
End Calibration B3	53:05:00:00
Start Burst 3	53:12:17:00
End Burst 3	53:12:18:30

TABLE C-4. GENERAL GROUPINGS OF DATA PLOTS CONTAINED ON MICROFICHE

Microfiche Titles	Card Number	Figure Numbers
PR-1 Prenuclear Instrument Checkout	C-1	C-1 through C-51
PR-1 Thermal Response Test Phase[a]	C-2	C-52 through C-205
PR-1 PCM Test Phase	C-3	C-206 through C-431
PR-1 PCM Transients 1, 2, & 3	C-4	C-432 through C-635
PR-1 PCM Transients 4, 5, & 6	C-5	C-636 through C-837
PR-1 PCM Transients 7, 8, & 9	C-6	C-840 through C-1039
PR-1 PCM Transients 10, 11, & 12	C-7	C-1042 through C-1242
PR-1 PCM Transients 13, 14, & 15	C-8	C-1243 through C-1443
PR-1 PCM Transients 16, 17, 18, 19, & 20	C-9	C-1444 through C-1644
PR-1 PCM Transients 21, 22, & 23	C-10	C-1645 through C-1845
PR-1 PCM Transients 24 & 25	C-11	C-1846 through C-1977
Power Burst 1	C-12	C-1978 through C-2168
Power Burst 2	C-13	C-2171 through C-2345
Power Burst 3	C-14	C-2347 through C-2514

a. Includes power calibration, preconditioning, and power oscillations.

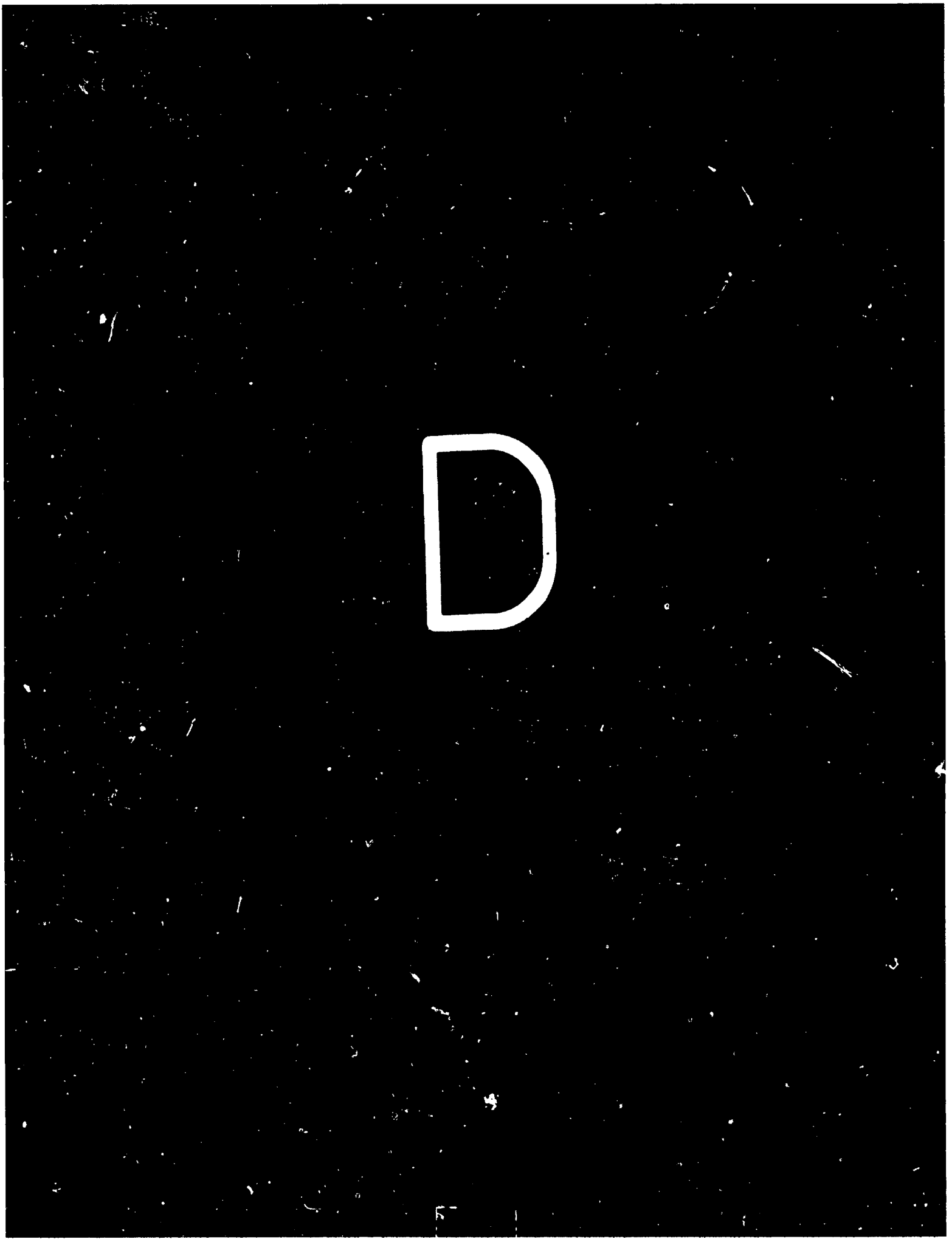
D

APPENDIX D

TEST ROD POWER DETERMINATION AND UNCERTAINTIES

BLANK

PAGE

APPENDIX D

TEST ROD POWER DETERMINATION AND UNCERTAINTIES

INTRODUCTION

Test rod powers for Test PR-1 were determined by two independent methods. The first method is a heat balance of the system based on measured thermal-hydraulic parameters (volumetric flow rate, coolant pressure, and coolant enthalpy rise). The thermal-hydraulic method provides the average linear heat generation of the rod, which can then be used to determine local test rod power. The second method is based on the radiochemical burnup analysis of a local fuel sample, and provides the total integrated power (energy) at the fuel sample elevation. Since the integrated test rod power is linearly related to neutron fluence, the instantaneous power can be determined using the burnup analysis and the measured self-powered neutron detector currents. To provide a common basis for comparison between the two methods, the axial power profile must be determined. The next section details the method for determining the axial power profile and local power determinations from the axial flux wires (see Appendix B). Subsequent sections detail the calculational techniques and results from the two methods for determining test rod power during Test PR-1.

POWER PROFILE AND LOCAL POWER DETERMINATION

Cobalt-aluminum (0.51% Co, 99.49% Al) flux wires were mounted axially on the shrouds of Rods 524-1 and 524-4. Gamma scanning of the flux-wires provided a method of determining the axial power profile within the in-pile tube and thereby the local test rod power. Data were obtained from the flux wires at 7.6-mm increments along the length of the fuel rod. A computer program called FLUXWR was used to smooth and normalize the data. The normalized curves for the two axially positioned flux wires are shown in Figure D-1. The local test rod powers of interest were then determined by the local peaking factor (PF) and the measured average test rod power. The local peaking factor is defined by the local-to-average power ratio and was determined from the flux wire data by PF = Local counts/Average counts.

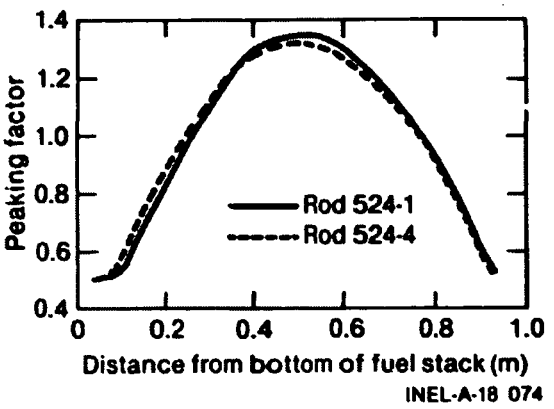

Figure D-1. Test PR-1 flux wire normalized peaking factor versus distance from bottom of fuel stack for Rods 524-1 and 524-4.

CALCULATIONAL METHODS FOR DETERMINING TEST ROD POWER

Thermal-Hydraulic Method

The determination of experimental fuel rod power can be based on the fact that, under equilibrium conditions, the heat added to the coolant flowing past the rod is equal to the rod heat generation, less any heat losses through the shroud wall. Thus,

$$Q_{in} = \rho V C_p(T_{out} - T_{in}) + \frac{T_{out} - T_{in}}{2R} \qquad (D\text{-}1)$$

where

ρ = coolant density

V = coolant volumetric flow rate

C_p = coolant specific heat

T_{out} = coolant outlet temperature

T_{in} = coolant inlet temperature

R = effective thermal resistance of the shroud.

A computer program (THSP) is used to compute the average rod power from the appropriate experimental measurements. Rod power is generally expressed as linear heat generation in kilowatts per meter of fuel.

A differential thermocouple (ΔTC) was mounted inside each shroud at 90 degrees in relation to the center of the in-pile tube. These ΔTCs measured the rise in coolant water temperature, and thereby the coolant enthalpy change, under subcooled steady state conditions. Uncertainty in test rod linear power density (instantaneous) determined by the thermal-hydraulic method are estimated to be 3.5 kW/m at a 95% confidence level.

Burnup Method

Burnup samples of the fuel rods were taken at various axial elevations (Appendix B). Analysis of the burnup samples is divided into several basic operations. First, the fuel in the sample is completely dissolved and filtered. Second, weighed aliquots of the dissolver solution are analyzed for the uranium content by isotope dilution mass spectrometry (IDMS), and the fission product concentrations via gamma-ray spectrometry. The principal radionuclides that are used as fission product monitors include ^{144}Ce, ^{141}Ce, and ^{95}Zr. Next, radionuclide decay corrections are made to compensate for the time and relative power variations of the irradiation, and, finally, the burnup and uncertainty computations are performed and checked.

The isotopic content of fission products remaining in the fuel is an indirect measurement of the number of atoms of uranium that fissioned, and can be correlated to the fission rate during the irradiation time of the test. From the number of fissions per gram of total uranium, the rod power can be calculated as follows. The total energy generated by the rod (E) is

$$E = M_u \times k \times B \qquad (D\text{-}2)$$

where

M_u = mass of uranium in fuel rod (g)

k = energy released per fission (physics calculations estimate 2.96×10^{-11} J/fission or 185.5 Mev)

B = fissions per gram of fuel.

Since only the mass of the UO_2 fuel is measured, the mass of uranium metal in the fuel rod is

$$M_U = \frac{\text{Atomic weight uranium}}{\text{Atomic weight } UO_2} \times M_{UO_2} . \qquad \text{(D-3)}$$

The average atomic weight (AW) of uranium can be determined from the uranium isotopic content (Appendix B) and individual isotopic atomic weights

$$AW_{average} = \Sigma\, ER_i \times AW_i$$

$$= (0.0006)\,(234) + (0.1006)\,(235) + (0.0011)\,(236)$$

$$+ (0.8978)\,(238) \qquad \text{(D-4)}$$

$$= 237.7$$

where

ER_i = uranium isotopic content of isotope i

AW_i = atomic weight of individual isotope (234, 235, 236, or 238).

The fraction of metallic uranium can be calculated, using the atomic weight of oxygen (16), by

$$\frac{AW_U}{AW_{UO_2}} = \frac{237.7}{237.7 + (2 \times 16)} = 0.881. \qquad \text{(D-5)}$$

The theoretical energy per fission is about 200 MeV. Because of irrecoverable losses from the system, only 185.5 MeV are recoverable as heat. This constant is used in converting burnup analysis results to the total energy generation.

Using Equation (D-2), the fuel rod energy expended at a particular axial location can be calculated per mass unit of uranium. To convert this value to an average fuel rod energy, the peaking factor at that specific location is used in the relationship

$$\text{Average rod energy} = \frac{\text{Local rod energy}}{\text{Local peaking factor}} . \qquad \text{(D-6)}$$

The test rod linear power at the axial peak power location can similarly be derived using the flux wire activation data. Uncertainty in the integrated test rod peak power (total energy) using the radiochemical burnup analyses is estimated to be less than 9% at a 95% confidence level.

Rod Power From SPND Current

The current produced by a self-powered neutron detector (SPND) is directly porportional to the thermal neutron flux within the PBF in-pile tube. Since the test rod power generation is also proportional to the thermal neutron flux, the SPNDs provide an alternate means of determining test rod power at any time during the nuclear test operation. Linear regression coefficients were determined between the individual test rod powers and SPND current for various times during Test PR-1. The time increments for which the various coefficients were chosen correspond to increments when the in-pile tube thermal conditions, and therefore neutronics, were constant.

The linear regression coefficients for the various time increments are listed in Table D-1. The coefficients will yield the test rod peak linear

TABLE D-1. COEFFICIENTS FOR DETERMINING TEST ROD PEAK POWER FROM SPND CURRENT DURING TEST PR-1

Test Phase	Rod	Regression Coefficients A_0	Regression Coefficients A_1	Integrated Rod Peak Power (kW•s/m)	
Power calibration	524-1	0.3136	0.5171	1 379 152	
	524-2	0.1602	0.3703	975 150	
	524-3	0.07014	0.4463	1 174 457	
	524-4	0.008270	0.4618	1 198 199	
Preconditioning and power oscillations	524-1	0.05113	0.4671	1 195 975	
	524-2	0.1789	0.3281	844 325	
	524-3	0.05220	0.3953	1 005 323	
	524-4	0.3561	0.4051	1 046 640	
DNB 1,2,3	524-1	-0.1620	0.5533	1 218 440	DNB 1-6
	524-2	-0.1043	0.3771	812 933	
	524-3	-0.1321	0.4601	1 013 514	
	524-4	-0.1391	0.4614	1 009 518	
DNB-4	524-1	0.8752	0.5295		
	524-2	-0.06016	0.3522		
	524-3	0.1607	0.4422		
	524-4	-0.07013	0.4407		
DNB-5	524-1	0.5249	0.5112		
	524-2	-0.02353	0.3456		
	524-3	0.1912	0.4526		
	524-4	0.02216	0.4440		
DNB-6	524-1	0.04767	0.5200		
	524-2	-0.06998	0.3514		
	524-3	-0.1016	0.4453		
	524-4	-0.09631	0.4501		
DNB-7	524-1	-0.09786	0.5470	1 372 009	DNB 7-12
	524-2	-0.009927	0.3783	1 062 313	
	524-3	-0.2230	0.4593	1 233 583	
	524-4	0.04887	0.4760	1 345 825	
DNB 8,9	524-1	3.9619	0.3554		
	524-2	-1.5173	0.3904		
	524-3	2.6575	0.3599		
	524-4	-0.3784	0.4754		
DNB 10,11,12	524-1	0.9893	0.4256		
	524-2	0.2324	0.3371		
	524-3	0.0930	0.4083		
	524-4	0.9258	0.4115		

TABLE D-1. (continued)

Test Phase	Rod	Regression Coefficients A_0	Regression Coefficients A_1	Integrated Rod Peak Power (kW•s/m)	
DNB 13	524-1	1.4610	0.3666	210548	
	524-2	-0.1066	0.3179	99333	
	524-3	0.4219	0.3688	151799	
	524-4	0.6385	0.3529	158693	
DNB 14, 15	524-1	1.4360	0.3424	2614204	DNB 14-23
	524-2	0.2680	0.3132	1951375	
	524-3	0.7854	0.3159	2277353	
	524-4	1.2141	0.3211	2439501	
DNB 16, 17	524-1	-0.4128	0.4369		
	524-2	-0.8415	0.3653		
	524-3	-1.1584	0.4297		
	524-4	-1.0477	0.4618		
DNB 18	524-1	1.6132	0.3638		
	524-2	0.00679	0.3318		
	524-3	0.4783	0.3511		
	524-4	1.4046	0.3735		
DNB 19	524-1	0.1780	0.5963		
	524-2	0.3520	0.3511		
	524-3	0.6093	0.3961		
	524-4	0.7854	0.4529		
DNB 20, 21, 22, 23	524-1	0.2567	0.4948		
	524-2	-1.795	0.3663		
	524-3	-2.292	0.4597		
	524-4	-2.179	0.4684		
Power calibration RIA Burst 1	524-1	-0.02737	0.4645	64181	
	524-2	-0.04242	0.3652	55686	
	524-3	-0.00398	0.4639	66169	
	524-4	10.2	0.4393	74492	
Power calibration RIA Burst 2	524-1	-0.00937	0.4956	64006	
	524-2	0.1165	0.3908	51152	
	524-3	-0.2422	0.5684	72149	
	524-4	-0.0555	0.4759	61205	
Power calibration RIA Burst 3	524-1	0.00252	0.4766	50705	
	524-2	0.0256	0.3932	42002	
	524-3	0.0389	0.4436	47452	
	524-4	0.0472	0.4366	46762	

TABLE D-1. (continued)

Test Phase	Rod	Regression Coefficients A_0	Regression Coefficients A_1	Integrated Rod Peak Power (kW•s/m)
Total integrated rod peak power	524-1		8.169×10^6	
	524-2		5.894×10^6	
	524-3		7.042×10^6	
	524-4		7.381×10^6	
Total average integrated rod peak power			7.122×10^6	

power with the parameter NEUTFLX 47-27008 (see Appendix C) as the independent variable. A peak-to-average power factor of 1.35 was determined from the flux wire analysis and is included in the regression coefficients. The correlation

$$\text{Peak linear power} = A_0 + [A_1 \times \text{SPND current (nA)}] \qquad \text{(D-6)}$$

is valid over both single- and two-phase coolant conditions during the appropriate time increment noted in Table D-1. Instantaneous SPND current (NEUTFLX 47-27008) can be obtained during each time segment from the data plots contained in Appendix C.

The rod peak linear power through the duration of Test PR-1 was determined by the above method for each of the fuel rods. Since there were no inherent differences in fuel loading or design for the four fuel rods, the scatter in individual powers was attributed to data uncertainty. The large disparity between powers for Rods 524-1 and 524-2 also suggested a mixup in instrumentation identifiers (flow or differential temperatures) between the two rods. The test rod powers used in the analysis of the Test PR-1 data were, therefore, averaged between the four rods.

Rod peak powers for each segment of Test PR-1 were integrated over time to provide a direct comparison with the radiochemical burnup analysis

(Table D-1). By using the calculation for energy release per fission (185.5 Mev), the integrated test rod powers (using the regressions to SPND current) could be directly compared to the total energy release determined from burnup analysis. In addition, the SPND current was integrated over time to allow determination of the instantaneous test rod power from the burnup results by the argument

$$\text{Local test rod power} = B_0 + B_1 \times (\text{SPND current}) \qquad \text{(D-7)}$$

where the slope, B_1, is the ratio of the burnup energy (kW.s/m) to the integrated SPND current (nA•s), and the intercept, B_0, is considered negligible or zero. The results of these analyses are presented in the following section.

CALCULATIONS

Table D-2 summarizes the material basis of the Test PR-1 burnup calculations. A summary comparison of fuel rod energy expended during Test PR-1, calculated from integrated rod power and from burnup analysis, is presented in Table D-3. Column 4 contains values of the percentage differences between Columns 2 and 3. These percentages were calculated by dividing the differences between Columns 2 and 3 by the average of Columns 2 and 3. Column 2 contains the total rod energy expended during the test calculated using rod powers from SPND currents. Column 3 contains values calculated directly from the burnup analyses results.

Two conclusions are drawn from Table D-3. First, the instantaneous test rod powers for Test PR-1 should be determined by averaging the powers determined for each of the four test rods. The average values based on thermal-hydraulics are within 2.1% of the average burnup values, excluding Rod 524-1. The data from Rod 524-1 are suspect due to the rod being water-logged during the test and possible biasing of the ^{95}Zr results. Second, the disparity between the thermal-hydraulic calculations for Rods 524-1 and 524-2 thermal-hydraulic calculations may be due to inadvertent switching of instrument leads for either the differential temperature thermocouples or the coolant flowmeters.

TABLE D-2. BURNUP RESULTS

Rod	Peaking Factor	Fissions/g Total U			U/UO_2	Fuel Height (m)	Fuel Mass[a] (g UO_2)
		Via ^{144}Ce	Via ^{95}Zr	Via ^{141}Ce			
524-1	0.962	1.90×10^{17}	2.09×10^{17}	1.87×10^{17}	0.881	0.9144	793
524-2	1.32	3.21×10^{17}	3.14×10^{17}	3.19×10^{17}	0.881	0.9144	793
524-3	1.042	2.62×10^{17}	2.59×10^{17}	2.63×10^{17}	0.881	0.9144	793
524-4	1.305	3.13×10^{17}	3.08×10^{17}	3.16×10^{17}	0.881	0.9144	793

a. Fuel stack masses were computed on the basis of pretest mass measurements for Rod 524-4. Complete characterization of the other three fuel rods was not conducted.

TABLE D-3. SUMMARY COMPARISON OF TEST PR-1 BURNUP WITH INTEGRATED ROD POWERS

Rod Number	Thermal-Hydraulic Rod Power (MWd/t)	Burnup Rod Power (MWd/t)	Percent of Difference
524-1	123.93	98.32[a]	23.05[a]
524-2	89.42	109.51	-20.20
524-3	106.84	114.03	-6.51
524-4	111.97	107.41	4.16
Average	108.04	110.32[b]	-2.09

a. Rod 524-1 burnup values suspect.

b. Rod 524-1 excluded from average.

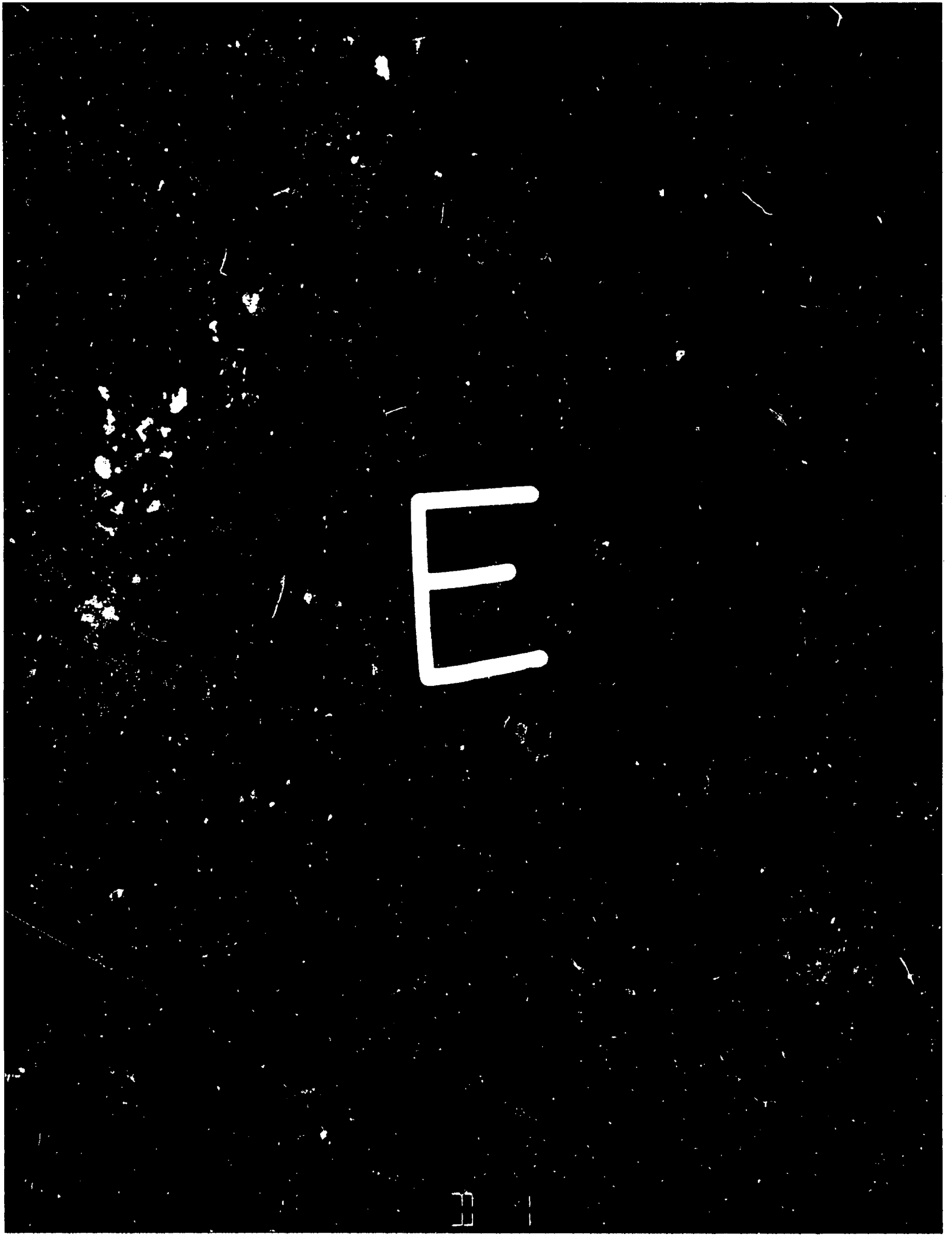
E

APPENDIX E

MEASUREMENT CORRECTION METHODS FOR FUEL AND CLADDING THERMOCOUPLES DURING RIA POWER BURSTS

BLANK PAGE

APPENDIX E

MEASUREMENT CORRECTION METHODS FOR FUEL AND CLADDING THERMOCOUPLES DURING RIA POWER BURSTS

FUEL TEMPERATURE MEASUREMENT CORRECTIONS

By definition, a reactivity initiated accident (RIA) in a nuclear reactor is the condition resulting when excess reactivity is introduced into the system, usually in an extremely short (approaching a step function) period of time. The response of the nuclear fuel to such a reactivity insertion is an exponential increase in the fission rate and, consequently, the temperature. The rise of fuel temperature is determined by the time constant of the fuel, which is a function of the prompt and delayed neutron lifetimes, fuel heat capacity, fuel thermal conductivity, and Doppler reactivity feedback. The use of thermocouples to measure nuclear fuel temperature response during an RIA introduces an error between the actual and measured temperatures due to the response time of the thermocouple system. The response of the thermocouple is determined by its geometry and the measurement medium. The response of the thermocouple signal to the exponential rise in fuel temperature is also exponential, but is delayed in time and has a time constant that is different from the fuel. Consequently, fuel temperature measurements during RIA testing are not accurate and must be corrected. An analytical method to correct fuel temperature measurements made during the RIA testing is presented in this section.

The actual increase in the fuel temperature is exponential and is described by the relationship[E-1]

$$T_{in} = T_{step} \left(1 - e^{-t/\tau_1}\right) \qquad \text{(E-1)}$$

where

T_{in} = temperature response of the fuel

T_{step} = temperature to which the fuel will rise for the amount of energy inserted

t = time

τ_1 = time constant of the fuel.

The value of T_{step} is estimated from enthalpy versus temperature tables for UO_2 fuel. The fuel enthalpy at the point of interest and the time constant, τ_1, can be estimated with a FRAP-T5 computer code calculation.

The time constant of the thermocouple system (τ_2) can be estimated from the measured temperature increase by the relationship[E-2]

$$\tau_2 = \frac{t_2 - t_1}{\ln\left(\frac{T_{step} - T_1}{T_{step} - T_2}\right)} \qquad \text{(E-2)}$$

where

T_1 = thermocouple temperature at time, t_1

T_2 = thermocouple temperature at time, t_2.

This estimate must be made with t_1 and t_2 sufficiently small that they are included in the rise time of the fuel temperature response.

The measured temperature increase (T_{out}) of the thermocouple system can now be calculated as an exponential response to an exponential driving function (T_{in}) by the relationship

$$T_{out} = T_{in} - T_{step}\left(\frac{\tau_2}{\tau_2 - \tau_1}\right)\left(e^{-t/\tau_2} - e^{-t/\tau_1}\right) . \qquad \text{(E-3)}$$

At times greater than that of the thermocouple peak temperature response, there is no error due to the response time of the thermocouple system. Therefore, the fuel temperature response is defined for the exponential rise and the decay beyond the time of the thermocouple peak temperature. The fuel temperature response between the initial rise and the time of the thermocouple peak temperature response must be estimated. The thermocouple response as a function of the fuel temperature response in this region in given by

$$T_{out} = T_{in} - T_{in}\left(\frac{\tau_2}{\tau_2 - \tau_1}\right)\left(e^{-t/\tau_2} - e^{-t/\tau_1}\right). \qquad \text{(E-4)}$$

At this point, estimates for T_{step}, τ_1, and τ_2 are used to iteratively solve the above equations and plot the temperature responses. When the calculated thermocouple system temperature response (T_{out}) is identical to the measured temperature response, the driving function (T_{in}) is the corrected thermocouple temperature response.

METHODS USED TO CORRECT CLADDING SURFACE THERMOCOUPLE TEMPERATURE MEASUREMENTS

The accuracy of externally mounted cladding surface thermocouples for measuring cladding surface temperatures is influenced by such factors as the location of the thermocouple junction relative to the surface of the cladding, the weld characteristics of the attachment method, and the coolant flow area and velocity in the vincinty of the thermocouple junction. The fact that a surface mounted thermocouple junction is not in intimate contact with the cladding surface introduces a response time effect which, during a fast transient, results in a delay time between when the cladding surface reaches a specific temperature and when the thermocouple signal indicates that same temperature. In addition, the thermocouple sheath itself acts as a cooling fin sticking out into the coolant stream, which increases the heat transfer coefficient to the coolant and reduces the magnitude of the measured temperature with respect to the true cladding surface temperature in the absence of a thermocouple.

An accurate evaluation of thermocouple response time and fin cooling effects on the measured temperature is practically impossible because of unavoidable variations in thermocouple attachment characteristics, location of the thermocouple junction within the sheath, etc. An empirical method has been used to obtain corrections to the measured cladding surface temperatures during the Test PR-1 power bursts. The method used involves modeling the test fuel rod, including the thermocouple assembly as attached to the cladding, with the computer code COUPLE/MOD3.[a] The FRAP-T5[b] computer code was used to calculate fuel rod and coolant conditions during the transient, and were used as input to the COUPLE calculations. The cladding surface heat transfer coefficients were then adjusted in the COUPLE calculations until satisfactory agreement was obtained between the calculated and measured cladding thermocouple temperature response. With the final surface heat transfer coefficients as input, the COUPLE calculation also predicts the cladding surface temperature in the absence of a thermocouple, which is used as the corrected cladding surface temperature. Although it is not expected that the described method provides exact cladding surface temperatures, it is considered that the resultant values are significant improvements over the measured surface temperatures.

COUPLE/MOD3 is a two-dimensional, finite element, steady state and transient heat conduction code with contiguous element and inverse capabilities. The code was developed by EG&G Idaho for use with the CDC CYBER 176/CYBER 173 computers. The main portion of COUPLE, aside from the contiguum elements, has been developed to handle multimaterial plane or axisymmetric solids with temperature-dependent anisotropic properties. The contiguum elements have been developed for single-material plane or axisymmetric solids with temperature-dependent isotropic properties. A heat conduction problem, aside from the contiguum elements, is formulated using the

---

a. COUPLE/MOD 3, Idaho National Engineering Laboratory Code Configuration Control Number M00001.

b. FRAP-T5, Idaho National Engineering Laboratory Code Configuration Control Number H0005838.

finite element method (FEM) [one of the approximate solution techniques classified under the method of weighted residuals (MWR)]. The name COUPLE reflects the two-dimensionality of the code and the increased coupling between nodal points due to the use of the finite element formulation.

Briefly, in the FEM, the temperature field throughout the continuum of interest is approximated by a discretization procedure that divides the solution region into finite regions (elements). The temperature field is then expressed in terms of an assumed approximating function within each element. The approximating or interpolating functions are defined in terms of the values of the temperature at specified points called nodes. These nodes usually lie on the element boundaries where adjacent elements are considered to be connected. Hence, in the FEM, the temperature at the nodes are unknowns. Once these unknowns are determined, the interpolating functions define the temperature throughout the assemblage of elements.

One of the important features of the FEM is the ability to formulate solutions for individual elements before putting them together (assembly) to represent the entire problem. Although there is more than one way to formulate the properties of an individual element, the Galerkin method is employed in COUPLE. The Galerkin method is an MWR technique for obtaining approximate solutions to linear and nonlinear partial differential equations. As applied in COUPLE, the general functional behavior of the temperature is assumed in some way so as to approximately satisfy the given differential equation and boundary conditions. Substitution of this approximation into the original differential equation and boundary conditions then results in some error called a residual. This residual is required to vanish in some average sense over the entire solution domain.

After the individual element properties are determined by the MWR, the element properties are assembled to obtain the overall system equations. These equations are then solved, giving the temperatures at each node point.

Figure E-1 shows a finite element model for a Test PR-1 fuel rod, including cladding and thermocouple, as formulated by COUPLE. Figure E-2 shows the detailed description, in COUPLE, of the thermocouple-cladding

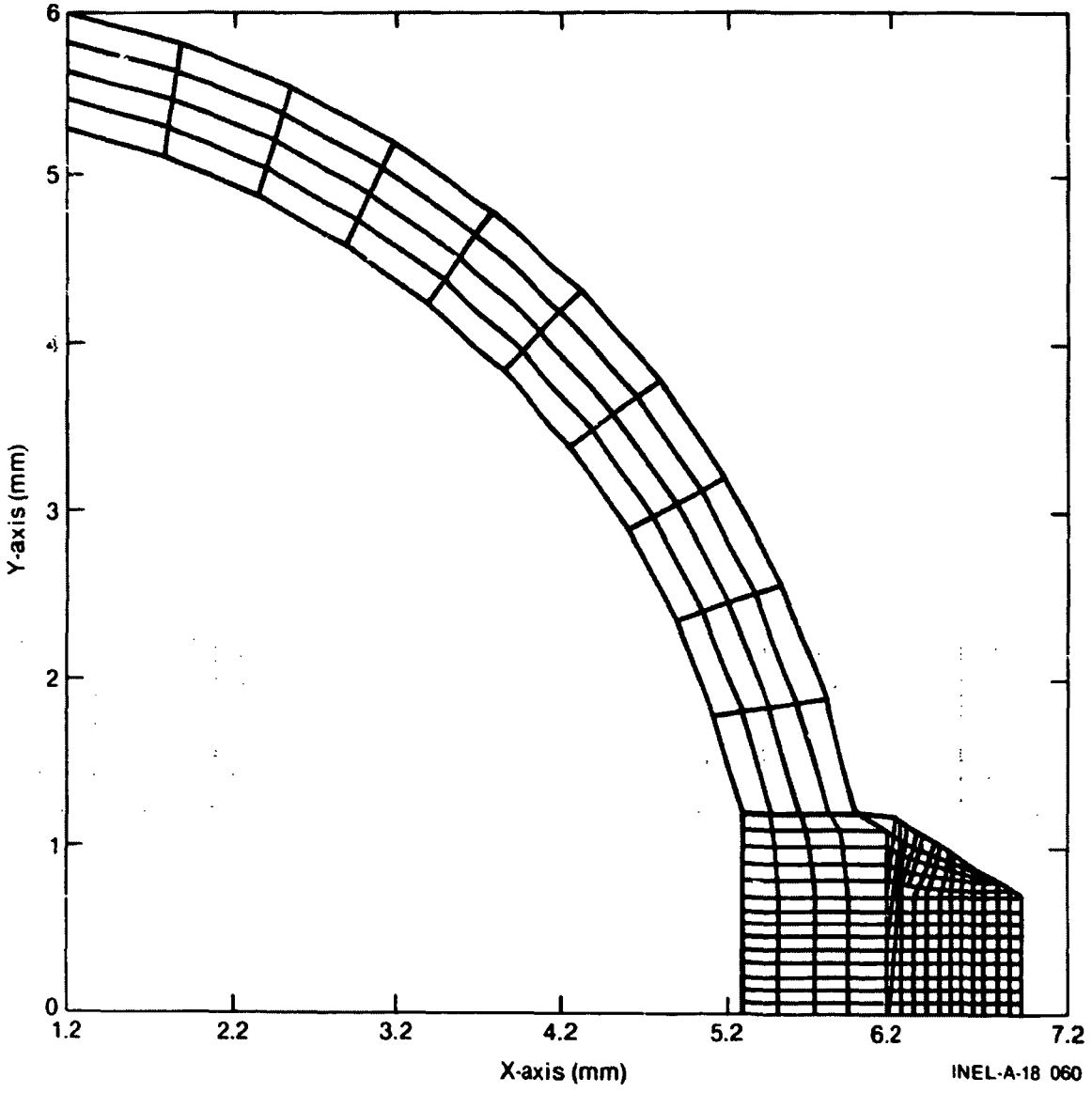

Figure E-1. Finite element model for Test PR-1 fuel rod, cladding, and thermocouple.

connection. Figure E-3 shows the conceptual attachment of a thermocouple to the cladding, and Figure E-4 shows a photomicrograph of the actual attachment of a thermocouple on a similar fuel rod.

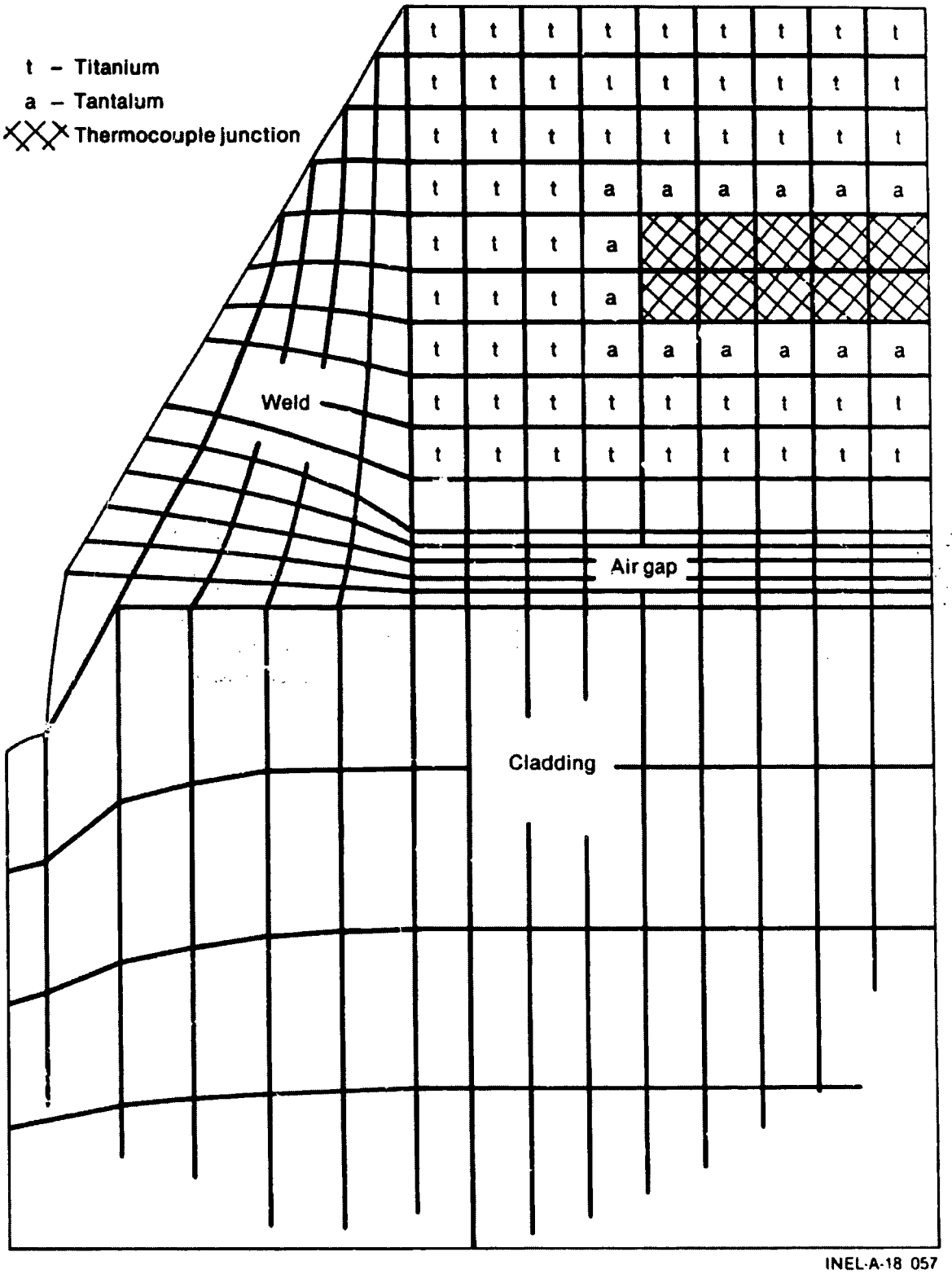

Figure E-2. Details of Test PR-1 cladding surface thermocouple model in the COUPLE code.

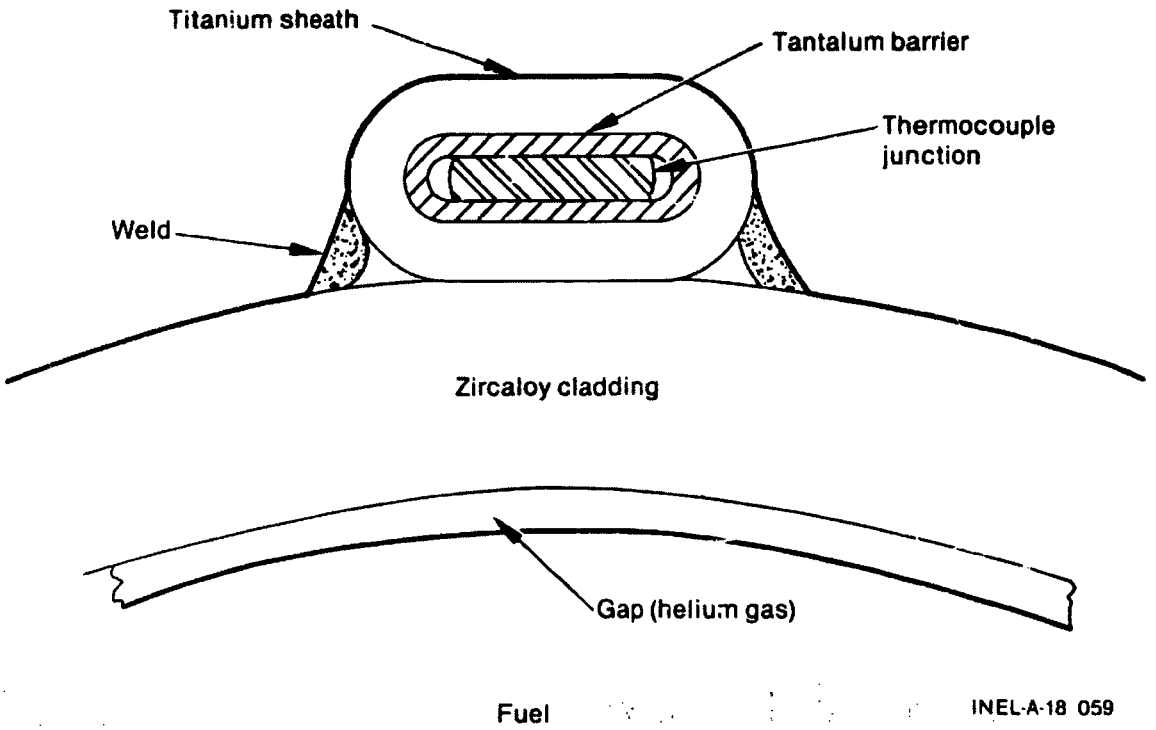

Figure E-3. Test PR-1 laser weld type thermocouple.

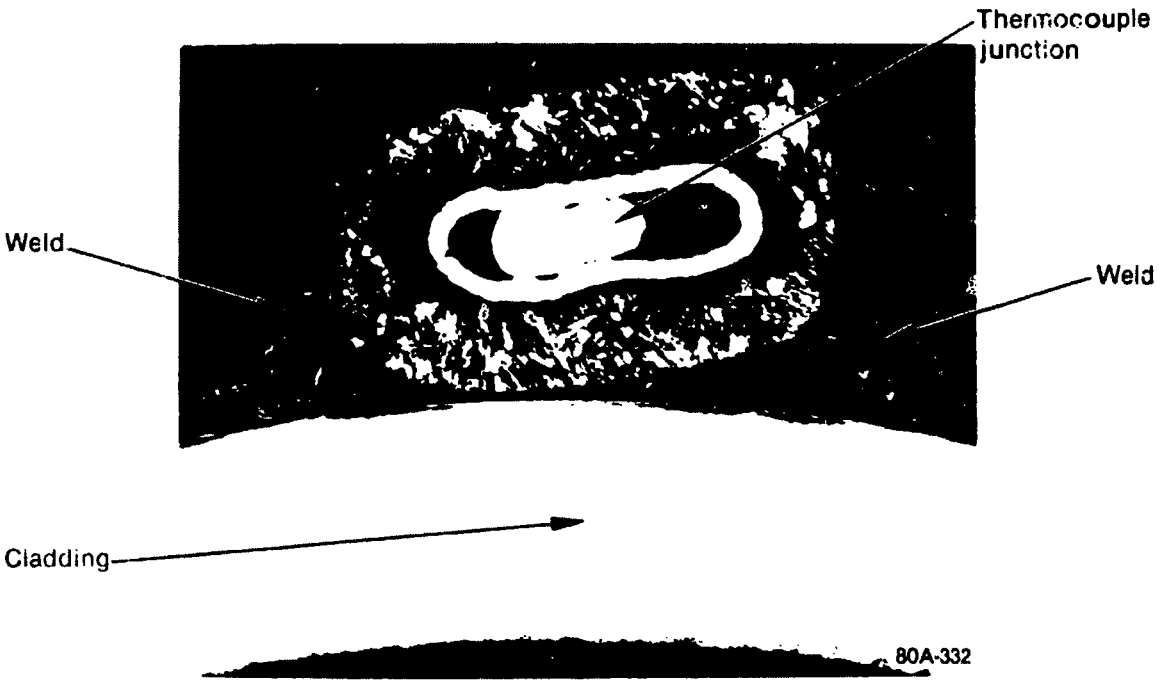

Figure E-4. Photomicrograph of Test PR-1 type thermocouple attached to the cladding of a fuel rod.

REFERENCES

E-1. Jacob Millman and Herbert Taub, Pulse, Digital, and Switching Waveforms, McGraw-Hill Book Company, 1965.

E-2. J. P. Holman, Heat Transfer, McGraw-Hill Book Company, 1976.

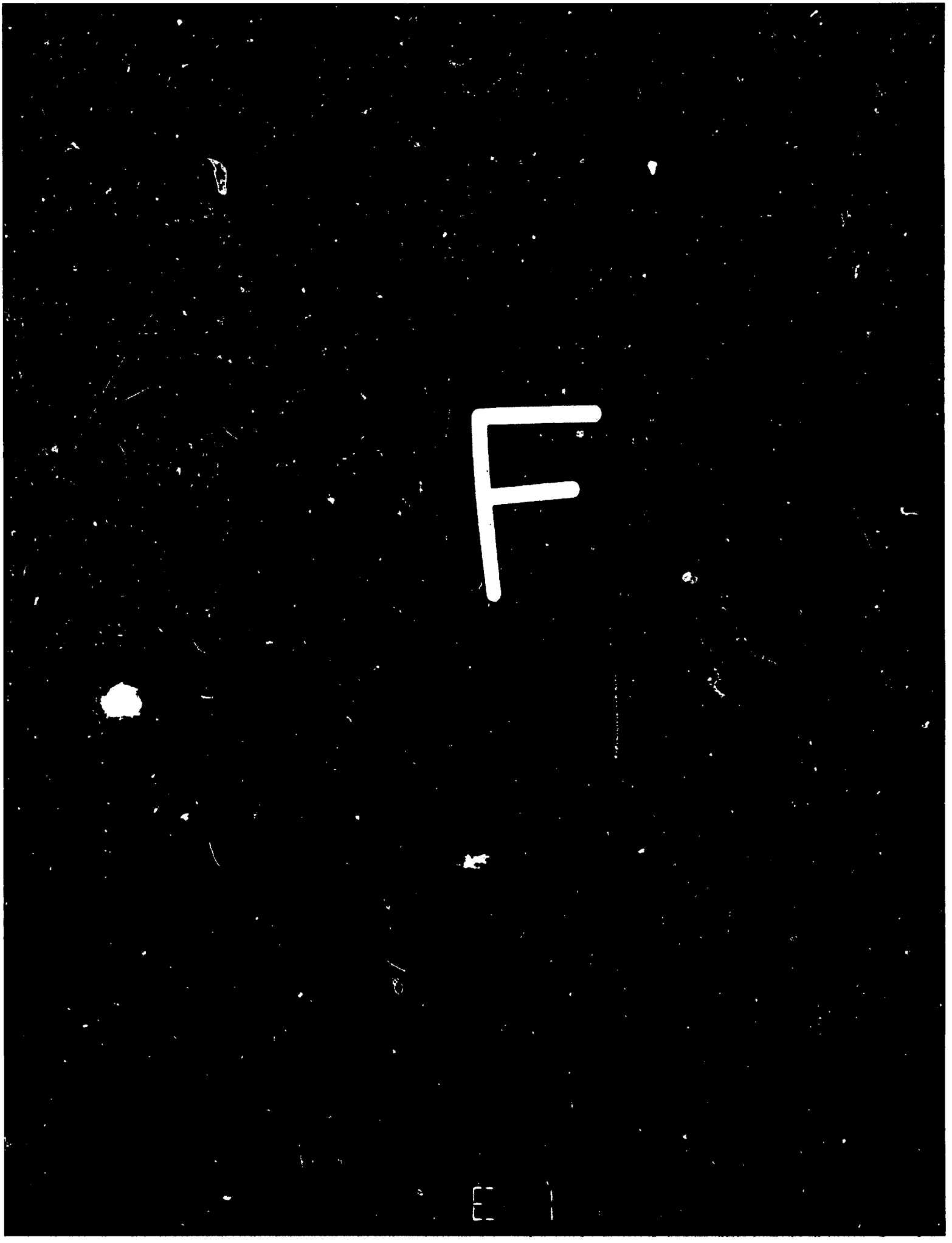
F

APPENDIX F

FRAPCON-2, FRAP-T5, AND RELAP5 MODELS AND INPUT

BLANK

PAGE

APPENDIX F

FRAPCON-2, FRAP-T5, AND RELAP5 MODELS AND INPUT

The FRAPCON-2[a] computer code was used to evaluate fuel rod parameters during the steady state portions of Test PR-1. The FRAP-T5[b] and RELAP5[c] computer codes were used to estimate thermal-hydraulic conditions and fuel rod behavior during the power-cooling-mismatch (PCM) and reactivity initiated accident (RIA) portions of Test PR-1.

FRAPCON is a FORTRAN IV computer code[F-1] developed to predict the steady state behavior of nuclear fuel rods during long-term operation. FRAPCON includes the coupled effects of thermal, mechanical, and internal gas pressure in the analysis of fuel rod behavior.

FRAP-T5 is a FORTRAN IV computer code[F-2] that calculates the transient response of light water reactor fuel rods during hypothesized accidents such as a power-cooling-mismatch. The code calculates the temperature, pressure, deformation, and failure histories of a fuel rod as functions of time-dependent fuel rod power and coolant boundary conditions. The phenomena modeled by the code include (a) heat conduction, (b) elastic-plastic fuel and cladding deformation, (c) fuel-cladding mechanical interaction, (d) fission gas release, (e) transient fuel rod gas pressure, (f) heat transfer between fuel and cladding, (g) cladding oxidation, (h) cladding annealing, and (i) heat transfer from cladding to coolant. The code contains the needed material properties, water properties, and heat transfer correlations. FRAP-T5 is programmed for the CDC 176 computer and is structured to enable direct linkage to a thermal-hydraulic code for

---

a. FRAPCON-2, Idaho National Engineering Laboratory Code Configuration Control Number H0019882B.

b. FRAP-T5, Idaho National Engineering Laboratory Code Configuration Control Number H0000583B.

c. RELAP5, Idaho National Engineering Laboratory Code Configuration Control Number F00021.

transient analysis. The FRAP-T5 code was used for the analysis of the Test PR-1 power-cooling-mismatch and RIA transients.

The RELAP5[F-3] code was used to calculate transient thermal-hydraulic conditions during the RIA power bursts. The output from RELAP5 was then linked to the FRAP-T5 code for calculation of the fuel rod transient response during the bursts.

The radial and axial power profiles used as input to the computer code calculations are listed in Tables F-1 and F-2, respectively. Table F-3 lists the pertinent fuel rod and flow shroud data used as input to the codes. With the exception of the cladding inner and outer diameters, the input data of Table F-3 were identical for the PCM and RIA portions of the experiment. Since the cladding was assumed to collapse onto the fuel stack during the PCM testing, the cladding inner and outer diameters were changed to 0.01057 and 0.01228 m, respectively, for the power burst operation. Table F-4 presents the correlations and modeling options used in the analyses. A FRAPCON-2 input listing for Rod 524-1 (helium fill gas, 95% theoretical density fuel) during steady state operation is presented in Table F-5. A FRAP-T5 input listing for Rod 524-4 (argon fill gas, 97% theoretical density fuel) during one of the PCM transients (PCM Cycle 23) is presented in Table F-6. A RELAP5 input listing for the RIA power burst analysis is presented in Table F-7.

TABLE F-1. RADIAL POWER PROFILES

PCM		RIA	
Mesh space	Normalized Power factor	Mesh space	Normalized Power factor
1	0.811	1	0.811
2	0.812	2	0.812
3	0.825	3	0.846
4	0.846	4	0.909
5	0.872	5	0.998
6	0.904	6	1.148
7	0.948		
8	1.008		
9	1.093		
10	1.186		

TABLE F-2. AXIAL POWER PROFILE

Elevation (m)	Normalized Power
0.	0.60
0.0213	0.69
0.0536	0.79
0.0963	0.90
0.1609	1.04
0.2146	1.13
0.2789	1.20
0.3219	1.33
0.3755	1.35
0.4292	1.34
0.4935	1.2
0.5368	1.17
0.6169	1.08
0.6706	1.00
0.7297	0.88
0.7888	0.77
0.8425	0.66
0.8781	0.57
0.9144	0.46

TABLE F-3. FUEL ROD AND FLOW SHROUD DATA

Fuel pellet	PCM	RIA
Diameter (m)	0.01057	0.01057
Height (m)	0.01057	0.01057
Stack length (m)	0.9144	0.9144
Density (g/cm^3)	10.413	10.413
Shoulder radius (m)	0	0
Dish depth (m)	0	0
Dish volume (m^3)	0	0
RMS roughness (μm)	2.16	2.16
Cladding		
Outer diameter (m)	0.0125	0.012282
Inner diameter (m)	0.01079	0.010572
RMS roughness (μm)	1.14	1.14

TABLE F-3. (continued)

	PCM	RIA
Plenum		
Plenum volume (m^3)	2.74E-05	2.74E-05
Gas pressure (MPa)	2.586	2.586
Gas composition	He or Ar	He or Ar
Spring length (m)	0.0508	0.0508
Spring coil OD (m)	0.00902	0.00902
Spring wire diameter (m)	0.001016	0.001016
Number of spring coils	17	17
Flow shroud		
Coolant flow area (m^2)	0.0001688	0.0001688
Hydraulic diameter (m)	0.00675	0.00675
Equivalent heated diameter (m)	0.01713	0.01713

TABLE F-4. CORRELATIONS AND MODELING OPTIONS USED

1. Fuel deformation model type = 0. (Free thermal expansion fuel deformation model specified.)
2. Modified Ross and Stoute model for gap conductance used.
3. Critical heat flux option = no cold wall or axial power factors used.
4. CHF correlation = General Electric Company.
5. Post-CHF heat transfer mode = Groeneveld Equation 5.9.

TABLE F-5. FRAPCON-2 INPUT LISTING FOR ROD 524-1

```
        1         2         3         4         5         6         7         8
12345678901234567890123456789012345678901234567890123456789012345678901234567890
 PWR ROD PR-1 FRAPCON RESTART
 &FRPCN
 MECHAN = 2,  IAXSYM = 0,
 IP = 10,  NA = 11,  NR = 11,
 &END
 &FRPCON
 CPL = .1597,  DCI = .0156,  DCO = .0125,  DE = .0112,  IEN = 95,
 DISRSO = .0[illegible]285,  DP = .0[illegible]167,  DSRO = .0[illegible]2,  DSRGW = .0[illegible]016,
 ENRCH = 10.0,  FRPAV = 2[illegible]0000.,  QF = 2[illegible]0.,  RDISP = 0.,  RPLT = .01[illegible]57,
 FA = 1.0,
 IGM = 4,  IDXGAS = 1,  IG = 2,  NDLFP = 1,  NUNITS = 0,
 IPLANT = 2,  IVARUP = 0,  NCPT = 0,  NSP = 0,
 JN = 13,
 JST = 0,
 P2 = 7.23[illegible]E3,  TOTL = .9144,  TA = 530.,  VS = 17.,
 QF(1) = .49,  .59,  .66,  1.[illegible],  1.24,  1.34,  1.3[illegible],  1.28,  1.12,
 QF(1[illegible]) = .9[illegible],  .72,  .47,  .34,
 CMPV(1) = 0.,  1.,  1[illegible].,  2[illegible].,  2[illegible].,  3[illegible].,  [illegible]5.,  4[illegible].,  45.,  5[illegible].
 TIME(1) = .01,  1.,  2.,  3.,  4.,  5.,  6.,  7.,  8.,  9.,
 X(1) = 0.,
 X(2) = .04156,  .12469,  .20782,  .29095,  .37407,  .45720,  .54033,
 X(8) = .62345,  .70658,  .78971,  .87284,  .9144,
 &END
        1         2         3         4         5         6         7         8
12345678901234567890123456789012345678901234567890123456789012345678901234567890
23 INPUT CARDS
```

TABLE F-6. REPRESENTATIVE FRAP-T5 INPUT LISTING FOR PCM TRANSIENT TESTING

```
12345678901234567890123456789012345678901234567890123456789012345678901234567890
    1    1   -7    0    0    1    0    1    0    0    0    0          0
    2    0    0    0    0         0         1
0.          500.          2.          0.          .9144       .012282     300.        .1
10473.        0.            0.        .01057      0.            0.          0.
            2.      1803.
.45452      .9144
 .001        .001                      .2                                 1.1
             1          1    1.0
.0653        .1959      .3266        .452        .5878        .7000       .8491
             0          0
  100   100    50    50
297.          4750.         297.          2500.
* PR-1 PCM CYCLE 23 ARGON ROD
* GENERAL DATA FOR HEAT-1
1 1 1 1 1 1 1 1 2 1 4 1 1.0 100 1.0 100
* GEOMETRY LOCATION AND MESH INCREMENT
0101020C      C  1
* MESH INCREMENT DATA - UNITS ARE METERS
1 1 1 1 1 1 C.0C0869  3    C.0002890   1    0.000595    3    0.006250
* COMPOSITION OVERLAY
C 0 1 0 3 0 1  6  3  7  2  10
* SOURCE POWER RADIAL DISTRIBUTION CARDS
0 1 0 1 0 1 1 .888  1  .898  2  .915  3  .948  4  1.0  5  1.096  6
0 1 0 1 0 1 0.  10
* INITIAL TEMPERATURE DISTRIBUTION
0 1 0 1 0 1 592.  11
*
    1    3   19
15.           0.          43.         300.         43.         500.
.6            0.          .69          .0213       .79          .0536     .9          .0963
1.04          .1009      1.13          .2146      1.2           .2789     1.31        .3219
1.33          .3759      1.32          .4292      1.2           .4935     1.17        .5368
1.08          .6169      1.0           .6706       .88          .7297      .77        .7888
.66           .8425       .57          .8781       .45          .9144
    0    2    2    2    3                    1   10
152CCCC0.     0.         152CCCC0.    1000.
1447367.      0.         1447367.     1000.
1860800.      0.         1860800.     1000.
400.14        0.         466.14       300.        361.66       500.
.01713
.00675
.000169
 1.14
     1    17.0321586E .0000274  2585625.  .0308       .00902     .0010162   300.
          1.
1234567890123456789012345678901234567890123456789012345678901234567890123456789012345678
42 INPUT CARDS
```

TABLE F-7. RELAP5 INPUT LISTING FOR RIA POWER BURST TESTING

```
RELAP5/MOD1/001
LISTING OF INPUT DATA FOR CASE  1

    1     =  TEST RUN FOR PBF          TEST SECTION - FULL LOOP MODEL
    2     100  NEW   TRANSNT
    3     101  RUN
    4     102  BRITISH  BRITISH
    5     201   2.00   1.0E-8   0.02   00002   1   25   25
    6     202   2.10   1.0E-8   0.001  00002   1   25   25
    7     203   3.00   1.0E-8   0.002  00002   1   50   50
    8     204   4.00   1.0E-8   0.005  00C02   1   40   40
    9     205   7.00   1.0E-8   0.010  00002   1  100  100
   10     206  32.00   1.0E-8   0.100  00002   1   40   40
   11     301  MFLOWJ   025000000
   12     302  MFLOWJ   300090000
   13     303       P   300090000
   14     304   VOIDG   300090000
   15     305    VELF   300090000
   16     306    VELG   300090000
   17     307  MFLOWJ   400090000
   18     308  HTTEMP   300000403
   19     501  TIME, 0  GE  NULL, 0  0.0  L
   20     *
   21     *  PUMP - BINGHAM PUMP USED
   22     *
   23     0100000  PUMP  PUMP
   24     0100101  0.0717 0.0 0.4106 0.0  00.0  0.000 0
   25     0100108  650010000 0.0717   0.0    0.0   0000
   26     0100109  020000000 0.0717 100.40 100.40 0000
   27     0100200  3 1133.000 509.0 0.0
   28     0100201  1 26.750 0.0 0.0
   29     0100202  1 26.750 0.0 0.0
   30     0100301  -1 -1 -1 -1 -1 0 0
   31     0100302  3550.0 1.0 800.0 960.0 2000.0 20.0 62.0 0.0 1000.8 0.0 0.0 0.0
   32     *
   33     *  PIPING FROM PUMP TO BYPASS JUNCTION
   34     *
   35     0200000  PIPE  SNGLVOL
   36     0200101  0.0717 50.800 0.0 0.0  00.0  0.000 0.00E-6 0.3027 00
   37     0200200  3 1331.555 509.0 0.0
   38     0250000  JUNCTION  SNGLJUN
   39     0250101  020010000 030000000 0.0717 1087.1 1087.1 0000
   40     0250201  1 26.750 0.0 0.0
   41     0300000  PIPE  BRANCH
   42     0300001  0 1
```

TABLE F-7. (continued)

```
0300101  0.0717 16.000 0.0 0.0  15.3  4.250 0.00E-6 0.3022 00
0300200  3 936.450 509.0 0.0
0350000  TESTFLOW  SNGLJUN
0350101  030010000 040000000 0.0717 0.01 0.01 0000
0350201  1 0.0 0.0 0.0
0370000  BYPASS  SNGLJUN
0370101  030010000 700000000 0.0717 21.0 21.0 0000
0370201  1 26.750 0.0 0.0
0390000  BYPASS  SNGLJUN
0390101  700000000 040000000 0.0717 21.0 21.0 0000
0390201  1 0.0 0.0 0.0
*
*  PIPING FROM TEST/BYPASS SPLIT TO ACF
*
0400000  TESTPIPE  BRANCH
0400001  0 1
0400101  0.0717 10.430 0.0 0.0  11.5  2.080 0.00E-6 0.3022 00
0400200  3  934.812 509.0 0.0
0450000  JUNCTION  SNGLJUN
0450101  040010000 050000000 0.0717 0.01 0.01 0000
0450201  1 0.0 0.0 0.0
0500000  TESTPIPE  SNGLVOL
0500101  0.0717 9.920 0.0 0.0   9.2  1.590 0.00E-6 0.3022 00
0500200  3  934.052 509.0 0.0
0550000  JUNCTION  SNGLJUN
0550101  050010000 090000000 0.0717 0.01 0.01 0000
0550201  1 0.0 0.0 0.0
0900000  TESTPIPE  SNGLVOL
0900101  0.0717 2.501 0.0 0.0  00.0  0.000 0.00E-6 0.3022 00
0900200  3  935.000 509.0 0.0
0950000  JUNCTION  SNGLJUN
0950101  090010000 100000000 0.0717 0.00 0.00 0000
0950201  1  0.000  0.000 0.0
*
*  PIPING FROM ACF TO INLET NOZZLE (INCLUDING ACF)
*
1000000  INLETPIPE  PIPE
1000001  5
1000101  1.0700, 3  0.0717, 5
1000301  4.0000, 3  3.6900, 5
1000601   00.00, 5
1000801  0.00 1.167, 3  0.00 0.0717, 5
1001001  00, 5
1001101  0100, 4
1001201  3 932.734 509.0 0.0 0.0  1
```

TABLE F-7. (continued)

```
1001202  3 932.734 509.0 0.0 0.0  2
1001203  3 932.734 509.0 0.0 0.0  3
1001204  3 932.734 509.0 0.0 0.0  4
1001205  3 932.734 509.0 0.0 0.0  5
1001300  1
1001301   0.000  0.000 0.0, 4
1050000  NOZZLE  SNGLJUN
1050101  100010000 200000000 0.0319 0.00 0.00 0100
1050201  1  0.000  0.000 0.0
*
*  DOWNCOMER REGION - INLET NOZZLE TO LOWER PLENUM
*
2000000  DOWNCOMER  PIPE
2000001  13
2000101  0.03191, 6  0.06330,13
2000201  0.03191, 6  0.06330,12
2000301  0.81500, 6  0.85700,13
2000601  -90.0,13
2000801  0.0 0.0417, 6  0.0 0.0867,13
2001001  00,13
2001101  0100,12
2001201  3  932.871 509.0 0.0 0.0  1
2001202  3  933.145 509.0 0.0 0.0  2
2001203  3  933.420 509.0 0.0 0.0  3
2001204  3  933.694 509.0 0.0 0.0  4
2001205  3  933.969 509.0 0.0 0.0  5
2001206  3  934.244 509.0 0.0 0.0  6
2001207  3  934.525 509.0 0.0 0.0  7
2001208  3  934.814 509.0 0.0 0.0  8
2001209  3  935.103 509.0 0.0 0.0  9
2001210  3  935.391 509.0 0.0 0.0 10
2001211  3  935.680 509.0 0.0 0.0 11
2001212  3  935.969 509.0 0.0 0.0 12
2001213  3  936.258 509.0 0.0 0.0 13
2001300  1
2001301   0.000  0.000 0.0,12
*
*  LOWER PLENUM REGION
*
2050000  EXPANSION  SNGLJUN
2050101  200010000 210000000 0.06330 0.00 0.00 0100
2050201  1  0.000  0.000 0.0
2100000  LPLENUM  BRANCH
2100001  0 1
2100101  0.12620 0.2090 0.0 0.0 -90.0 -0.2090 0.00E-6 0.4914 00
```

TABLE F-7. (continued)

```
2100200  3 936.293 509.0 0.0
2150000  CONTRACT  SNGLJUN
2150101  210000000 220000000 0.06540 0.00 0.00 0100
2150201  1  0.000  0.000 0.0
2200000  ANNULUS  SNGLVOL
2200101  0.06540 0.5330 0.0 0.0  90.0  0.5330 0.00E-6 0.0877 00
2200200  3 936.203 509.0 0.0
2250000  HOLES     SNGLJUN
2250101  220010000 230000000 0.03190 0.00 0.00 0100
2250201  1  0.000  0.000 0.0
2300000  SPLIT  BRANCH
2300001  0 1
2300101  0.13300 0.5170 0.0 0.0  90.0  0.3310 0.00E-6 0.1920 00
2300200  3 935.700 509.0 0.0
2350000  LOWER-TEST  SNGLJUN
2350101  230010000 300000000 0.00545 0.00 0.00 0100
2350201  1  0.000  0.000 0.0
*
*  TEST SECTION COMPONENT - INLET TO UPPER MIXING REGION
*
3000000  TESTSECT  PIPE
3000001  17
3000101  0.00612, 2  0.01132, 4  0.00880, 5  0.00776,12  0.01084,13
3000102  0.02012,15  0.00616,17
3000201  0.00612, 1  0.00450, 2  0.01132, 3  0.00117, 4  0.00776,12
3000202  0.01084,13  0.02012,14  0.00616,16
3000301  0.35400, 2  0.49800, 4  0.31500, 5  0.35300,12  0.70600,13
3000302  0.42000,15  0.38700,17
3000601  90.0,17
3000801  0.0 0.0441, 2  0.0 0.0191, 4  0.0 0.0257, 5  0.0 0.0220,12
3000802  0.0 0.0320,13  0.0 0.0800,15  0.0 0.0442,17
3000901  0.00  0.00, 1  3.25  3.25, 2  0.00  0.00, 3
3000902  1.50  1.50, 4  0.00  0.00,16
3001001  00,17
3001101  0100, 1  0000, 2  0100, 3  0000, 4  0100,16
3001201  3  936.051 509.0 0.0 0.0  1
3001202  3  935.931 509.0 0.0 0.0  2
3001203  3  935.798 509.0 0.0 0.0  3
3001204  3  935.620 509.0 0.0 0.0  4
3001205  3  935.482 509.0 0.0 0.0  5
3001206  3  935.371 509.0 0.0 0.0  6
3001207  3  935.238 509.0 0.0 0.0  7
3001208  3  935.119 509.0 0.0 0.0  8
3001209  3  935.000 509.0 0.0 0.0  9
3001210  3  934.881 509.0 0.0 0.0 10
3001211  3  934.762 509.0 0.0 0.0 11
```

TABLE F-7. (continued)

```
3001212  3  934.643 509.0 0.0 0.0 12
3001213  3  934.465 509.0 0.0 0.0 13
3001214  3  934.294 509.0 0.0 0.0 14
3001215  3  934.190 509.0 0.0 0.0 15
3001216  3  934.072 509.0 0.0 0.0 16
3001217  3  933.939 509.0 0.0 0.0 17
3001300  1
3001301   0.000  0.000 0.0    16
3050000  TEST-UPPER  SNGLJUN
3050101  300010000 410000000 0.00545 0.0   .. 0 0100
3050201  1  0.000  0.000 0.0
*
*  BYPASS REGION - INLET TO UPPER MIXING BRANCH
*
2370000  BYPASSBOT  SNGLJUN
2370101  230010000 400000000 0.00170 1.45 1.45 0000
2370201  1  0.000  0.000 0.0
4000000  BYPASS  PIPE
4000001  15
4000101  0.06P00, 1  0.07360, 5  0.10180,11  0.08620,15
4000201  0.06800, 1  0.07360, 5  0.10180,10  0.02083,11  0.08620,14
4000301 00.33800, 1  0.33900, 5  0.55200,11  0.45100,15
4000601  90.0,15
4000801  0.0  0.1850, 1  0.0 0.0950, 5  0.0 0.1510,11  0.0 0.1110,15
4001001  00,15
4001101  0100,14
4001201  3  936.051 509.0 0.0 0.0  1
4001202  3  935.936 509.0 0.0 0.0  2
4001203  3  935.822 509.0 0.0 0.0  3
4001204  3  935.707 509.0 0.0 0.0  4
4001205  3  935.593 509.0 0.0 0.0  5
4001206  3  935.443 509.0 0.0 0.0  6
4001207  3  935.257 509.0 0.0 0.0  7
4001208  3  935.071 509.0 0.0 0.0  8
4001209  3  934.902 509.0 0.0 0.0  9
4001210  3  934.733 509.0 0.0 0.0 10
4001211  3  934.564 509.0 0.0 0.0 11
4001212  3  934.395 509.0 0.0 0.0 12
4001213  3  934.243 509.0 0.0 0.0 13
4001214  3  934.091 509.0 0.0 0.0 14
4001215  3  933.939 509.0 0.0 0.0 15
4001300  1
4001301   0.000  0.000 0.0    14
4050000  BYPASSTOP  SNGLJUN
4050101  400010000 410000000 0.08620 0.00 0.00 0100
4050201  1  0.000  0.000 0.0
```

TABLE F-7. (continued)

```
225     *
226     *  UPPER MIXING BRANCH
227     *
226     4100000  UPPERMIX  BRANCH
229     4100001  0 1
230     4100101  0.11880 0.3200 0.0 0.0  90.0  0.3200 0.00E-6 0.3070 00
231     4100200  3 933.700 509.0 0.0
232     *
233     *  UPPER STRUCTURE REGION - UPPER MIXING REGION TO OUTLET NOZZLE
234     *
235     4150000  JUNCTION  SNGLJUN
236     4150101  410010000 500000000 0.11880 0.00 0.00 0100
237     4150201  1  0.000  0.000 0.0
238     5000000  UPPLENUM  PIPE
239     5000001  7
240     5000101  0.11880, 1  0.01030, 2  0.11590, 4  0.06270, 7
241     5000301  0.32000, 1  0.94800, 2  0.43700, 4  0.90000, 7
242     5000601  90.0, 7
243     5000801  0.00 0.3070, 1  0.0 0.0573, 2  0.00 0.2440, 4  0.0 0.2820,7
244     5001001  00, 7
245     5001101  0100, 6
246     5001201  3 933.000 509.0 0.0 0.0  1
247     5001202  3 932.786 509.0 0.0 0.0  2
248     5001203  3 932.533 509.0 0.0 0.0  3
249     5001204  3 932.406 509.0 0.0 0.0  4
250     5001205  3 932.181 509.0 0.0 0.0  5
251     5001206  3 931.678 509.0 0.0 0.0  6
252     5001207  3 931.575 509.0 0.0 0.0  7
253     5001300  1
254     5001301   0.000  0.000 0.0, 6
255     5050000  OUTNOZZLE  SNGLJUN
256     5050101  500010000 600000000 0.0219 0.45 0.45 0000
257     5050201  1  0.000  0.000 0.0
258     *
259     *  OUTLET PIPING COMPONENT - OUTLET NOZZLE THROUGH ACF
260     *
261     6000000  OUTPIPING  PIPE
262     6000001  5
263     6000101  0.07170, 2  1.07000, 5
264     6000301  3.69000, 2  4.00000, 5
265     6000601   00.0, 5
266     6000801  0.00 0.3022, 2  0.0 1.167, 5
267     6001001  00,5
268     6001101  0100, 4
269     6001201  3 931.423 509.0 0.0 0.0  1
270     6001202  3 931.423 509.0 0.0 0.0  2
```

TABLE F-7. (continued)

```
6001203  3 931.423 509.0 0.0 0.0  3
6001204  3 931.423 509.0 0.0 0.0  4
6001205  3 931.423 509.0 0.0 0.0  5
6001300  1
6001301   0.000   0.000 0.0, 4
6050000  JUNCTION   SNGLJUN
6050101  600010000 610000000 0.07170 0.00 0.00 0100
6050201  1  0.000  0.000 0.0
*
*  PIPING FROM OUTLET ACF TO TEST/BYPASS MIXING
*
6100000  TESTPIPE  PIPE
6100001  10
6100101  0.0717, 9  0.7857,10
6100301  2.501, 1  3.068, 2  4.193, 5  4.420, 6  4.784, 9  1.998,10
6100601   -3.4, 1  -13.0, 2  -14.2, 5    0.0,10
6100701  -0.150,1  -0.690,2  -1.008,5  0.000,10
6100801  0.00 0.3022, 9  0.00 0.7500,10
6101001  00,10
6101101  0100, 9
6101201  3  928.900 509.0 0.0 0.0,10
6101300  1
6101301  0.00 0.00 0.0, 9
6150000  JUNCTION   SNGLJUN
6150101  610010000 620000000 0.0717 0.00 0.00 010C
6150201  1 0.0 0.0 0.0
*
*  TEST/BYPASS MIXING
*
6200000  BRANCH  BRANCH
6200001  0 1
6200101  0.0717 4.729 0.0 0.0  00.0  0.000 0.00E-6 0.3022 00
6200200  3  928.721 509.0 0.0
6210000  REGJUNCT  SNGLJUN
6210101  620010000 630000000 0.0717 0.15 0.15 0000
6210201  1 0.0 0.0 0.0
6230000  BYPASSJUN  SNGLJUN
6230101  620010000 720010000 0.0717 0.01 0.01 0000
6230201  1 0.0 0.0 0.0
6250000  HXLOOPJUN  SNGLJUN
6250101  620010000 800000000 0.0098 0.00 0.00 010C
6250201  1 0.0 0.0 0.0
6270000  BYPASSJUN  SNGLJUN
6270101  720010000 630000000 0.0717 0.01 0.01 0000
6270201  1 26.750 0.0 0.0
6290000  HXLOOPJUN  SNGLJUN
```

TABLE F-7. (continued)

```
317     6290101  630000000 800000000 0.0098 0.00 0.00 0100
318     6290201  1 0.0 0.0 0.0
319     6300000  BRANCH  BRANCH
320     6300001  0 1
321     6300101  0.0717 1.501 0.0 0.0  00.0  0.000 0.00E-6 0.3022 00
322     6300200  3  928.086 509.0 0.0
323     *
324     *  TEST/BYPASS MIXING TO PUMP
325     *
326     6350000  JUNCTION  SNGLJUN
327     6350101  630010000 640000000 0.0717 34.60 34.60 0000
328     6350201  1 26.750 0.0 0.0
329     6400000  BRANCH  BRANCH
330     6400001  0 1
331     6400101  0.0717 2.700 0.0 0.0  00.0  0.000 0.00E-6 0.3022 00
332     6400200  3  918.152 509.0 0.0
333     6430000  JUNCTION  SNGLJUN
334     6430101  640010000 650000000 0.0717 3.57 3.57 0000
335     6430201  1 26.750 0.0 0.0
336     6450000  HXLOOP  SNGLJUN
337     6450101  640010000 830010000 0.0376 0.01 0.01 0000
338     6450201  1 0.0 0.0 0.0
339     6470000  HXLOOP  SNGLJUN
340     6470101  830010000 650000000 0.0376 0.01 0.01 0000
341     6470201  1 0.0 0.0 0.0
342     6500000  BRANCH  BRANCH
343     6500001  0 1
344     6500101  0.0717 9.439 0.0 0.0 -38.8 -6.002 0.00E-6 0.3022 00
345     6500200  3  928.116 509.0 0.0
346     *
347     *  LOOP BYPASS
348     *
349     7000000  BYPASS  BRANCH
350     7000001  0 1
351     7000101  0.0717 5.510 0.0 0.0  10.5  0.918 0.00E-6 0.3022 00
352     7000200  3 932.763 509.0 0.0
353     7050000  BYPASSJUN  SNGLJUN
354     7050101  700010000 710000000 0.0717 1.10 1.10 0000
355     7050201  1 26.750 0.0 0.0
356     7100000  BYPASS  SNGLVOL
357     7100101  0.0717 5.510 0.0 0.0  10.5  0.918 0.00E-6 0.3022 00
358     7100200  3  928.532 509.0 0.0
359     7150000  BYPASSJUN  SNGLJUN
360     7150101  710010000 720000000 0.0717 0.01 0.01 0000
361     7150201  1 26.750 0.0 0.0
362     7200000  BYPASS  SNGLVOL
```

TABLE F-7. (continued)

```
7200101   ?.0717 5.510 0.0 0.0 -00.9 -0.034 0.00E-6 0.3022 00
7200200   3  928.109 509.0 0.0
*
*  HEAT EXCHANGER AND PRESSURIZER BRANCH
*
8000000  HXLOOP  BRANCH
8000001  0 1
8000101  0.0098 27.670 0.0 0.0 -11.5 -5.489 0.00E-6 0.1115 00
8000200  3  920.988 509 0 0.0
8050000  HXLOOP  SNGLJUN
8050101  800010000 810000000 0.0098 0.02 0.02 0000
8050201  1 0.0 0.0 0.0
8100000  HXLOOP  SNGLVOL
8100101  0.0276 2.000 0.0 0.0   1.6  0.056 0.00E-6 0.1874 00
8100200  3  920.890 509.0 0.0
8150000  HXLOOP  SNGLJUN
8150101  810010000 820000000 0.0098 0.01 0.01 0000
8150201  1 0.0 0.0 0.0
8200000  HXLOOP  BRANCH
8200001  0 1
8200101  0.0098 15.143 0.0 0.0  32.3  8.100 0.00E-6 0.1115 00
8200200  3  919.049 509.0 0.0
8230000  PRESSURE  SNGLJUN
8230101  820010000 900000000 0.0036 0.06 0.06 0000
8230201  1 0.0 0.0 0.0
8250000  HXLOOP  SNGLJUN
8250101  820010000 830000000 0.0098 0.01 0.01 0000
8250201  1 0.0 0.0 0.0
8270000  PRESSURE  SNGLJUN
8270101  830000000 900000000 0.0036 0.06 0.06 0000
8270201  1 0.0 0.0 0.0
8300000  HXLOOP  BRANCH
8300001  0 1
8300101  0.0376 14.162 0.0 0.0 -10.8 -2.667 0.00E-6 0.2187 00
8300200  3  918.100 509.0 0.0
*
*  PRESSURIZER DEAD END
*
9000000  PRESSURE BRANCH
9000001  0 1
9000101  0.0036 19.469 0.0 0.0 -27.0 -8.833 0.00E-6 0.0679 00
9000200  3  919.000 509.0 0.0
9050000  PRESSURE  SNGLJUN
9050101  900010000 910000000 0.0036 0.50 0.50 0000
9050201  1 0.0 0.0 0.0
9100000  PRESURIZ  TMDPVOL
```

TABLE F-7. (continued)

```
409     9100101  3.978 10.500 0.0 0.0  90.0  10.500 0.00E-6 2.250 00
410     9100200  3
411     9100201   0.00  929.000 509.0
412     *
413     *  FUEL ROD HEAT STRUCTURE
414     *
415     13000000  7 9 2 1 0.0000
416     13000100  0 1
417     13000101  1 0.01096  1 0.01450  1 0.01550  1 0.01644
418     13000102  1 0.01733  1 0.01771  2 0.02054
419     13000201  100, 5  200, 6  300, 8
420     13000301  0.927, 1  0.956, 2  0.999, 3  1.054, 4
421     13000302  1.374, 5  0.000, 6  0.012, 8
422     13000401   509.0, 9
423     13000501  0 0 0 0 0.0, 7
424     13000601  300060000 10000 1 1 1.410, 7
425     13000701  100 447.0E-6 0.0 3.900E-6, 1
426     13000702  100 621.0E-6 0.0 5.400E-6, 2
427     13000703  100 663.0E-6 0.0 5.800E-6, 3
428     13000704  100 698.0E-6 0.0 6.100E-6, 4
429     13000705  100 628.0E-6 0.0 5.500E-6, 5
430     13000706  100 524.0E-6 0.0 4.600E-6, 6
431     13000707  100 384.0E-6 0.0 3.400E-6, 7
432     13000901  0 0.0220 0.0603 1.410, 7
433     *
434     *  BYPASS MODERATOR HEATING
435     *
436     14000000  6 4 1 1 0.0000
437     14000100  0 1
438     14000101  3 0.0015
439     14000201  200, 3
440     14000301  1.0, 3
441     14000401  509.0, 4
442     14000501  400060000 10000 1 0 1.000, 6
443     14000601  0 0 0 0 1.000, 6
444     14000701  100 0.001E-6 56.70E-6 0.0, 1
445     14000702  100 0.001E-6 75.60E-6 0.0, 2
446     14000703  100 0.001E-6 94.50E-6 0.0, 3
447     14000704  100 0.001E-6 94.50E-6 0.0, 4
448     14000705  100 0.001E-6 75.60E-6 0.0, 5
449     14000706  100 0.001E-6 56.70E-6 0.0, 6
450     14000801  0 0.0 0.0 0.552, 6
451     *
452     *  DOWNCOMER MODERATOR HEATING
453     *
454     12000000  4 4 1 1 0.0000
```

TABLE F-7. (continued)

```
12000100  0 1
12000101  3 0.0015
12000201  200, 3
12000301  1.0, 3
12000401  509.0, 4
120005C1  200070000 10000 1 0 1.369, 4
1200060.  0 0 0 0 1.369, 4
12000701  100 0.001E-6 56.40E-6 0.0, 1
12000702  100 0.001E-6 56.40E-6 0.0, 2
12000703  100 0.001E-6 56.40E-6 0.0, 3
12000704  100 0.001E-6 56.40E-6 0.0, 4
12000801  0 0.0 0.0 0.367, 4
*
*  UO2 PROPERTIES
*
20110000  TBLFECN 1 1
*  THERMAL CONDUCTIVITY (BTU/SEC-FT-F)
20110001    32.0 0.00013,   212.0 0.00170   392.0 0.00095   572.0 0.00083
20110002   752.0 0.00077,   932.0 0.00065  1112.0 0.00060  1292.0 0.00055
20110003  1472.0 0.00051  1832.0 0.00045  2192.0 0.00040  2552.0 0.00037
20110004  2912.0 0.00033  3272.0 0.00030  3632.0 0.00028  3992.0 0.00042
20110005  4352.0 0.00055  5144.0 0.00060  9000.0 0.00069
*  SPECIFIC HEAT (BTU/LB-F) - NOTE INCLUSION OF HEAT OF FUSION
20110051    32.0  34.9   120.0  38.1   200.0  40.1   400.0  43.4   800.0  46.6
20110052  1200.0  48.3  1600.0  49.5  2000.0  50.8  2400.0  52.4  2800.0  54.9
20110053  3200.0  59.1  3500.0  55.7  4000.0  75.2  4400.0  87.5  4800.0 102.9
20110054  5440.0 117.7  5148.  1610.3  5190.  1610.3  5198.0  79.2  9000.0  79.2
*
*  HELIUM PROPERTIES
*
20120000  TBLFECN 1 1
*  THERMAL CONDUCTIVITY (BTU/SEC-FT-F) - THIS CURVE WAS CHOSEN TO
*        GIVE THE GAP A PRESCRIBED GAP CONDUCTANCE VERSUS GAP
*        TEMPERATURE DEPENDENCE.
20120001  -100.0 0.00009   500.0 0.00009  1520.0 0.00022  1890.0 0.00037
20120002  2420.0 0.00056  2780.0 0.00083  4940.0 0.00083
*  SPECIFIC HEAT (BTU/LB-F)
20120051  0.03620
*
*  CLAD (ZR-2) PROPERTIES
*
20130000  TBLFECN 1 1
*  THERMAL CONDUCTIVITY (BTU/SEC-FT-F)
20130001    32.0 0.00193   212.0 0.00220   392.0 0.00240   572.0 0.00260
20130002   752.0 0.00279   932.0 0.00294  1112.0 0.00318  1292.0 0.00340
20130003  1472.0 0.00355  1652.0 0.00373  1832.0 0.00425  2012.0 0.00449
```

TABLE F-7 (continued)

```
501     20130004  2192.0 0.00004  2372.0 0.00352  2552.0 0.00607  2732.0 0.00571
502     20130005  3092.0 0.00004  3317.0 0.00352  3000.0 0.00362
503     *  SPECIFIC HEAT (BTU/LB-F) - LAST DEFINITE VALUE ABOVE MELTING TEMP.
504     20130051    80.0 25.7    250.0 28.7    392.0 31.4  1502.0 35.6  1508.0 47.7
505     20130052  1044.0 55.0  1340.0 53.4  1515.0 58.3  1652.0 77.5  1698.0 73.1
506     20130053  1724.0 68.0  1750.0 44.9  1797.0 33.8  3317.0 33.8  3320.0 1.0E6
507     20130054  3000.0 1.0E6
508     *
509     *  REACTOR POWER HISTORY (INTEGRAL 0-10SEC IS 717.6MW-SEC)
510     *
511     20210000  POWER 501 1.0 0.804
512     20210001    0.0 0.0  2.0 0.115 2.045 0.456 2.05 0.533 2.15 3.026
513     20210002  2.25  26.25  2.30  77.5  2.35  173.0  2.40  252.5
514     20210003  2.414  254.8  2.428  259.2  2.45  234.2  2.55  139.5
515     20210004  2.65  114.4  2.85  100.7  3.15  81.6  3.55  69.4
516     20210005  4.05  59.5  4.55  49.3  5.05  43.0  5.13  2.2
517     20210006  5.14  39.5  5.15  39.3  5.43  12.0  5.20  5.9
518     20210007  5.31  3.9  5.45  3.4  52.0  1.2
519     *
```

REFERENCES

F-1. G. A. Berna et al., FRAPCON-2: A Computer Code for the Calculation of Steady State Thermal-Mechanical Behavior of Oxide Fuel Rods, NUREG/CR-1845, December 1980.

F-2. L. J. Siefken et al., FRAP-T5 A Computer Code for the Transient Analysis of Oxide Fuel Rods, NUREG/CR-0840, TREE-1281, June 1979.

F-3. V. H. Ransom et al., RELAP5/MOD1 Code Manual, Volume 1: System Models and Numerical Methods, and Volume 2: Users Guide and Input Requirements, NUREG/CR-1826, EGG-2070, November 1980.

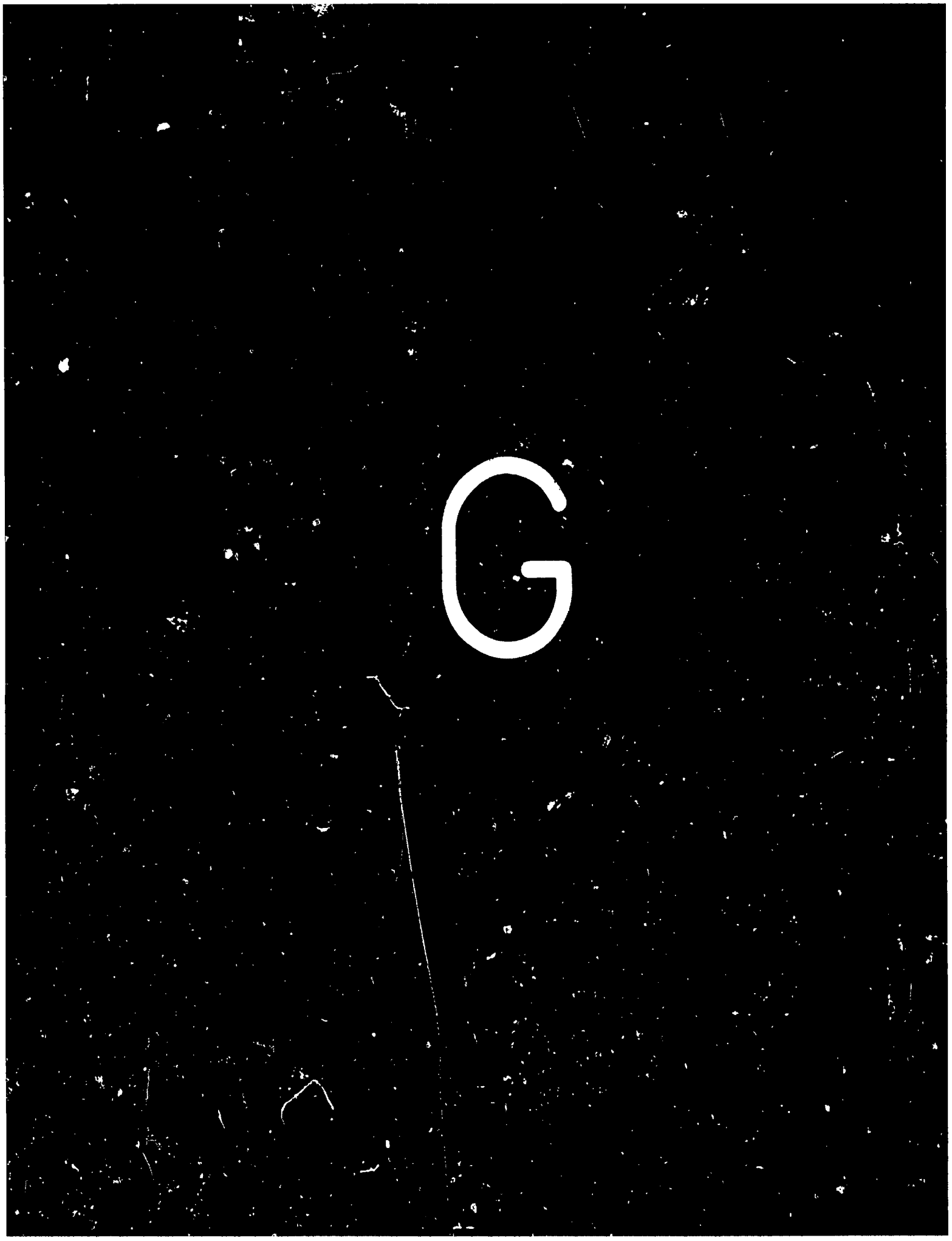

APPENDIX G

TEST PR-1 DOCUMENT AND RECORDS TRACEABILITY

BLANK

PAGE

APPENDIX G

TEST PR-1 DOCUMENT AND RECORDS TRACEABILITY

This appendix provides a description of the documentation and data gathering processes involved in preparing for, performing, and gathering data from tests at the Power Burst Facility (PBF).

PURPOSE

The purpose of this appendix is to provide a set of instructions for retrieving records, documents, data tapes, etc., for Test PR-1. By explaining what is available and where to look for it, much of the activity could be reconstructed, if necessary. These materials and records would be necessary to (a) reconstruct the processing, correction, and presentation of data; (b) retrieve data tapes in the raw or corrected form; (c) determine the type and location of instruments used; (d) determine the calibrations, zero settings, offsets, etc., for the transducers and instruments used; (e) find details of the test train design, fabrication, and instrumentation; and (f) retrieve calculations used in the discussions presented in this report. Much of this information is contained in various reports, documents, files, and drawings produced during the planning, building, and operation of the test, as well as during the data processing and qualification procedure.

Unfortunately, there is no unified filing system where one can find all the information in one place. Some of the files and documentation systems are formal, but many are not. Material is physically located in three major areas: the Power Burst Facility, the Idaho National Engineering Laboratory (INEL) Computer Facility, and the Experiment Specification and Analysis organization work area. Some items are located in the INEL Technical Library and the EG&G Idaho drawing vault.

FILES, DOCUMENTS, AND RECORD SYSTEMS

This section lists all the major files, documents, and record systems, as well as an explanation of what they contain. It also lists the various data tapes and how to retrieve them.

Interim and Informal Reports

These reports are prepared primarily for preliminary or internal use and are generally intended as working documents. They have not received full review and approval. Since these documents may undergo substantial changes, they should not be considered final.

Each document has a unique number assigned by the Publication Processing Office. This organization, as well as the INEL Technical Library, files copies of each report. Copies are also available from the National Technical Information Service and the Nuclear Regulatory Commission's Division of Technical Information and Document Control. The specific documents covered under this category will be discussed in subsequent sections.

Data Acquisition Specification (DAS)

This document is designed as a working tool for setting up the experiment instrumentation. It details the amplifiers to be used, gain settings, zero offsets, instrument ranges, patch panel connections, and provides a cross index between the measurement identifiers of the Experiment Operating Specification, the working parameter channels, and the patch panel numbers. This document is used to set up and check out the facility instrumentation for each experiment. It does not have a unique number, but is filed in the Configuration Document Control (CDC) generic file for the particular experiment.

Transducer Report

Information on the transducers used in the particular experiment is contained in the transducer report. These reports list the transducers by serial number and by the measurement identifier. They also contain the basic equations necessary to translate transducer output voltage (current) into engineering units. These equations are based on calibration data if available. A brief description of the transducers is given and calibration techniques are discussed. These reports are contained in the Engineering Design File (discussed in a subsequent section) and have a unique number.

Experiment Operating Procedure (EOP)

This document describes in detail how the experiment will be operated from the PBF control room. It includes instrument check lists to ensure proper operation at specific points in the experiment. This document, prepared by PBF Operations Division, is assigned a unique number by the CDC, and the original is retained in the CDC files.

Experiment Specification Document (ESD)

This document is prepared by the Experiment Specification and Analysis group and it describes, in specific terms, the purpose of the experiment and, in general terms, the instrumentation required. These documents are interim reports and are available as described previously.

Experiment Configuration Specification (ECS)

This document is prepared by the Test Train Assembly and instrumentation organization and describes in specific terms how the test train will be constructed and instrumented. It is from this report that the experiment apparatus is designed and the Site Work Releases (described in a subsequent section) are prepared. This is an interim report.

Experiment Operating Specification (EOS)

This is an informal report prepared by the Experiment Specification and Analysis group. The purpose of this document is to explain, in general, how the experiment will be performed, what data are to be recorded, and where measurements are to be made. In most cases, there is detail of the instrument locations, desired operating ranges, necessary response times, and measurement accuracy. This document also establishes the official identifiers that will accompany each measurement.

Experiment Predictions Document (EP)

This is an interim document which explains the objectives of the experiment as well as giving a general description of the test conduct, measurements to be made, and instruments to be used. The results of the test prediction calculations are presented, along with references to computer codes and input conditions.

Engineering Design File (EDF)

This is an informal file system operated by the Thermal Fuels Behavior Program (TFBP). The purpose of this file is to record engineering work, done in support of the Power Burst Facility or experiments, which requires more formal recording. The originals of all material are filed near the TFBP management offices. Copies of these files are kept at the PBF in the CDC files.

Blue Book

This is an informal file system used by the Test Train Assembly organization to record the design, instrumentation, fabrication, and checkout of the test train. The file consists of a number of looseleaf binders, each titled according to subject. Each specific test has a Blue Book; however, no unique number is assigned. The Blue Book can be retrieved by using

the generic test title. Blue Books are on file at CDC, in the test train assembly area, and with the test train and experiment project engineers. Following is a list of the Blue Book contents:

1. Experiment Configuration Specification

2. Design Process Records (design documentation package provided by the cognizant design engineer with a cover letter describing section contents)

3. Assembly Site Work Releases (SWR)

4. Indentured Parts List

5. Fuel Train Assembly Procedures (applicable Assembly Disassembly Procedures (ADPs) and hot cell Detailed Operating Procedures (DOPs) are listed by the cognizant assembly engineer)

6. Test Train Assembly Procedures (applicable ADPs are listed by the cognizant assembly engineer)

7. Test Train Disassembly Procedures (applicable ADPs are listed by the cognizant assembly engineer)

8. Quality Discrepancy Reports

9. Instrument Schedule.

Site Work Release (SWR)

The SWR is a document that can contain other documents, records, drawings, etc. It has a unique number issued by Configuration Document Control. A Site Work Release is issued to cover specific areas of work. These documents are on file at CDC.

Configuration Document Control (CDC)

The CDC is physically located at the Power Burst Facility. This is a formal control system that is used to file the SWRs, drawings, plant operation manuals, PBF facility Technical Specifications, PBF System Design Documents, Experiment Operating Procedures, Detailed Operation Procedures, Engineering Design Files, and Document Revision Records. Many of these documents are filed by a unique number, but there are also generic files by test that contain items such as the Data Acquisition Documents and the Blue Books.

Drawing File

All drawings used in the construction and instrumentation of TF8P test trains have a unique drawing number. The originals are filed in the EG&G Idaho drawing vault. Copies of particular test drawings are usually filed at the Configuration Document Control station at the Power Burst Facility.

Data Tapes

All raw test data generated at the PBF are recorded on tape by the Data Acquisition and Reduction System (DARS) in pulse code modulated (PCM) form. These PCM tapes are kept at the PBF until after the Fuel Behavior Report is published. They are then sent to the EG&G Idaho central file where they are retained for about one year. They are then sent to the Federal Tape Storage Center in Seattle, Washington, where they are retained indefinitely. These tapes can be retrieved at any time. Records of tapes and methods of retrieval are kept at the PBF. These tapes can only be used in conjunction with the DARS.

Data tapes are also stored at the INEL Computer Science Center in qualified (corrected) form. SEARCH 1.0 is the Common Word Addressable File (CWAF) directory and retrieval program residing in the Idaho National

Engineering Laboratory Scientific Data Management System (ISDMS). It is designed to maintain a resident directory and to "backup" and "restore" files cataloged under specified user identifications.

The code is currently implemented on a CDC CYBER 173 and CYBER 176, running under the NOS/BE operating system at the INEL.

Data Processing History File

This is an informal file kept by the Data Processing Organization. Records are kept on the location of data tapes that have been processed. Microfiche of all processed data in graphical form, as well as all changes made to the data, are recorded here. Both raw and finished data fiche are stored.

Computer Code Configuration Control (CCCC)

This is a formal control system operated by the INEL Computer Science Center. This system is designed for historical storage and retrieval of tapes or cards. Each stored item is given a unique number and is stored either to a specified date or indefinitely.

User-Supplied Data Configuration Control Log (USDCC)

This log is maintained in the TFBP office area and is designed to ensure traceability and reproducibility of computer aided analyses and Cyber data processing performed for the TFBP. The USDCC lists references to computer codes in the CCCC, tapes in the INEL Tape Library, and support documents. Each major document has a specific list. The USDCC listing for this document is under the heading "PR-1 Test Results Report."

Photographs

The photographs presented in TFBP documents are retrievable from either of two separate sources. Photographs identified by a letter followed by a

number (e.g., A234), or the year followed by a letter and number (e.g., 79B-332), are on file at the Test Reactor Area hot cell organization. Photographs identified by the year followed by only a number (e.g., 79-4567) are on file with the EG&G Idaho Photography section.

TEST PR-1 EXPERIMENT MATERIALS IDENTIFICATON

This section lists the specific Test PR-1 documentation. It should be noted that the PR-1 experiment was originally the Gap Conductance 2-4 experiment; therefore, some of the earlier documentation is labeled GAPCON 2-4. References to this will be found throughout the record material. Major documents can be used in turn to locate lower levels of documentation. The following major documents are for Test PR-1:

1. Experiment Operating Specification--EGG-TFBP-5027, October 1979

2. Site Work Release--PR-1 SWR 71125X

3. Transducer Report--EDF 1516 "PR-1 Test Train and Fuel and Transducer Description and Performance"

4. Transducer Report--EDF 1515 "PR-1 Flow Loop and Plant Instrumentation Description and Performance"

5. Experiment Predictions--EGG-TFBP-5056, January 1980

6. Transmittal of PR-1 Qualified Data--EG&G letter SMA-1-80.

DOCUMENT AND FILE AVAILABILITY

Some documents, materials, tapes, records, etc., maintained by a Department of Energy (DOE) contractor such as EG&G Idaho, Inc., are not generally available without either EG&G Idaho or Nuclear Regulatory Commission (NRC)/DOE approval.

Data Tapes

Tapes of the raw DARS PCM data can be obtained through the PBF Operations organization. Listings and locations of the data tapes are maintained. For this data to be usable it must be processed by the DARS.

Tapes of qualified data in the INEL CYBER format can be obtained from the INEL Tape Library and/or from the NRC Data Bank. The NRC/Reactor Safety Research Data Bank is accessible only with NRC approval. Contact can be made through the NRC Data Bank coordinator in Silver Spring, Maryland, or through the EG&G Idaho coordinator. Tapes can also be located by the INEL Scientific Data Management System and then obtained from the INEL Tape Library.

Interim or Informal Documents

Interim or informal documents are available from the National Technical Information Service, the Nuclear Regulatory Commission's Division of Technical Information and Document Control, and the INEL Technical Library, as well as from the Thermal Fuels Behavior Program.

Drawings

Formal drawings and blueprints used for any EG&G Idaho program can be obtained from the EG&G Idaho drawing vault, by specific number and with appropriate approval.

Access to Informal Files

Access to the various informal files at the INEL is possible only by traveling to the physical location. Generally, information is retrievable only when code numbers or nomenclature are known. Local knowledge of the file contents is probably necessary.

Calculations

The inputs to computer calculations made for predicting experimental conditions are contained in the experimental prediction document along with computer code configuration control numbers for the program(s) used. The inputs for posttest calculations are contained in an appendix to the final report (such as a test results report), along with the corresponding computer code configuration control numbers.

END

DATE FILMED

6-2-81

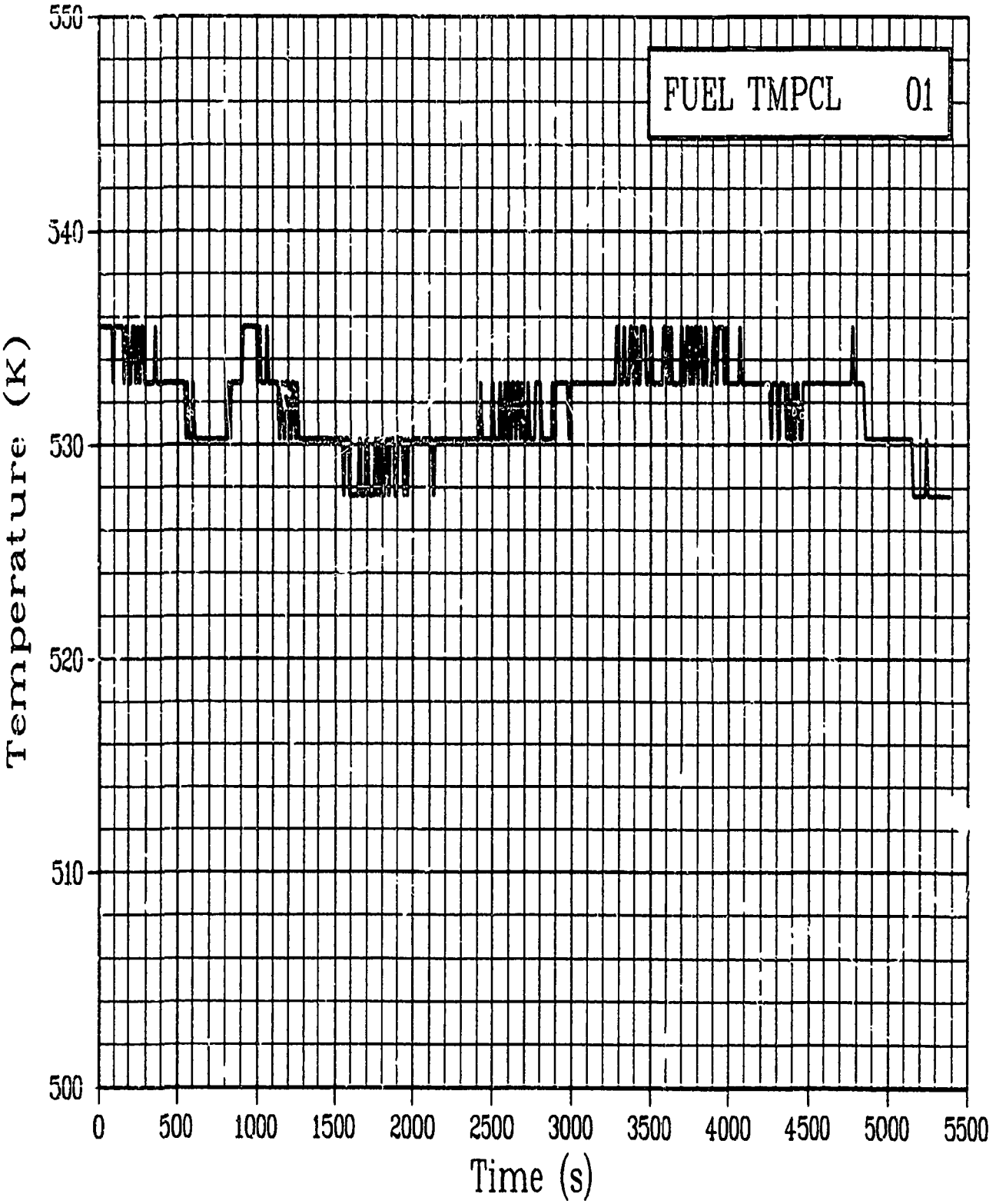

Figure C-1. Fuel centerline temperature Rod GC 524-1, 0.4521 m during Test PR-1 instrument checkout (calibration not shown) (FUEL TMPCL 01).

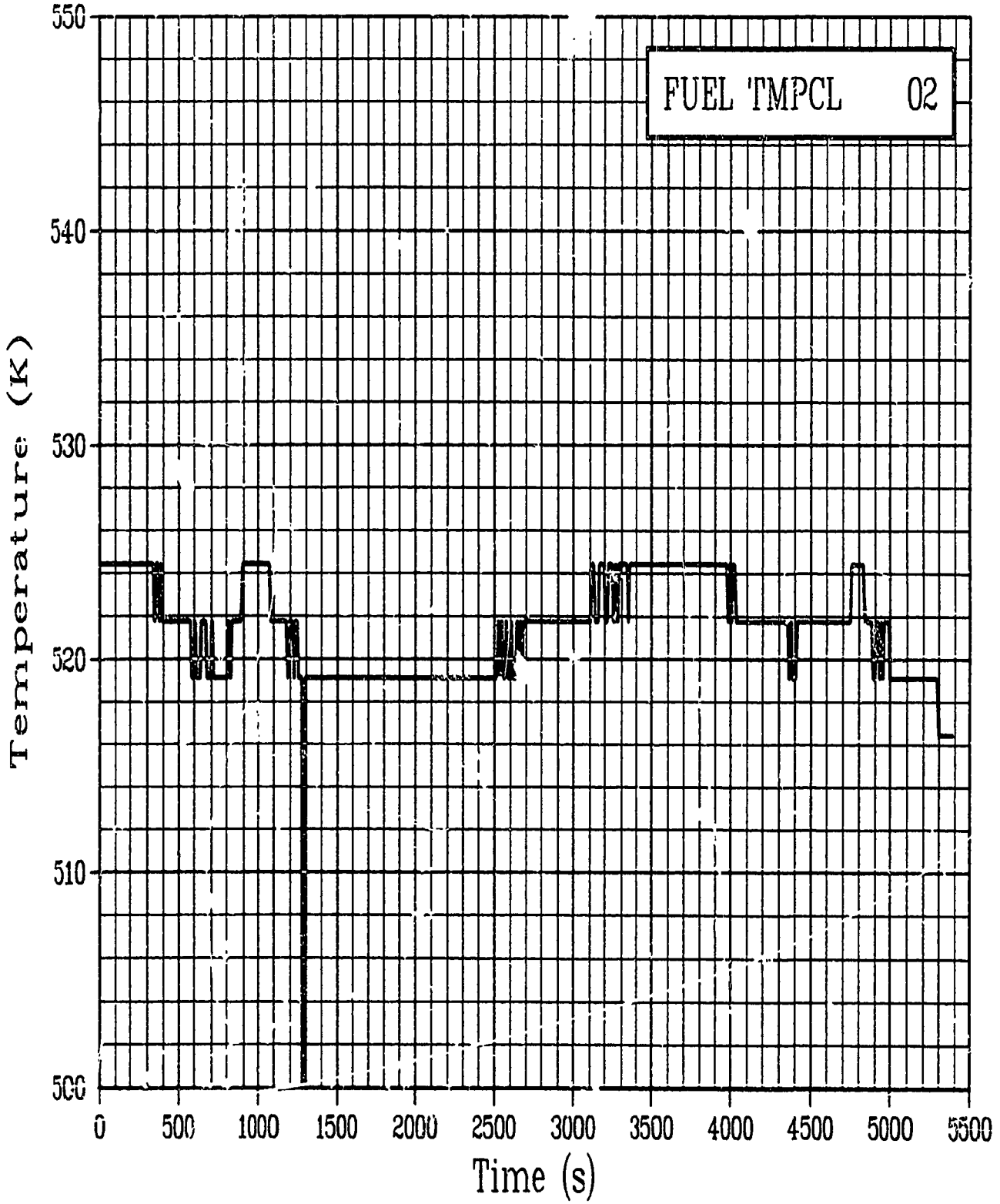

Figure C-2. Fuel centerline temperature Rod GC 524-2, 0.4521 m during Test PR-1 instrument checkout (calibration not shown) (FUEL TMPCL 02).

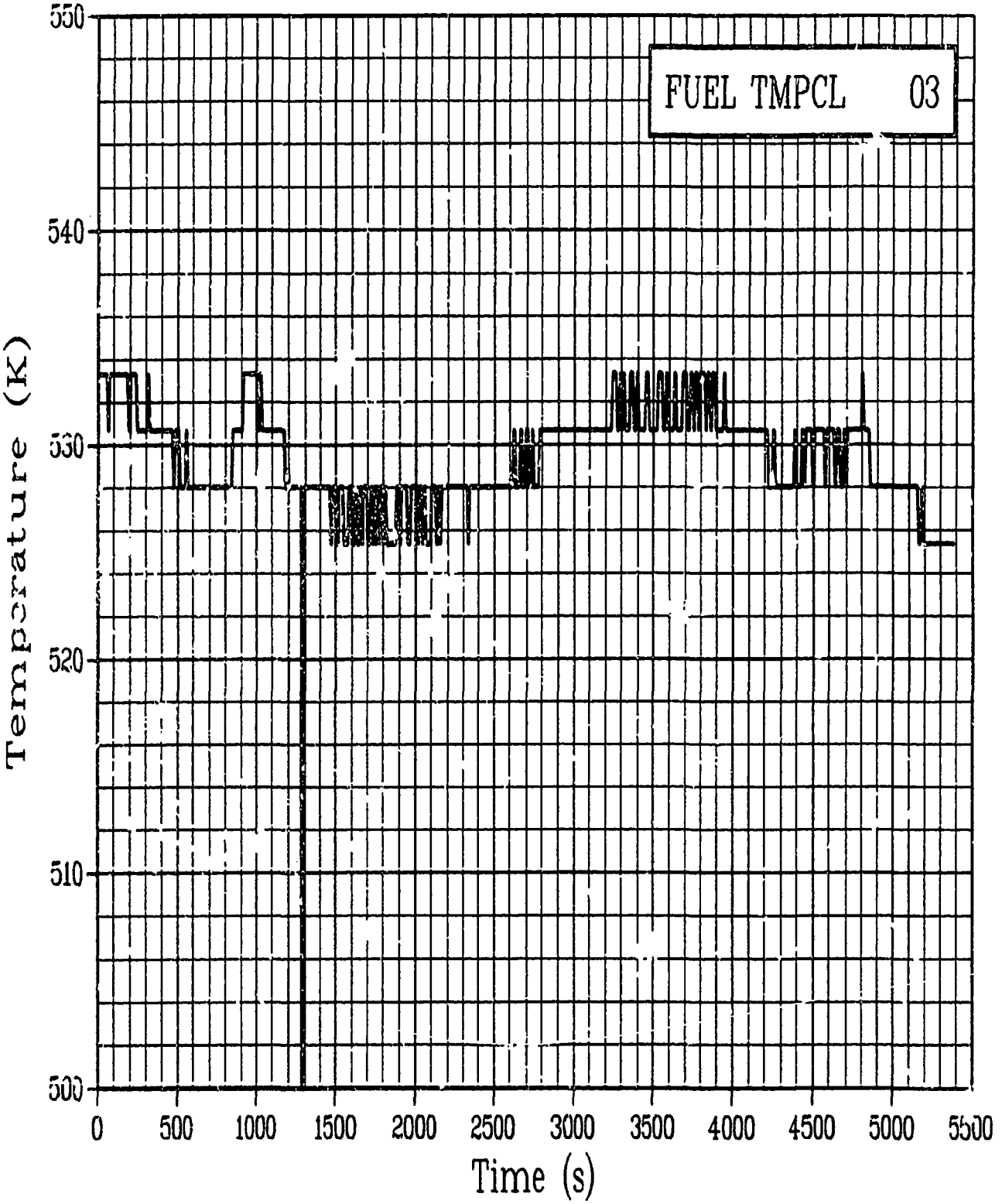

Figure C-3. Fuel centerline temperature Rod GC 524-3, 0.4521 m during Test PR-1 instrument checkout (calibration not shown) (FUEL TMPCL 03).

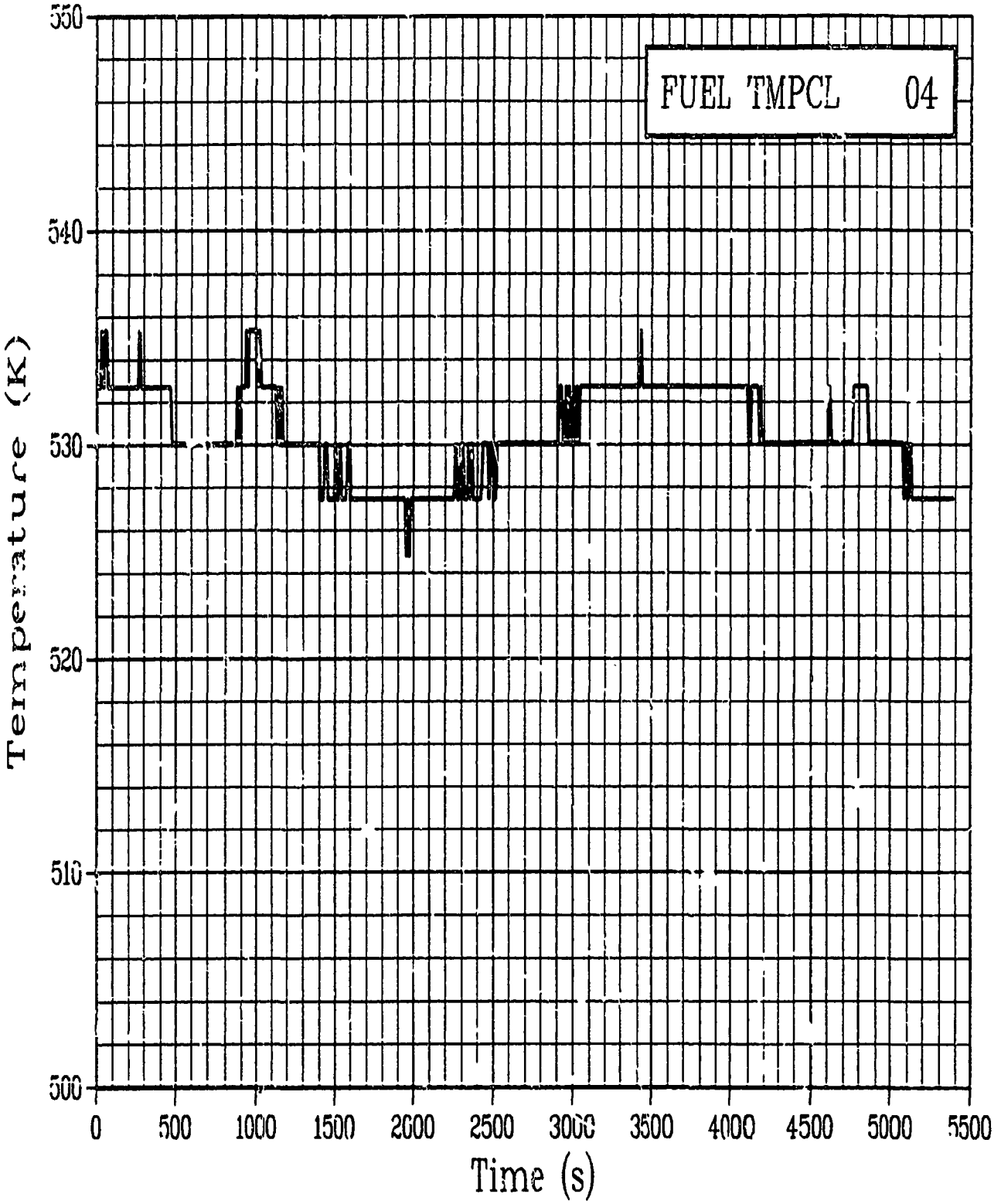

Figure C-4. Fuel centerline temperature Rod GC 524-4, 0.4521 m during Test PR-1 instrument checkout (calibration not shown) (FUEL TMPCL 04).

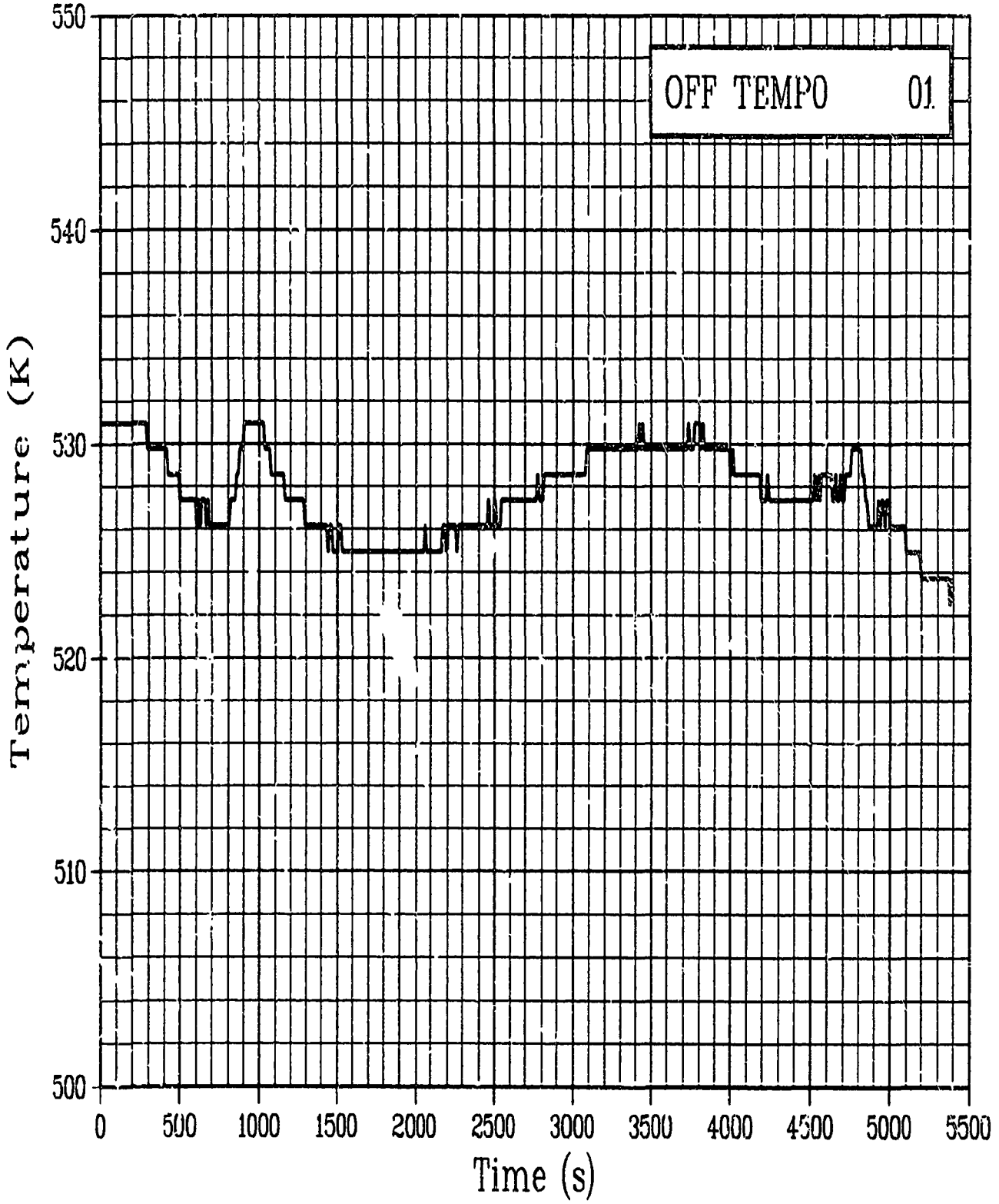

Figure C-5. Fuel off-center temperature Rod GC 524--1, at 0 degrees and 0.4521 m during Test PR-1 instrument checkout (calibration not shown) (OFF TEMPO 01).

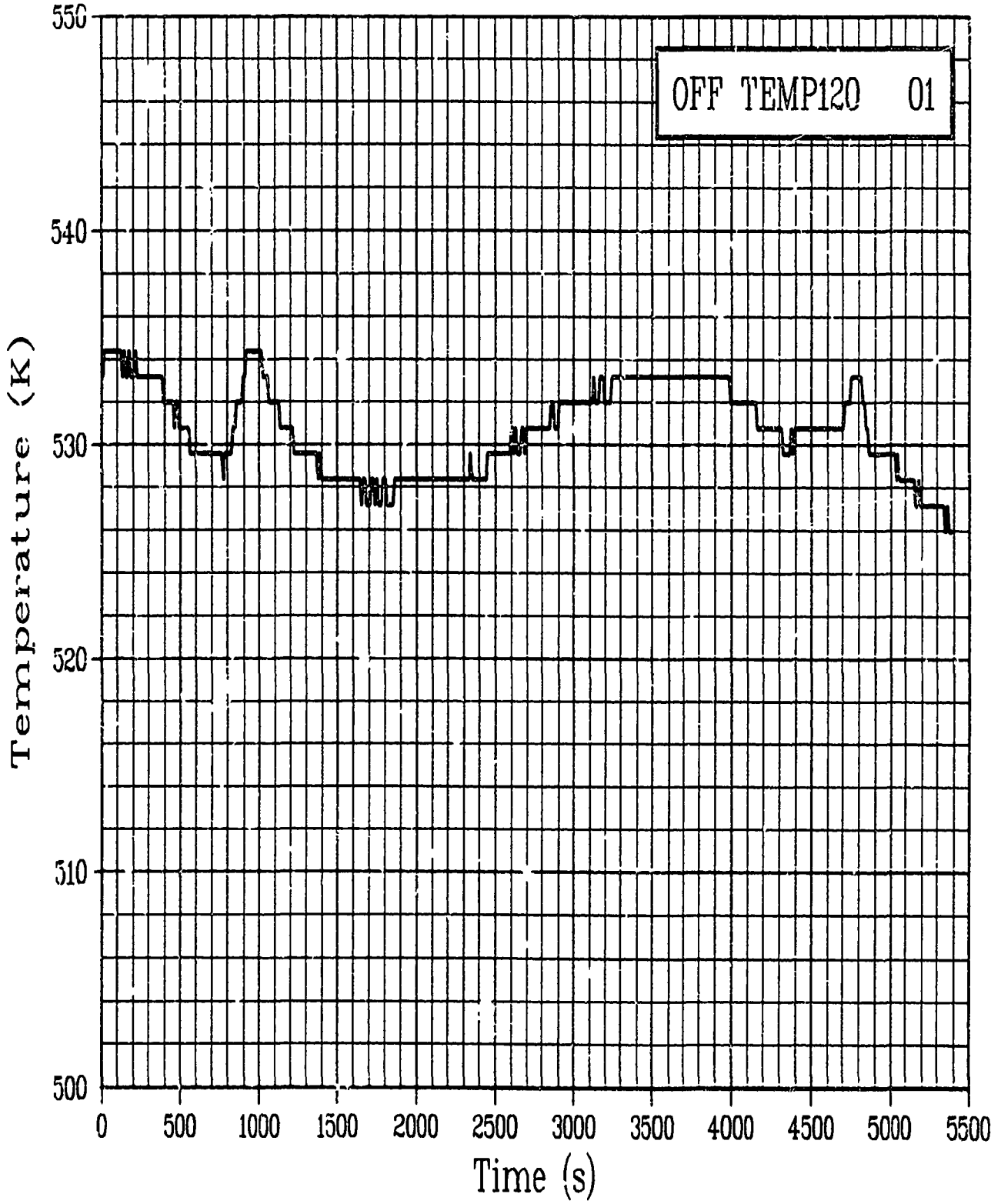

Figure C-6. Fuel off-center temperature Rod GC 524-1, at 120 degrees and 0.4521 m during Test PR-1 instrument checkout (calibration not shown) (OFF TEMP120 01).

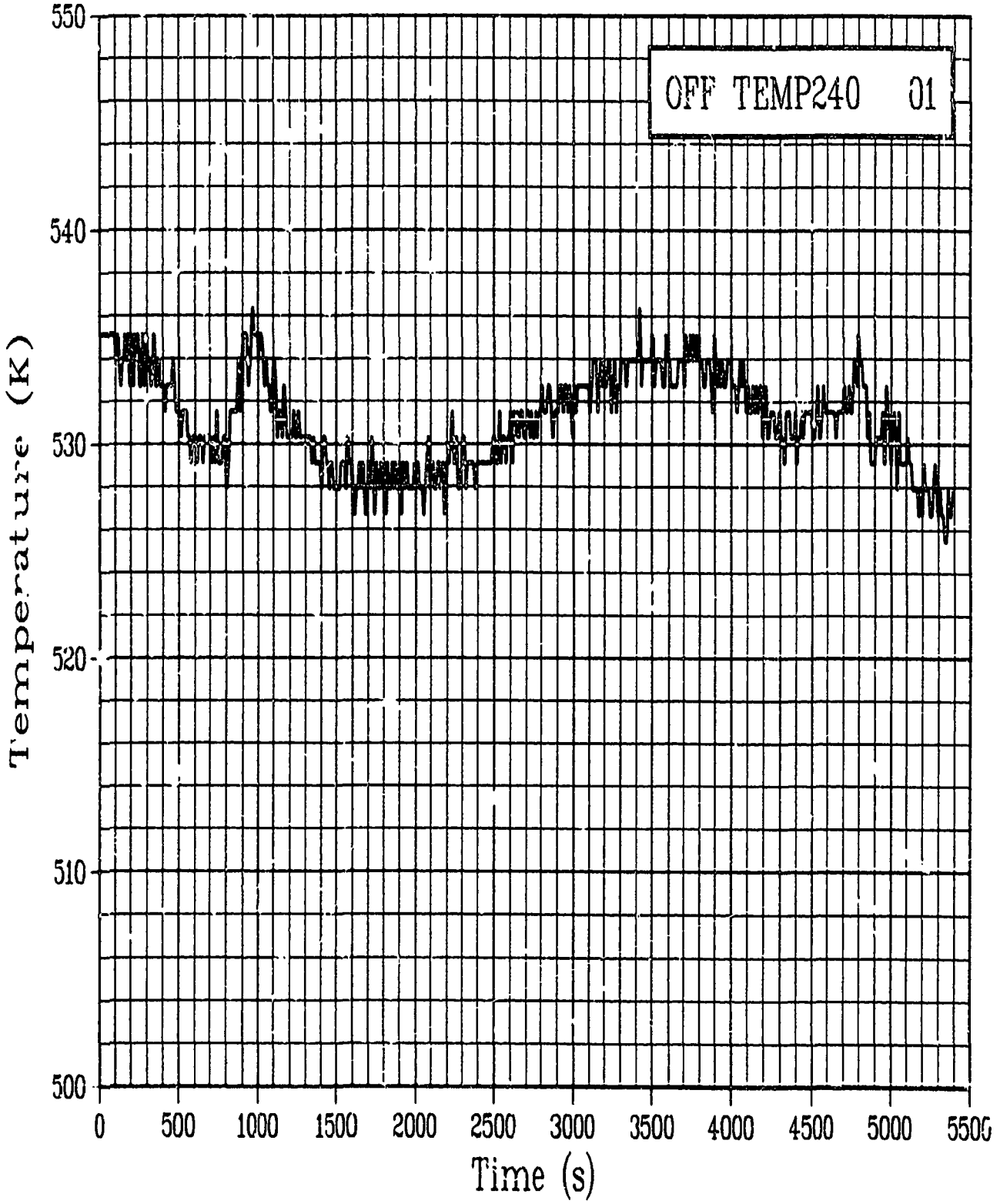

Figure C-7. Fuel off-center temperature Rod GC 524-1, at 240 degrees and 0.4521 m during Test PR-1 instrument checkout (calibration not shown) (OFF TEMP240 01).

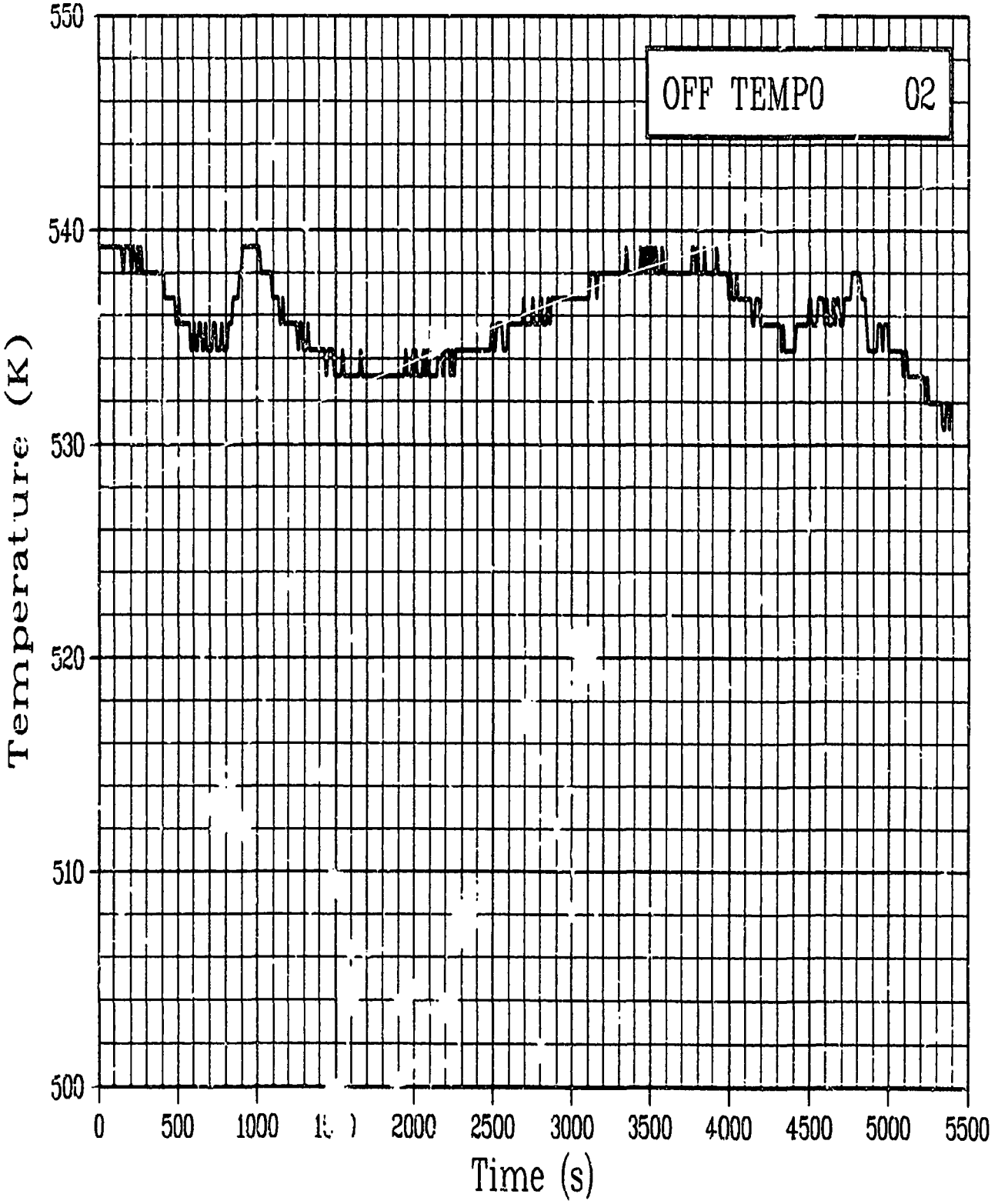

Figure C-8. Fuel off-center temperature Rod GC 524-2, at 0 degrees and 0.4521 m during Test PR-1 instrument checkout (calibration not shown) (OFF TEMPO 02).

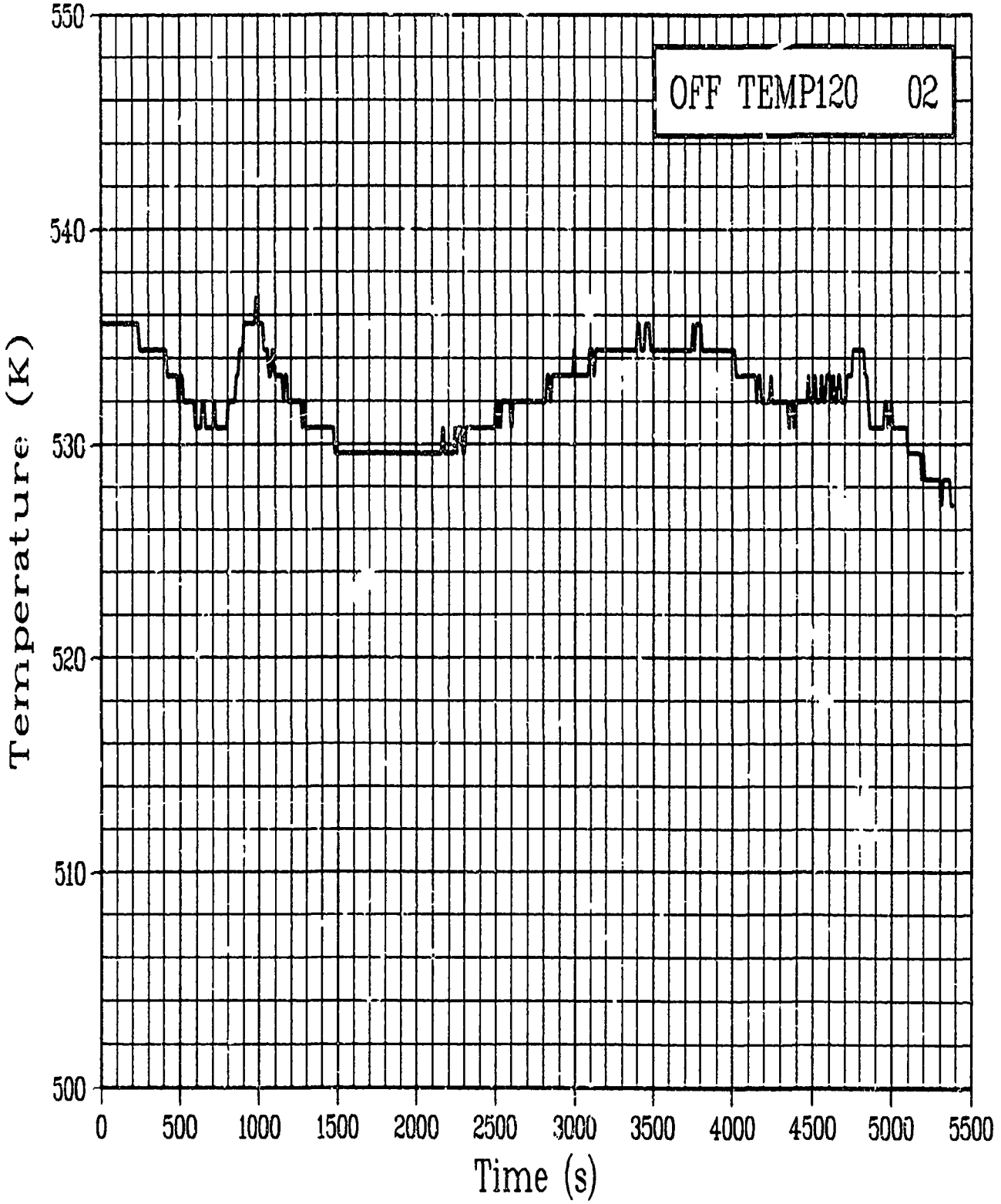

Figure C-9. Fuel off-center temperature Rod GC 524-2, at 120 degrees and 0.4521 m during Test PR-1 instrument checkout (calibration not shown) (OFF TEMP120 02).

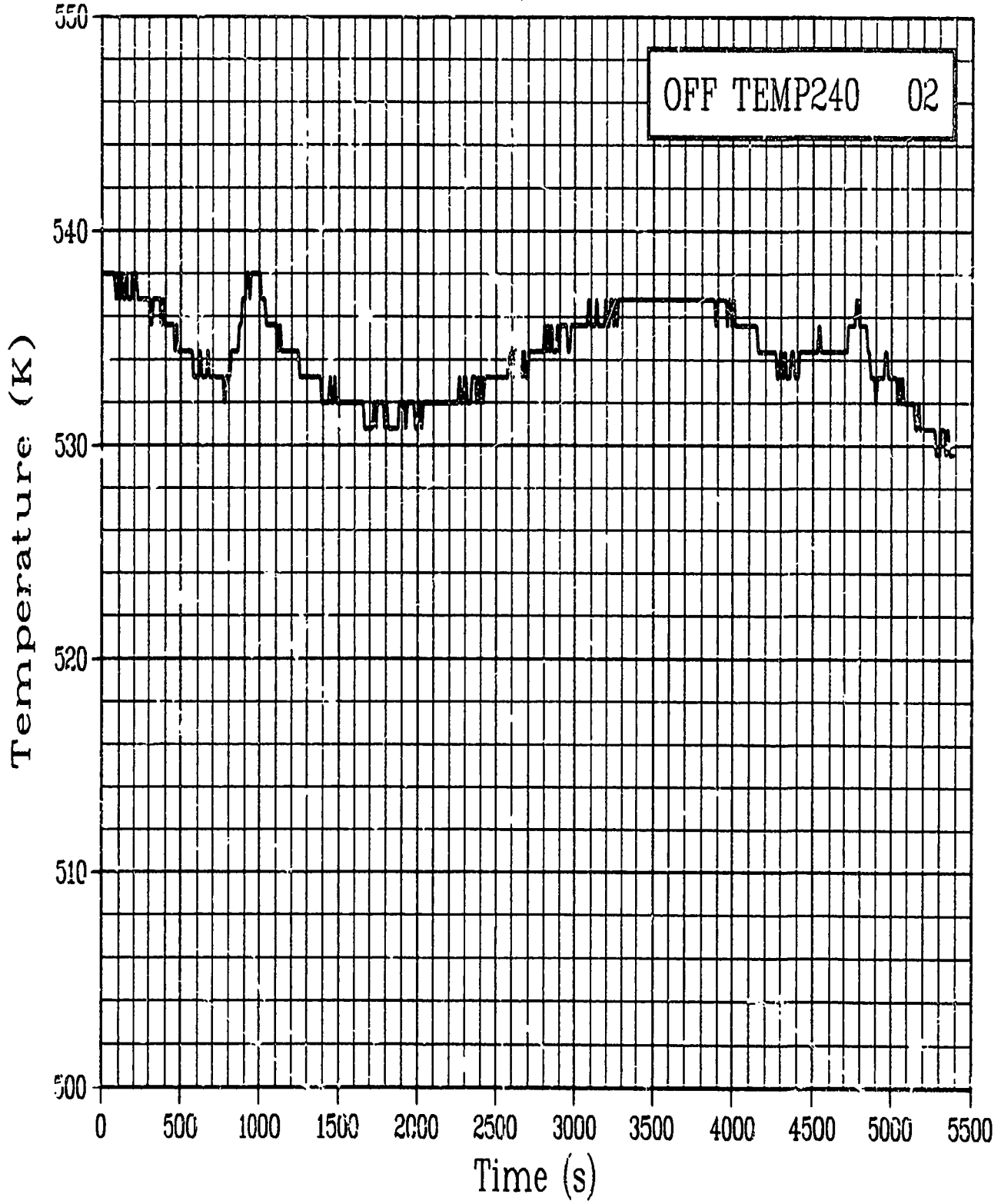

Figure C-10. Fuel off-center temperature Rod GC 524-2, at 240 degrees and 0.4521 m during Test PR-1 instrument checkout (calibration not shown) (OFF TEMP240 02).

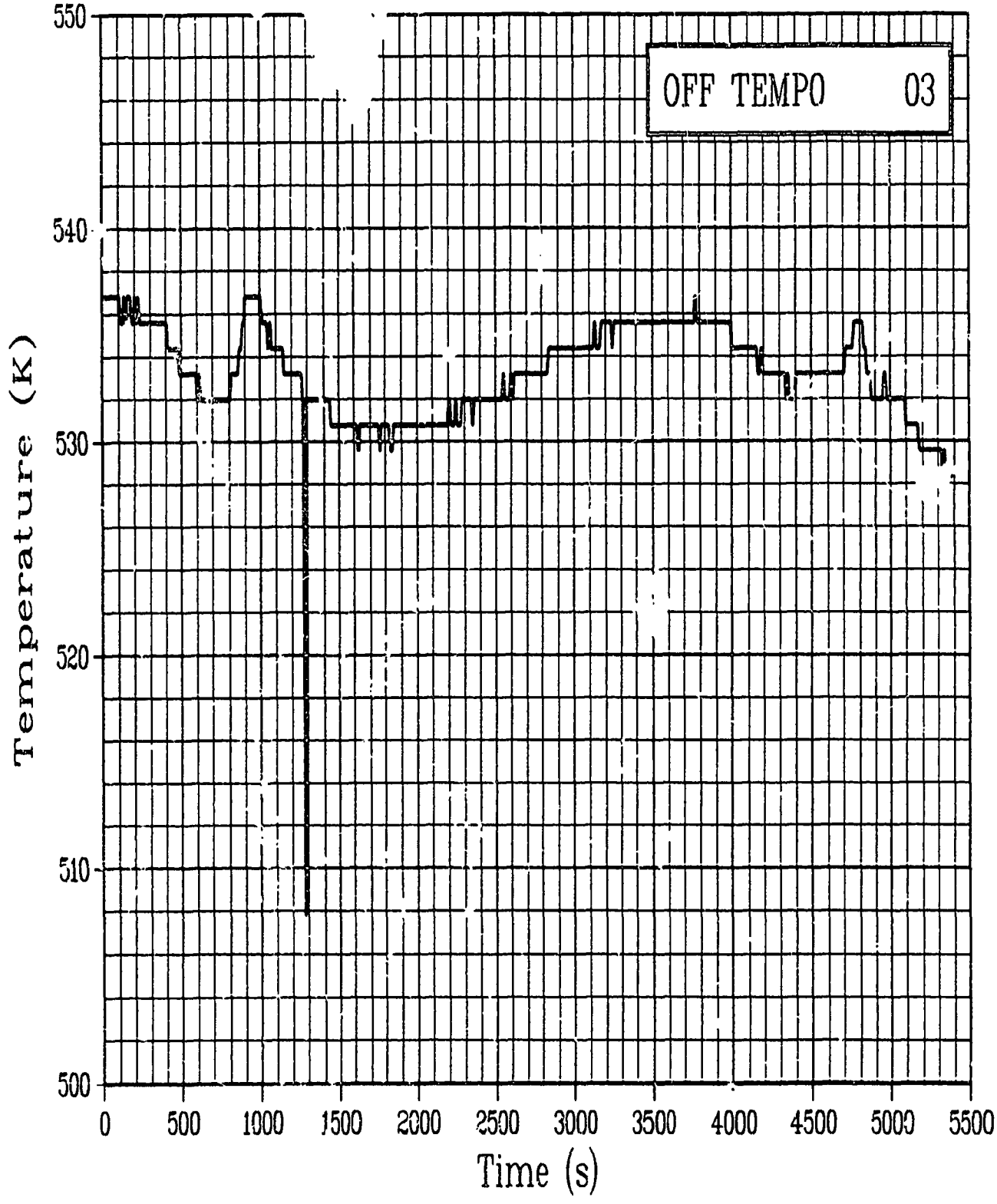

Figure C--11. Fuel off-center temperature Rod GC 524-3, at 0 degrees and 0.4521 m during Test PR-1 instrument checkout (calibration not shown) (OFF TEMPO 03).

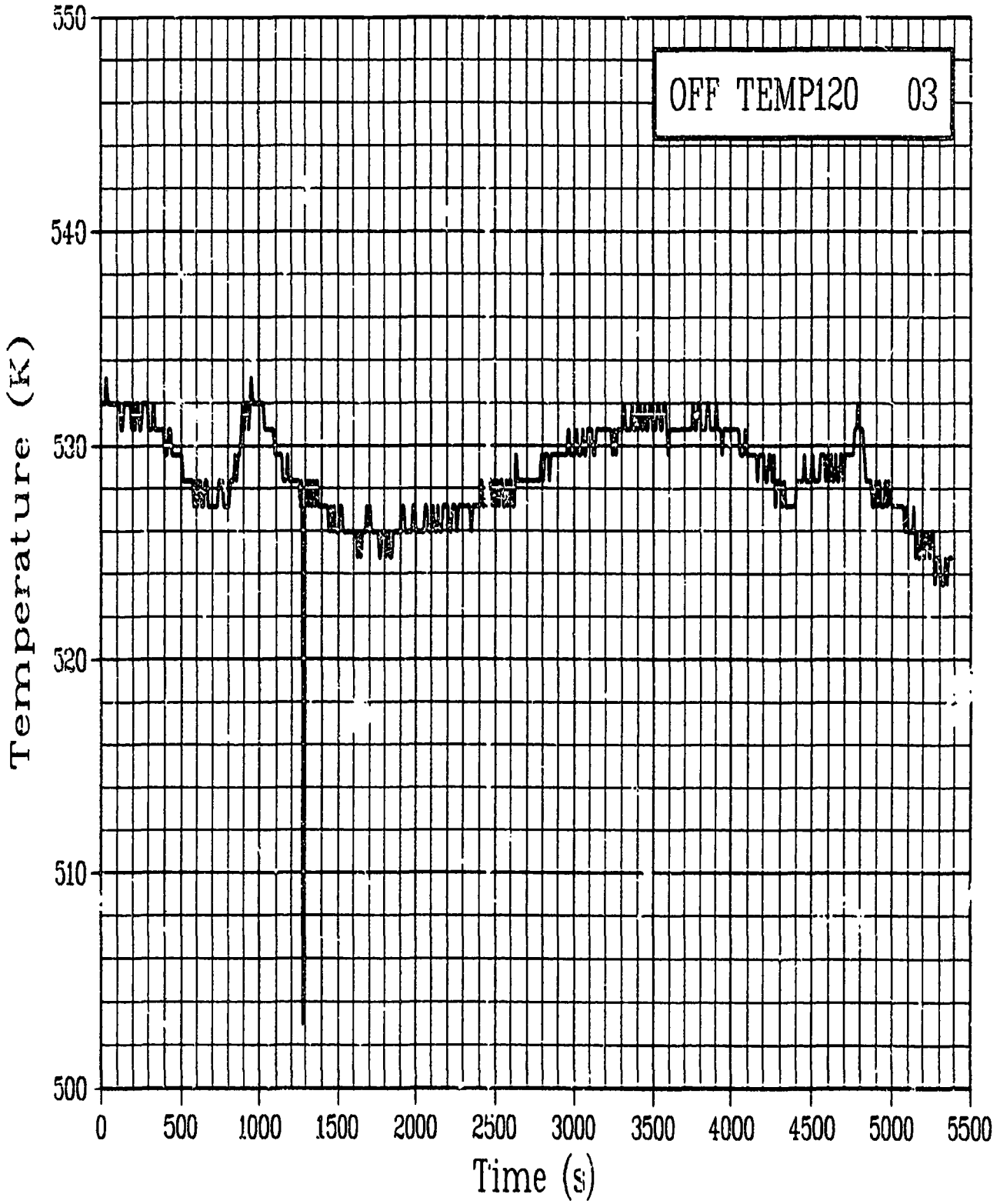

Figure C-12. Fuel off-center temperature Rod GC 524-3, at 120 degrees and 0.4521 m during Test PR-1 instrument checkout (calibration not shown) (OFF TEMP120 03).

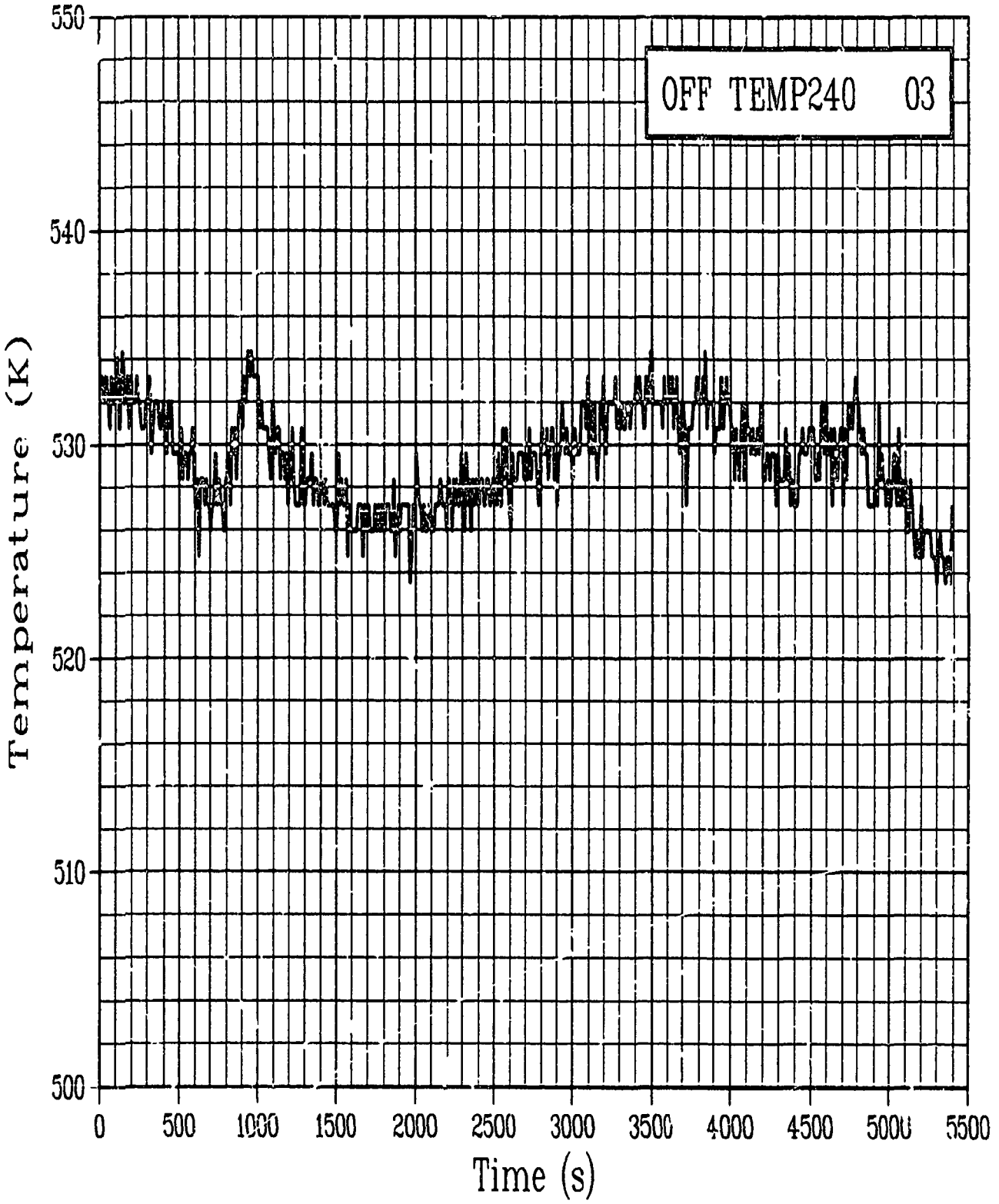

Figure C-13. Fuel off-center temperature Rod GC 524-3, at 240 degrees and 0.4521 m during Test PR-1 instrument checkout (calibration not shown) (OFF TEMP240 03).

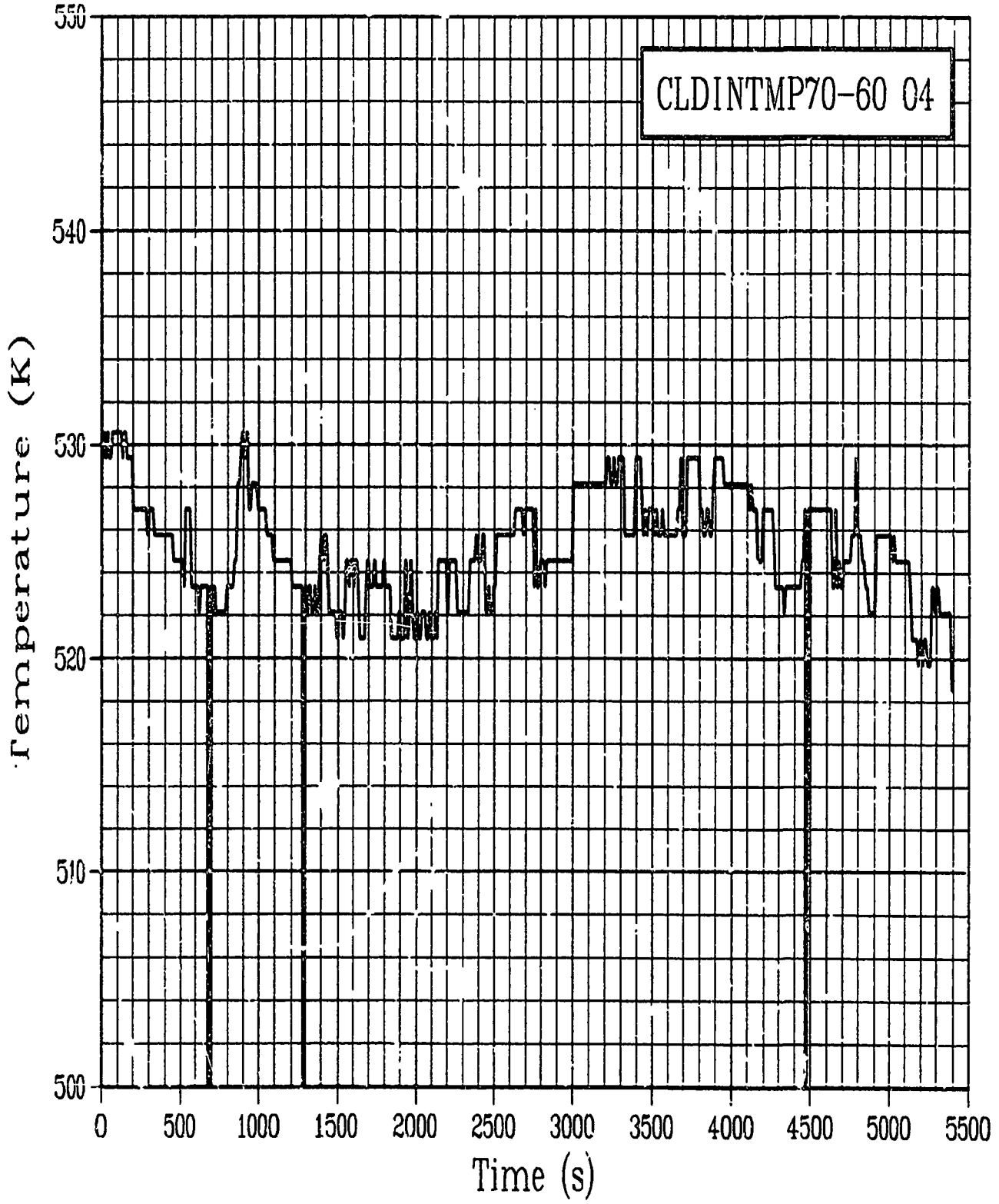

Figure C-14. Cladding internal temperature Rod GC 524-4, 0.70 m and 60 degrees during Test PR-1 instrument checkout (calibration not shown) (CLDINTMP70-60 04).

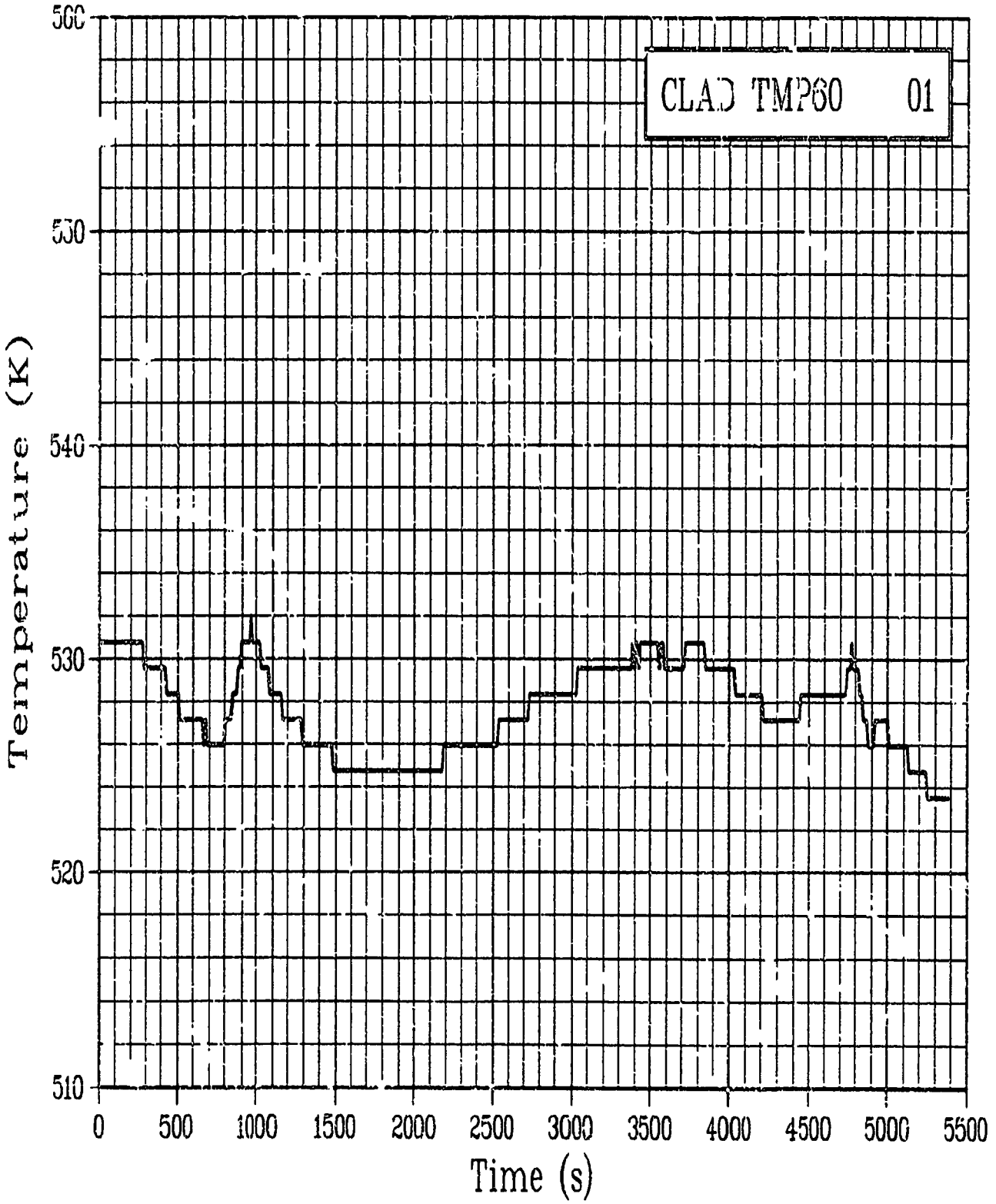

Figure C-15. Cladding surface temperature Rod GC 524-1, at 60 degrees and 0.4521 m during Test PR-1 instrument checkout (calibration not shown) (CLAD TMP60 01).

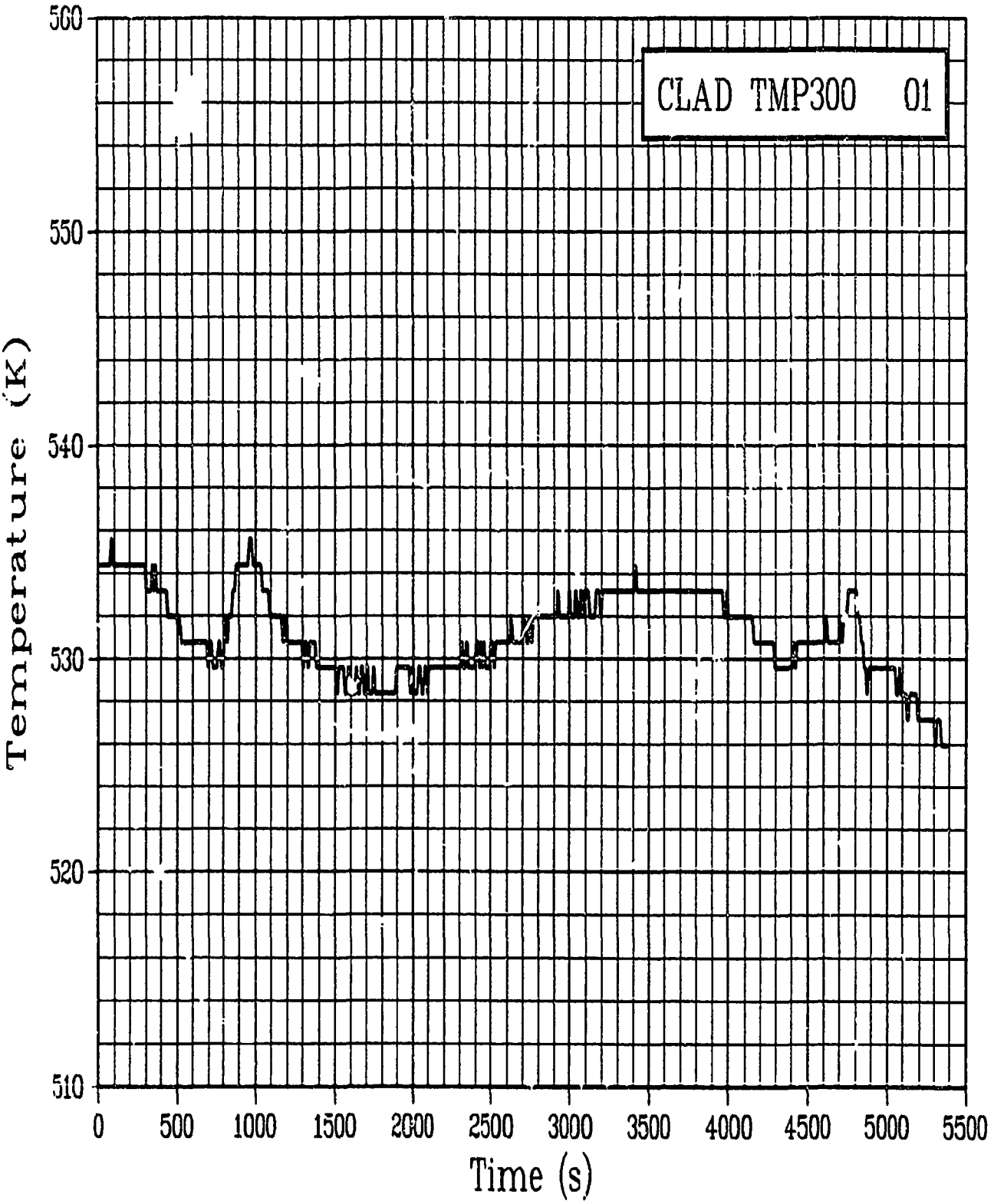

Figure C-16. Cladding surface temperature Rod GC 524-1, at 300 degrees and 0.4521 m during Test PR-1 instrument checkout (calibration not shown) (CLAD TMP300 01).

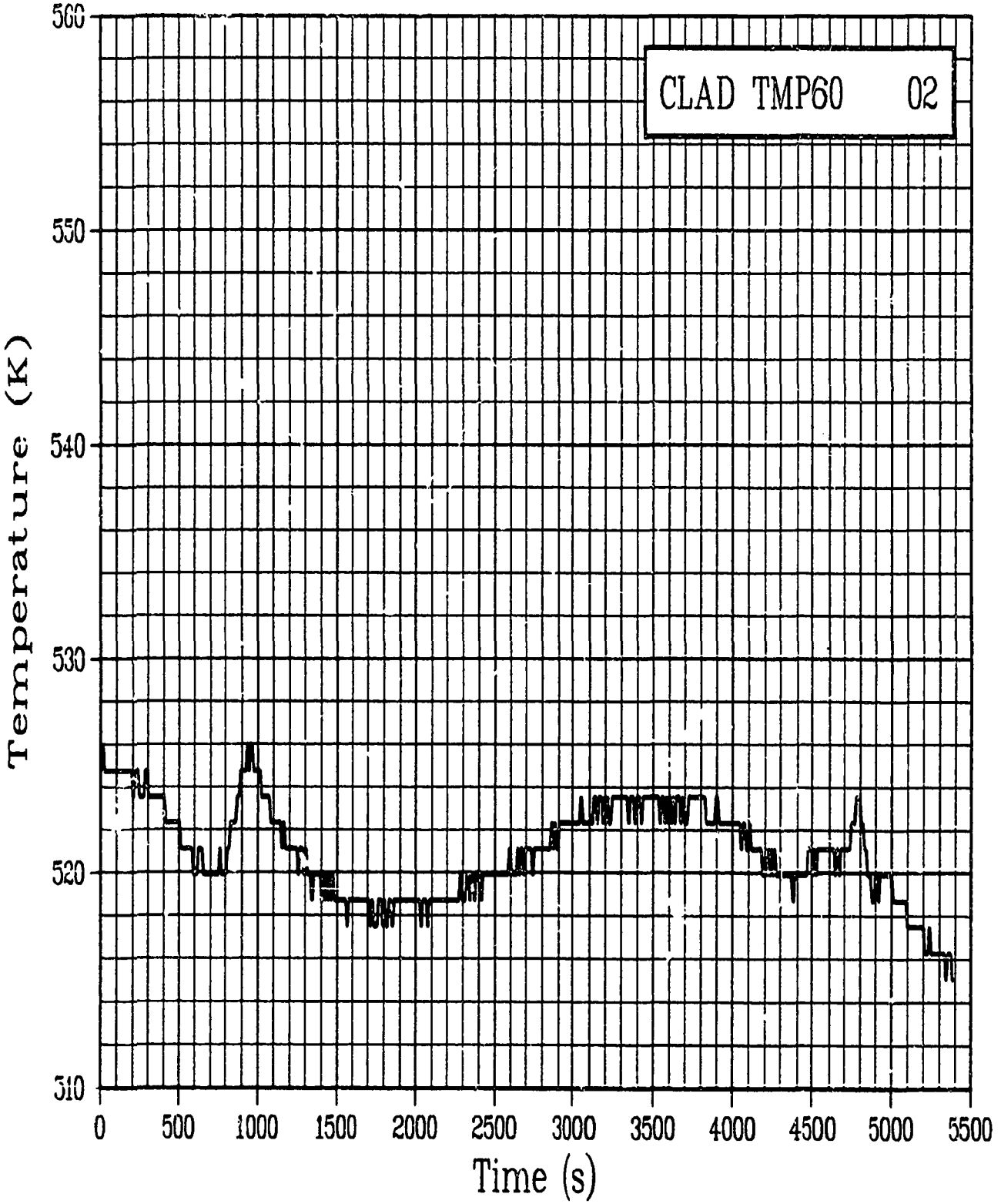

Figure C-17. Cladding surface temperature Rod GC 524-2, at 60 degrees and 0.4521 m during Test PR-1 instrument checkout (calibration not shown) (CLAD TMP60 02).

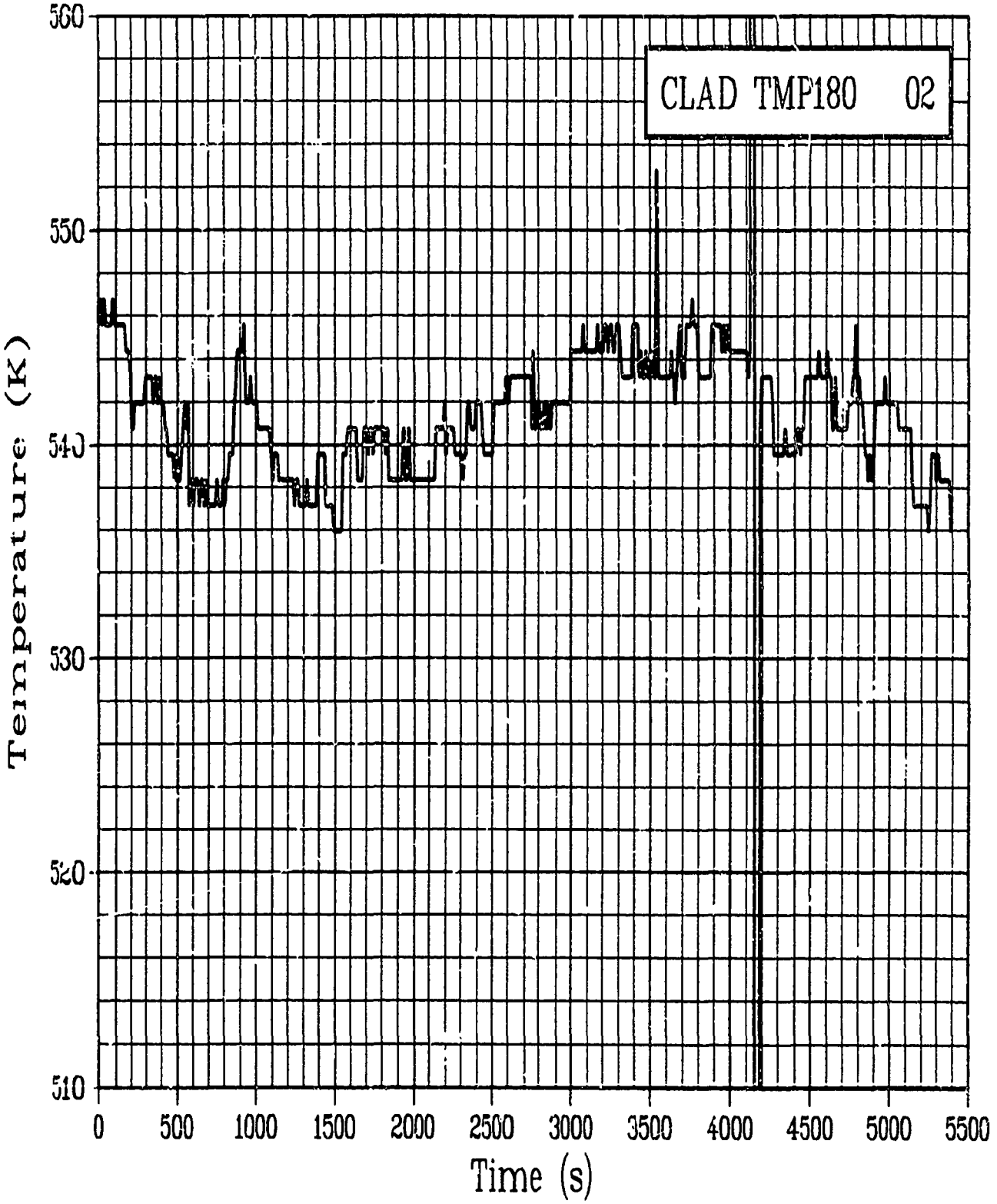

Figure C-18. Cladding surface temperature Rod GC 524-2, at 180 degrees and 0.4521 m during Test PR-1 instrument checkout (calibration not shown) (CLAD TMP180 02).

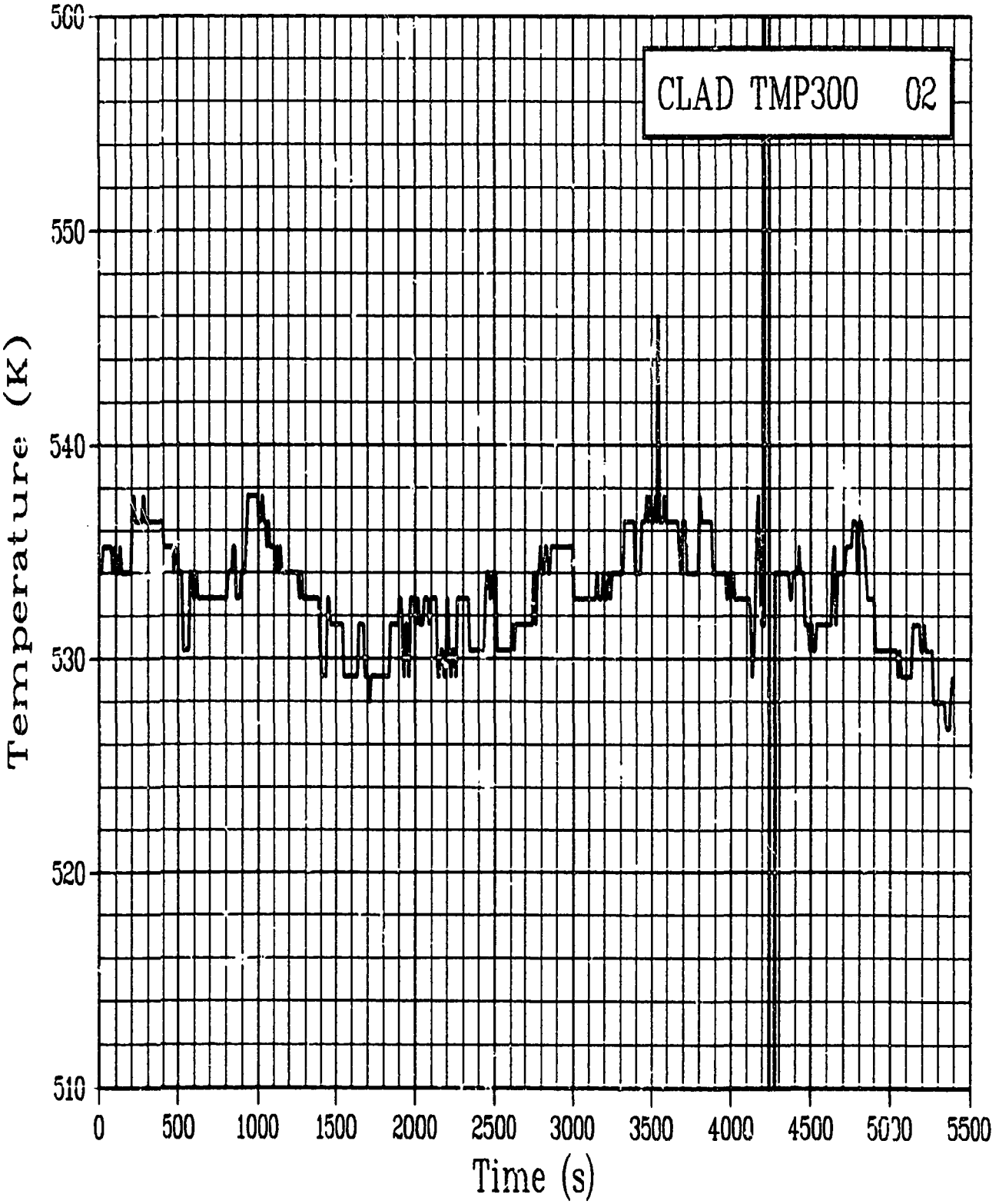

Figure C-19. Cladding surface temperature Rod GC 524-2, at 300 degrees and 0.4521 m during Test PR-1 instrument checkout (calibration not shown) (CLAD TMP300 02).

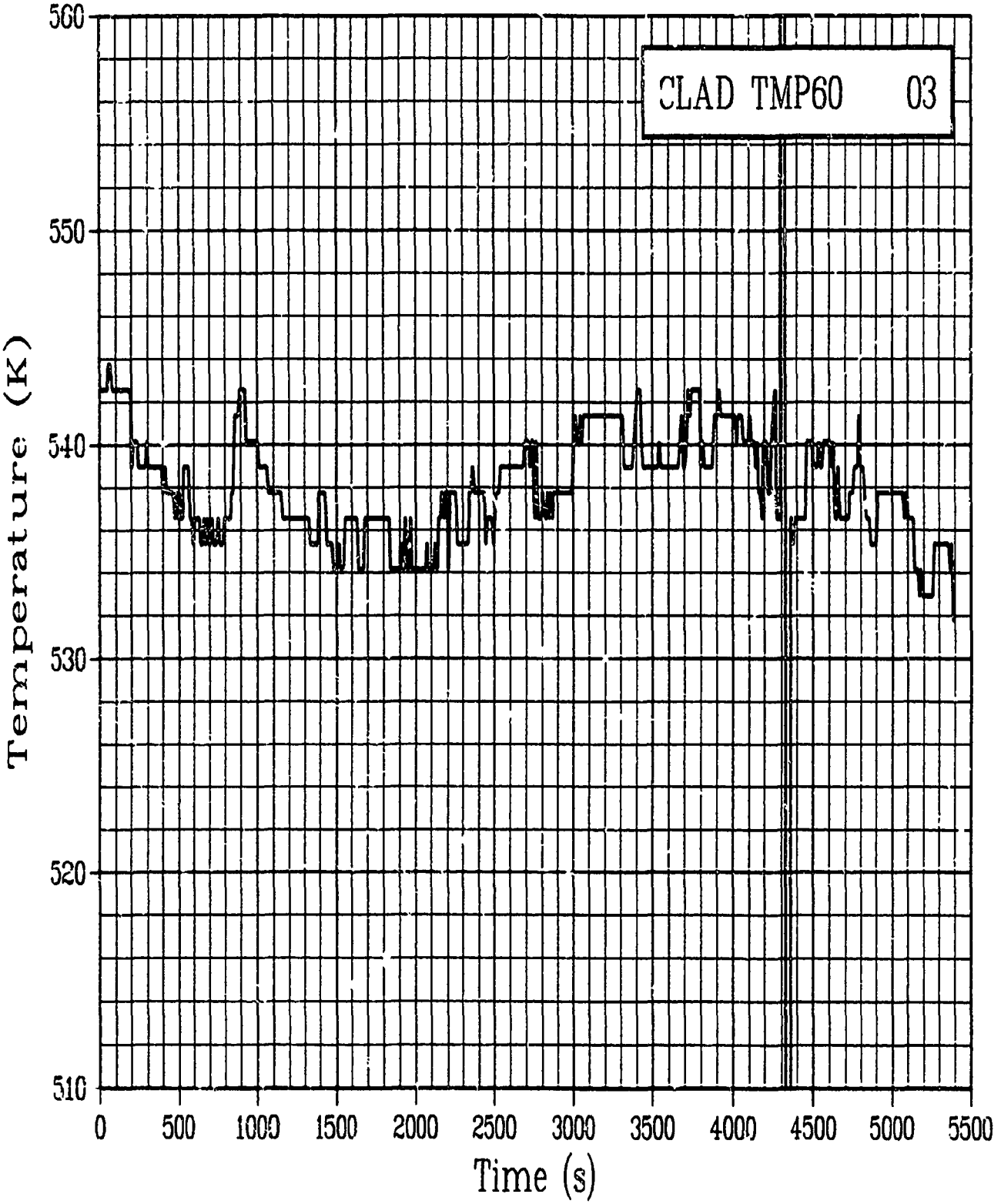

Figure C-20. Cladding surface temperature Rod GC 524-3, at 60 degrees and 0.4521 m during Test PR-1 instrument checkout (calibration not shown) (CLAD TMP60 03).

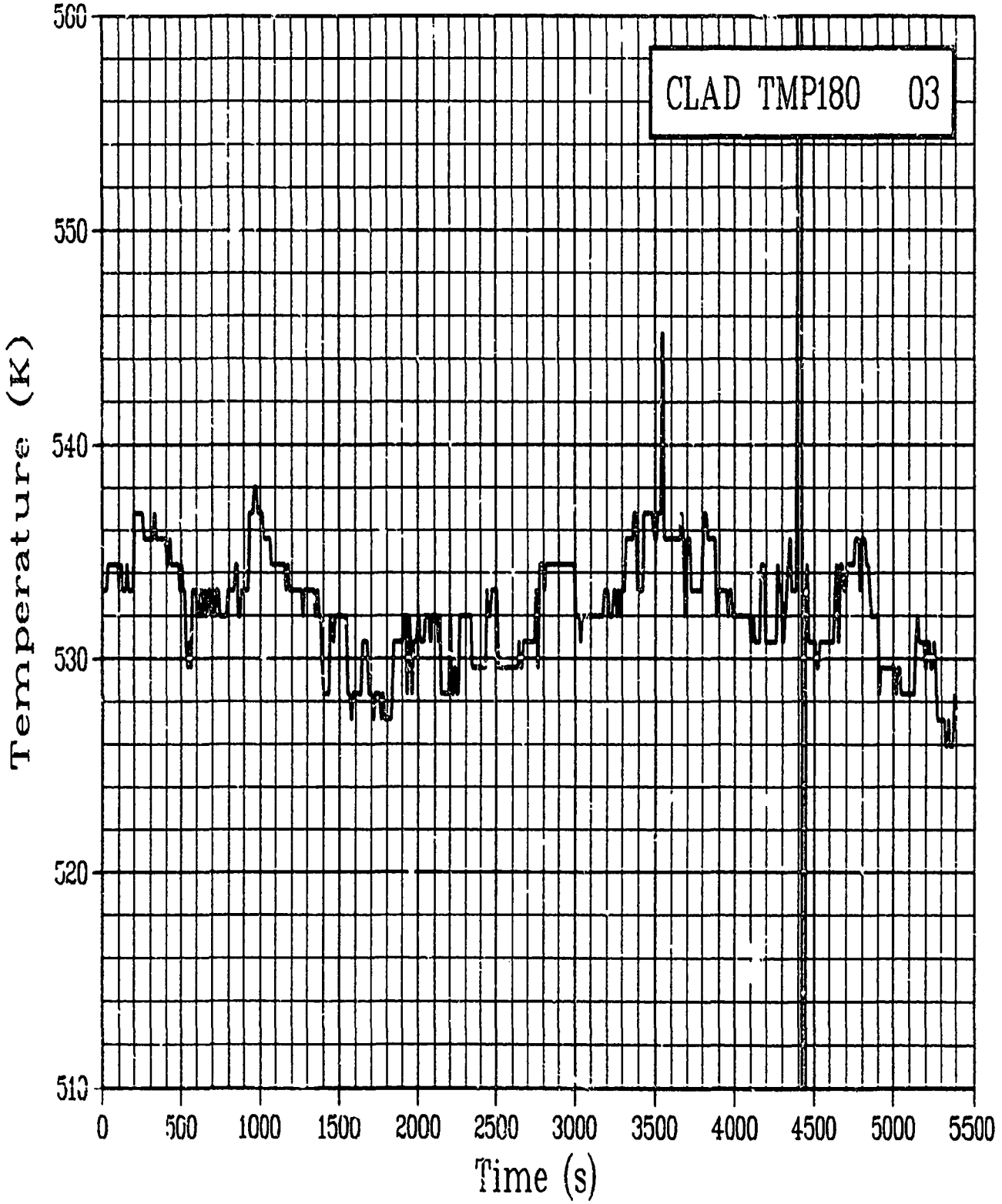

Figure C-21. Cladding surface temperature Rod GC 524-3, at 180 degrees and 0.4521 m during Test PR-1 instrument checkout (calibration not shown) (CLAD TMP180 03).

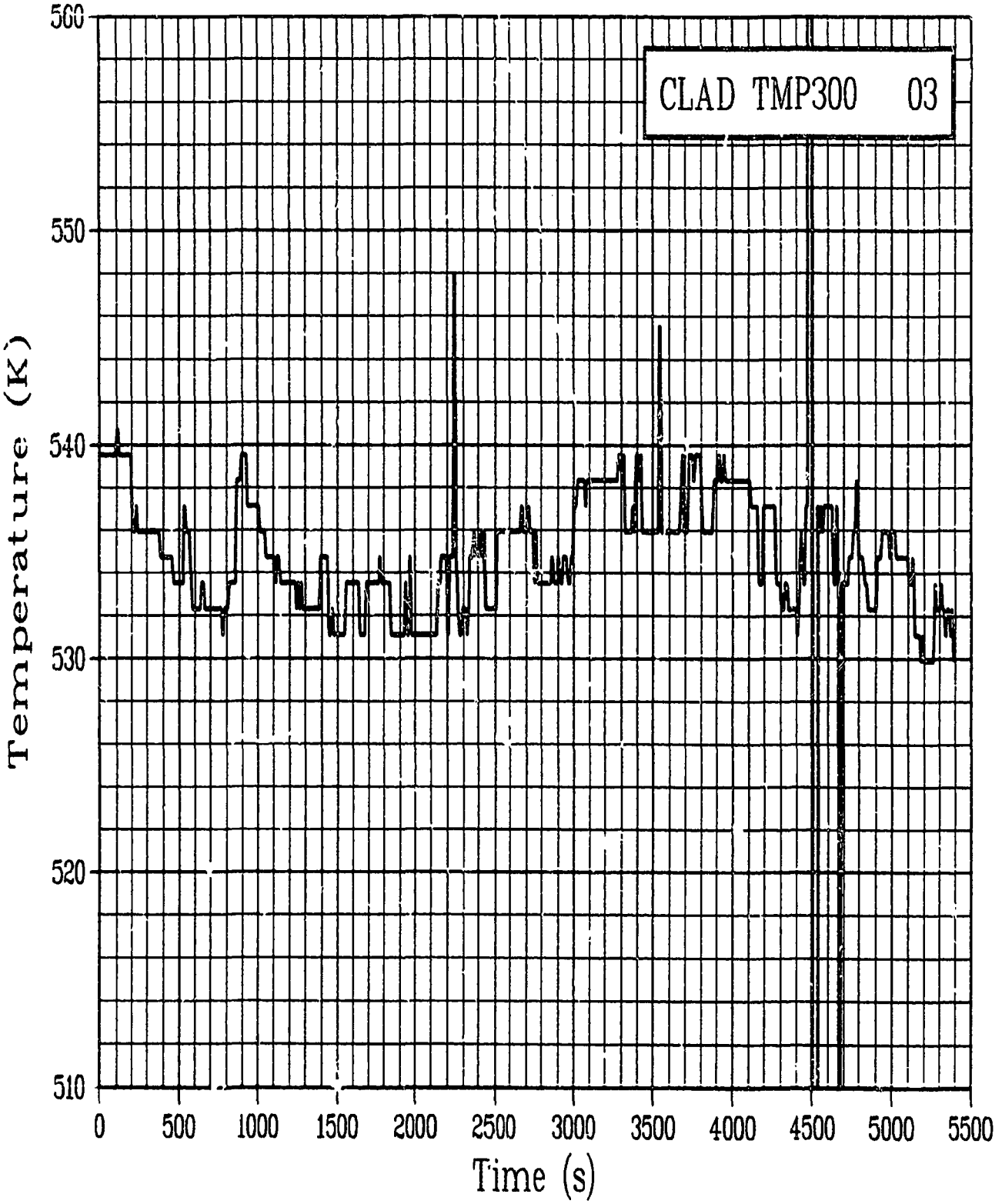

Figure C-22. Cladding surface temperature Rod GC 524-3, at 300 degrees and 0.4521 m during Test PR-1 instrument checkout (calibration not shown) (CLAD TMP300 03).

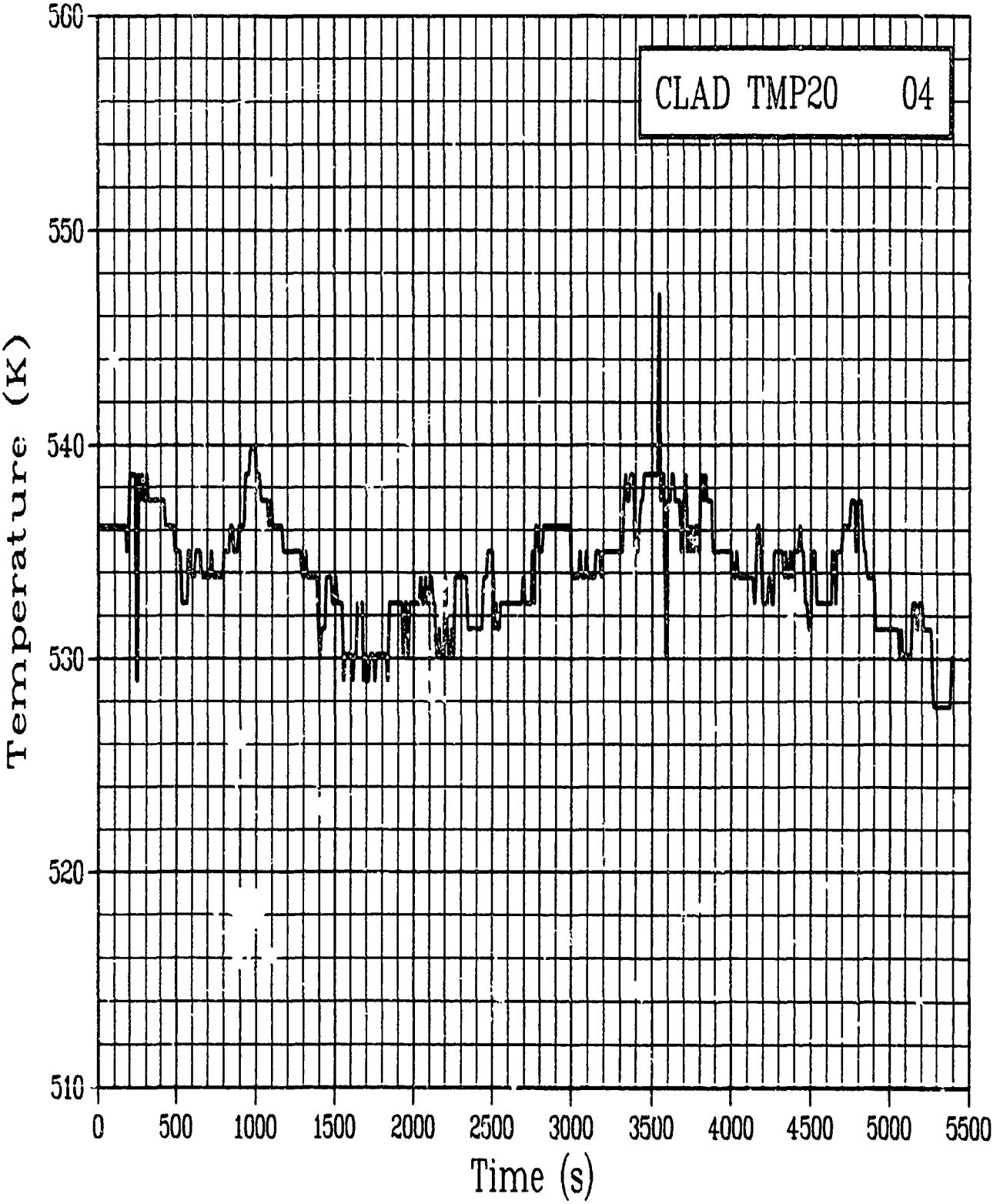

Figure C-23. Cladding surface temperature Rod GC 524-4, at 20 degrees and
n) 0.70 m during Test PR-1 instrument checkout (calibration not shown)
(CLAD TMP20 04).

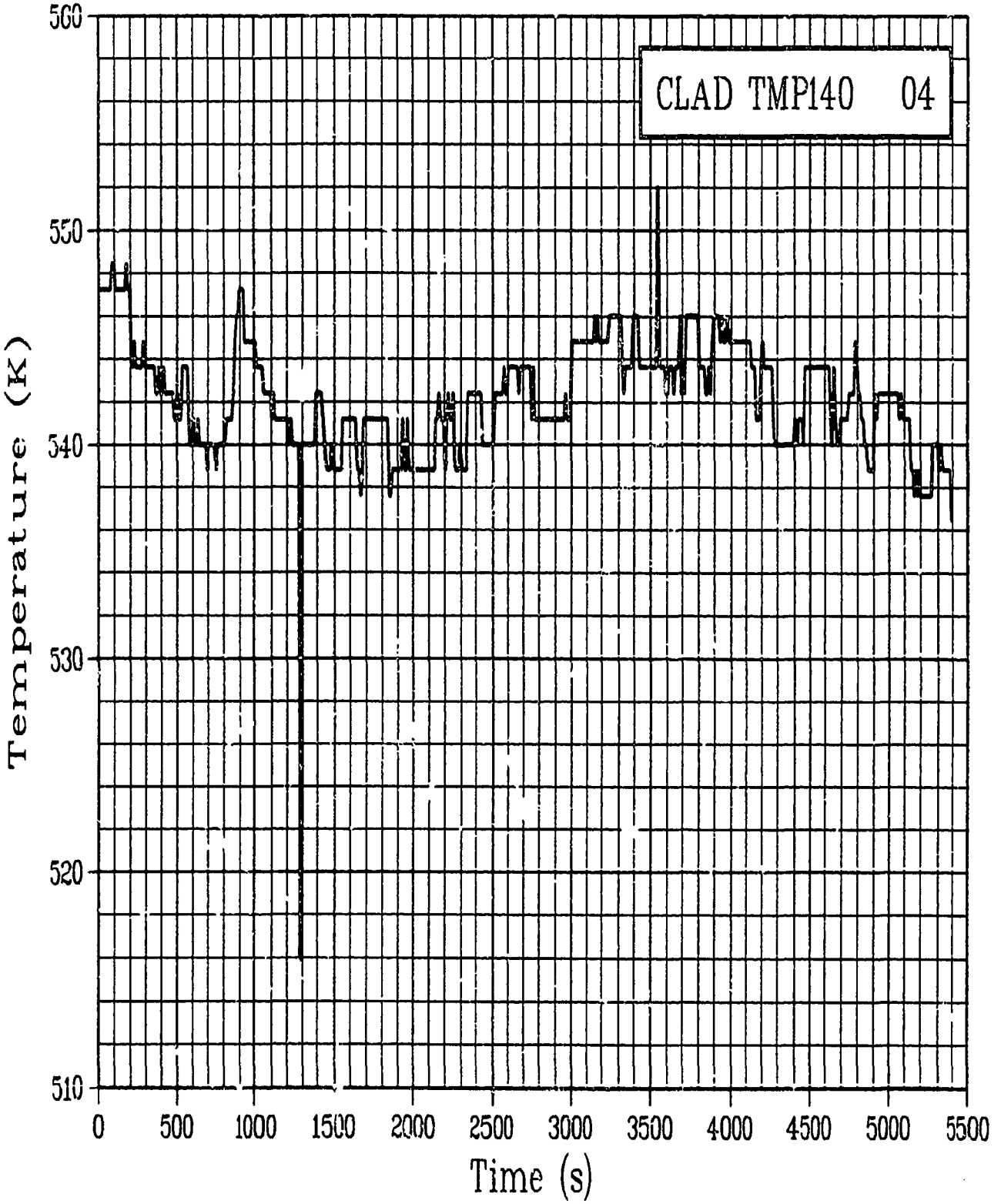

Figure C-24. Cladding surface temperature Rod GC 524-4, at 140 degrees and 0.4521 m during Test PR-1 instrument checkout (calibration not shown) (CLAD TMP140 04).

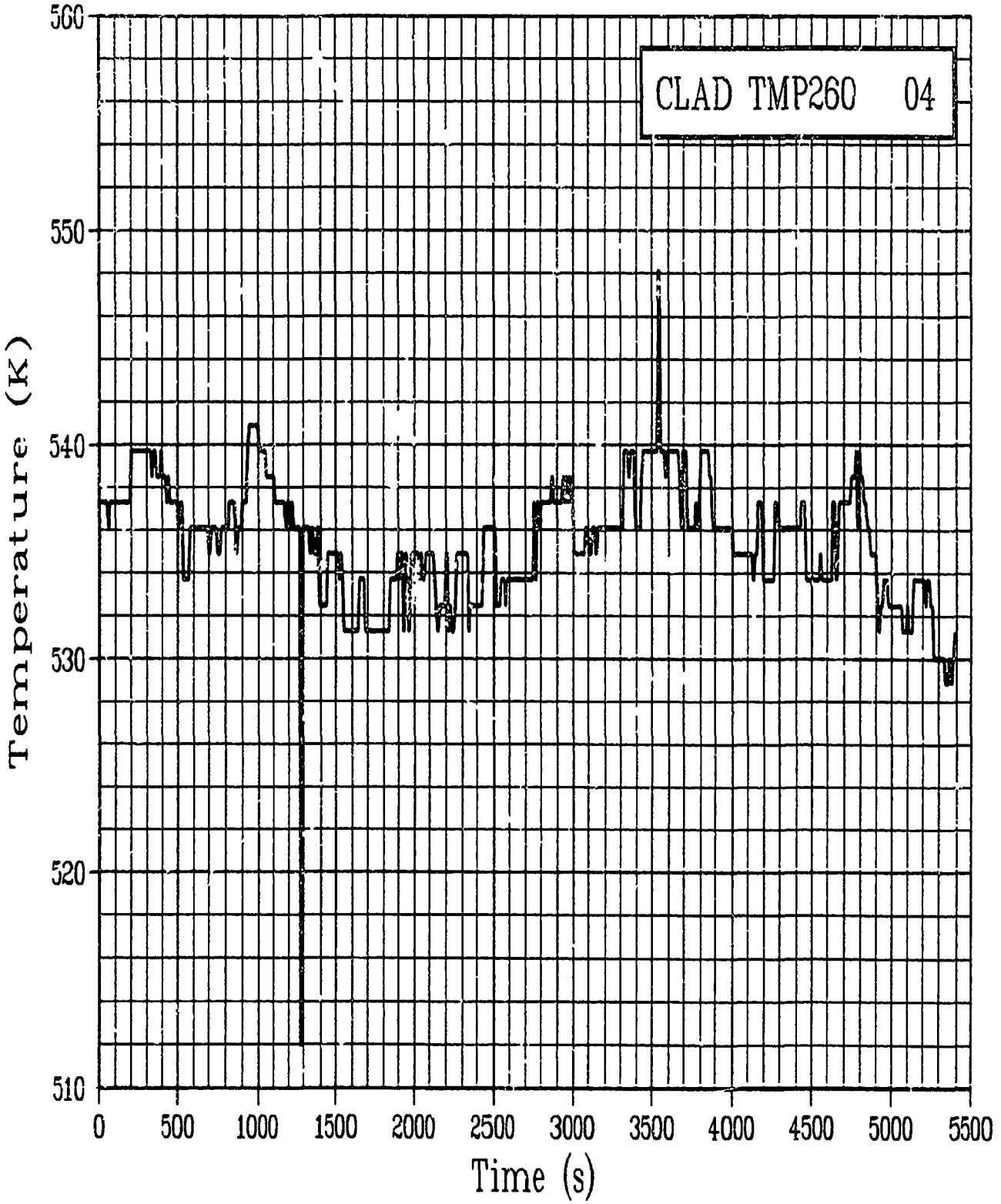

Figure C-25. Cladding surface temperature Rod GC 524-4, at 260 degrees and
n) 0.70 m during Test PR-1 instrument checkout (calibration not shown)
(CLAD TMP260 04).

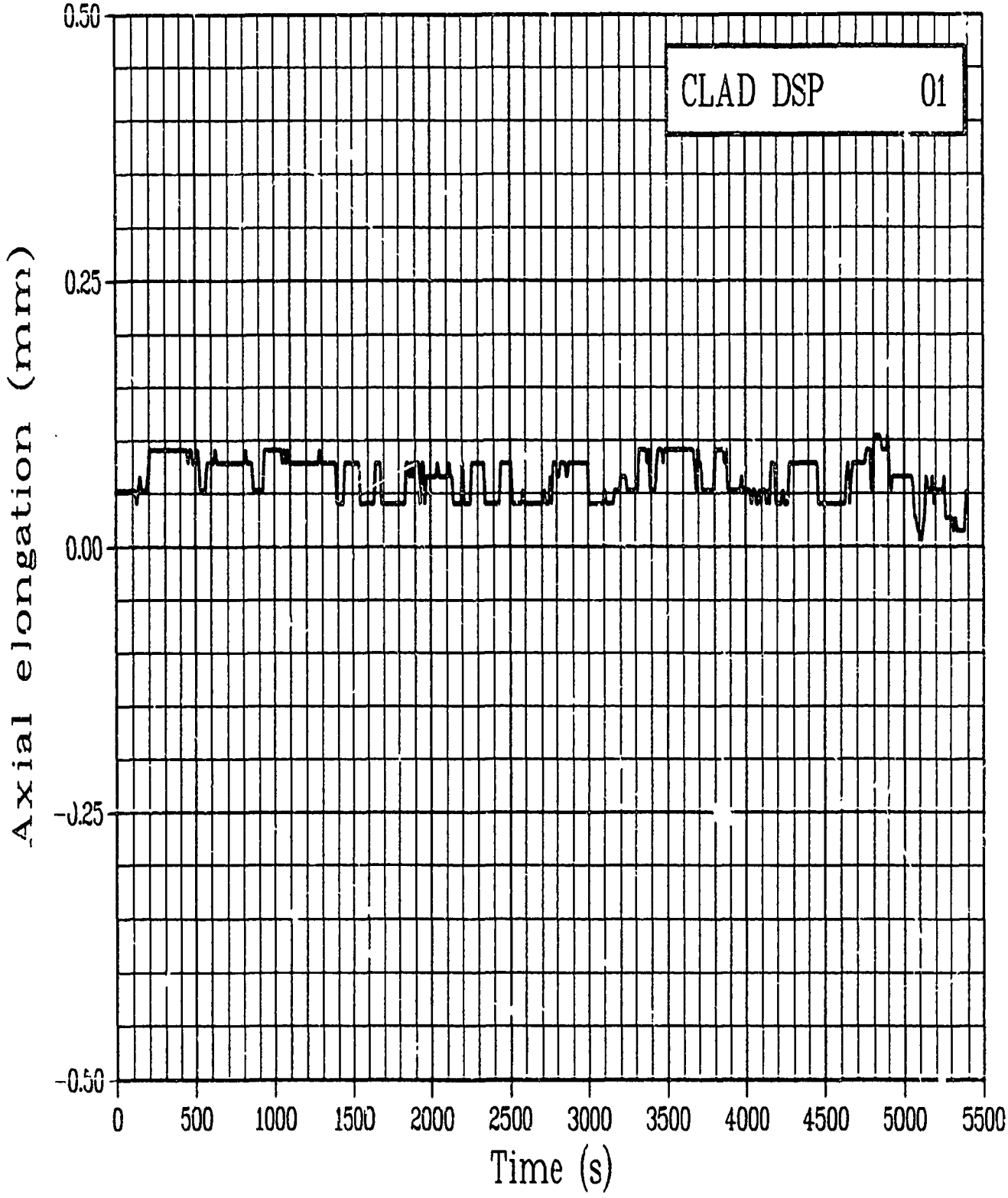

Figure C-26. Cladding axial elongation of Rod GC 524-1 during Test PR-1 instrument checkout (calibration not shown) (CLAD DSP 01).

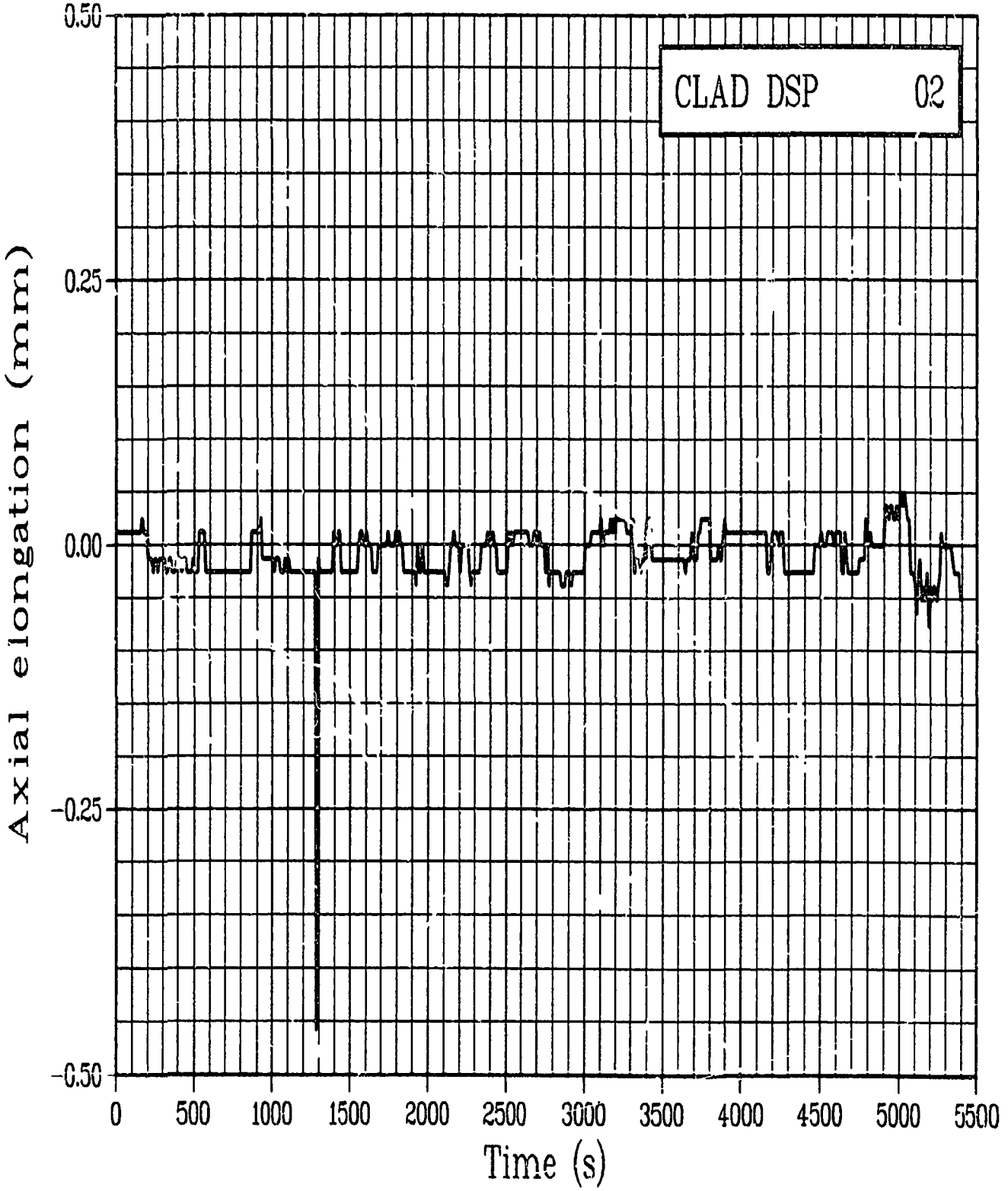

Figure C-27. Cladding axial elongation of Rod GC 524-2 during
n) Test PR-1 instrument checkout (calibration not shown)
(CLAD DSP 02).

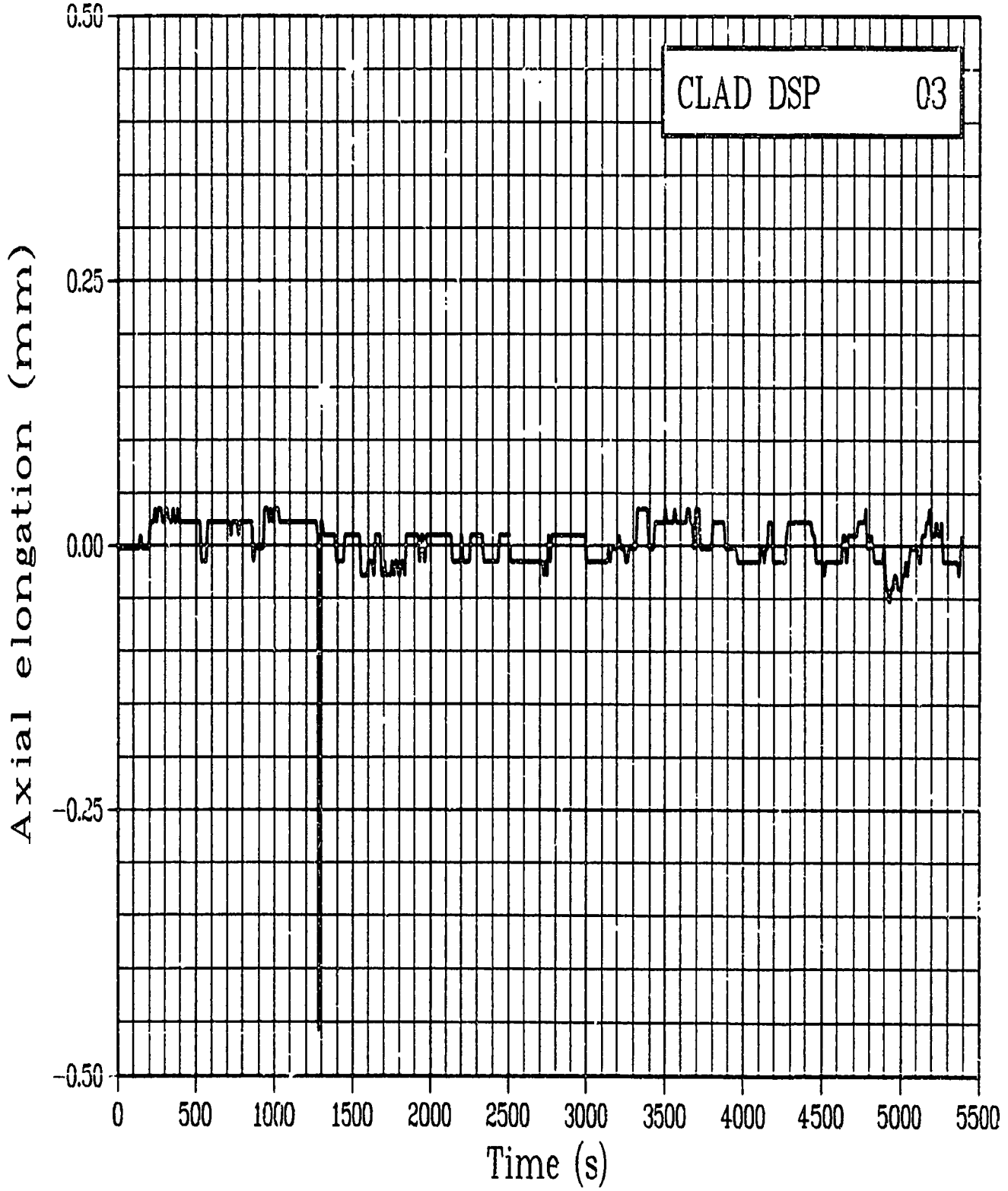

Figure C-28. Cladding axial elongation of Rod GC 524-3 during Test PR-1 instrument checkout (calibration not shown) (CLAD DSP 03).

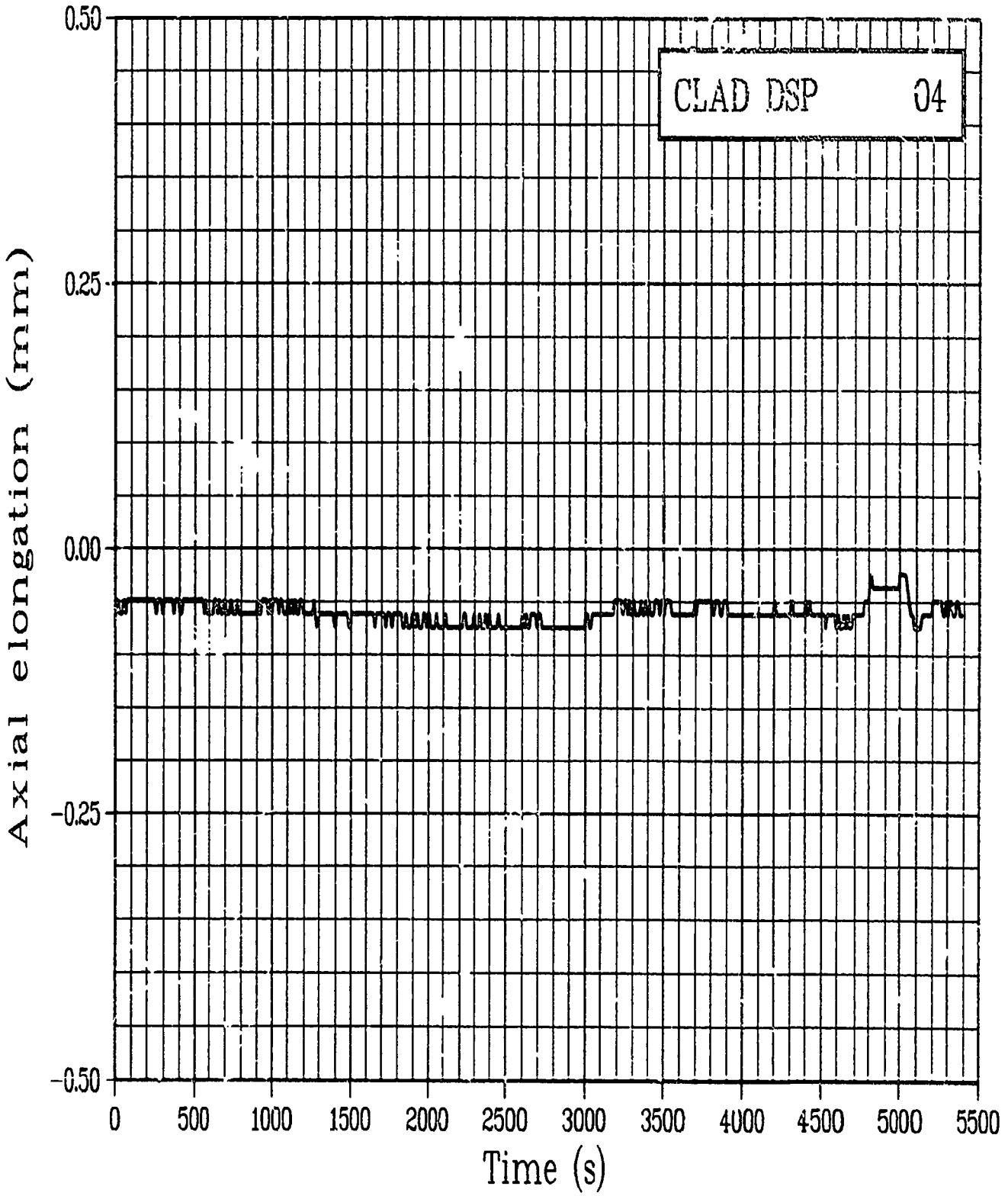

Figure C-29. Cladding axial elongation of Rod GC 524-4 during Test PR-1 instrument checkout (calibration not shown) (CLAD DSP 04).

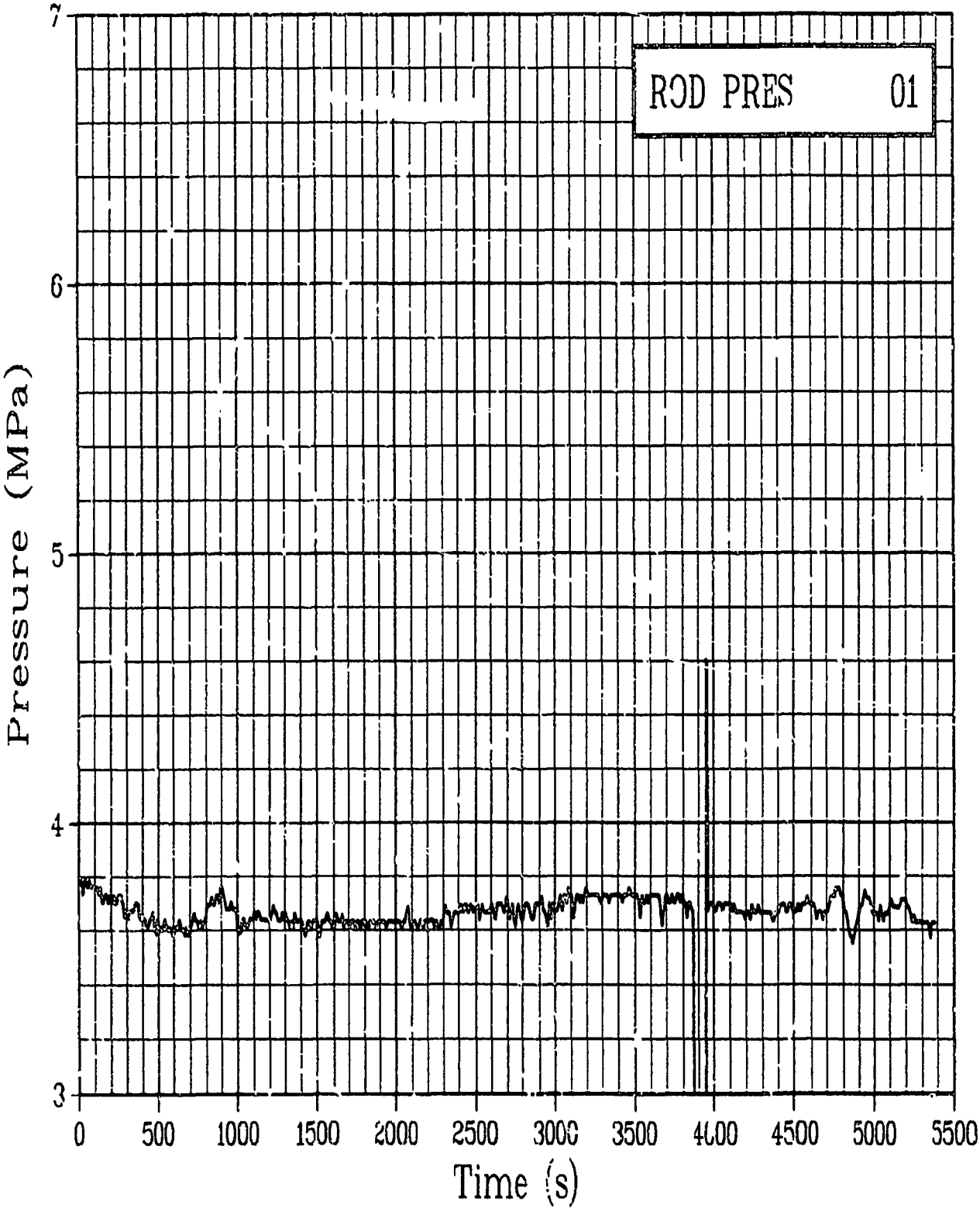

Figure C-30. Absolute pressure in Rod GC 524-1 plenum during Test PR-1 instrument checkout (calibration not shown) (ROD PRES 01).

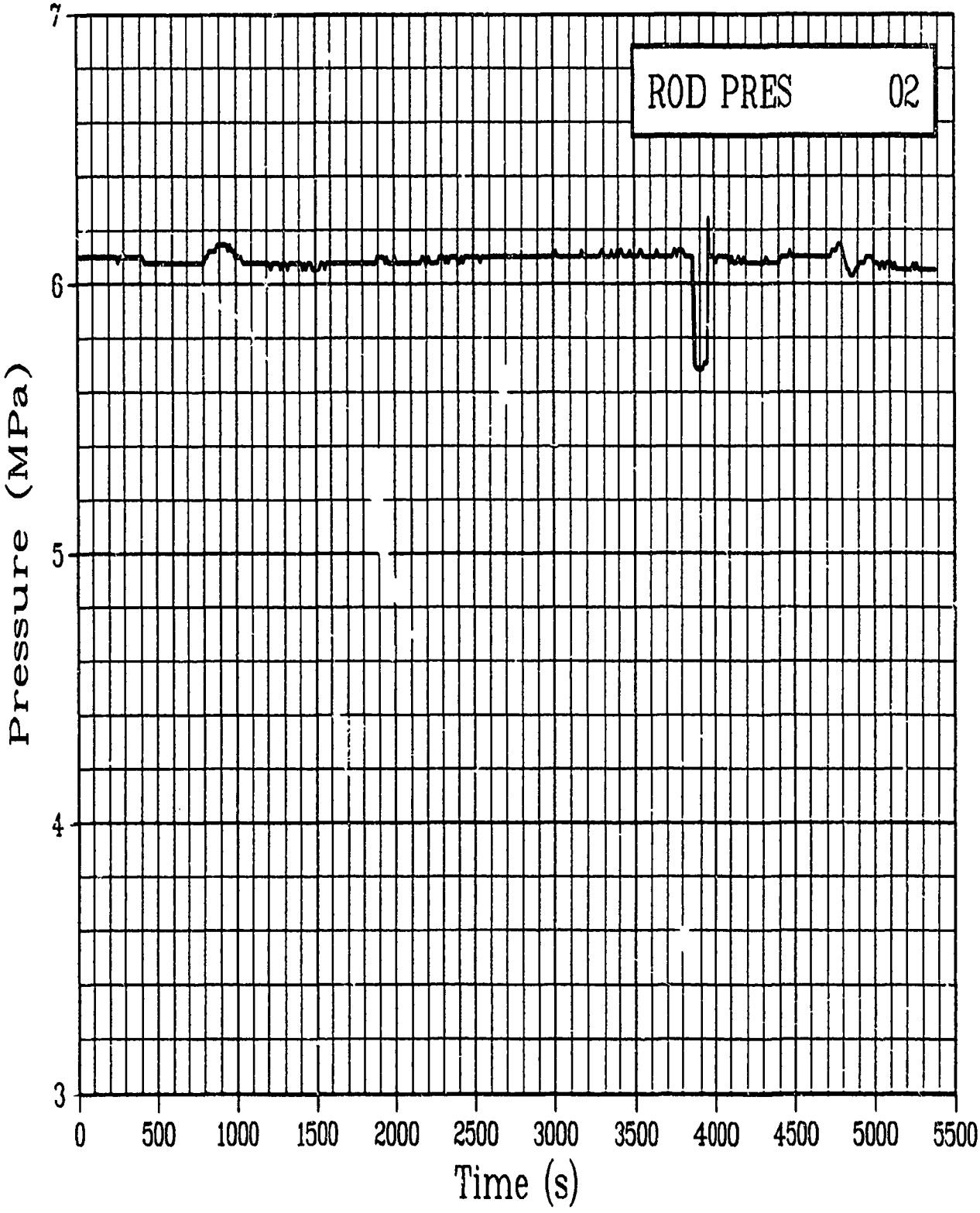

Figure C-31. Absolute pressure in Rod GC 524-2 plenum during Test PR-1 instrument checkout (calibration not shown) (ROD PRES 02).

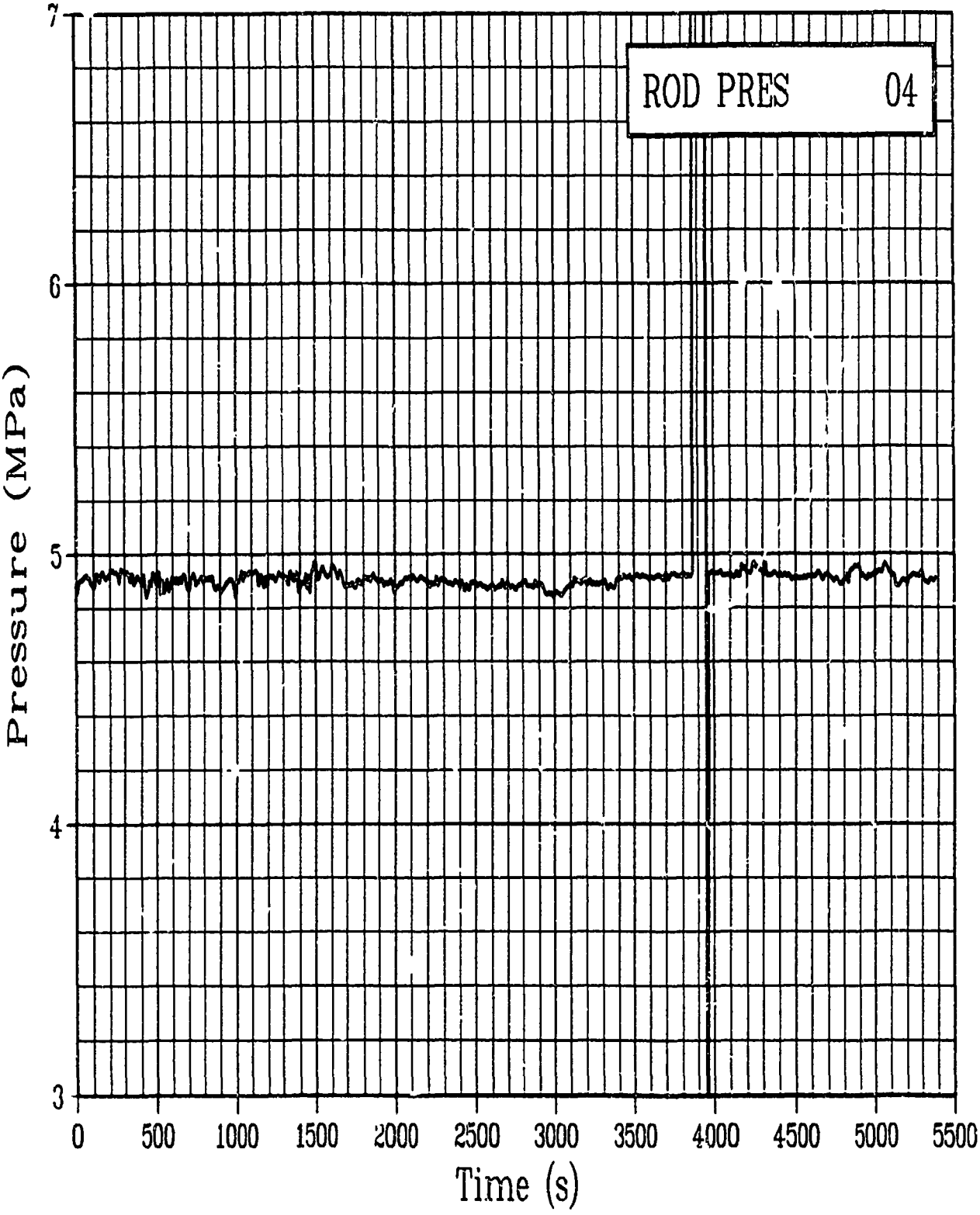

Figure C-32. Absolute pressure in Rod GC 524-4 plenum during Test PR-1 instrument checkout (calibration not shown) (ROD PRES 04).

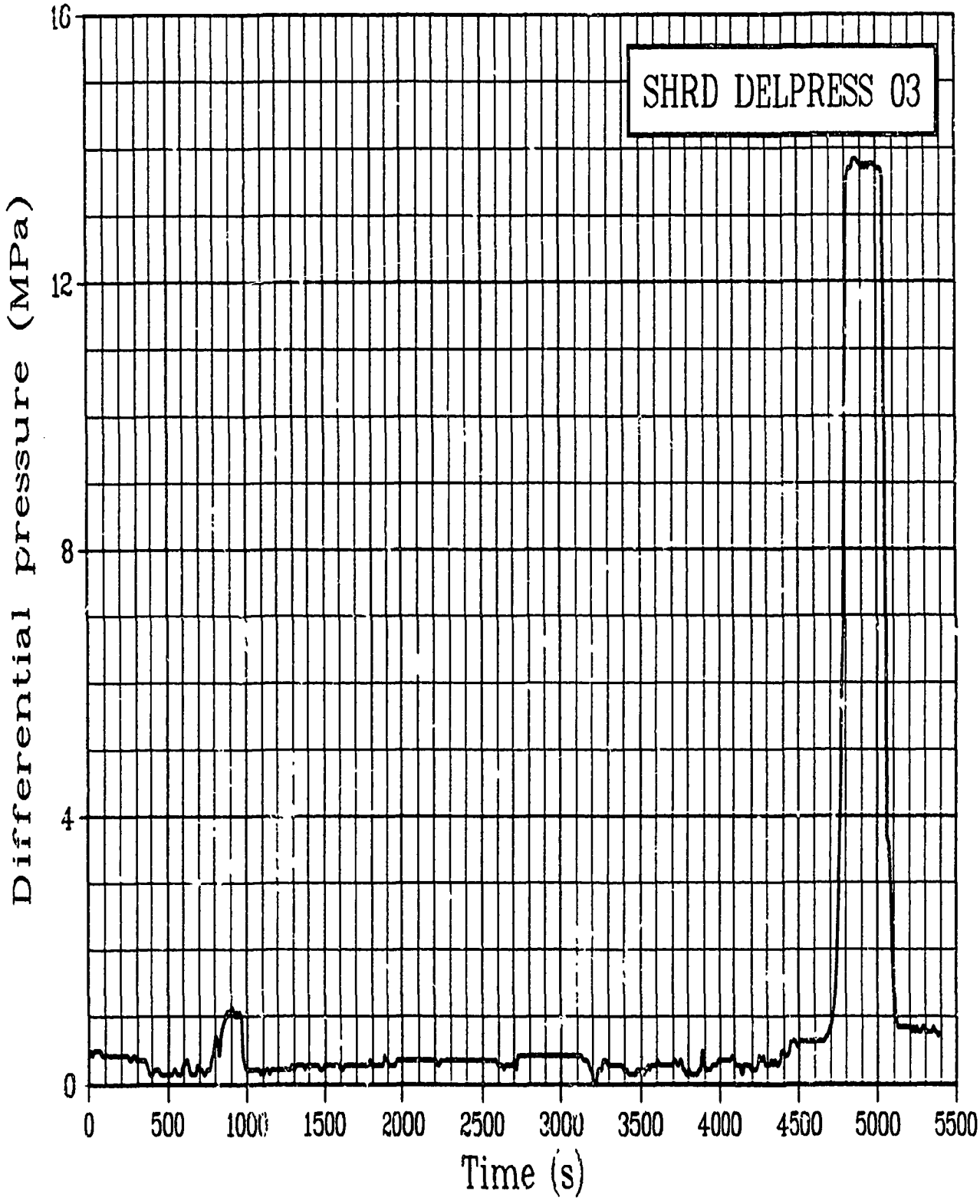

Figure C-33. Differential pressure across Rod GC 524-3 shroud during Test PR-1 instrument checkout (calibration not shown) (SHRD DELPRESS 03).

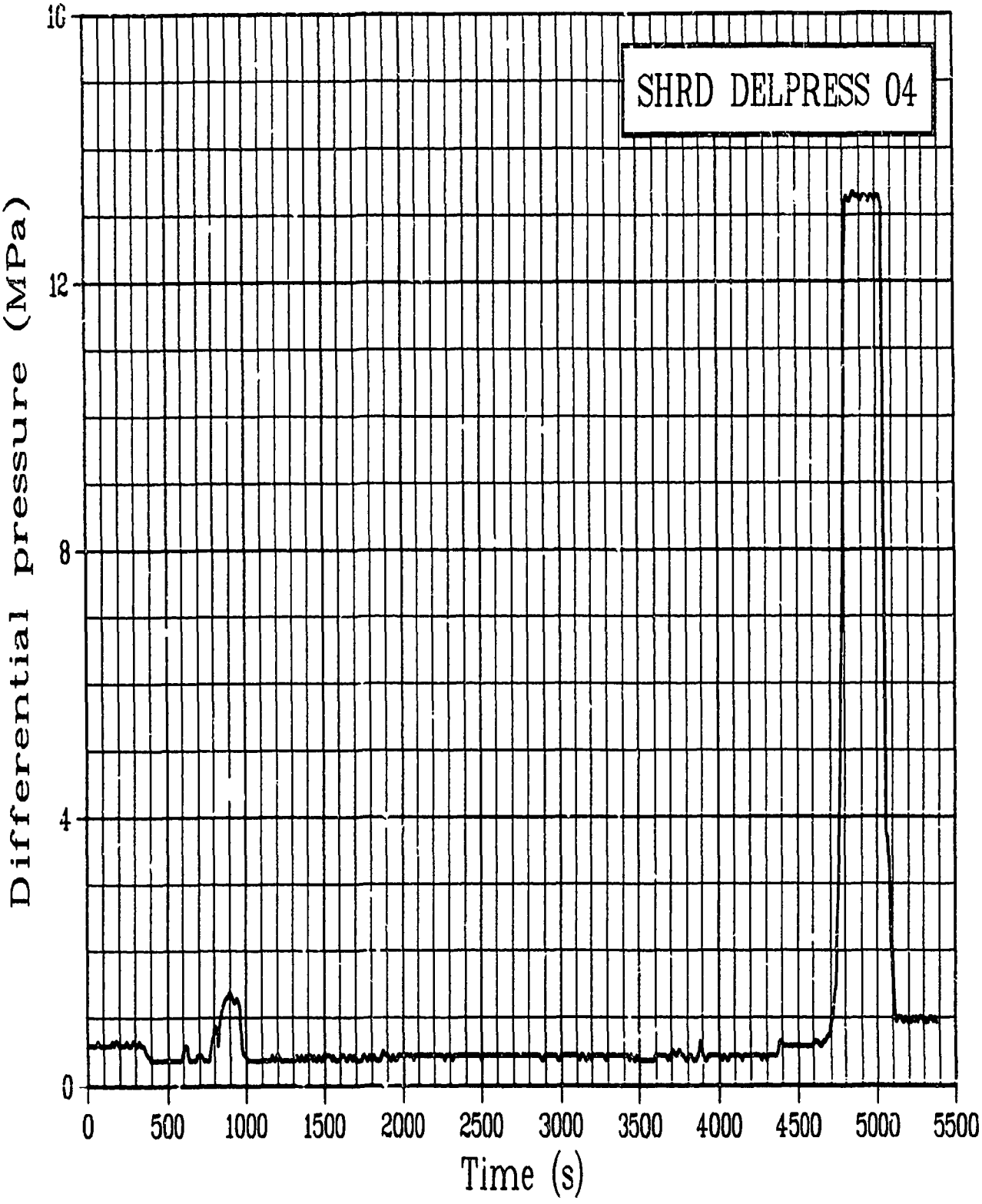

Figure C-34. Differential pressure across Rod GC 524-4 shroud during Test PR-1 instrument checkout (calibration not shown) (SHRD DELPRESS 04).

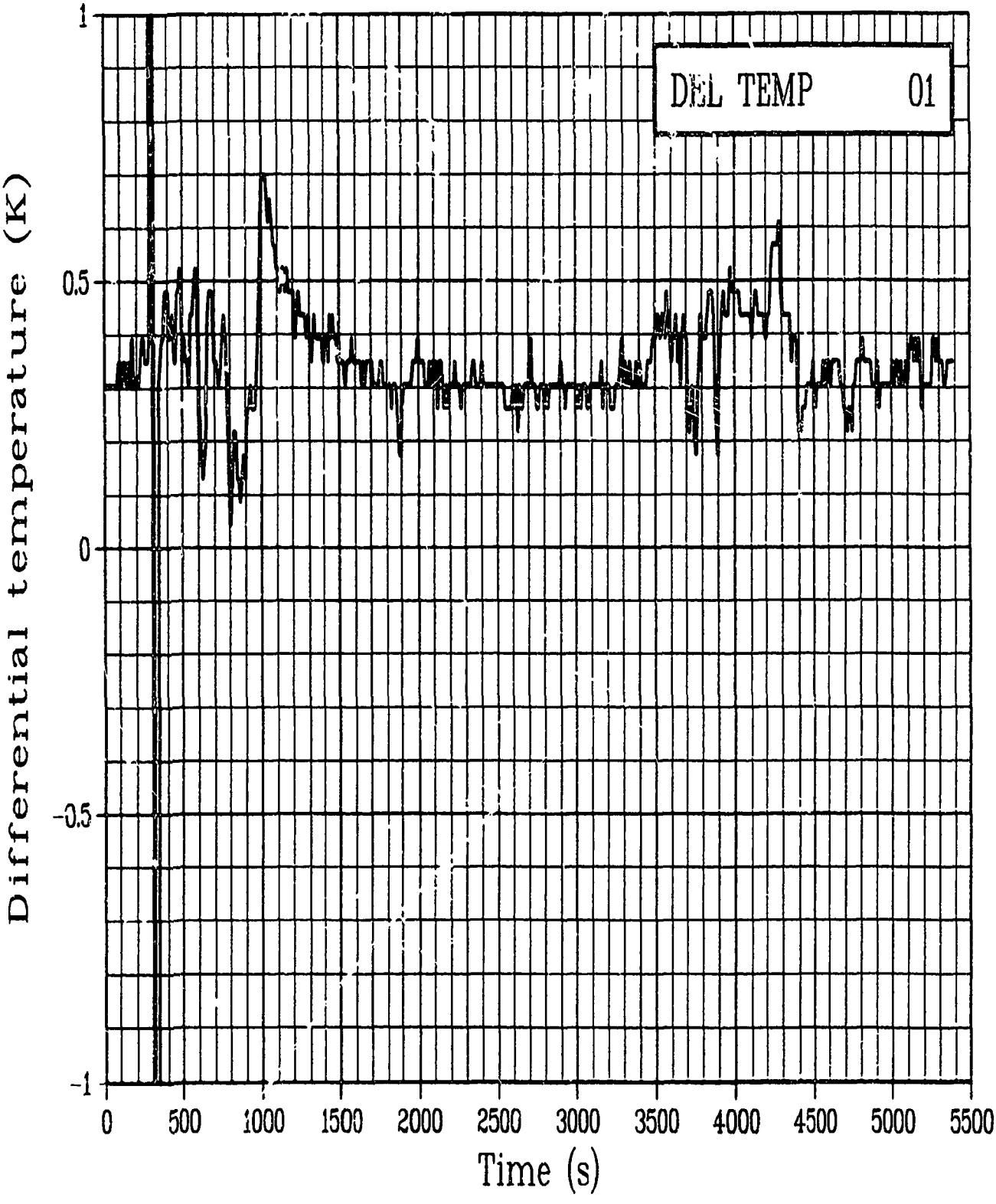

Figure C-35. Differential temperature of Rod GC 524-1 coolant inlet and outlet during Test PR-1 instrument checkout (calibration not shown) (DEL TEMP 01).

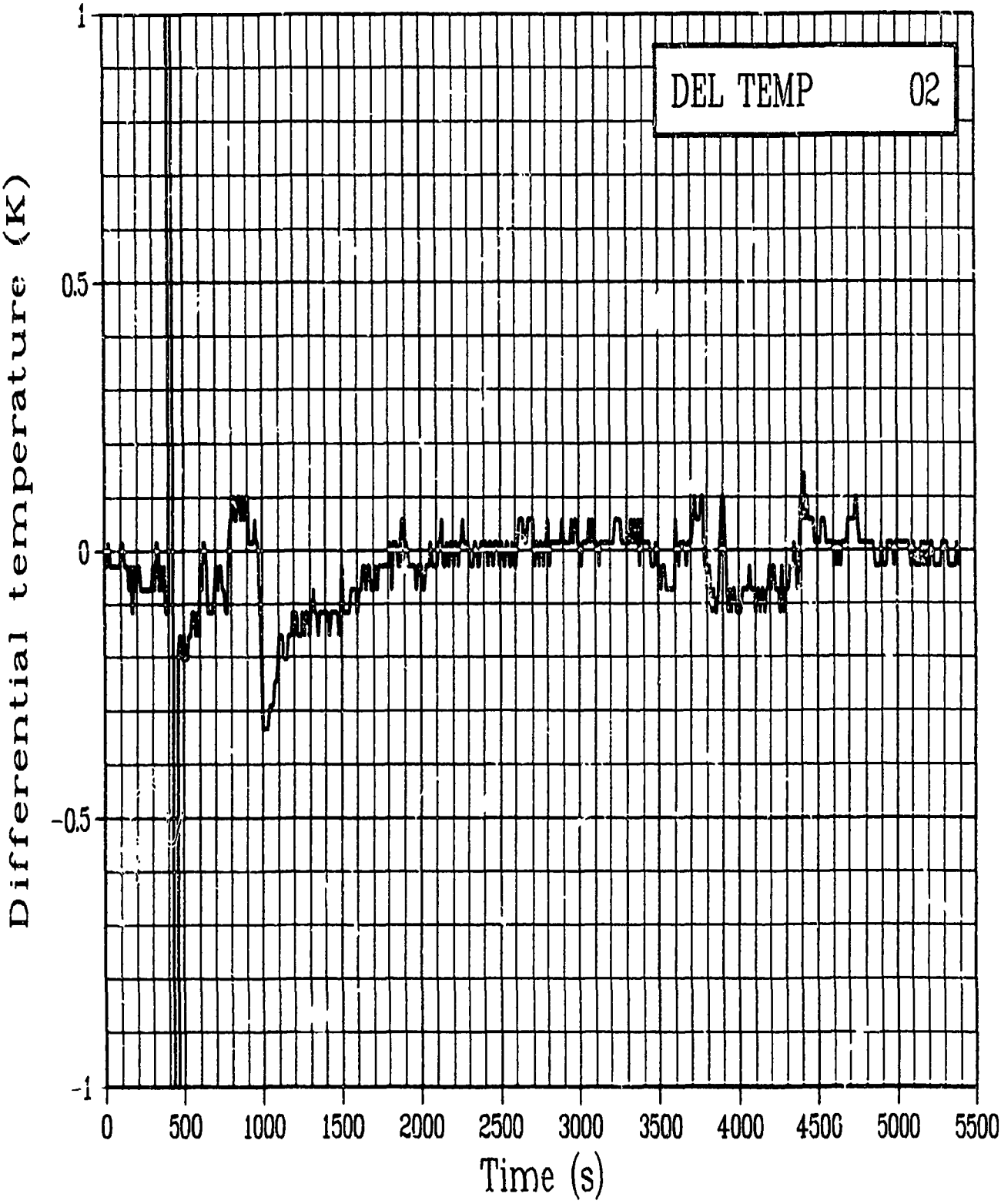

Figure C-36. Differential temperature of Rod GC 524-2 coolant inlet and outlet during Test PR-1 instrument checkout (calibration not shown) (DEL TEMP 02).

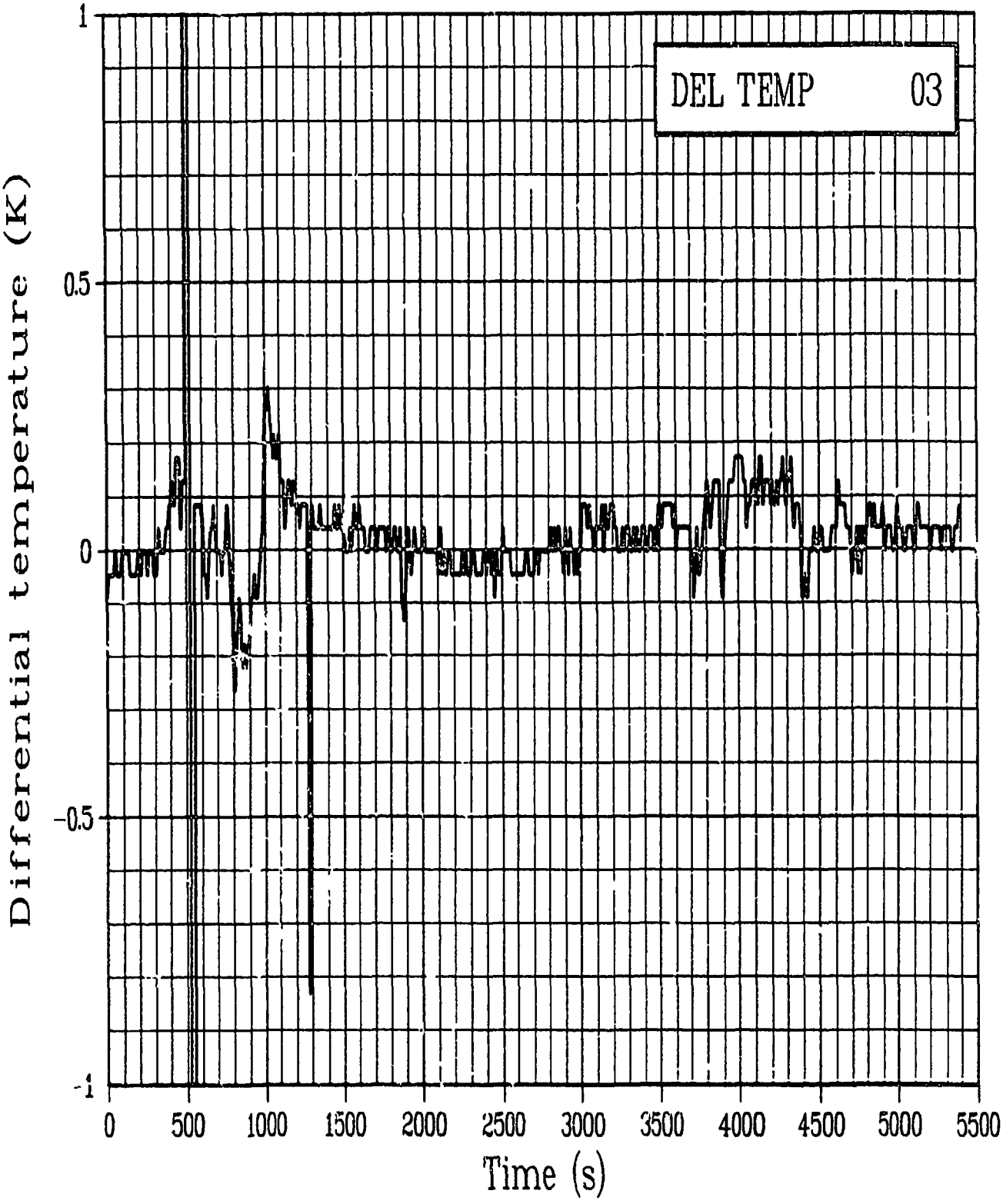

Figure C-37. Differential temperature of Rod GC 524-3 coolant inlet and outlet during Test PR-1 instrument checkout (calibration not shown) (DEL TEMP 03).

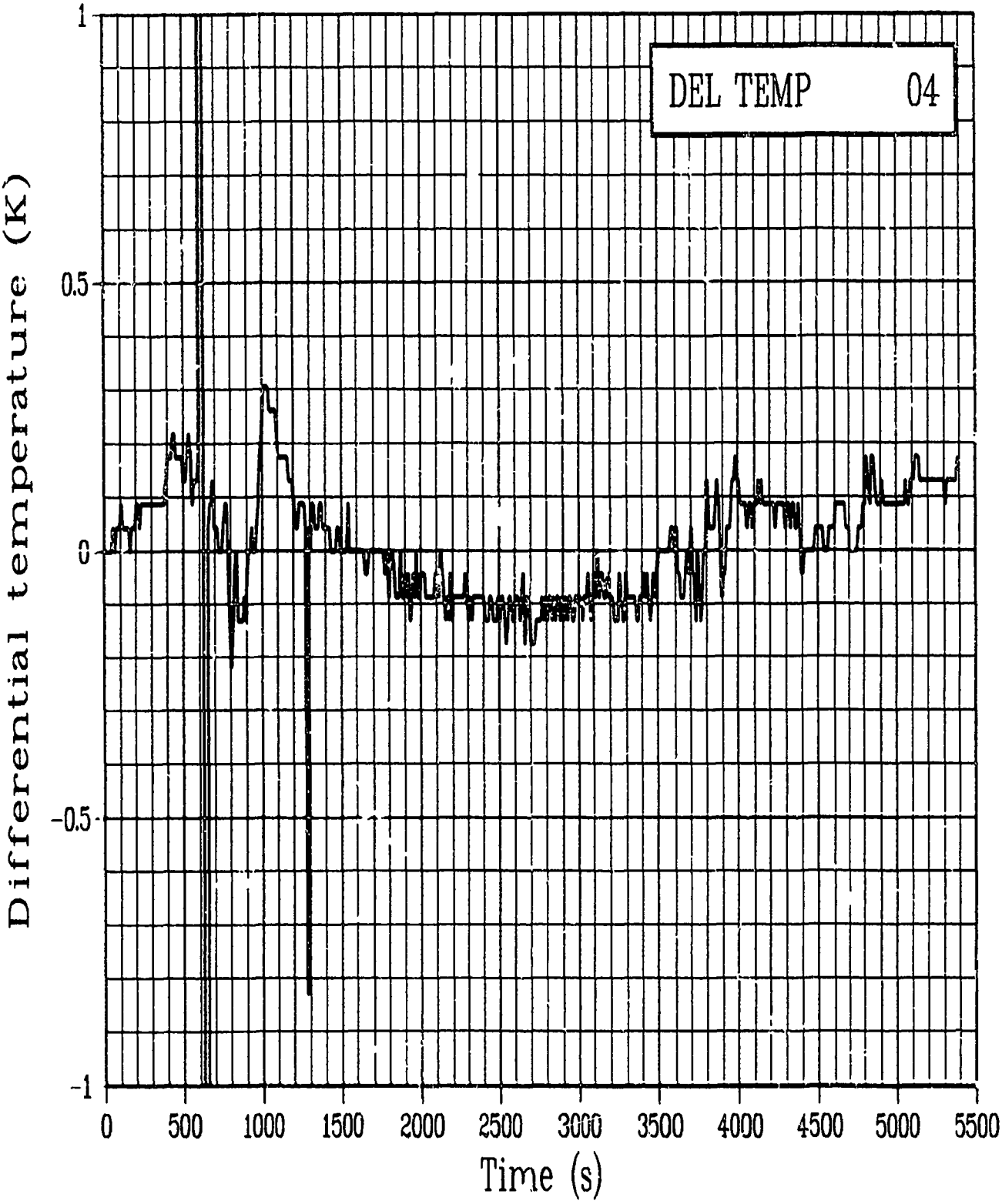

Figure C-38. Differential temperature of Rod GC 524-4 coolant inlet and outlet during Test PR-1 instrument checkout (calibration not shown) (DEL TEMP 04).

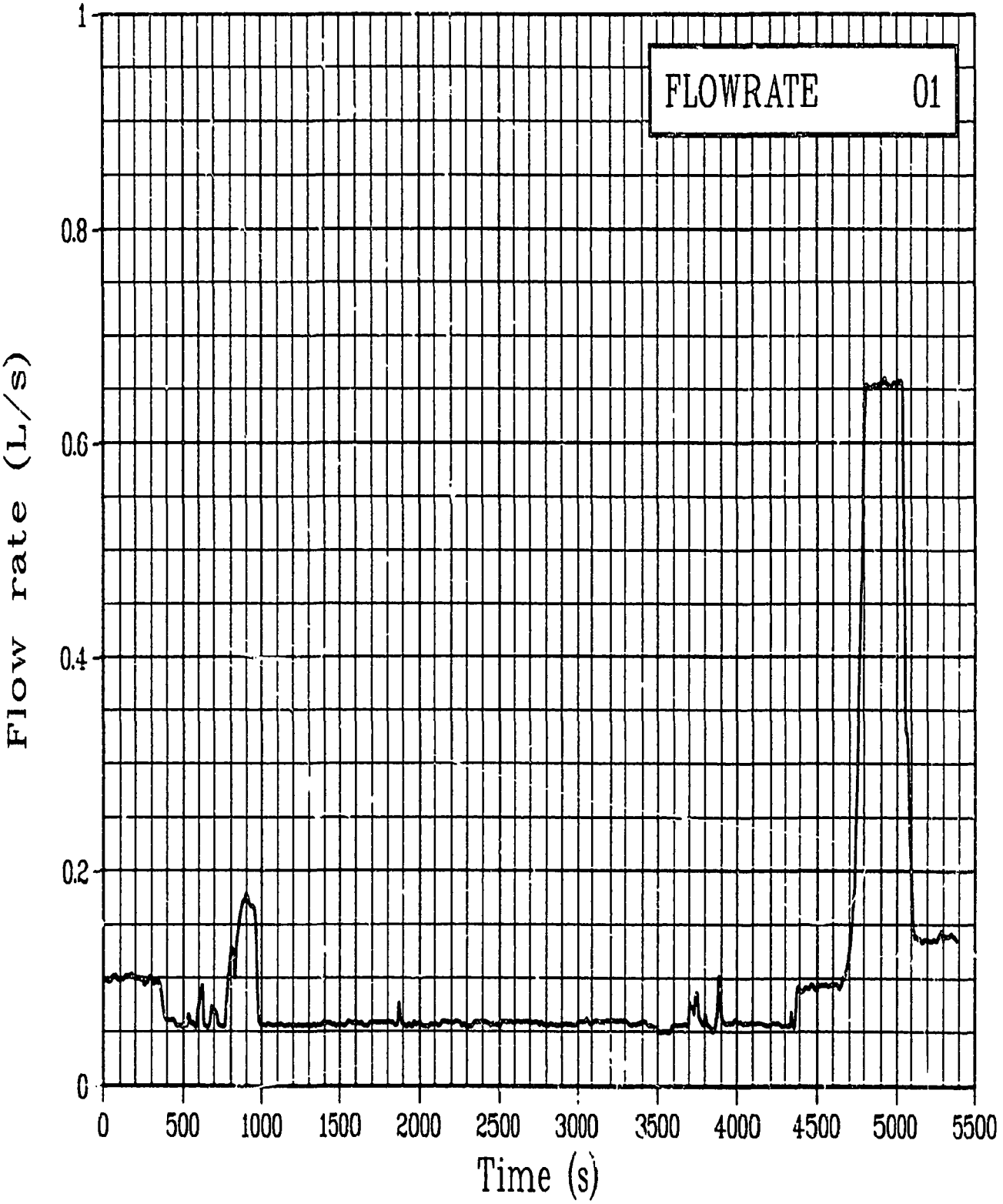

Figure C-39. Volumetric flow rate in Rod GC 524-1 lower shroud during Test PR-1 instrument checkout (calibration not shown) (FLOWRATE 01).

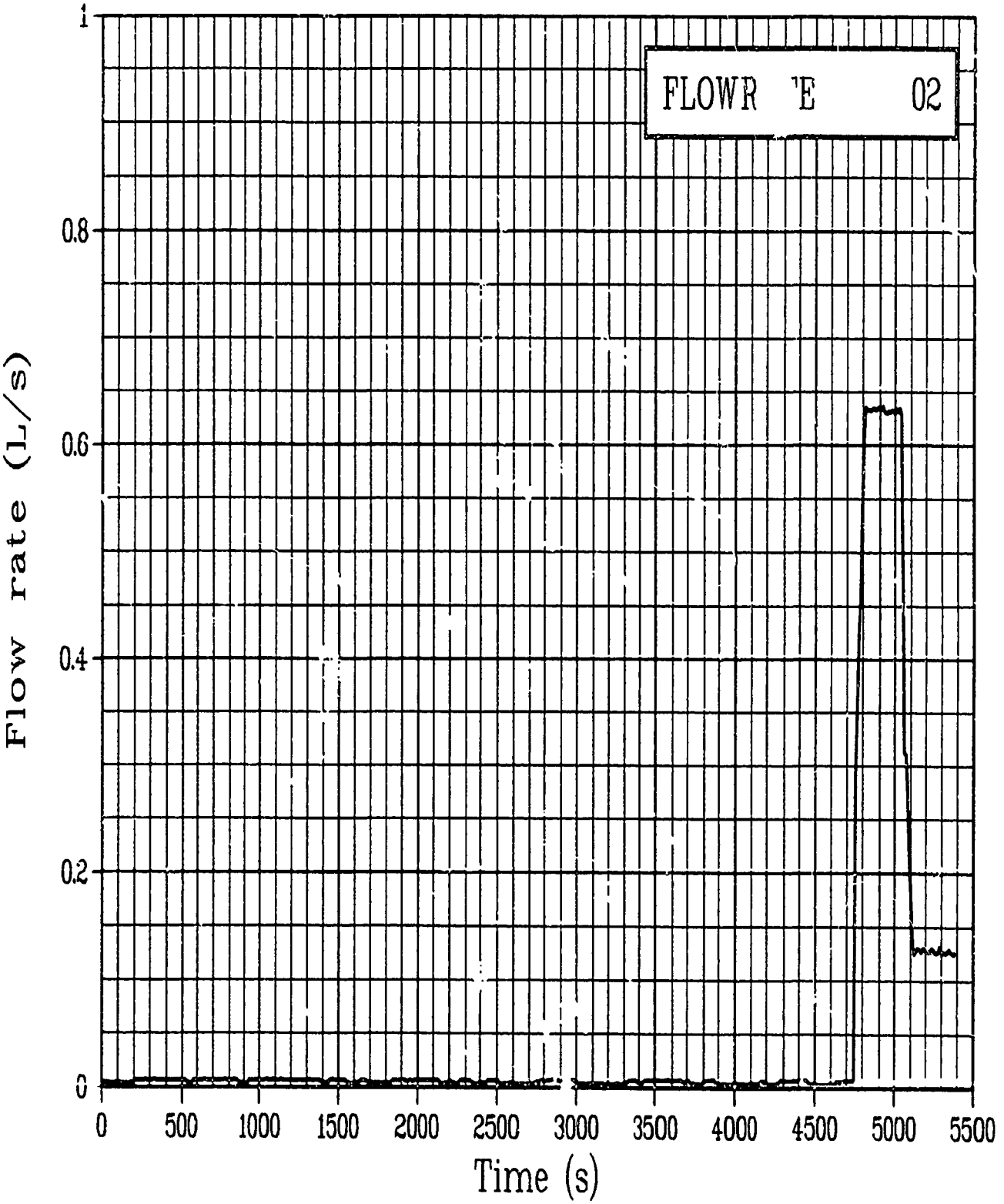

Figure C-40. Volumetric flow rate in Rod GC 524-2 lower shroud during Test PR-1 instrument checkout (calibration not shown) (FLOWRATE 02).

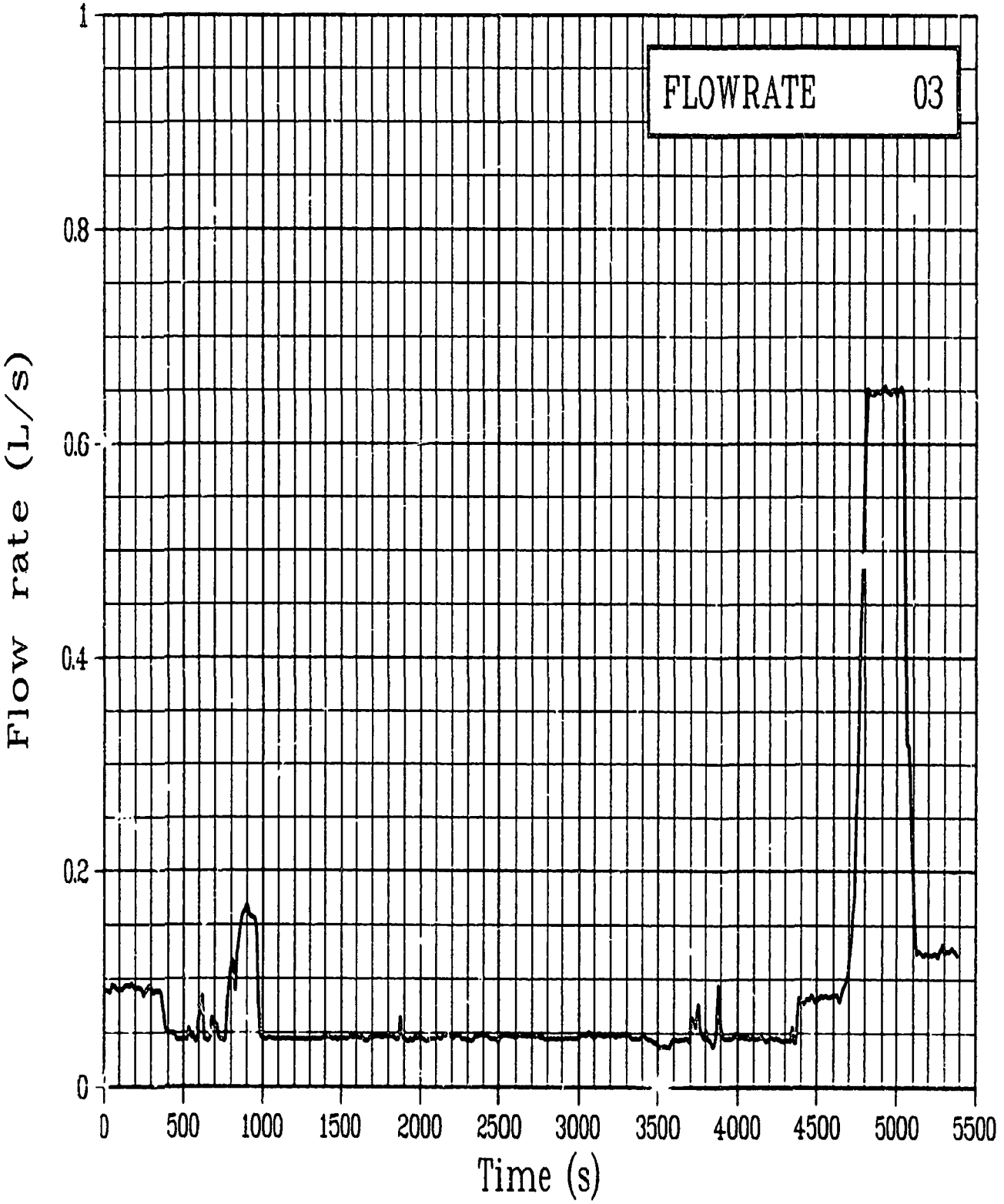

Figure C-41. Volumetric flow rate in Rod GC 524-3 lower shroud during Test PR-1 instrument checkout (calibration not shown) (FLOWRATE 03).

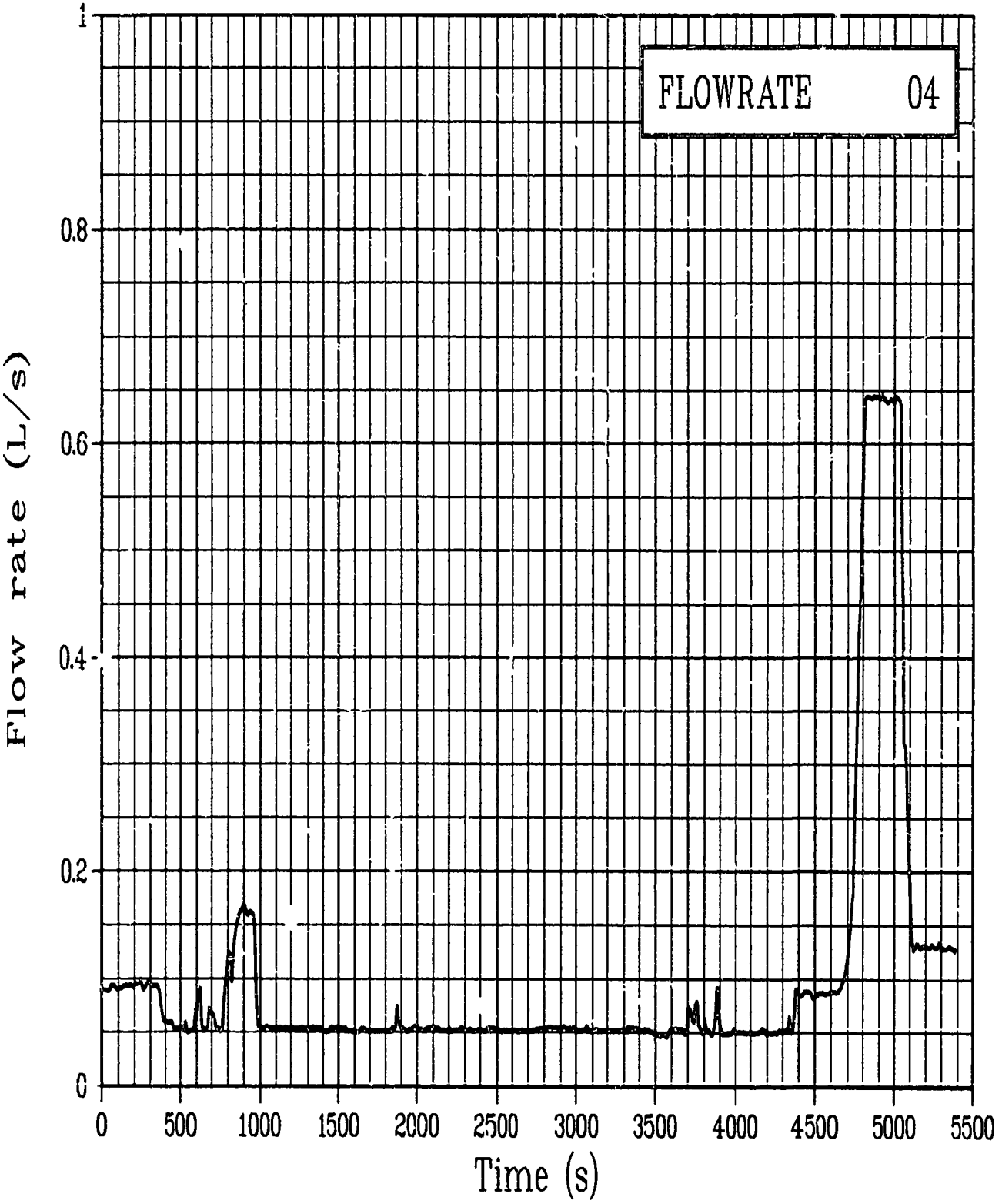

Figure C-42. Volumetric flow rate in Rod GC 524-4 lower shroud during Test PR-1 instrument checkout (calibration not shown) (FLOWRATE 04).

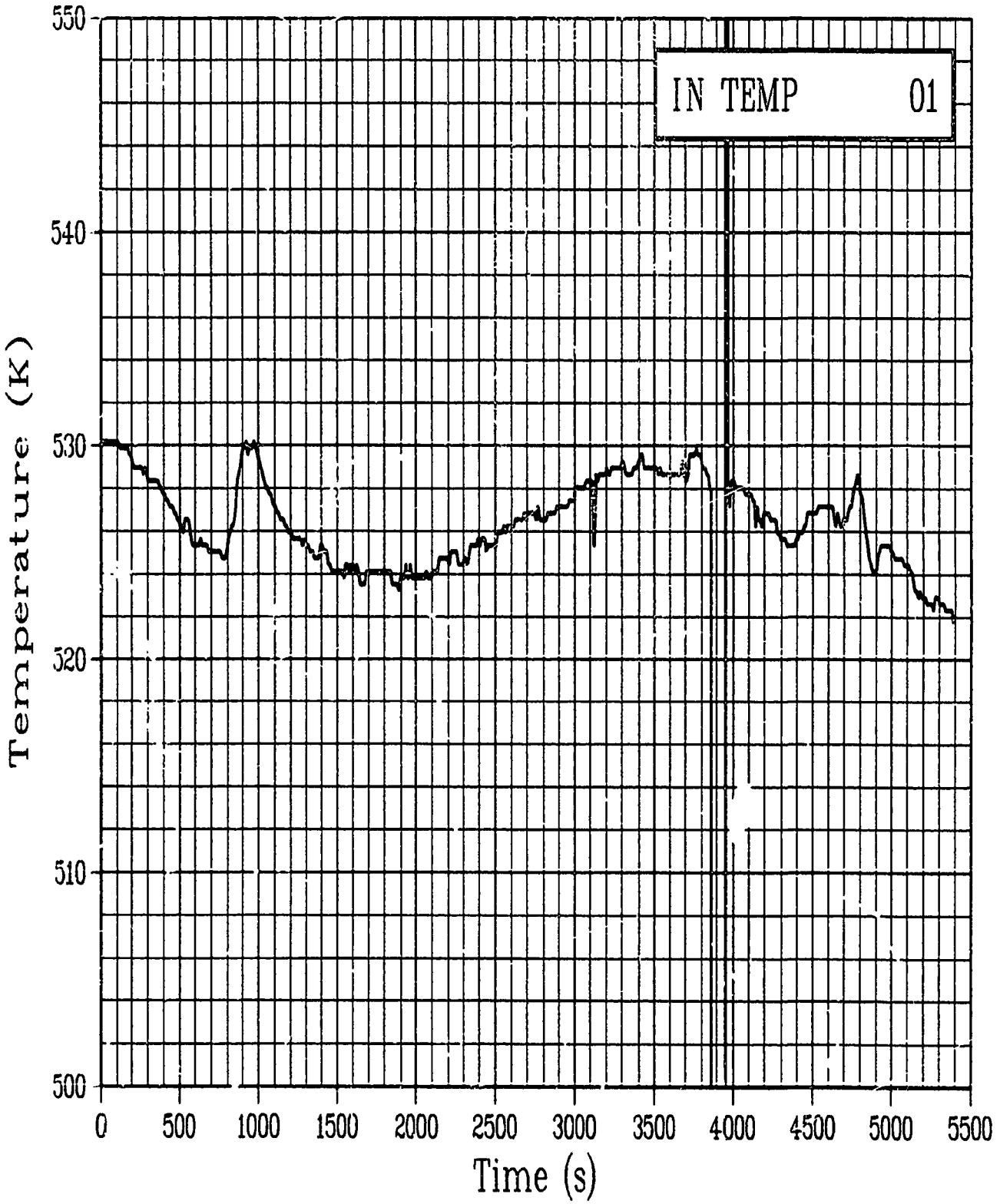

Figure C-43. Fluid temperature No. 1 at the flow shroud inlet during Test PR-1 instrument checkout (calibration not shown) (IN TEMP 01).

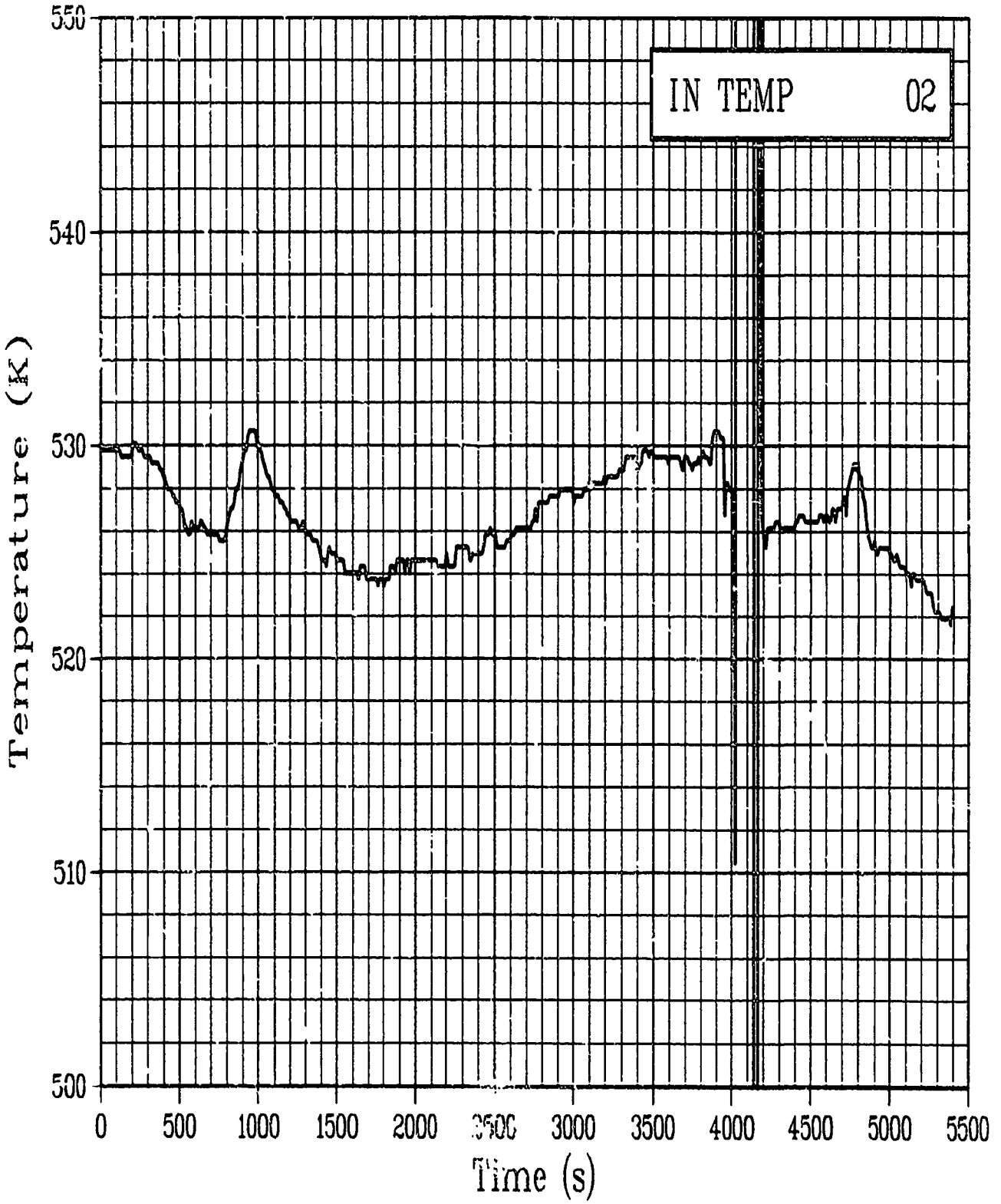

Figure C-44. Fluid temperature No. 2 at the flow shroud inlet during Test PR-1 instrument checkout (calibration not shown) (IN TEMP 02).

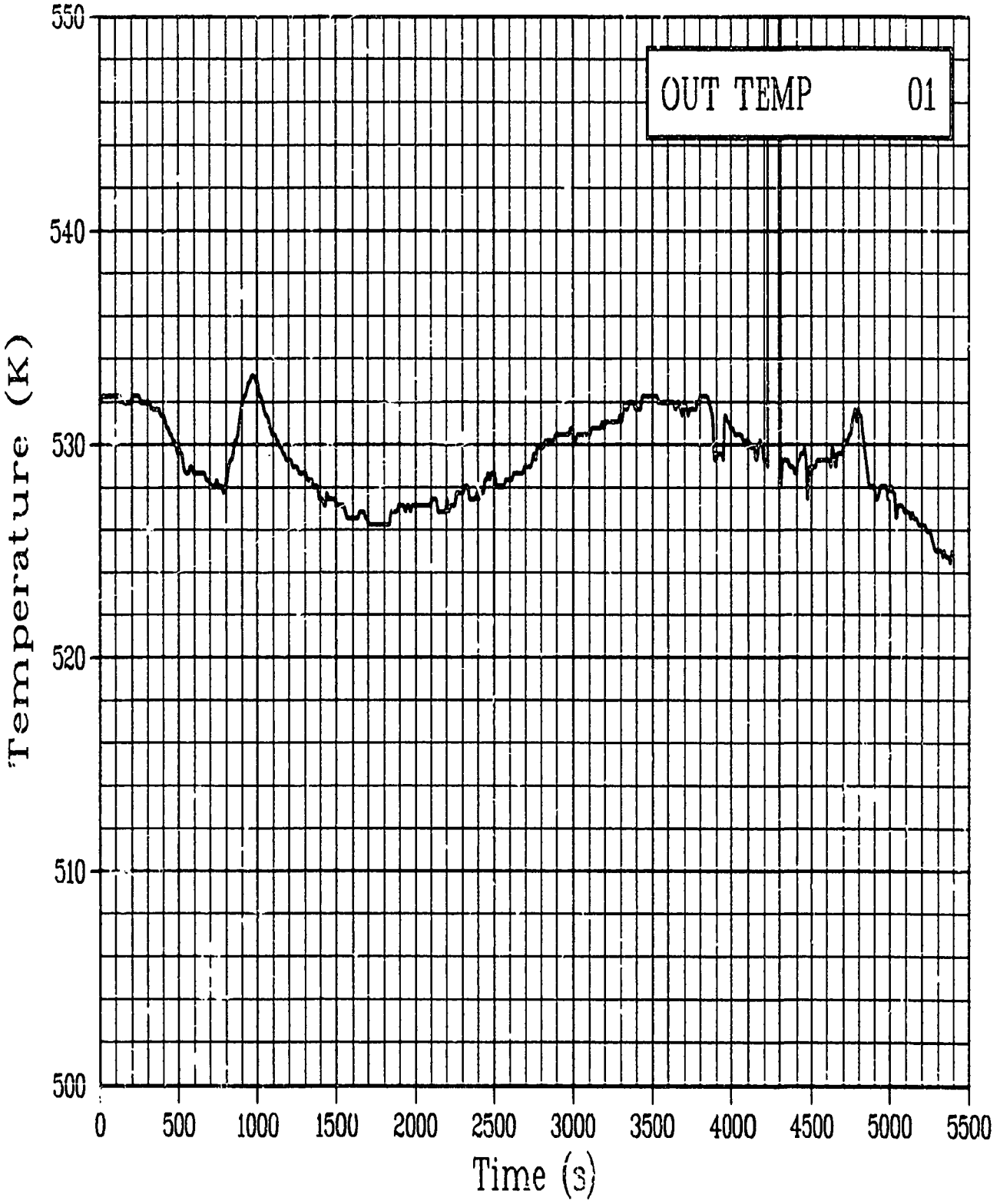

Figure C-45. Fluid temperature of Rod GC 524-1 coolant outlet during Test PR-1 instrument checkout (calibration not shown) (OUT TEMP 01).

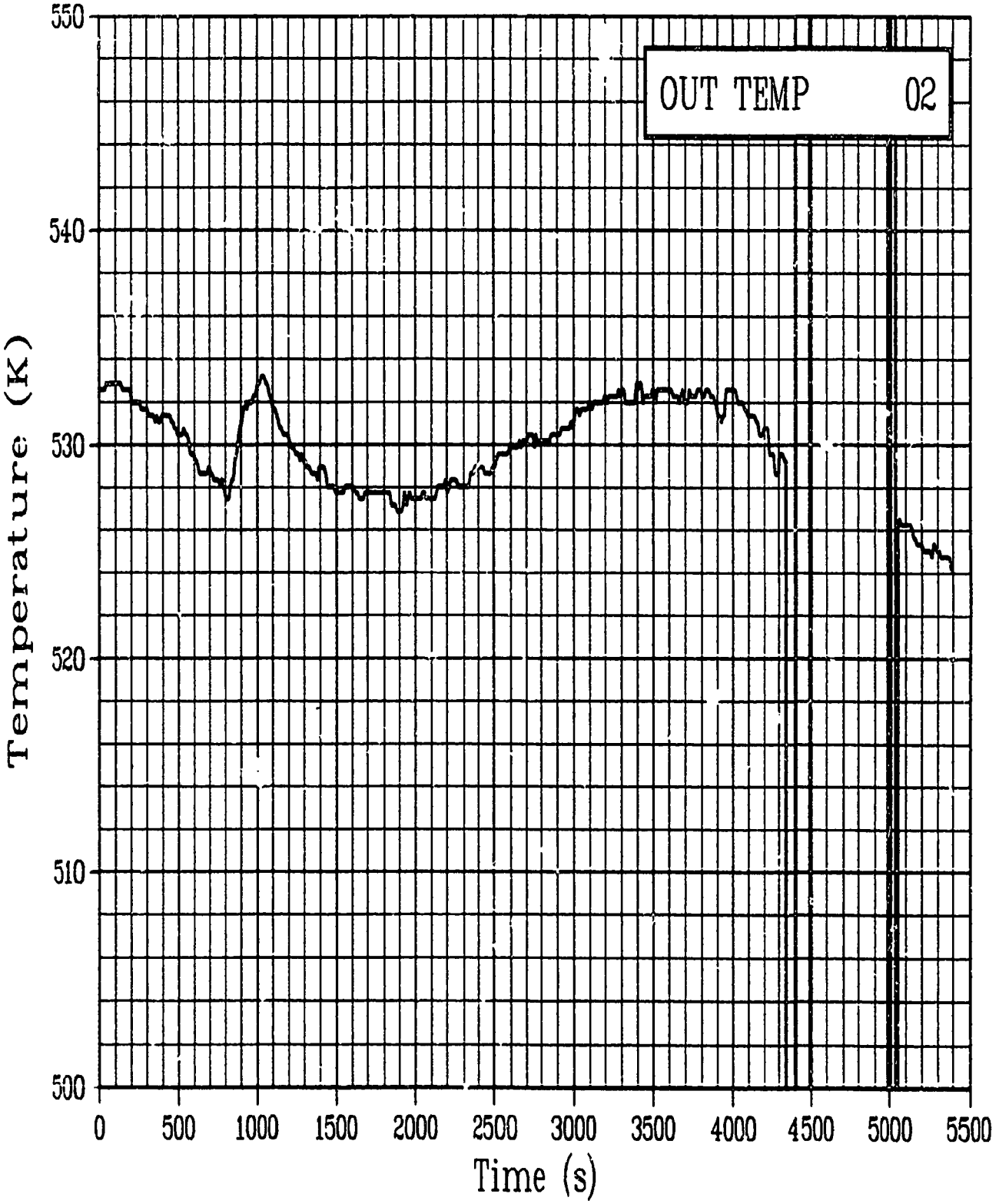

Figure C-46. Fluid temperature of Rod GC 524-2 coolant outlet during Test PR-1 instrument checkout (calibration not shown) (OUT TEMP 02).

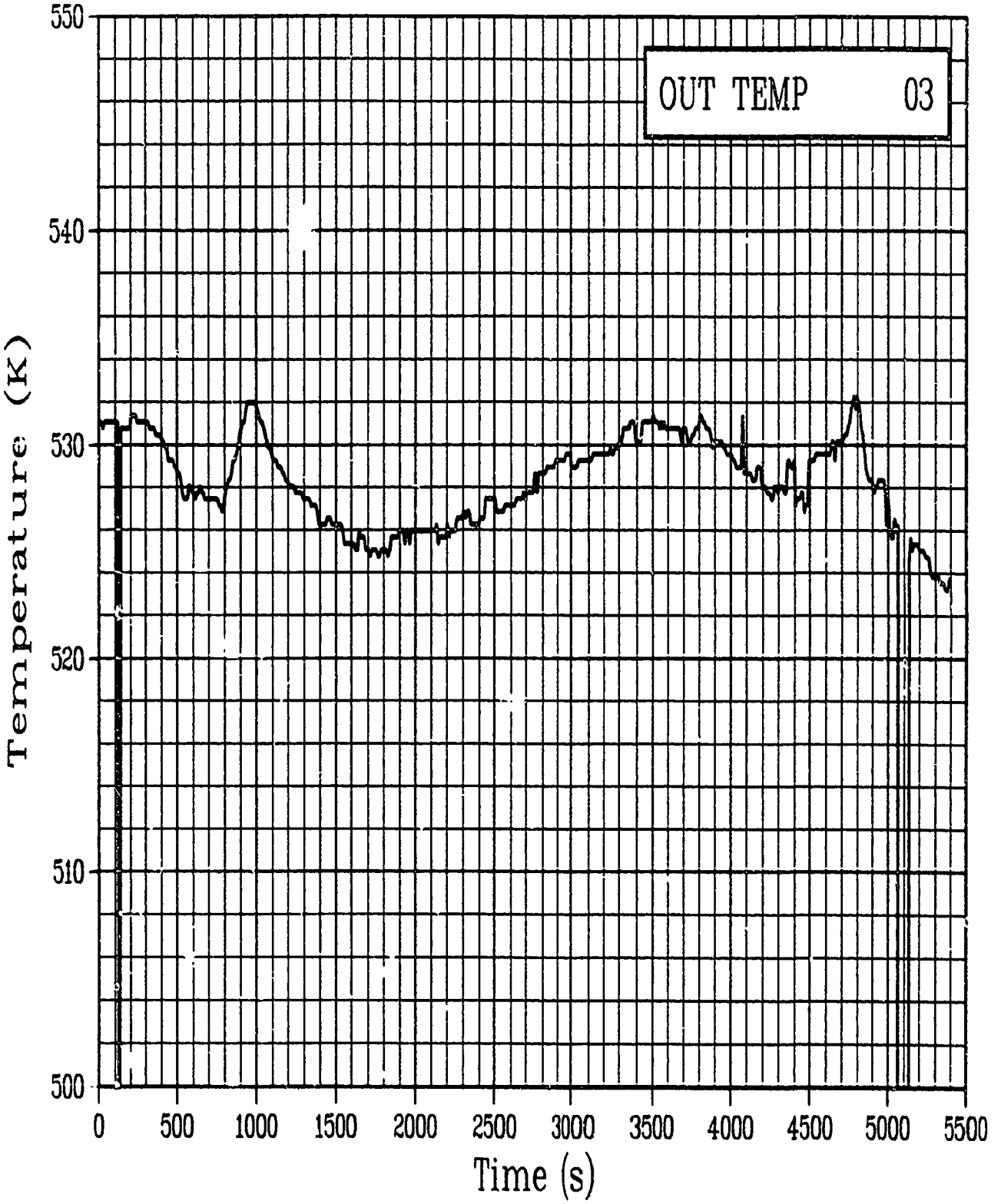

Figure C-47. Fluid temperature of Rod GC 524-3 coolant outlet during Test PR-1 instrument checkout (calibration not shown) (OUT TEMP 03).

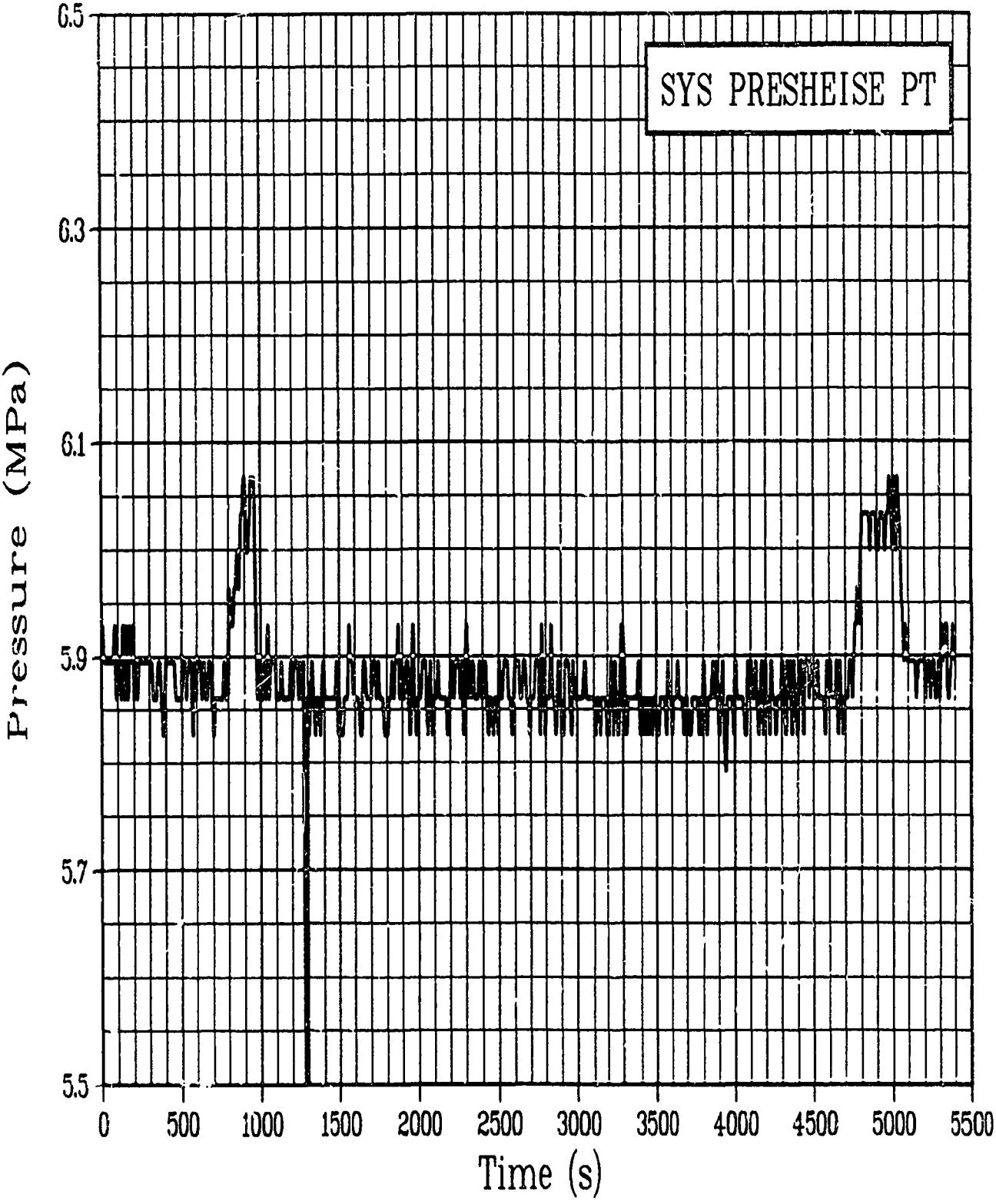

Figure C-48. Plant system pressure, Heise pressure guage during Test PR-1 instrument checkout (calibration not shown) (SYS PRESHEISE PT).

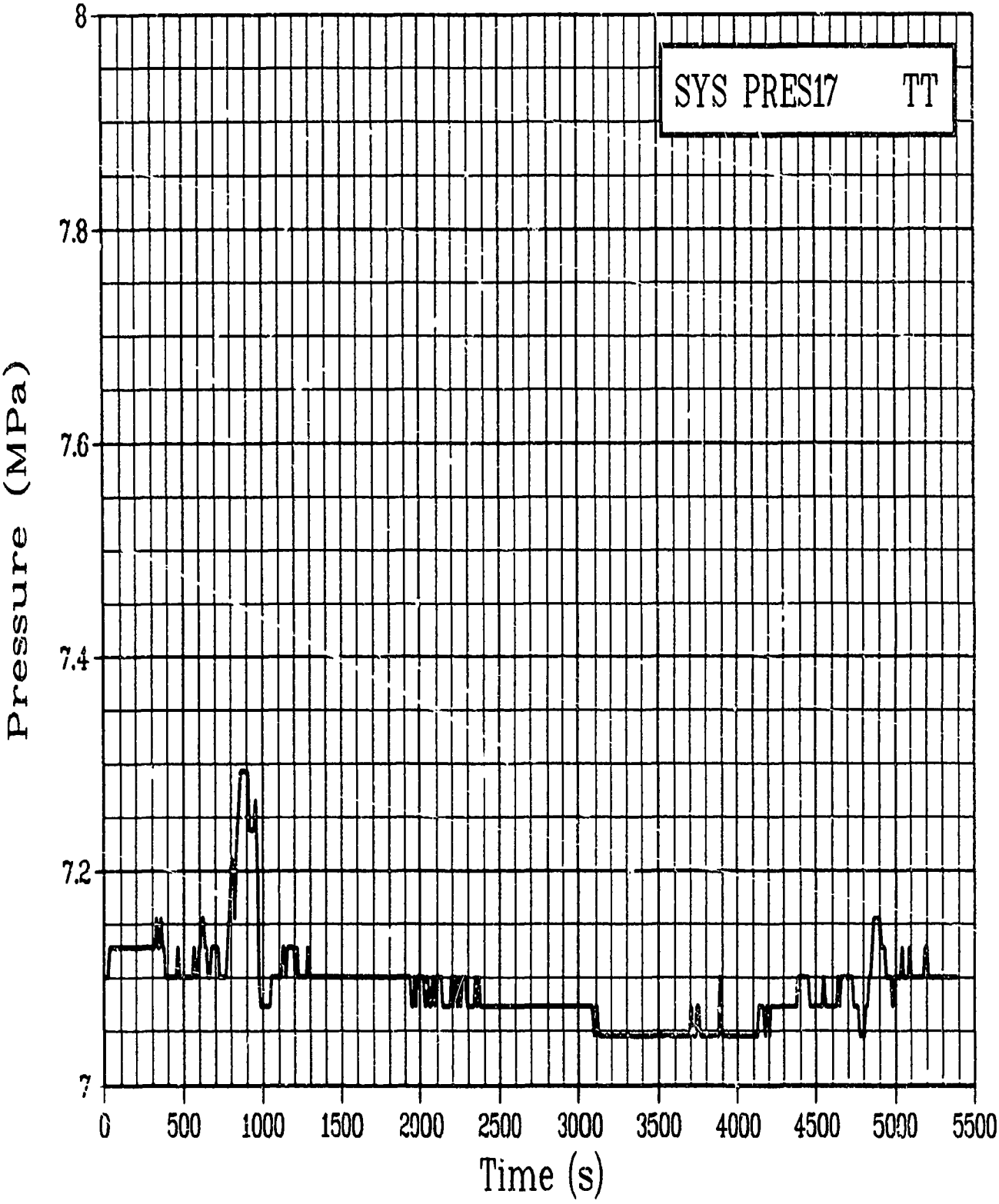

Figure C-49. Coolant pressure in the IPT outlet, 0-17 MPa range during Test PR-1 instrument checkout (calibration not shown) (SYS PRES17 TT).

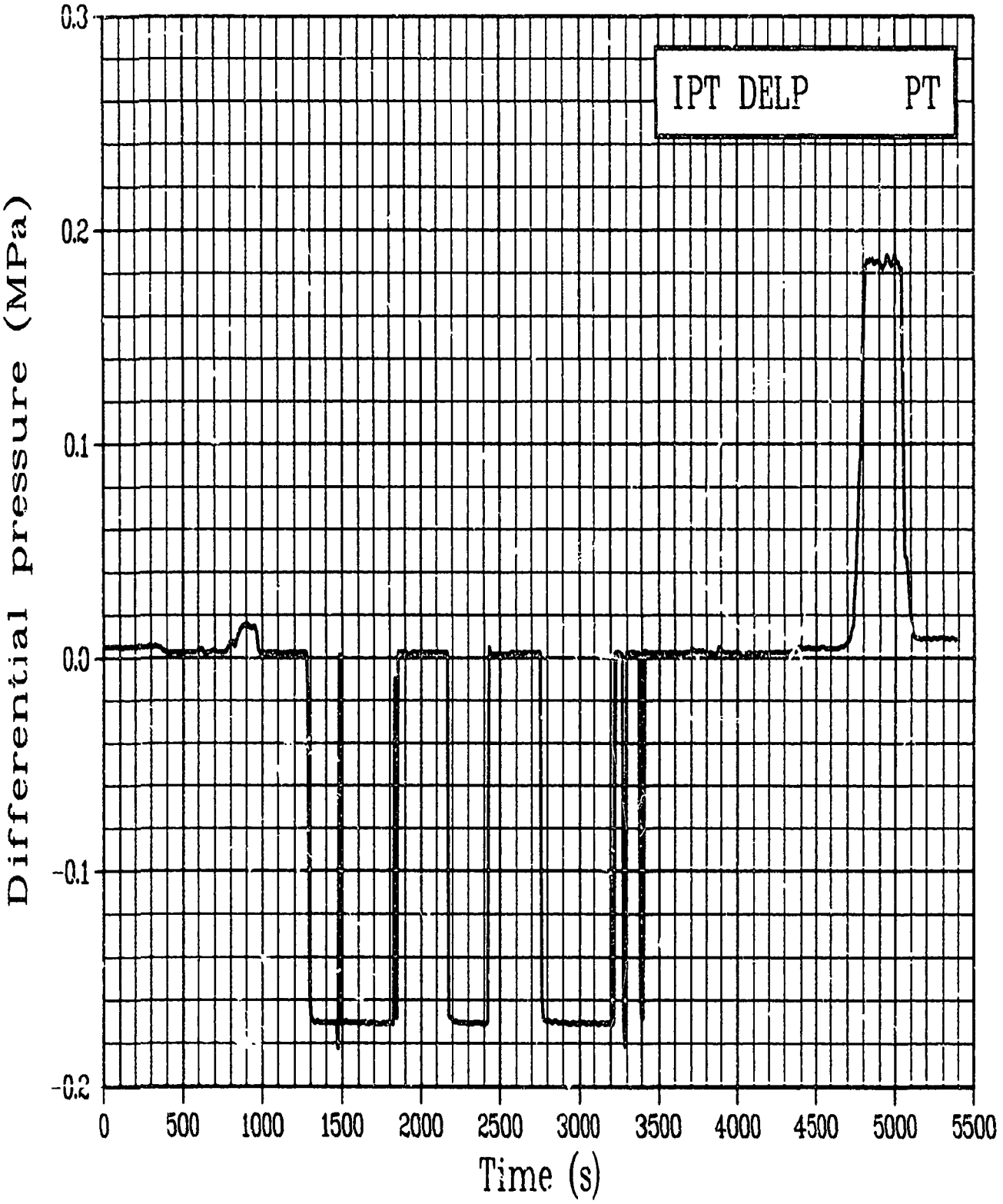

Figure C--50. Differential pressure across the in-pile tube during Test PR-1 instrument checkout (calibration not shown) (IPT DELP PT).

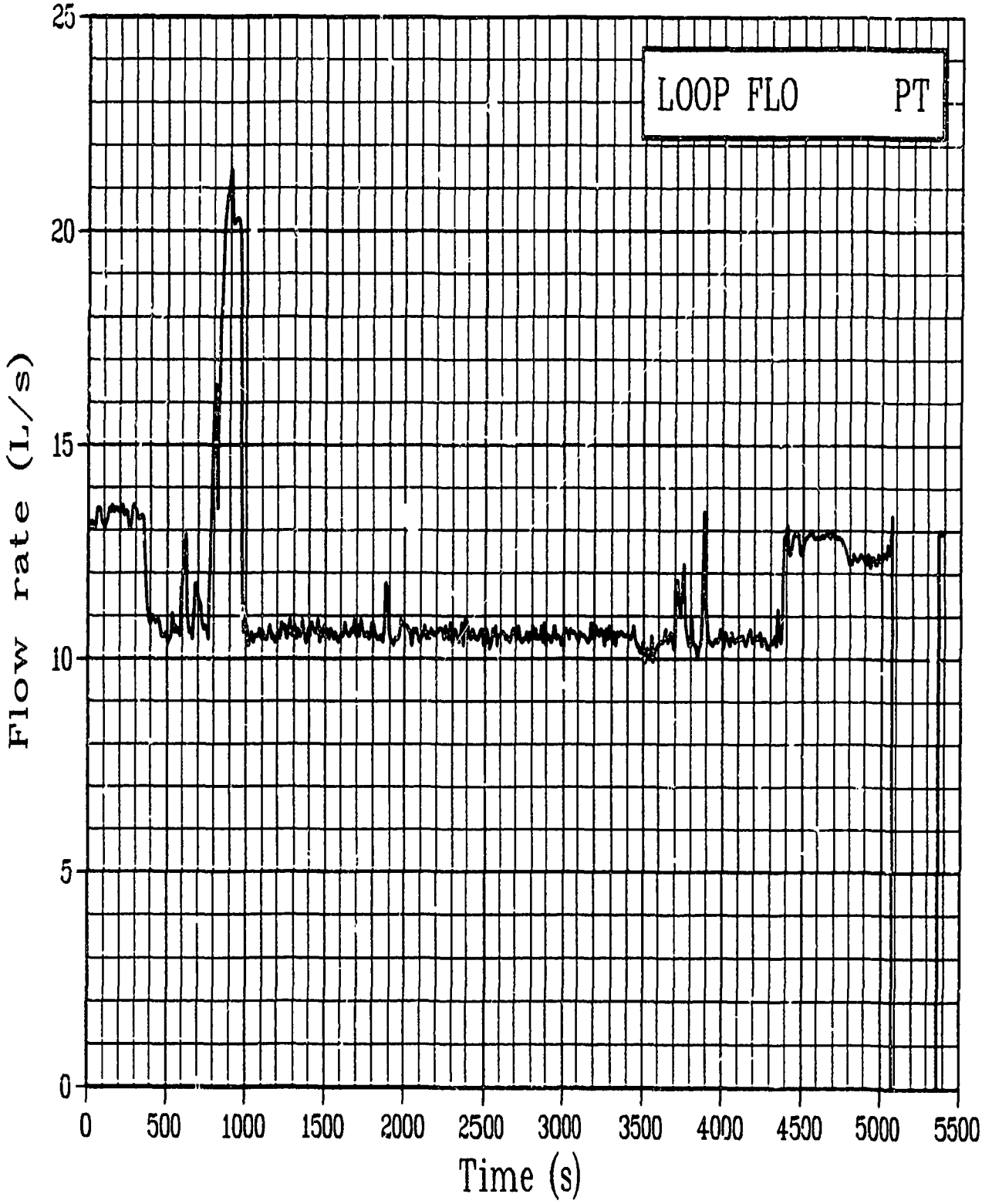

Figure C-51. Volumetric flow rate in experimental loop system during Test PR-1 instrument checkout (calibration not shown) (LOOP FLO PT).

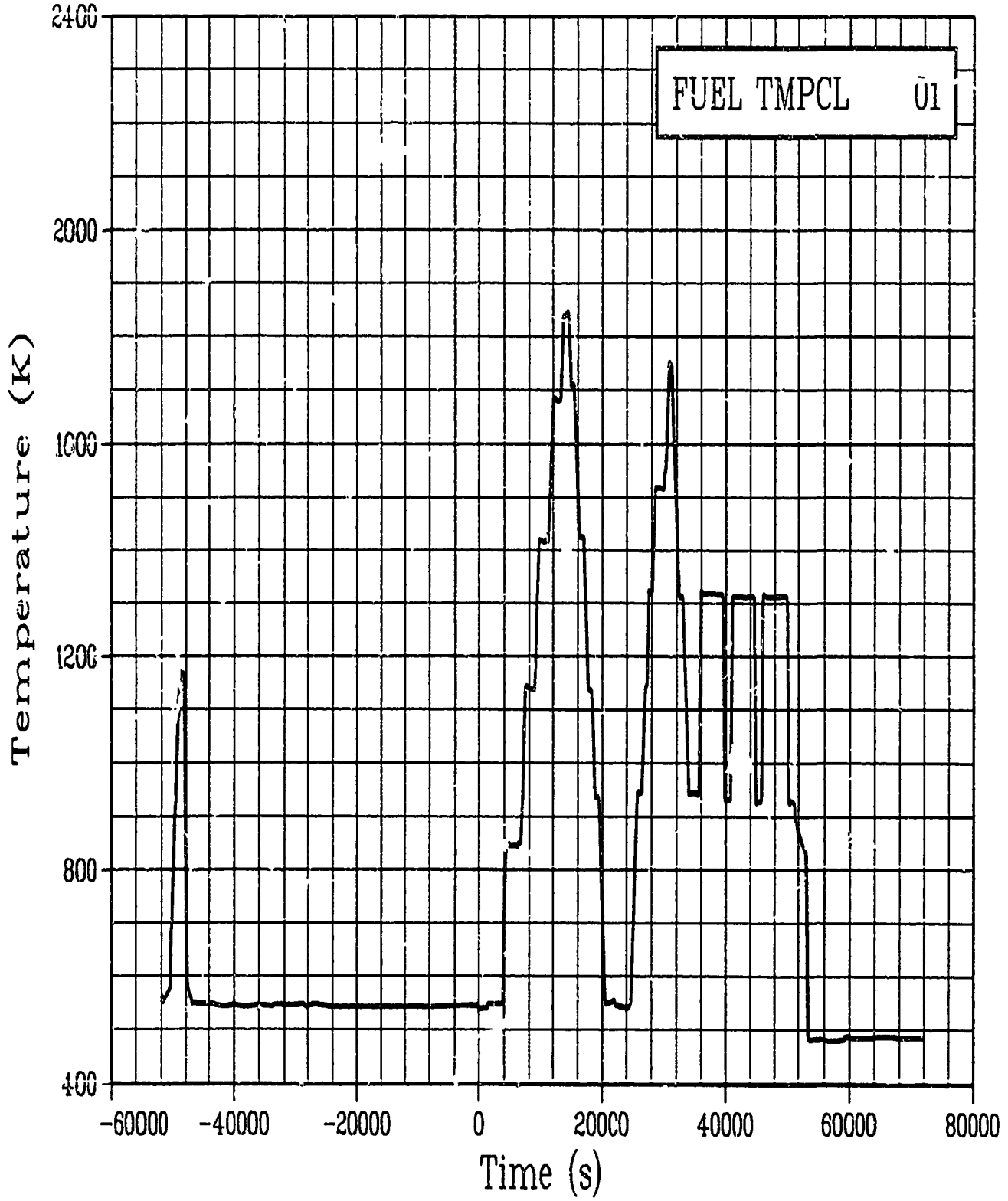

Figure C-52. Fuel centerline temperature Rod GC 524-1, 0.4521 m during Test PR-1 power calibration and preconditioning periods (FUEL TMPCL 01).

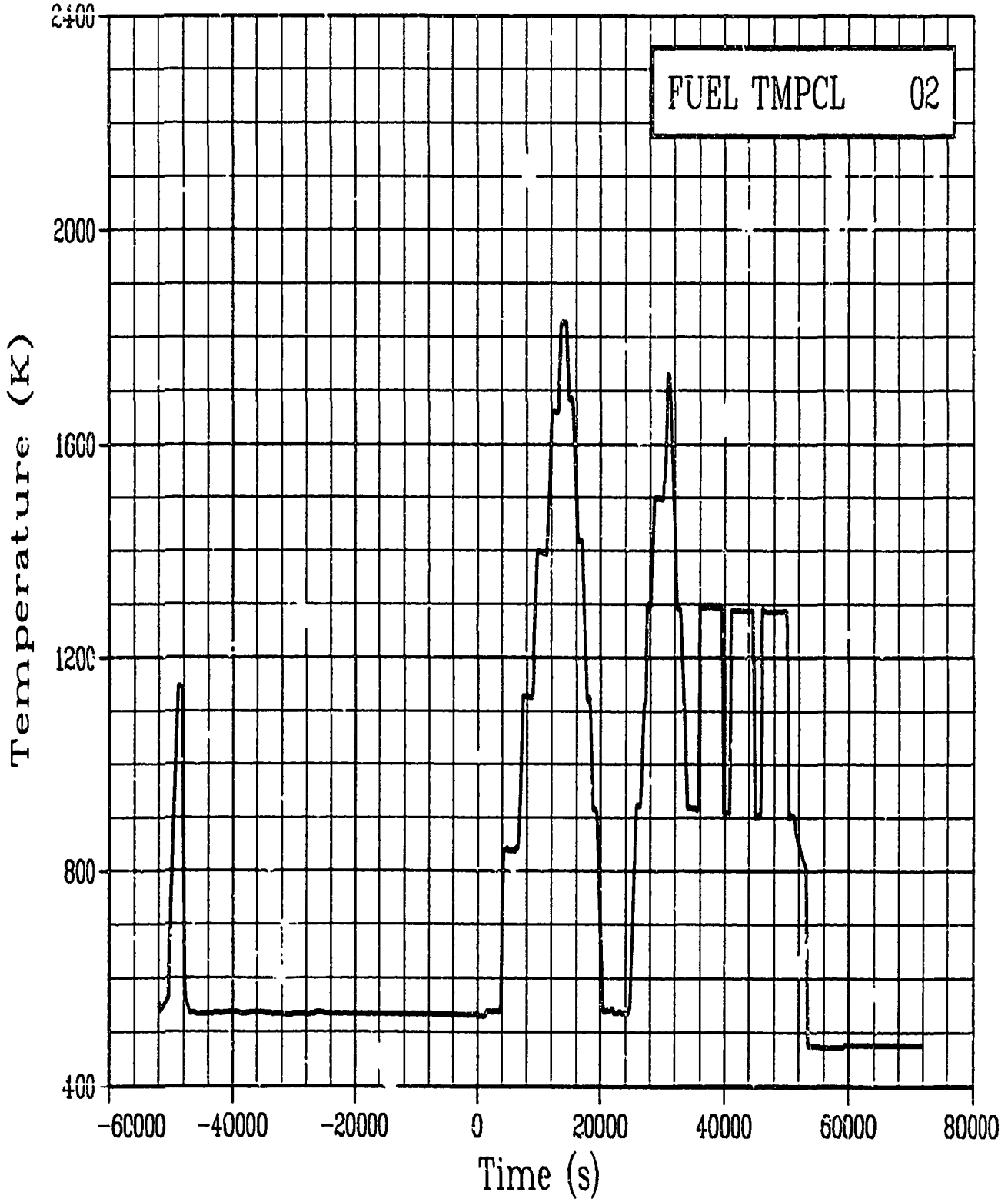

Figure C-53. Fuel centerline temperature Rod GC 524-2, 0.4521 m during Test PR-1 power calibration and preconditioning periods (FUEL TMPCL 02).

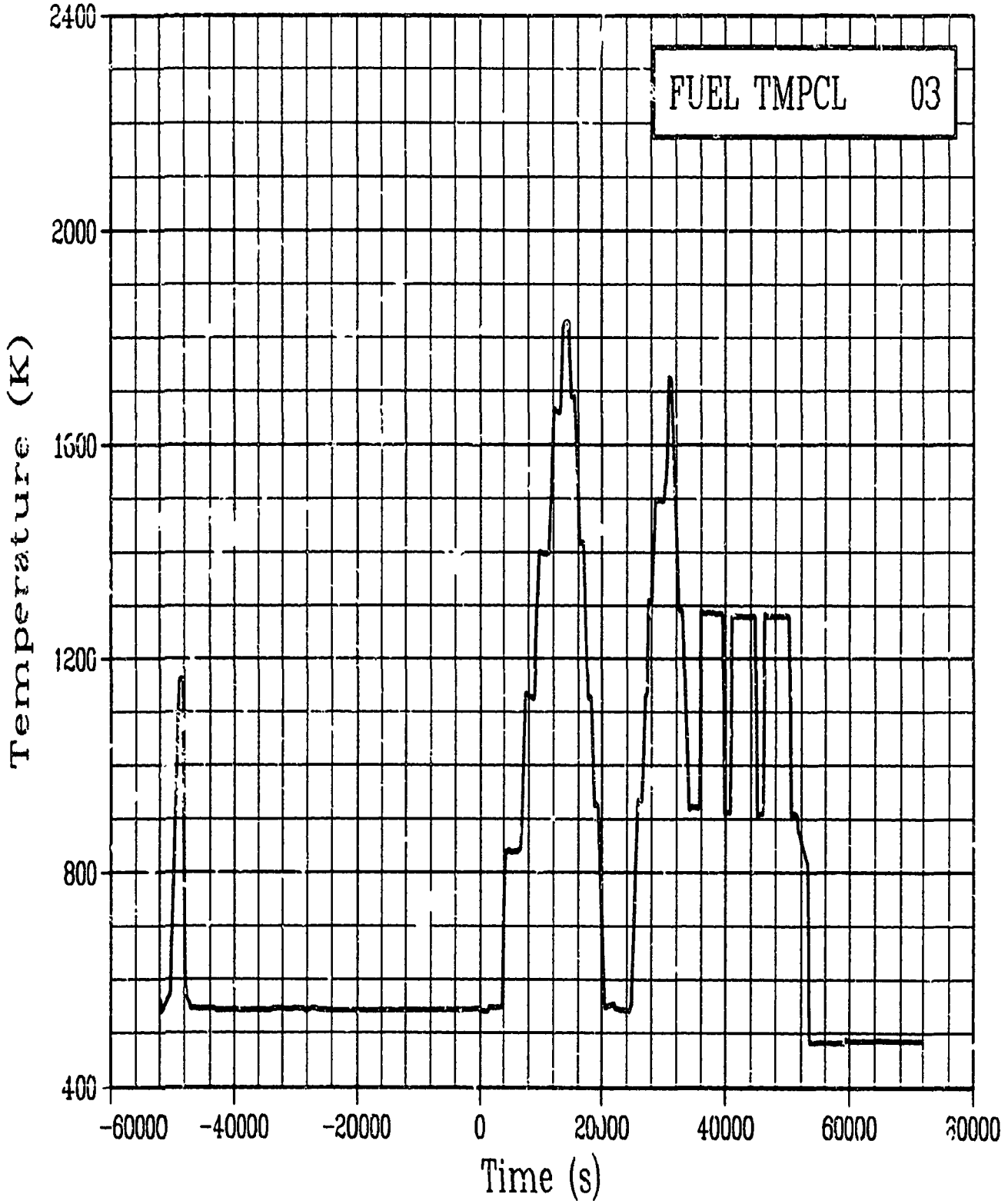

Figure C-54. Fuel centerline temperature Rod GC 524-3, 0.4521 m during Test PR-1 power calibration and preconditioning periods (FUEL TMPCL 03).

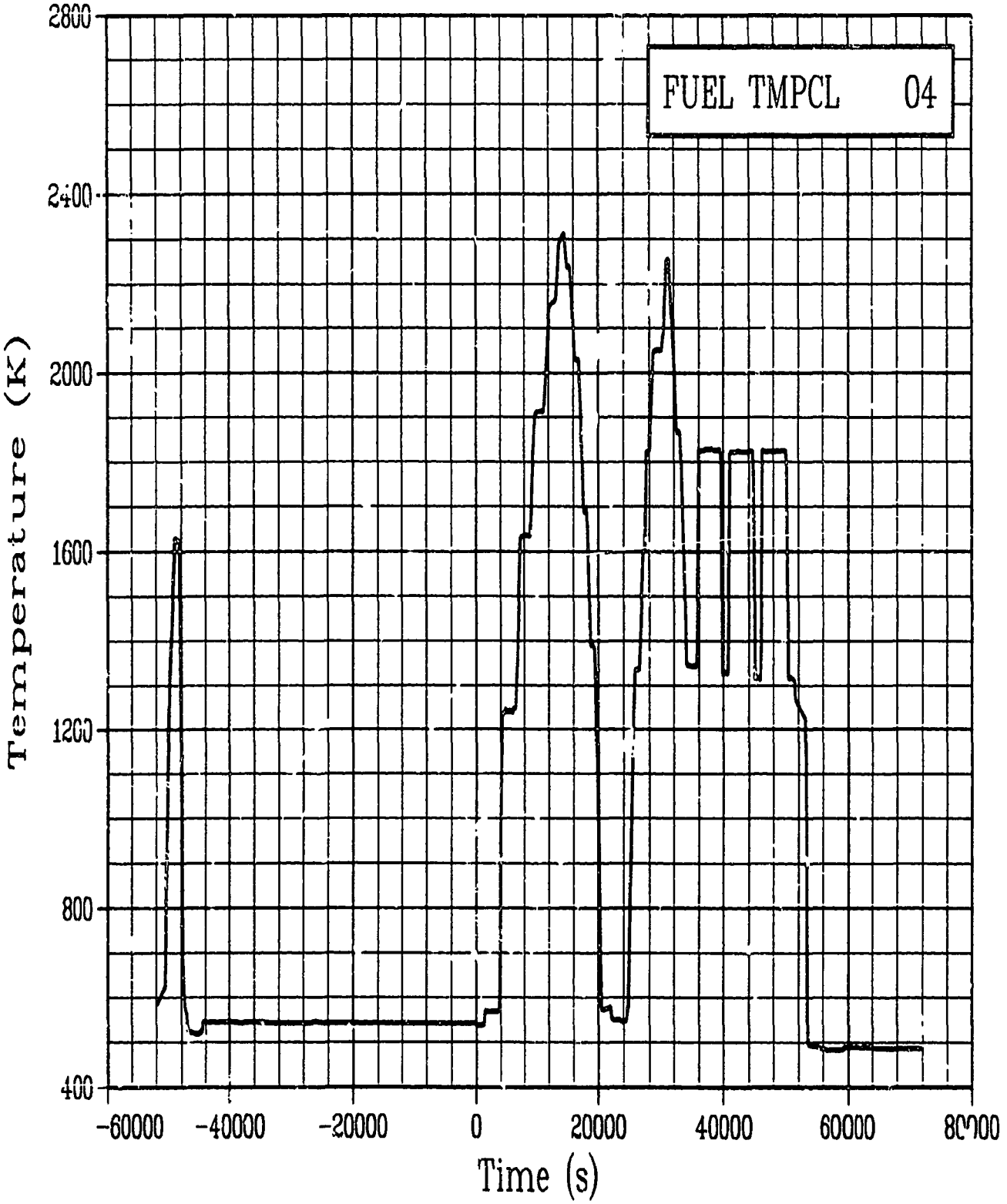

Figure C-55. Fuel centerline temperature Rod GC 524-4, 0.4521 m during Test PR-1 power calibration and preconditioning periods (FUEL TMPCL 04).

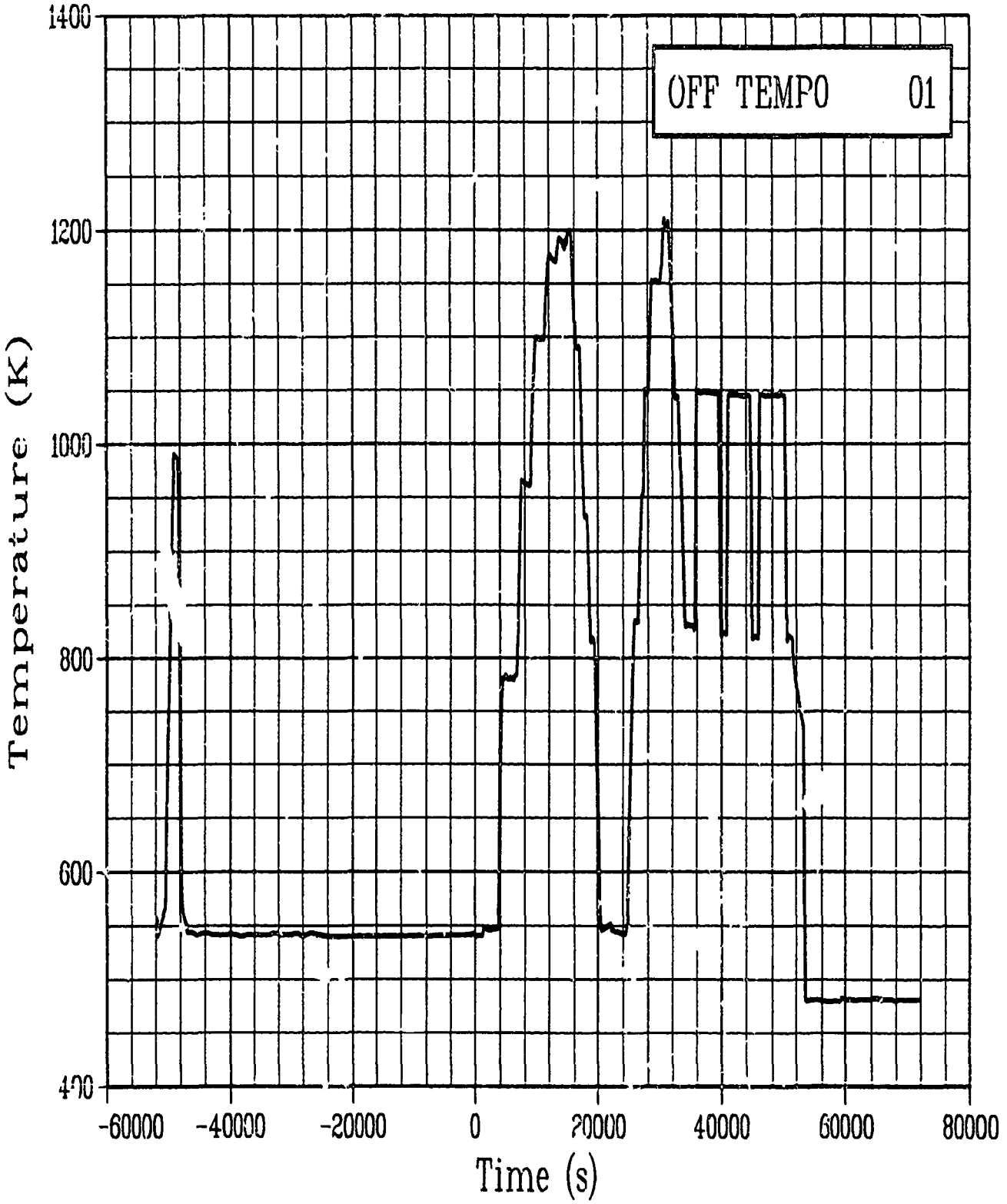

Figure C-56. Fuel off-center temperature Rod GC 524-1, at 0 degrees and 0.4521 m during Test PR-1 power calibration and preconditioning periods (OFF TEMPO 01).

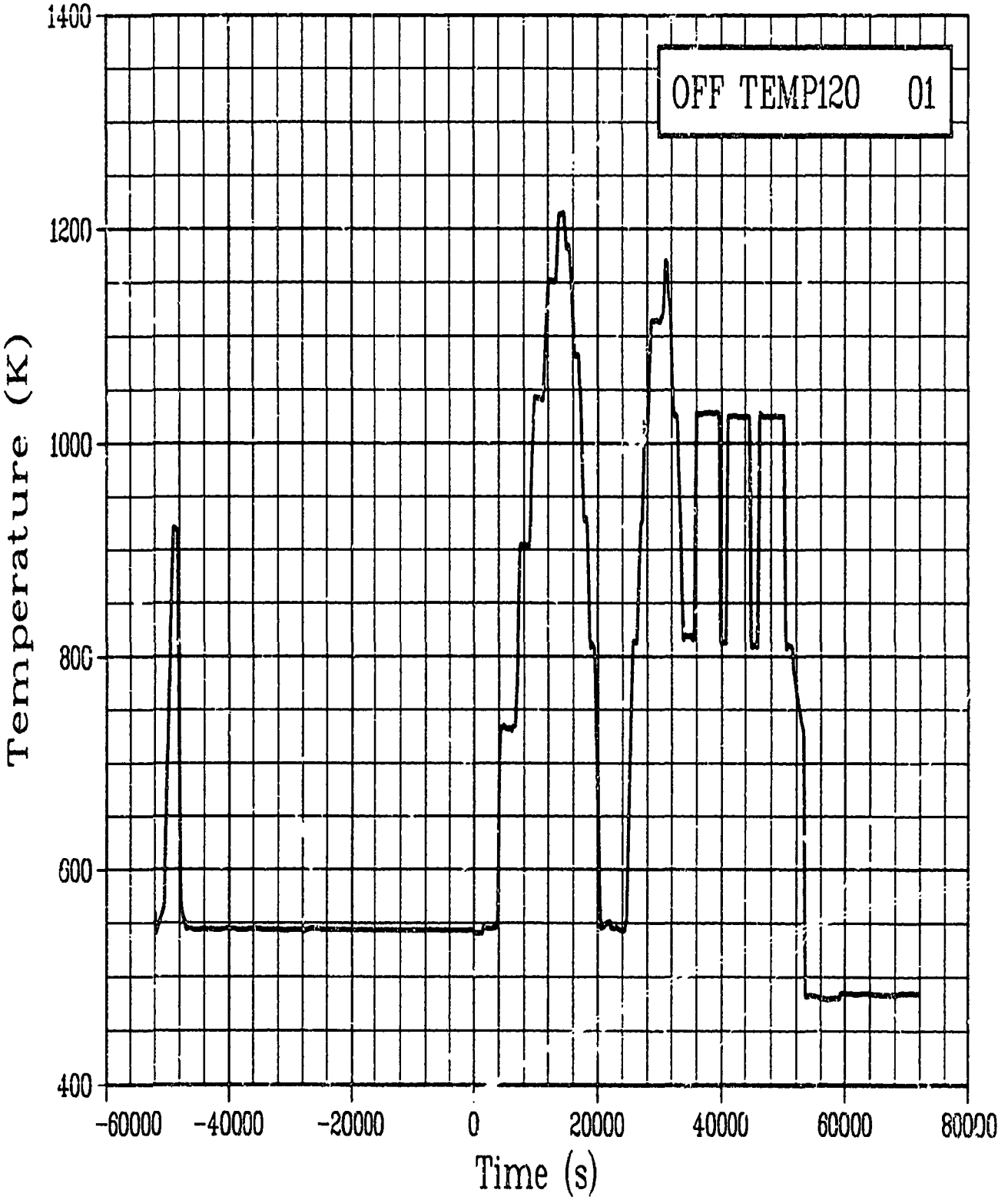

Figure C-57. Fuel off-center temperature Rod GC 524-1, at 120 degrees and 0.4521 m during Test PR-1 power calibration and preconditioning periods (OFF TEMP120 01).

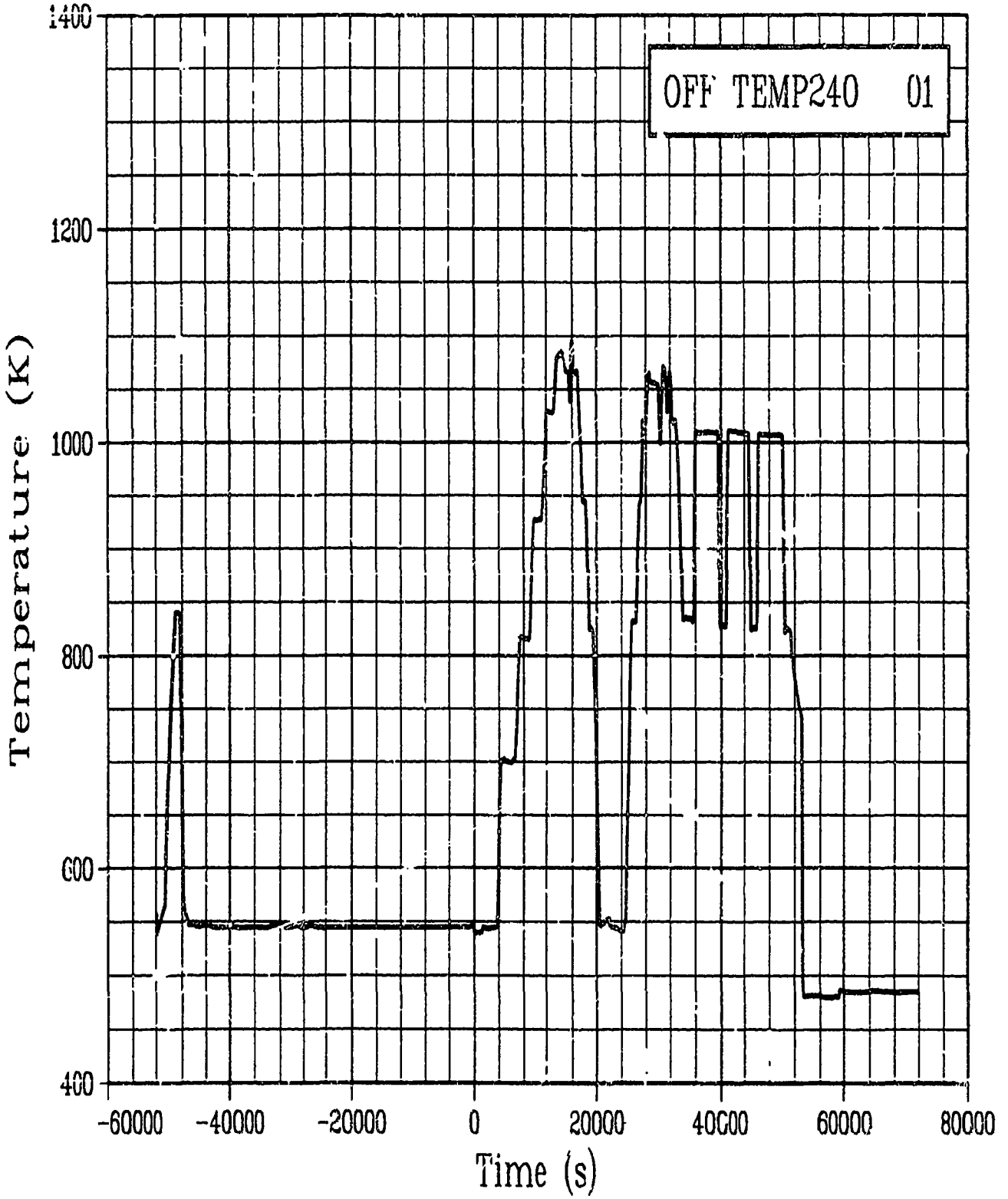

Figure C-58. Fuel off-center temperature Rod GC 524-1, at 240 degrees and 0.4521 m during Test PR-1 power calibration and preconditioning periods (OFF TEMP240 01).

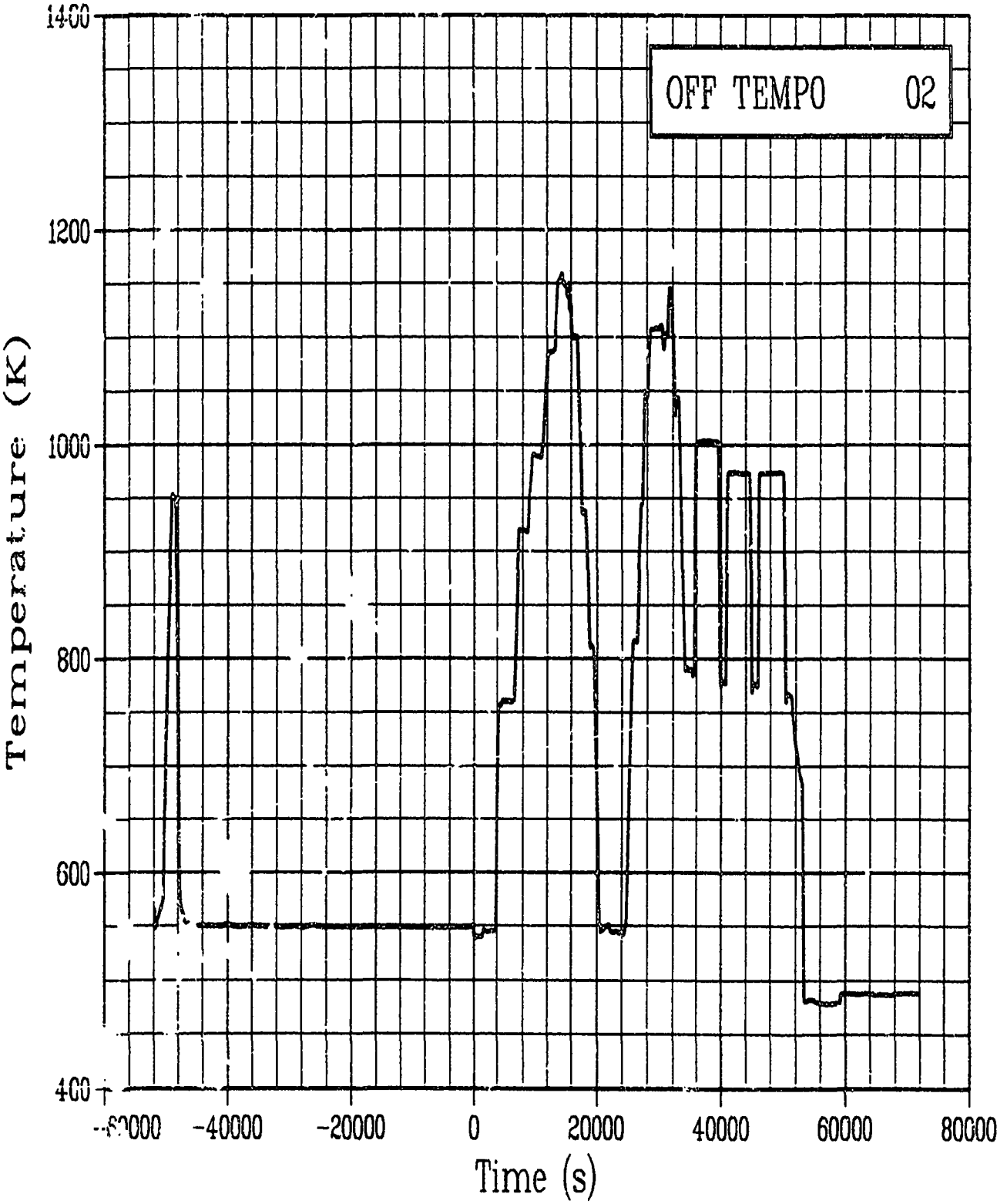

Figure 3-59. Fuel off-center temperature Rod GC 524-2, at 0 degrees and 0.4521 m during Test PR-1 power calibration and preconditioning periods (OFF TEMPO 02).

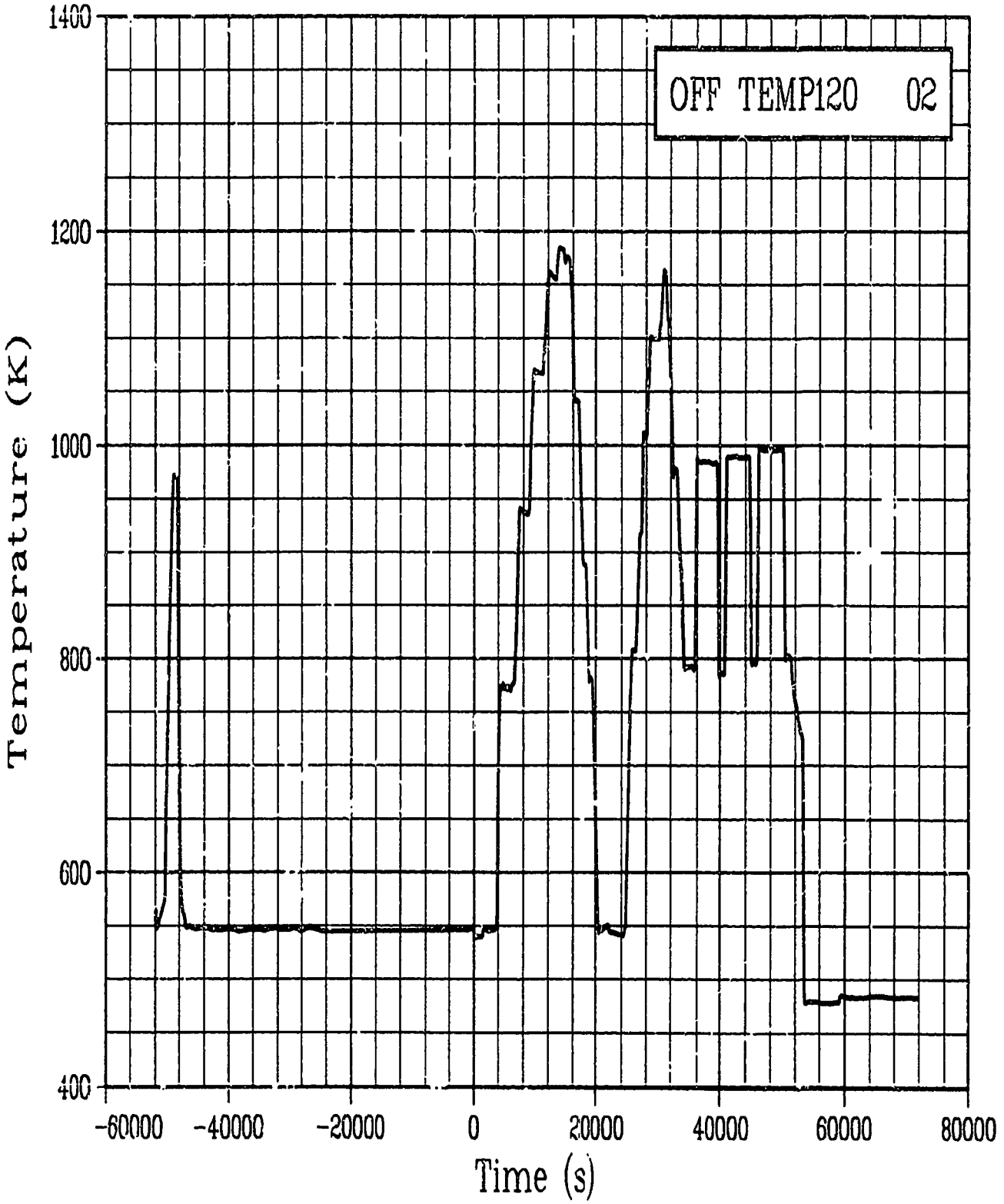

Figure C-60. Fuel off-center temperature Rod GC 524-2, at 120 degrees and 0.4521 m during Test PR-1 power calibration and preconditioning periods (OFF TEMP120 02).

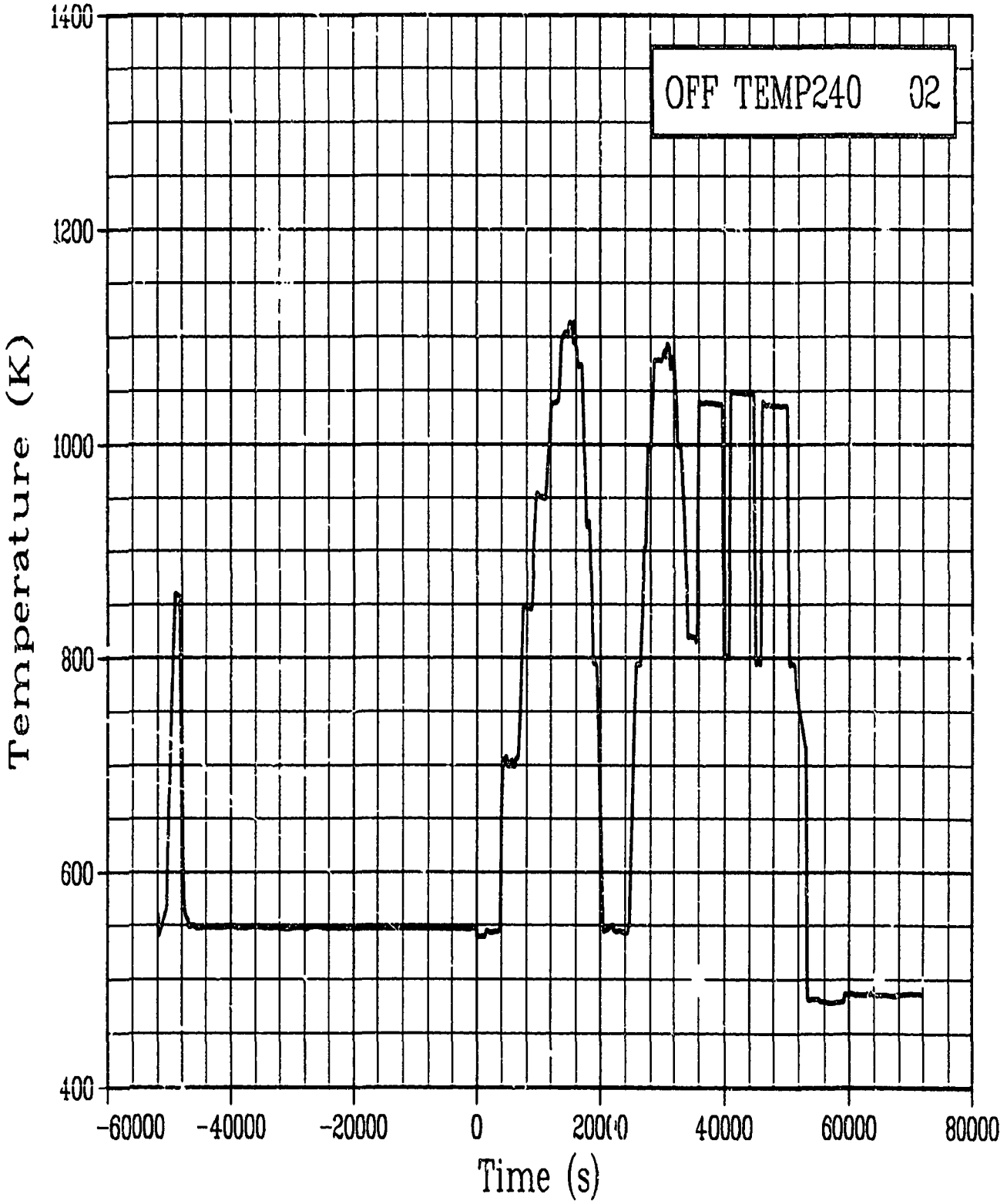

Figure C-61. Fuel off-center temperature Rod GC 524-2, at 240 degrees and 0.4521 m during Test PR-1 power calibration and preconditioning periods (OFF TEMP240 02).

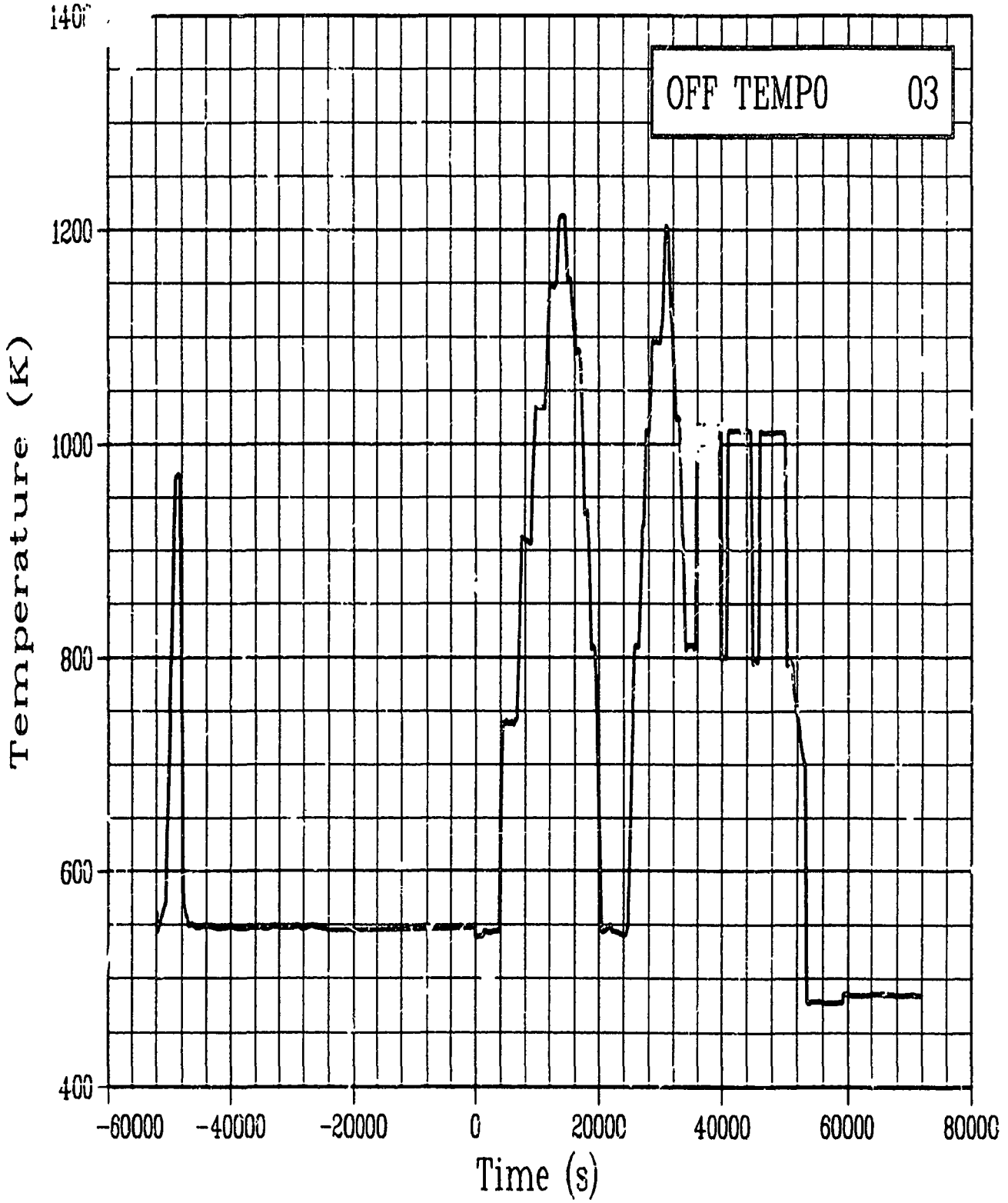

Figure C-62. Fuel off-center temperature Rod GC 524-3, at 0 degrees and 0.4521 m during Test PR-1 power calibration and preconditioning periods (OFF TEMP0 03).

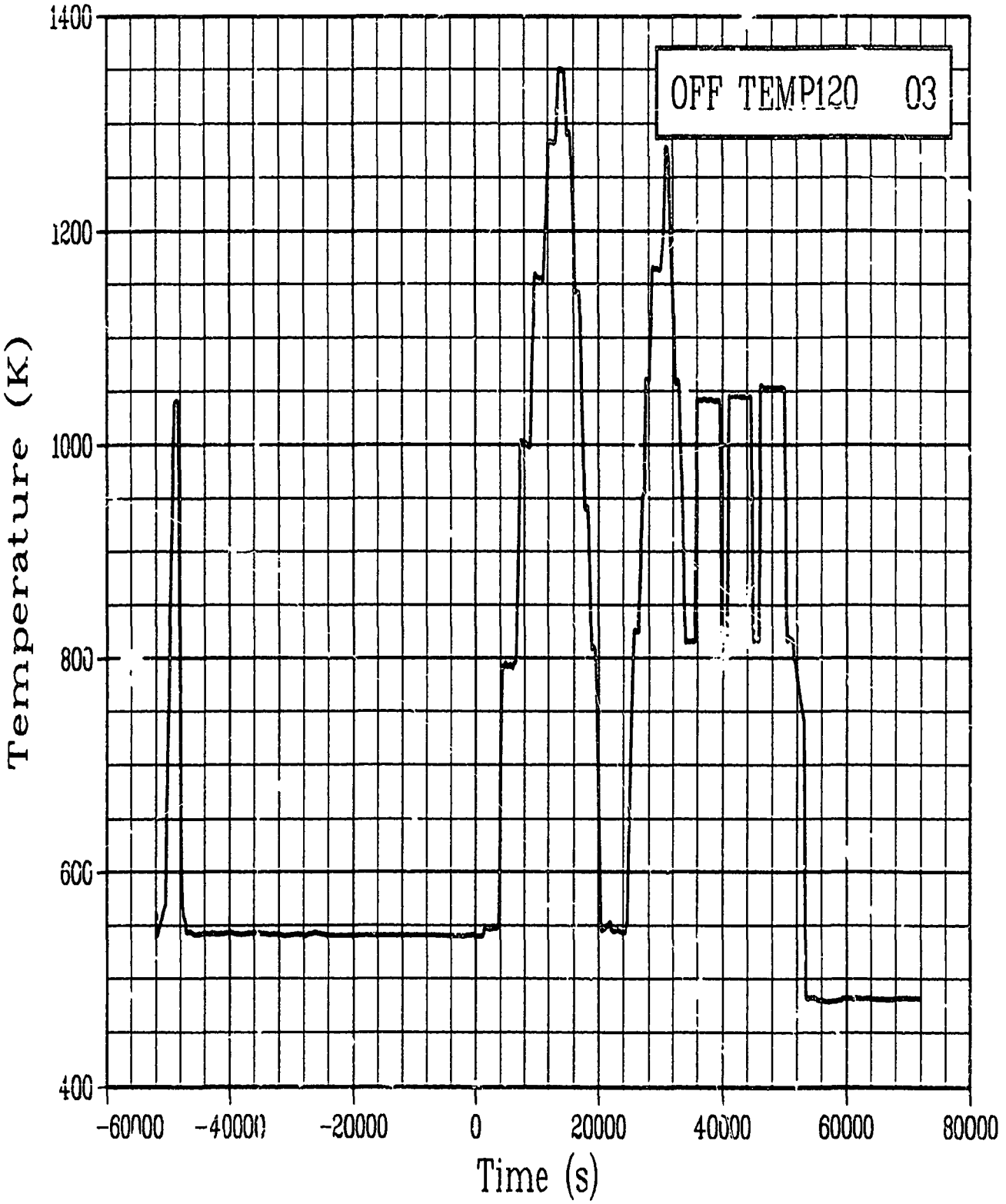

Figure C-63. Fuel off-center temperature Rod GC 524-3, at 120 degrees and 0.4521 m during Test PR-1 power calibration and preconditioning periods (OFF TEMP120 03).

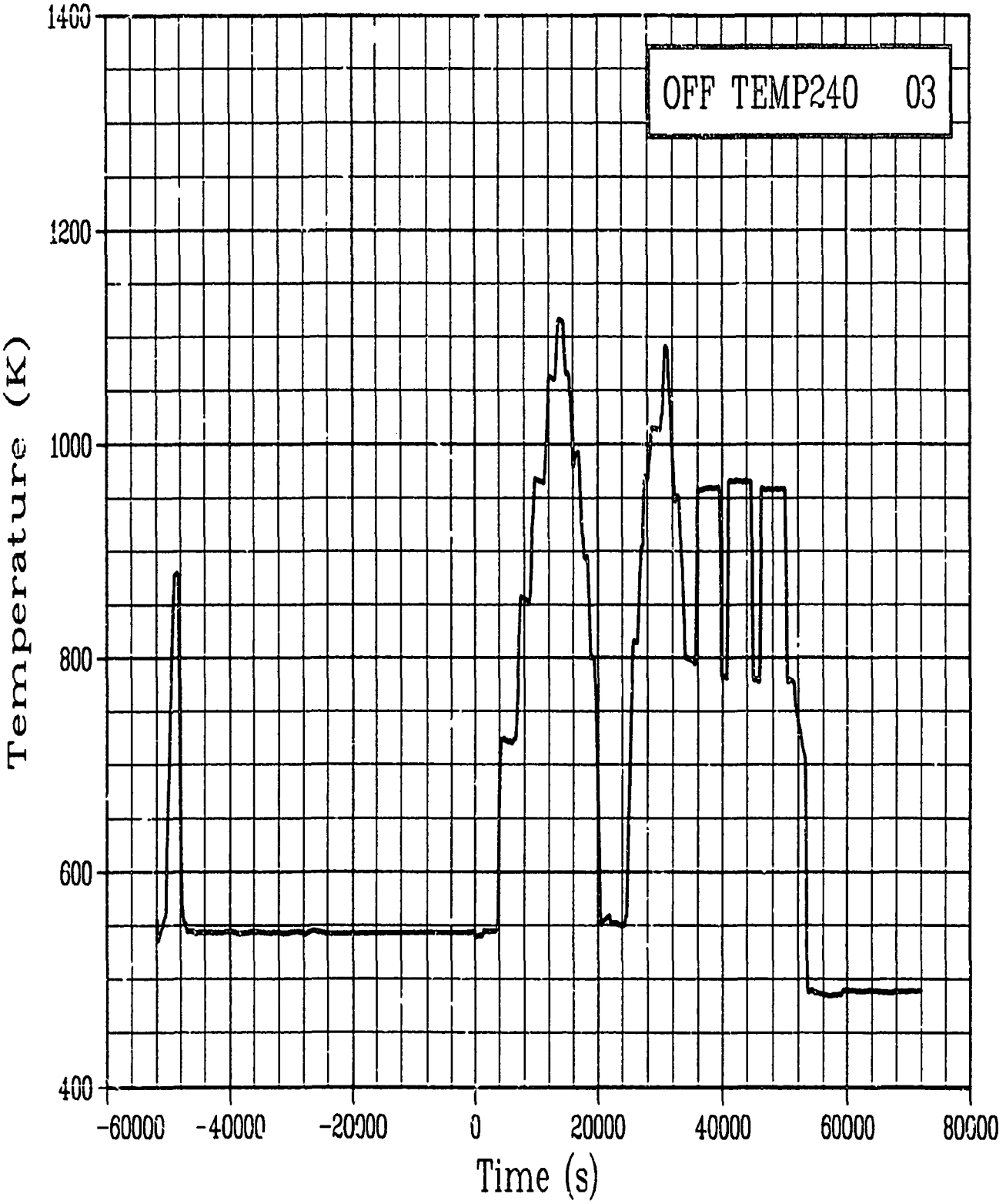

Figure C-64. Fuel off-center temperature Rod GC 524-3, at 240 degrees and 0.4521 m during Test PR-1 power calibration and preconditioning periods (OFF TEMP240 03).

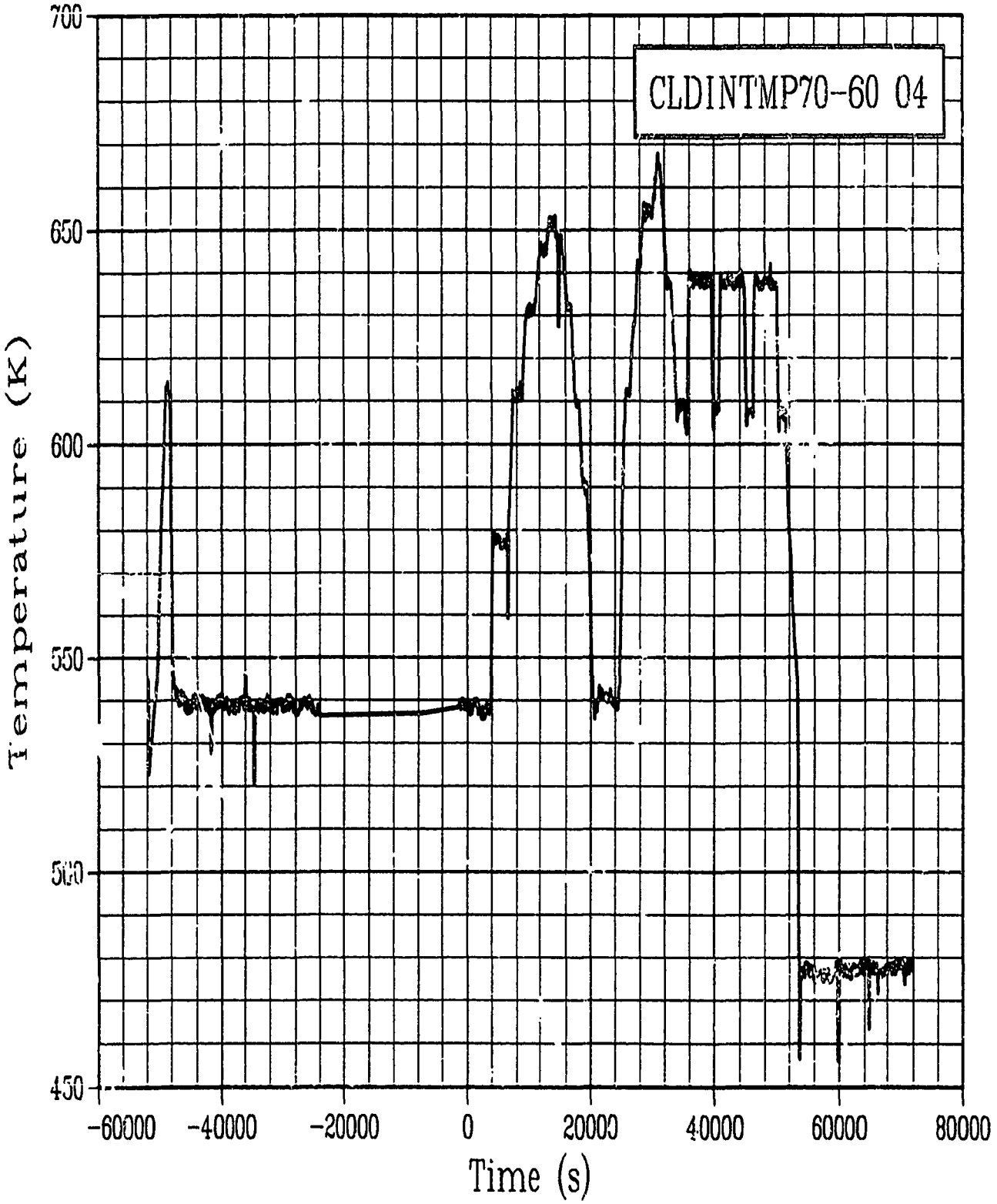

Figure C-65. Cladding internal temperature Rod GC 524-4, 0.70 m and 60 degrees during Test PR-1 power calibration and preconditioning periods (CLDINTMP70-60 04).

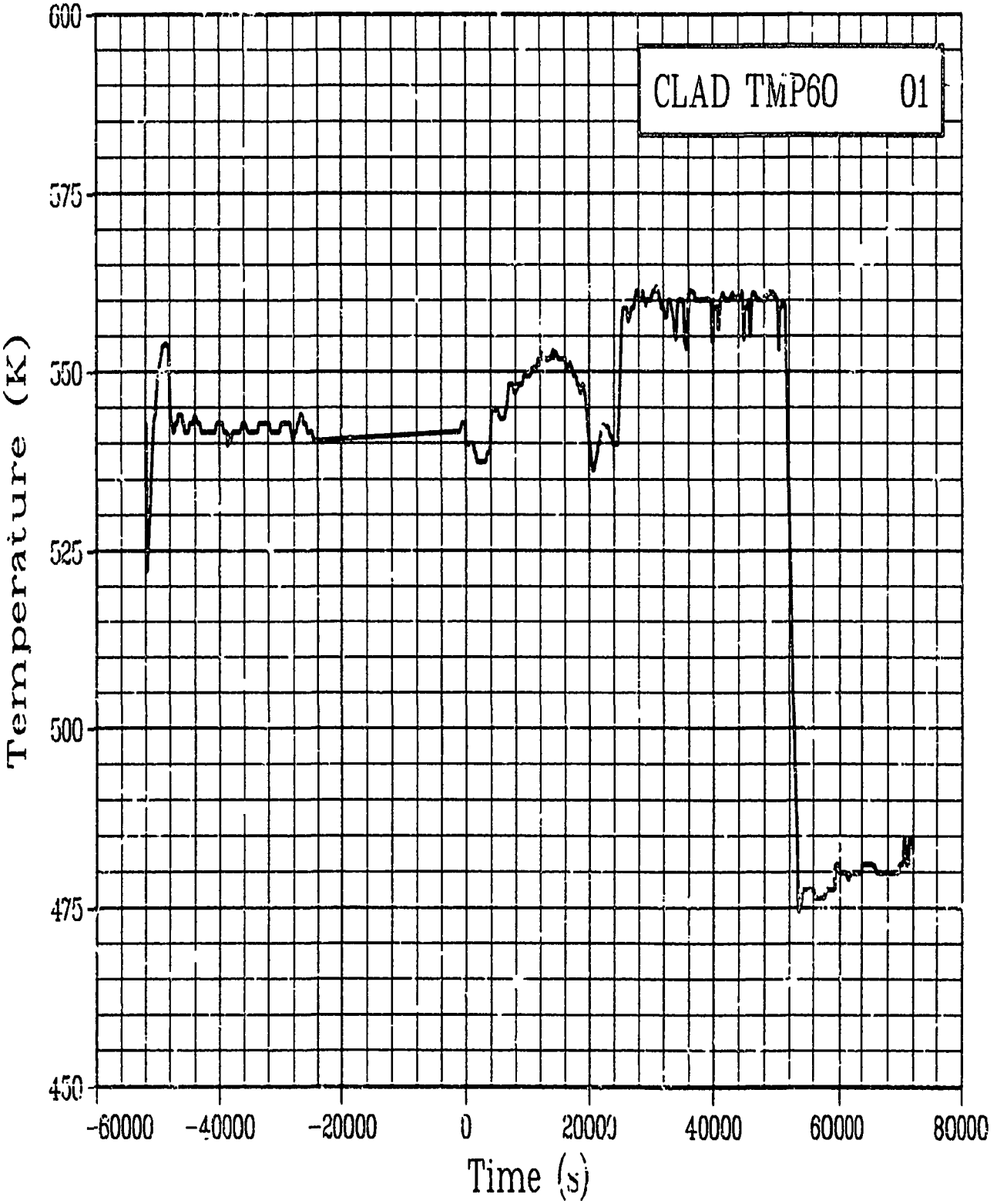

Figure C-66. Cladding surface temperature Rod GC 524-1, at 60 degrees and 0.4521 m during Test PR-1 power calibration and preconditioning periods (CLAD TMP60 01).

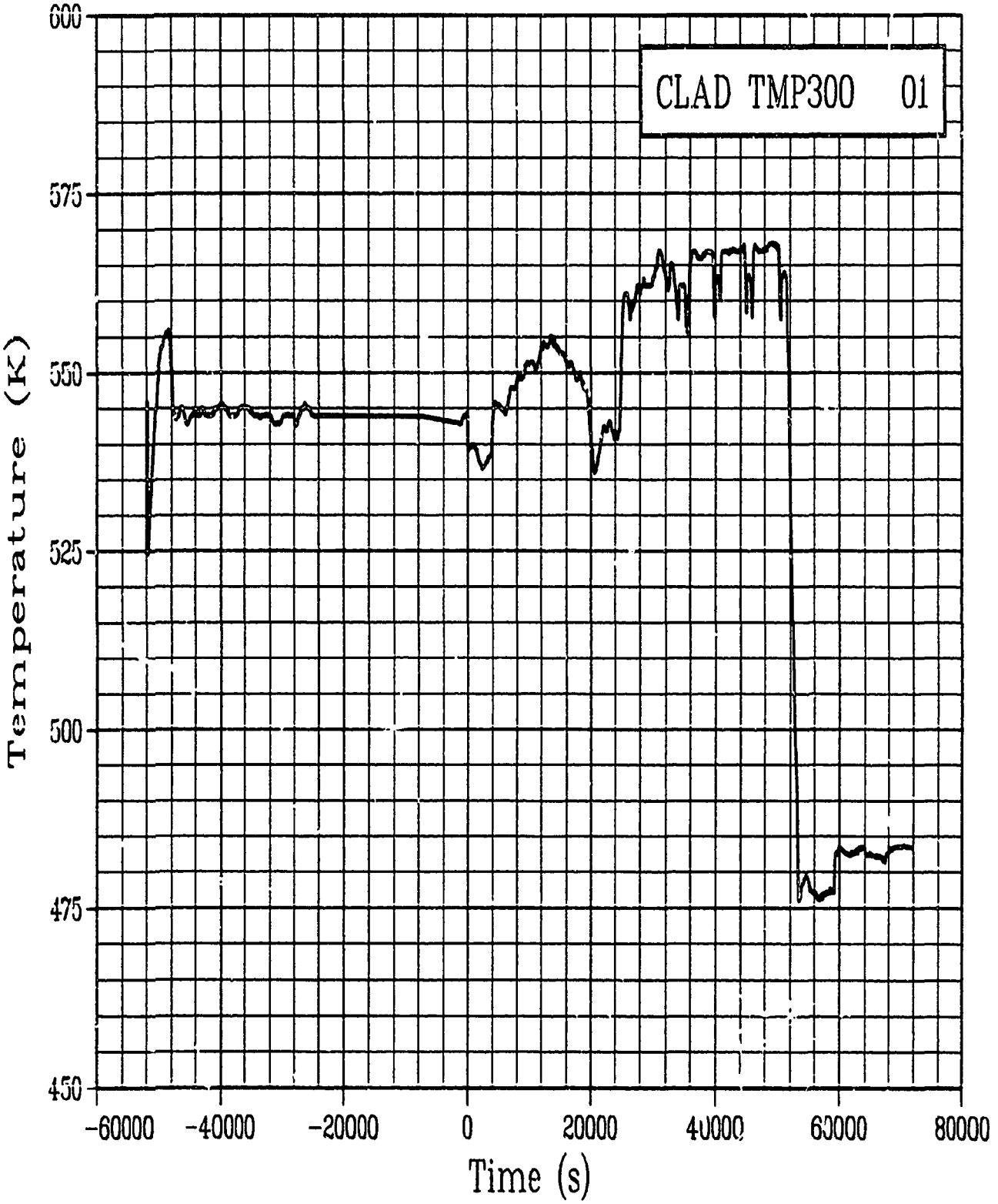

Figure C-67. Cladding surface temperature Rod GC 524-1, at 300 degrees and 0.4521 m during Test PR-1 power calibration and preconditioning periods (CLAD TMP300 01).

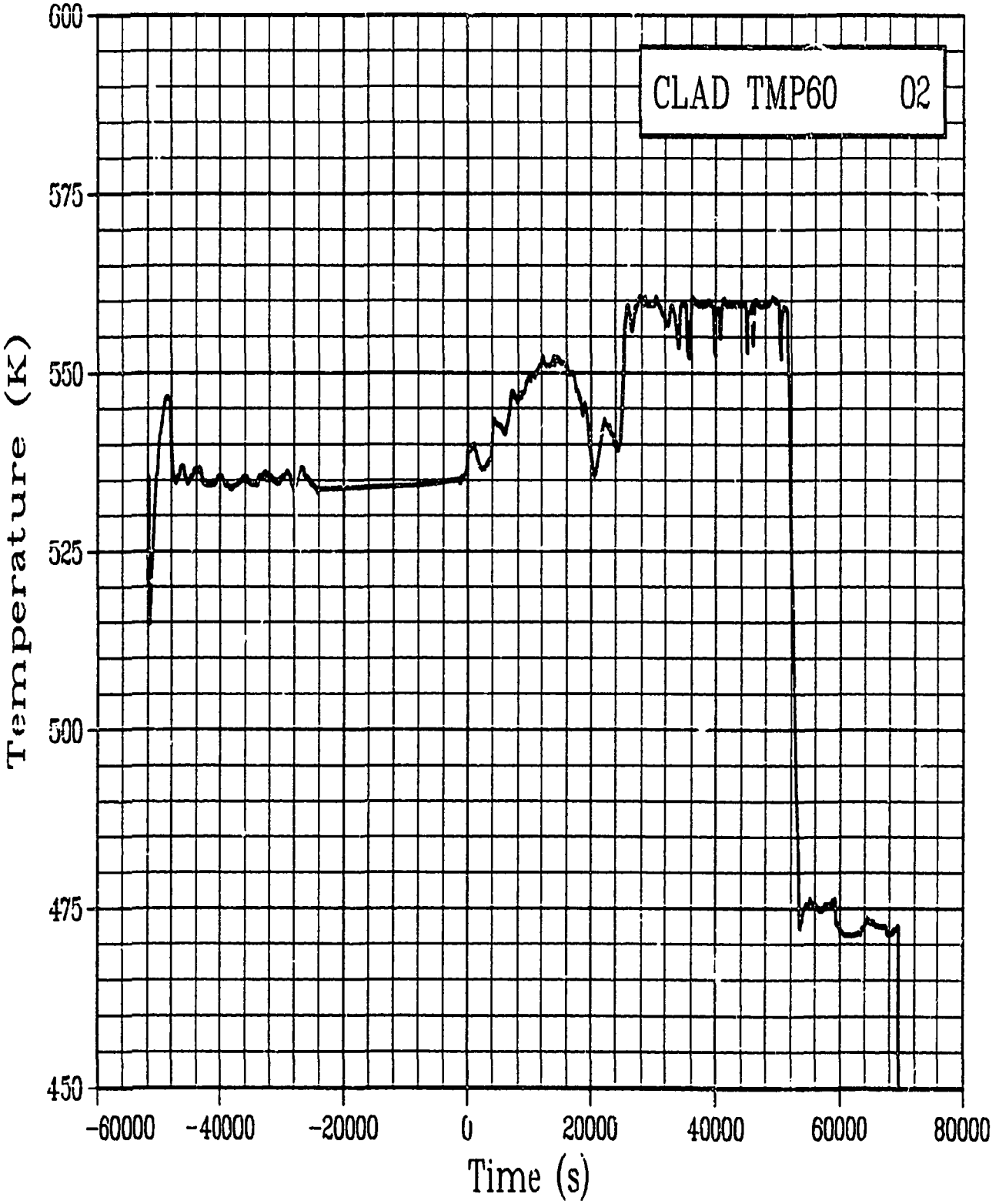

Figure C-68. Cladding surface temperature Rod GC 524-2, at 60 degrees and 0.4521 m during Test PR-1 power calibration and preconditioning periods (CLAD TMP60 02).

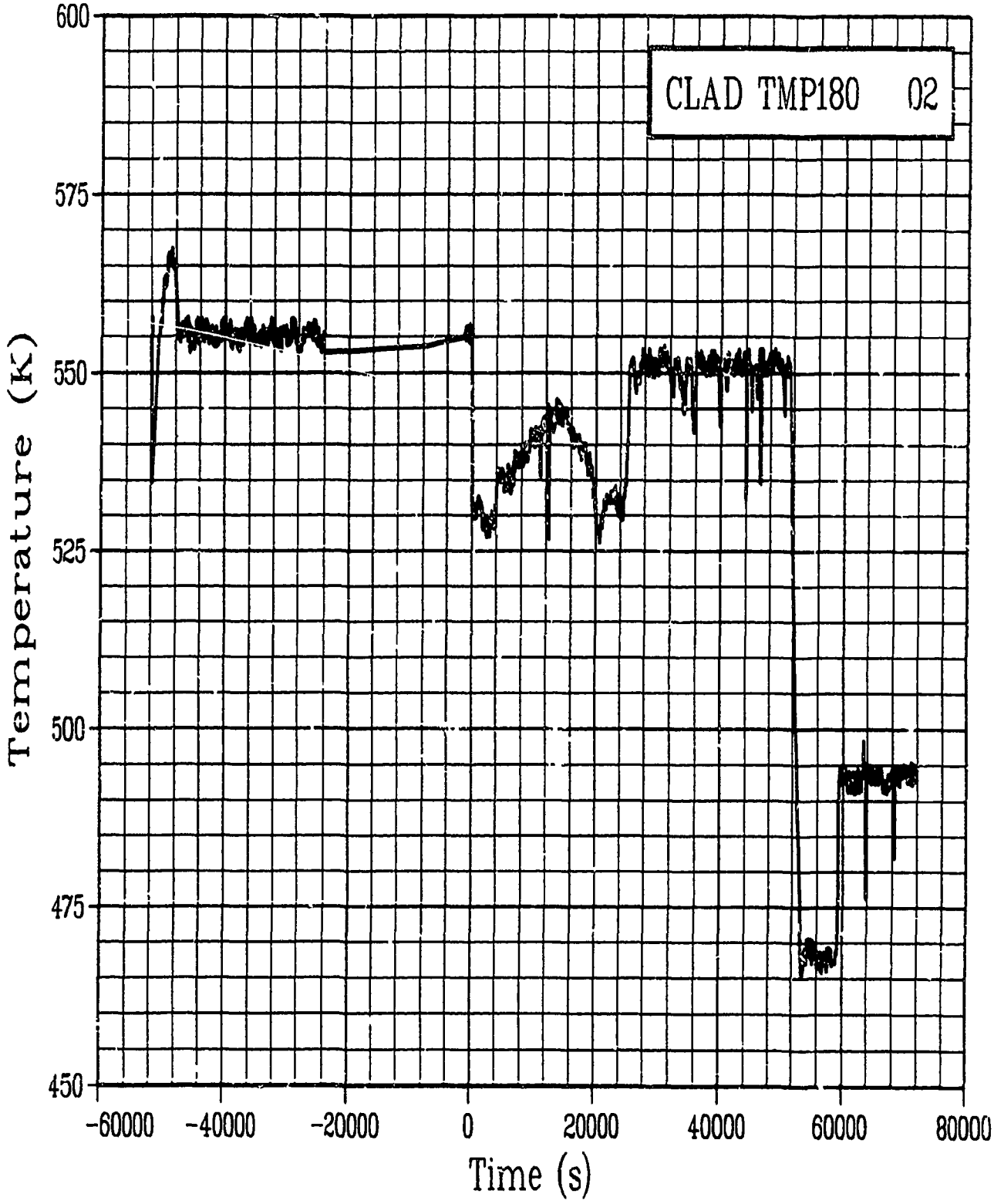

Figure C-69. Cladding surface temperature Rod GC 524-2, at 180 degrees and 0.4521 m during Test PR-1 power calibration and preconditioning periods (CLAD TMP180 02).

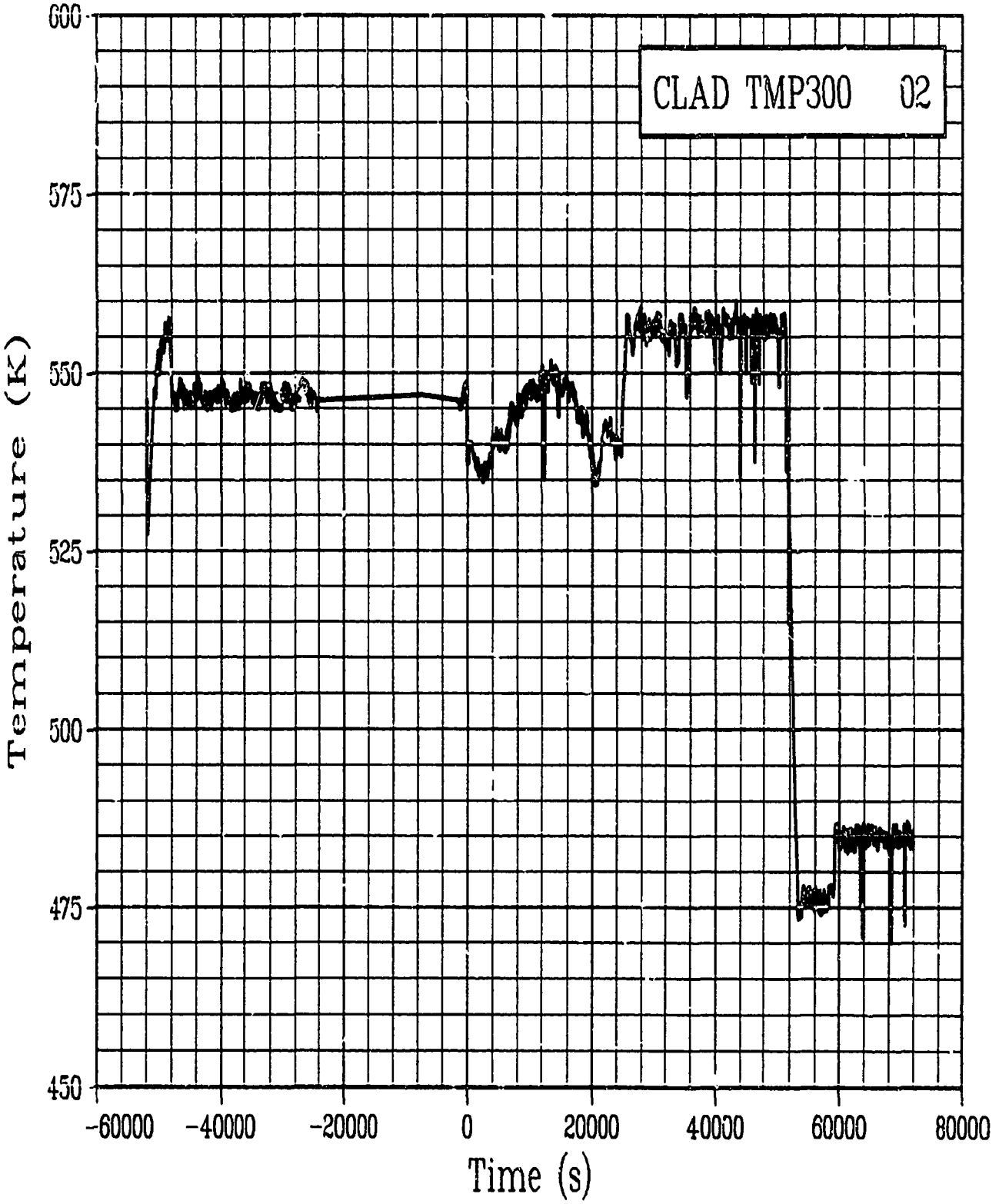

Figure C-70. Cladding surface temperature Rod GC 524-2, at 300 degrees and 0.4521 m during Test PR-1 power calibration and preconditioning periods (CLAD TMP300 02).

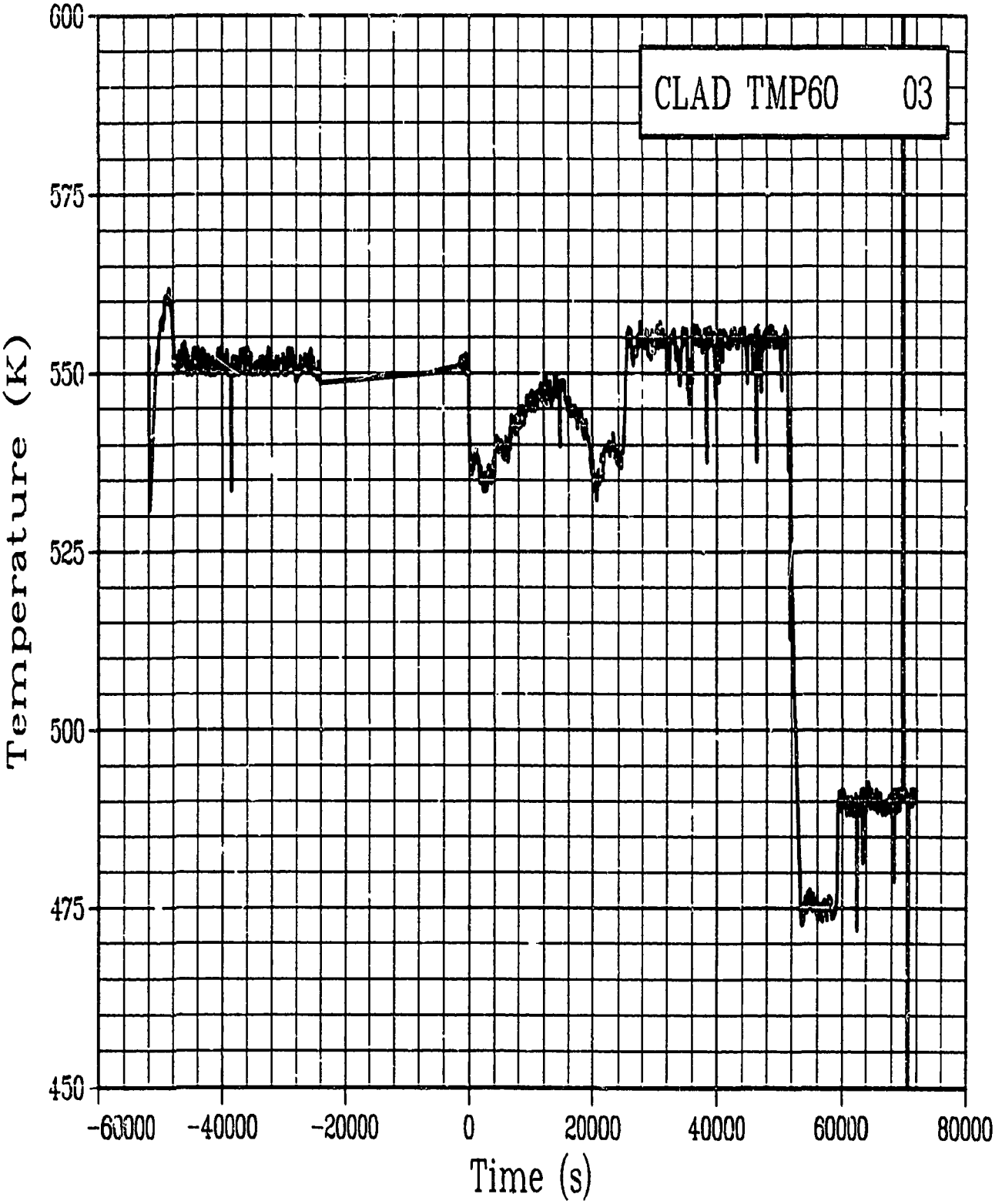

Figure C-71. Cladding surface temperature Rod GC 524-3, at 60 degrees and
ls 0.1521 m during Test PR-1 power calibration and preconditioning periods
(CLAD TMP60 03).

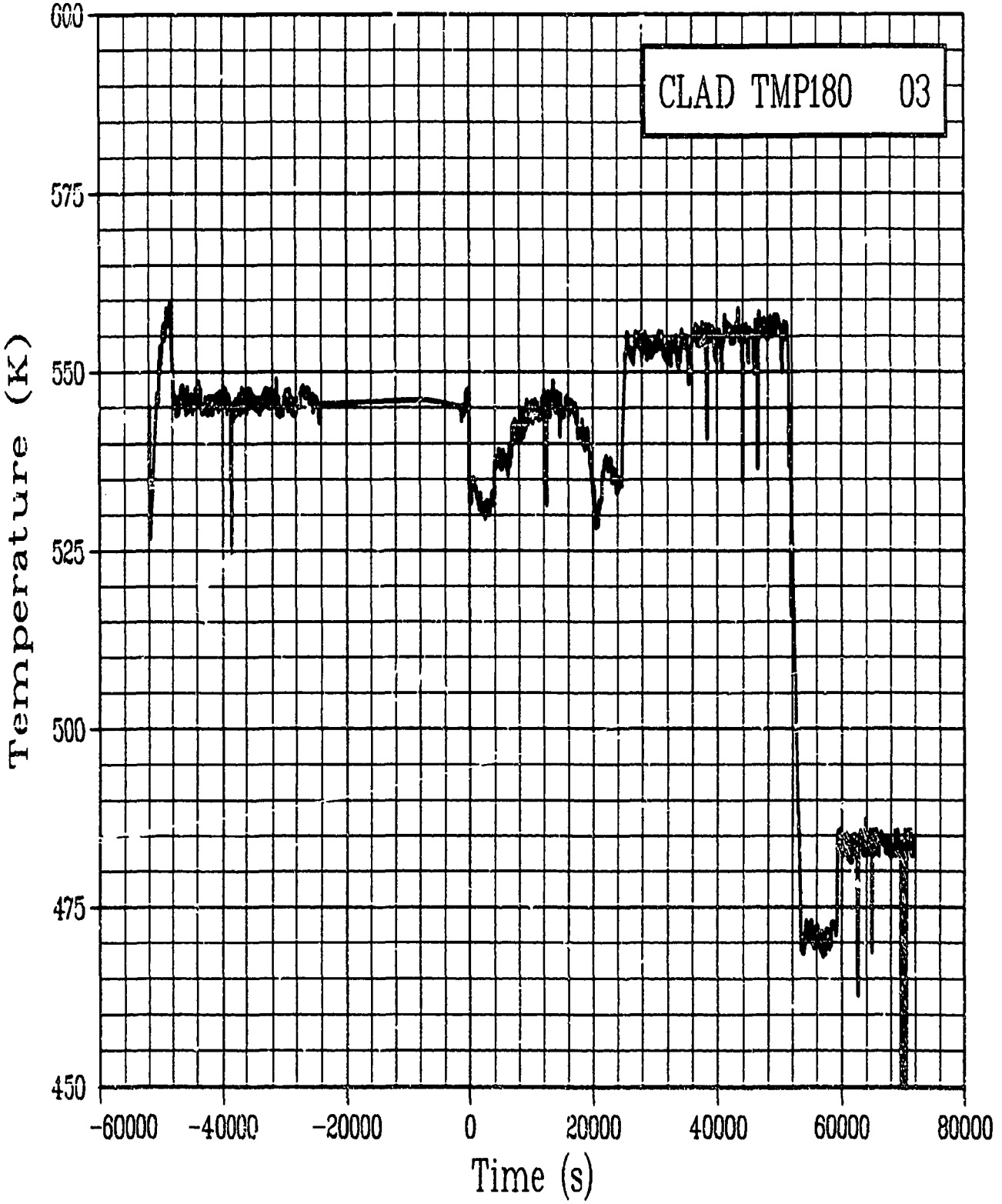

Figure C-72. Cladding surface temperature Rod GC 524-3, at 180 degrees and 0.4521 m during Test PR-1 power calibration and preconditioning periods (CLAD TMP180 03).

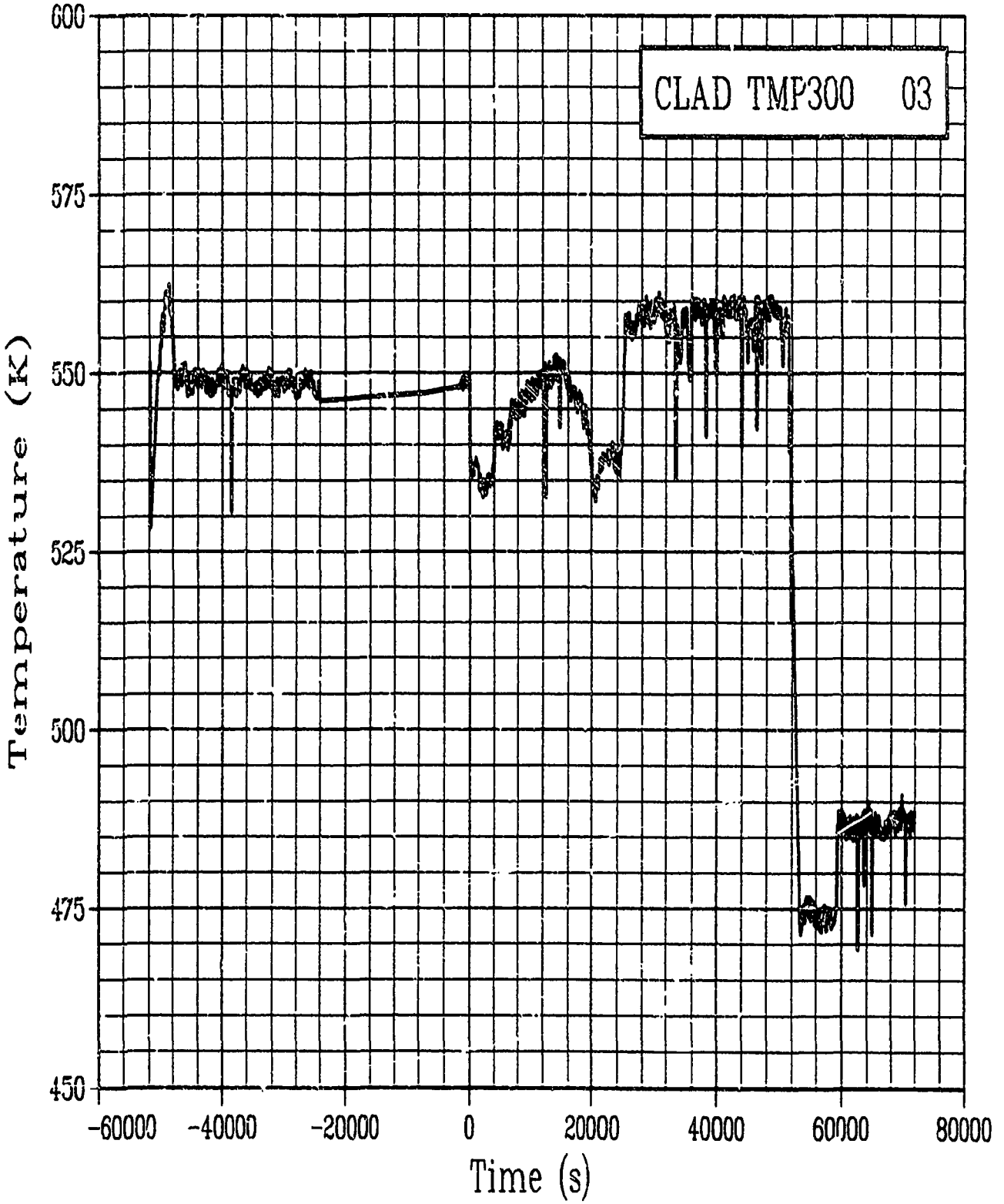

Figure C-73. Cladding surface temperature Rod GC 524-3, at 300 degrees and 0.4521 m during Test PR-1 power calibration and preconditioning periods (CLAD TMP300 03).

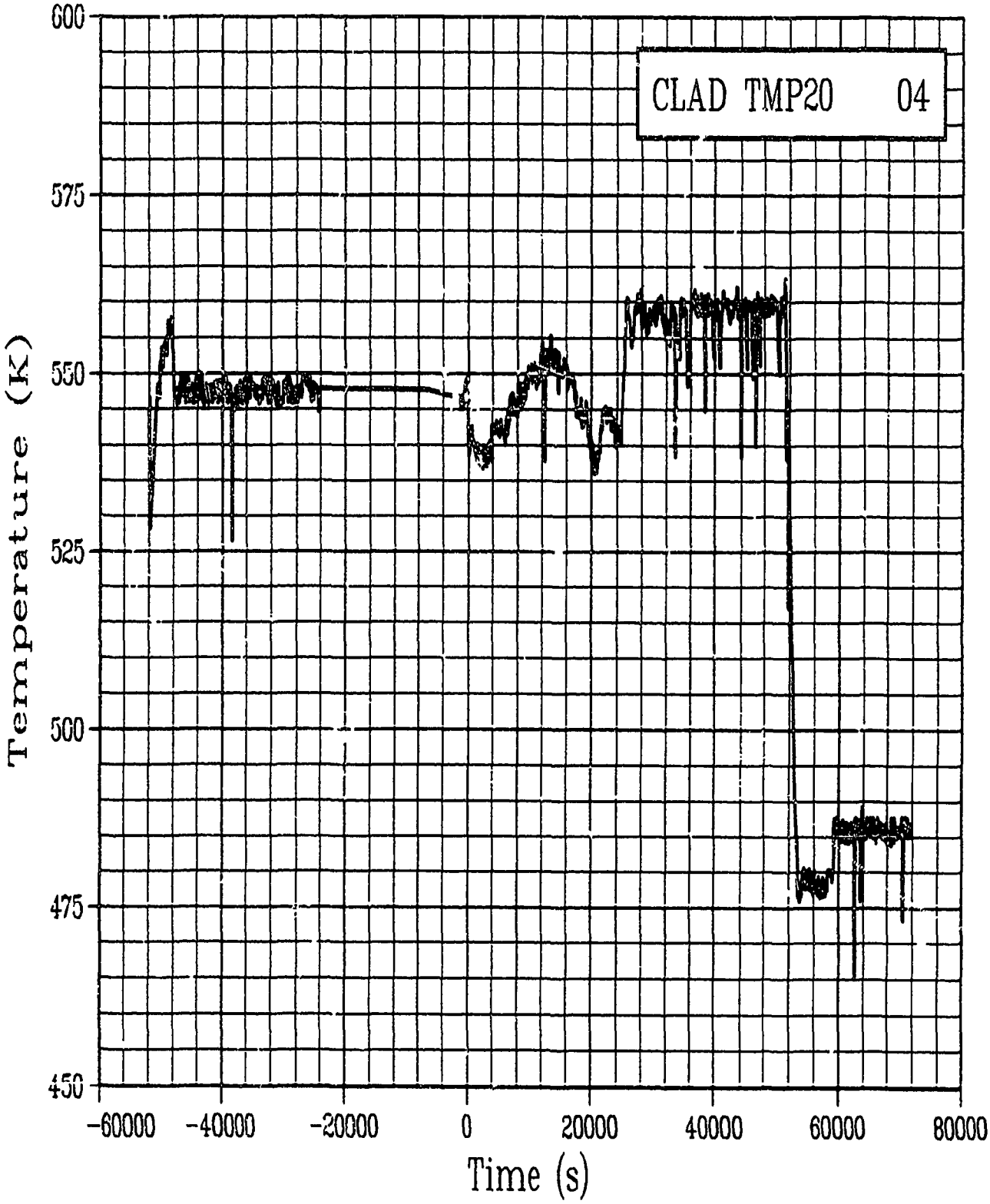

Figure C-74. Cladding surface temperature Rod GC 524-4, at 20 degrees and 0.70 m during Test PR-1 power calibration and preconditioning periods (CLAD TMP20 04).

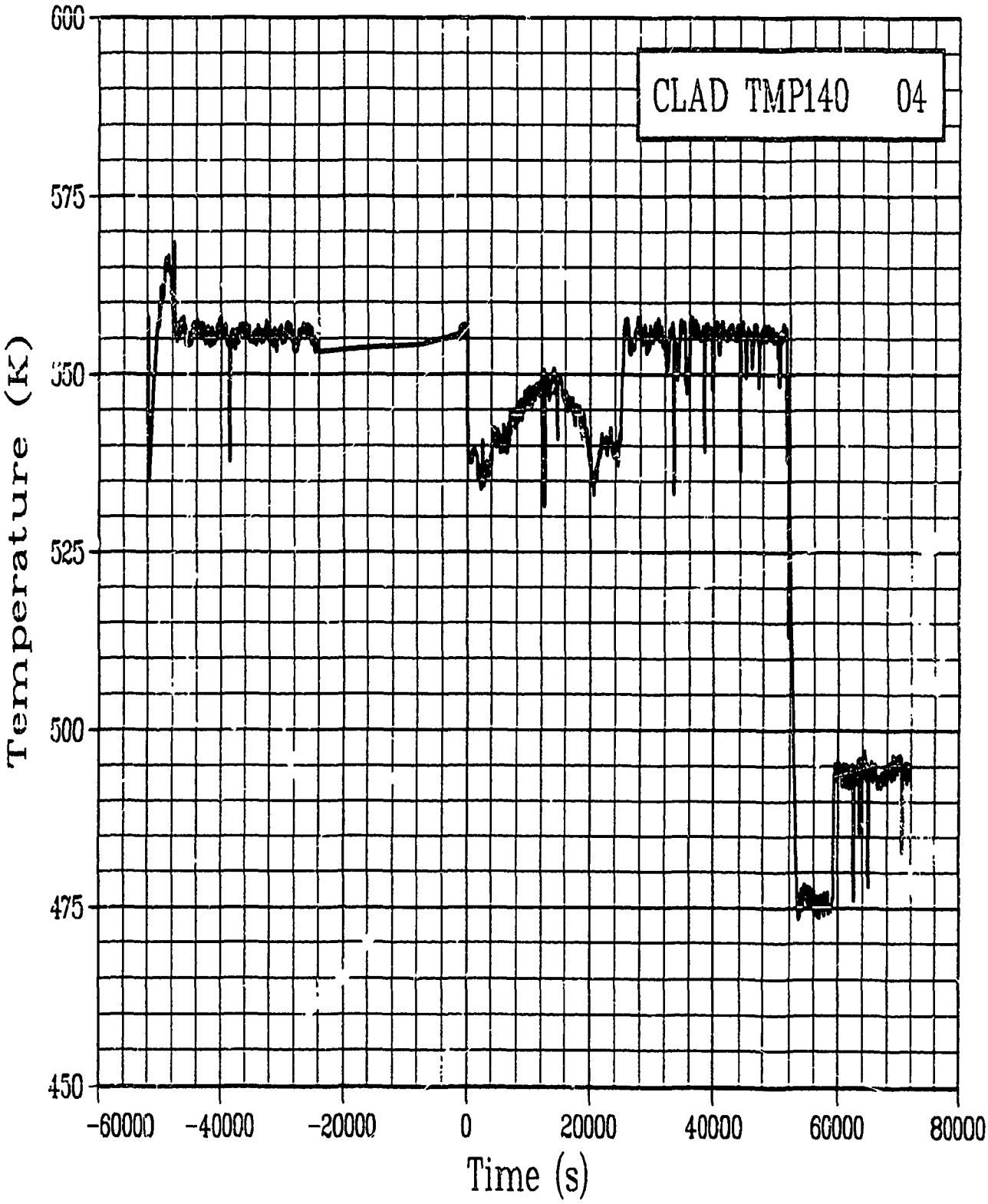

Figure C-75. Cladding surface temperature Rod GC 524-4, at 140 degrees and 0.4521 m during Test PR-1 power calibration and preconditioning periods (CLAD TMP140 04).

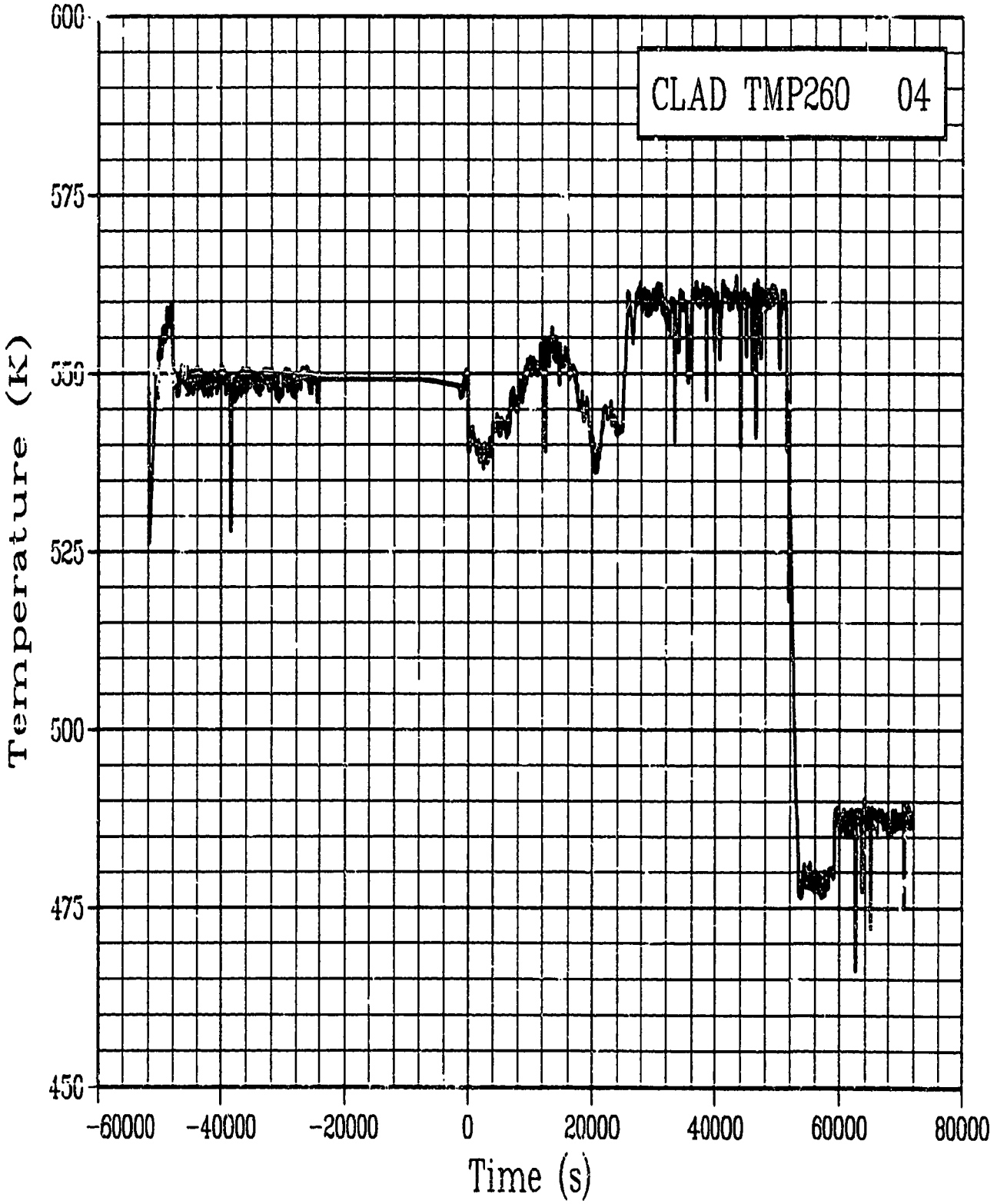

Figure C-76. Cladding surface temperature Rod GC 524--4, at 260 degrees and 0.70 m during Test FR-1 power calibration and preconditioning periods (CLAD TMP260 04).

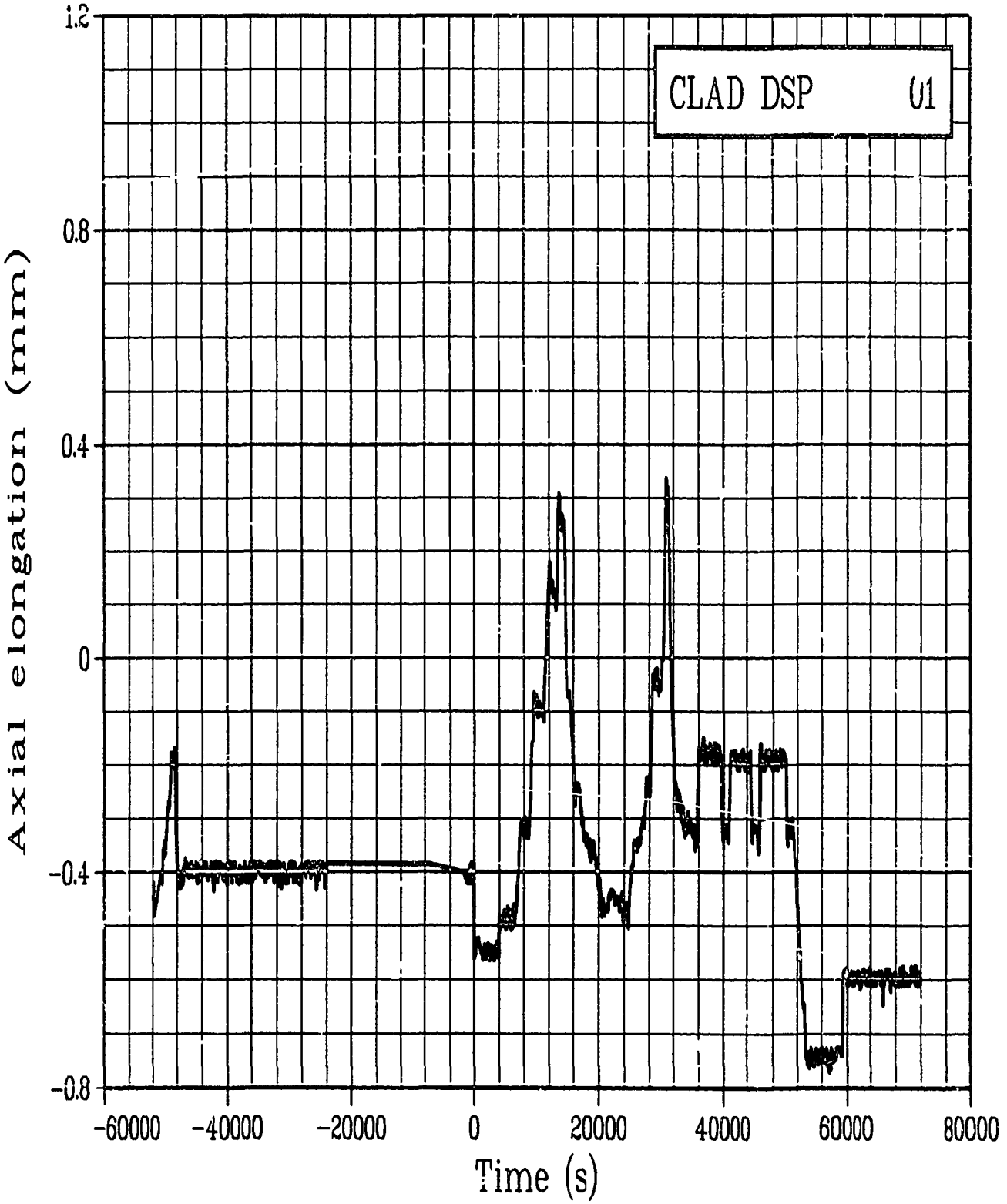

Figure C-77. Cladding axial elongation of Rod GC 524-1 during Test PR-1 power calibration and preconditioning periods (CLAD DSP 01).

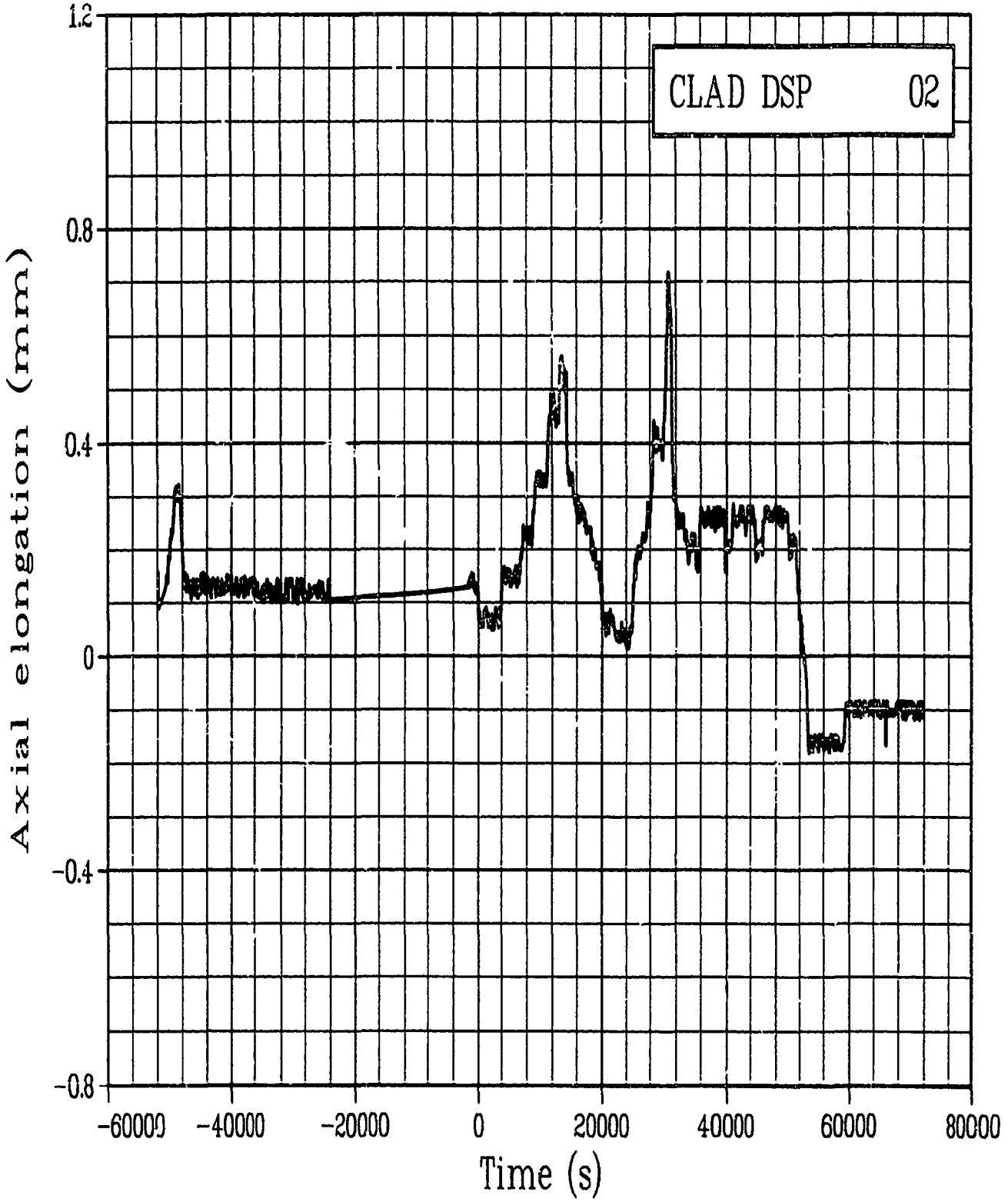

Figure C-78. Cladding axial elongation of Rod GC 524-2 during
ls Test PR-1 power calibration and preconditioning periods
(CLAD DSP 02).

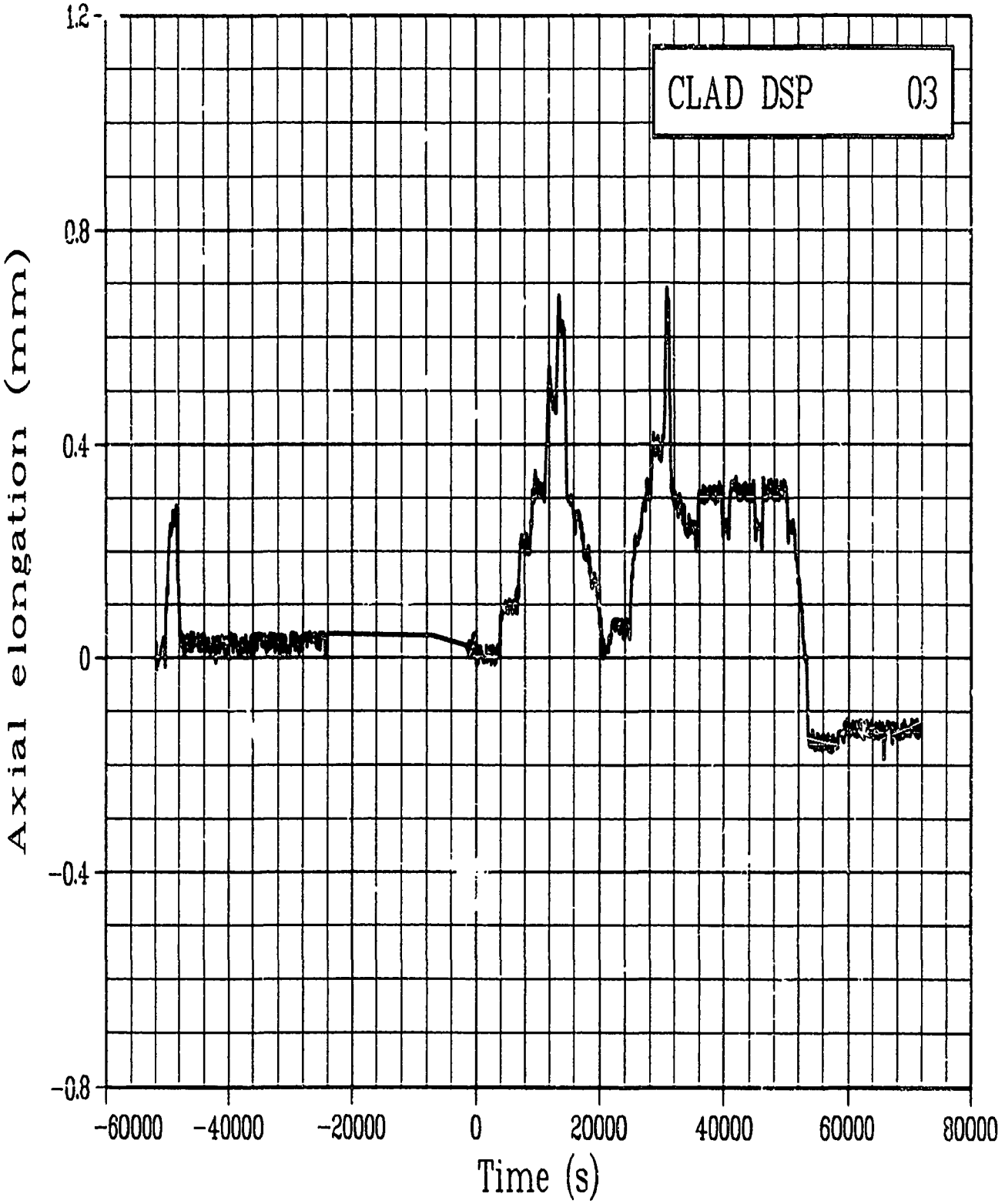

Figure C-79. Cladding axial elongation of Rod CC 524-3 during Test PR-1 power calibration and preconditioning periods (CLAD DSP 03).

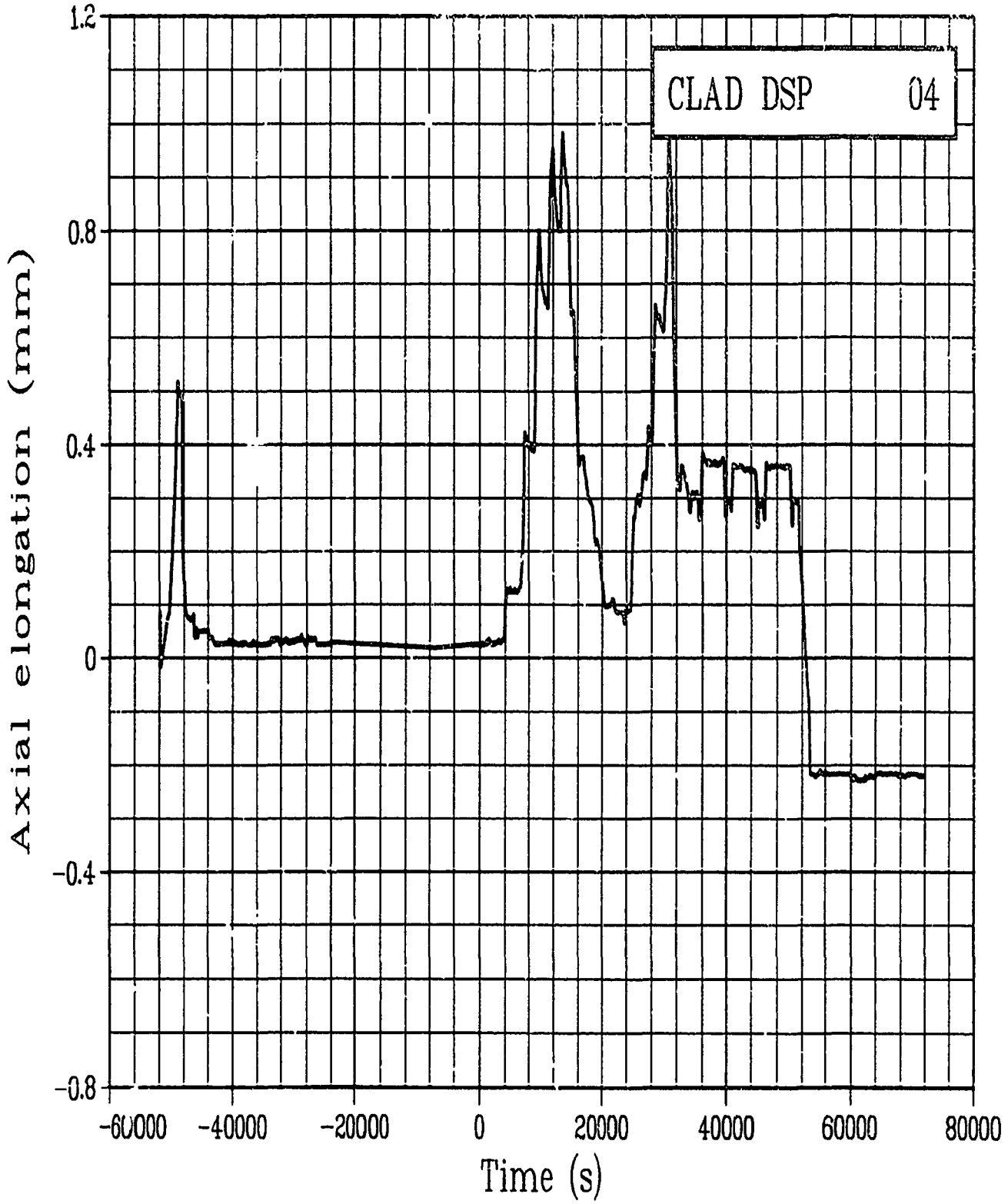

Figure C-80. Cladding axial elongation of Rod GC 524-4 during Test PR-1 power calibration and preconditioning periods (CLAD DSP 04).

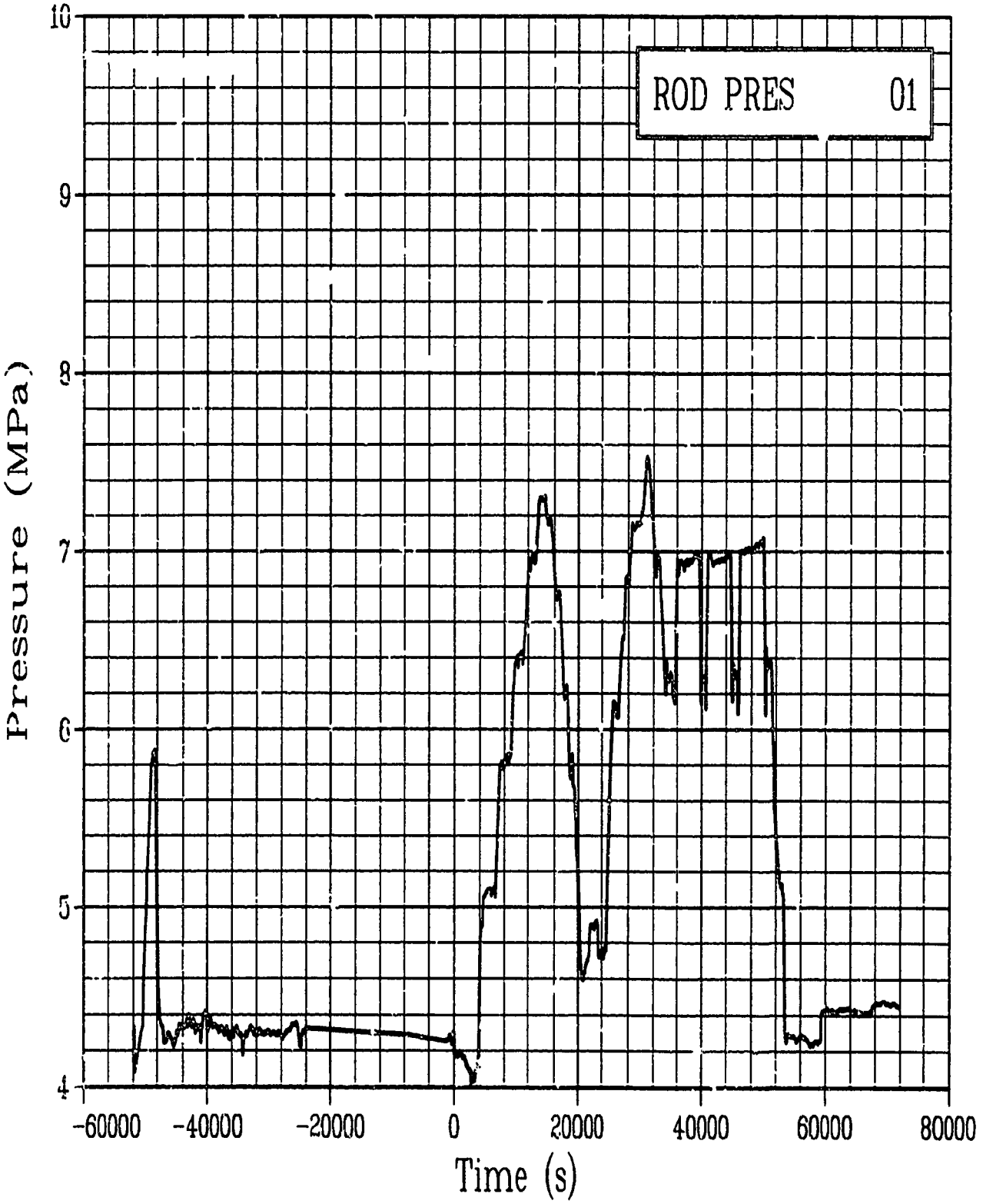

Figure C-81. Absolute pressure in Rod GC 524-1 plenum during Test PR-1 power calibration and preconditioning periods (ROD PRES 01).

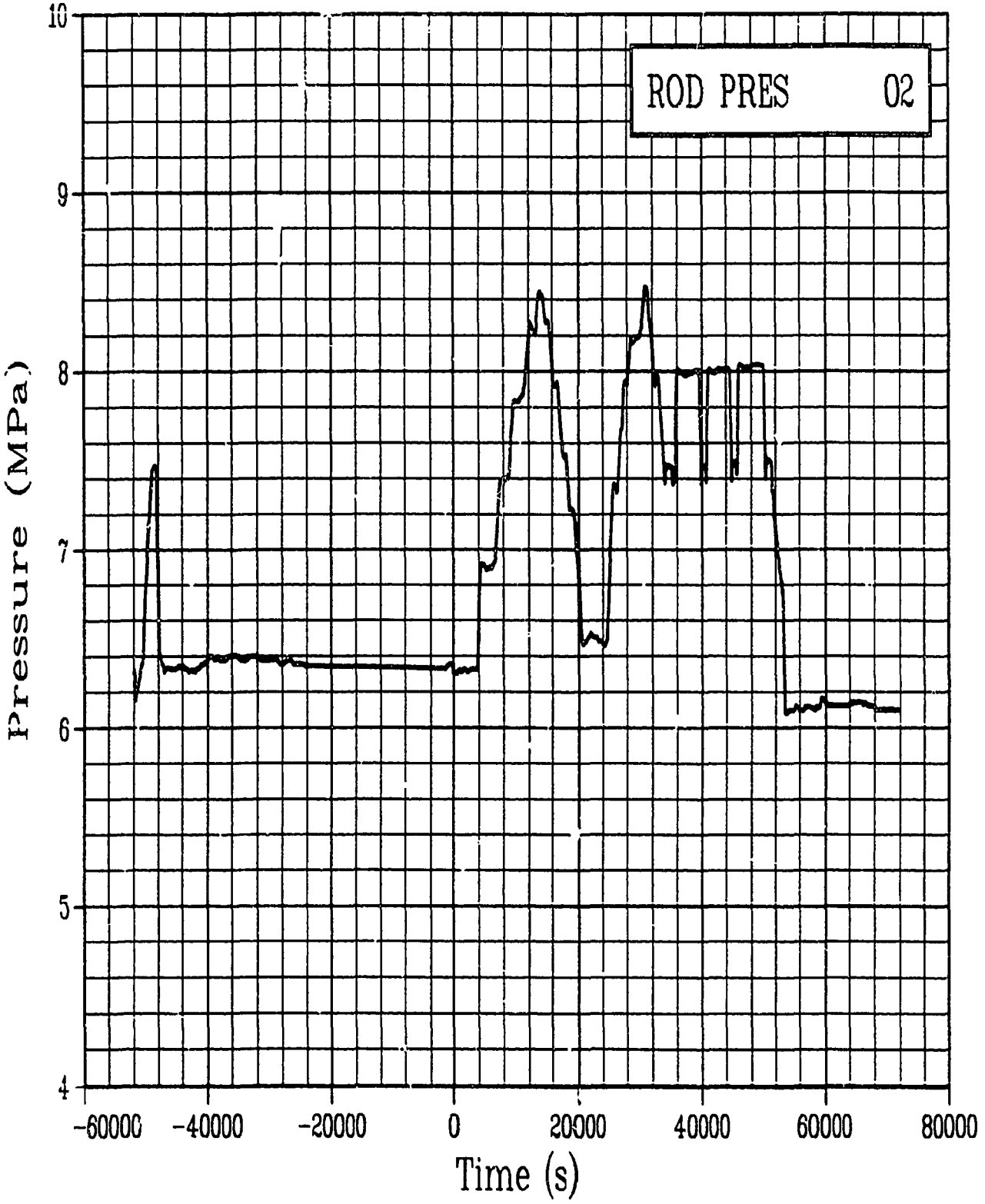

Figure C-82. Absolute pressure in Rod GC 524-2 plenum during Test PR-1 power calibration and preconditioning periods (ROD PRES 02).

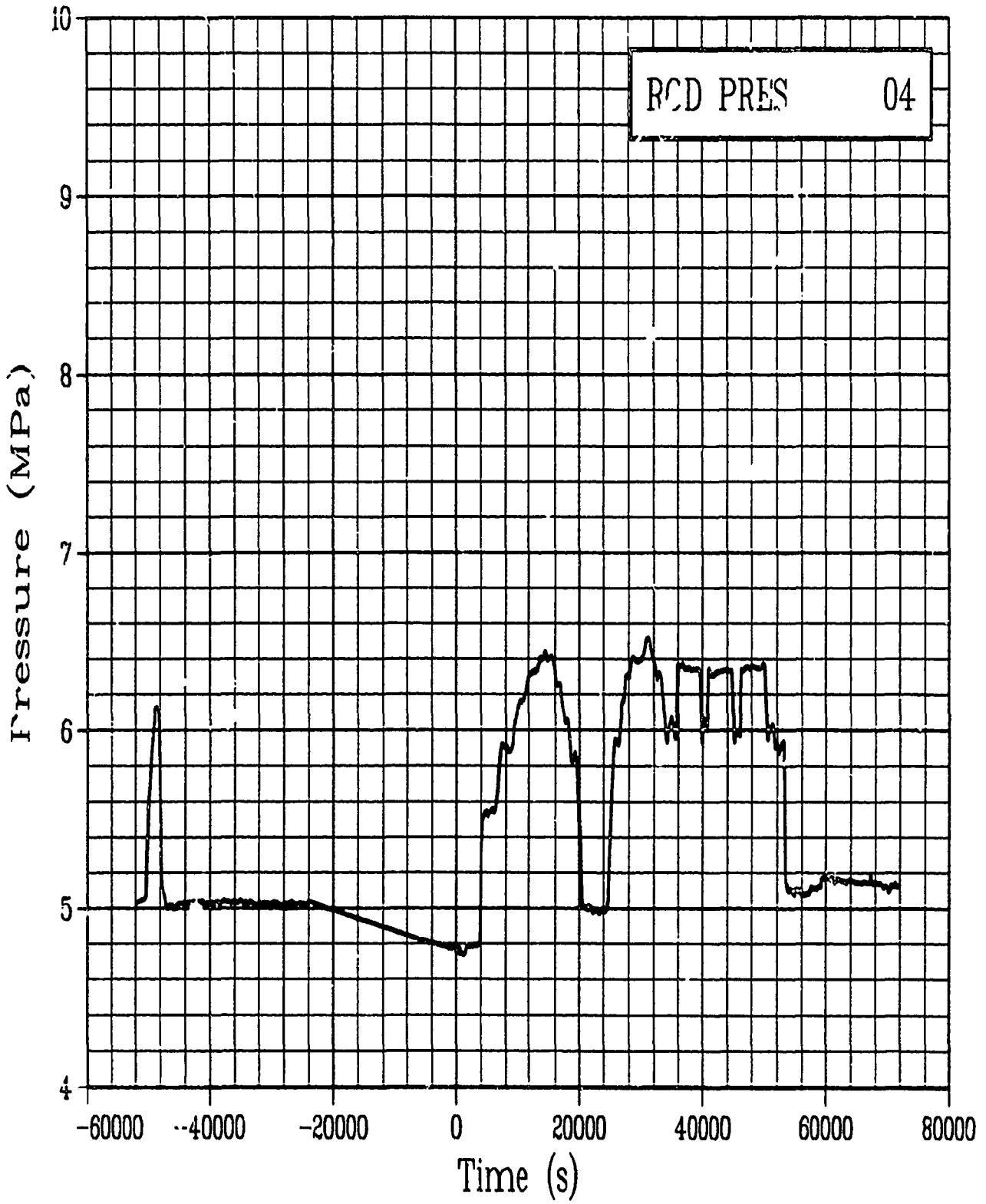

Figure C-83. Absolute pressure in Rod GC 524-4 plenum during Test PR-1 power calibration and preconditioning periods (ROD PRES 04).

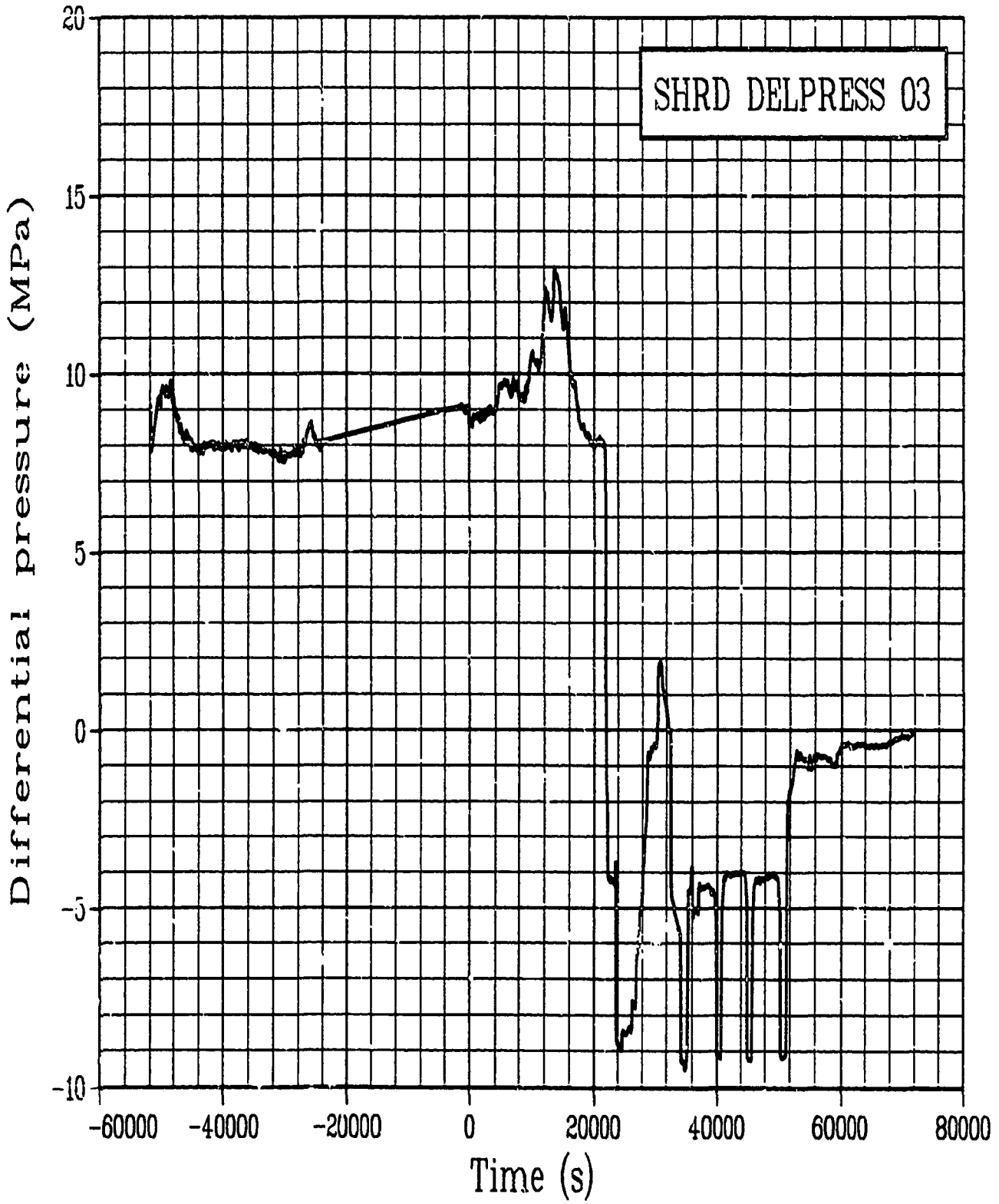

Figure C-84. Differential pressure across Rod GC 524-3 shroud during Test PR-1 power calibration and preconditioning periods (SHRD DELPRESS 03).

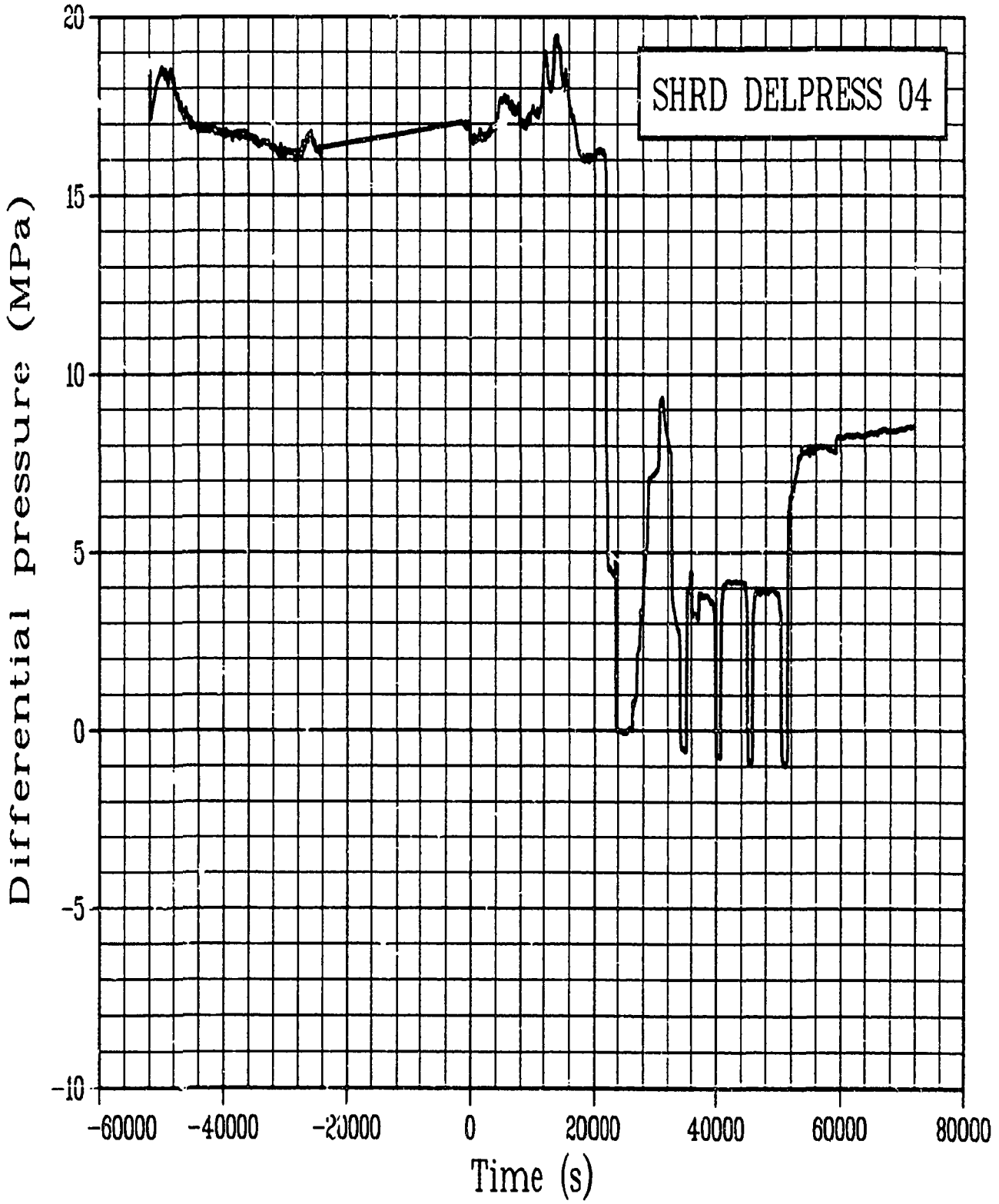

Figure C-85. Differential pressure across Rod GC 524-4 shroud during Test PR-1 power calibration and preconditioning periods (SHRD DELPRESS 04).

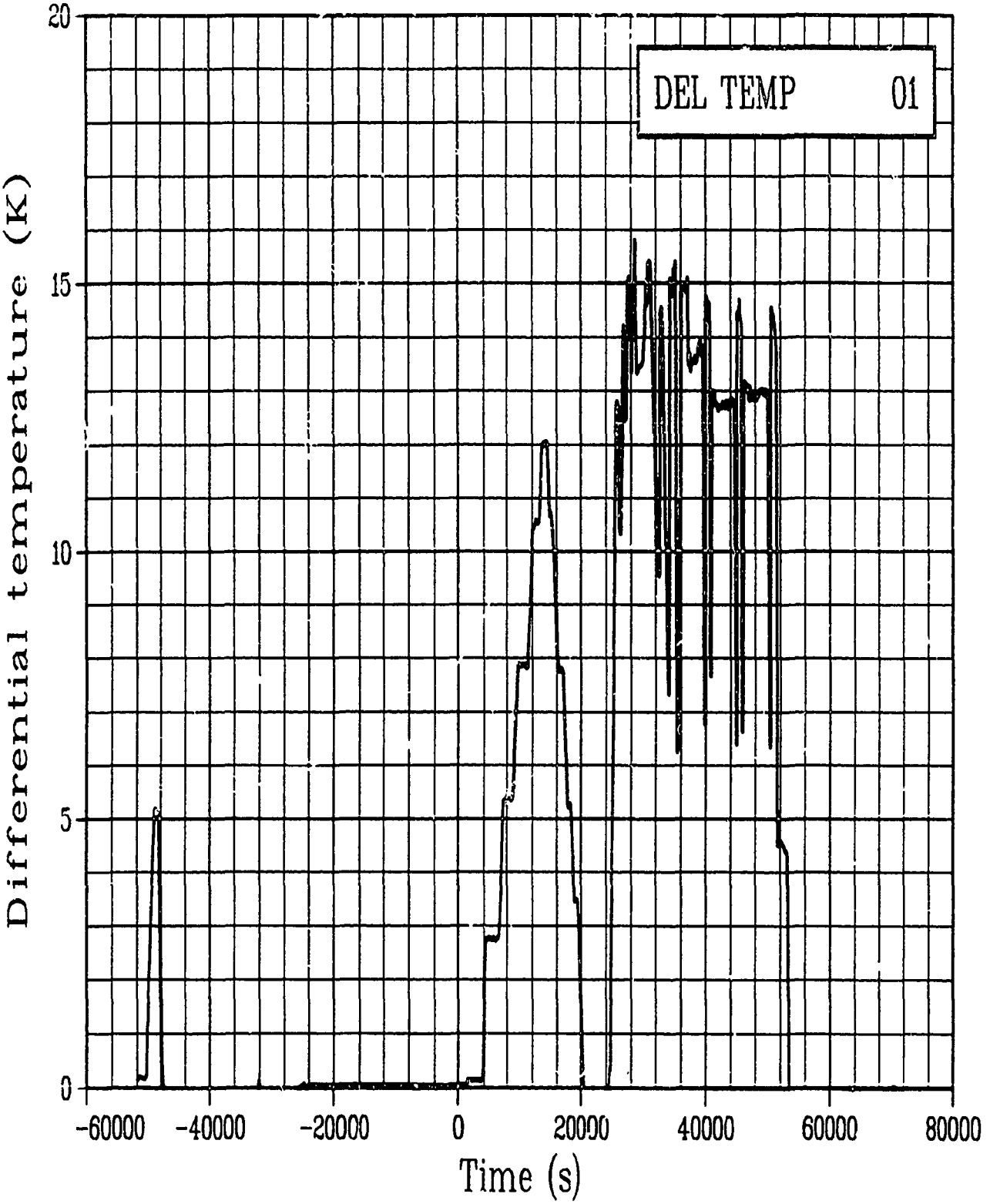

Figure C-86. Differential temperature of Rod GC 524-1 coolant inlet and outlet during Test PR--1 power calibration and preconditioning periods (DEL TEMP 01).

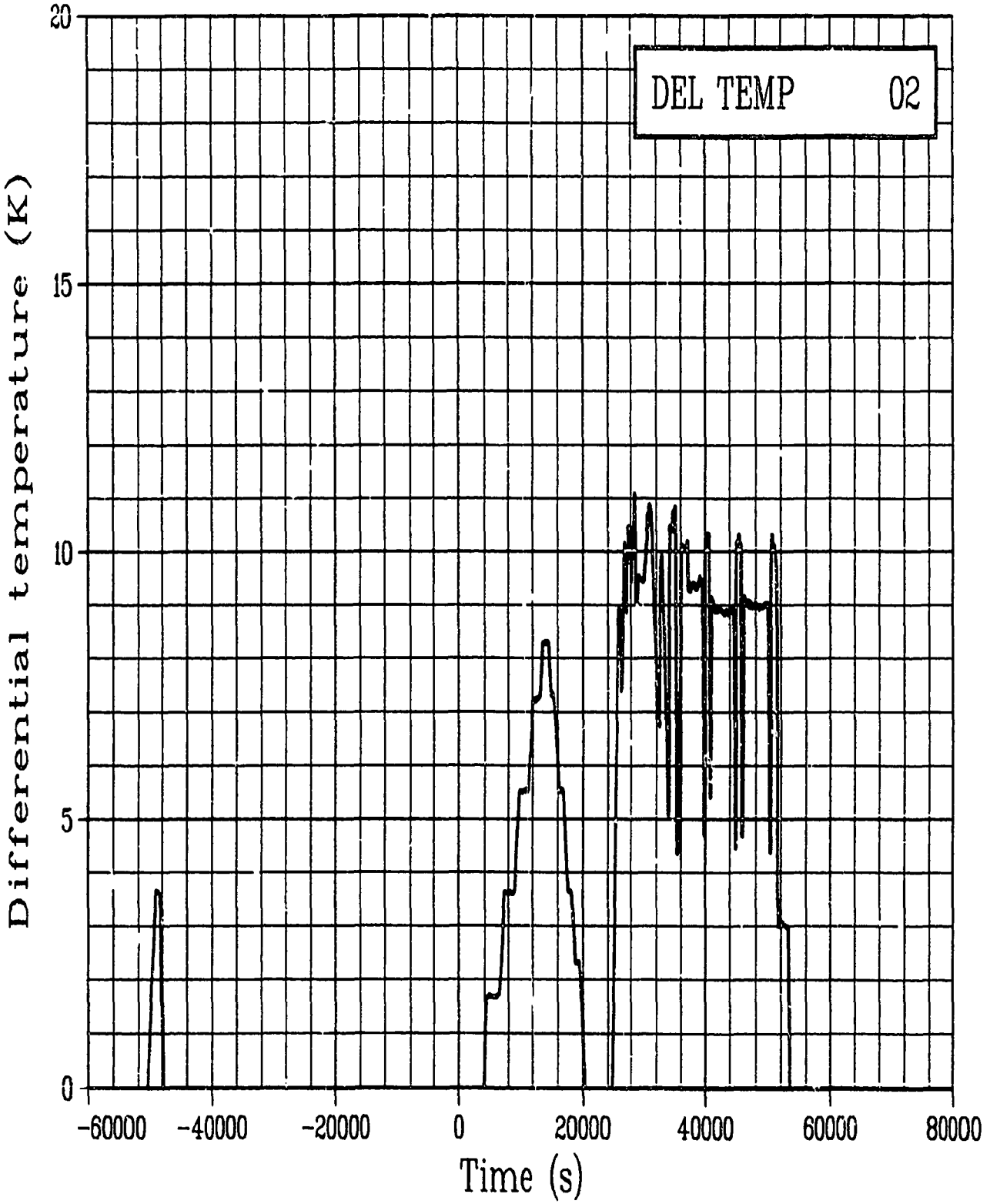

Figure C-87. Differential temperature of Rod GC 524-2 coolant inlet and outlet during Test PR-1 power calibration and preconditioning periods (DEL TEMP 02).

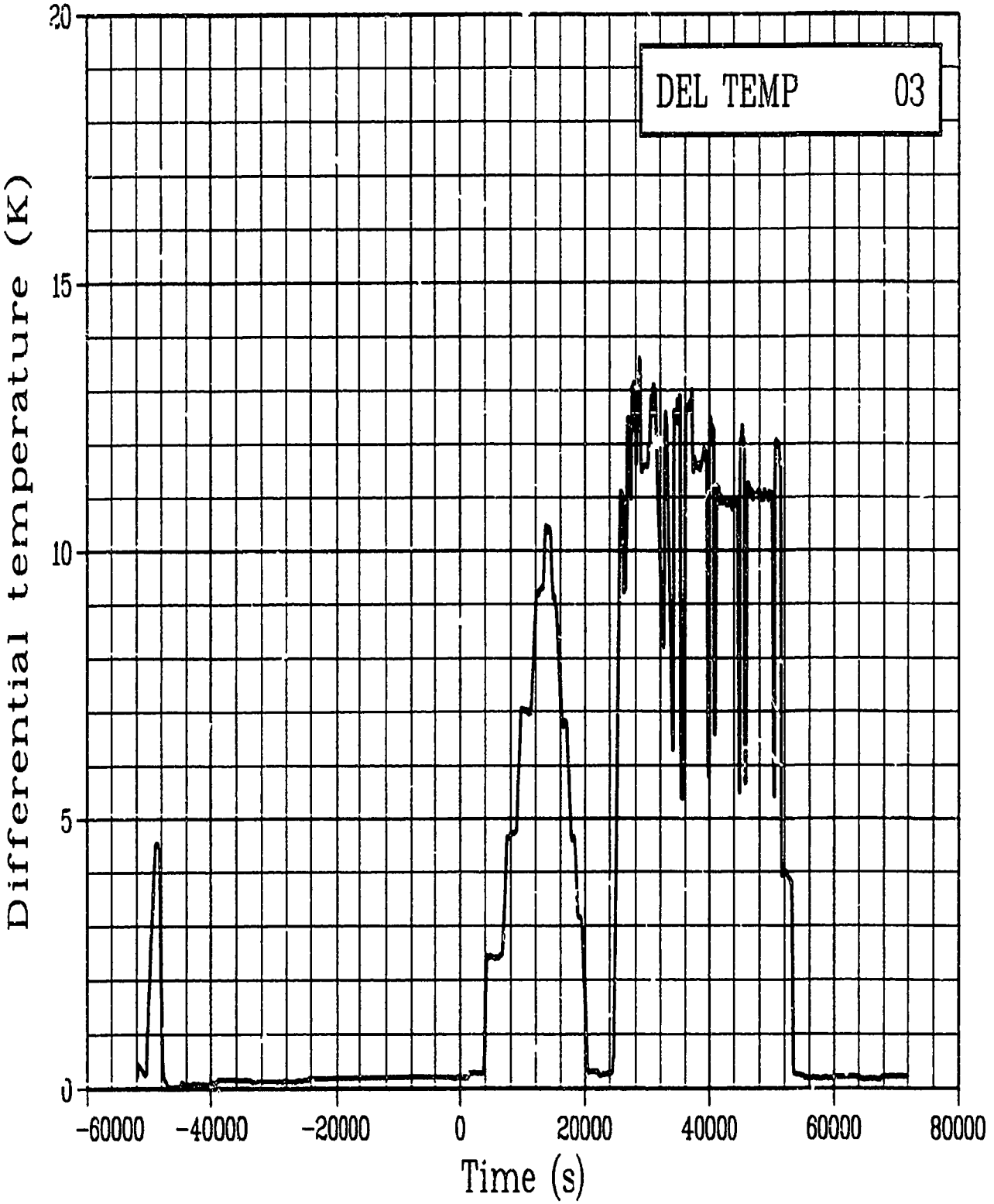

Figure C-38. Differential temperature of Rod GC 524-3 coolant inlet and outlet during Test PR-1 power calibration and preconditioning periods (DEL TEMP 03).

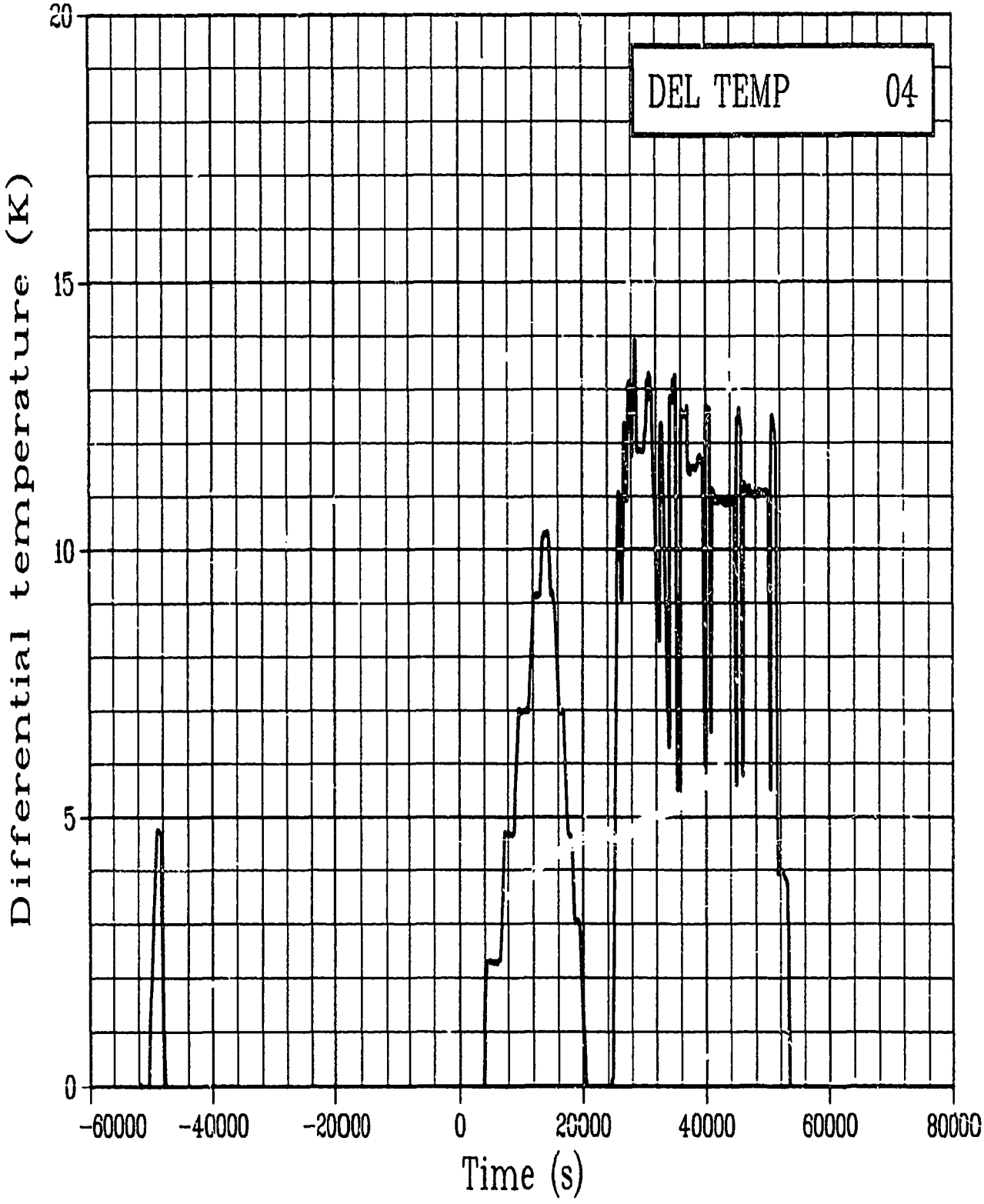

Figure C-89. Differential temperature of Rod GC 524-4 coolant inlet and outlet during Test PR-1 power calibration and preconditioning periods (DEL TEMP 04).

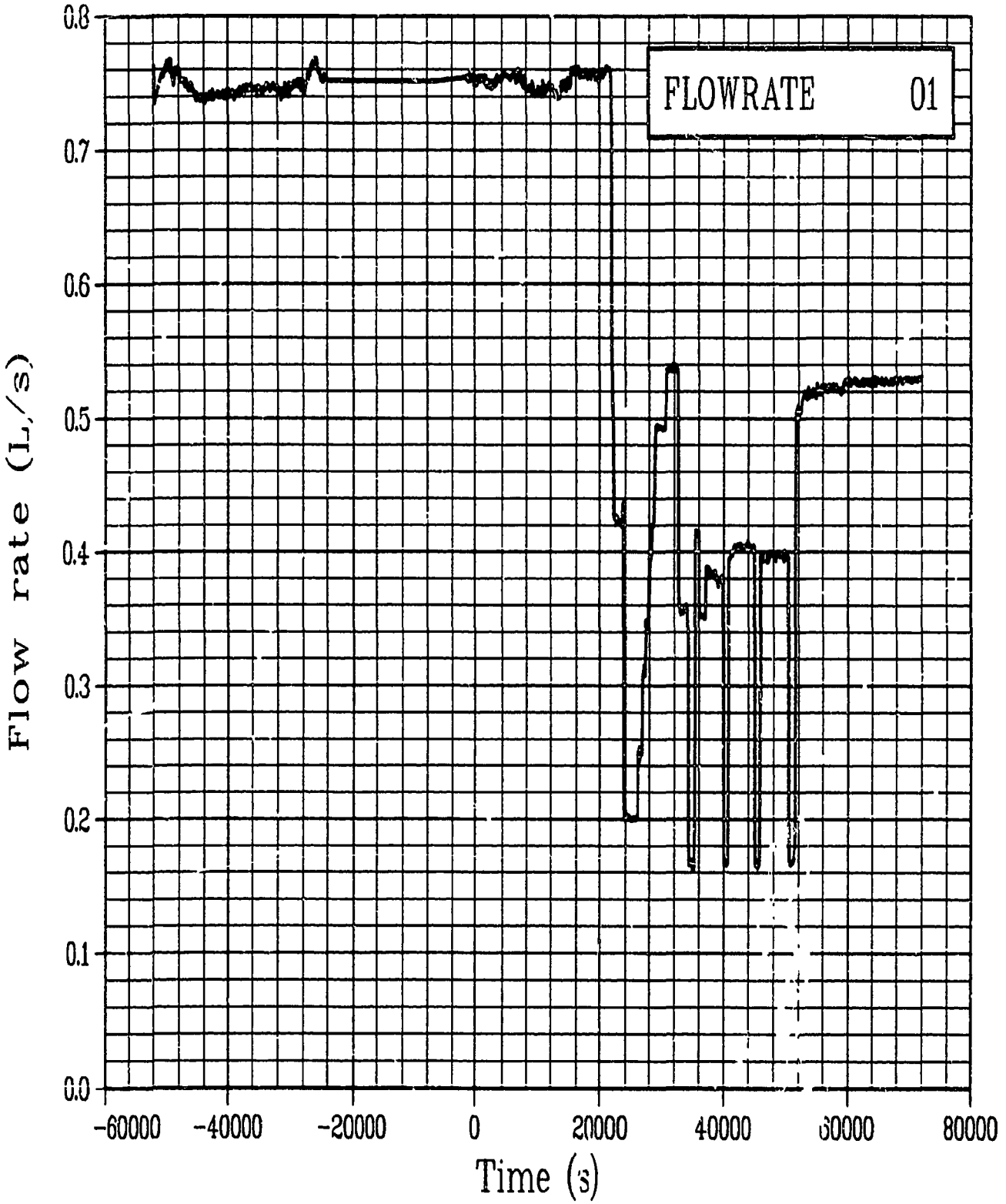

Figure C-90. Volumetric flow rate in Rod GC 524-1 lower shroud during Test PR-1 power calibration and preconditioning periods (FLOWRATE 01).

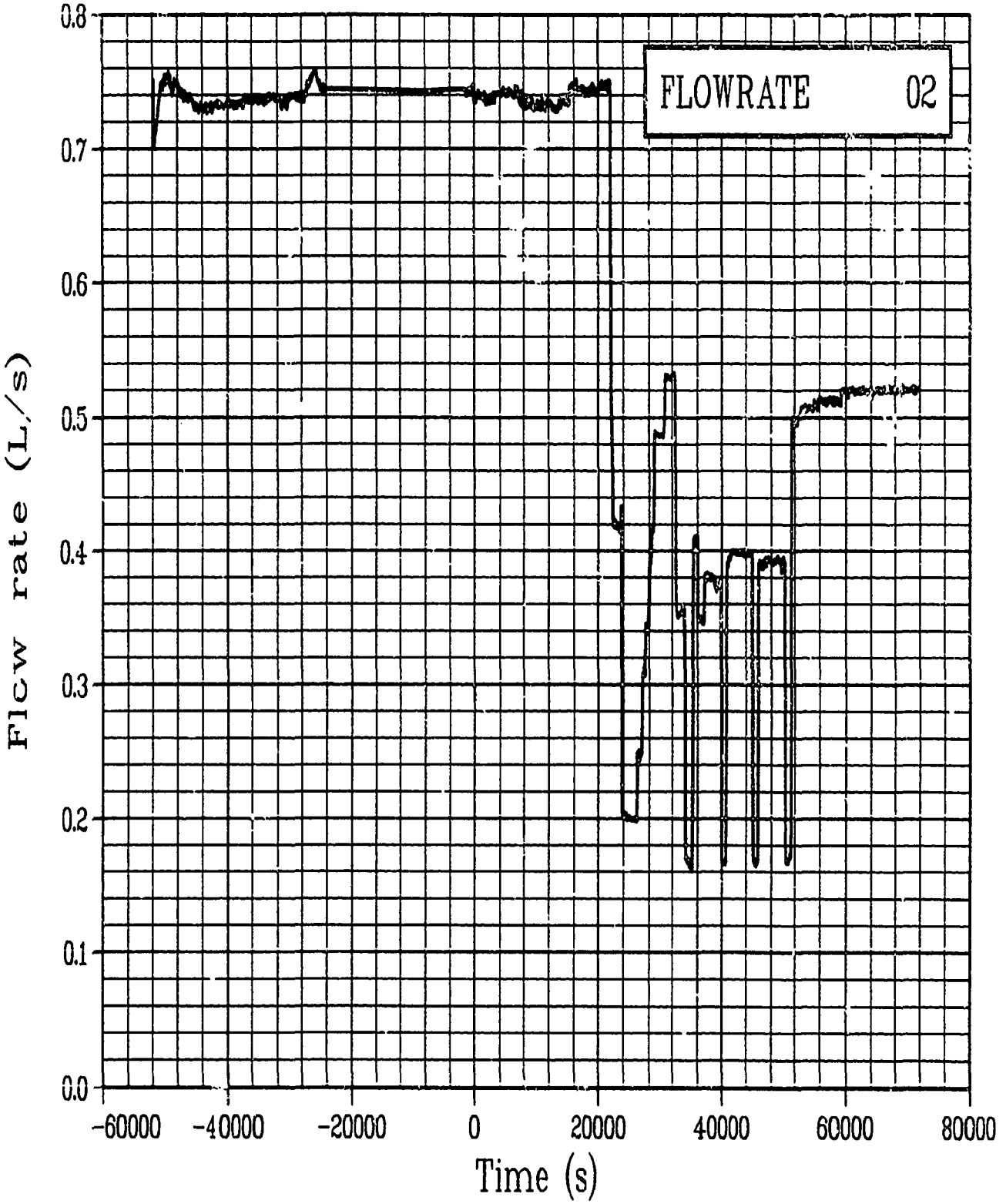

Figure C-91. Volumetric flow rate in Rod GC 524-2 lower shroud during Test PR-1 power calibration and preconditioning periods (FLOWRATE 02).

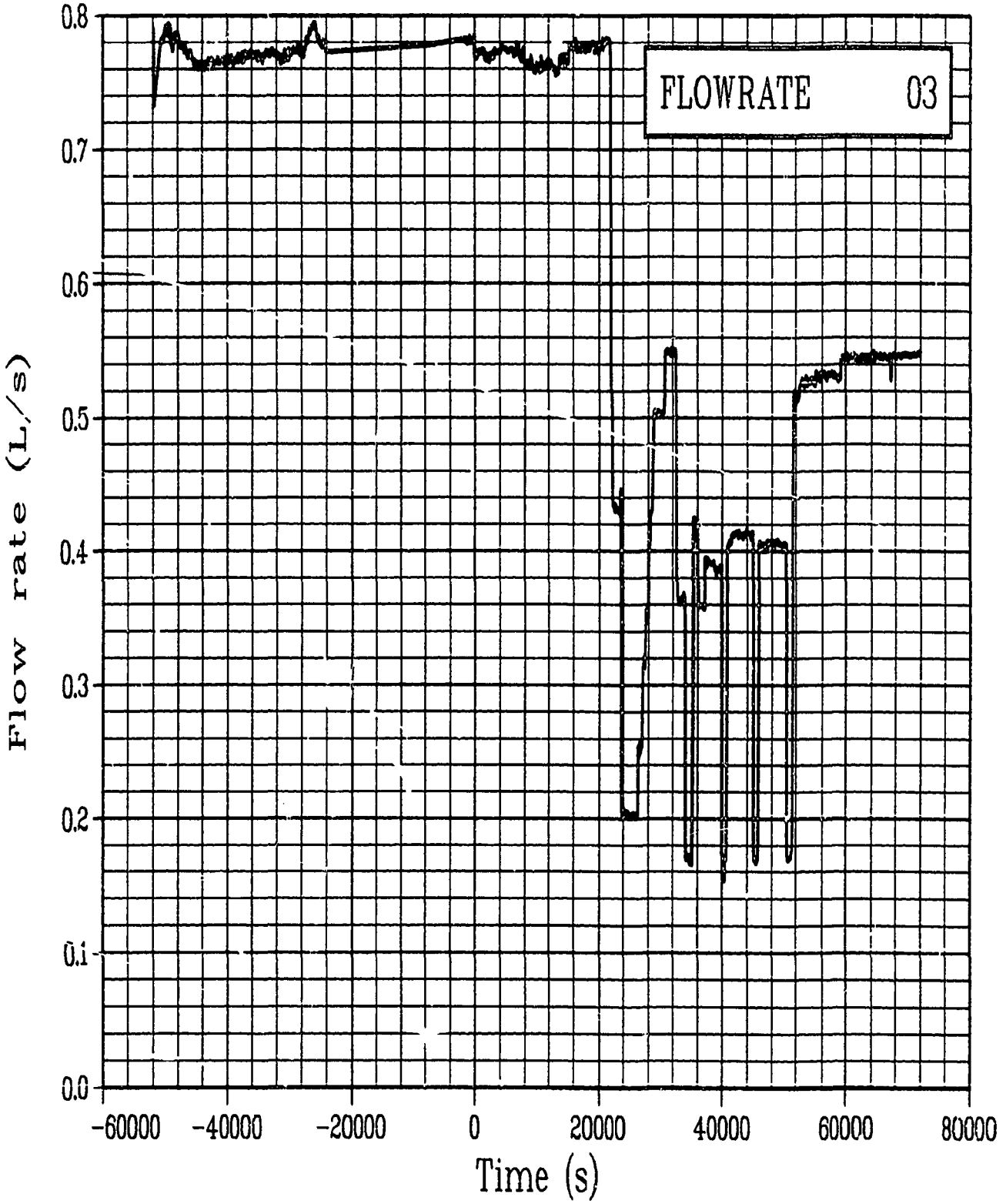

Figure C-92. Volumetric flow rate in Rod GC 524-3 lower shroud during Test PR-1 power calibration and preconditioning periods (FLOWRATE 03).

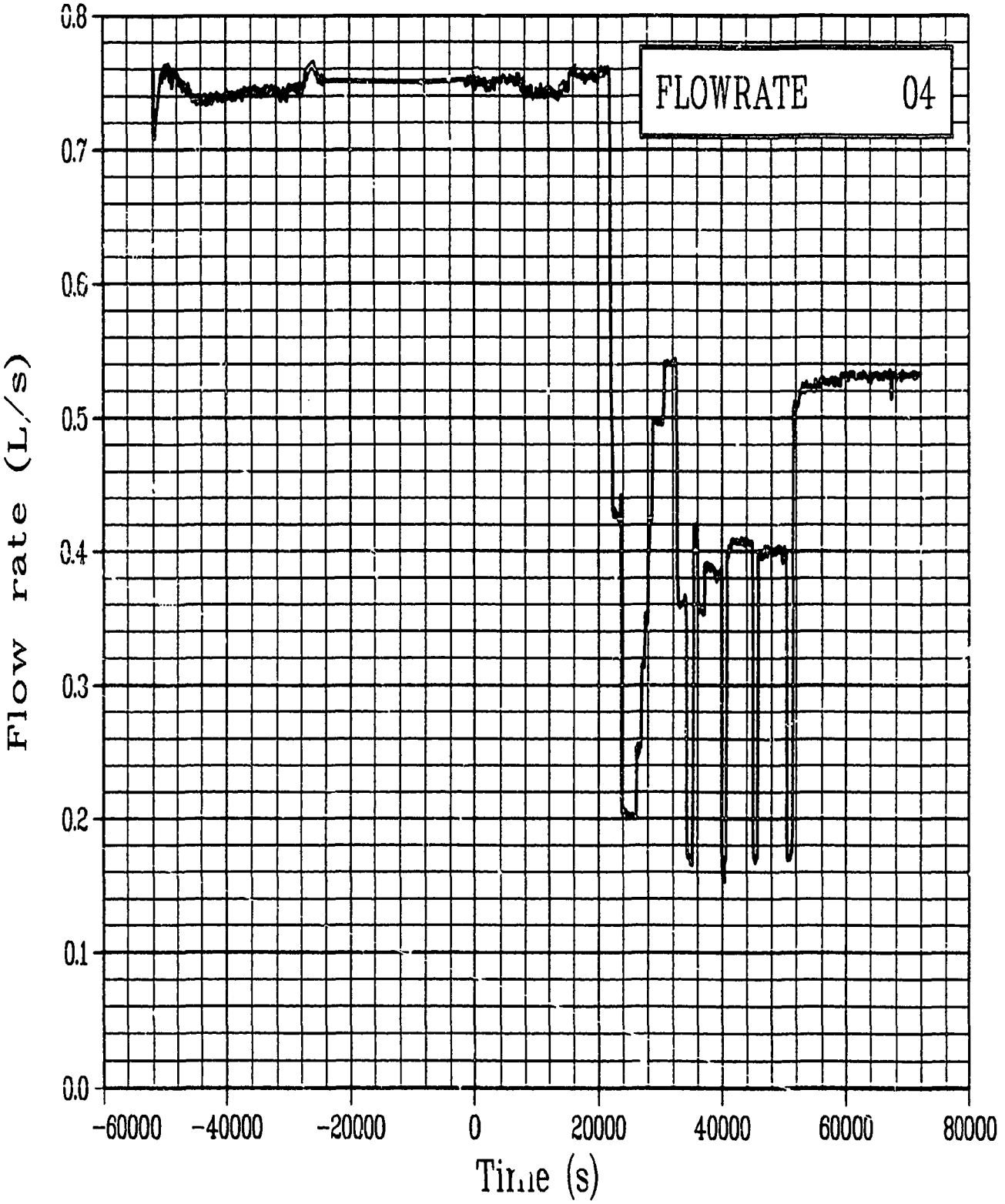

Figure C-93. Volumetric flow rate in Rod GC 524-4 lower shroud during Test PR-1 power calibration and preconditioning periods (FLOWRATE 04).

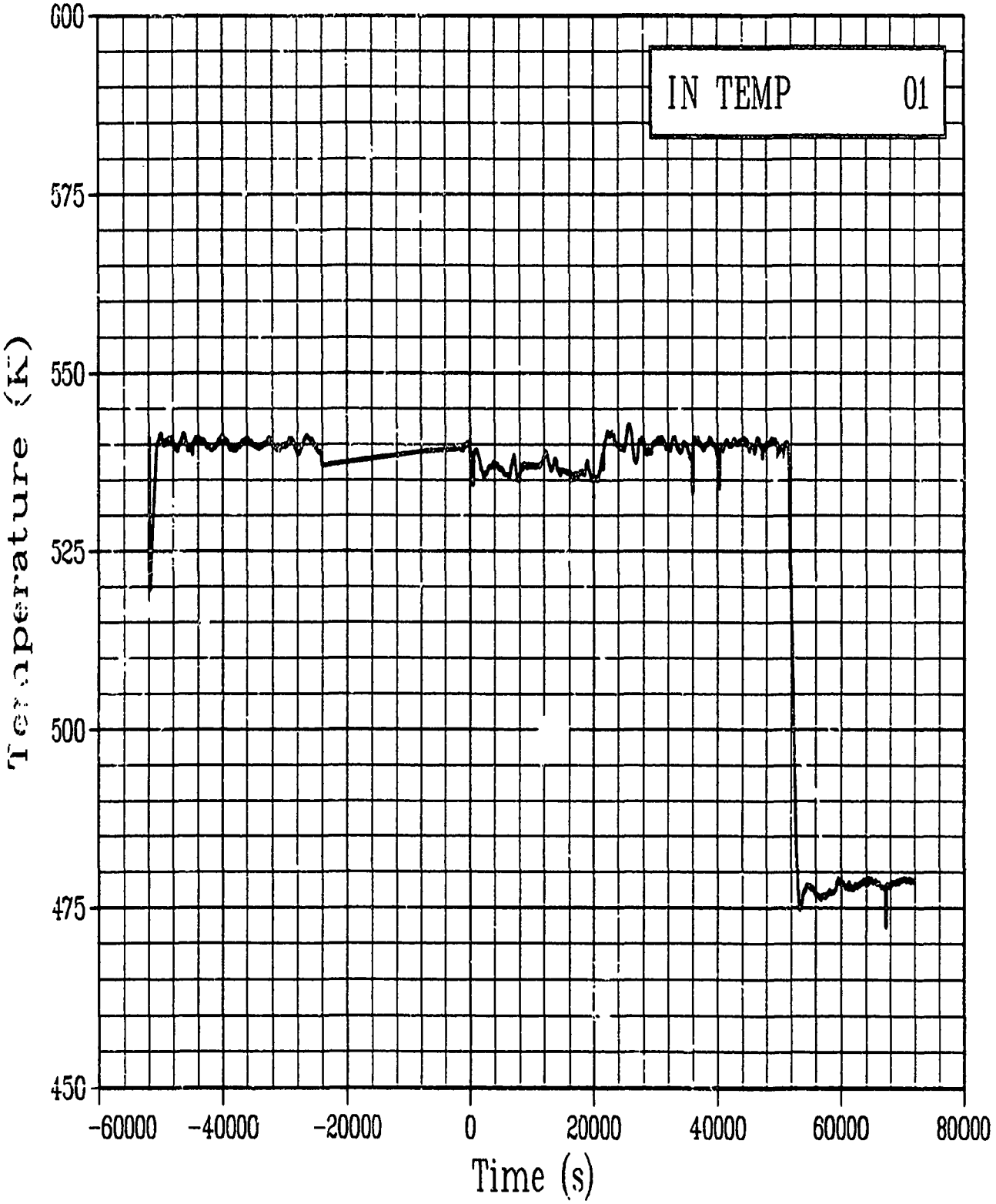

Figure C-94. Fluid temperature No. 1 at the flow shroud inlet during Test PR-1 power calibration and preconditioning periods (IN TEMP 01).

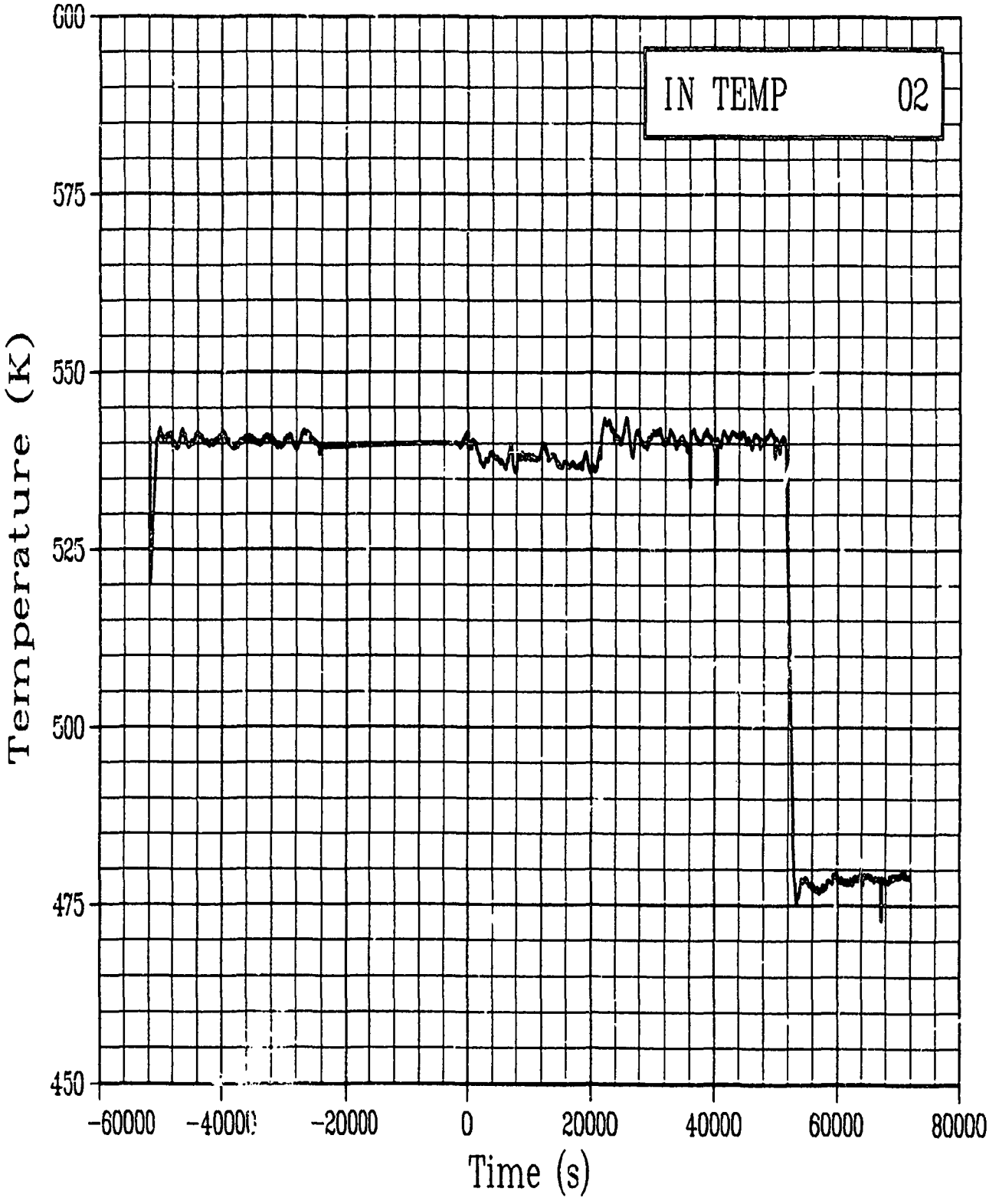

Figure C--95. Fluid temperature No. 2 at the flow shroud inlet during Test PR-1 power calibration and preconditioning periods (IN TEMP 02).

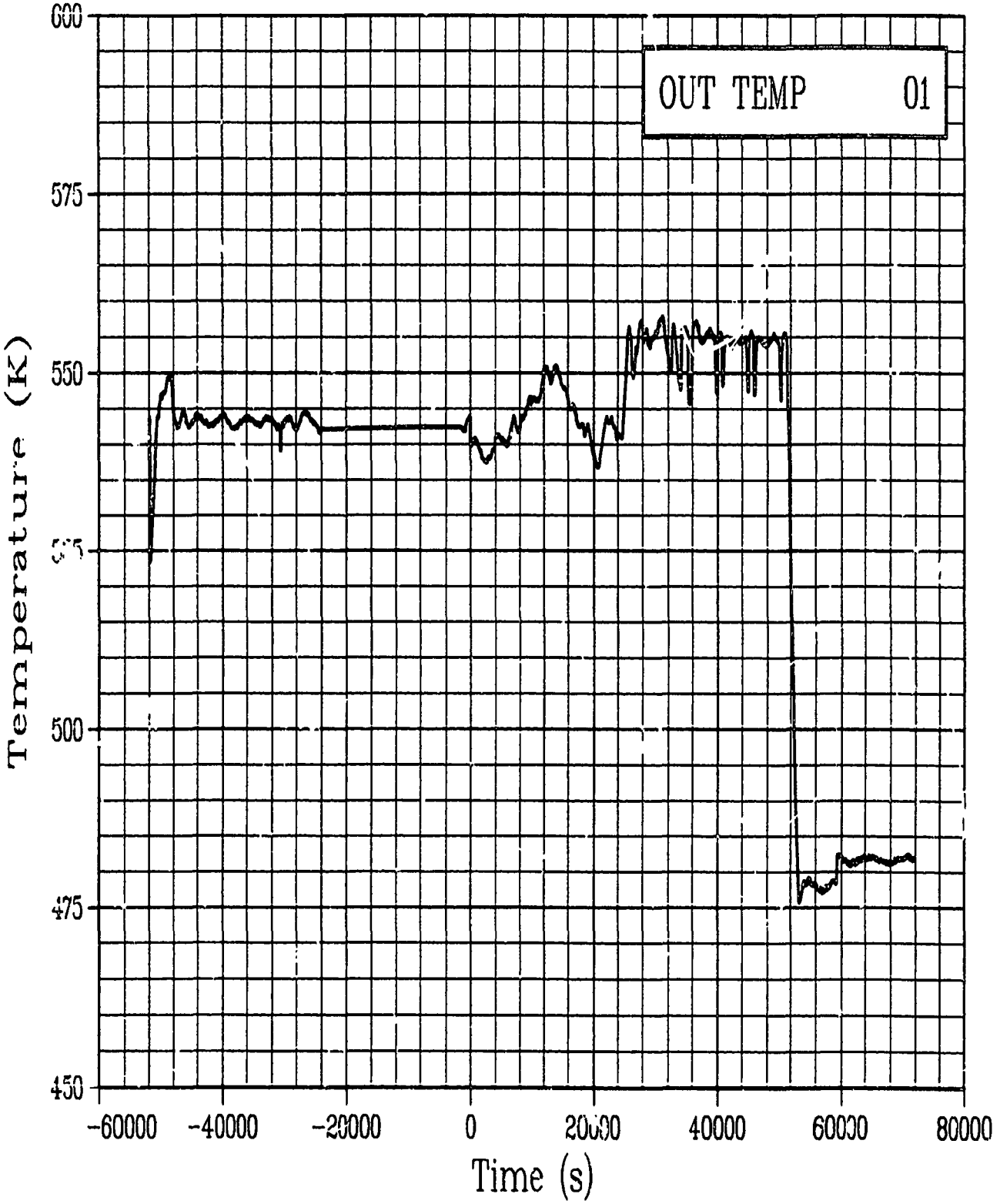

Figure C-96. Fluid temperature of Rod GC 524-1 coolant outlet during Test PR-1 power calibration and preconditioning periods (OUT TEMP 01).

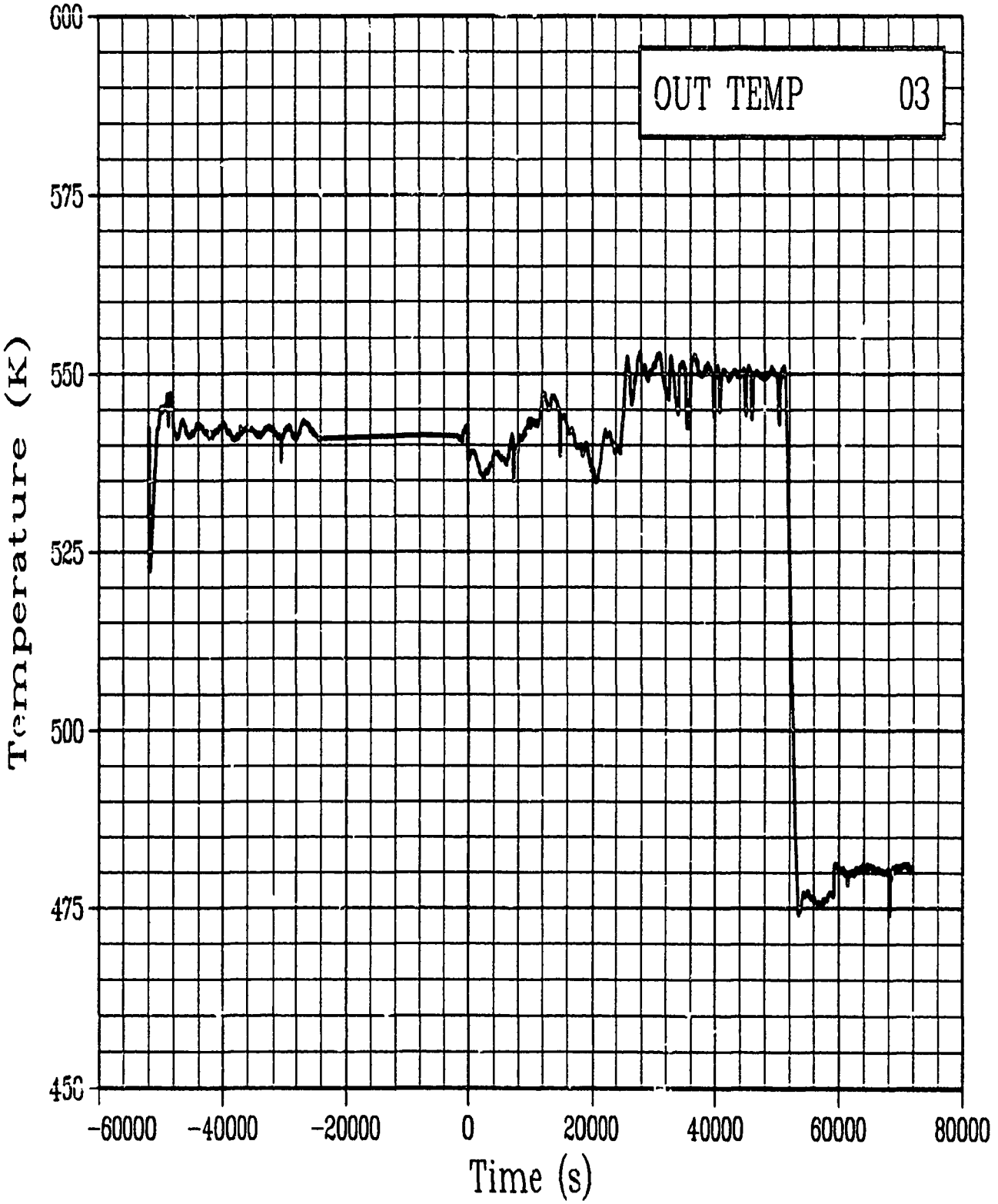

Figure C-97. Fluid temperature of Rod GC 524-3 coolant outlet during Test PR-1 power calibration and preconditioning periods (OUT TEMP 03).

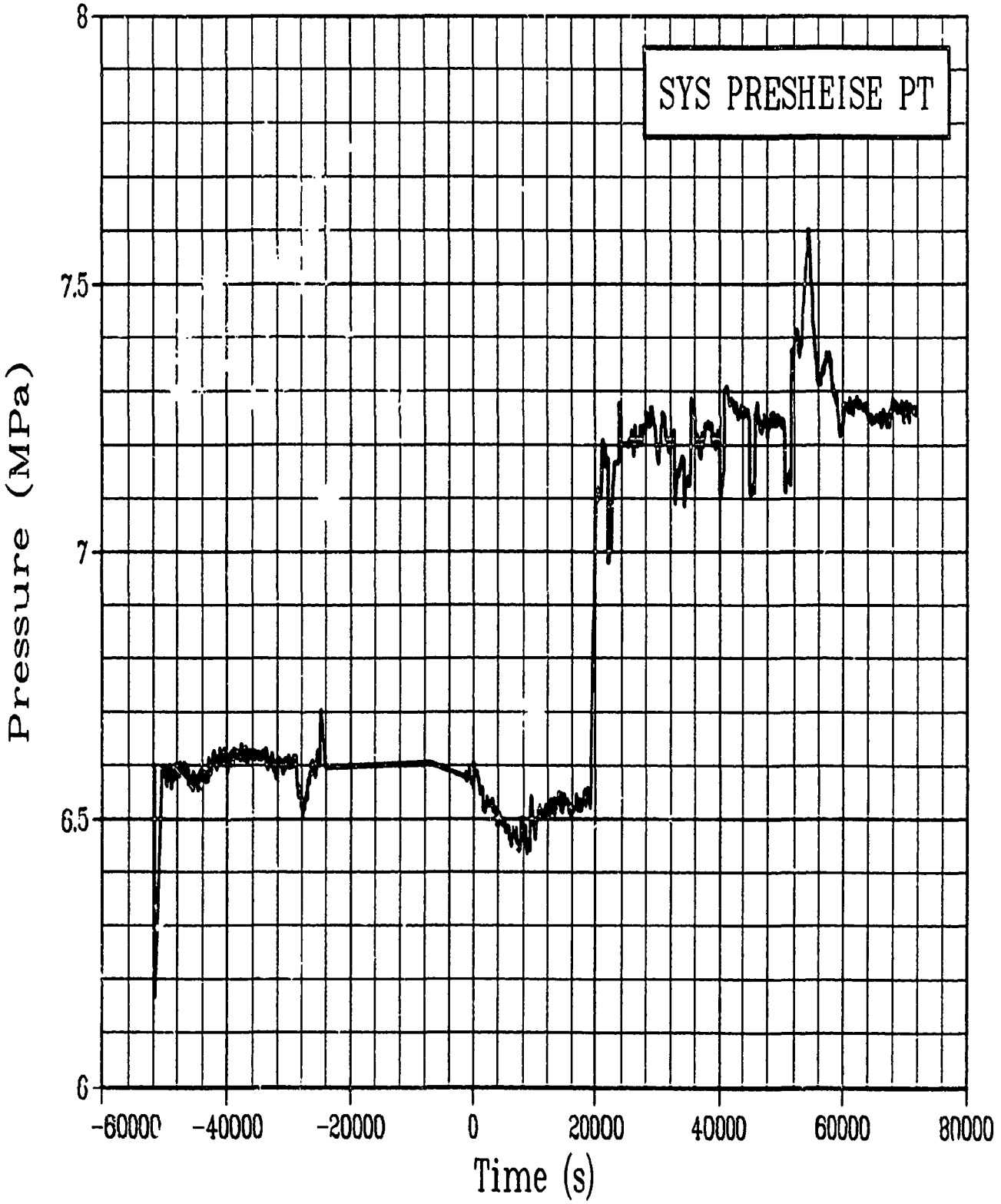

Figure C-98. Plant system pressure, Heise pressure guage during Test PR-1 power calibration and preconditioning periods (SYS PRESHEISE PT).

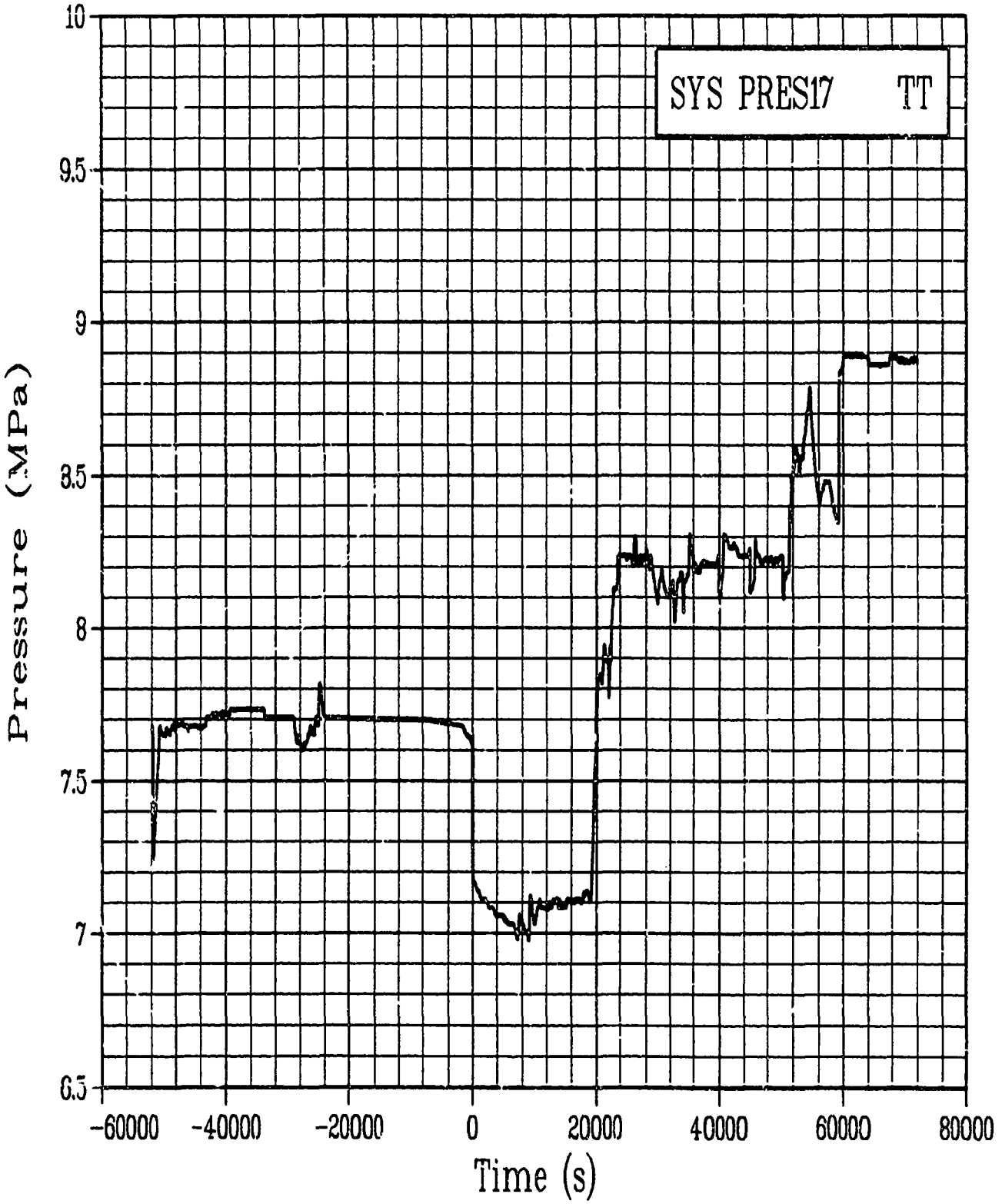

Figure C-99. Coolant pressure in the IPT outlet, 0-17 MPa range during Test PR-1 power calibration and preconditioning periods (SYS PRES17 TT).

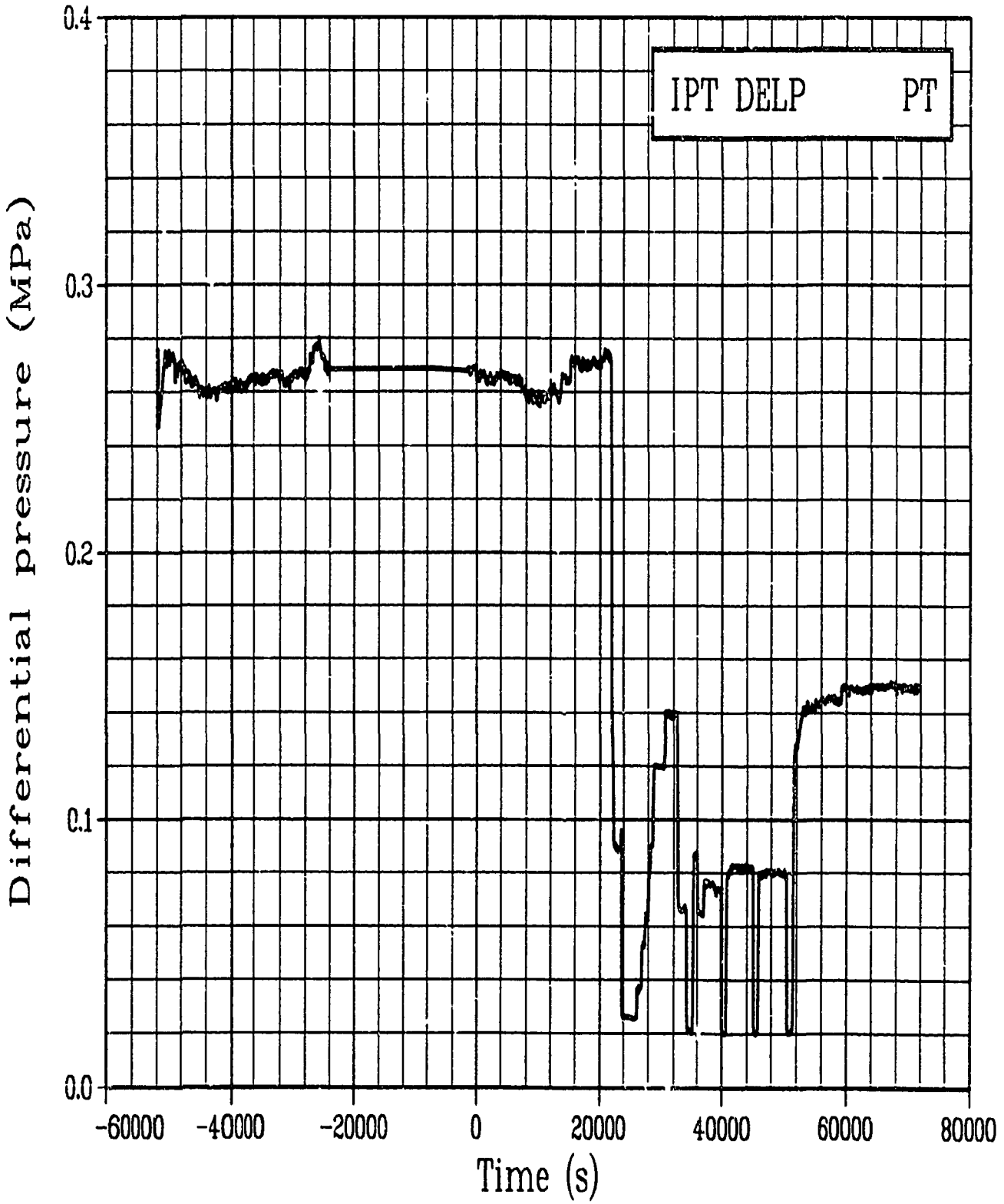

Figure C-100. Differential pressure across the in-pile tube during Test PR-1 power calibration and preconditioning periods (IPT DELP PT).

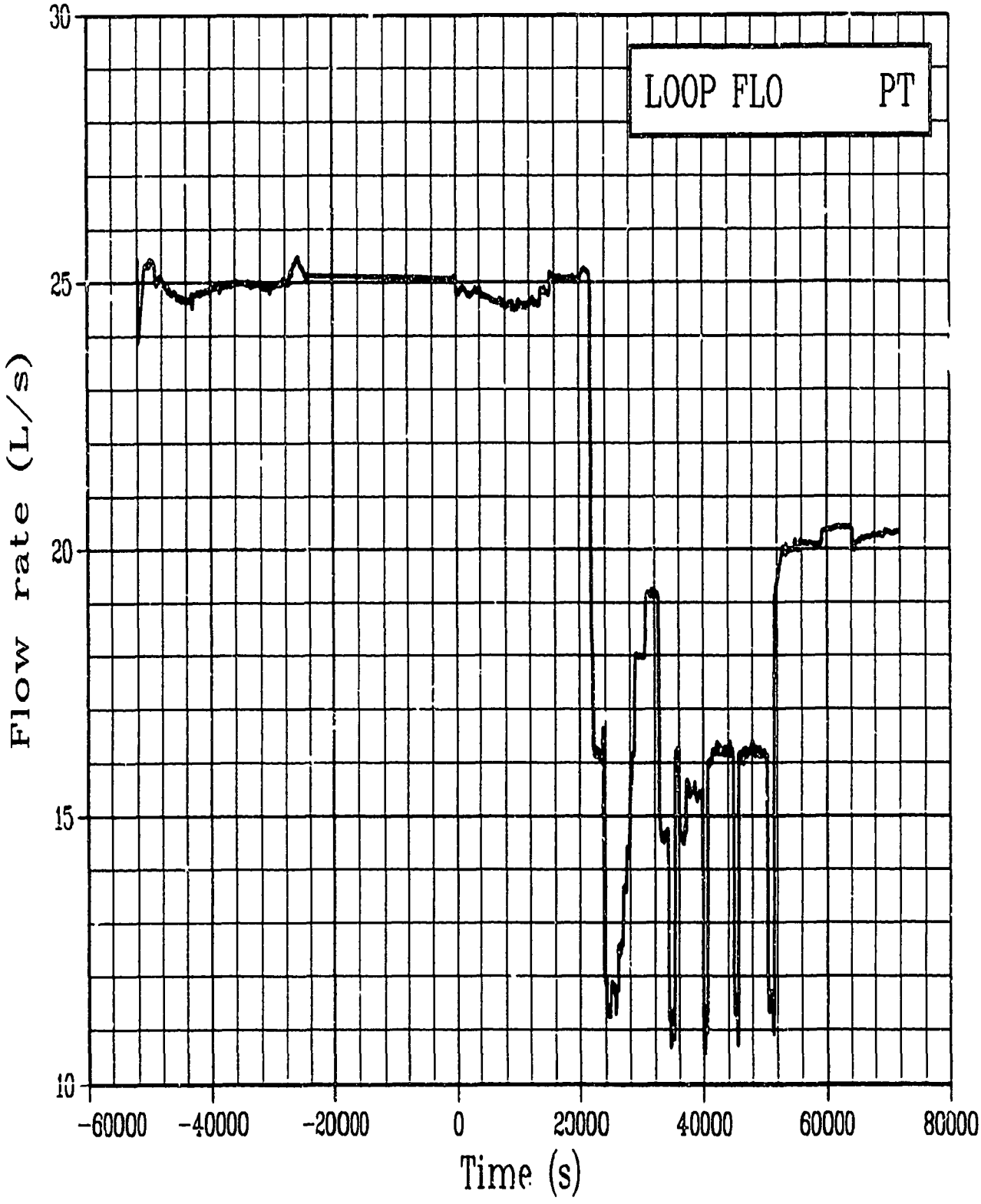

Figure C-101. Volumetric flow rate in experimental loop system during Test PR-1 power calibration and preconditioning periods (LOOP FLO PT).

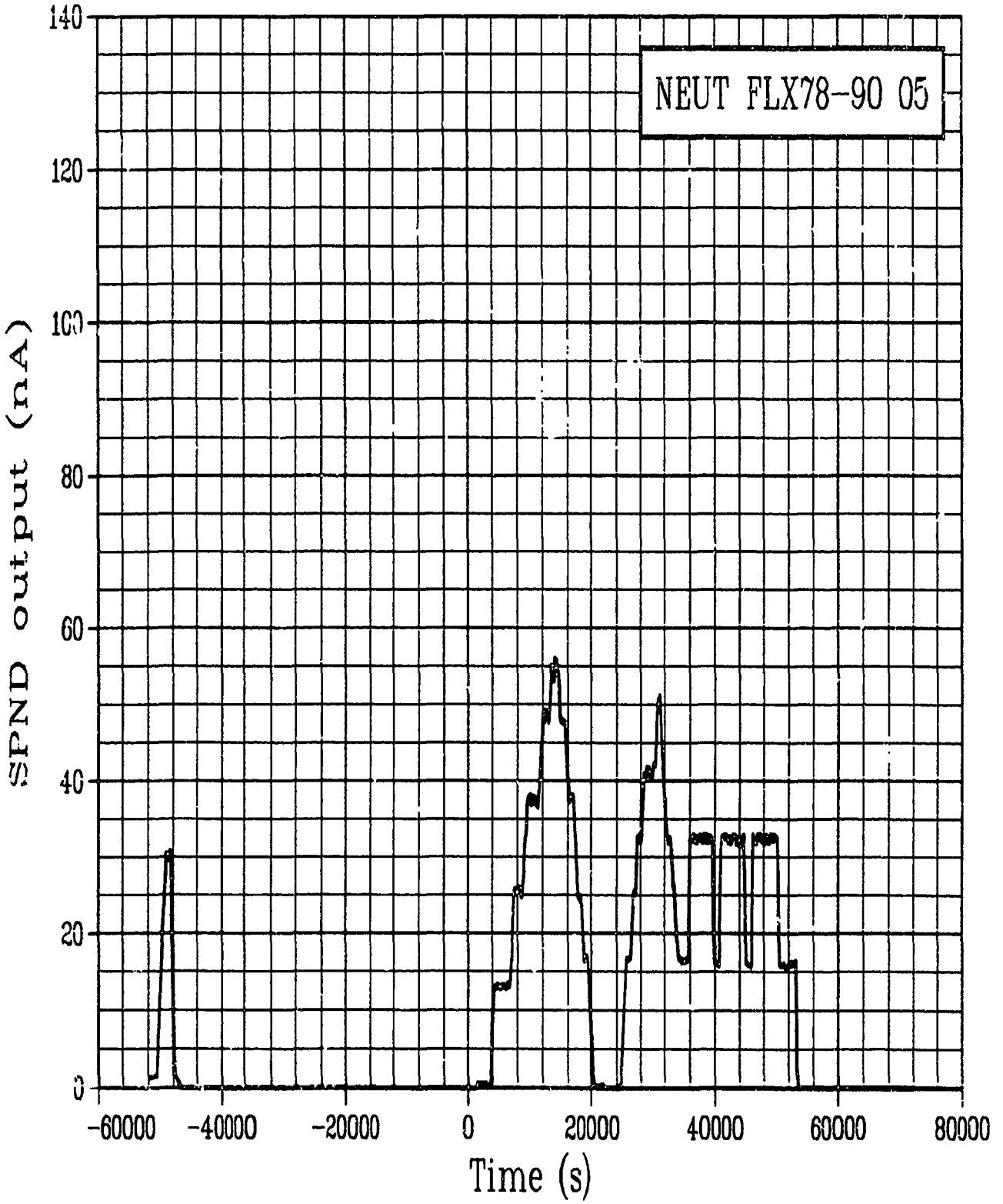

Figure C-102. Neutron flux 0.78 m from bottom of fuel stack during Test PR-1 power calibration and preconditioning periods (NEUT FLX78-90 05).

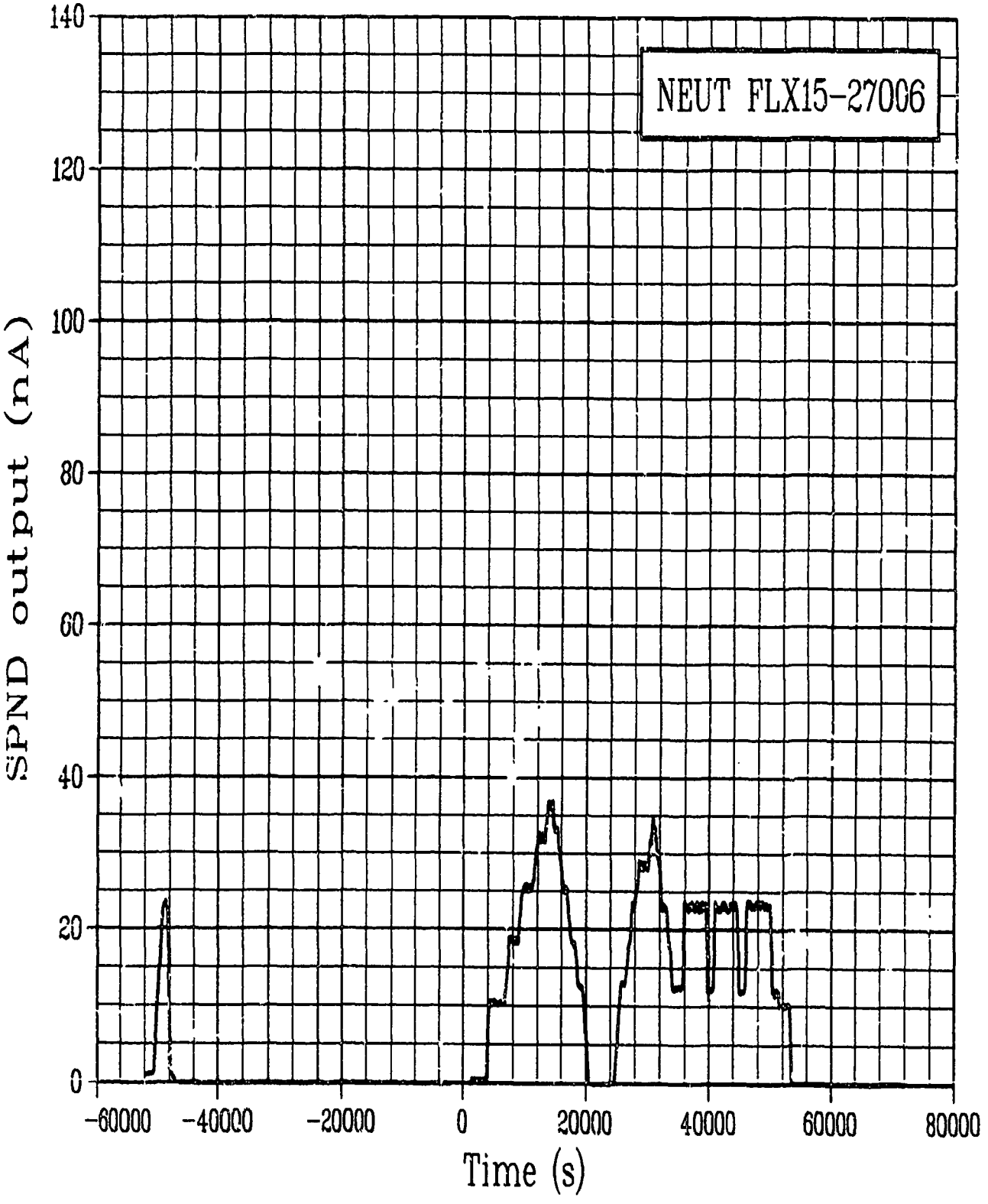

Figure C-103. Neutron flux 0.15 m from bottom of fuel stack during Test PR-1 power calibration and preconditioning periods (NEUT FLX15-27006).

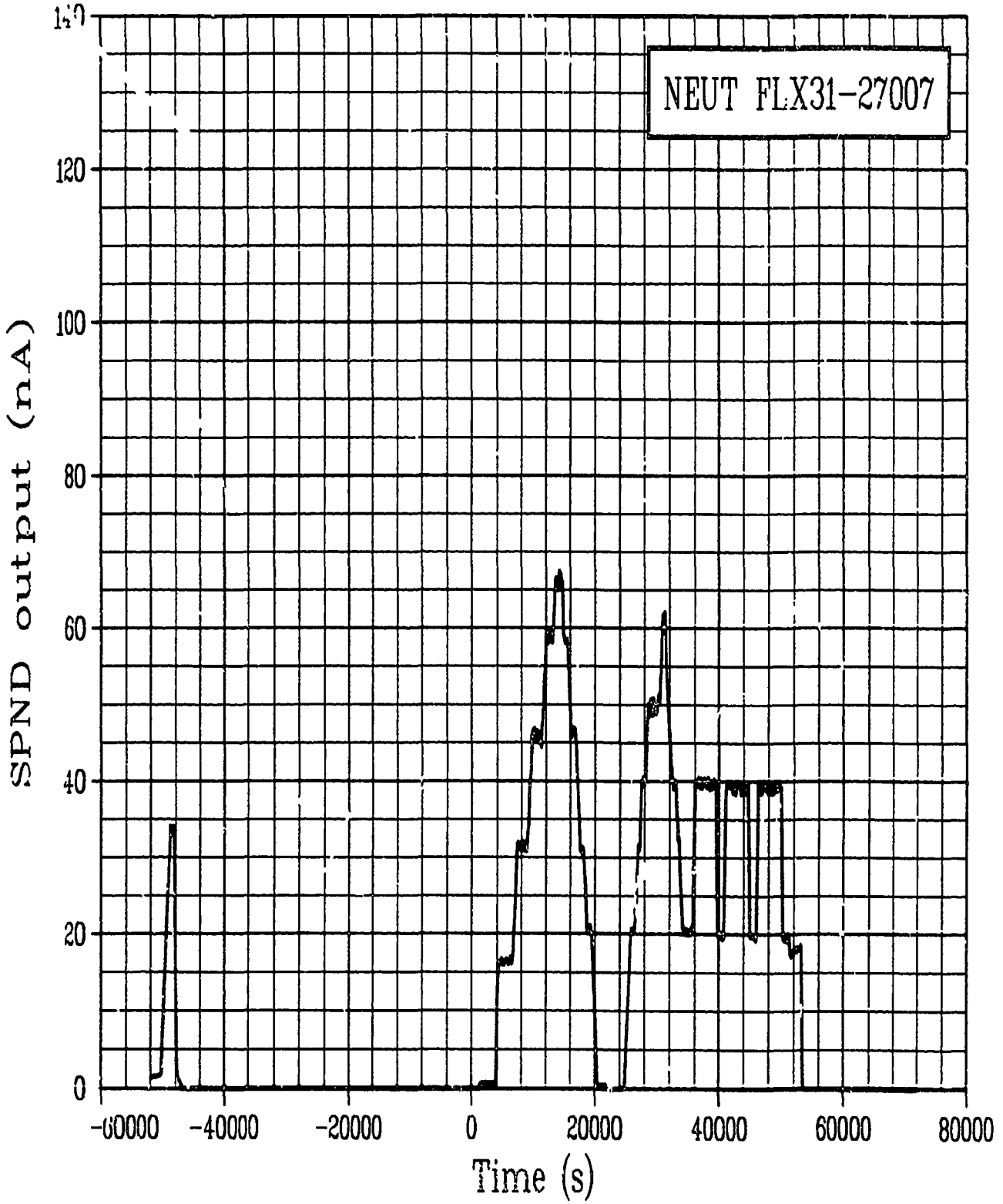

Figure C-104. Neutron flux 0.31 m from bottom of fuel stack during Test PR-1 power calibration and preconditioning periods (NEUT FLX31-27007).

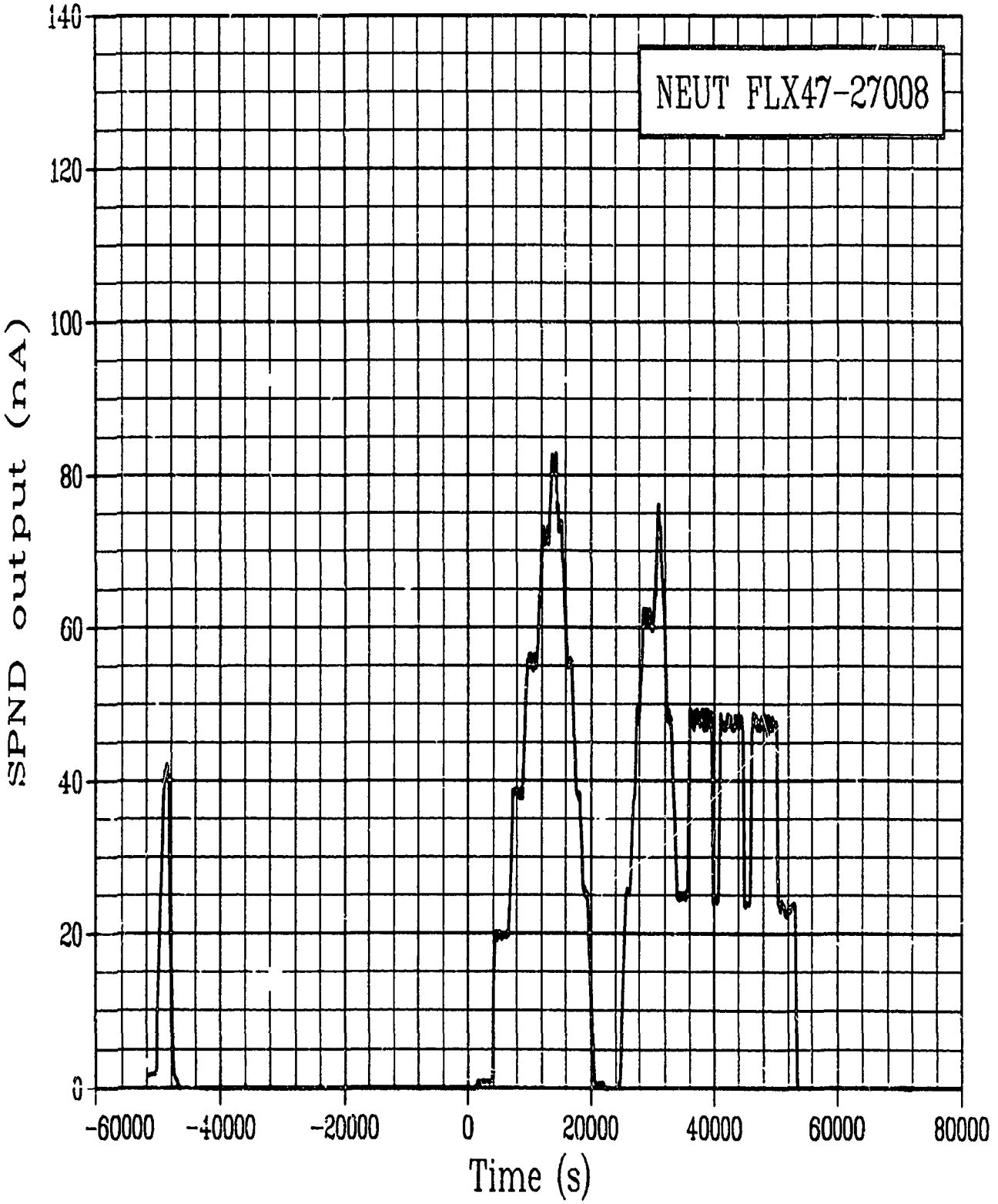

Figure C-105. Neutron flux 0.47 m from bottom of fuel stack during Test PR-1 power calibration and preconditioning periods (NEUT FLX47-27008).

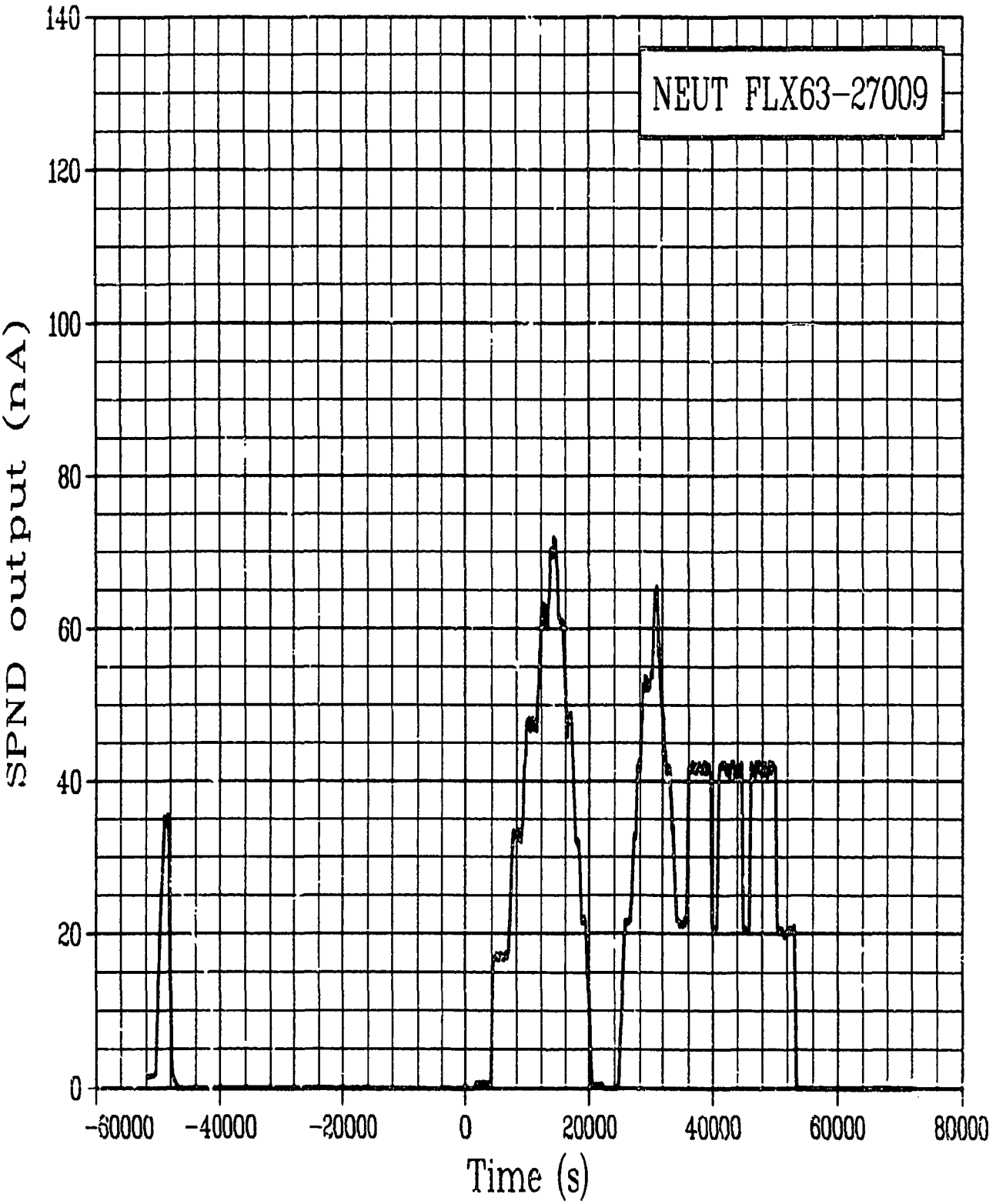

Figure C-106. Neutron flux 0.63 m from bottom of fuel stack during Test PR-1 power calibration and preconditioning periods (NEUT FLX63-27009).

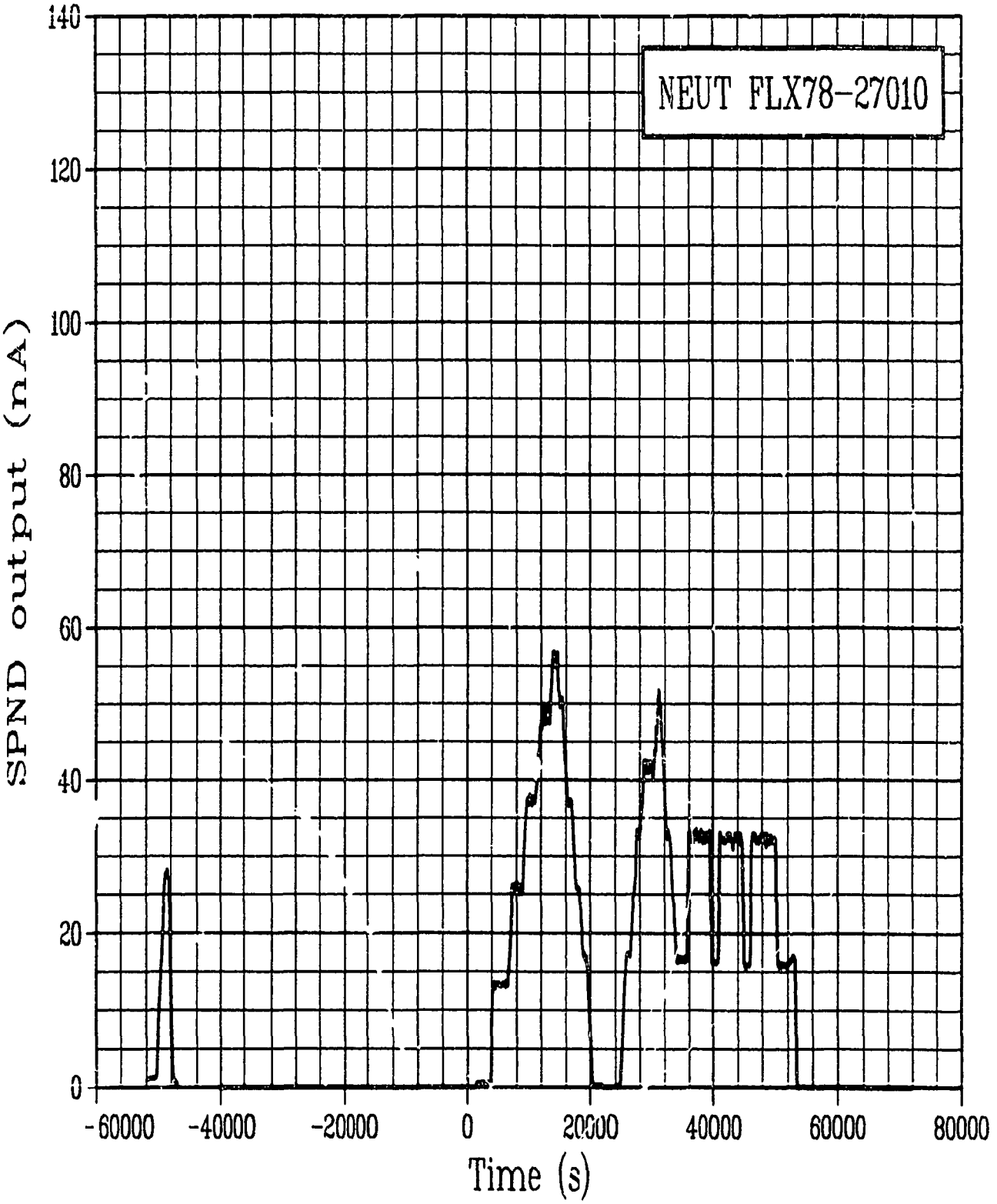

Figure C-107. Neutron flux 0.78 m from bottom of fuel stack during Test PR-1 power calibration and preconditioning periods (NEUT FLX78-27010).

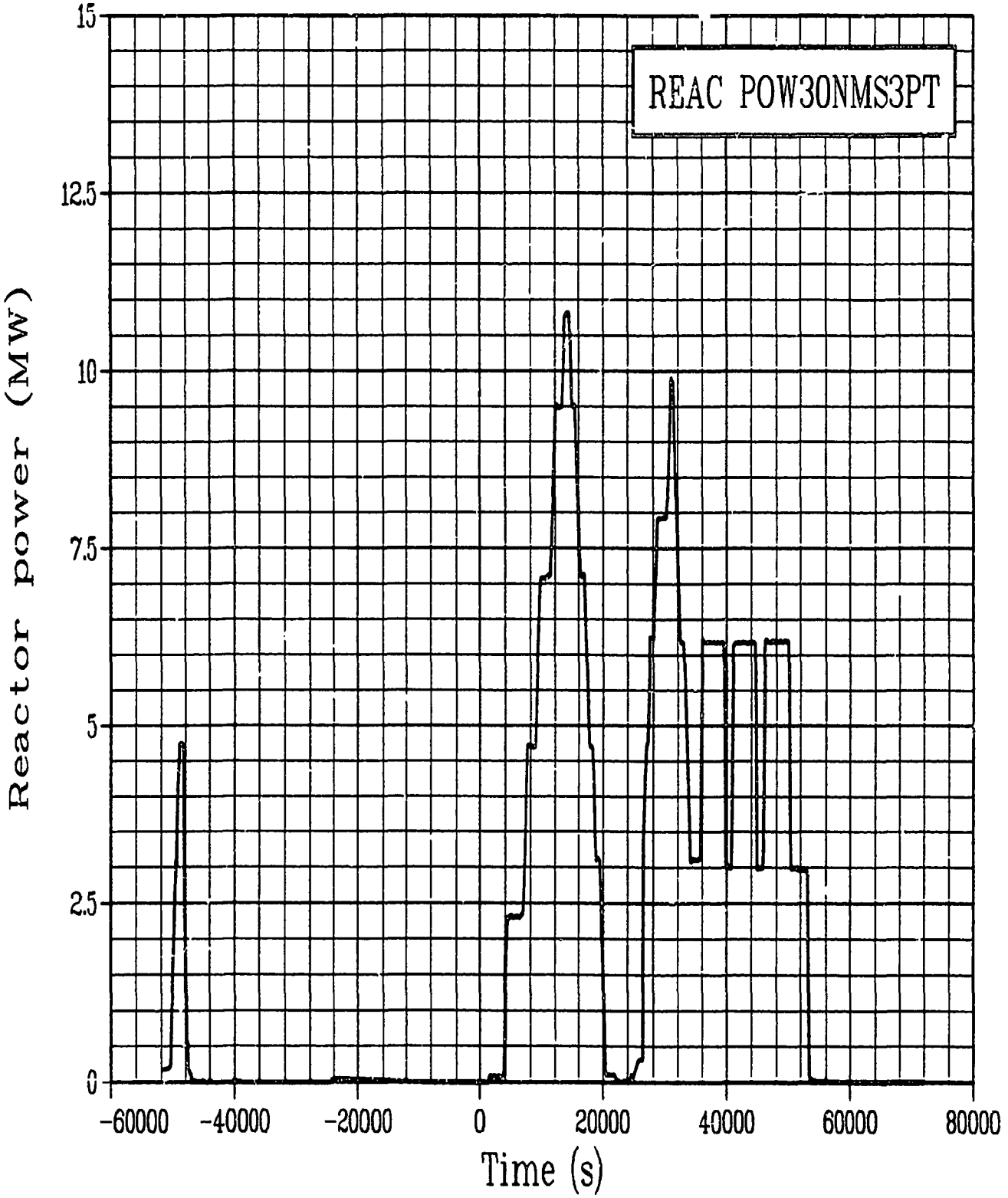

Figure C-108. Reactor power from Core Ionization Chamber NMS 3 during Test PR-1 power calibration and preconditioning periods (REAC POW30NMS3PT).

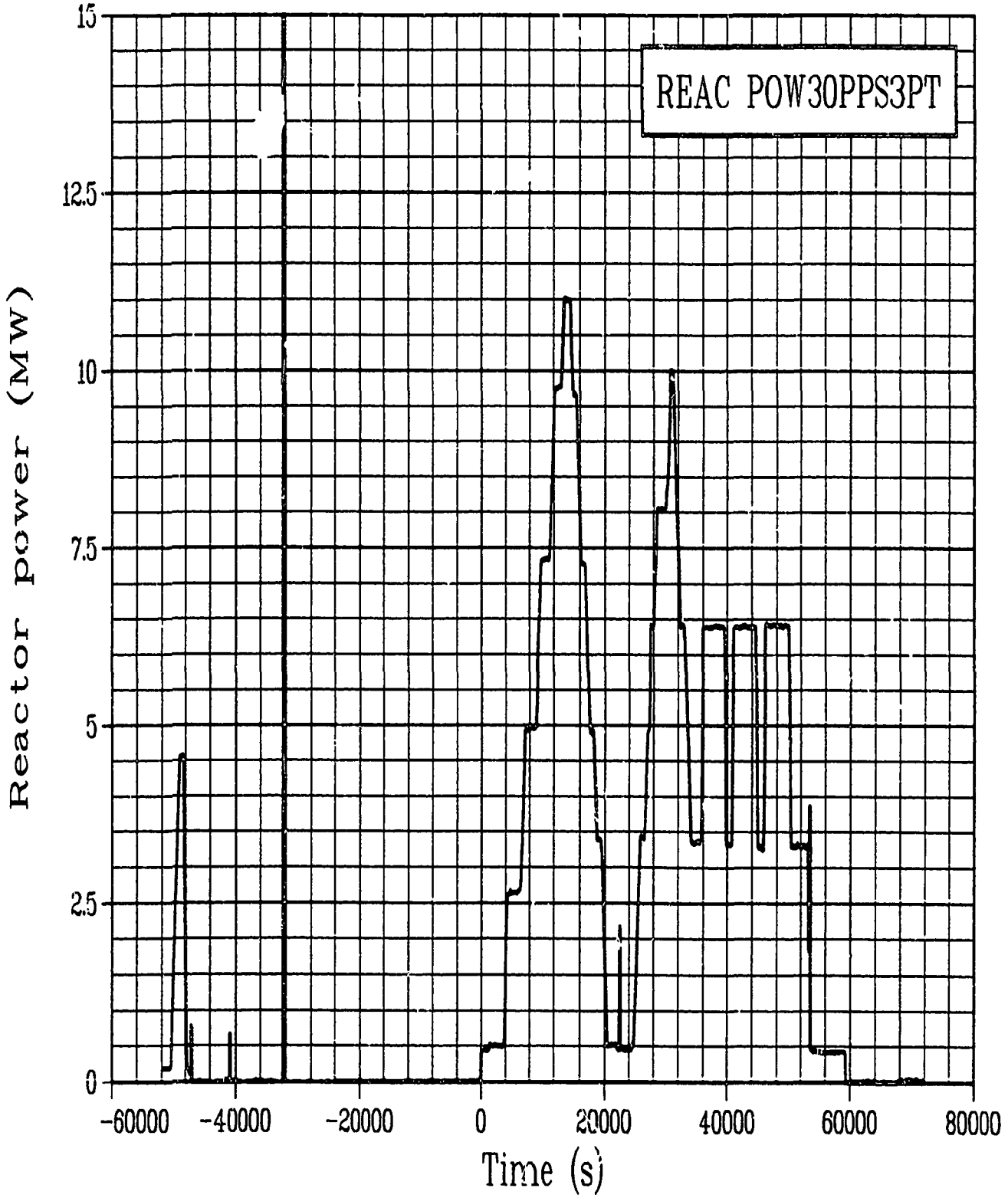

Figure C-109. Reactor power from Core Ionization Chamber PPS 3 during Test PR-1 power calibration and preconditioning periods (REAC POW30PPS3PT).

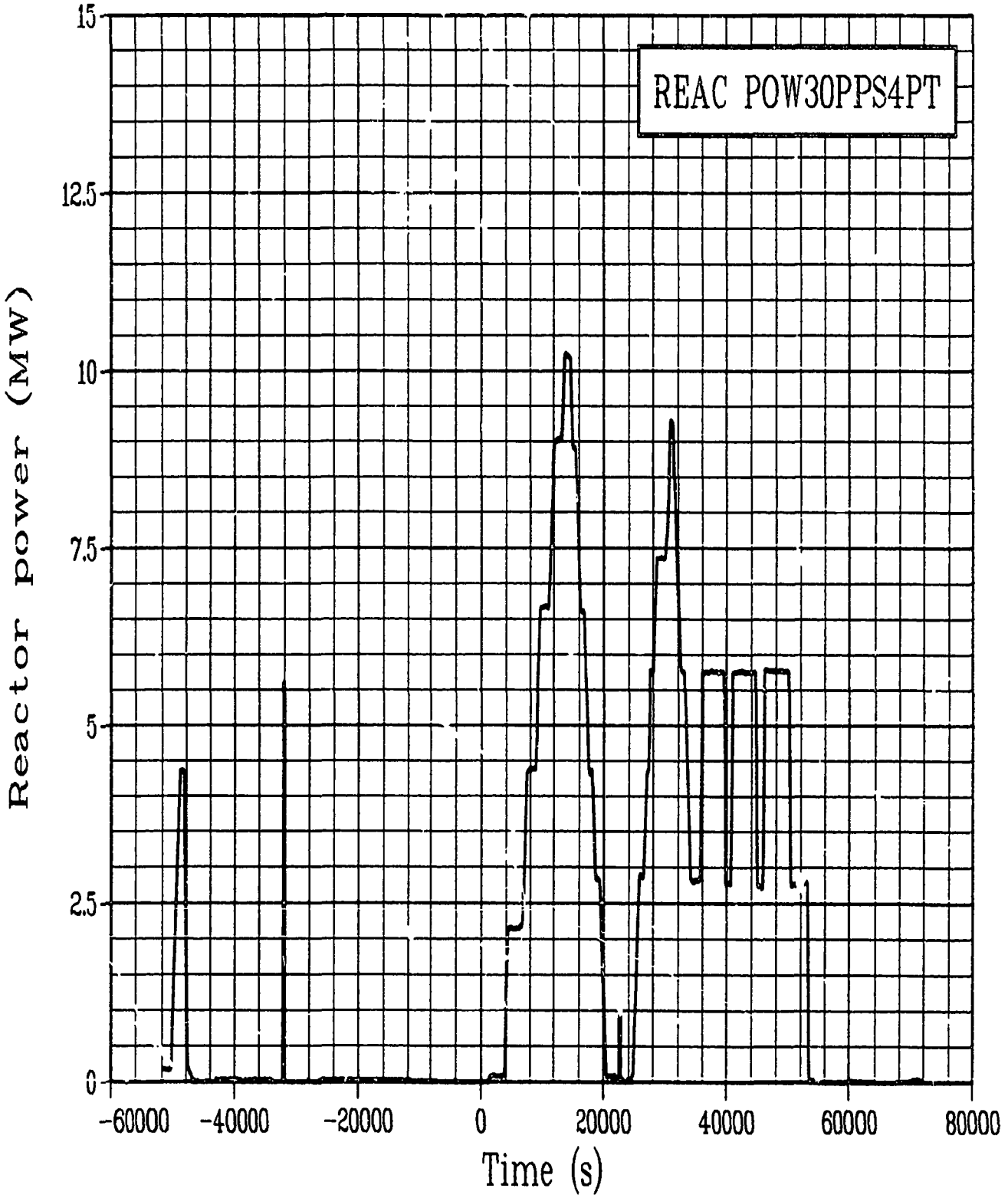

Figure C-110. Reactor power from Core Ionization Chamber PPS 4 during Test PR-1 power calibration and preconditioning periods (REAC POW30PPS4PT).

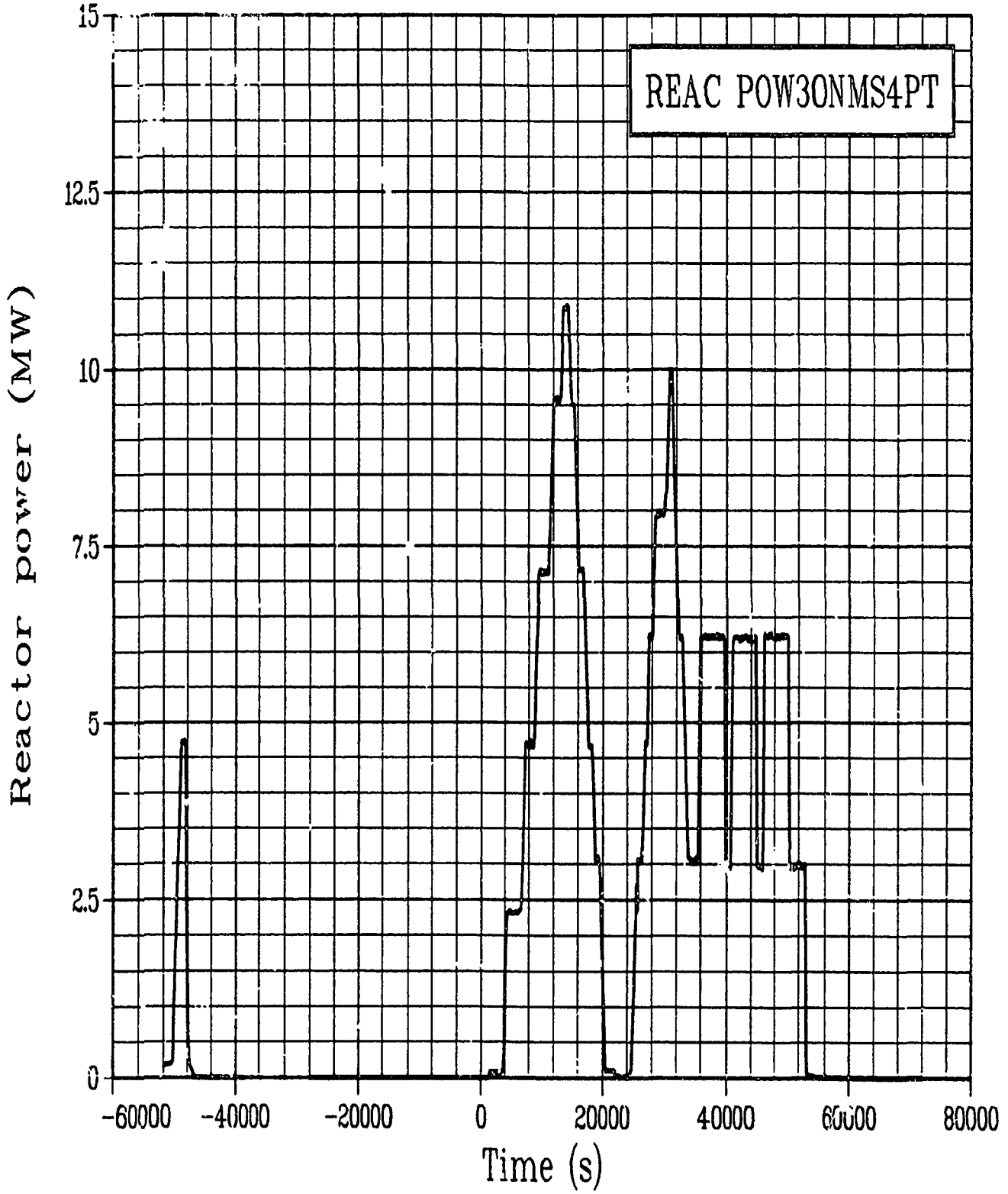

Figure C-111. Reactor power from Core Ionization Chamber NMS 4 during Test PR-1 power calibration and preconditioning periods (REAC POW30NMS4PT).

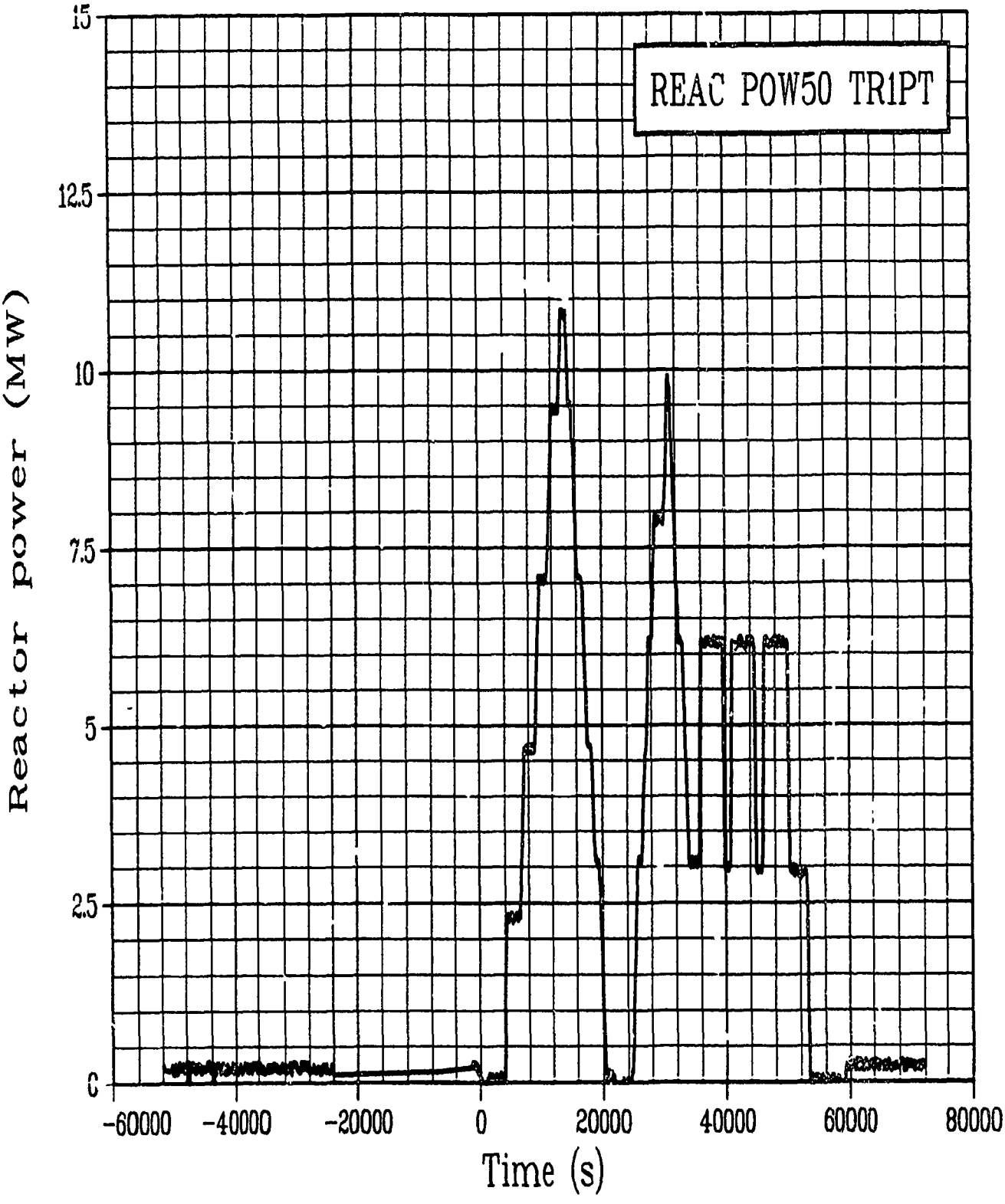

Figure C-112. Reactor power from Core Ionization Chamber TR 1 during Test PR-1 power calibration and preconditioning periods (REAC POW50 TR1PT).

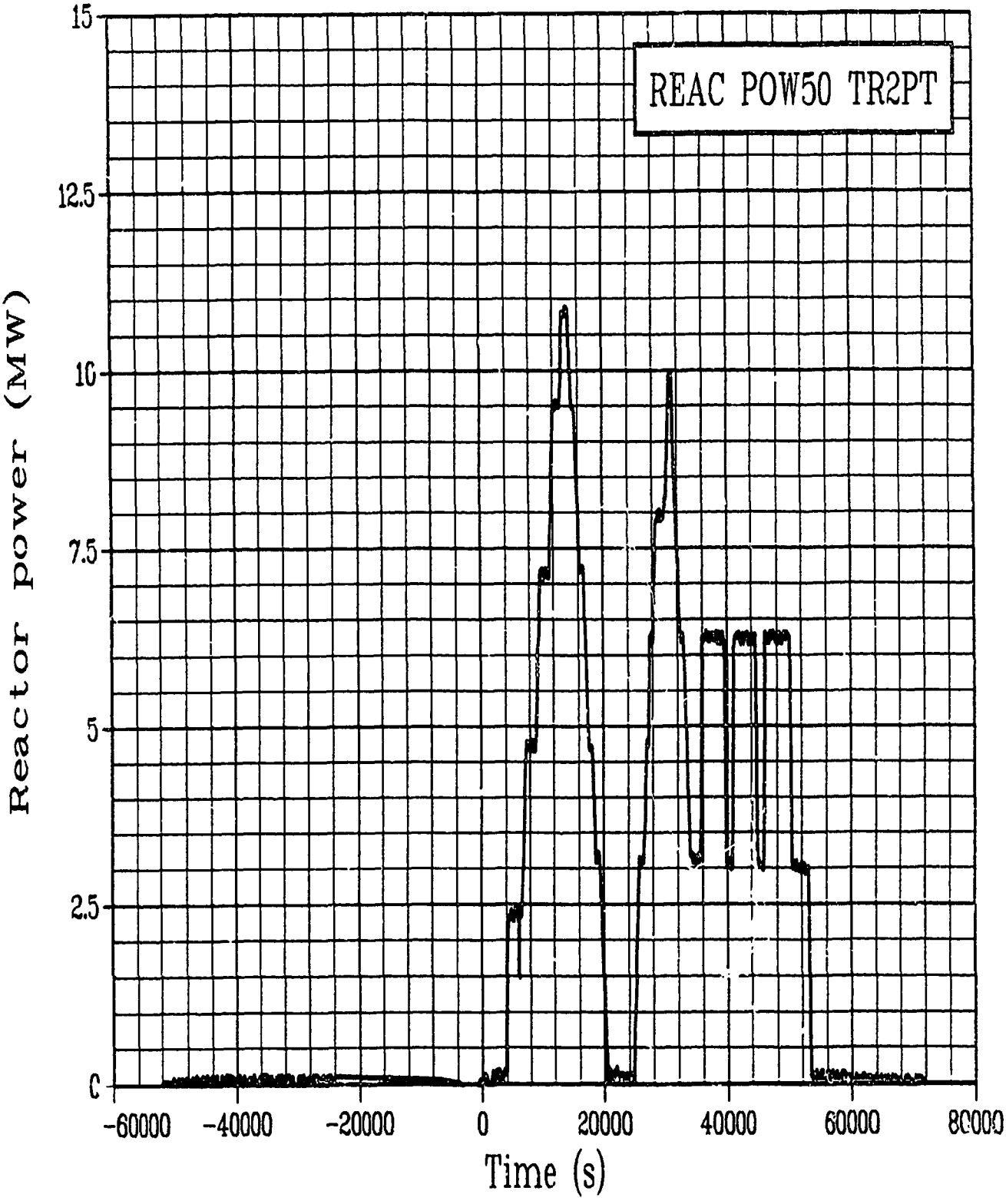

Figure C-113. Reactor power from Core Ionization Chamber TR 2 during Test PR-1 power calibration and preconditioning periods (REAC POW50 TR2PT).

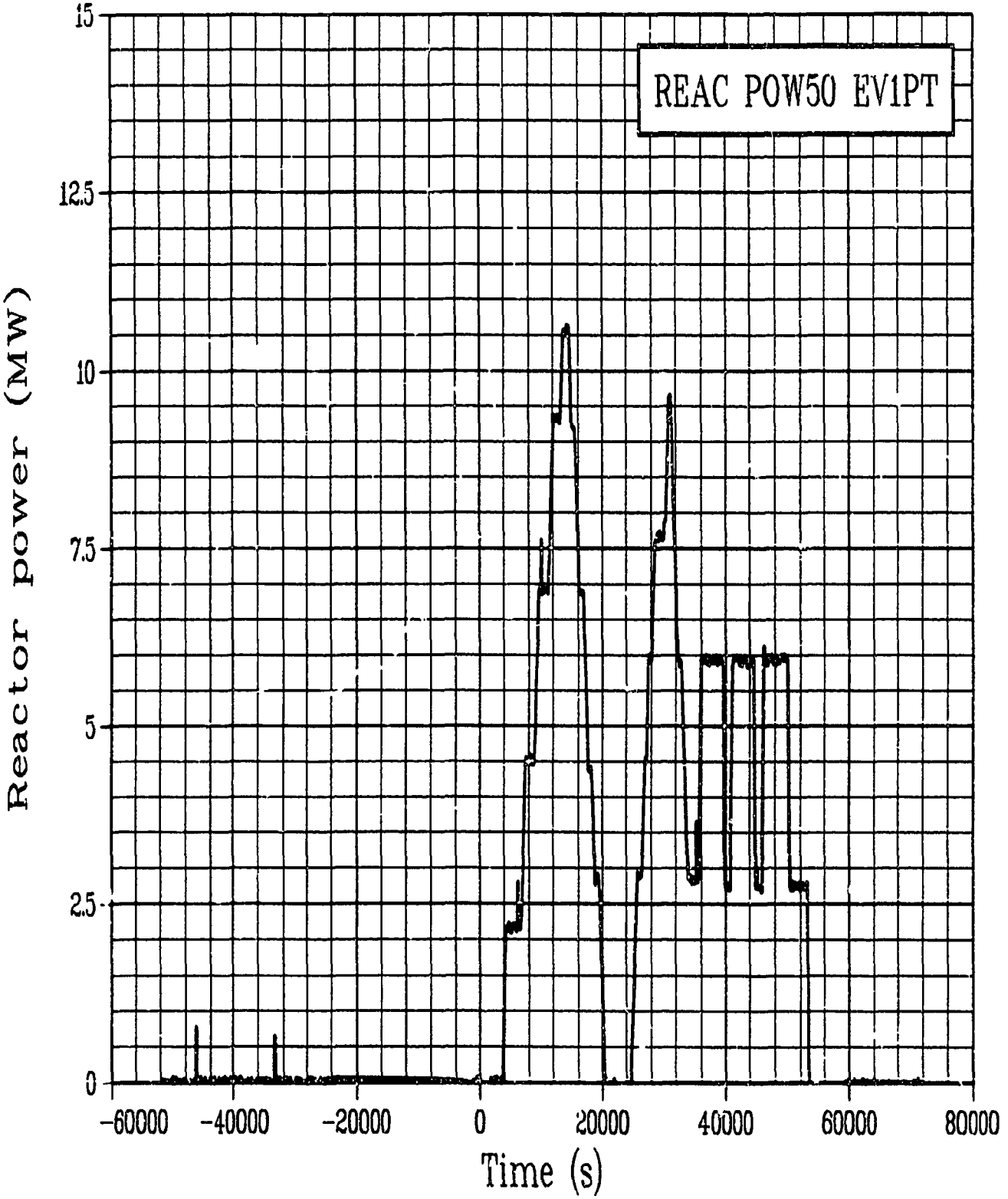

Figure C-114. Reactor power from Core Ionization Chamber EV 1 during Test PR-1 power calibration and preconditioning periods (REAC POW50 EV1PT).

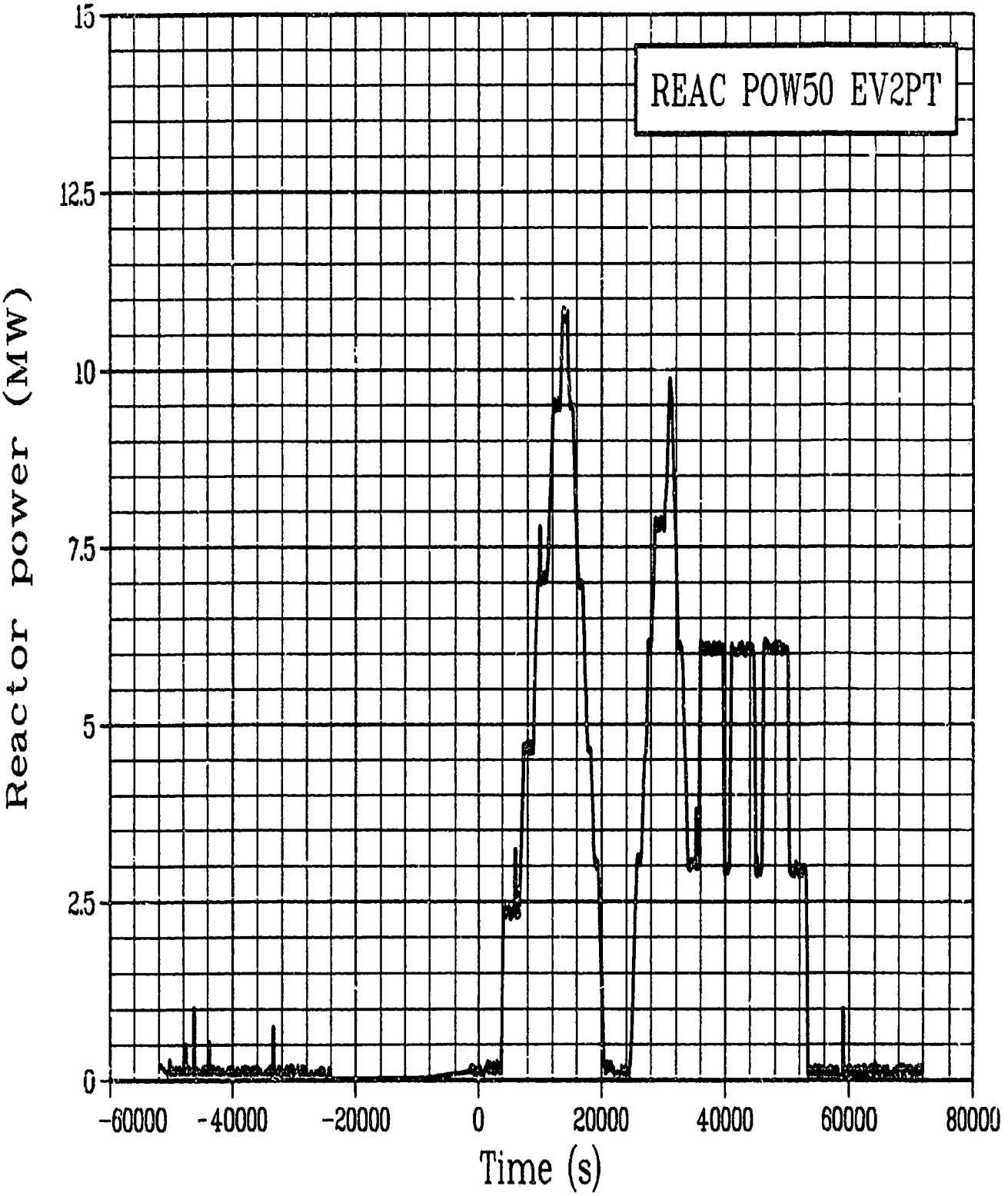

Figure C-115. Reactor power from Core Ionization Chamber EV 2 during Test PR-1 power calibration and preconditioning periods (REAC POW50 EV2PT).

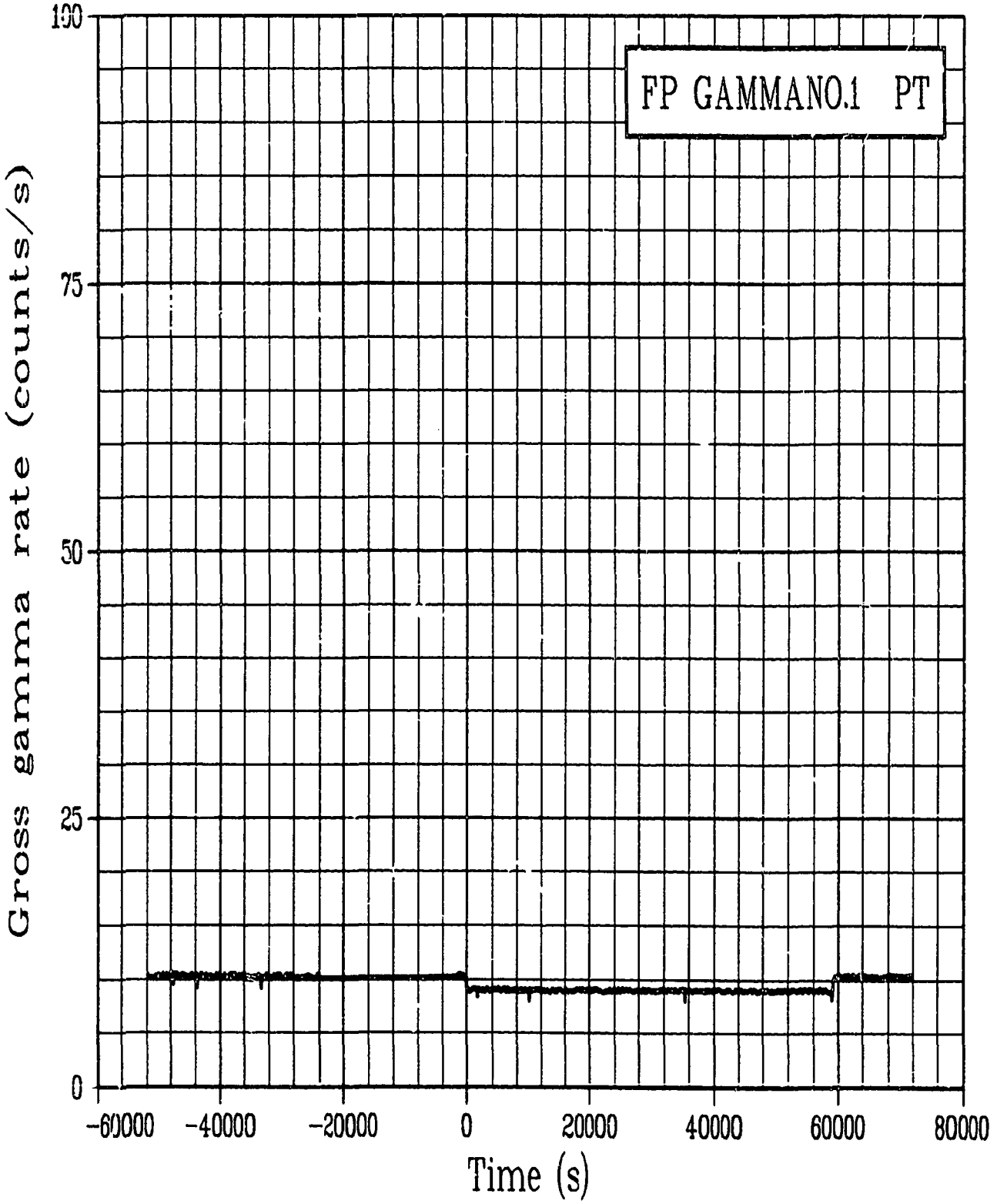

Figure C-116. Gross gamma rate of fission product detector 1 during Test PR-1 power calibration and preconditioning periods (FP GAMMANO.1 PT).

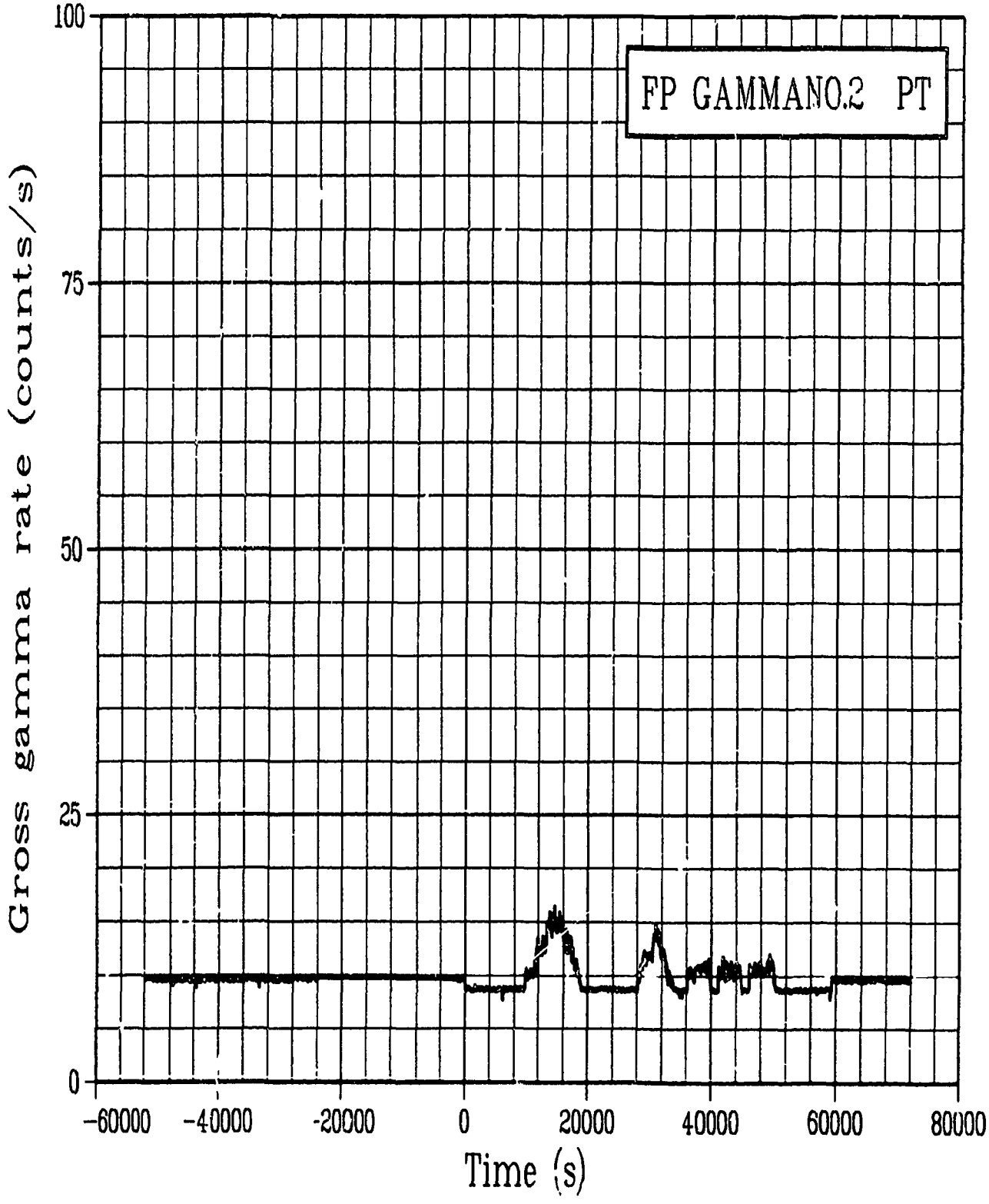

Figure C-117. Gross gamma rate of fission product detector 2 during Test PR-1 power calibration and preconditioning periods (FP GAMMANO.2 PT).

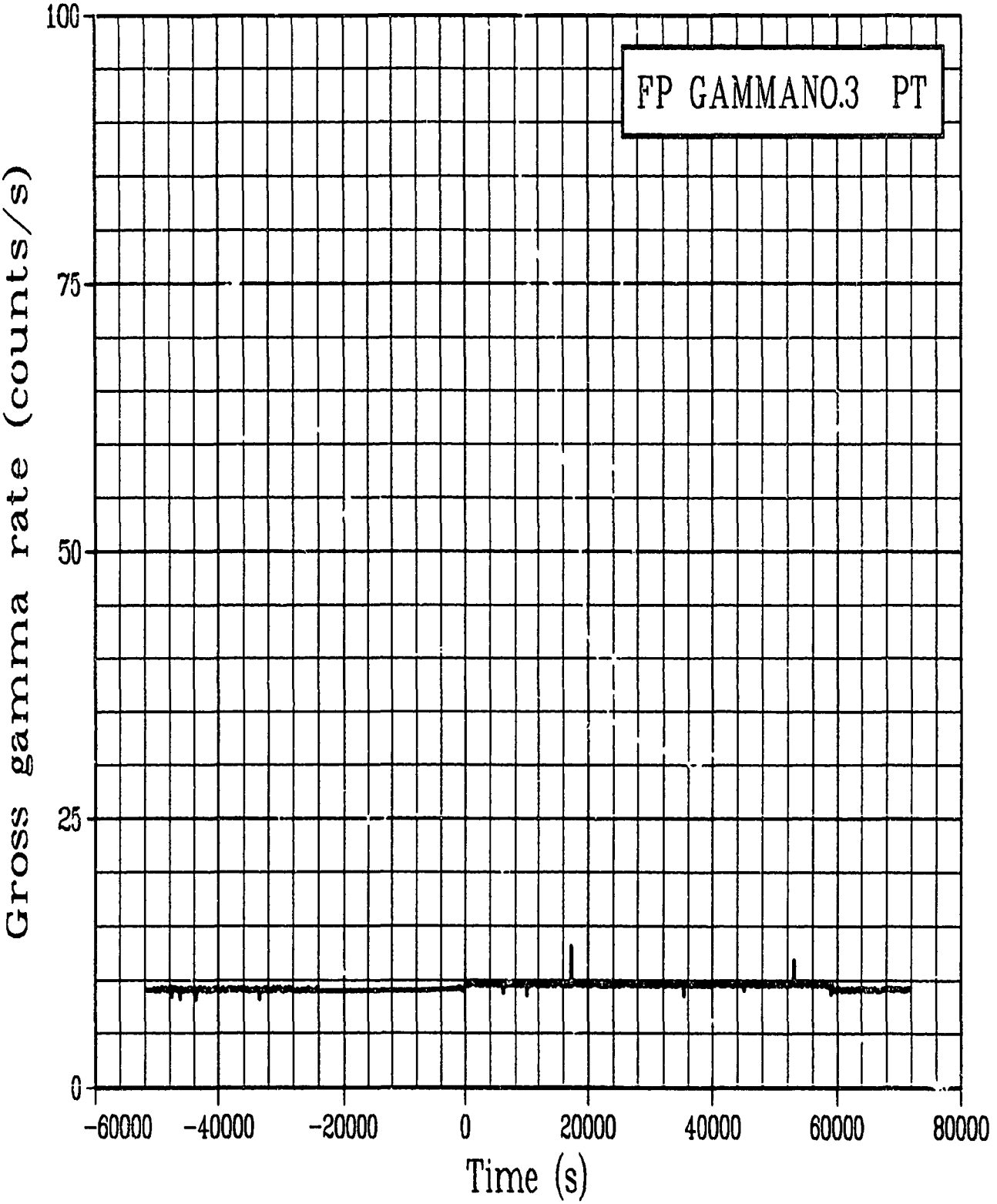

Figure C-118. Gross gamma rate of fission product detector 3 during Test PR-1 power calibration and preconditioning periods (FP GAMMANO.3 PT).

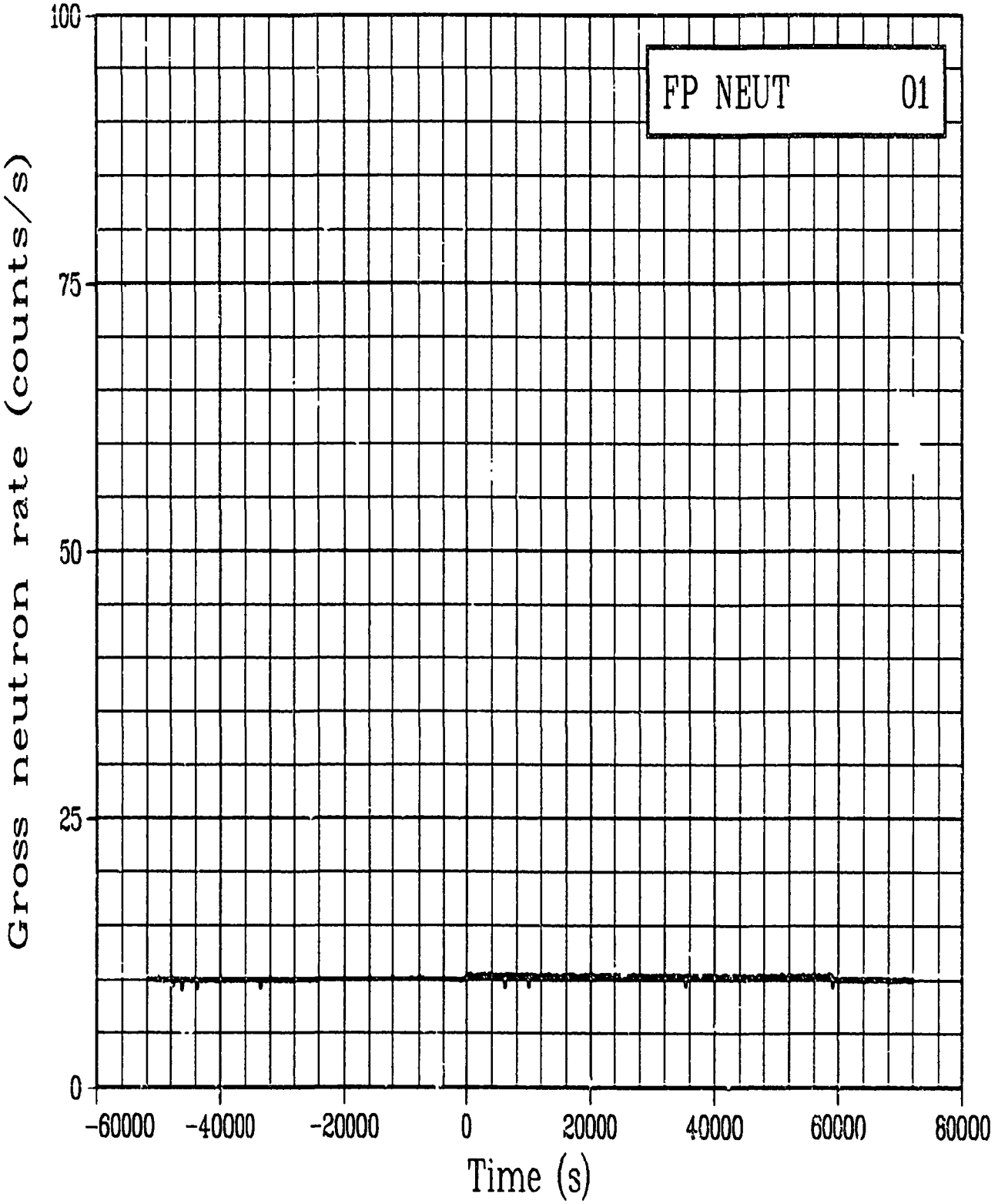

Figure C-119. Gross neutron rate of fission product detector system during Test PR-1 power calibration and preconditioning periods (FP NEUT 01).

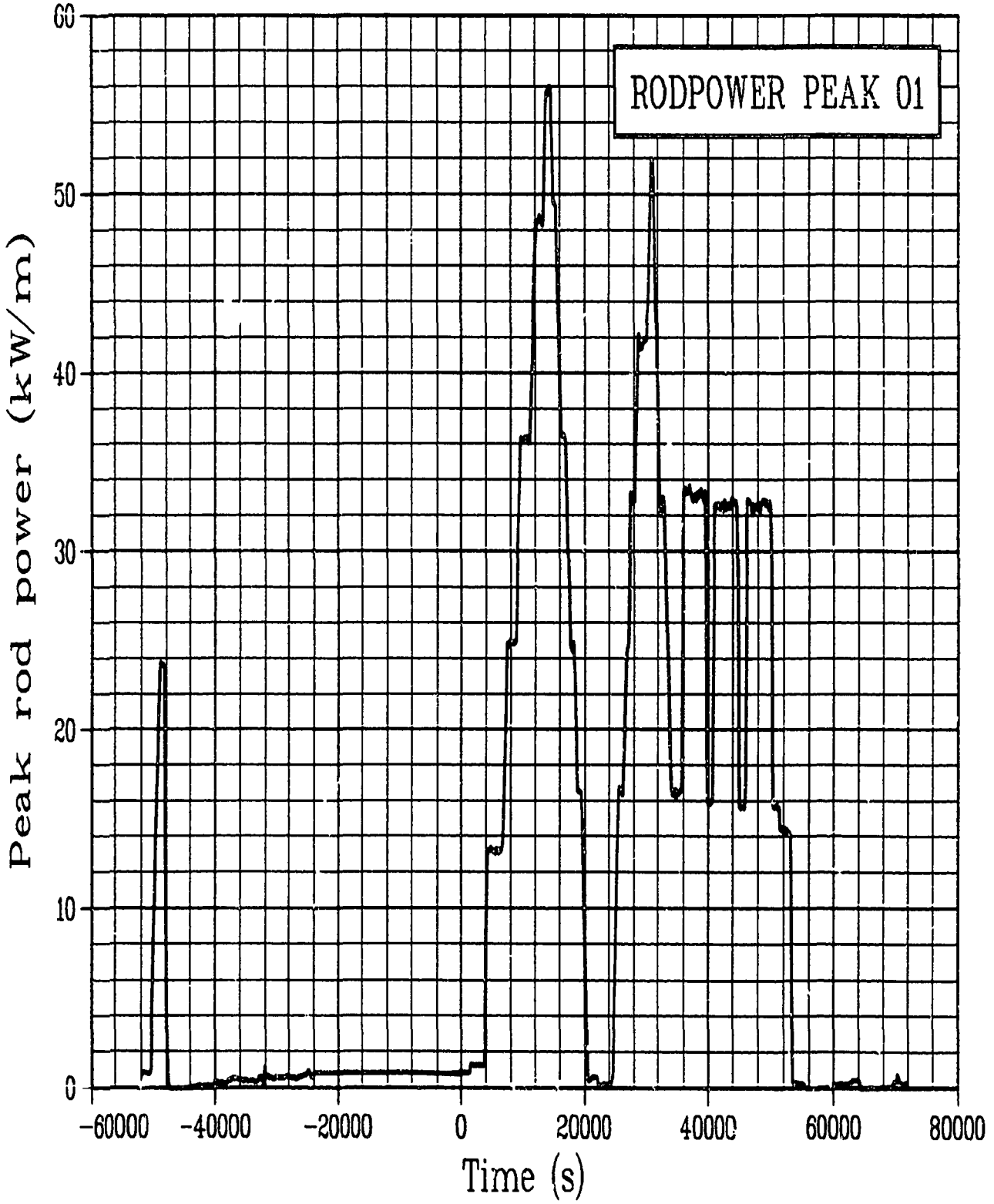

Figure C--120. Calculated peak rod power Rod GC 524-1 during Test PR-1 power calibration and preconditioning periods (RODPOWER PEAK 01).

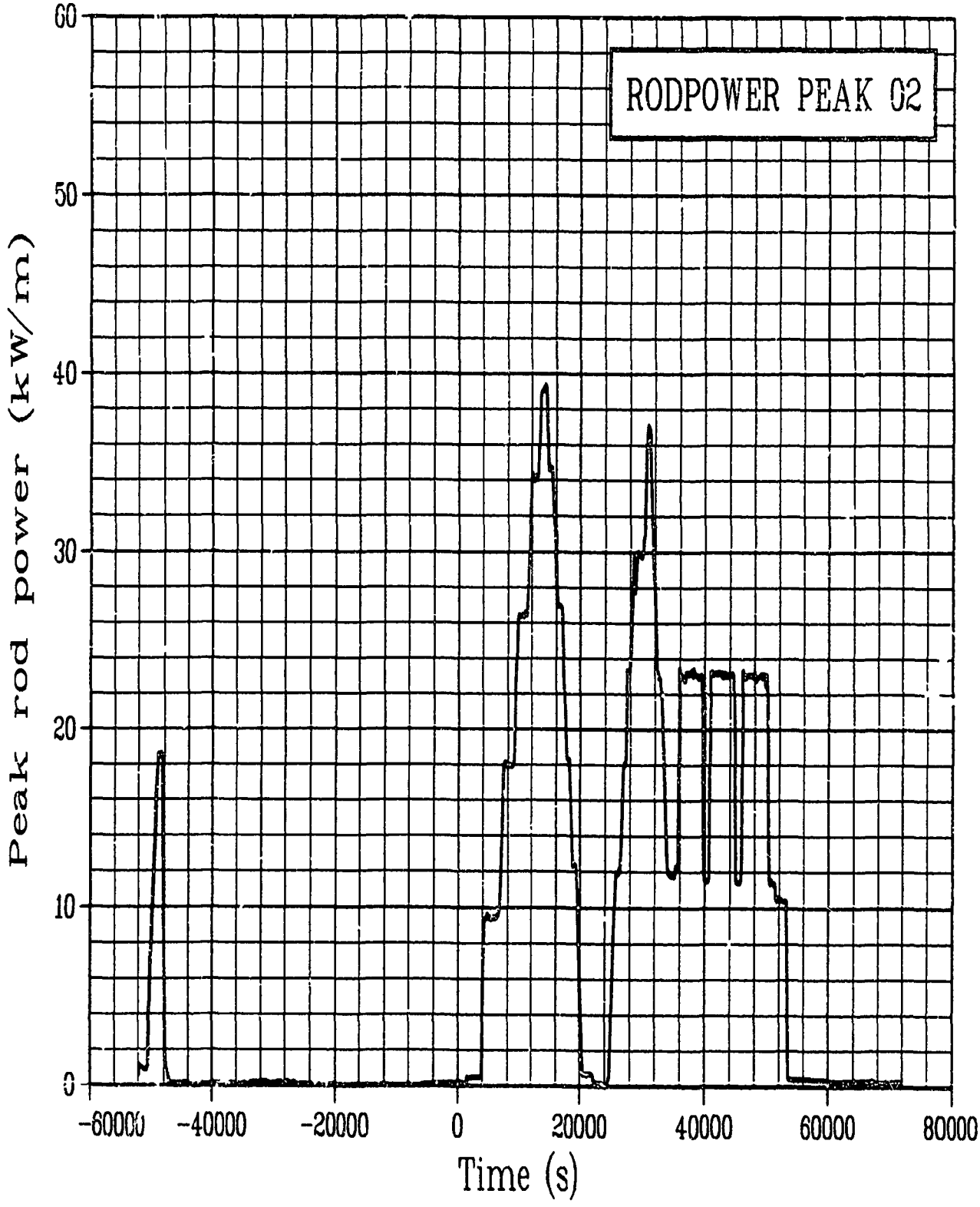

Figure C-121. Calculated peak rod power Rod GC 524-2 during Test PR-1 power calibration and preconditioning periods (RODPOWER PEAK 02).

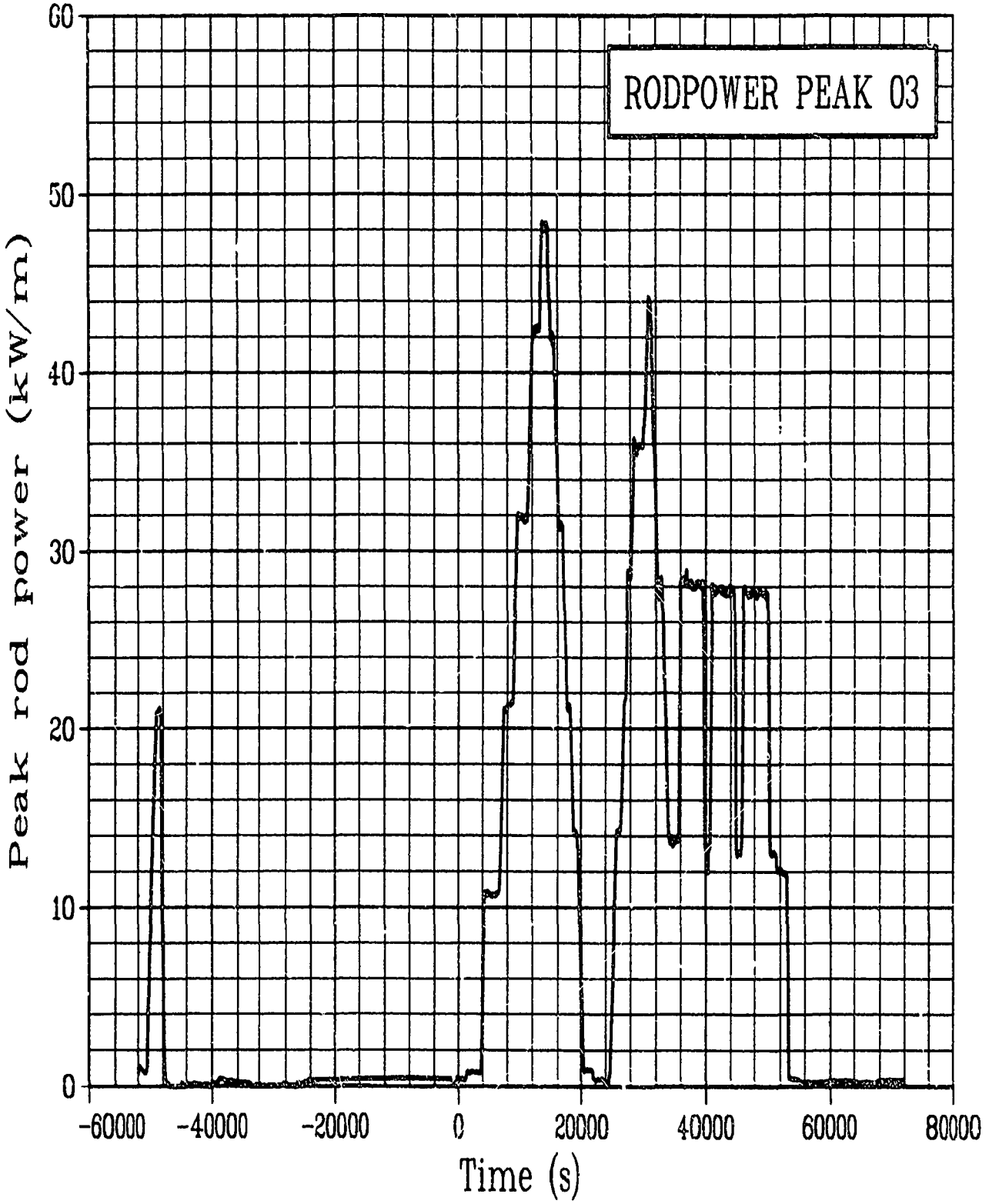

Figure C-122. Calculated peak rod power Rod GC 524-3 during Test PR-1 power calibration and preconditioning periods (RODPOWER PEAK 03).

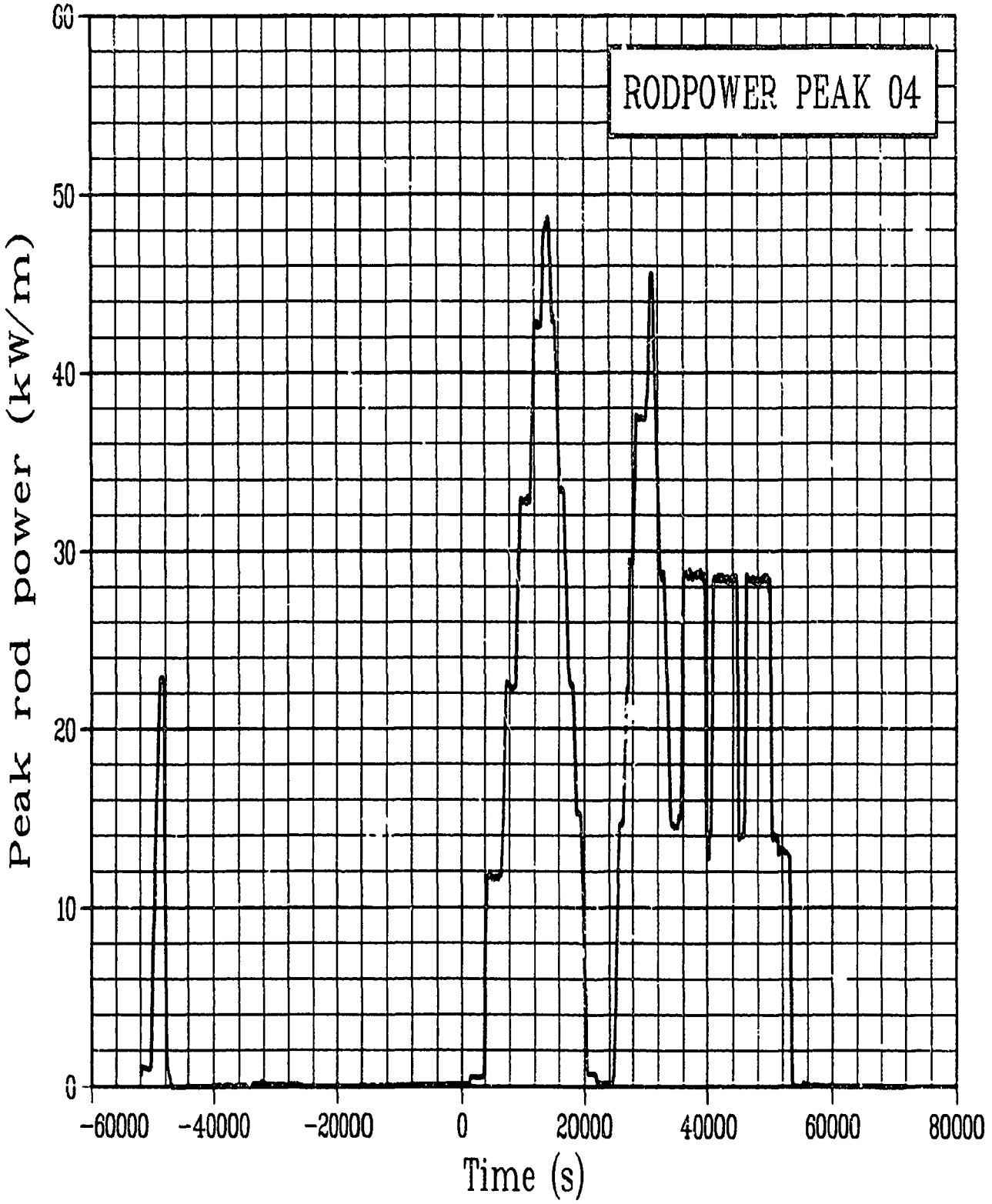

Figure C-123. Calculated peak rod power Rod GC 524-4 during Test PR-1 power calibration and preconditioning periods (RODPOWER PEAK 04).

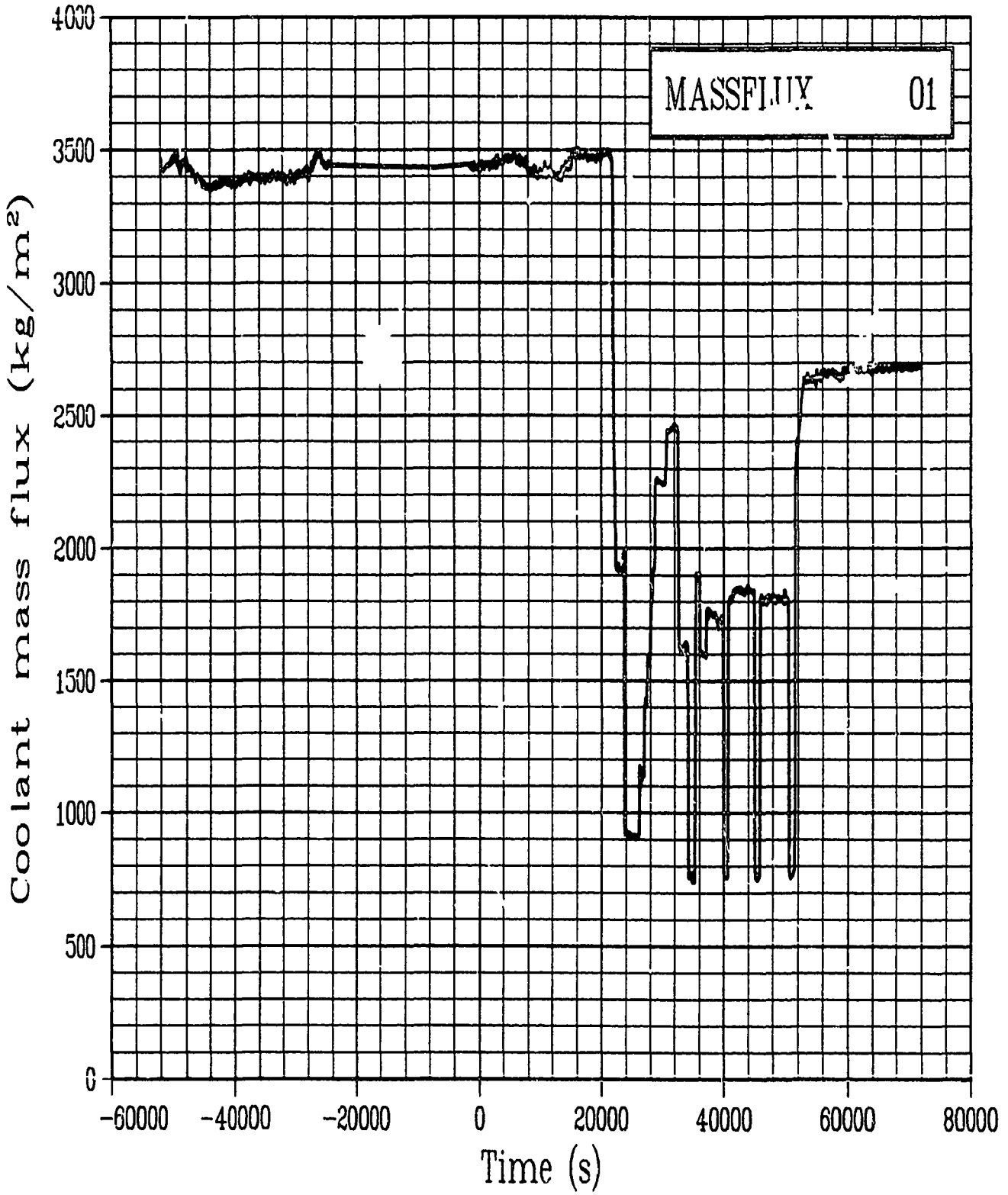

Figure C-124. Calculated coolant mass flux Rod GC 524-1 during Test PR-1 power calibration and preconditioning periods (MASSFLUX 01).

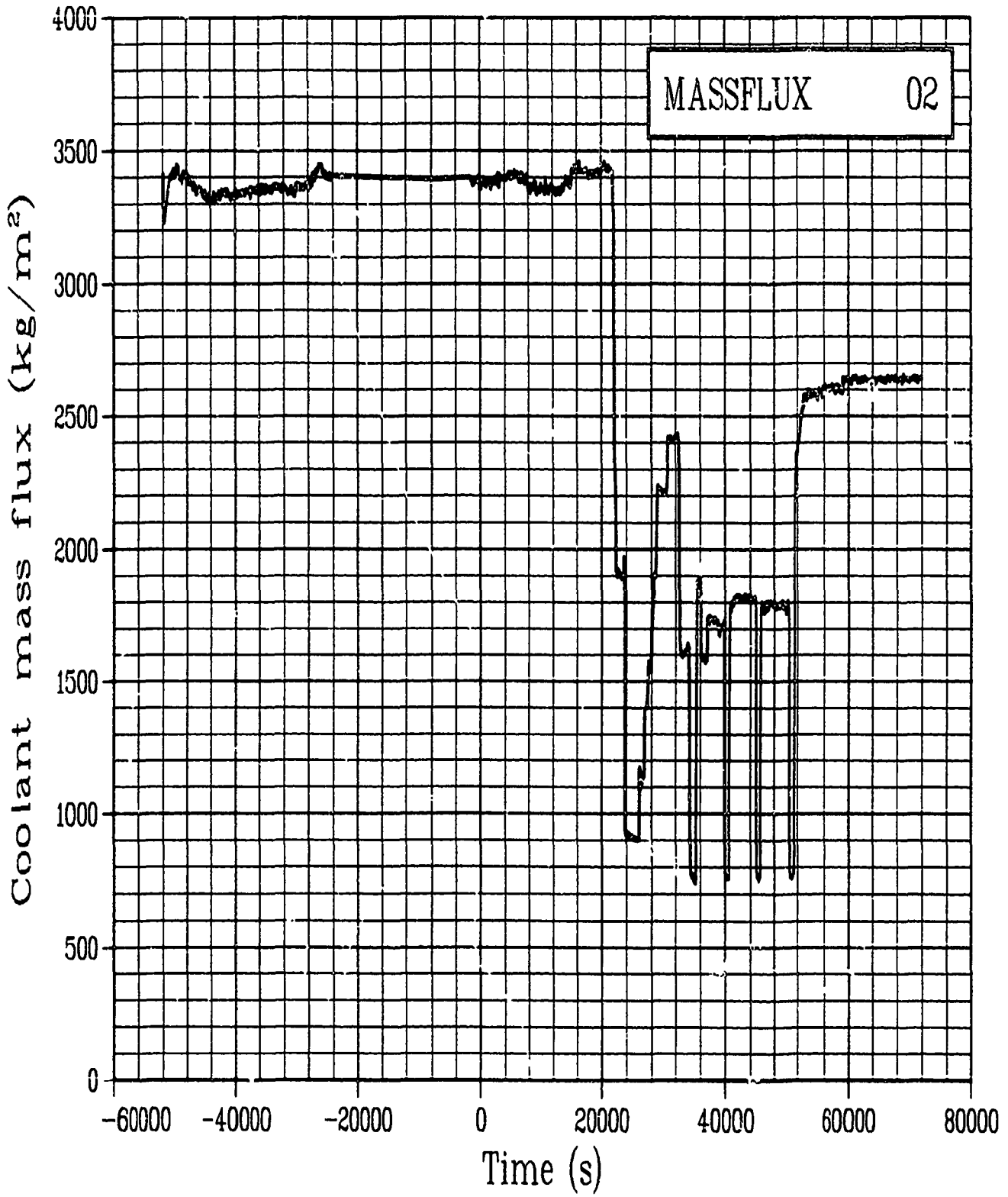

Figure C-125. Calculated coolant mass flux Rod GC 524-2 during Test PR-1 power calibration and preconditioning periods (MASSFLUX 02).

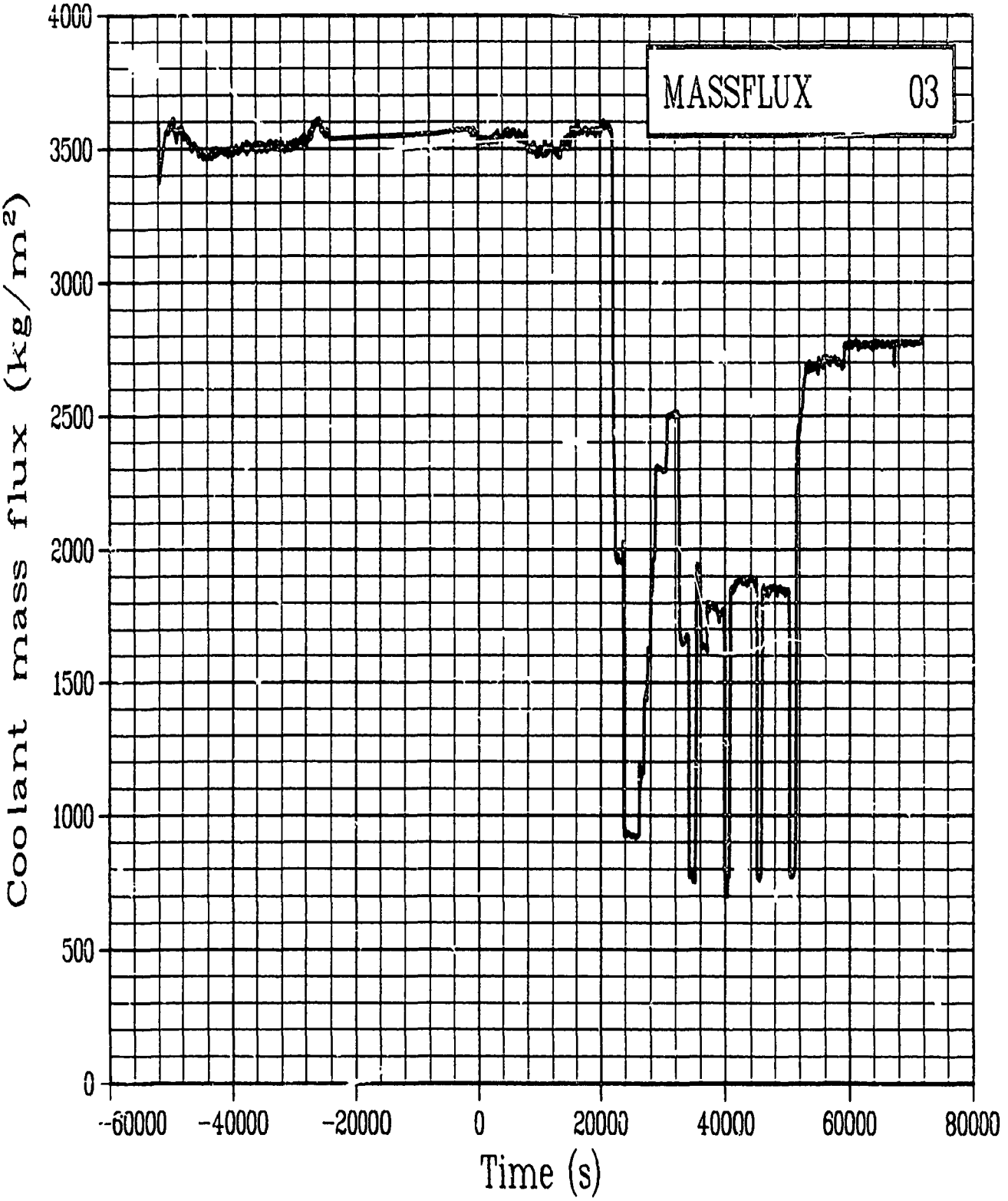

Figure C-126. Calculated coolant mass flux Rod GC 524-3 during Test PR-1 power calibration and preconditioning periods (MASSFLUX 03).

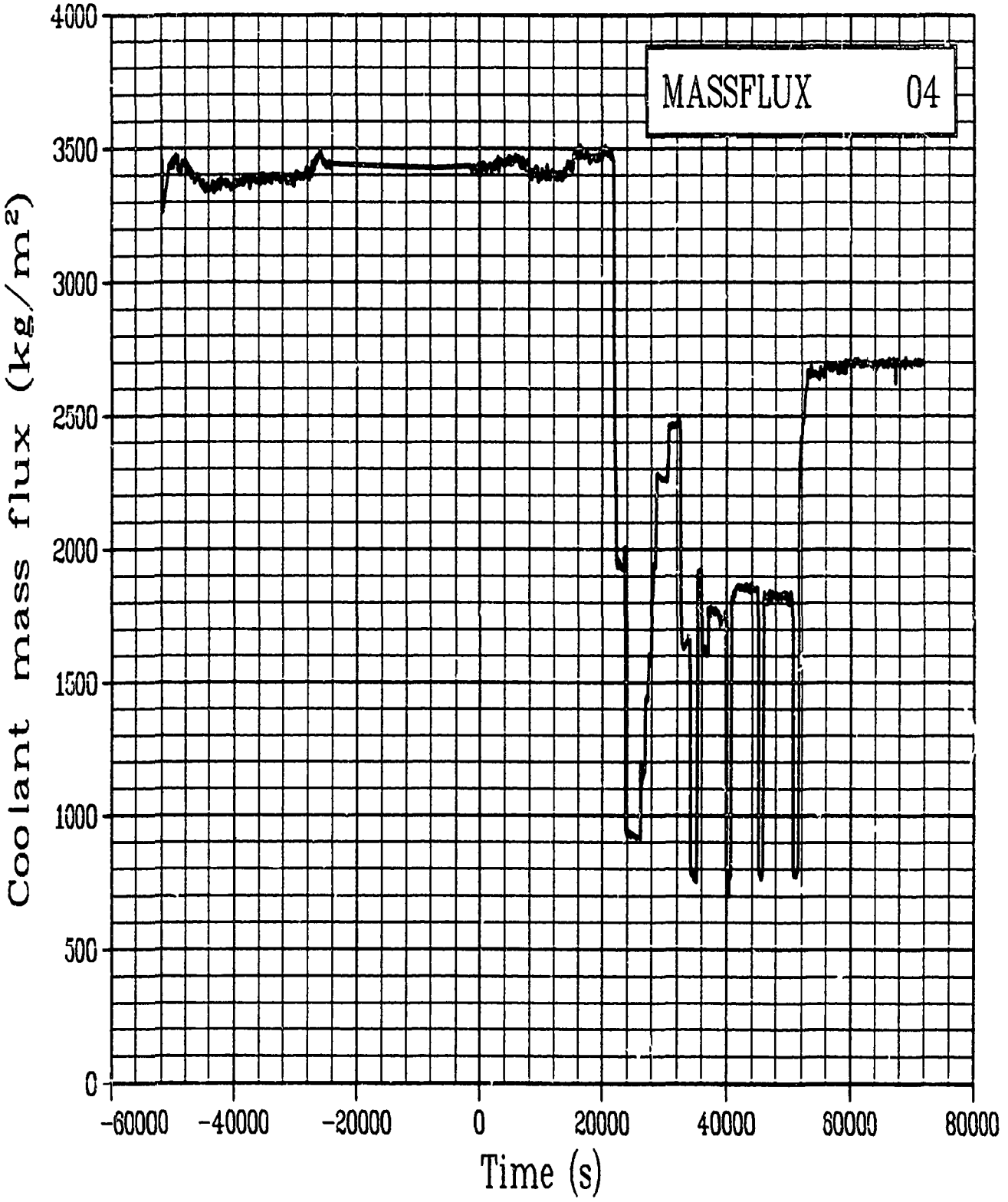

Figure C-127. Calculated coolant mass flux Rod GC 524-4 during Test PR-1 power calibration and preconditioning periods (MASSFLUX 04).

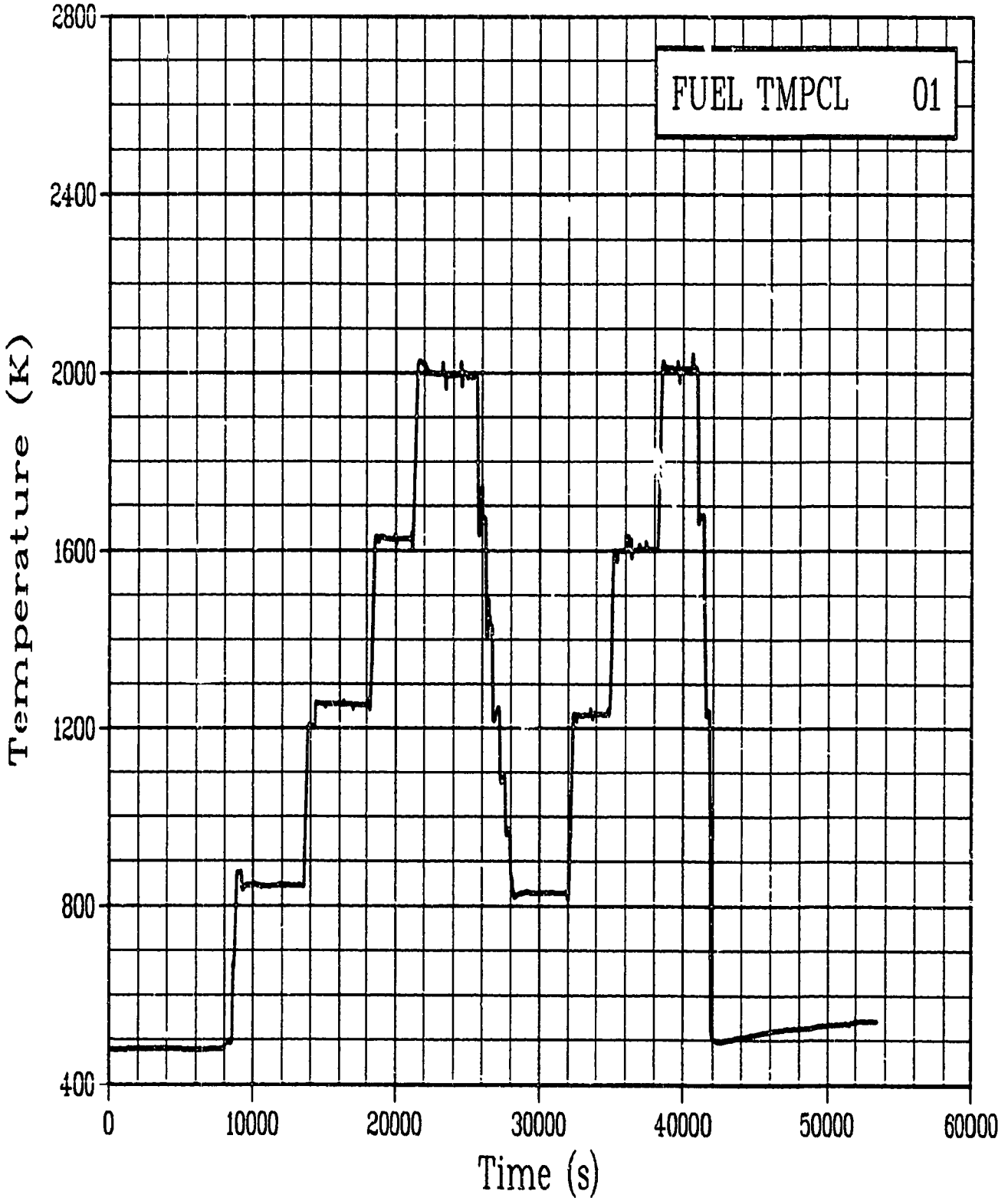

Figure C-128. Fuel centerline temperature Rod GC 524-1, 0.4521 m during Test PR-1 power oscillation period (FUEL TMPCL 01).

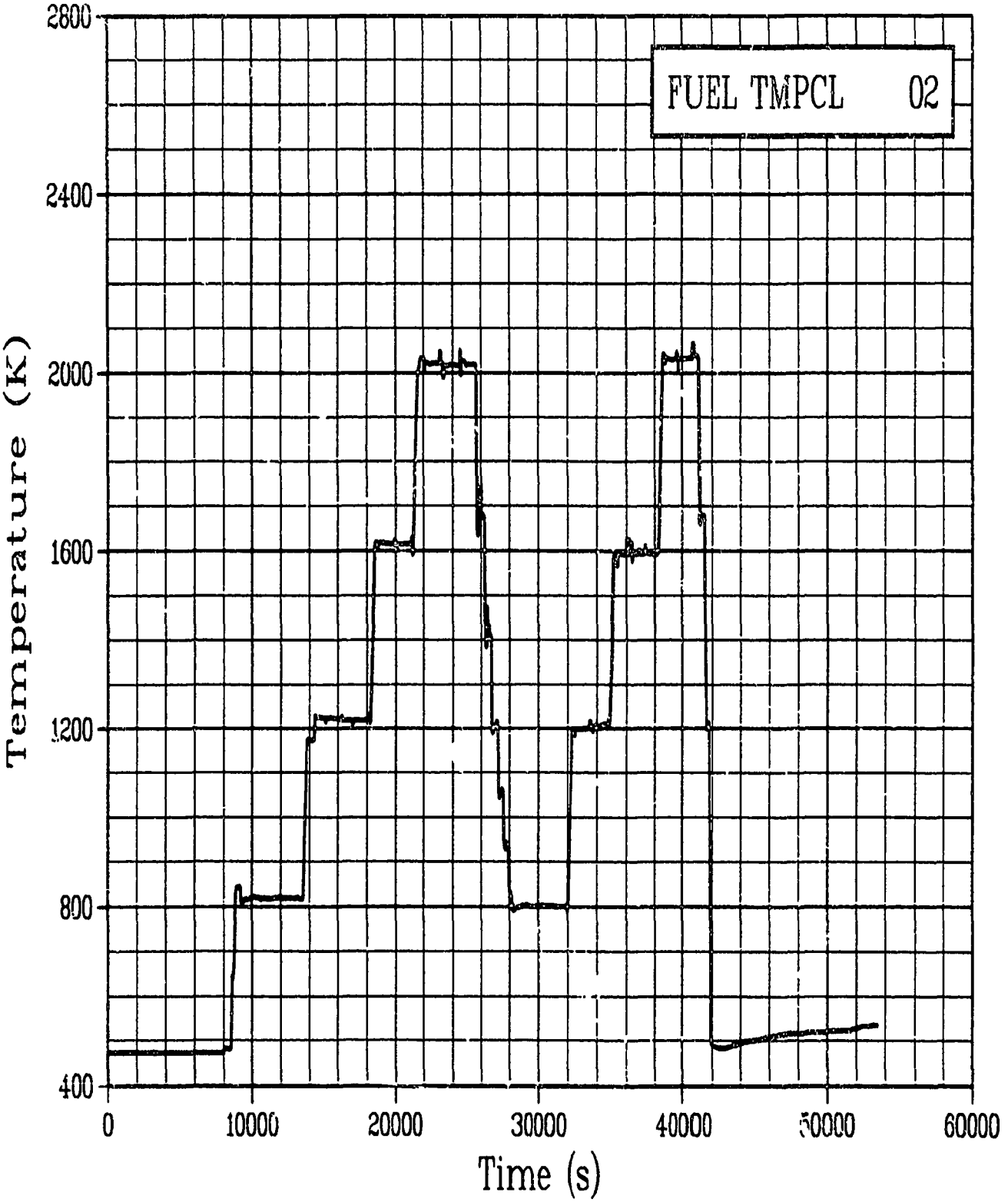

Figure C-129. Fuel centerline temperature Rod GC 524-2, 0.4521 m during Test PR-1 power oscillation period (FUEL TMPCL 02).

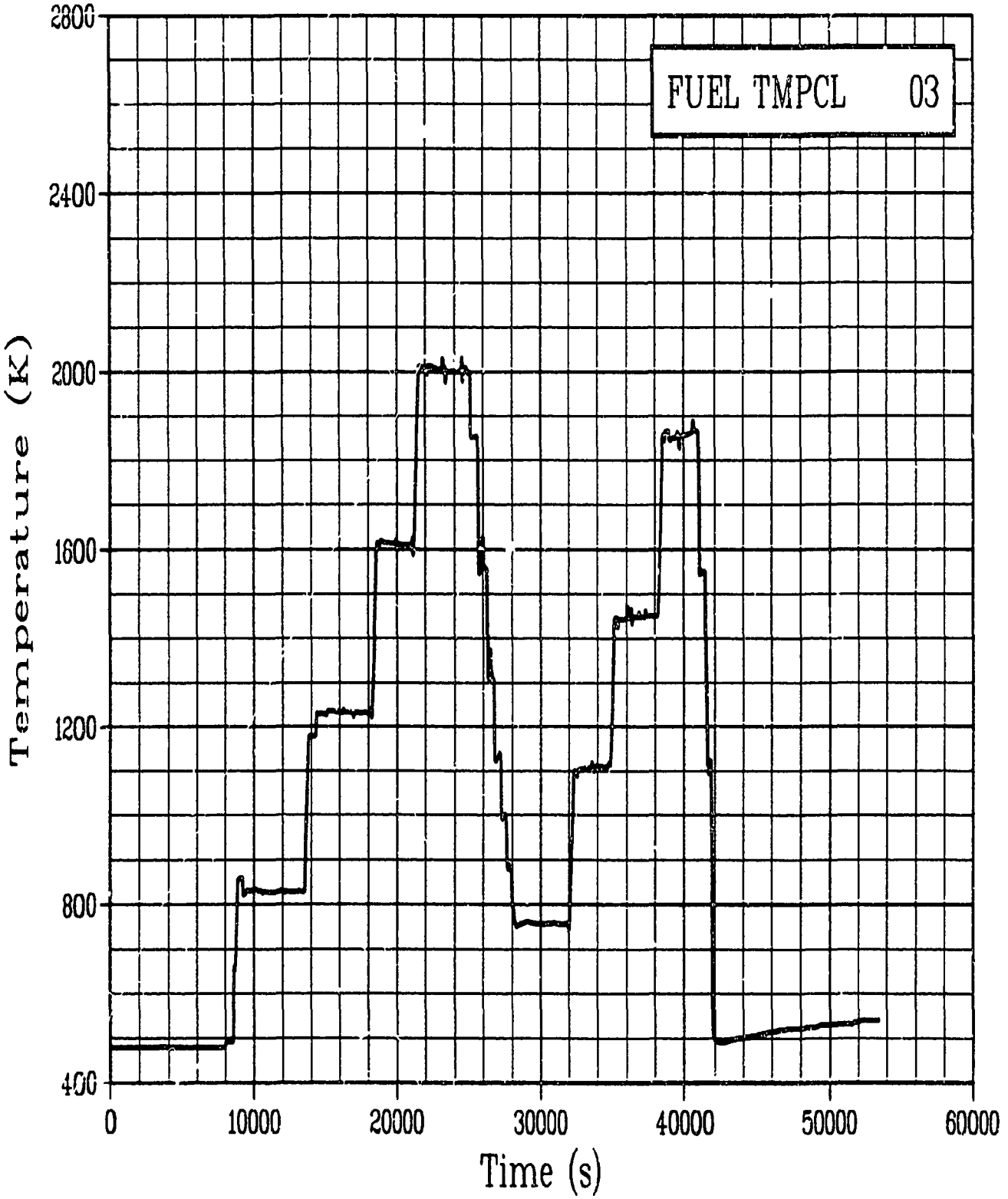

Figure C-130. Fuel centerline temperature Rod GC 524-3, 0.4521 m during Test PR-1 power oscillation period (FUEL TMPCL 03).

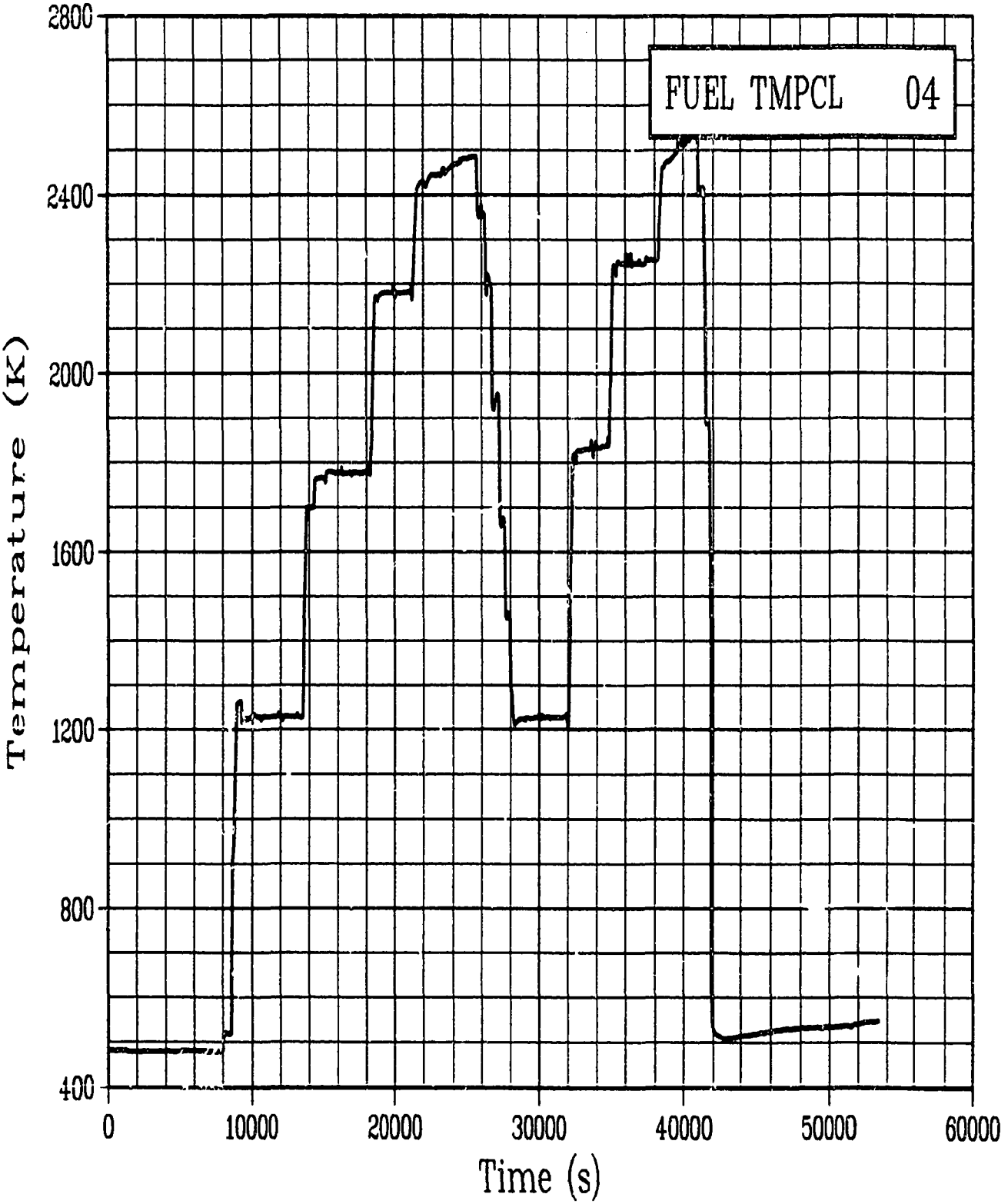

Figure C-131. Fuel centerline temperature Rod GC 524-4, 0.4521 m during Test PR-1 power oscillation period (FUEL TMPCL 04).

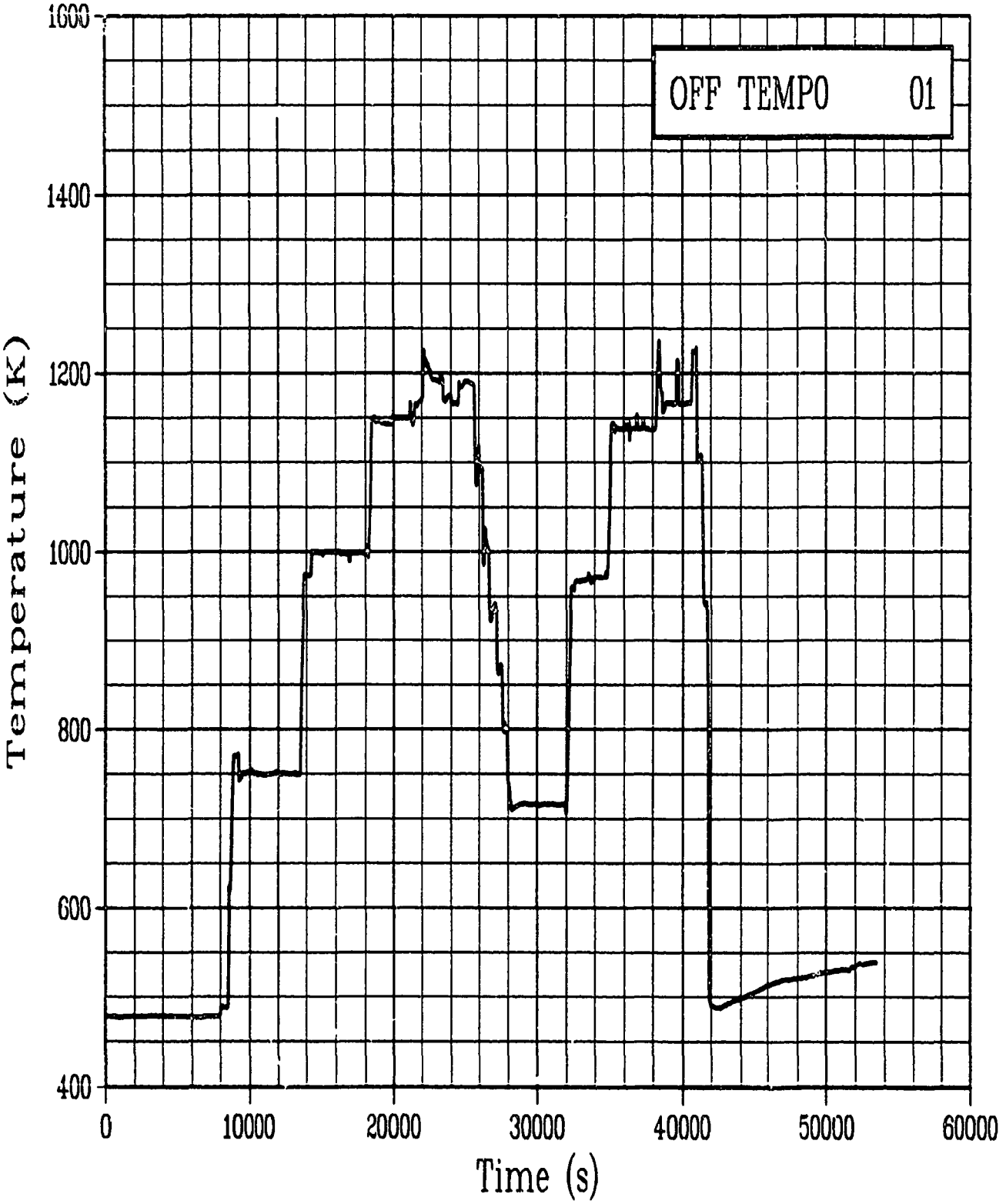

Figure C-132. Fuel off-center temperature Rod GC 524-1, at 0 degrees and 0.4521 m during Test PR-1 power oscillation period (OFF TEMPO 01).

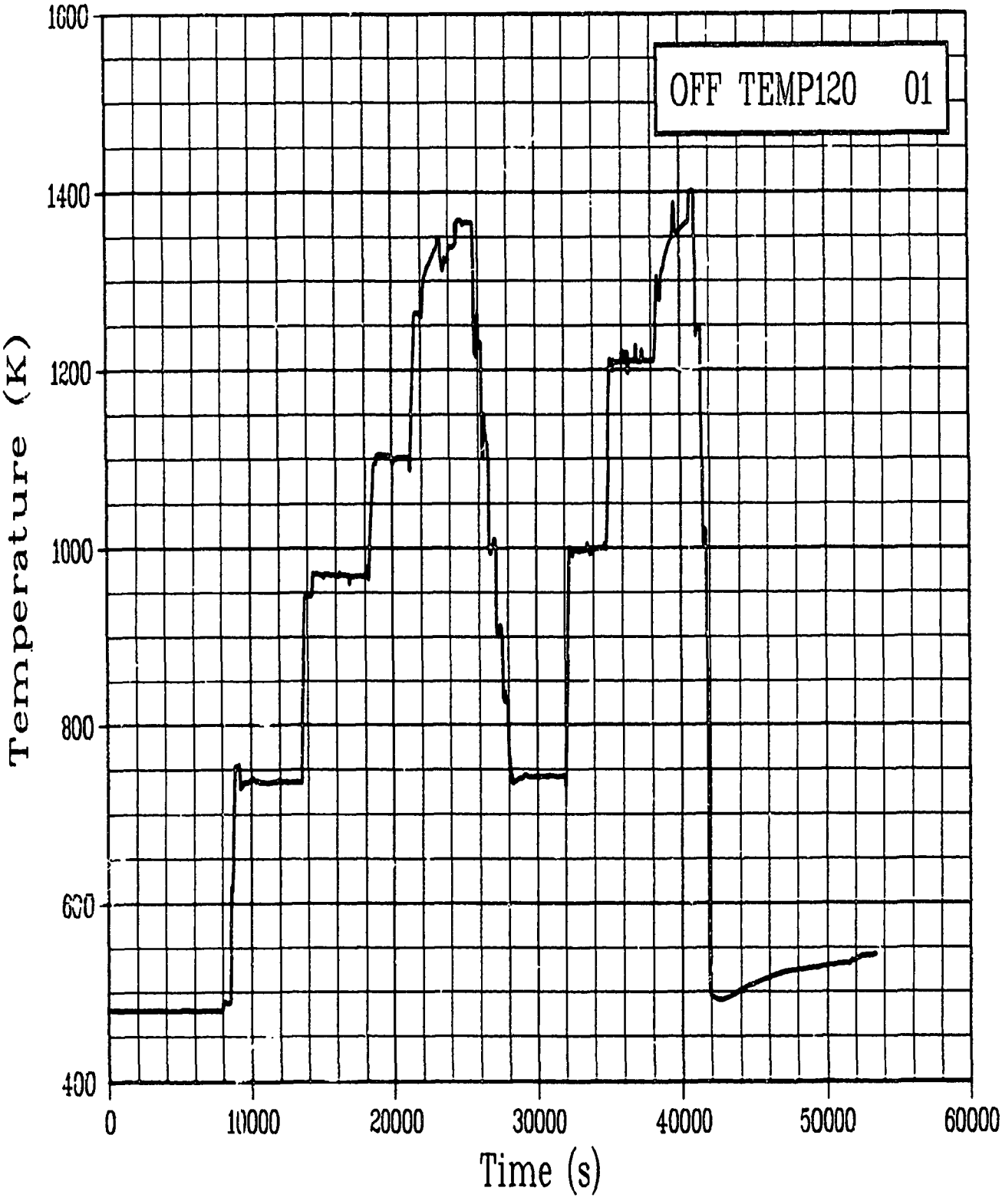

Figure C-133. Fuel off-center temperature Rod GC 524-1, at 120 degrees and 0.4521 m during Test PR-1 power oscillation period (OFF TEMP120 01).

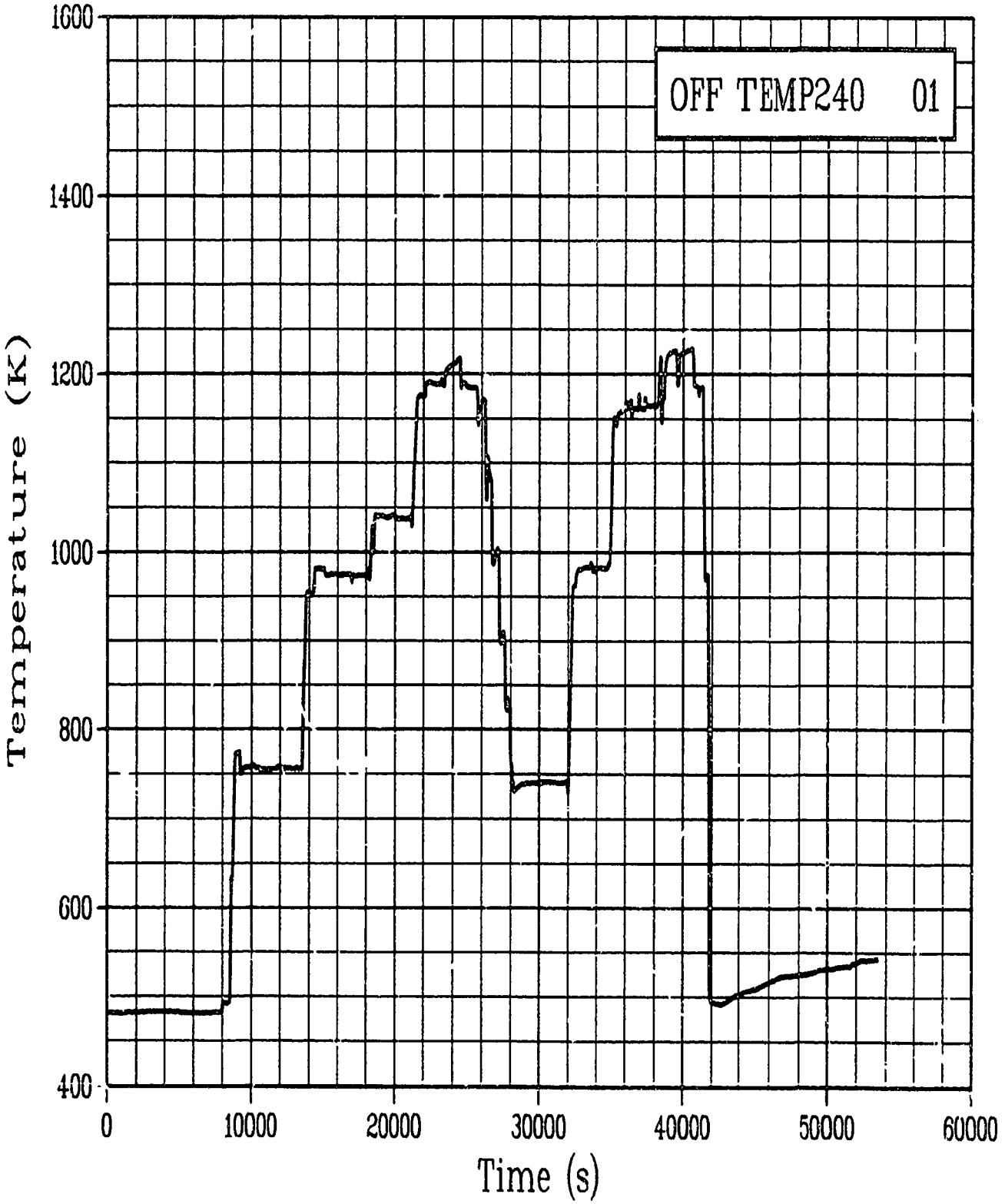

Figure C-134. Fuel off-center temperature Rod GC 524-1, at 240 degrees and 0.4521 m during Test PR-1 power oscillation period (OFF TEMP240 01).

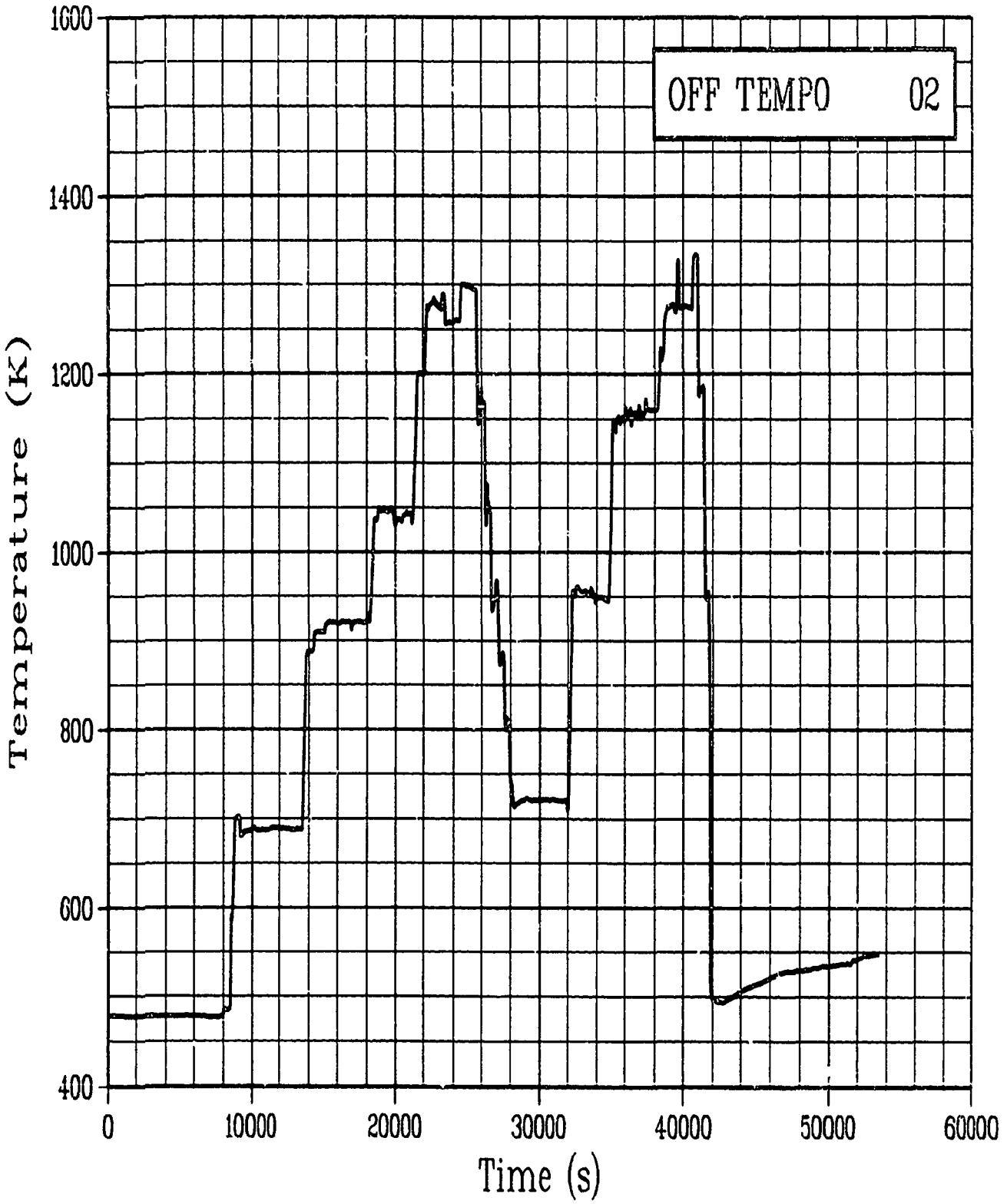

Figure C-135. Fuel off-center temperature Rod GC 524-2, at 0 degrees and 0.4521 m during Test PR-1 power oscillation period (OFF TEMPO 02).

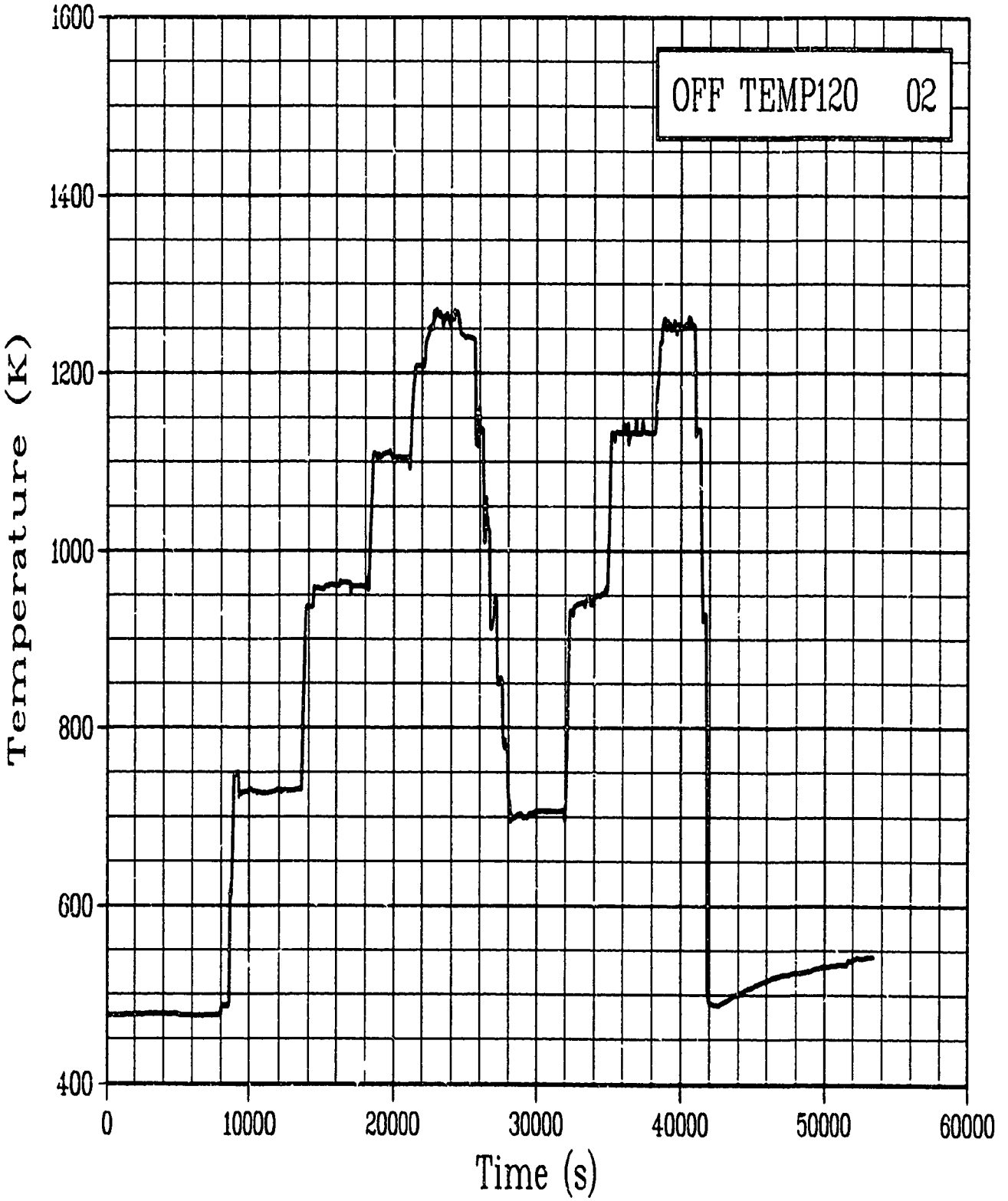

Figure C-136. Fuel off-center temperature Rod GC 524-2, at 120 degrees and 0.4521 m during Test PR-1 power oscillation period (OFF TEMP120 02).

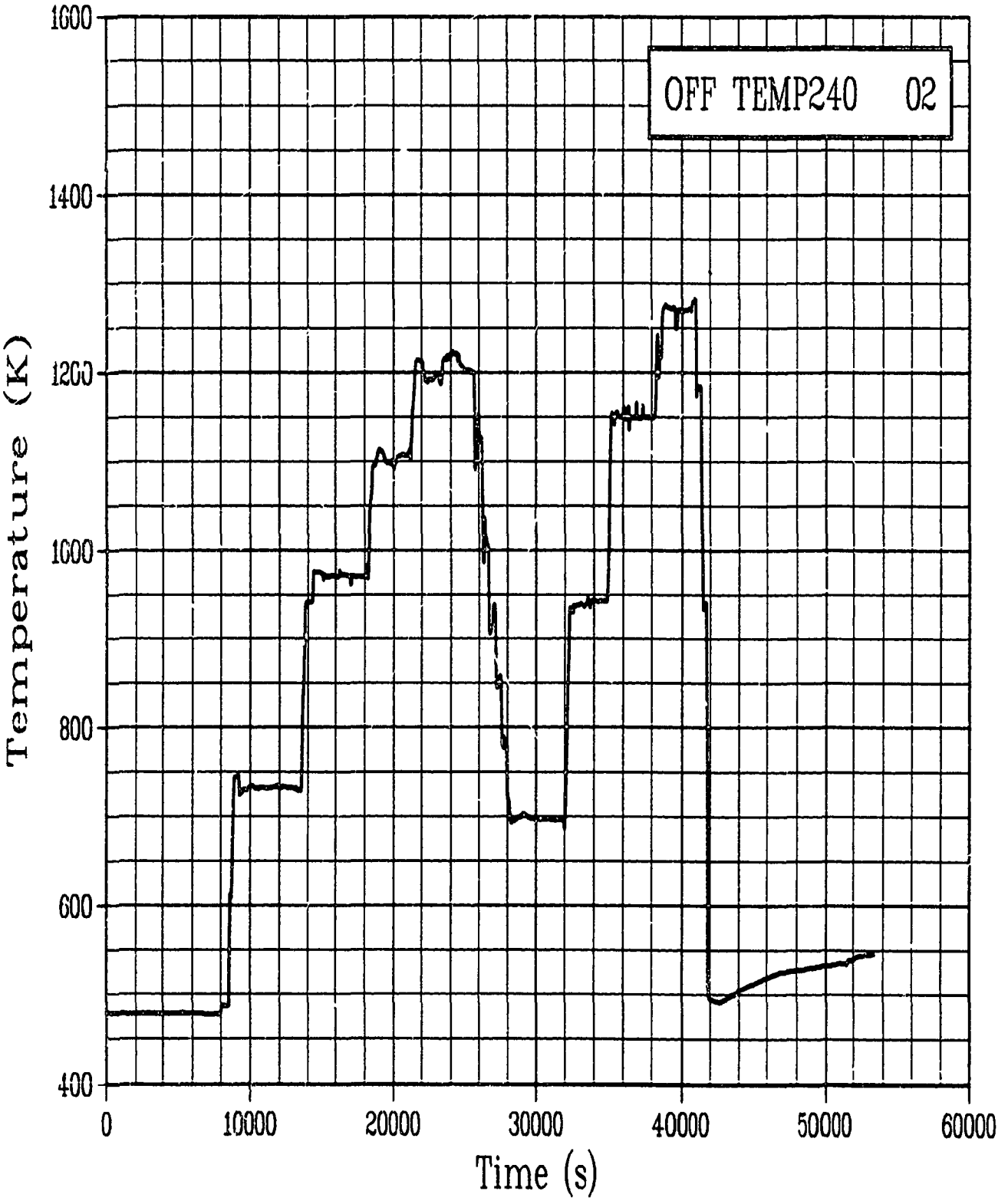

Figure C-137. Fuel off-center temperature Rod GC 524-2, at 240 degrees and 0.4521 m during Test PR-1 power oscillation period (OFF TEMP240 02).

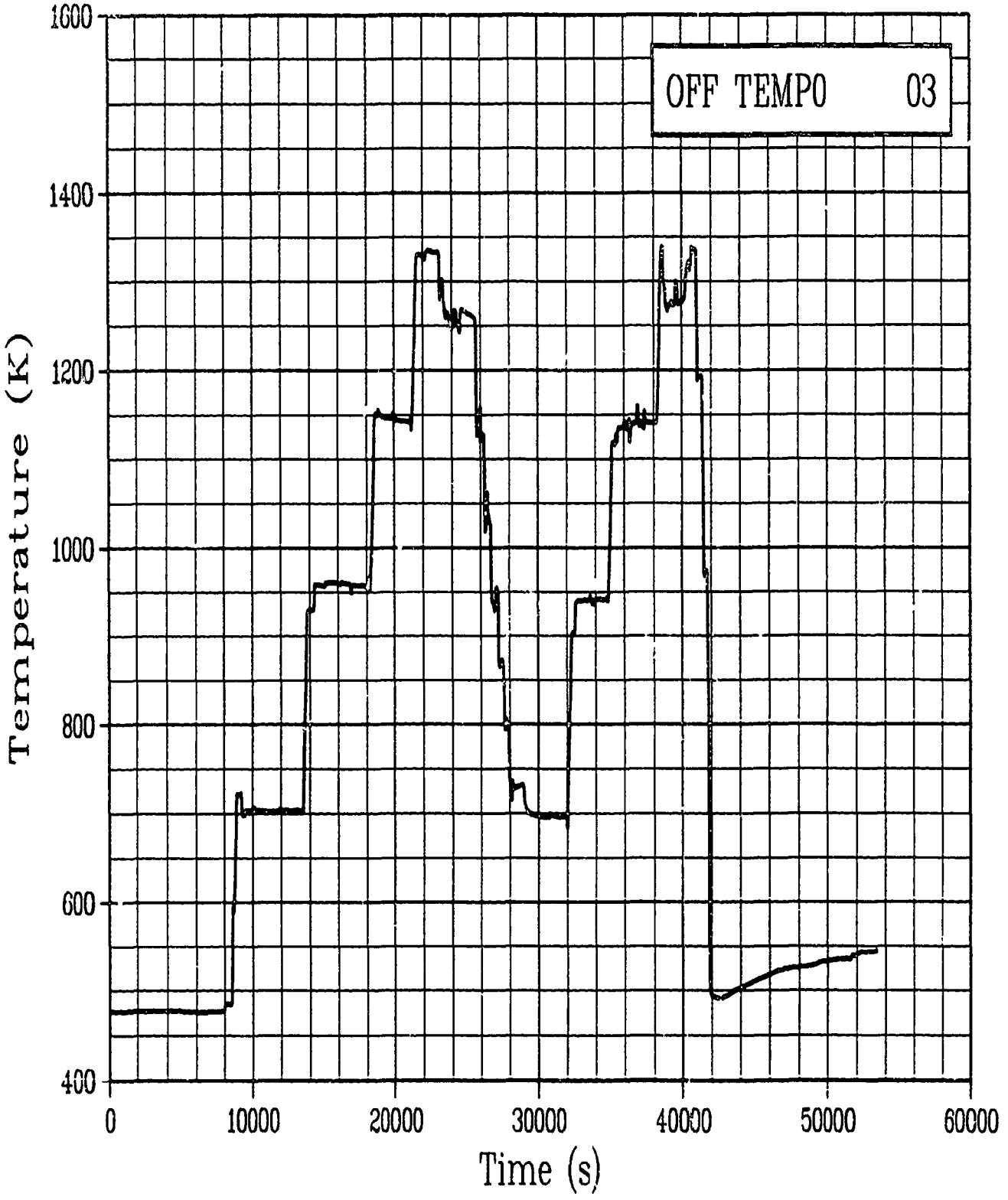

Figure C-138. Fuel off-center temperature Rod GC 524-3, at 0 degrees and 0.4521 m during Test PR-1 power oscillation period (OFF TEMPO 03).

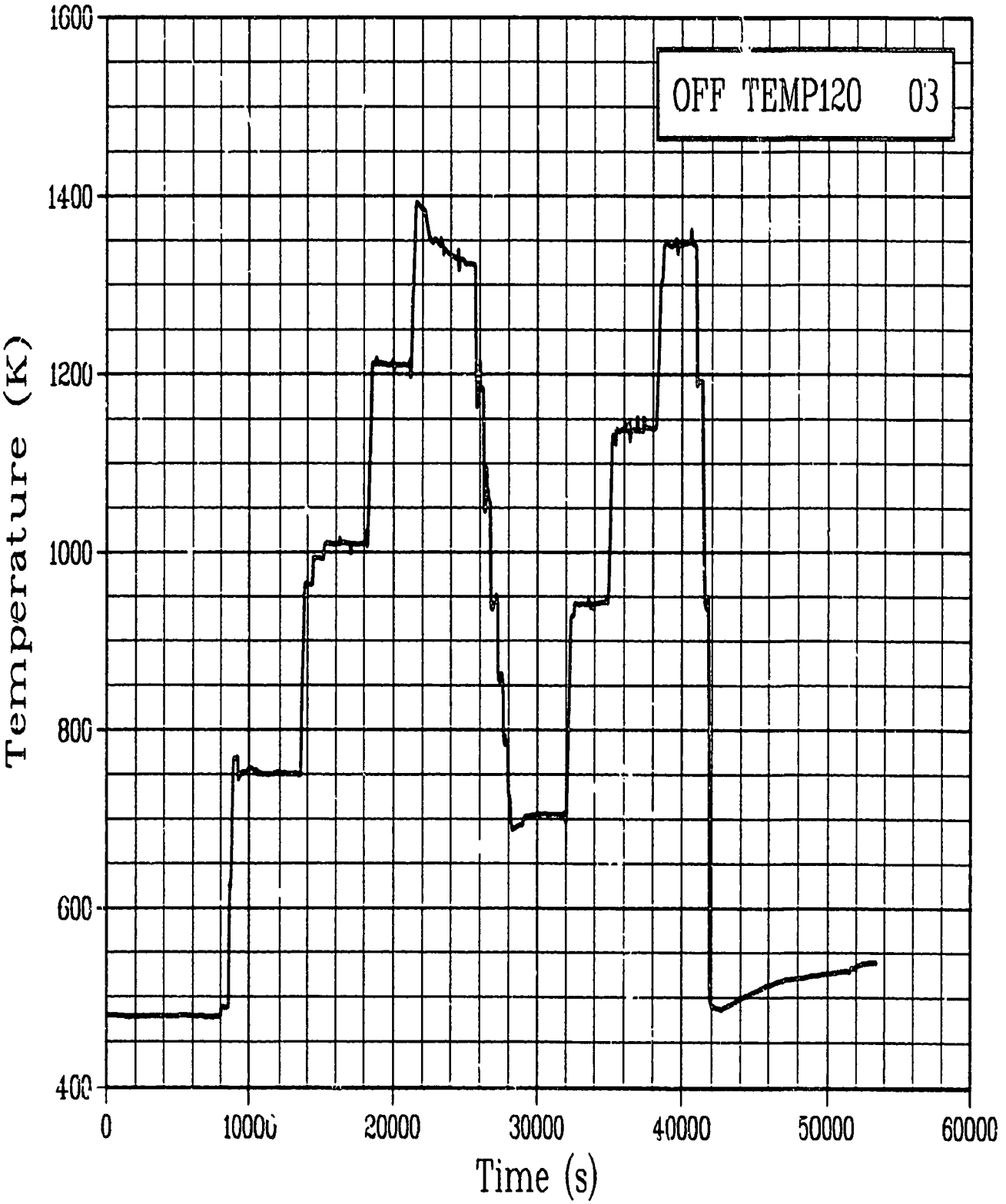

Figure C-139. Fuel off-center temperature Rod GC 524-3, at 120 degrees and 0.4521 m during Test PR-1 power oscillation period (OFF TEMP120 03).

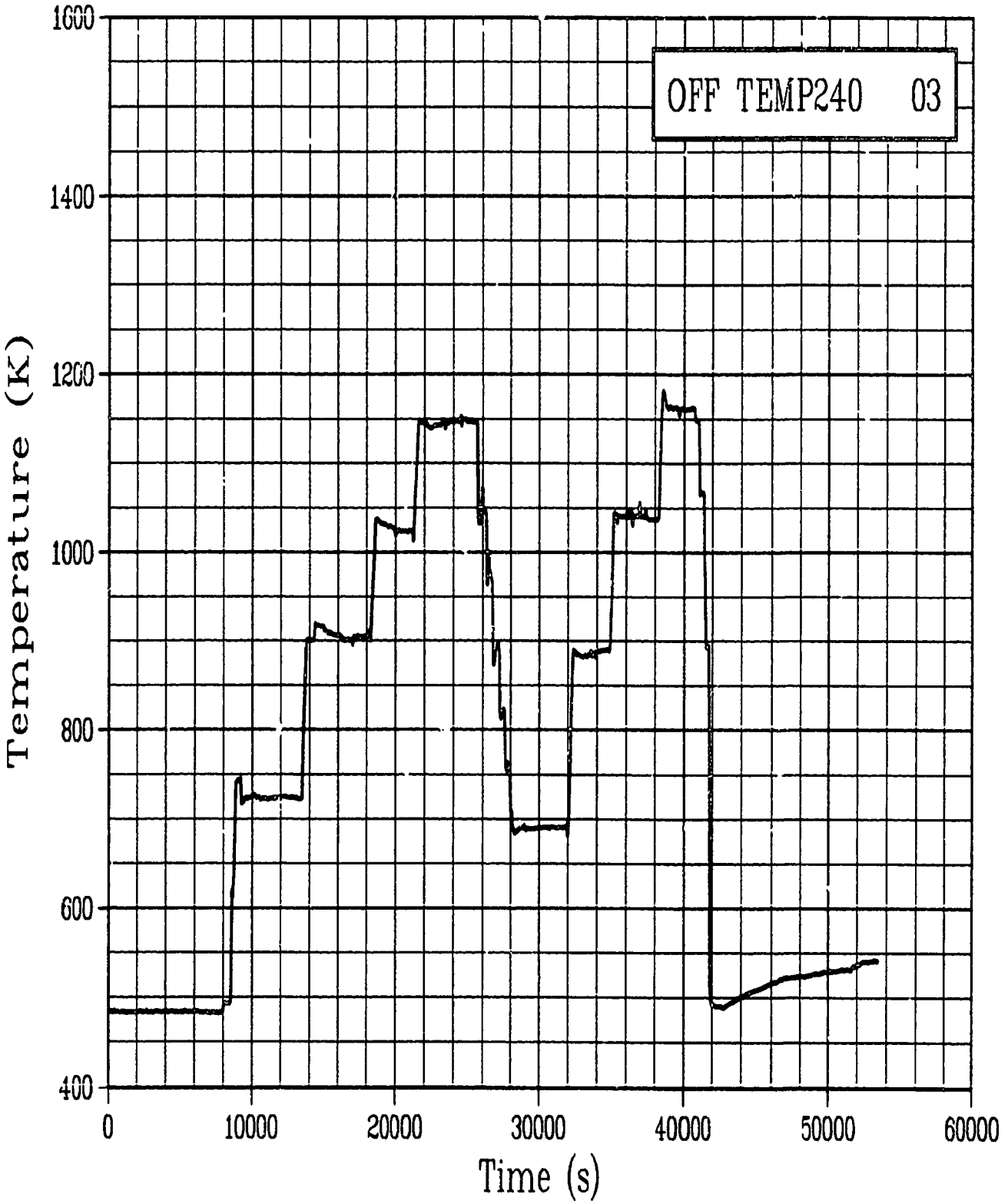

Figure C-140. Fuel off-center temperature Rod GC 524-3, at 240 degrees and 0.4521 m during Test PR-1 power oscillation period (OFF TEMP240 03).

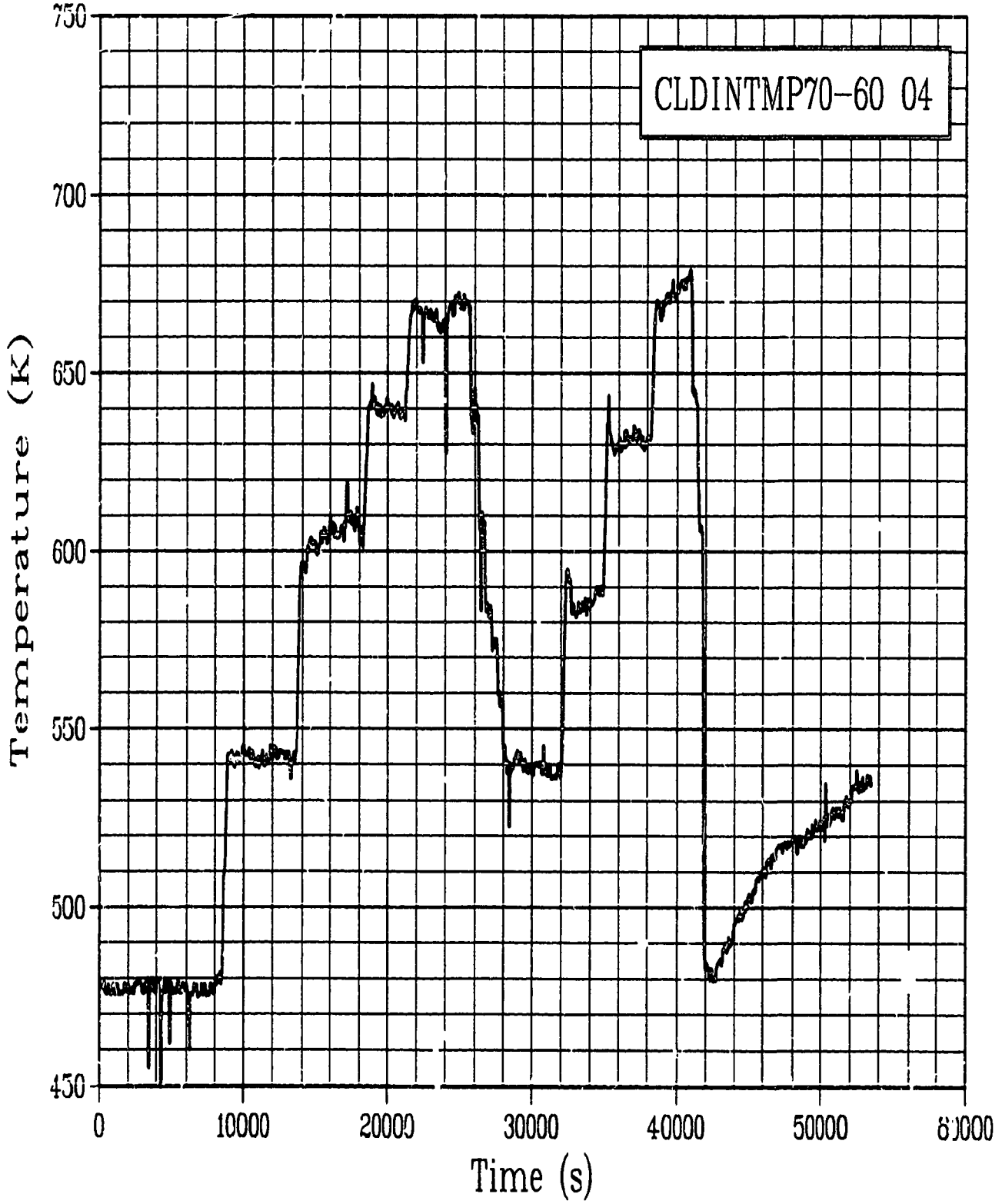

Figure C-141. Cladding internal temperature Rod GC 524-4, 0.70 m and 60 degrees during Test PR-1 power oscillation period (CLDINTMP70-60 04).

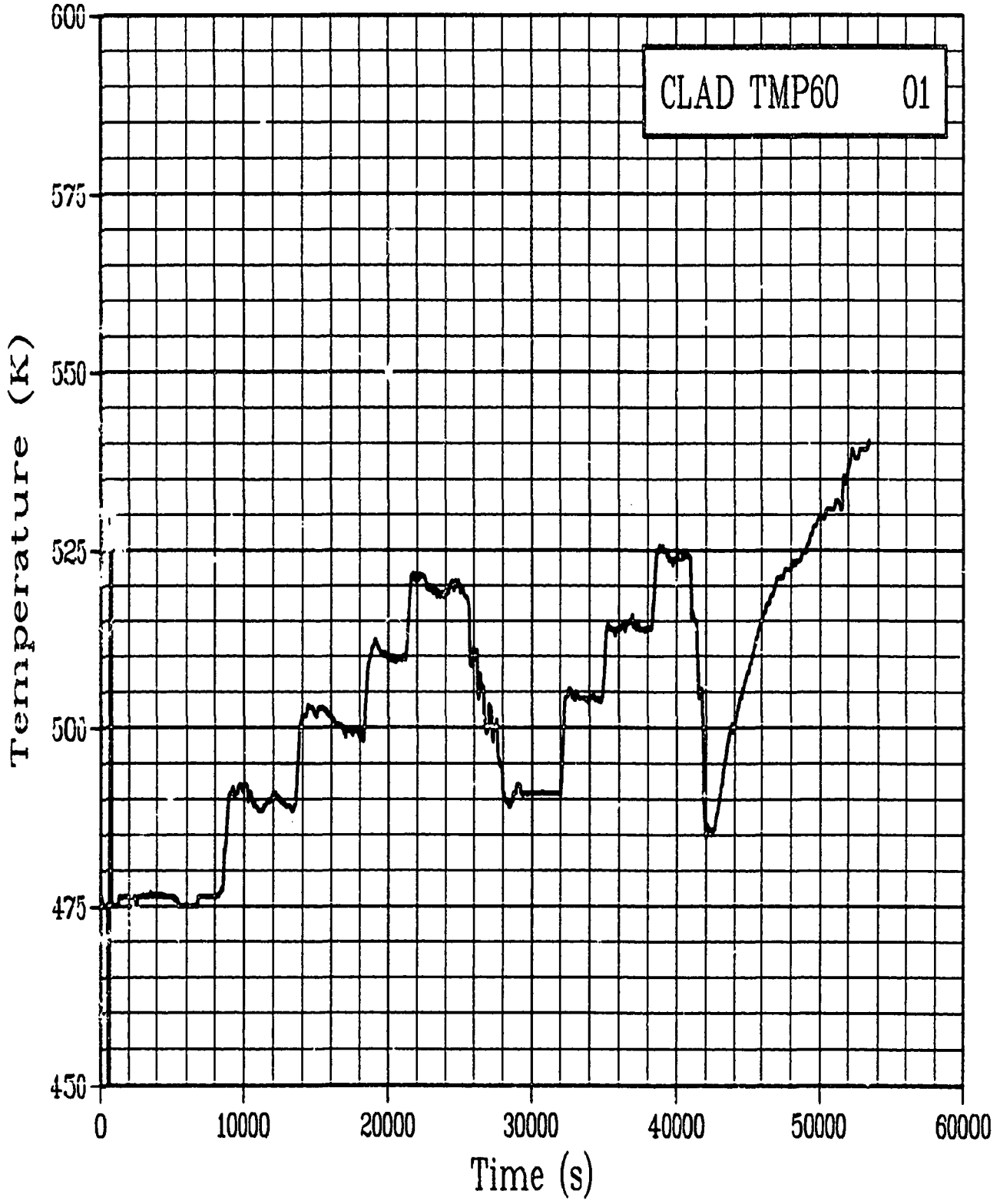

Figure C-142. Cladding surface temperature Rod GC 524-1, at 60 degrees and 0.4521 m during Test PR-1 power oscillation period (CLAD TMP60 01).

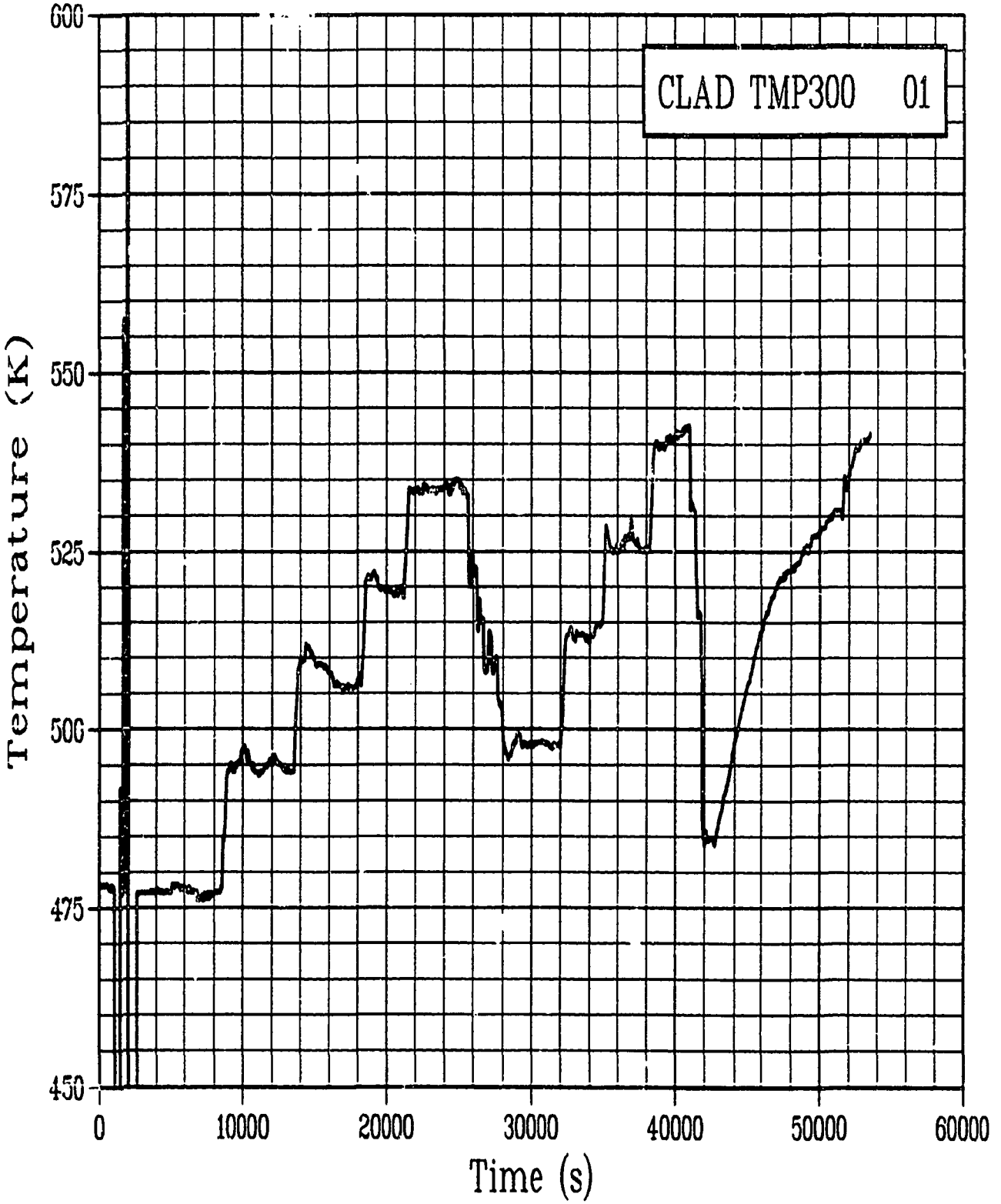

Figure C-143. Cladding surface temperature Rod GC 524-1, at 300 degrees and 0.4521 m during Test PR-1 power oscillation period (CLAD TMP300 01).

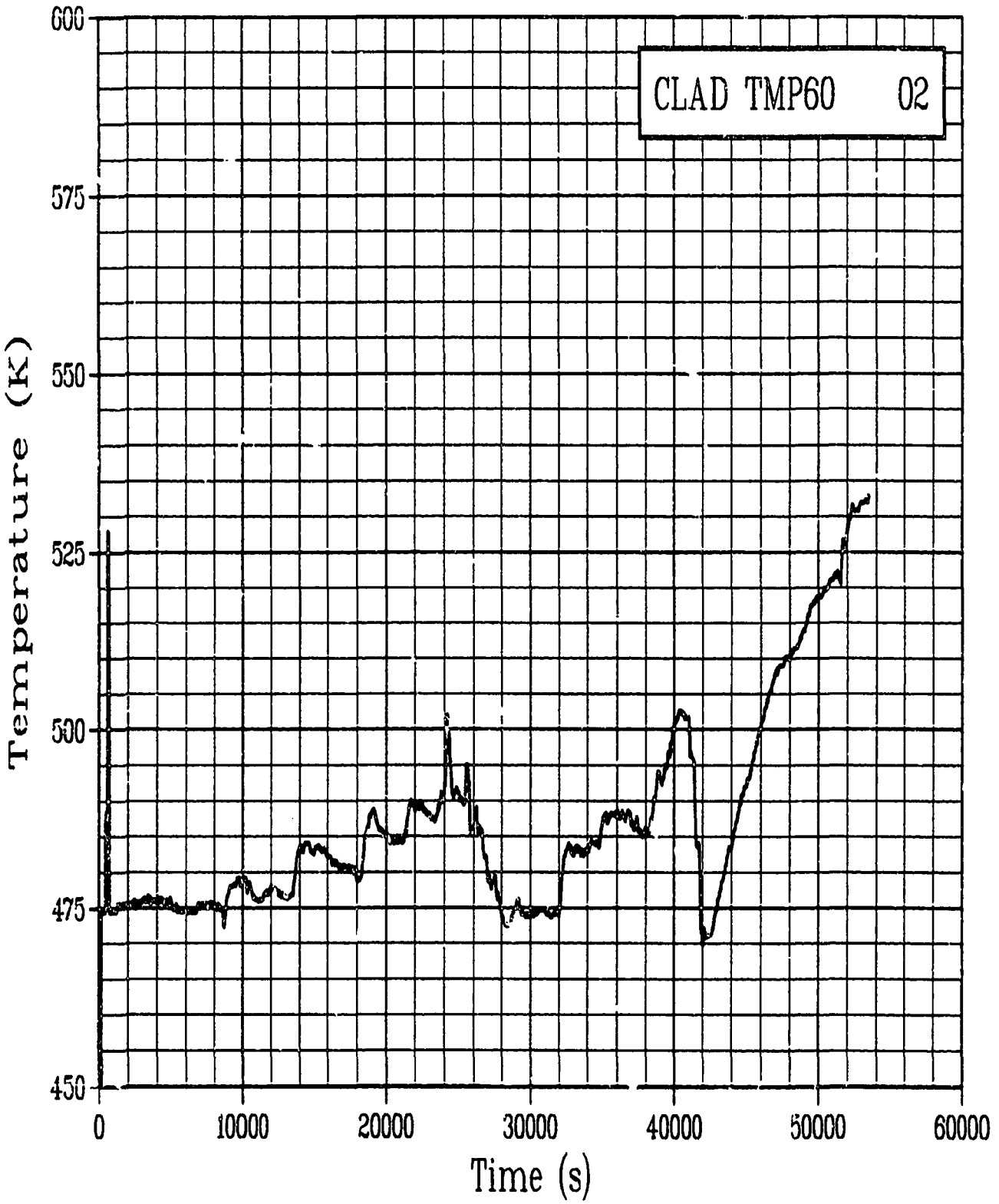

Figure C-144. Cladding surface temperature Rod GC 524-2, at 60 degrees and 0.4521 m during Test PR-1 power oscillation period (CLAD TMP60 02).

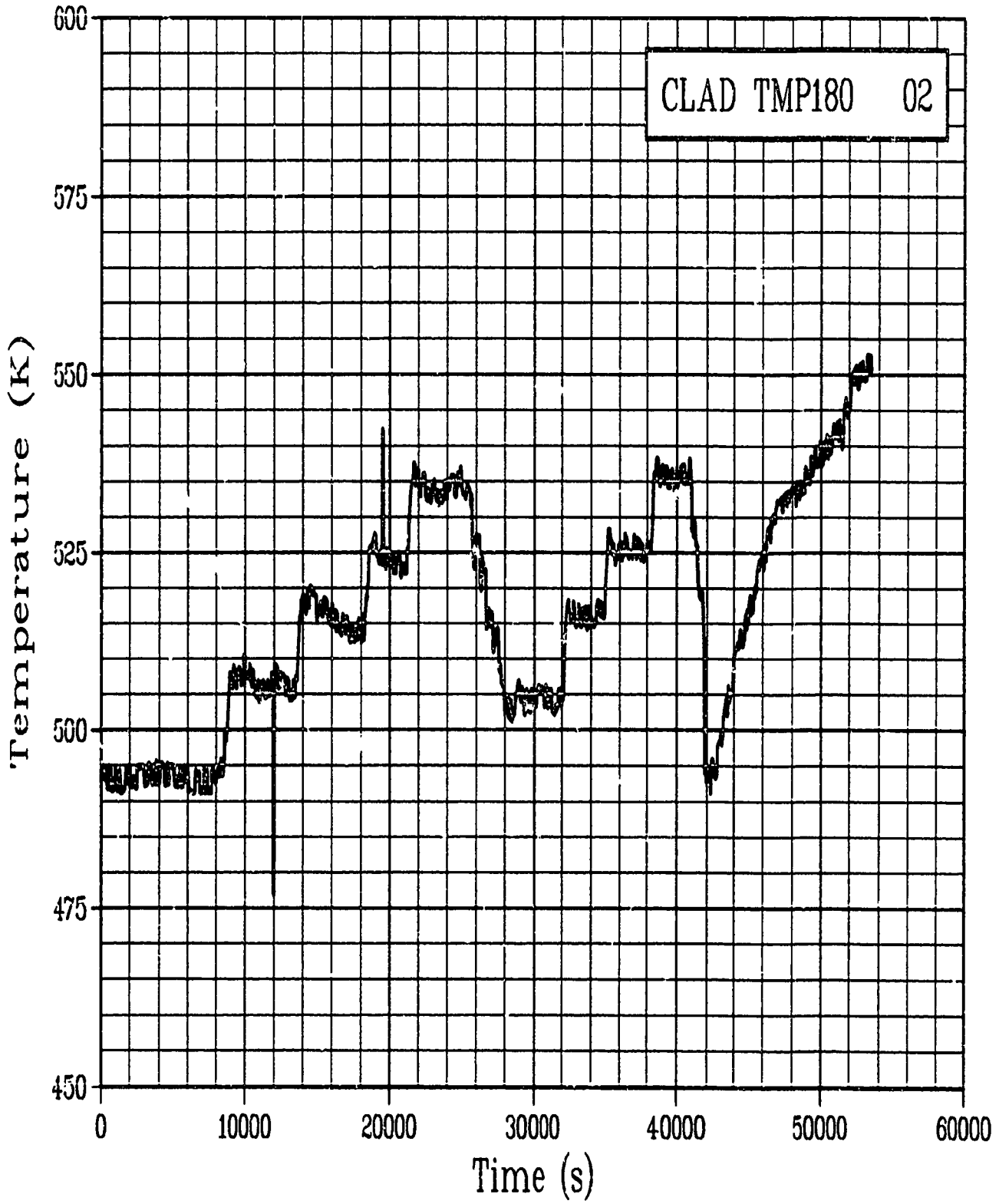

Figure C-145. Cladding surface temperature Rod GC 524-2, at 180 degrees and 0.4521 m during Test PR-1 power oscillation period (CLAD TMP180 02).

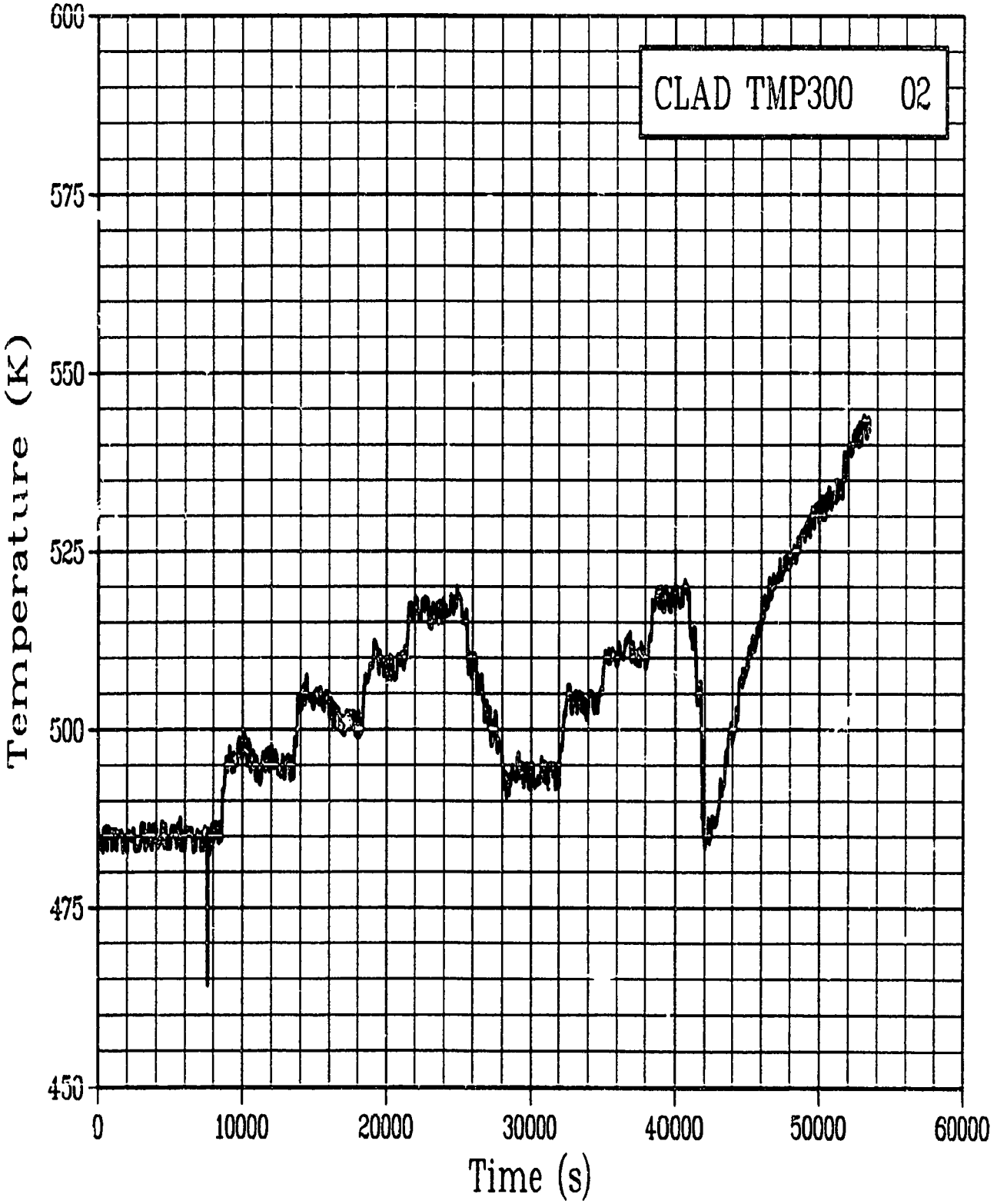

Figure C-146. Cladding surface temperature Rod GC 524-2, at 300 degrees and 0.4521 m during Test PR-1 power oscillation period (CLAD TMP300 02).

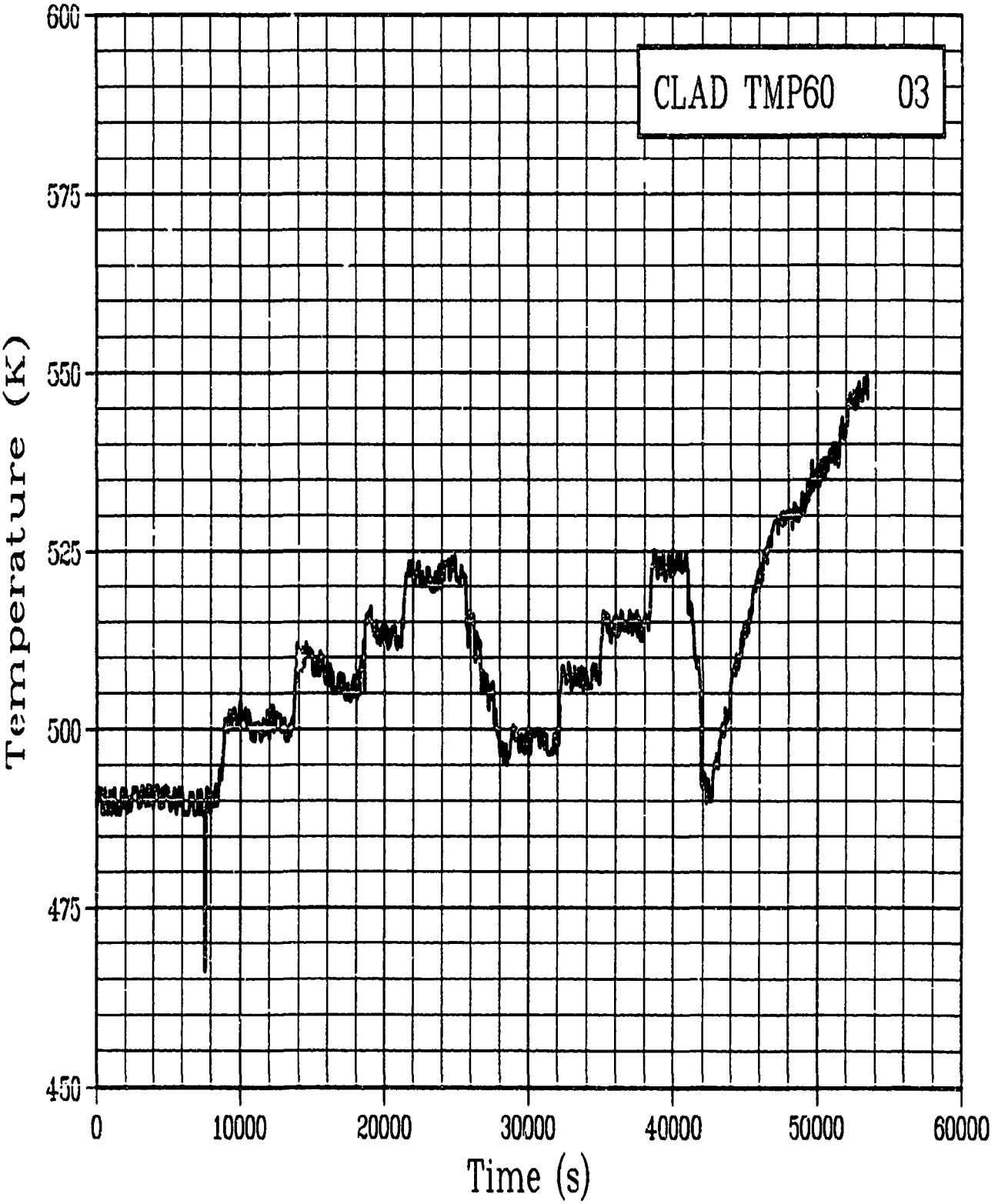

Figure C-147. Cladding surface temperature Rod GC 524-3, at 60 degrees and 0.4521 m during Test PR-1 power oscillation period (CLAD TMP60 03).

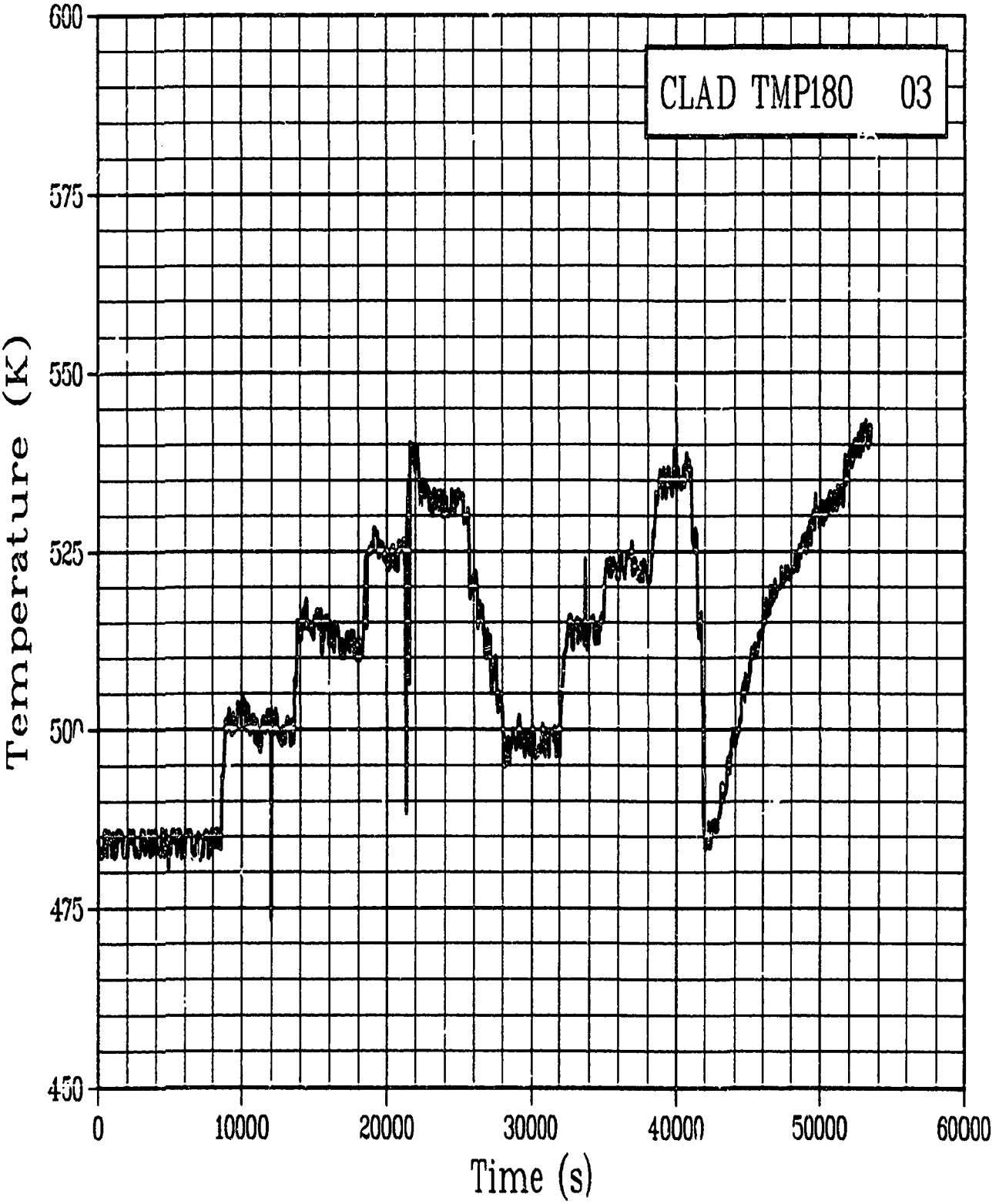

Figure C-148. Cladding surface temperature Rod GC 524-3, at 180 degrees and 0.4521 m during Test PR-1 power oscillation period (CLAD TMP180 03).

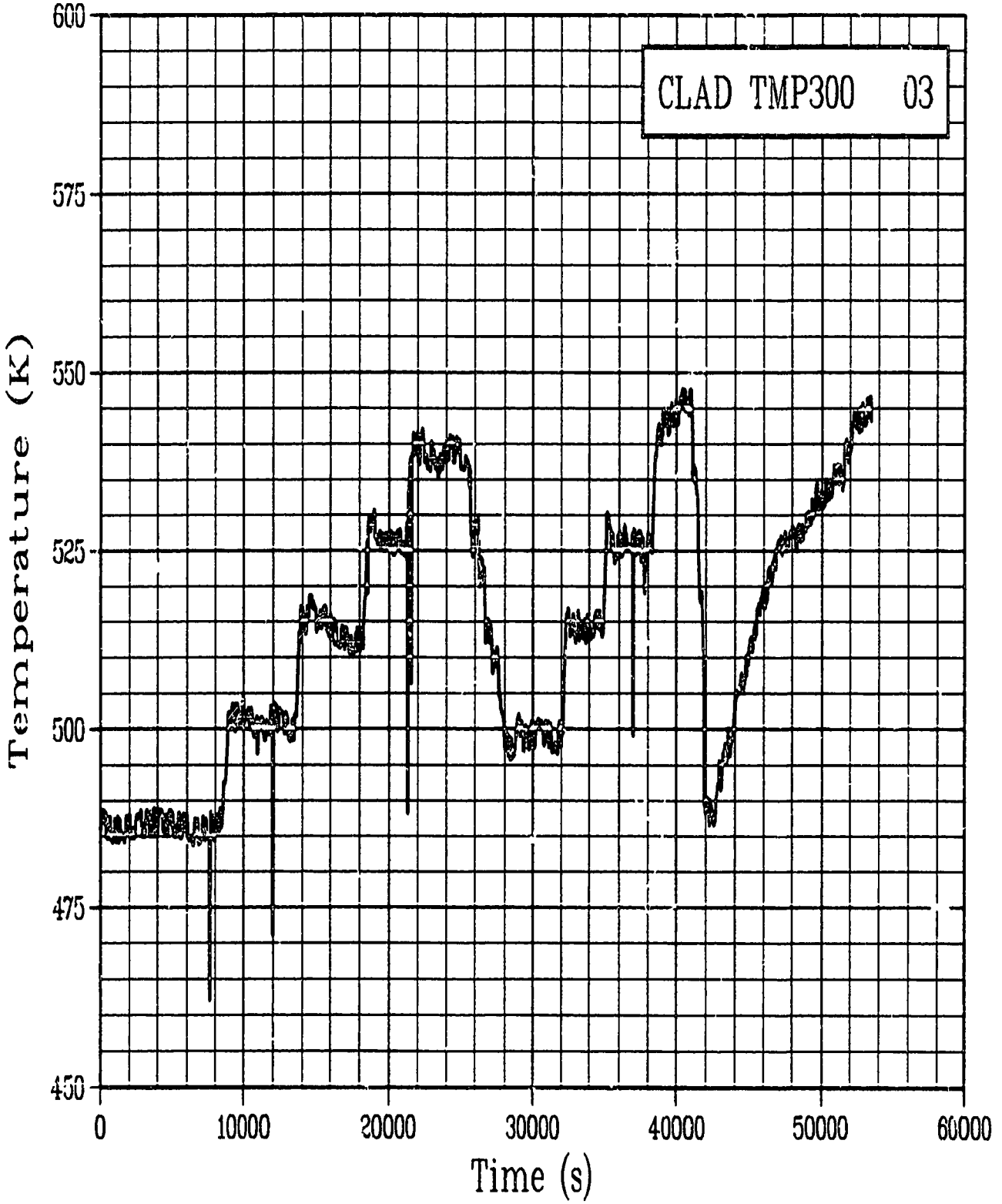

Figure C-149. Cladding surface temperature Rod GC 524-3, at 300 degrees and 0.4521 m during Test PR-1 power oscillation period (CLAD TMP300 03).

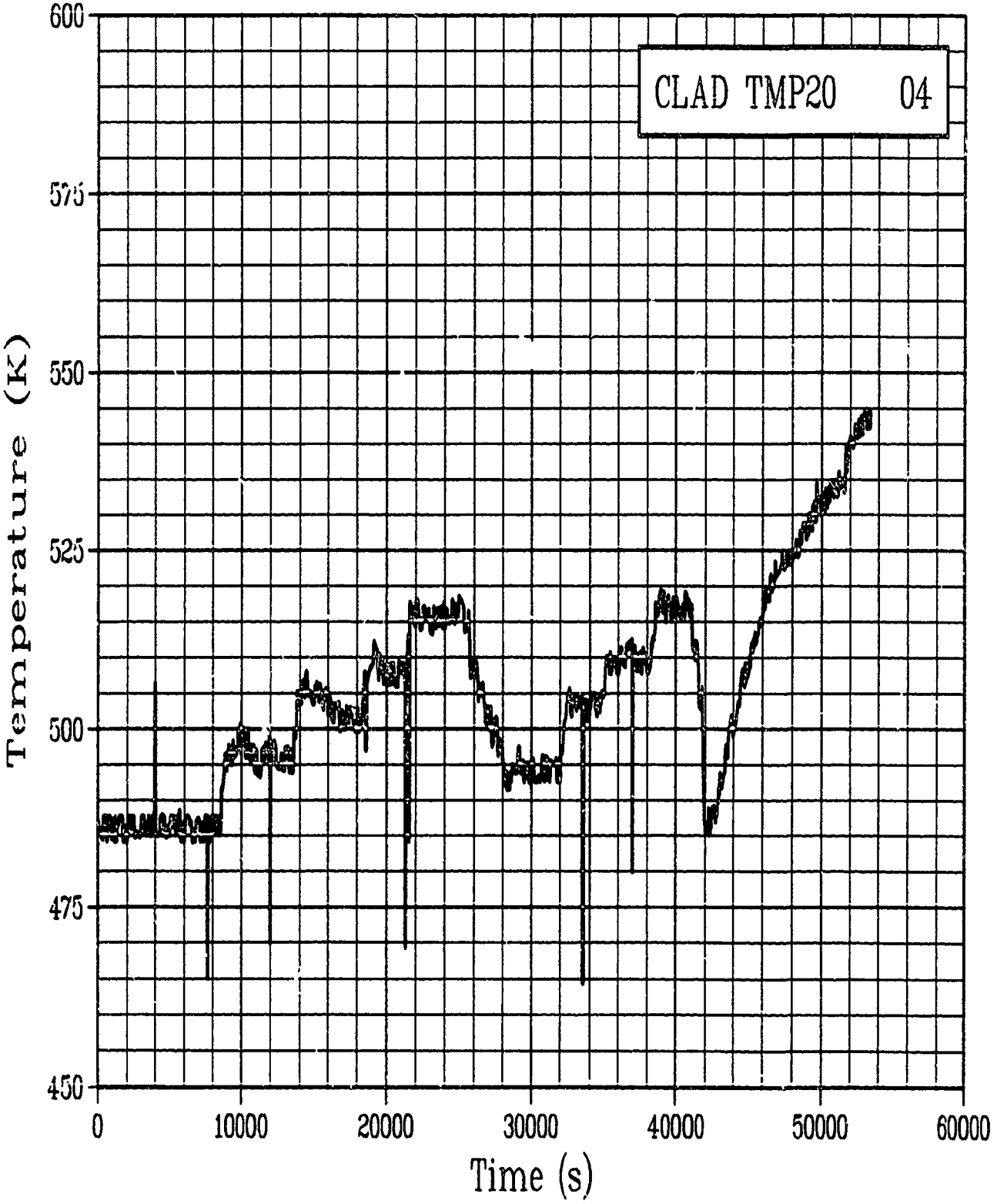

Figure C-150. Cladding surface temperature Rod GC 524-4, at 20 degrees and 0.70 m during Test PR-1 power oscillation period (CLAD TMP20 04).

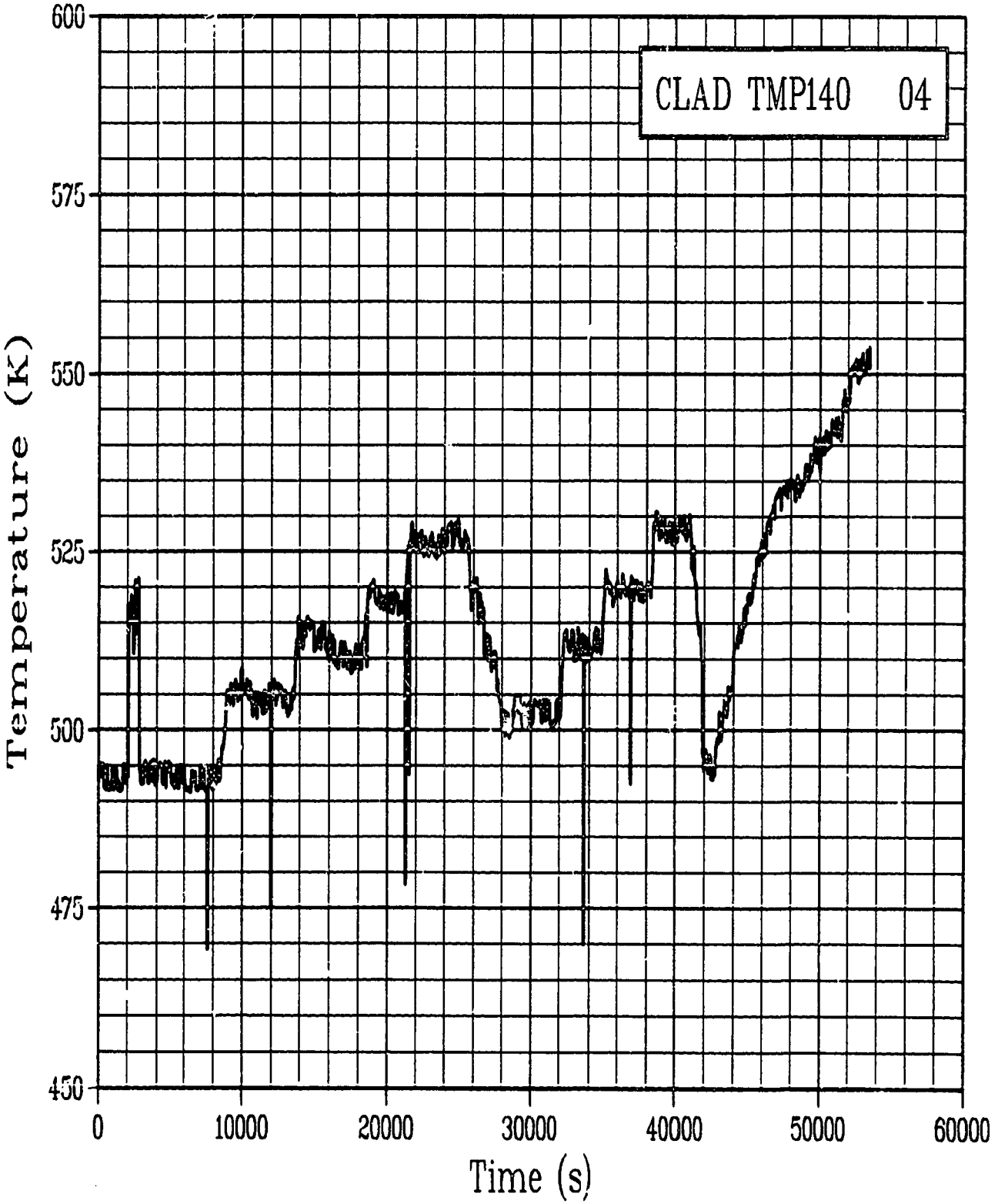

Figure C-151. Cladding surface temperature Rod GC 524-4, at 140 degrees and 0.4521 m during Test PR-1 power oscillation period (CLAD TMP140 04).

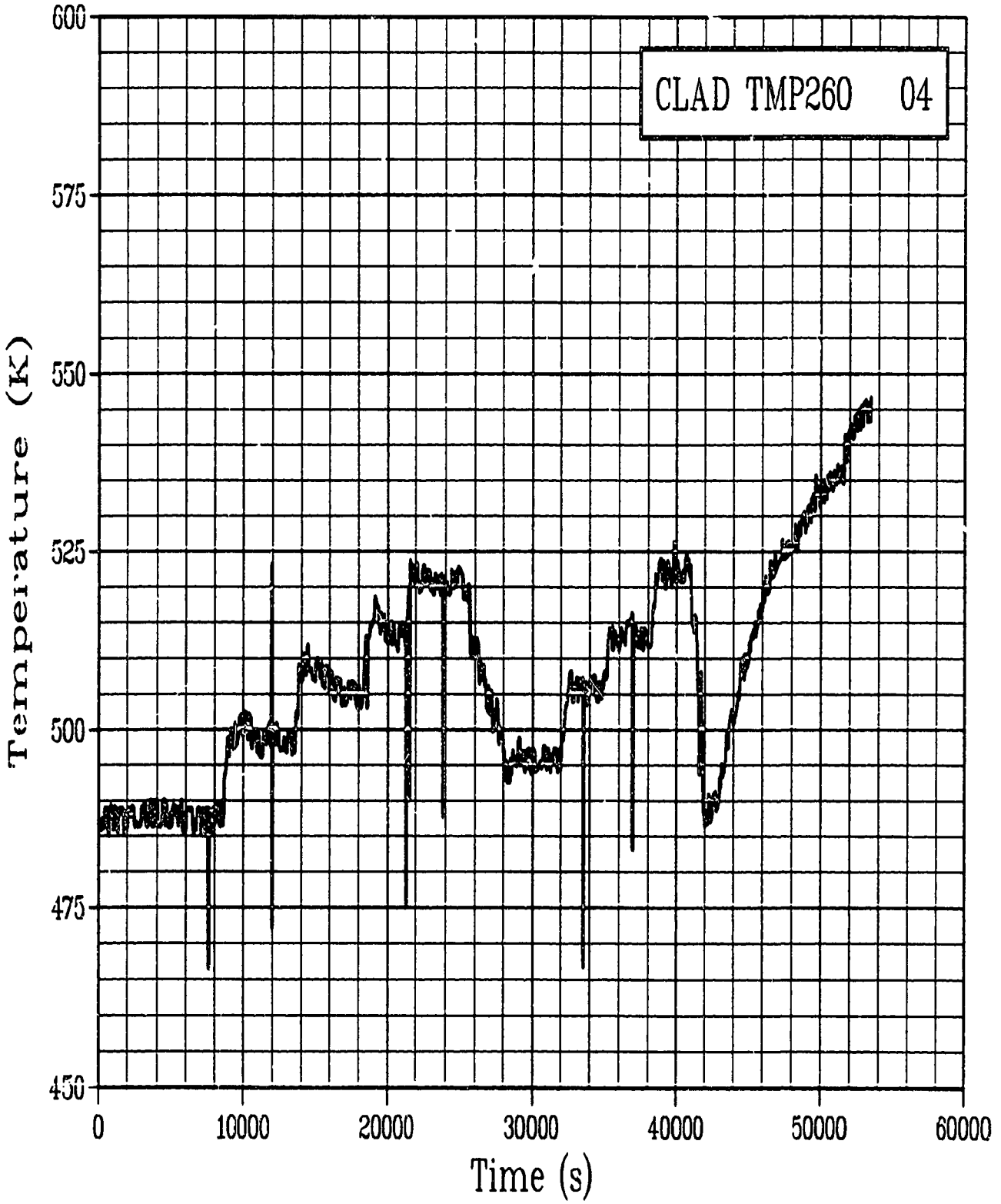

Figure C-152. Cladding surface temperature Rod GC 524-4, at 260 degrees and 0.70 m during Test PR-1 power oscillation period (CLAD TMP260 04).

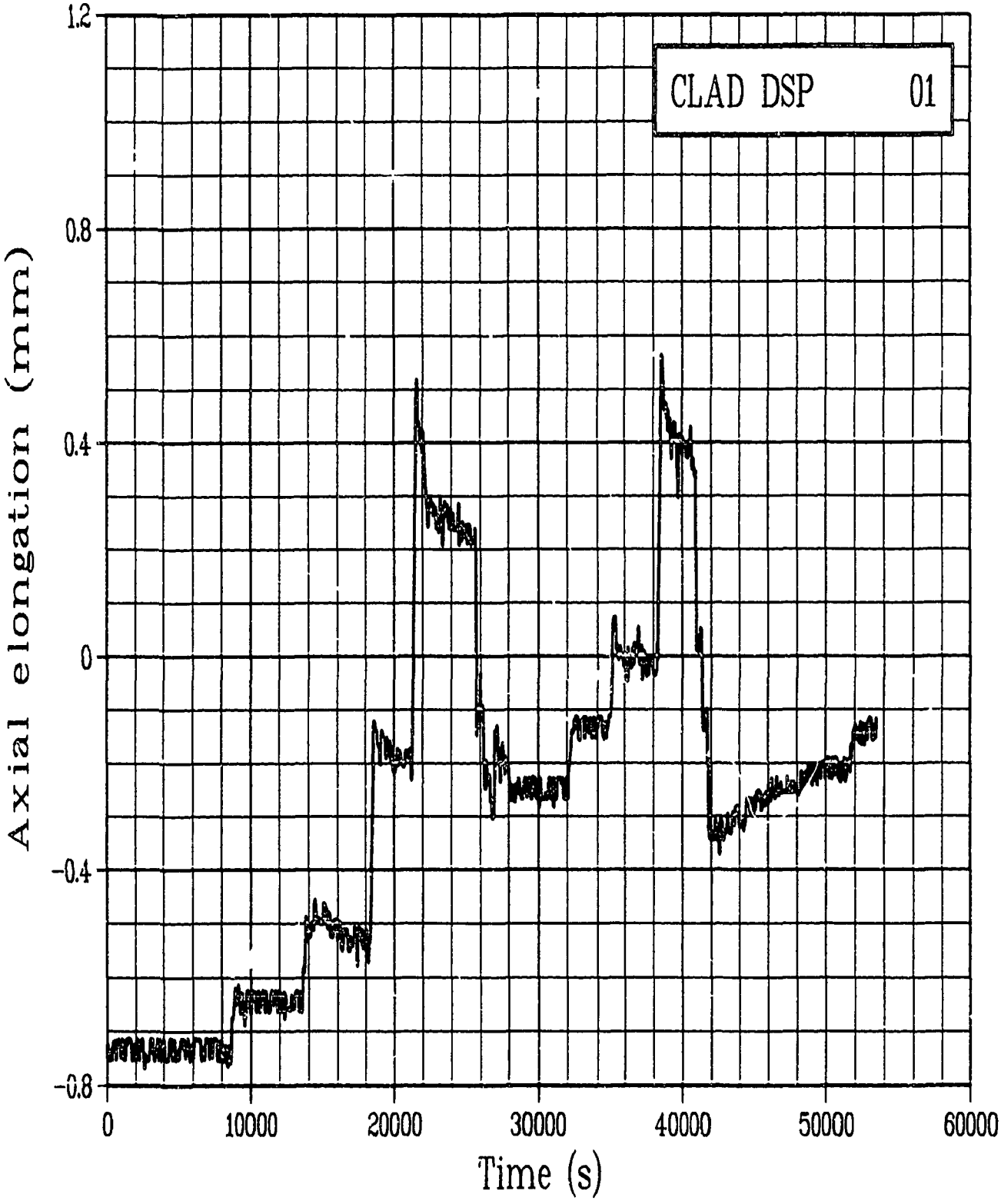

Figure C-153. Cladding axial elongation of Rod GC 524-1 during Test PR-1 power oscillation period (CLAD DSP 01).

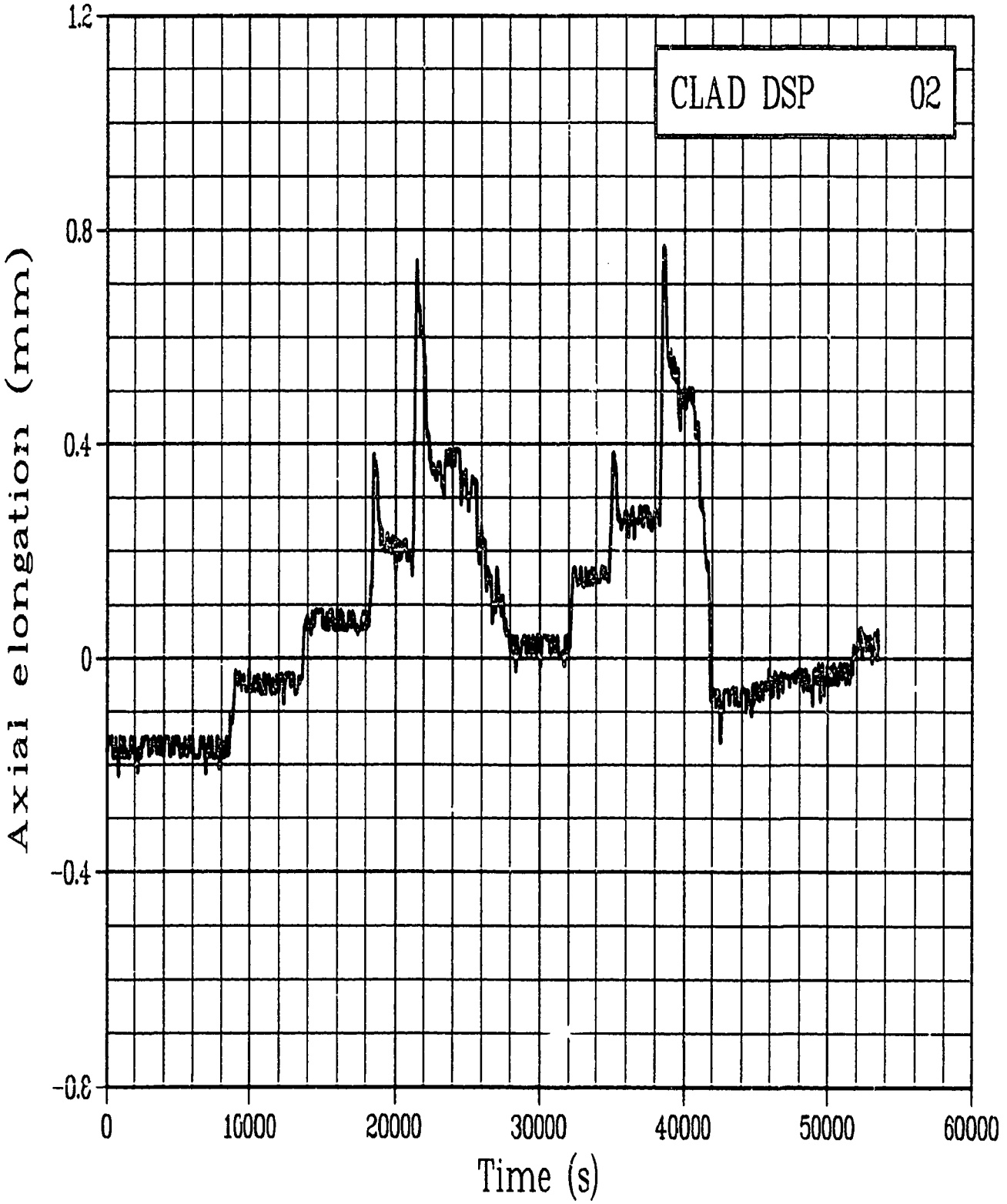

Figure C-154. Cladding axial elongation of Rod GC 524-2 during Test PR-1 power oscillation period (CLAD DSP 02).

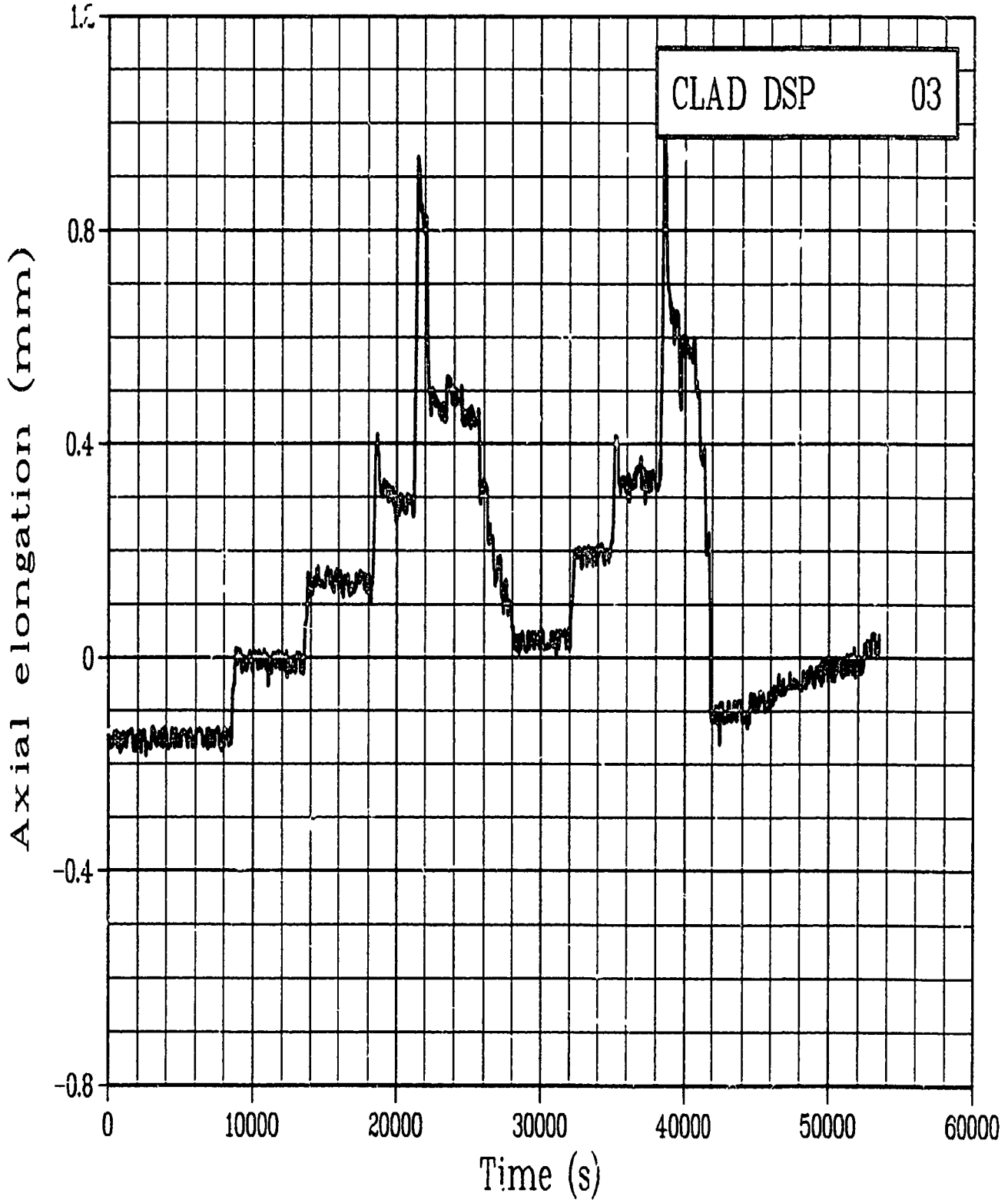

Figure C-155. Cladding axial elongation of Rod GC 524-3 during Test PR-1 power oscillation period (CLAD DSP 03).

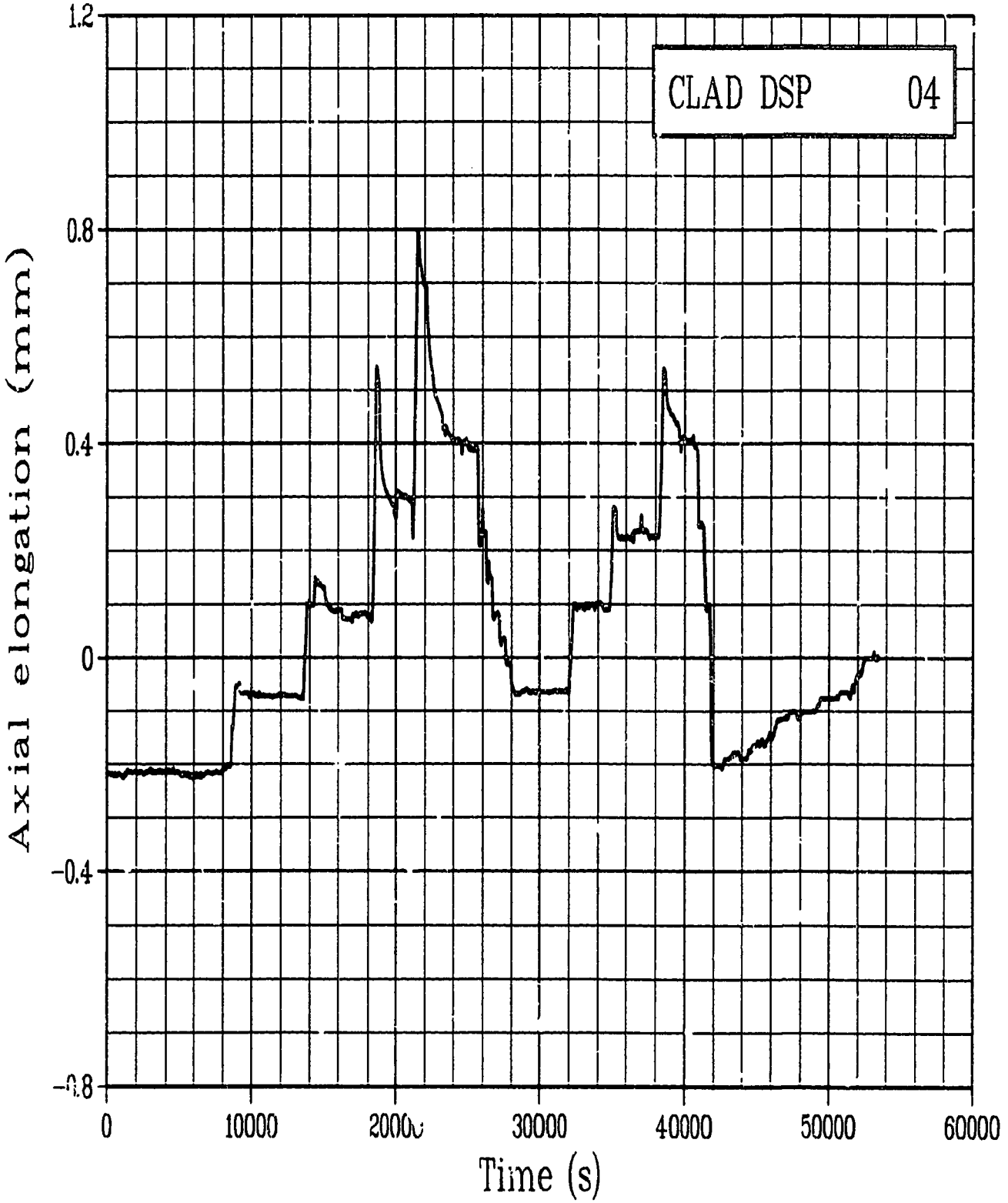

Figure C-156. Cladding axial elongation of Rod GC 524-4 during Test PR-1 power oscillation period (CLAD DSP 04).

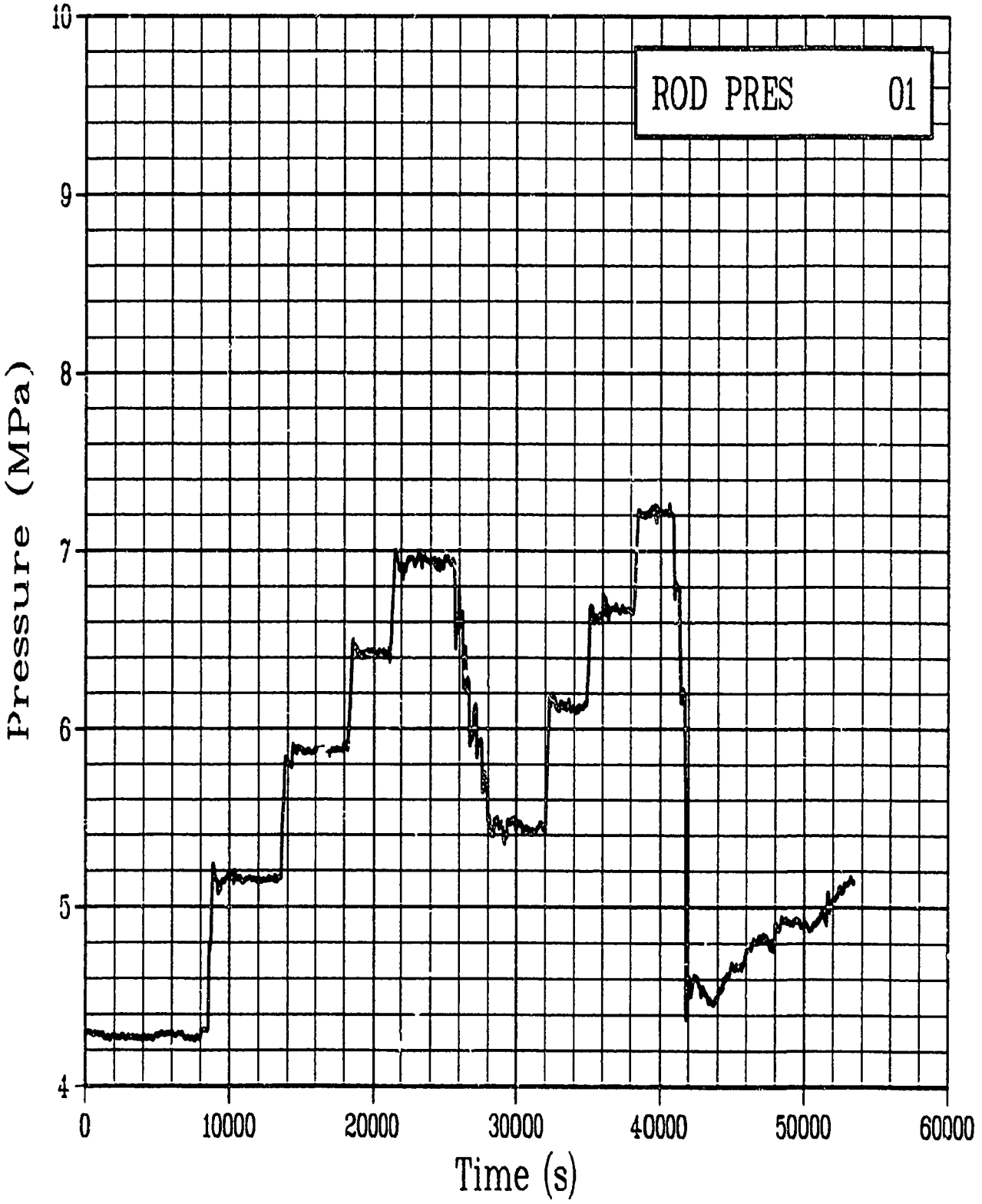

Figure C-157. Absolute pressure in Rod GC 524-1 plenum during Test PR-1 power oscillation period (ROD PRES 01).

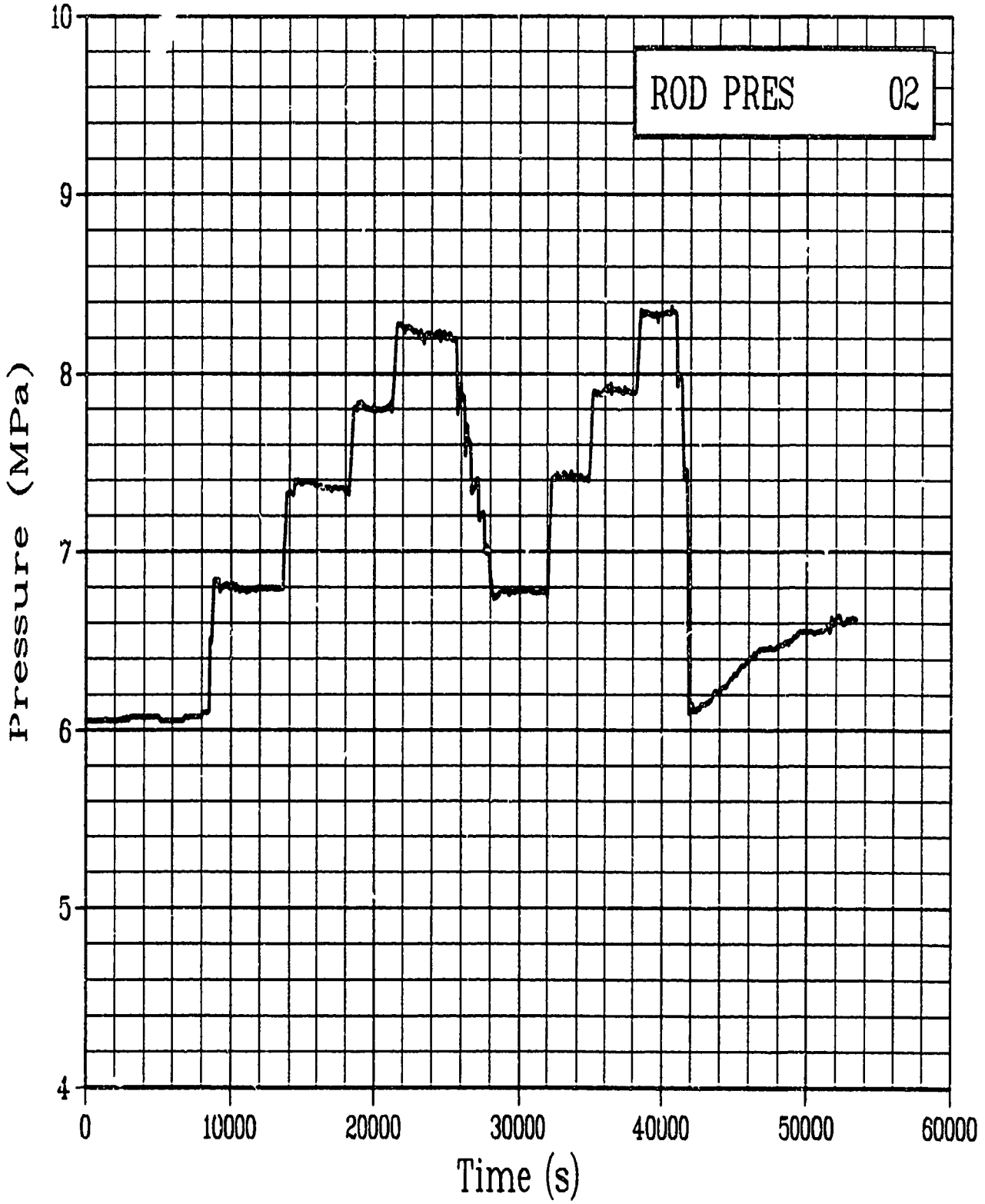

Figure C-158. Absolute pressure in Rod GC 524-2 plenum during Test PR-1 power oscillation period (ROD PRES 02).

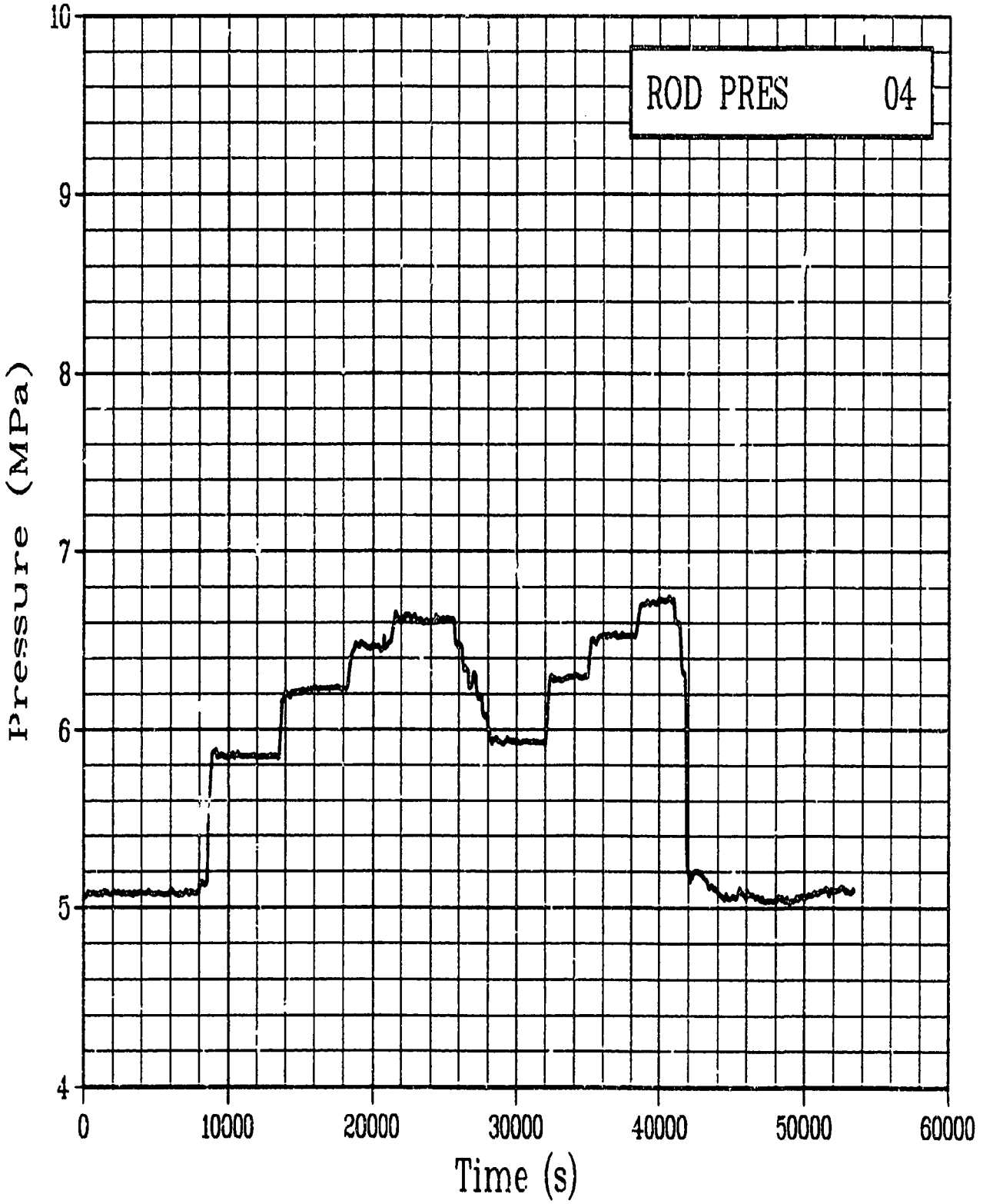

Figure C-159. Absolute pressure in Rod GC 524-4 plenum during Test PR-1 power oscillation period (ROD PRES 04).

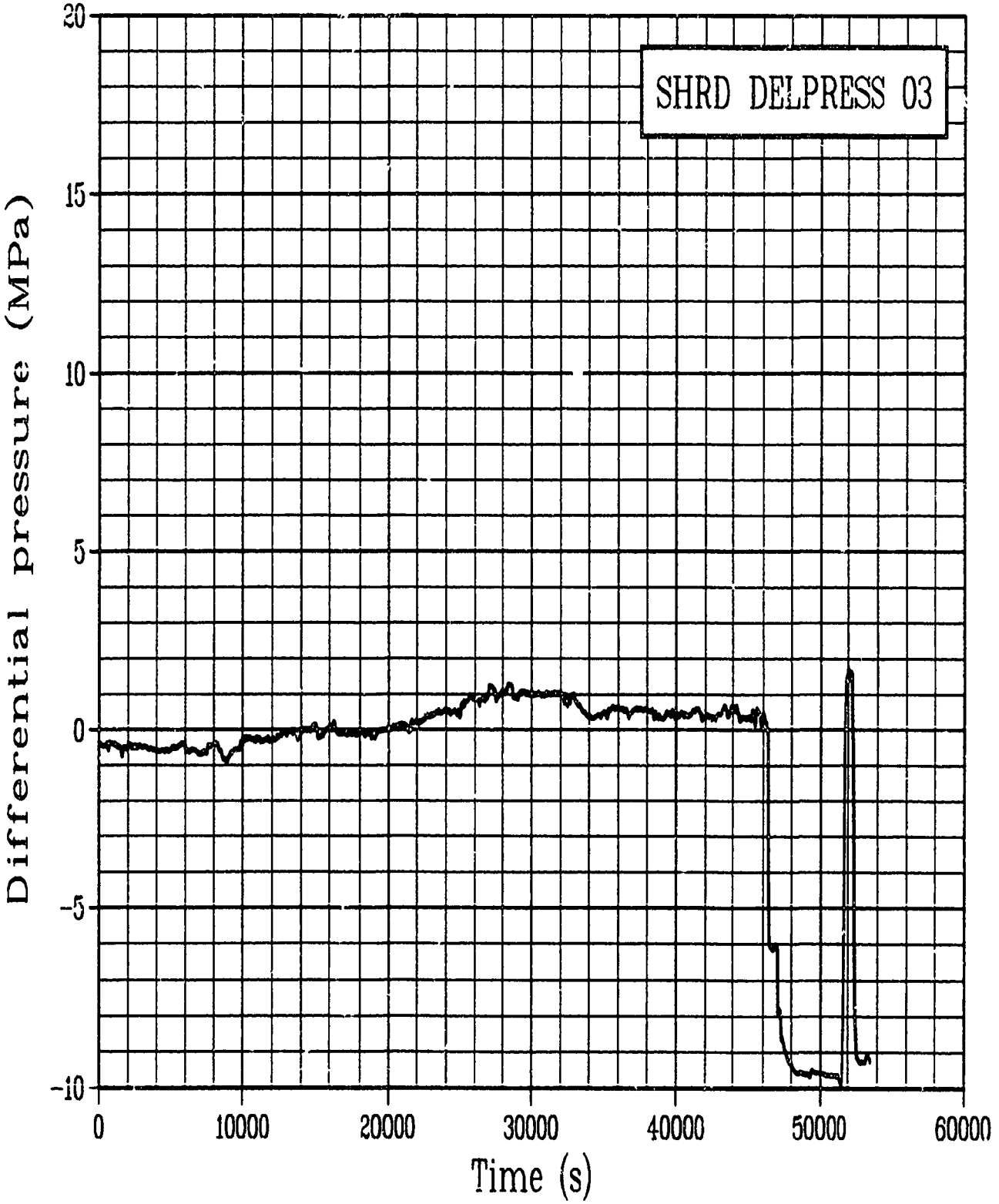

Figure C-160. Differential pressure across Rod GC 524-3 shroud during Test PR-1 power oscillation period (SHRD DELPRESS 03).

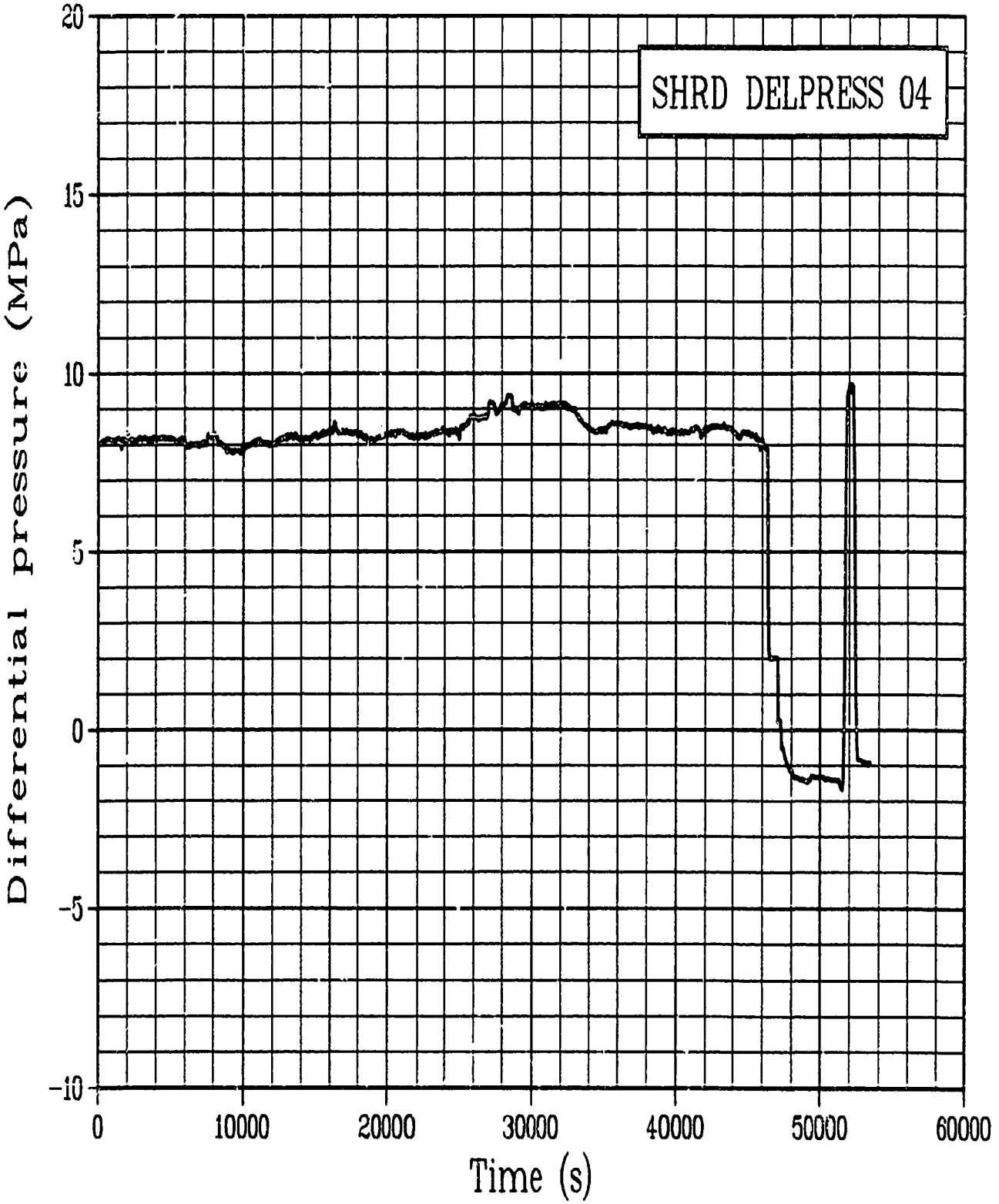

Figure C-161. Differential pressure across Rod GC 524-4 shroud during Test PR-1 power oscillation period (SHRD DELPRESS 04).

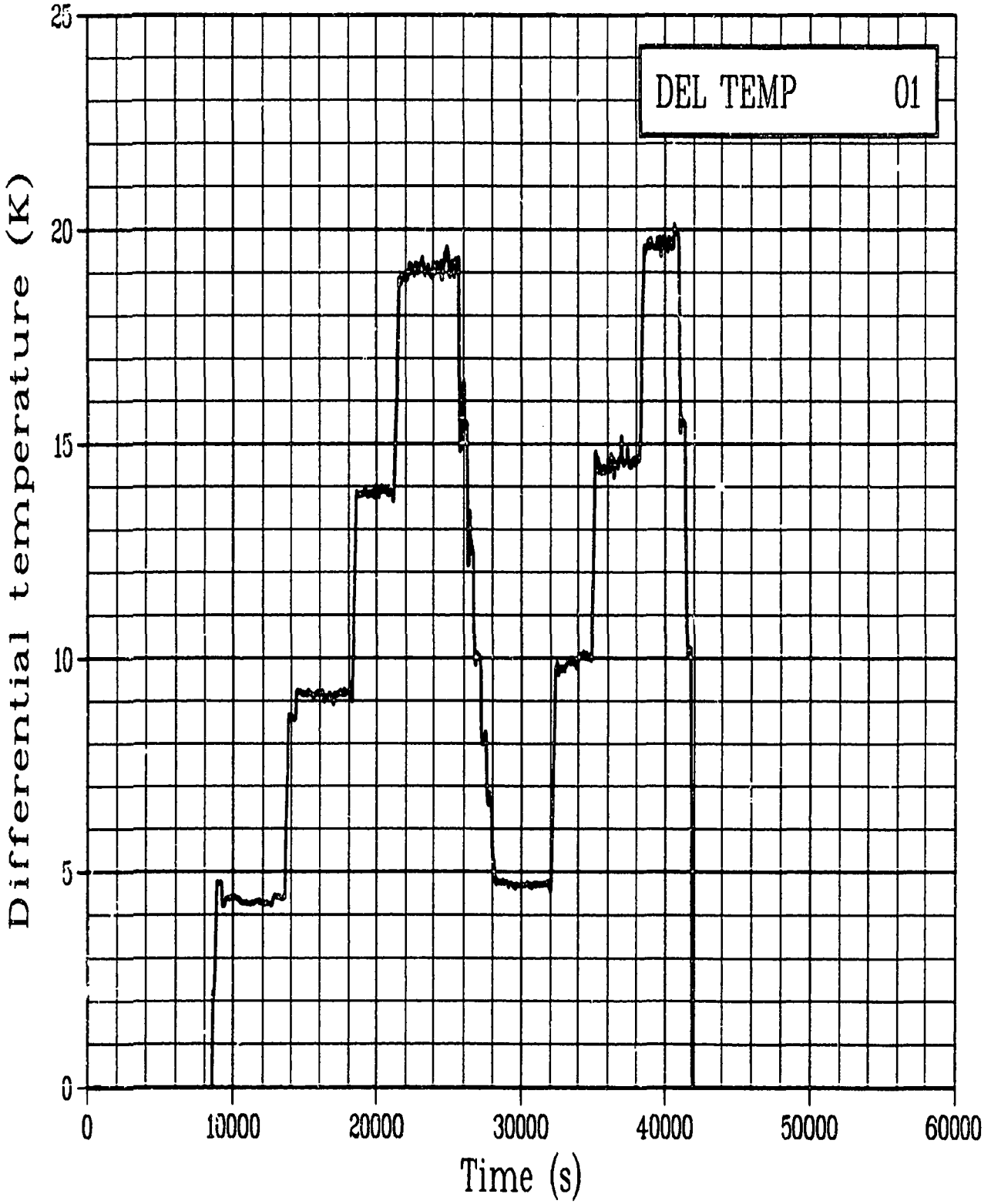

Figure C-162. Differential temperature of Rod GC 524-1 coolant inlet and outlet during Test PR-1 power oscillation period (DEL TEMP 01).

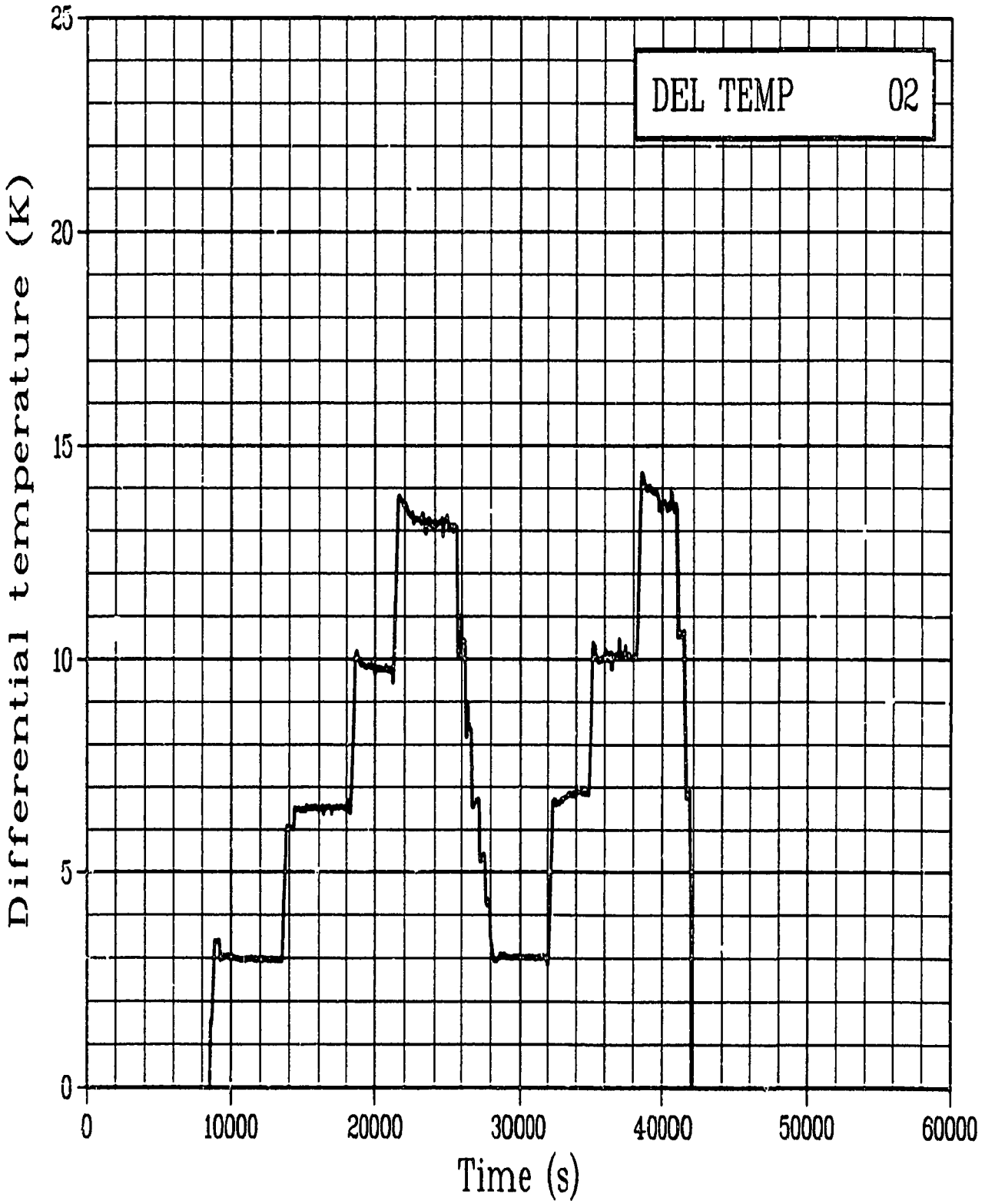

Figure C-163. Differential temperature of Rod GC 524-2 coolant inlet and outlet during Test PR-1 power oscillation period (DEL TEMP 02).

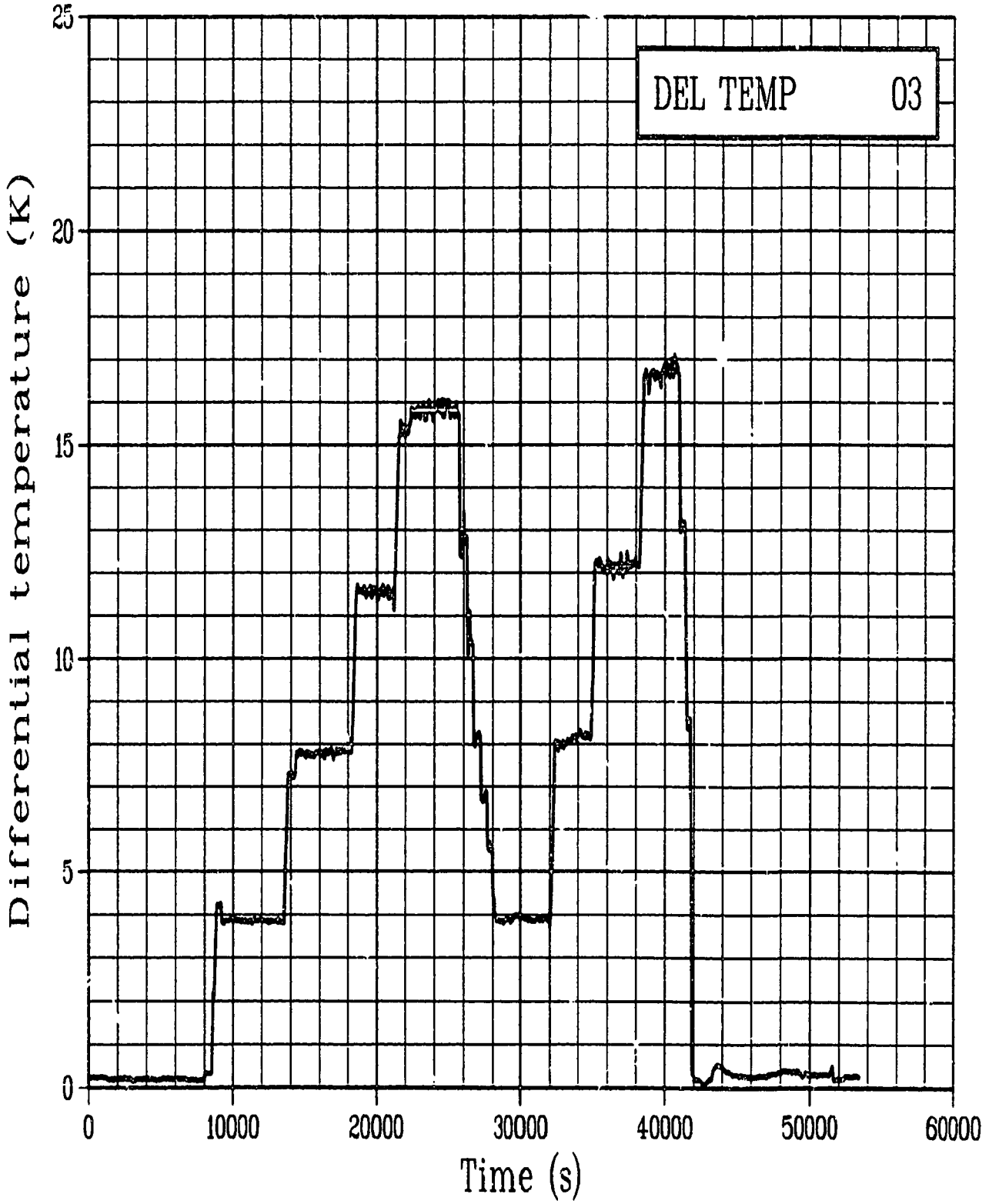

Figure C-164. Differential temperature of Rod GC 524-3 coolant inlet and outlet during Test PR-1 power oscillation period (DEL TEMP 03).

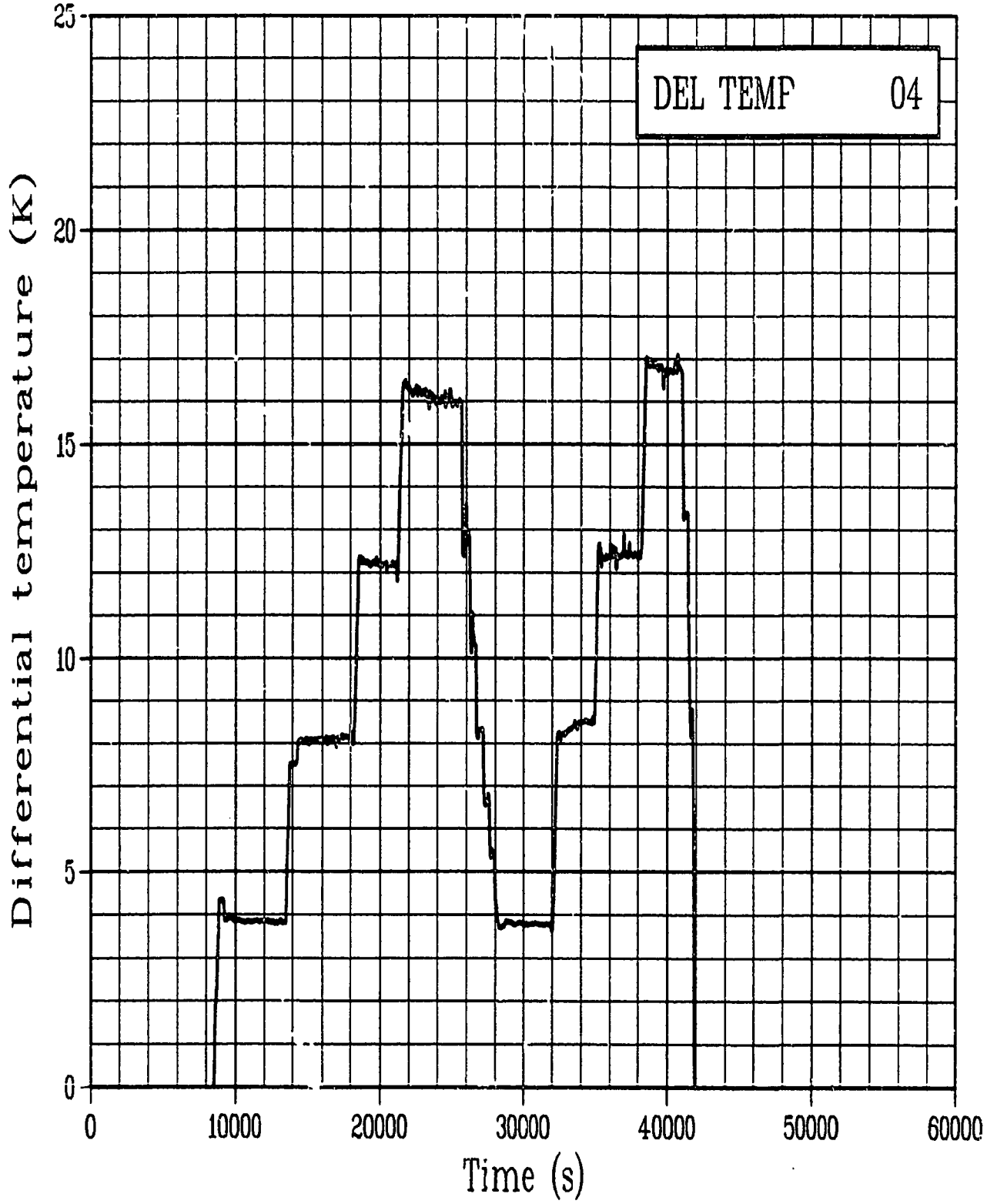

Figure C-165. Differential temperature of Rod GC 524-4 coolant inlet and outlet during Test PR-1 power oscillation period (DEL TEMP 04).

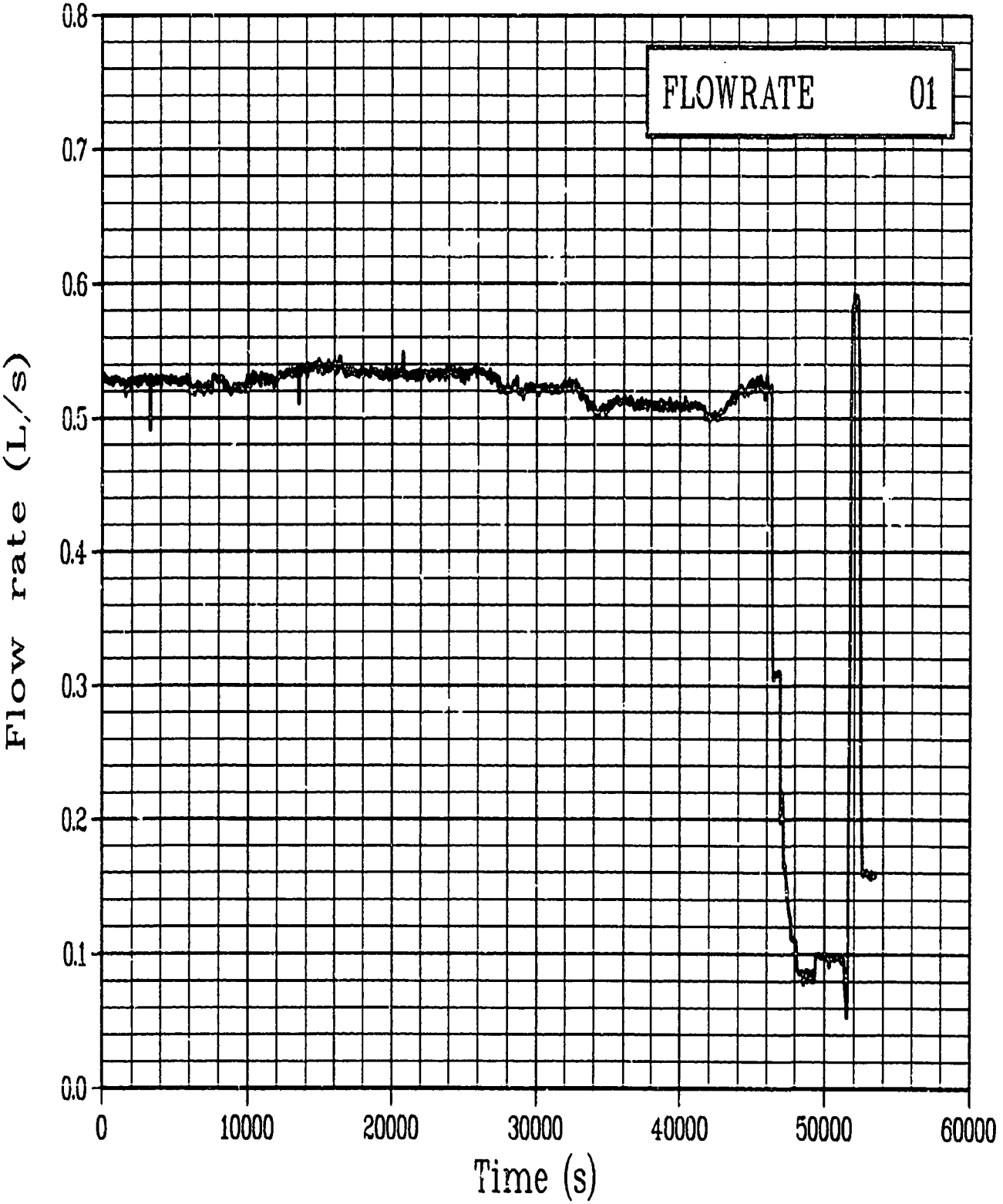

Figure C-166. Volumetric flow rate in Rod GC 524-1 lower shroud during Test PR-1 power oscillation period (FLOWRATE 01).

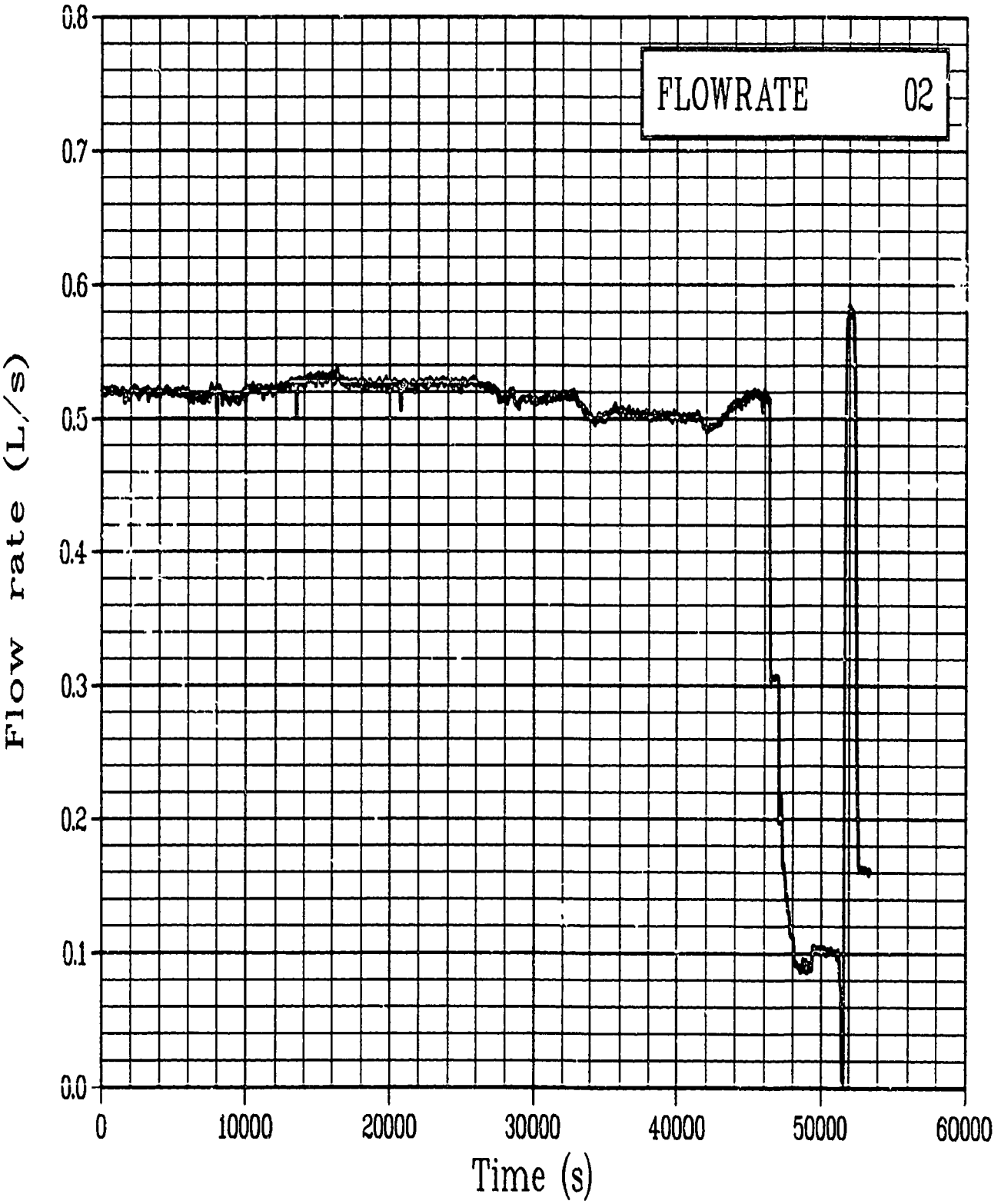

Figure C-167. Volumetric flow rate in Rod GC 524-2 lower shroud during Test PR-1 power oscillation period (FLOWRATE 02).

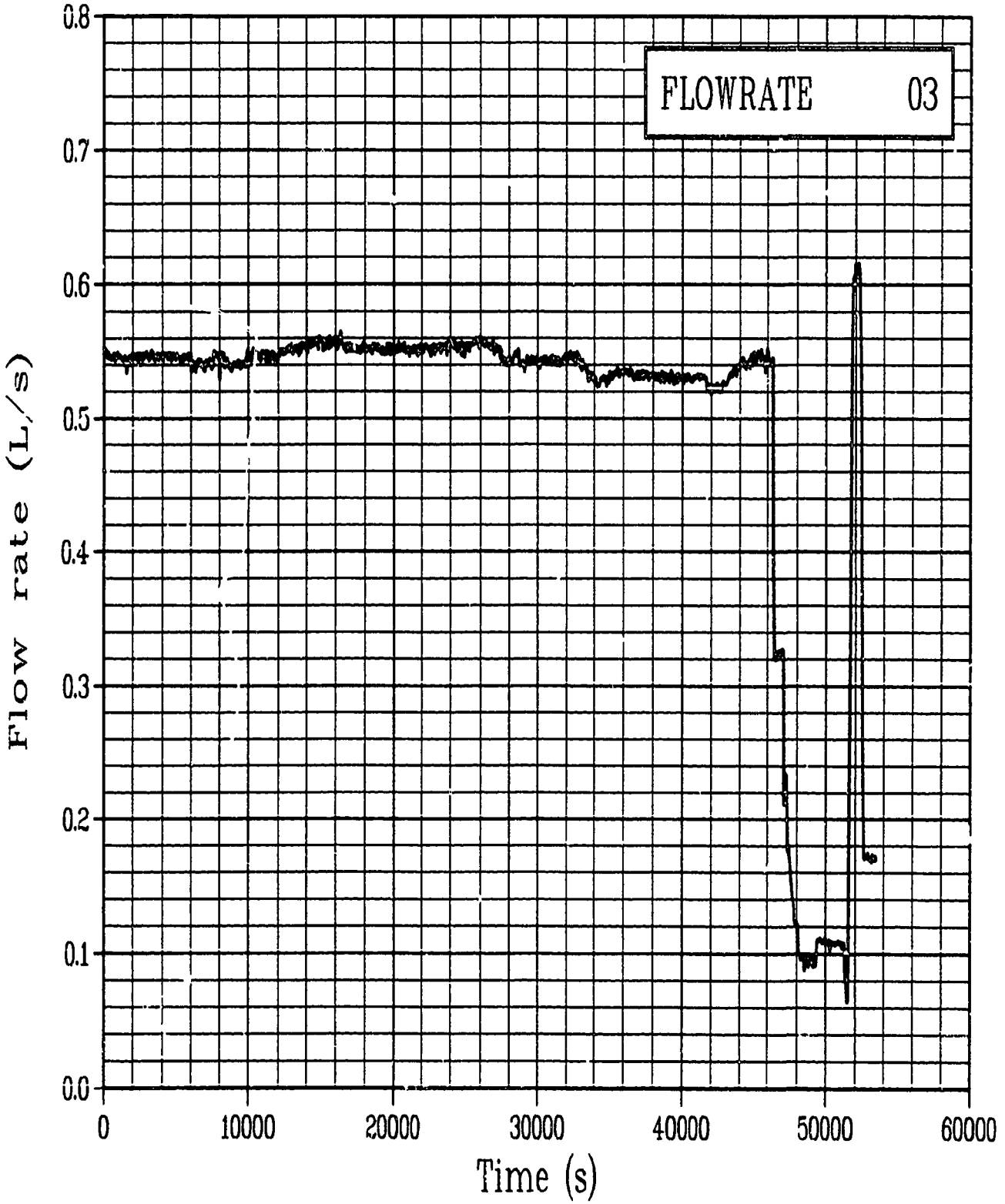

Figure C-168. Volumetric flow rate in Rod GC 524-3 lower shroud during Test PR-1 power oscillation period (FLOWRATE 03).

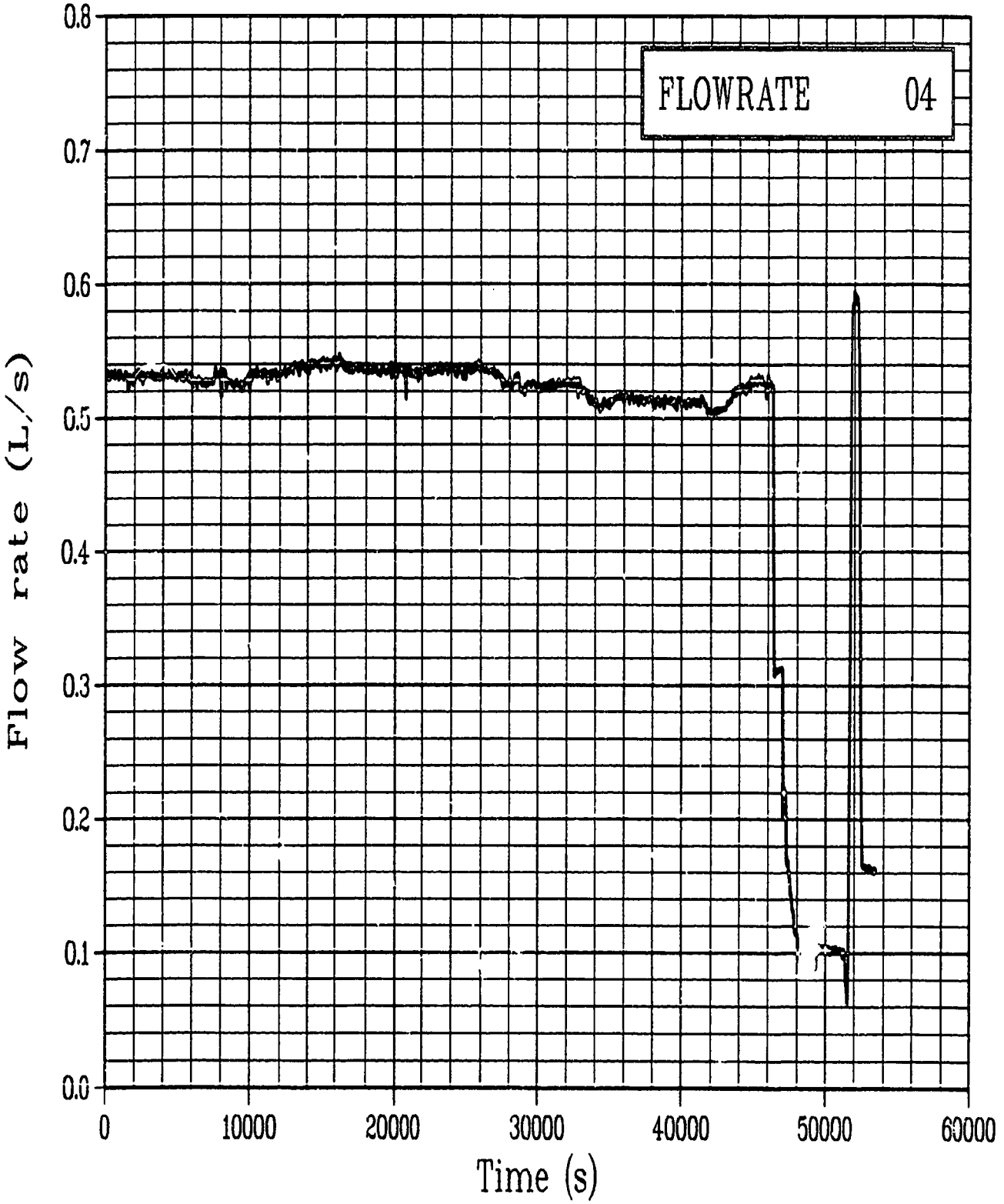

Figure C-169. Volumetric flow rate in Rod GC 524-4 lower shroud during Test PR-1 power oscillation period (FLOWRATE 04).

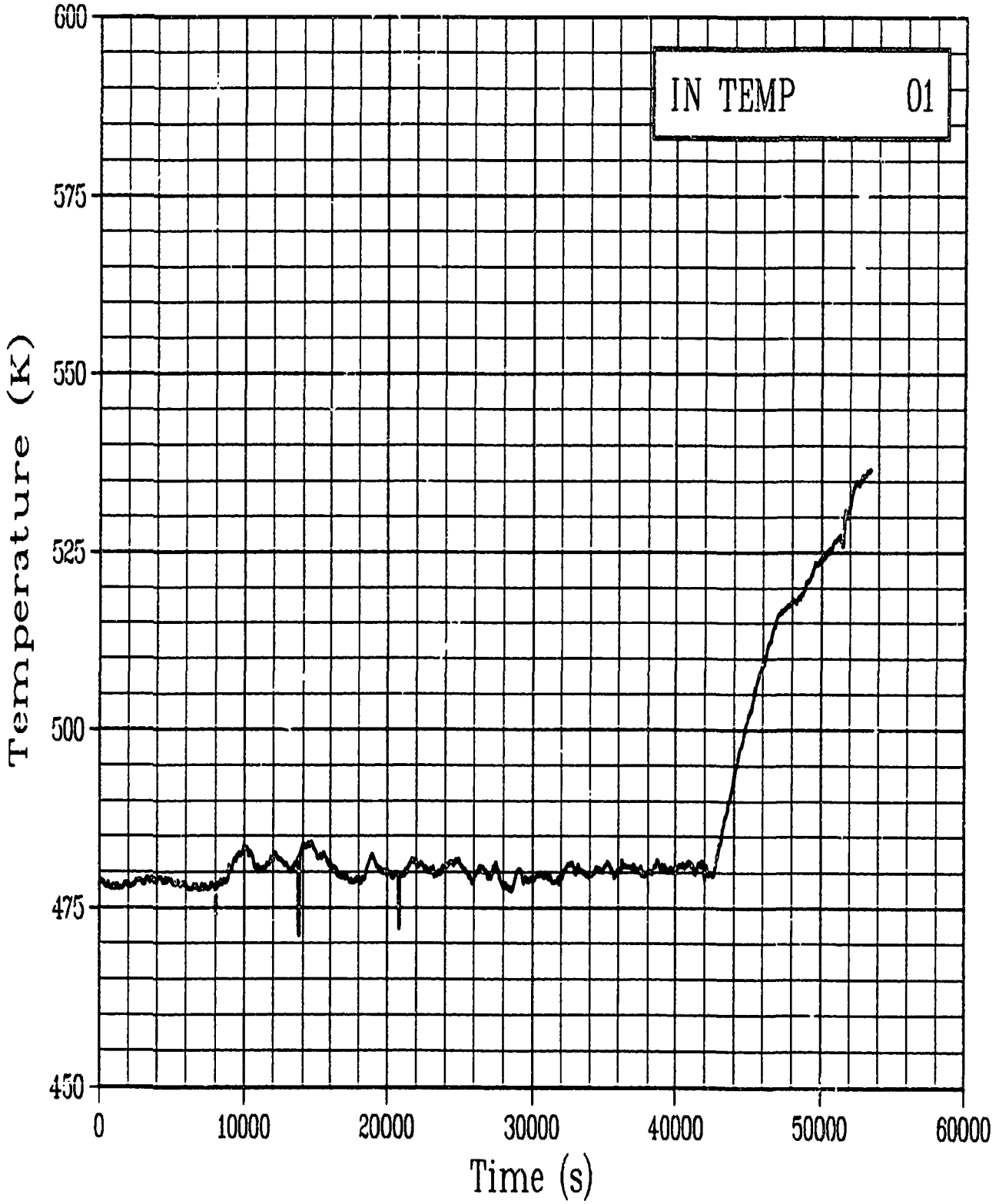

Figure C-170. Fluid temperature No. 1 at the flow shroud inlet during Test PR-1 power oscillation period (IN TEMP 01).

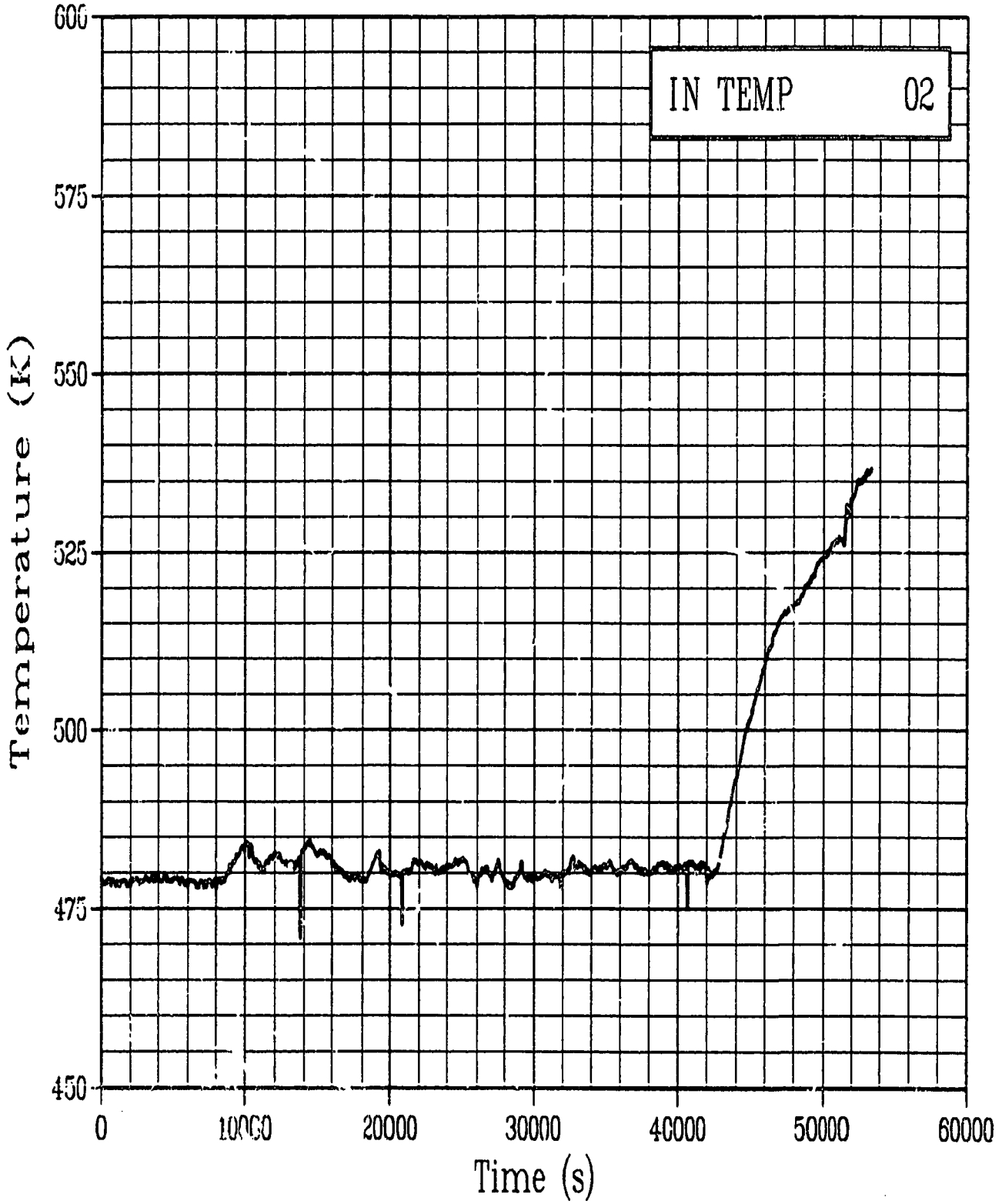

Figure C-171. Fluid temperature No. 2 at the flow shroud inlet during Test PR-1 power oscillation period (IN TEMP 02).

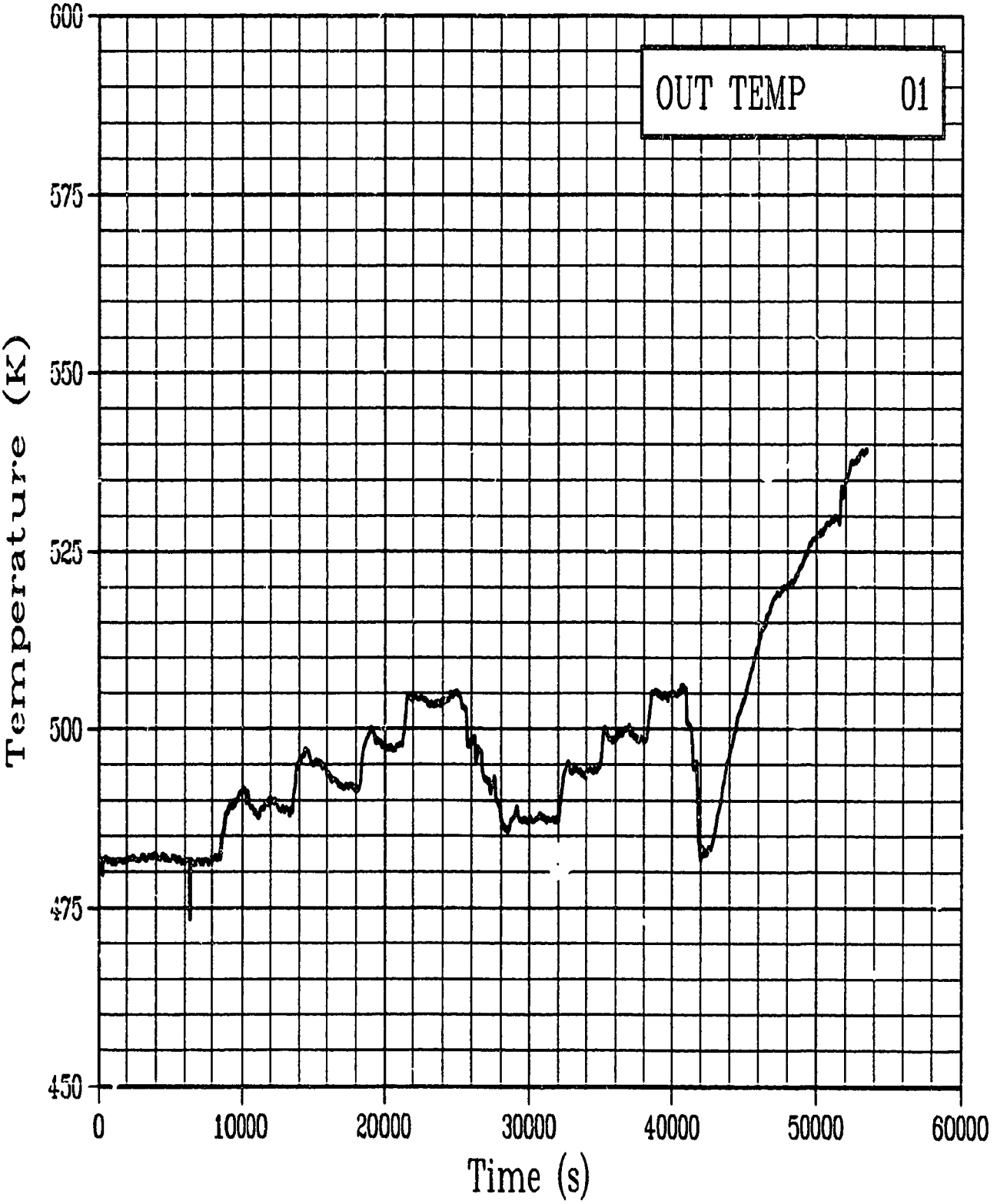

Figure C-172. Fluid temperature of Rod GC 524-1 coolant outlet during Test PR-1 power oscillation period (OUT TEMP 01).

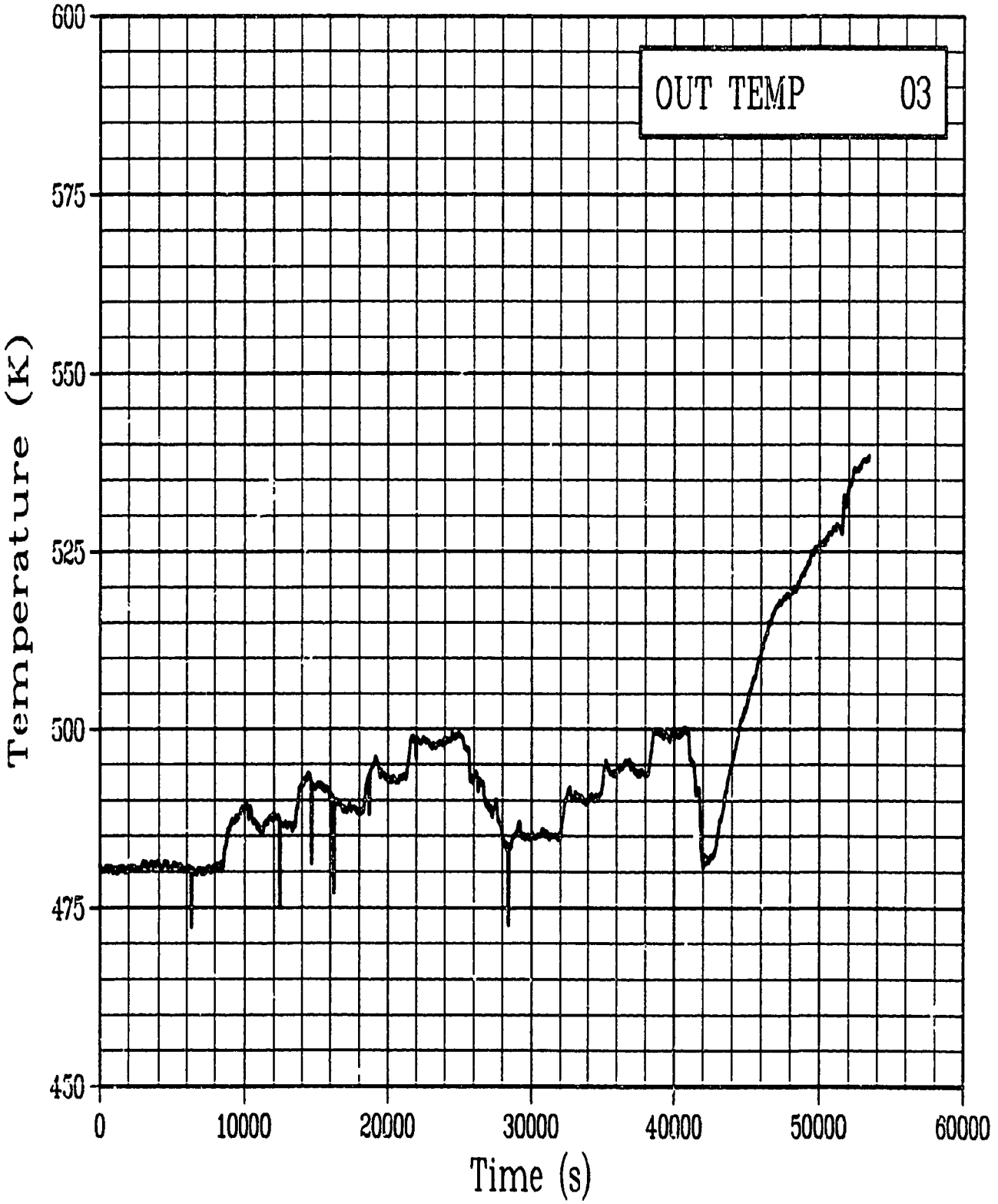

Figure C-173. Fluid temperature of Rod GC 524-3 coolant outlet during Test PR-1 power oscillation period (OUT TEMP 03).

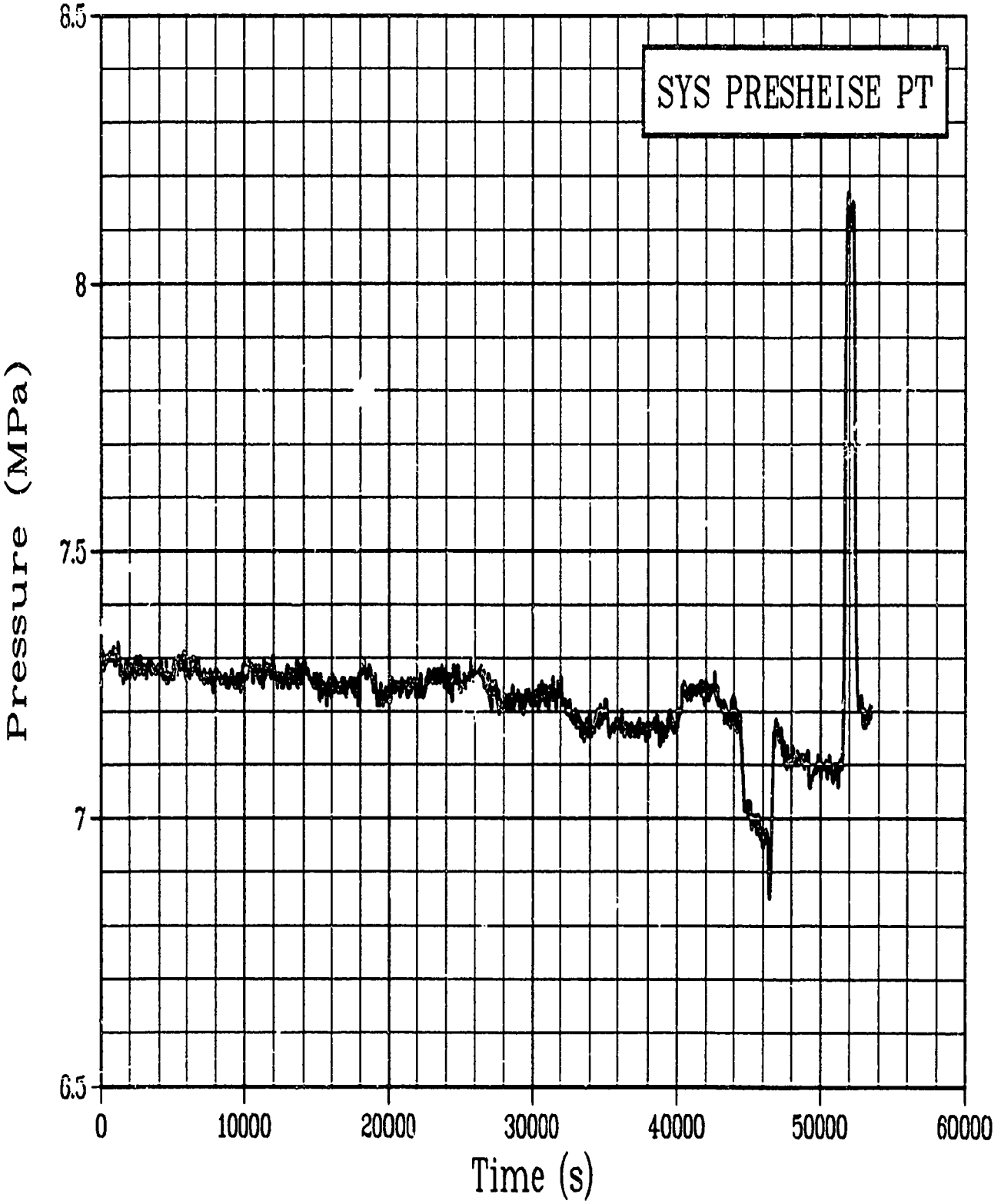

Figure C-174. Plant system pressure, Heise pressure guage during Test PR-1 power oscillation period (SYS PRESHEISE PT).

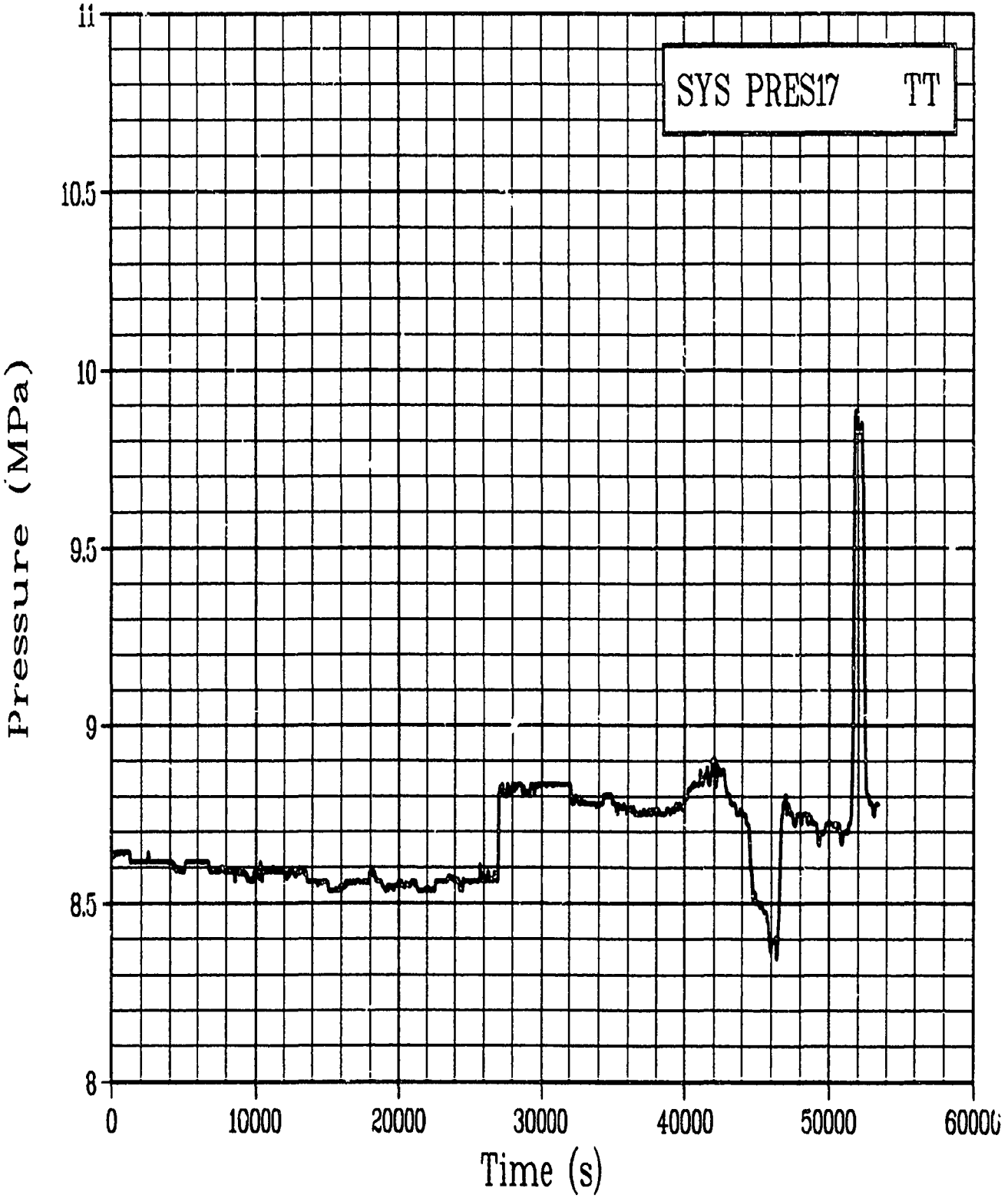

Figure C-175. Coolant pressure in the IPT outlet, 0-17 MPa range during Test PR-1 power oscillation period (SYS PRES17 TT).

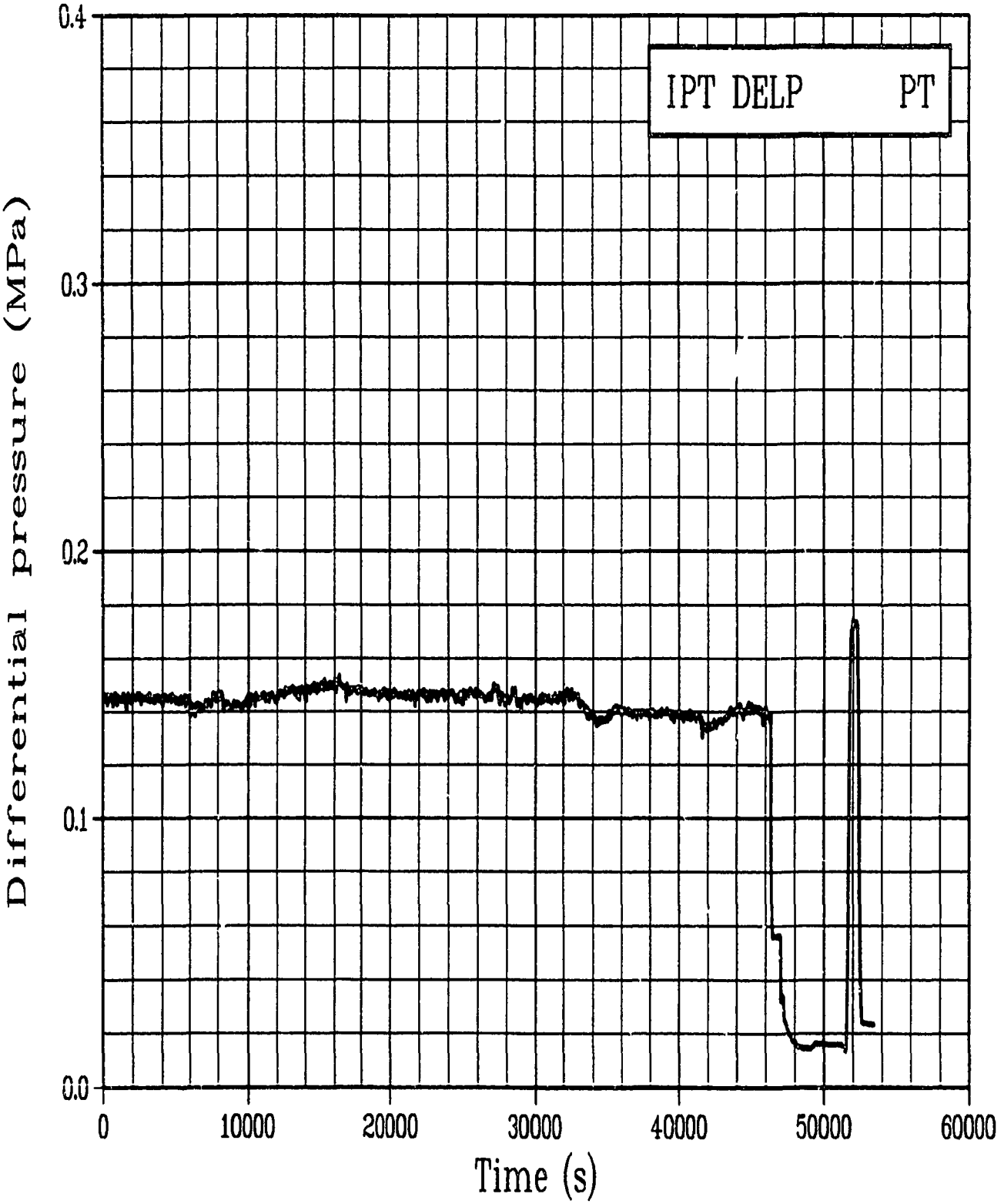

Figure C-176. Differential pressure across the in-pile tube during Test PR-1 power oscillation period (IPT DELP PT).

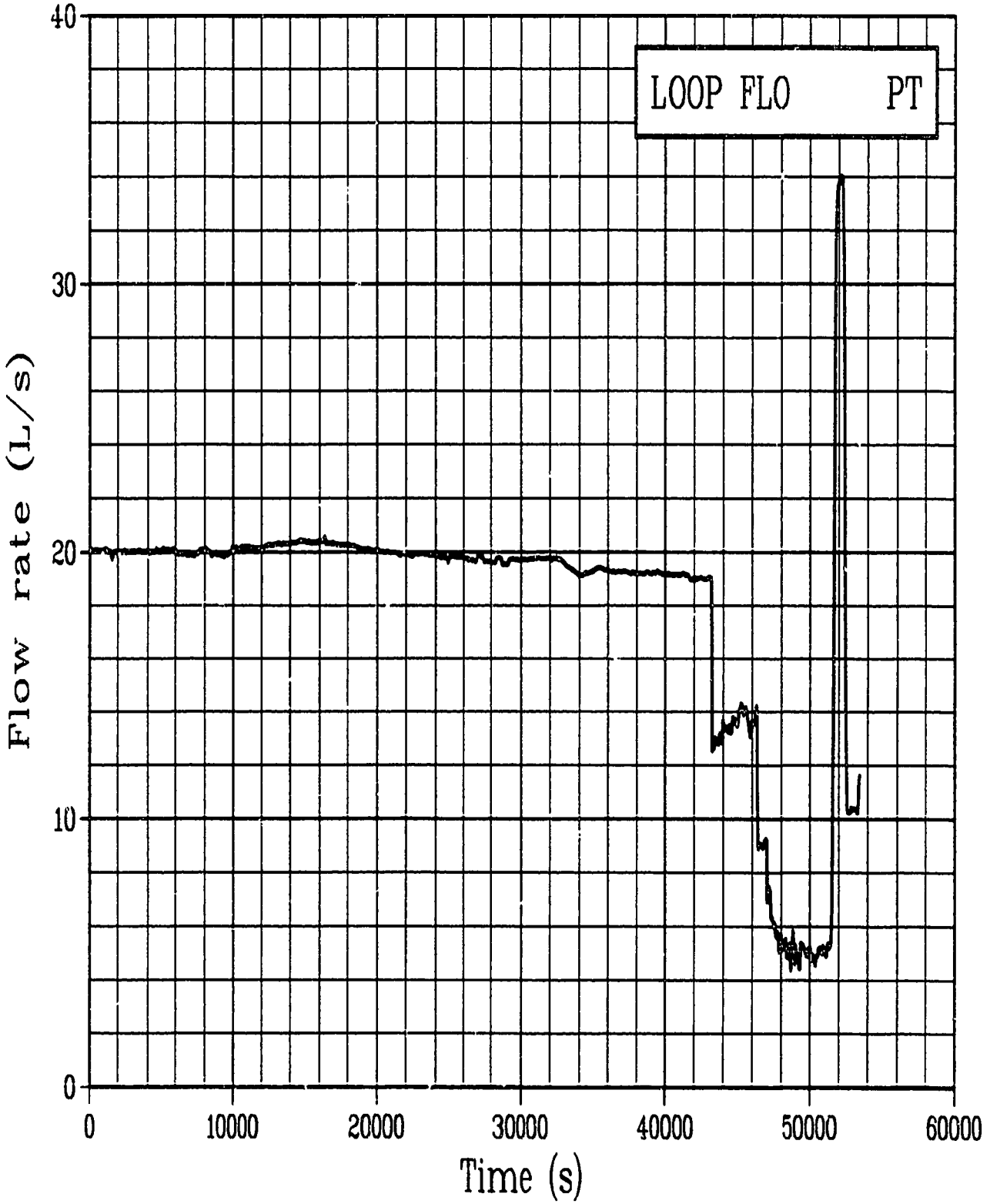

Figure C-177. Volumetric flow rate in experimental loop system during Test PR-1 power oscillation period (LOOP FLO PT).

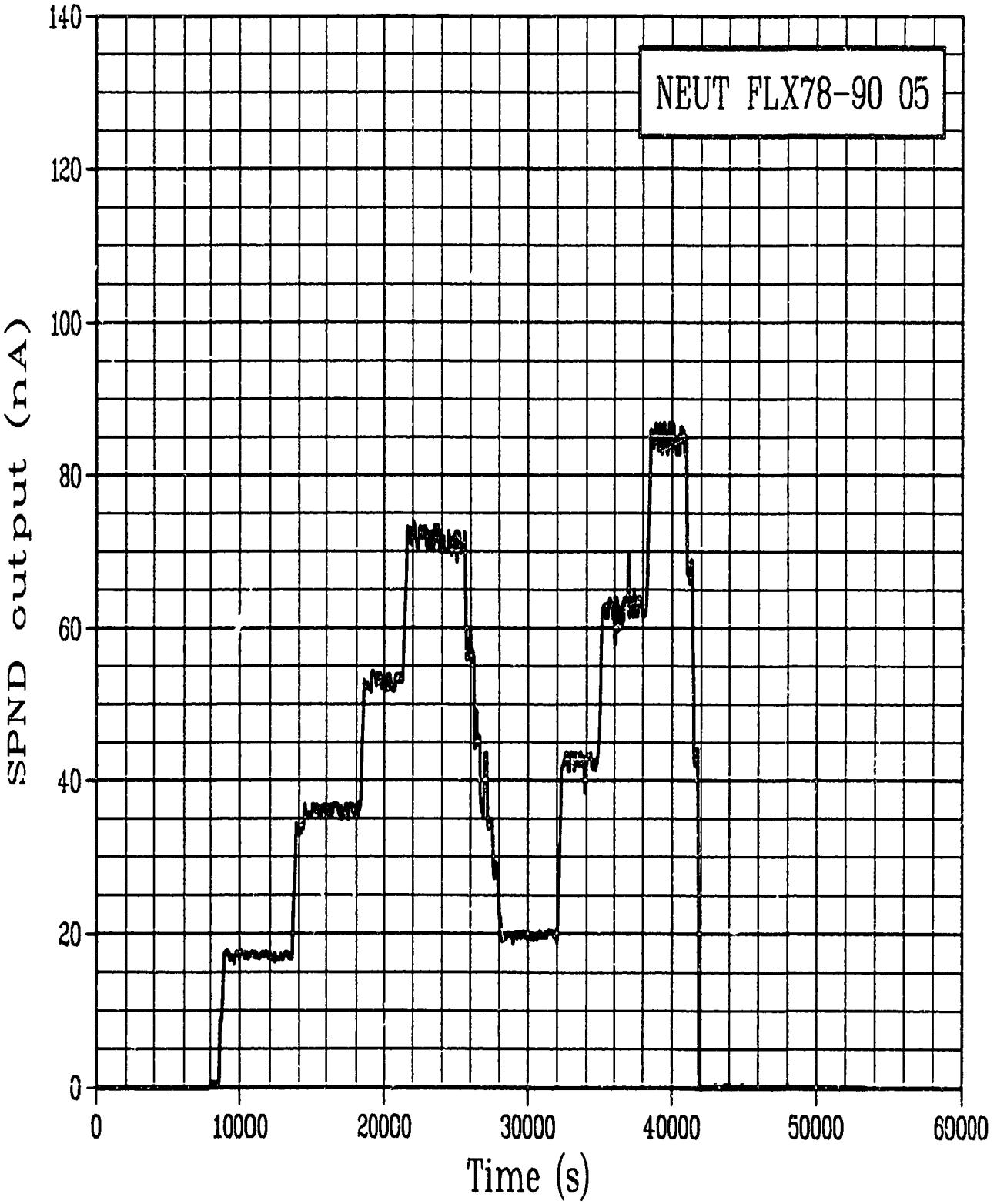

Figure C-178. Neutron flux 0.78 m from bottom of fuel stack during Test PR-1 power oscillation period (NEUT FLX78-90 05).

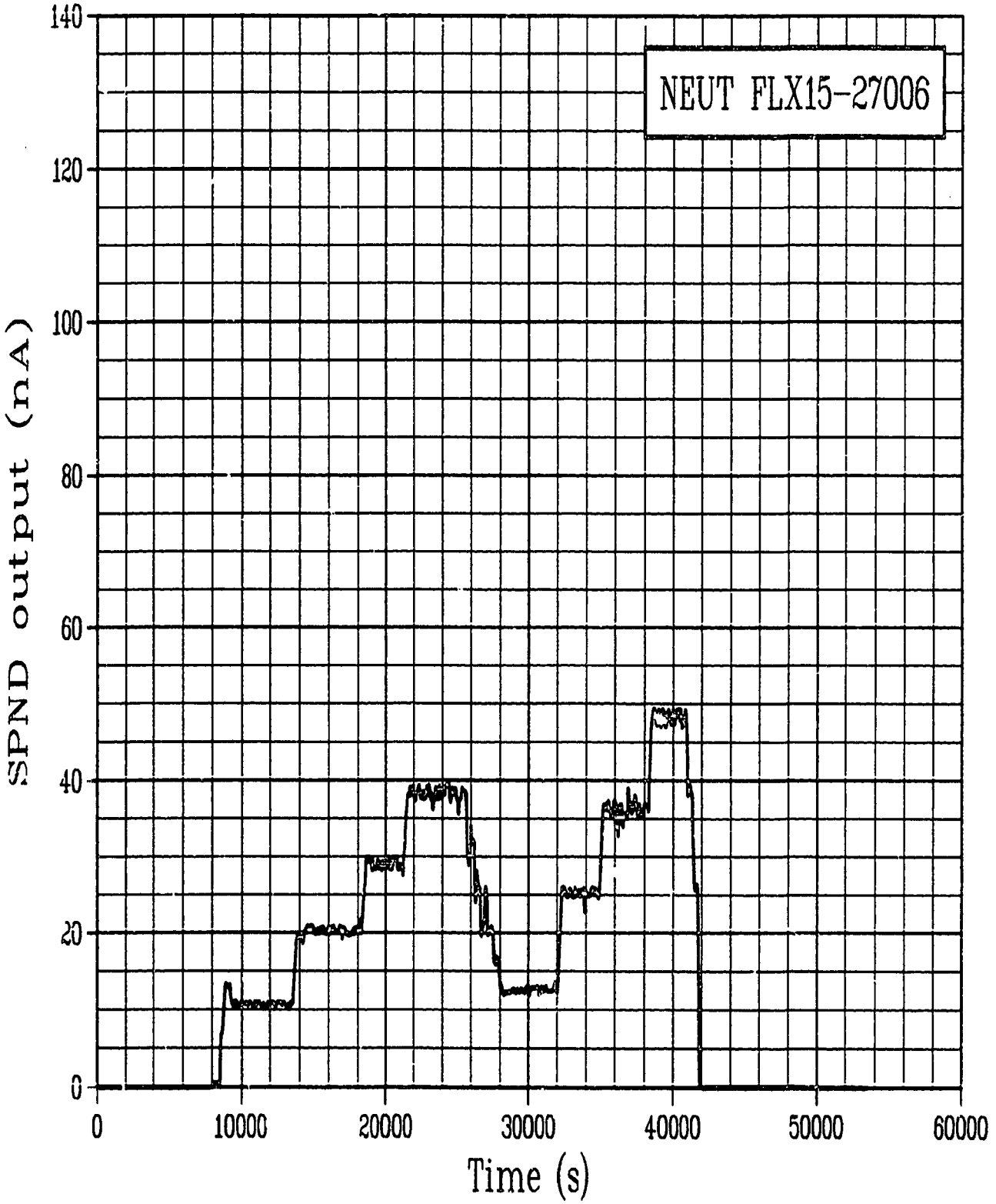

Figure C-179. Neutron flux 0.15 m from bottom of fuel stack during Test PR-1 power oscillation period (NEUT FLX15-27006).

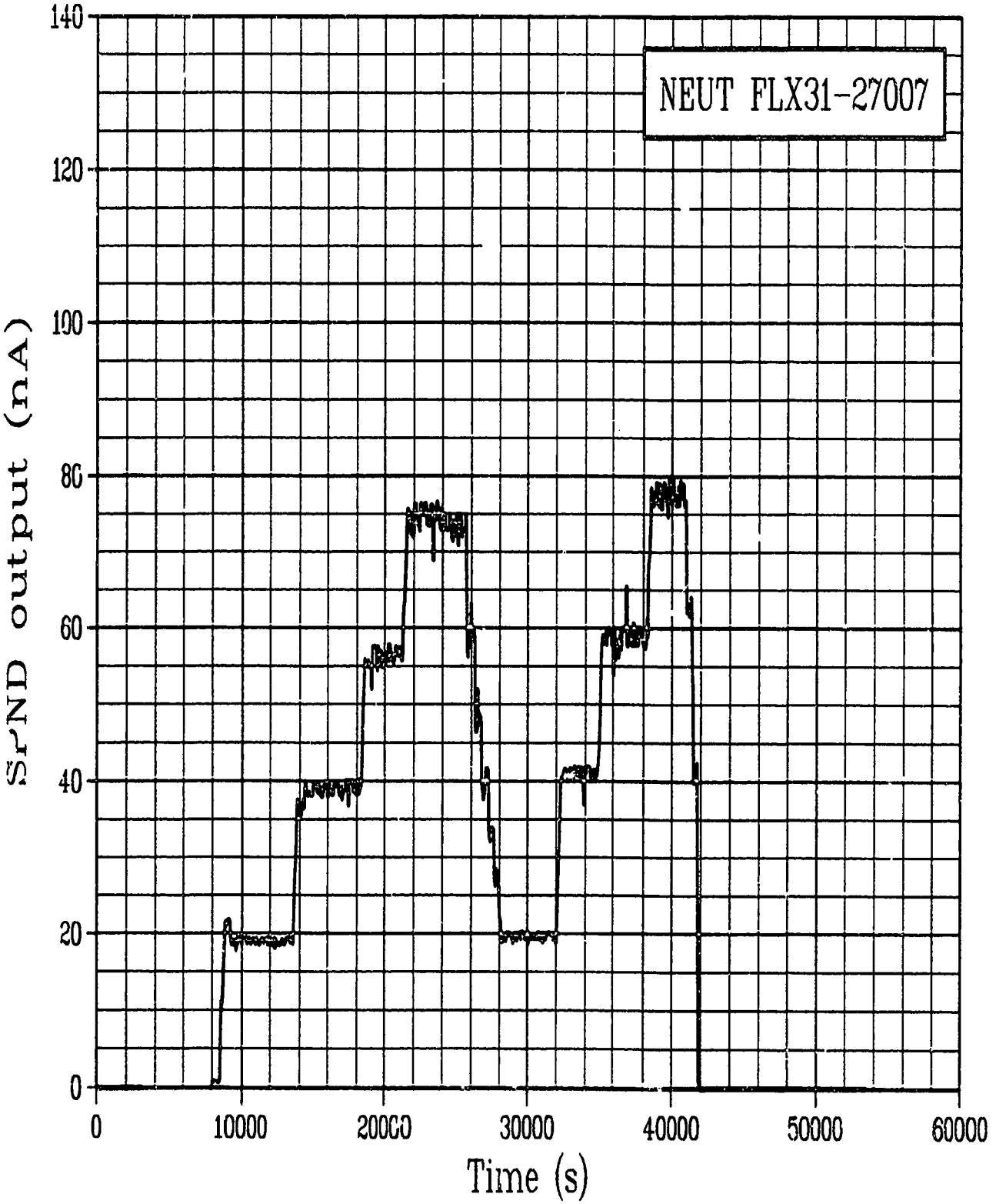

Figure C-180. Neutron flux 0.31 m from bottom of fuel stack during Test PR-1 power oscillation period (NEUT FLX31-27007).

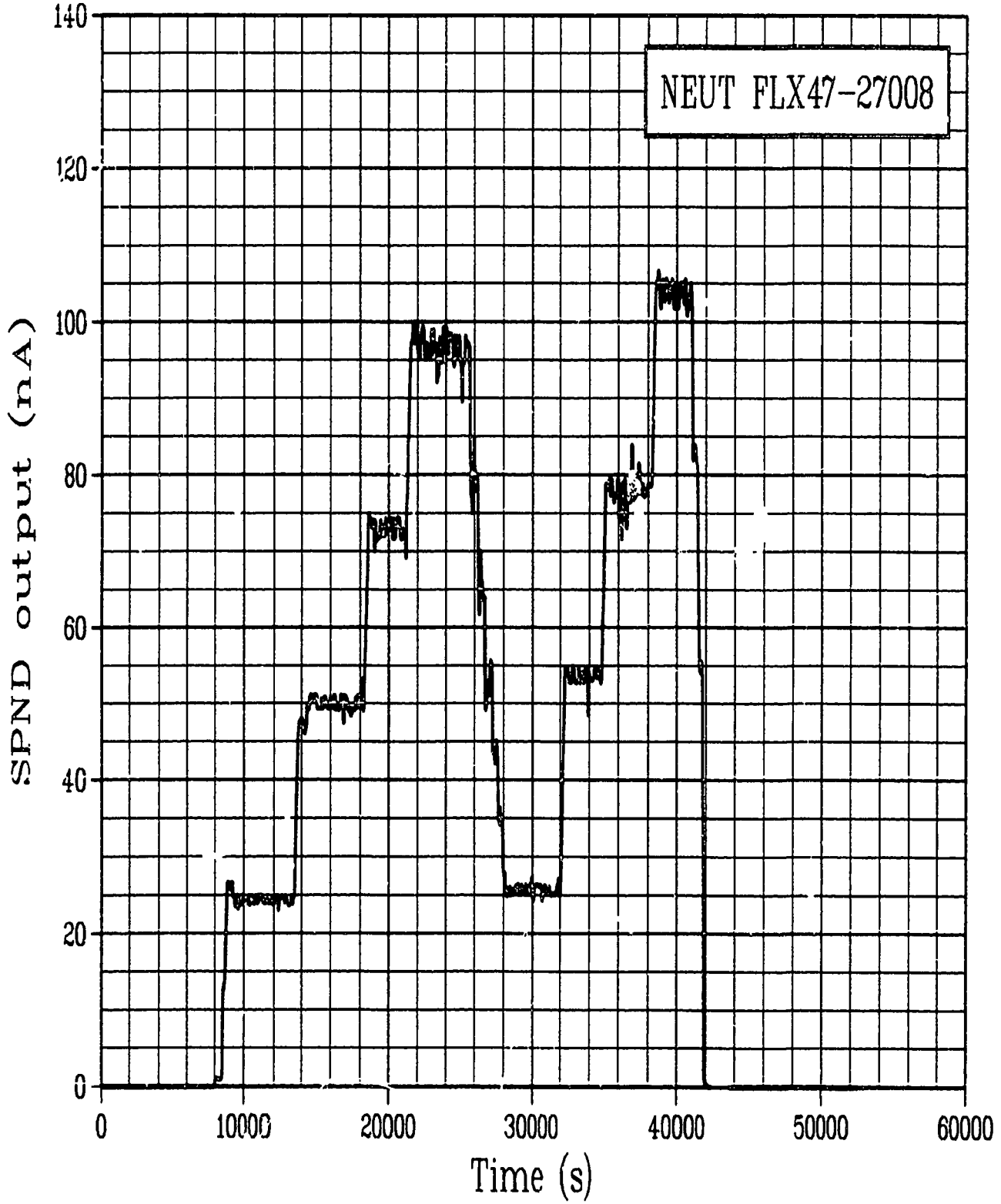

Figure C-181. Neutron flux 0.47 m from bottom of fuel stack during Test PR-1 power oscillation period (NEUT FLX47-27008).

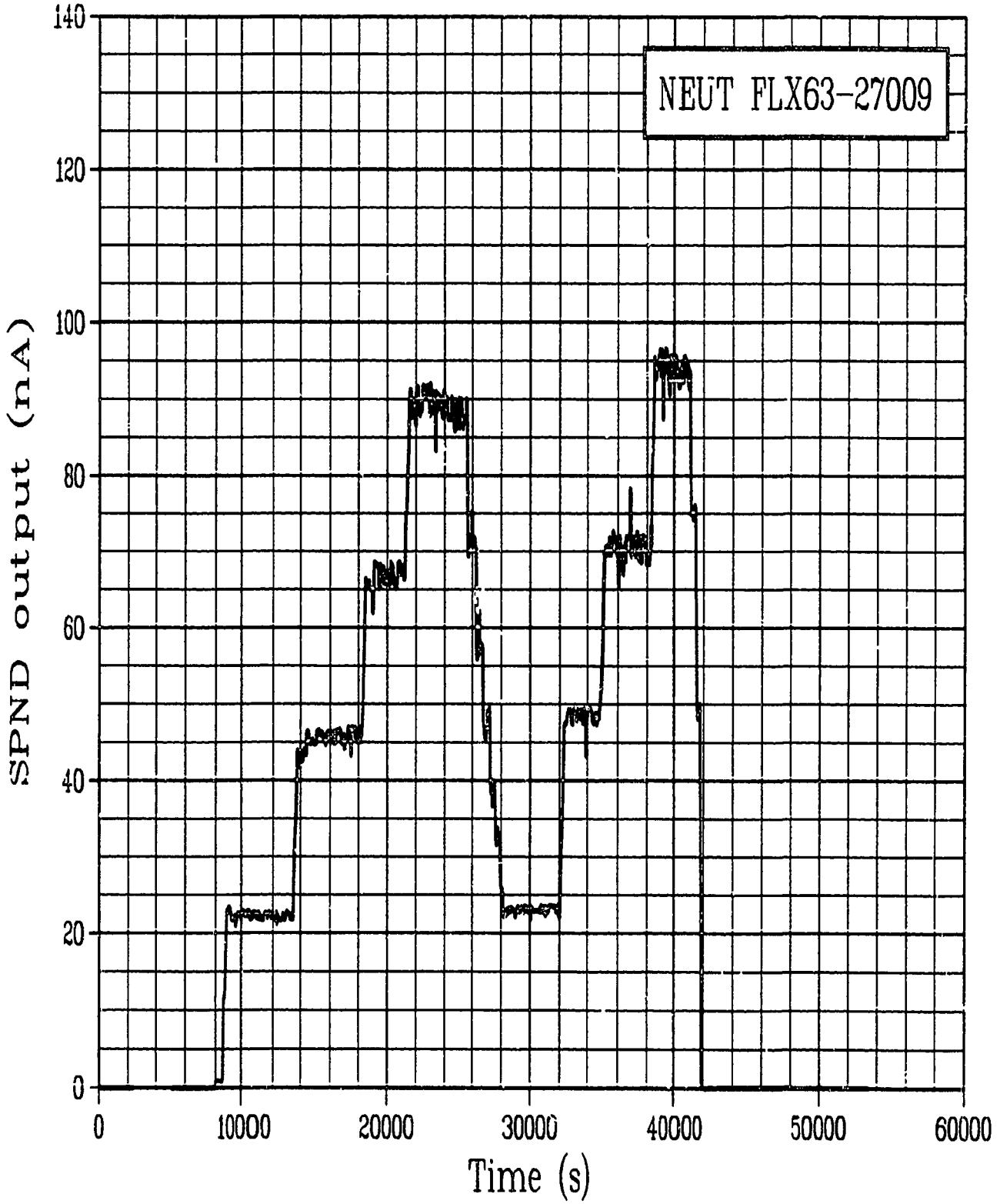

Figure C-182. Neutron flux 0.63 m from bottom of fuel stack during Test PR-1 power oscillation period (NEUT FLX63-27009).

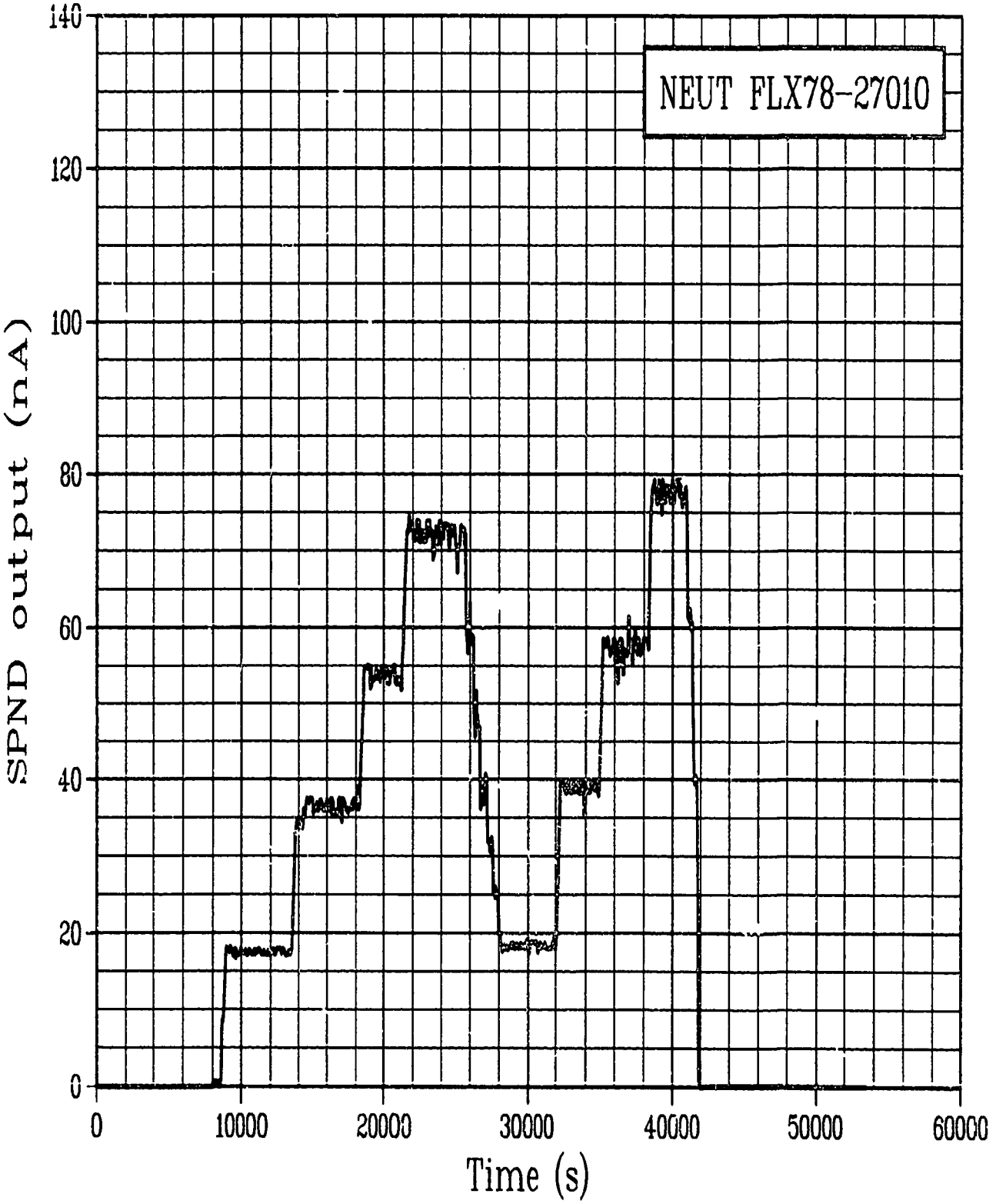

Figure C-183. Neutron flux 0.78 m from bottom of fuel stack during Test PR-1 power oscillation period (NEUT FLX78-27010).

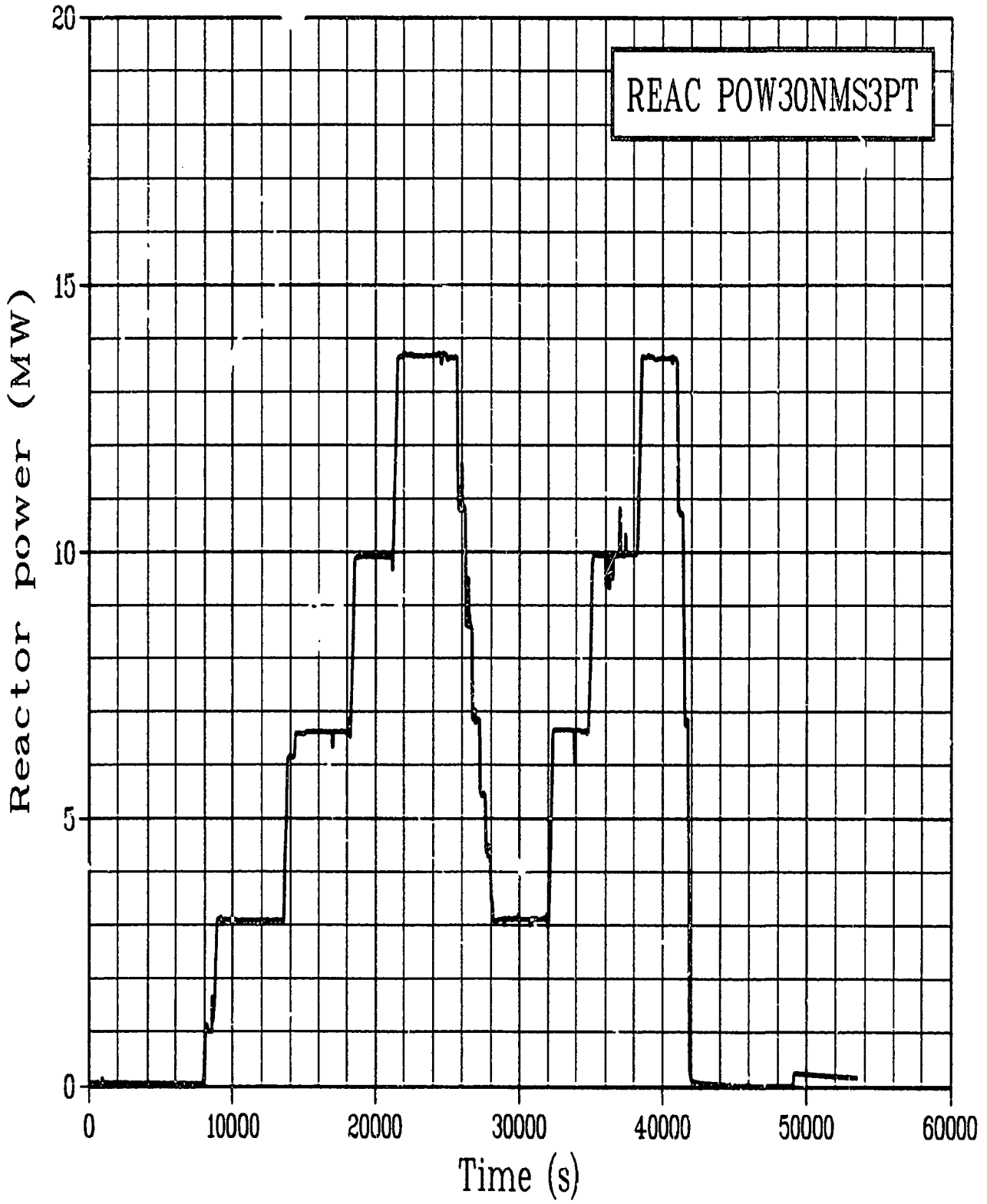

Figure C-184. Reactor power from Core Ionization Chamber NMS 3 during Test PR-1 power oscillation period (REAC POW30NMS3PT).

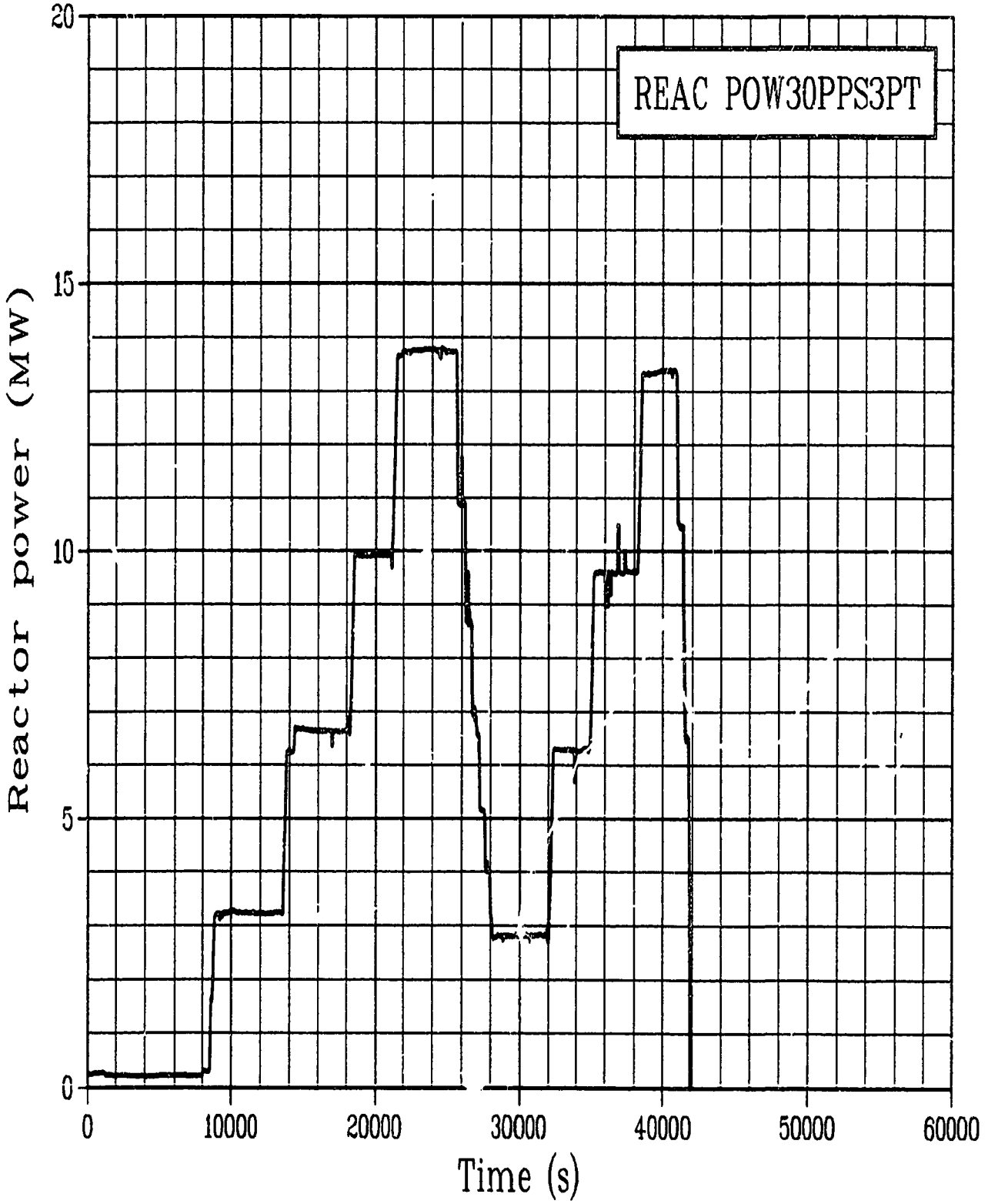

Figure C-185. Reactor power from Core Ionization Chamber PPS 3 during Test PR-1 power oscillation period (REAC POW30PPS3PT).

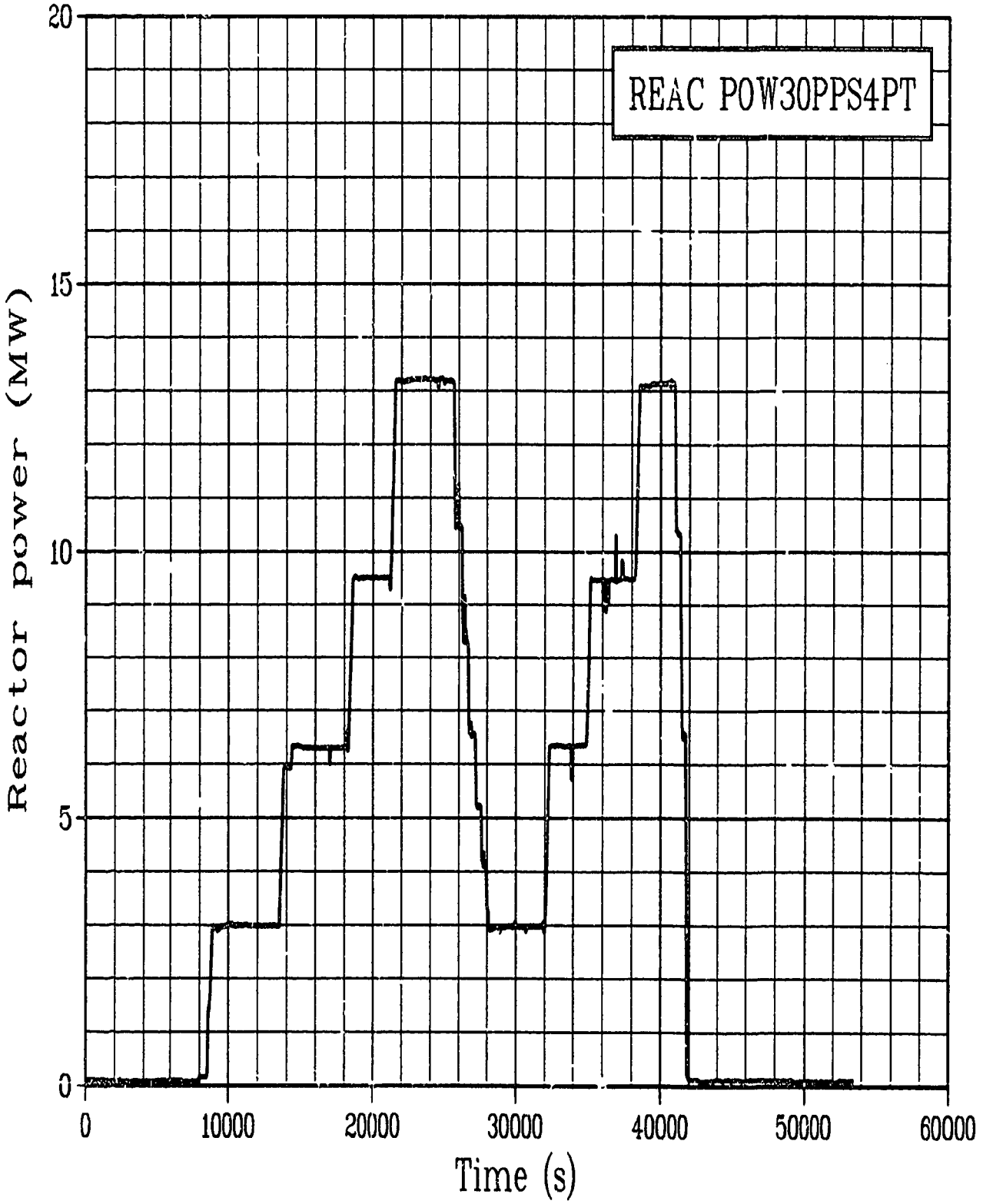

Figure C-186. Reactor power from Core Ionization Chamber PPS 4 during Test PR-1 power oscillation period (REAC POW30PPS4PT).

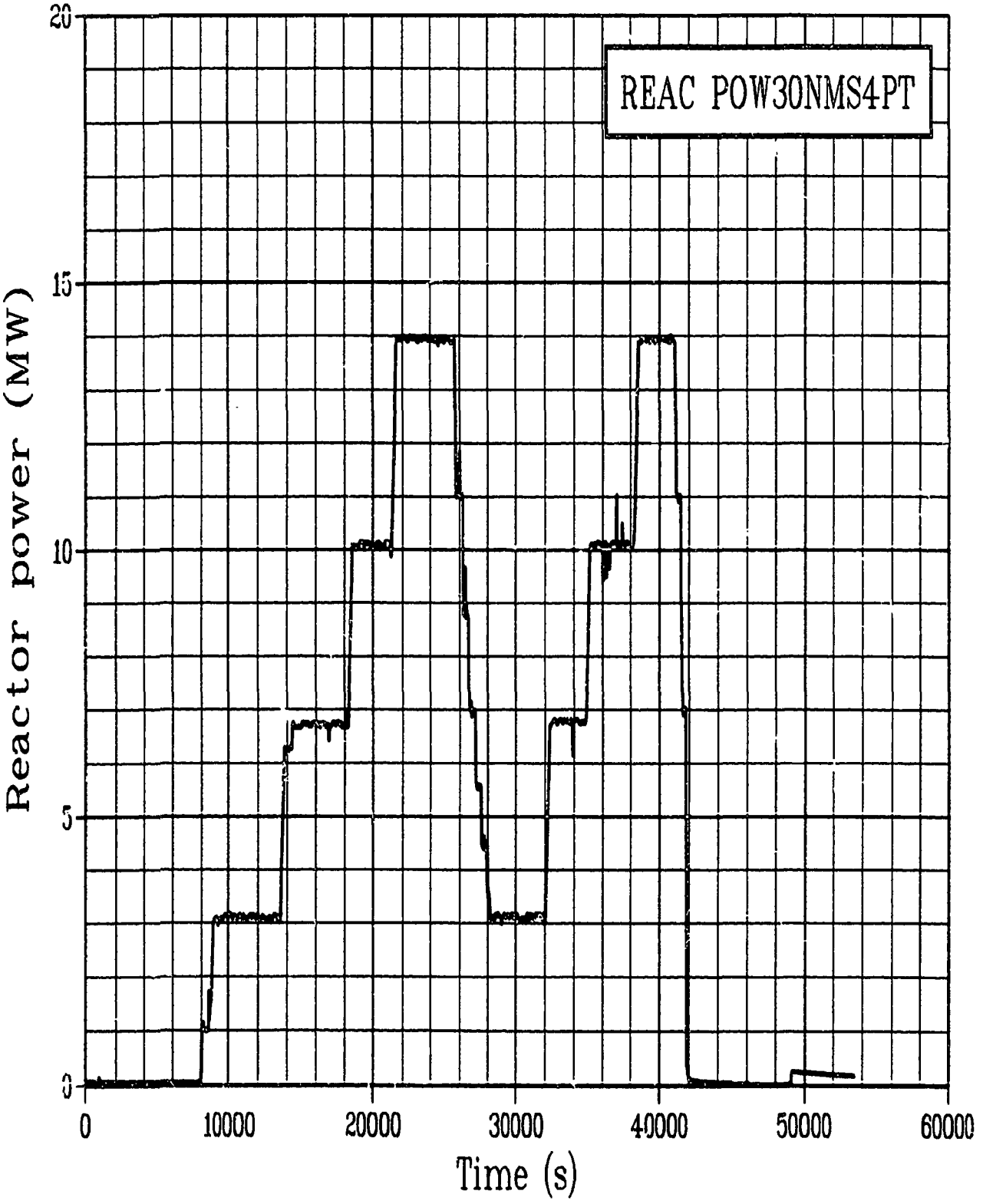

Figure C-187. Reactor power from Core Ionization Chamber NMS 4 during Test PR-1 power oscillation period (REAC POW30NMS4PT).

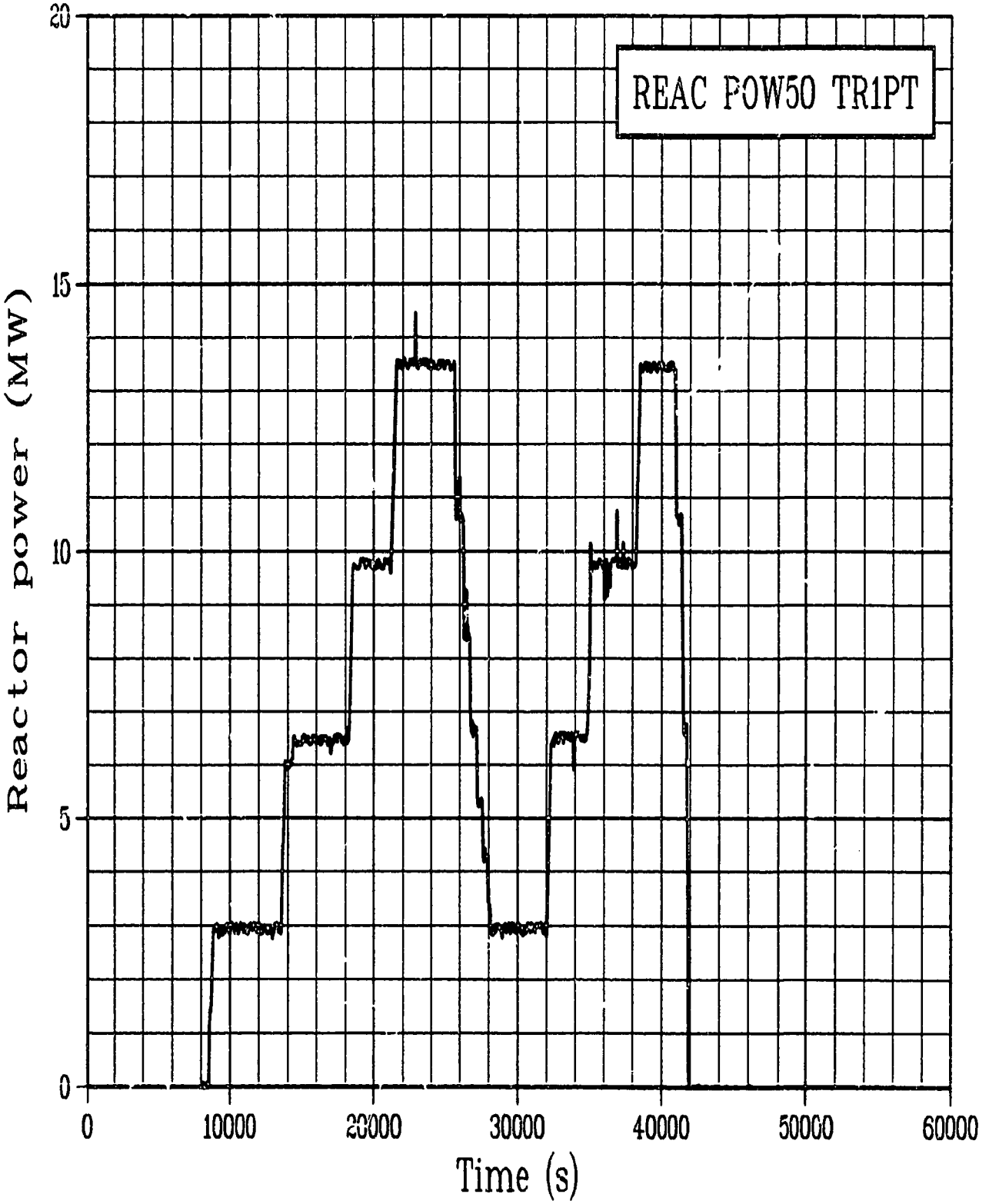

Figure C-188. Reactor power from Core Ionization Chamber TR 1 during Test PR-1 power oscillation period (REAC POW50 TR1PT).

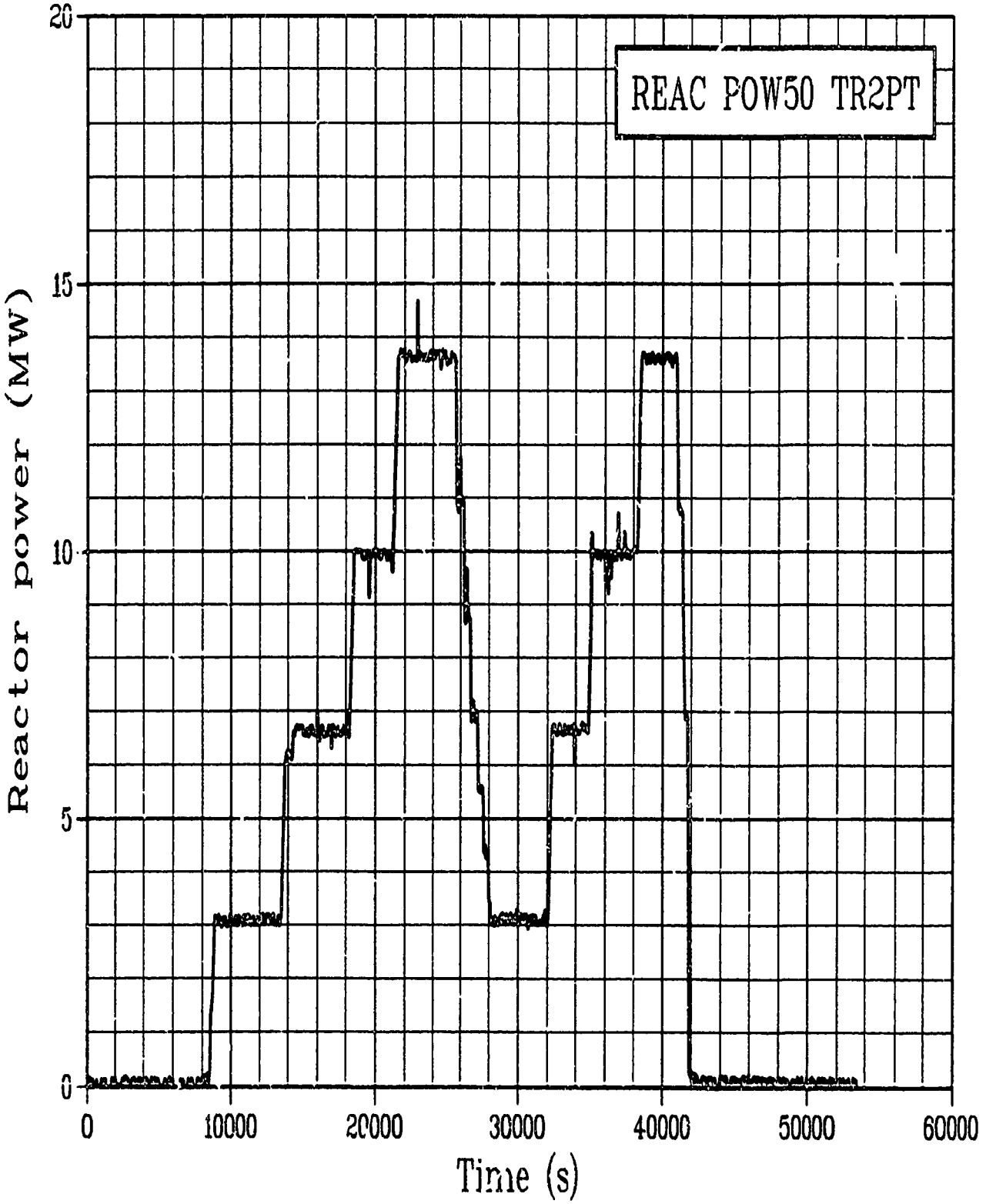

Figure C-189. Reactor power from Core Ionization Chamber TR 2 during Test PR-1 power oscillation period (REAC POW50 TR2PT).

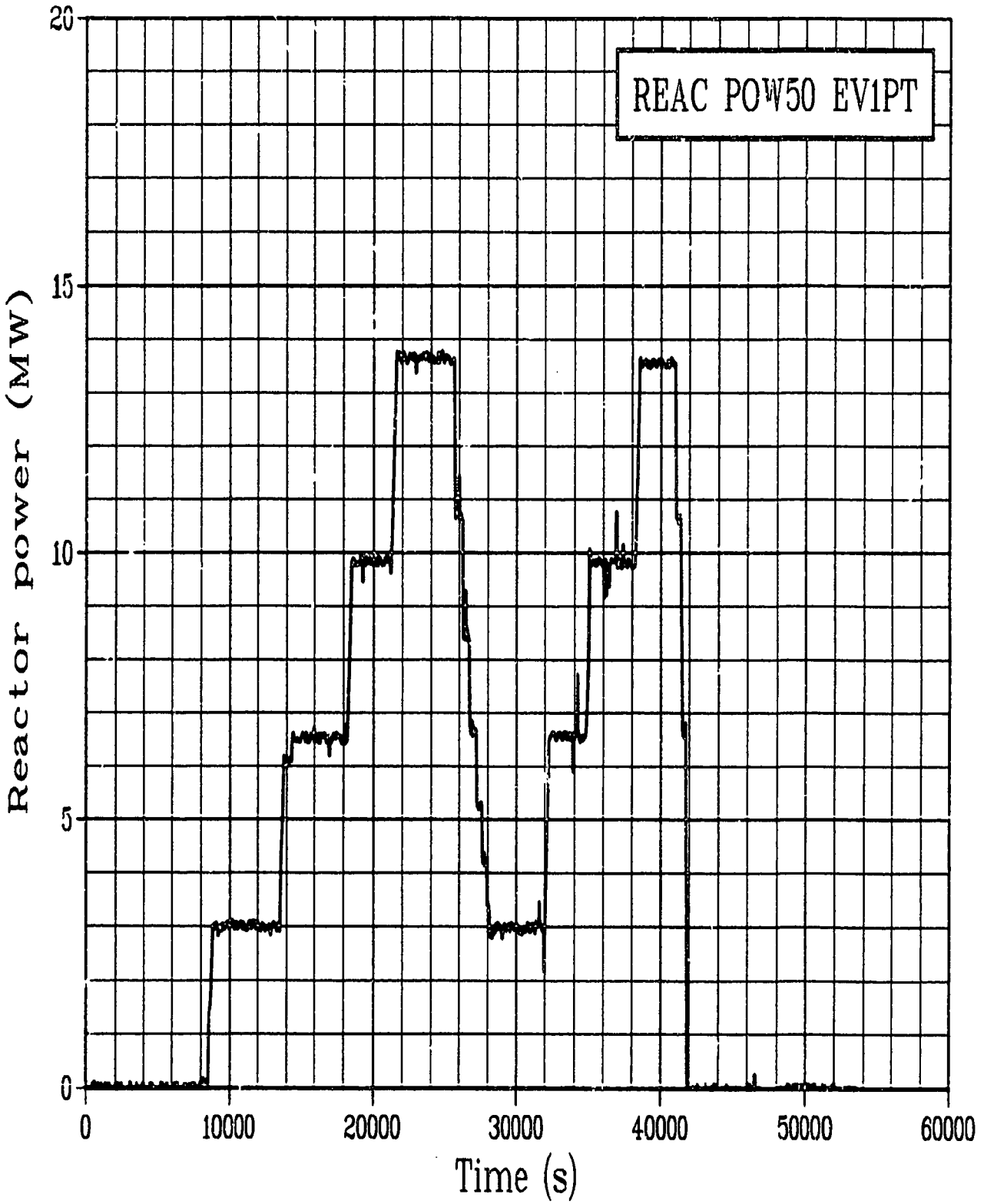

Figure C-190. Reactor power from Core Ionization Chamber EV 1 during Test PR-1 power oscillation period (REAC POW50 EV1PT).

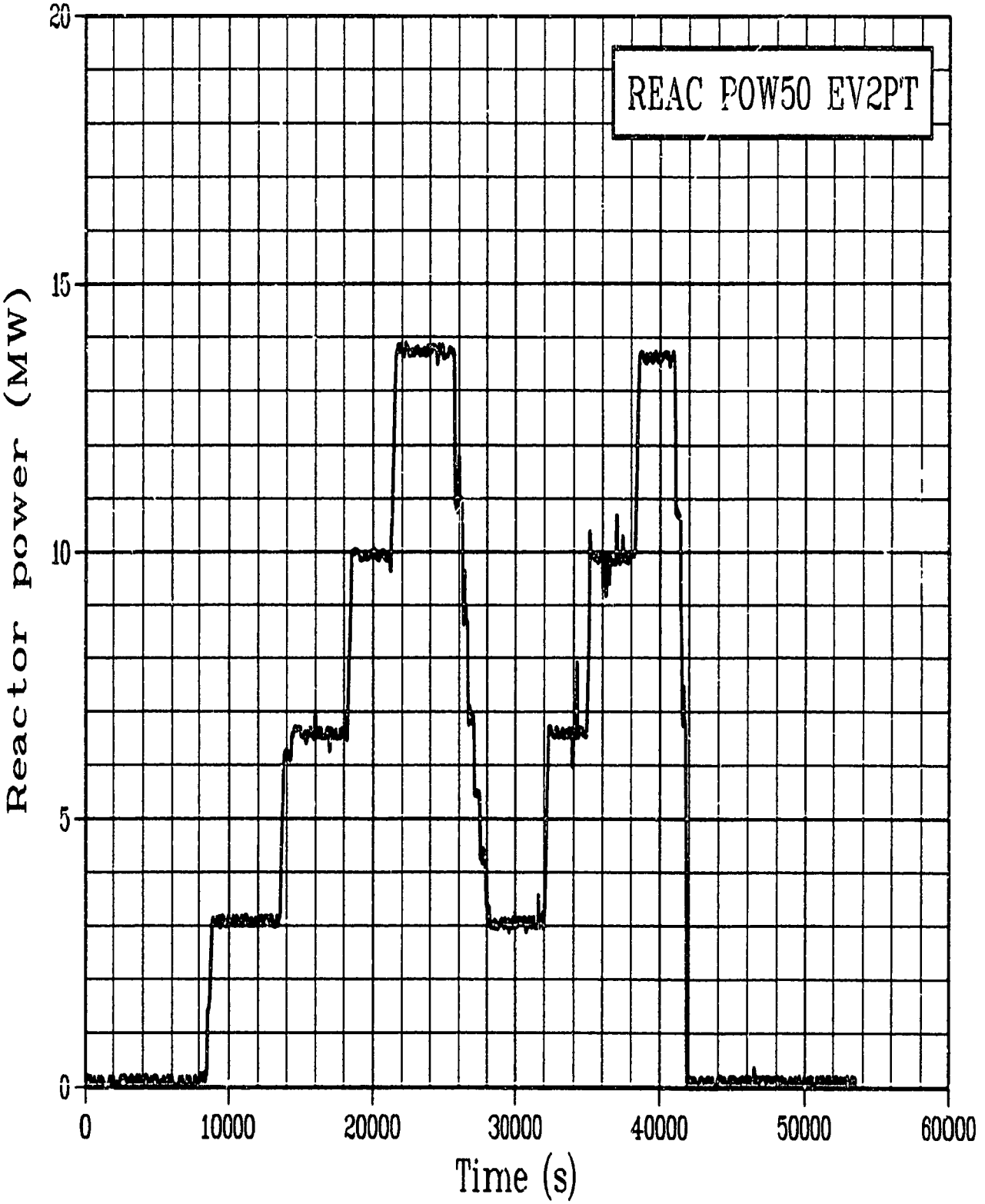

Figure C-191. Reactor power from Core Ionization Chamber EV 2 during Test PR-1 power oscillation period (REAC POW50 EV2PT).

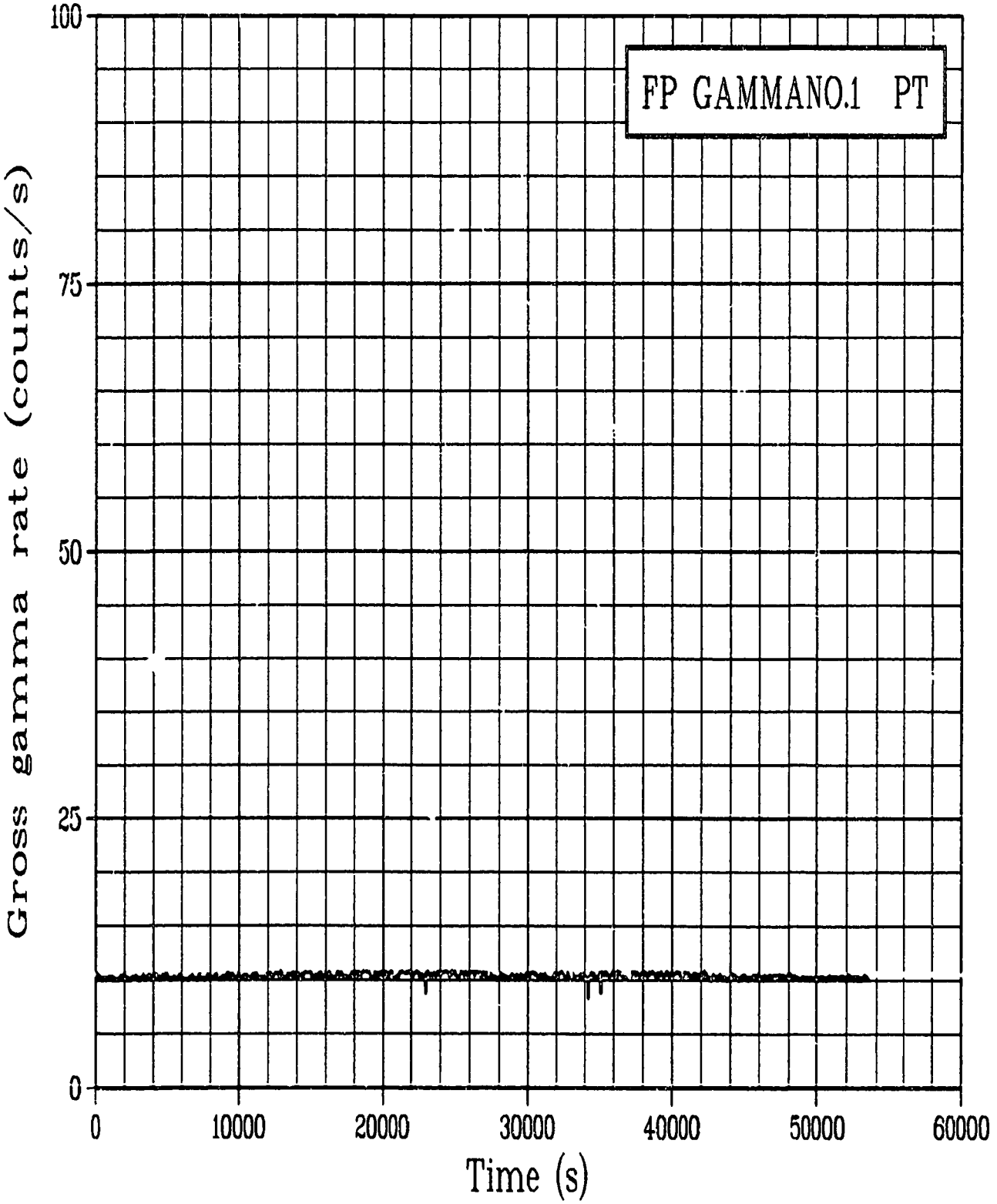

Figure C-192. Gross gamma rate of fission product detector 1 during Test PR-1 power oscillation period (FP GAMMANO.1 PT).

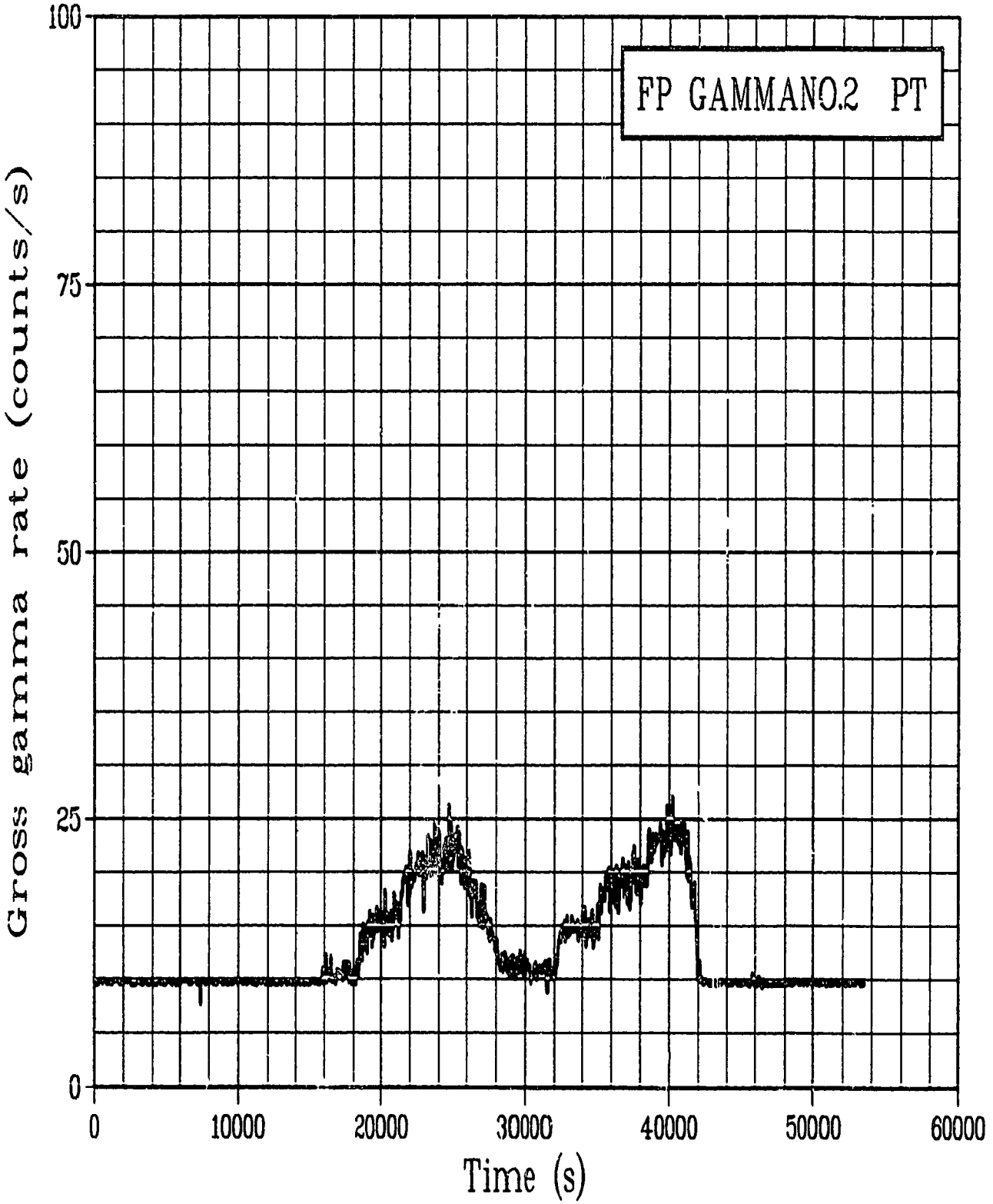

Figure C-193. Gross gamma rate of fission product detector 2 during Test PR-1 power oscillation period (FP GAMMANO.2 PT).

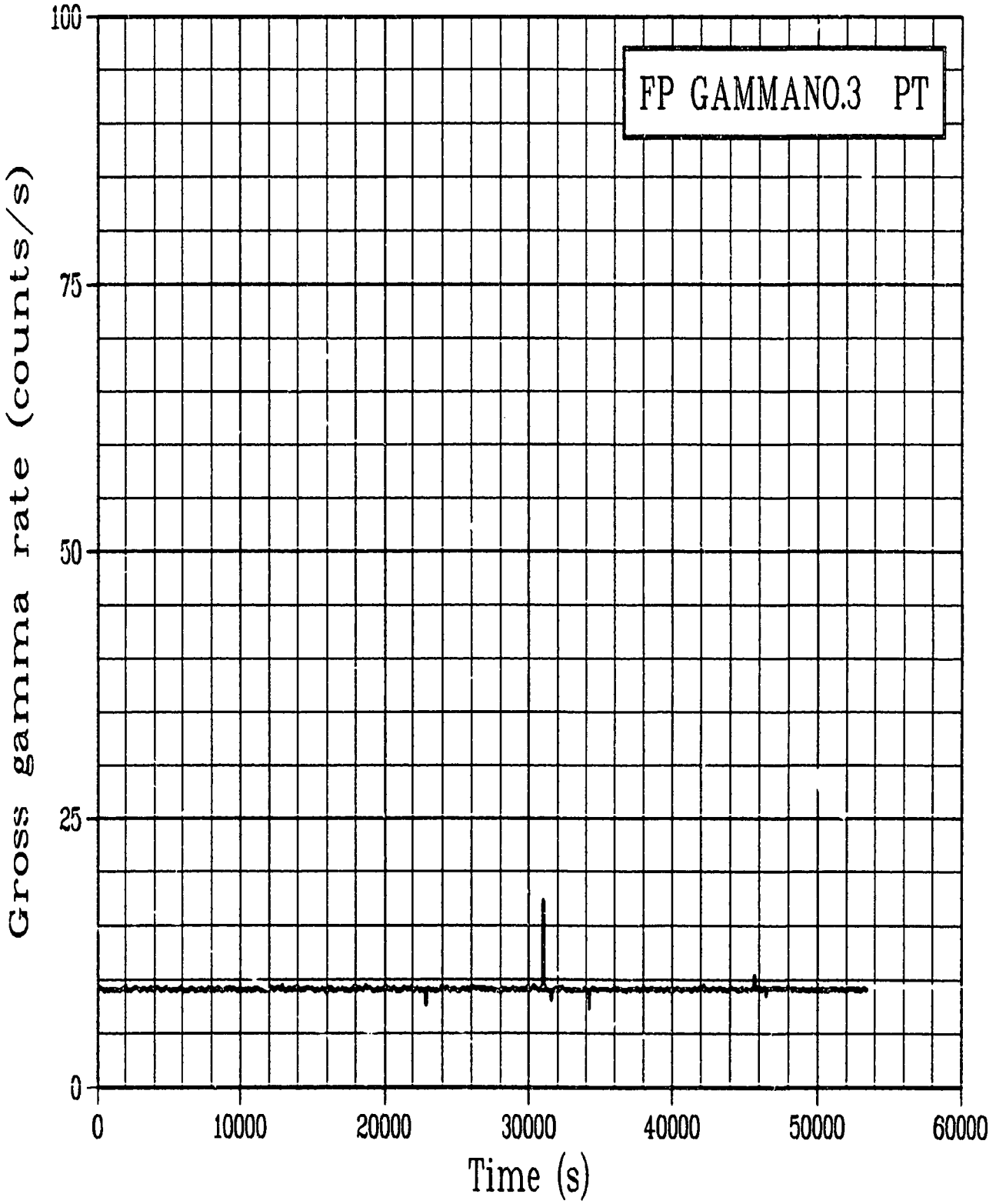

Figure C-194. Gross gamma rate of fission product detector 3 during Test PR-1 power oscillation period (FP GAMMANO.3 PT).

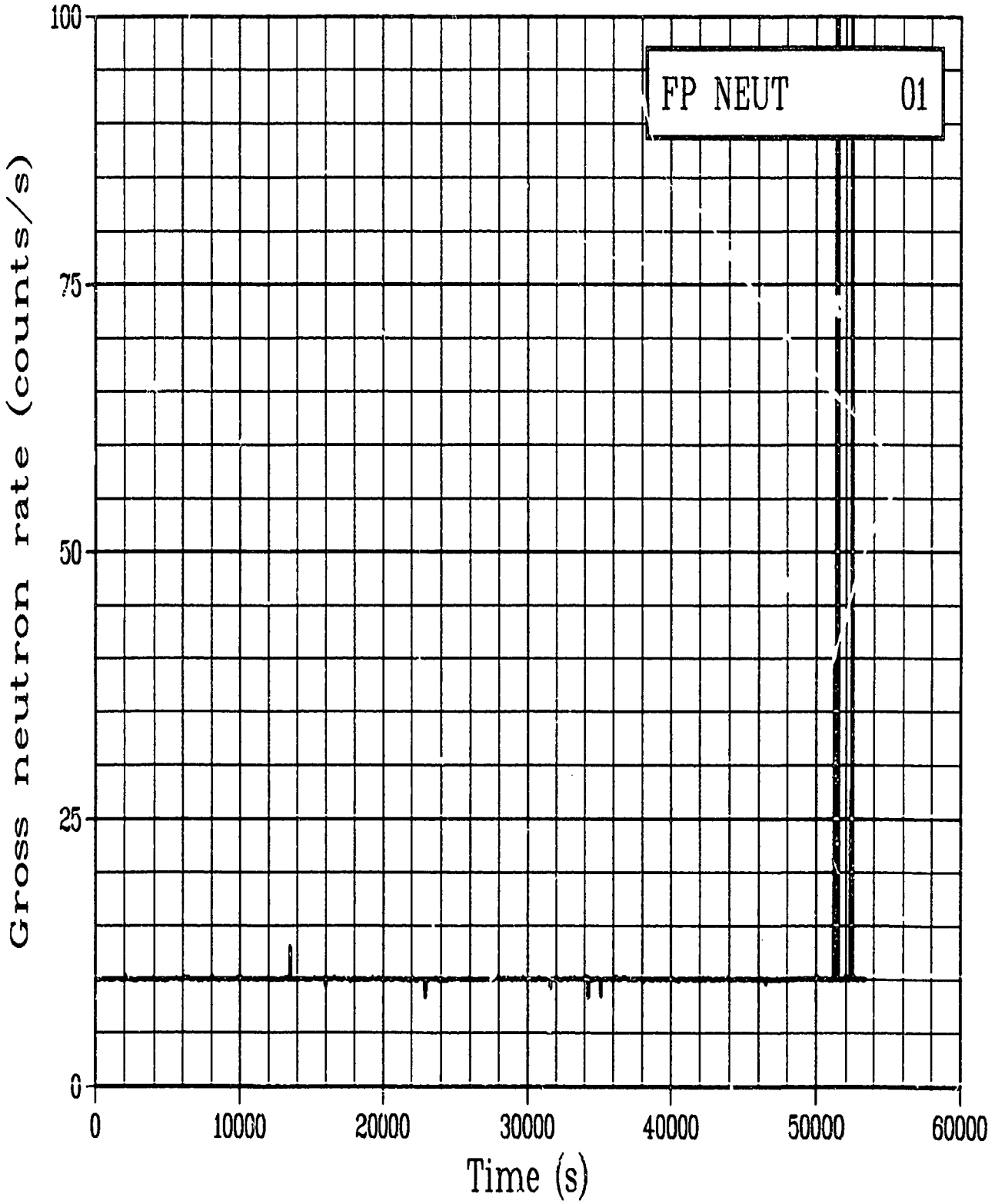

Figure C-195. Gross neutron rate of fission product detector system during Test PR-1 power oscillation period (FP NEUT 01).

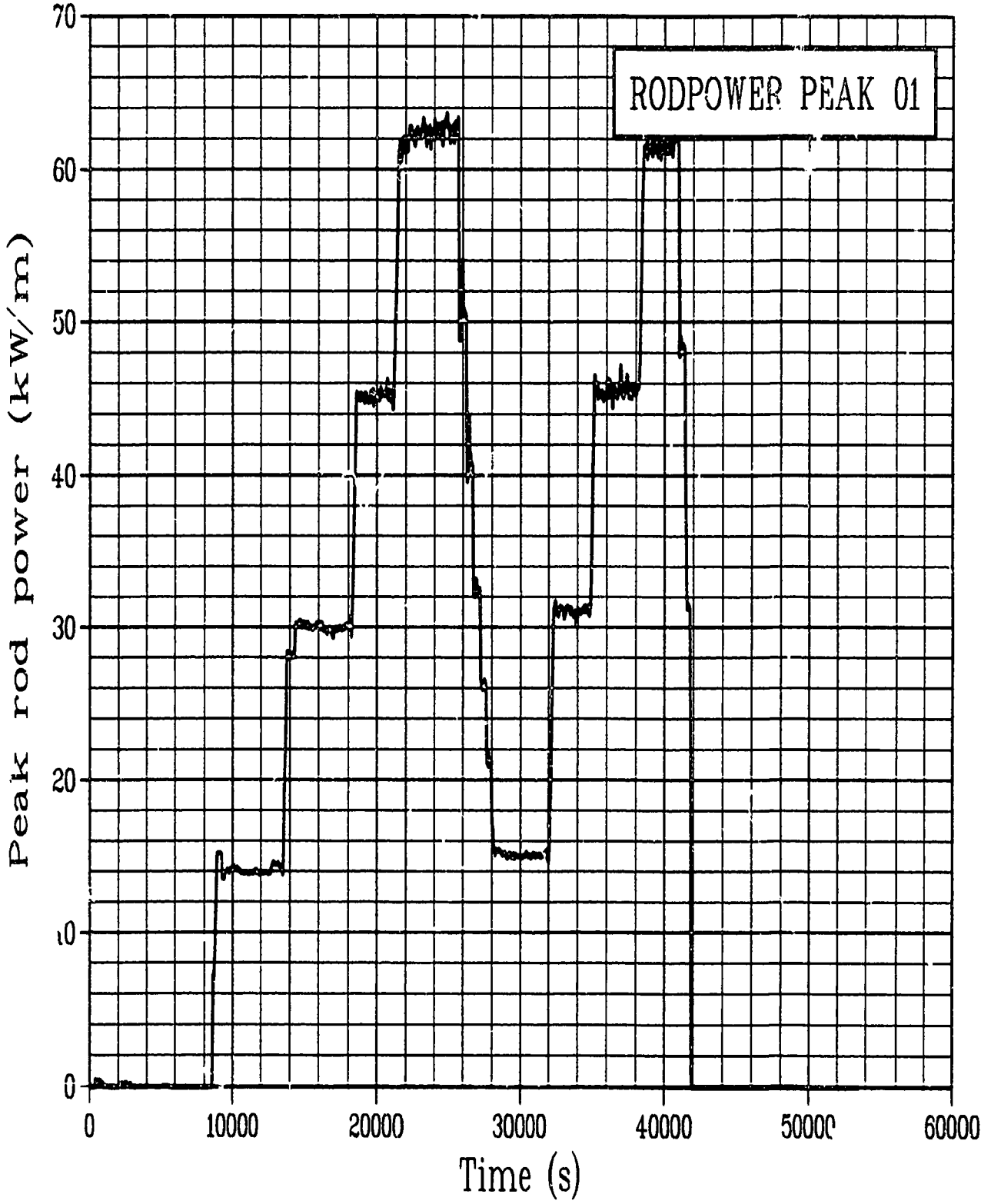

Figure C-196. Calculated peak rod power Rod GC 524-1 during Test PR-1 power oscillation period (RODPOWER PEAK 01).

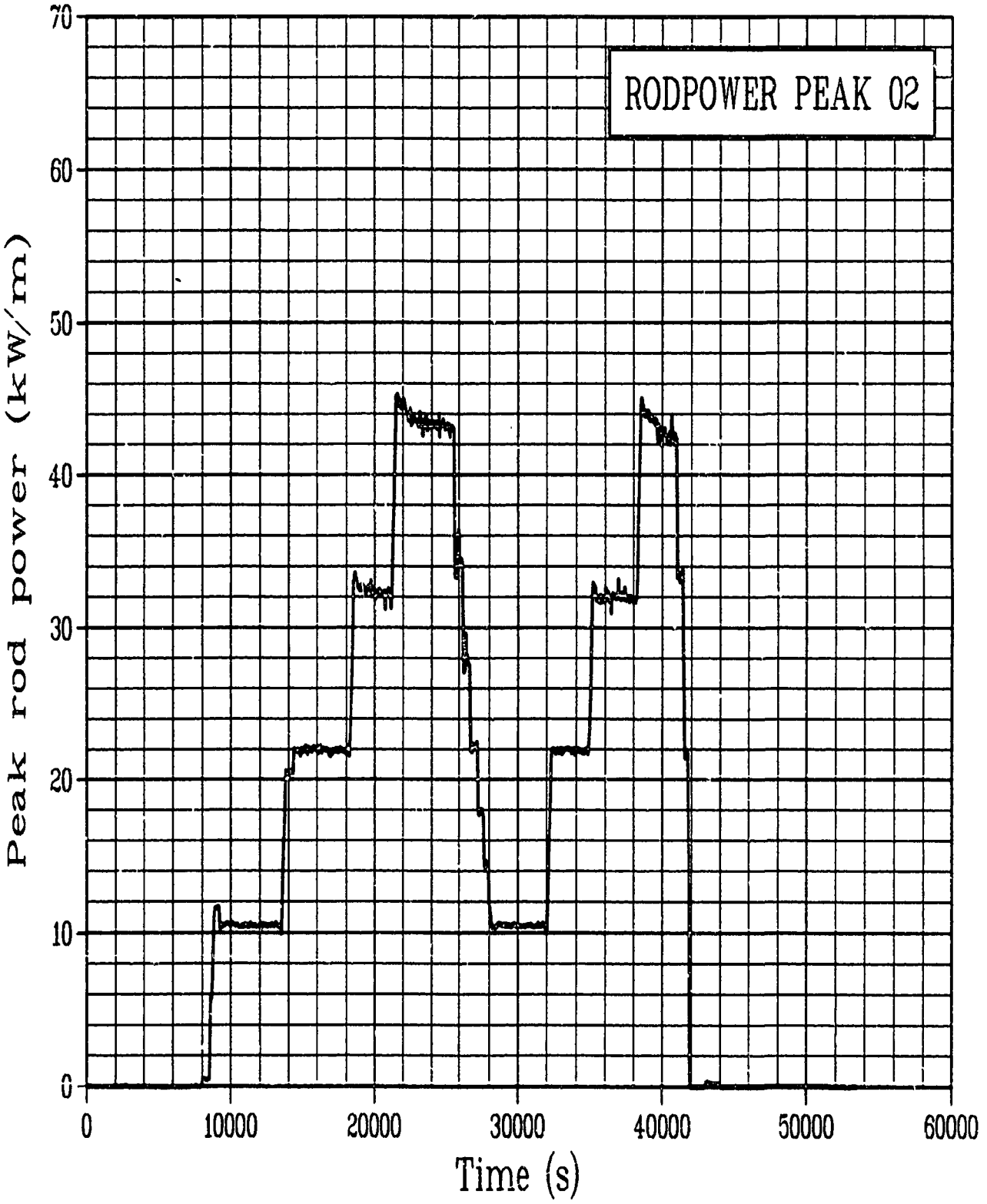

Figure C-197. Calculated peak rod power Rod GC 524-2 during Test PR-1 power oscillation period (RODPOWER PEAK 02).

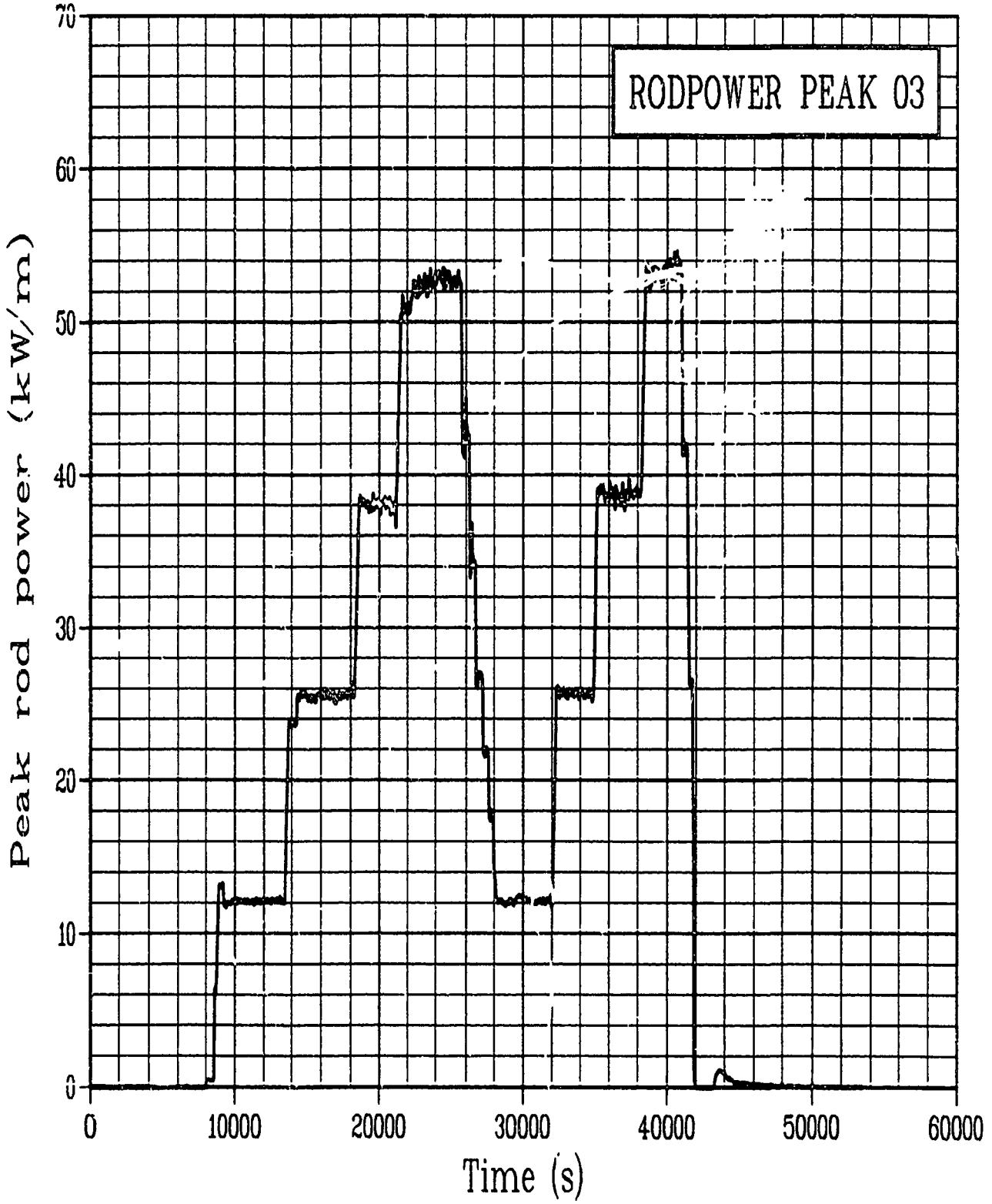

Figure C-198. Calculated peak rod power Rod GC 524-3 during Test PR-1 power oscillation period (RODPOWER PEAK 03).

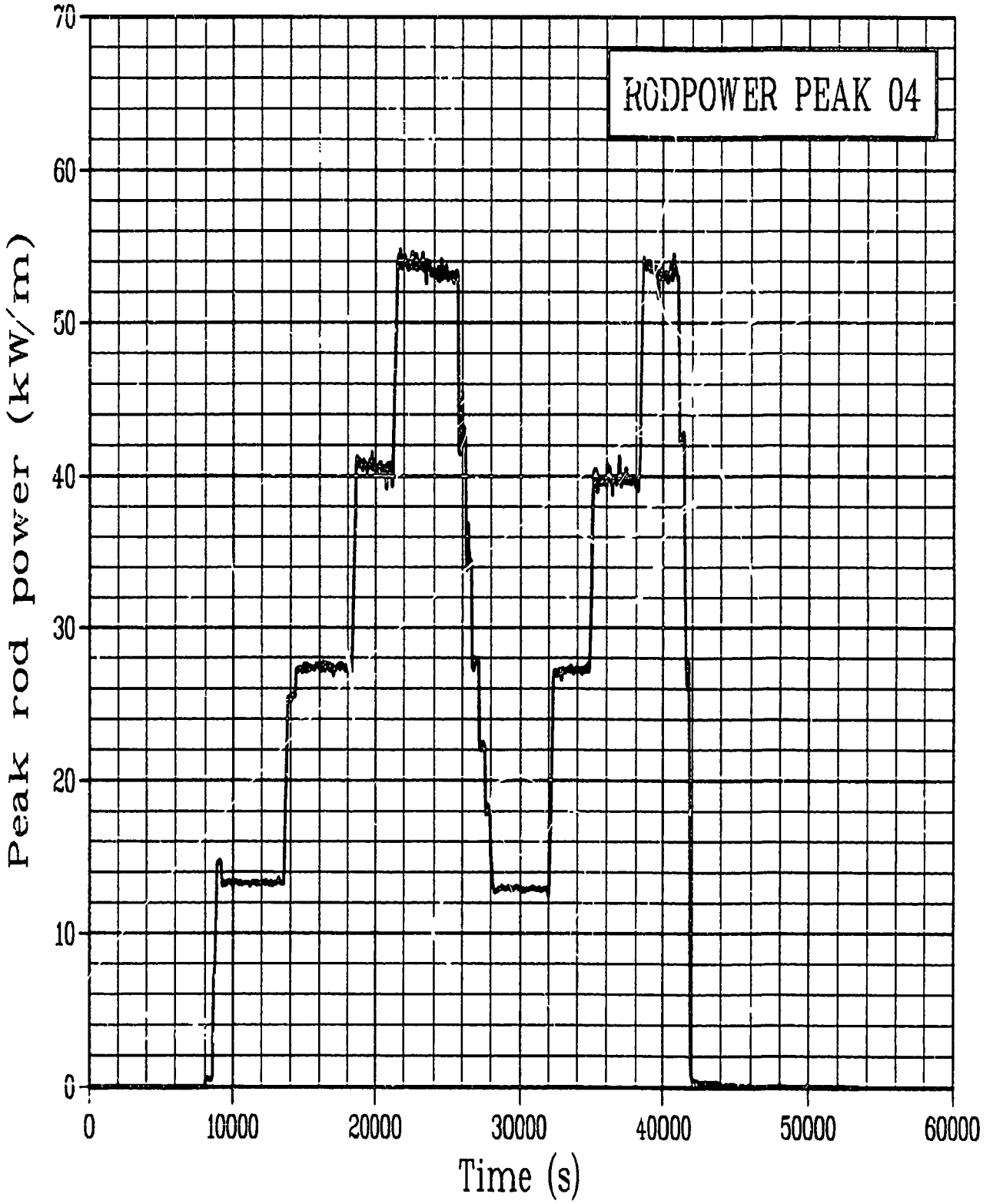

Figure C-199. Calculated peak rod power Rod GC 524-4 during Test PR-1 power oscillation period (RODPOWER PEAK 04).

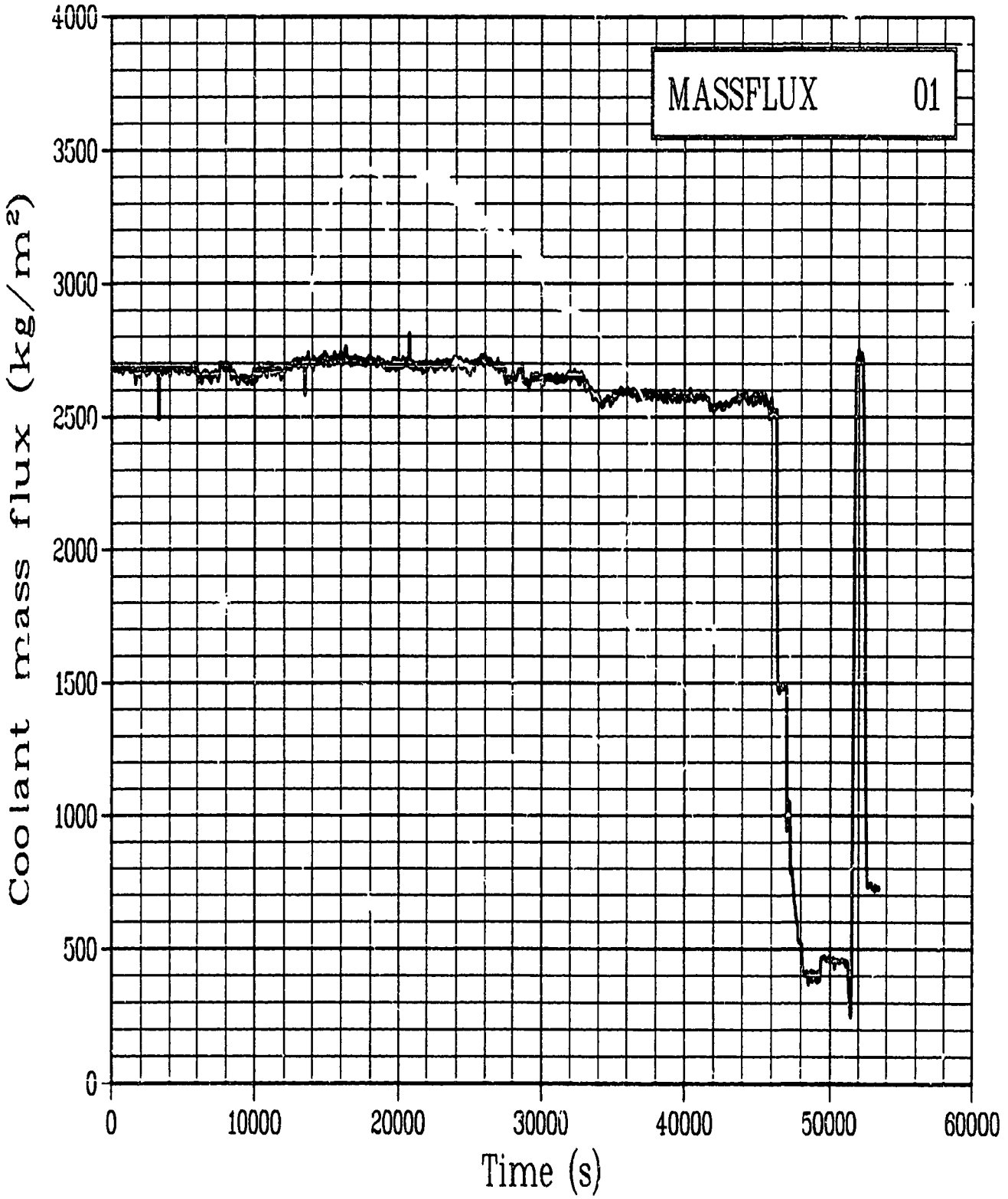

Figure C-200. Calculated coolant mass flux Rod GC 524-1 during Test PR-1 power oscillation period (MASSFLUX 01).

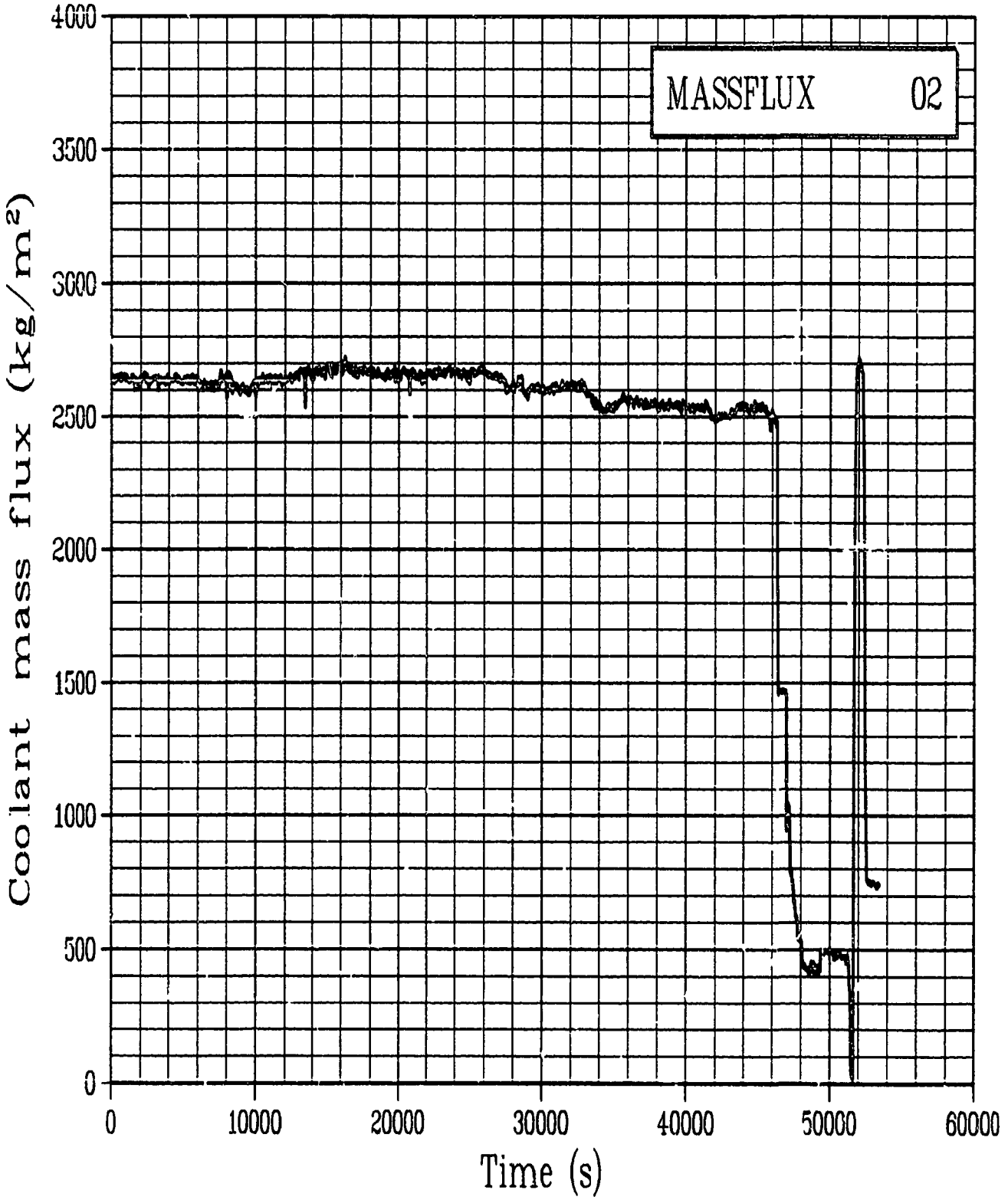

Figure C-201. Calculated coolant mass flux Rod GC 524-2 during Test PR-1 power oscillation period (MASSFLUX 02).

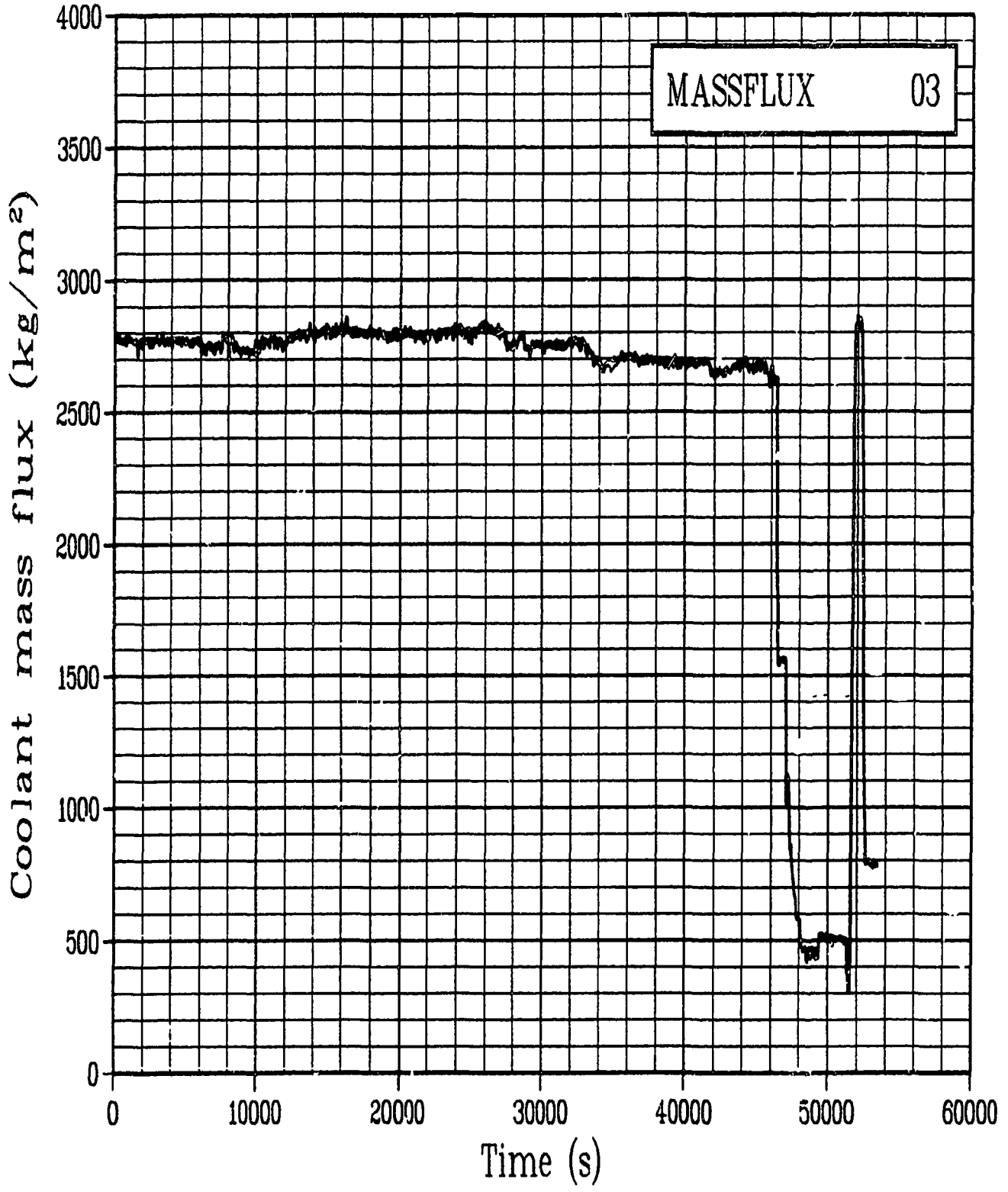

Figure C-202. Calculated coolant mass flux Rod GC 524-3 during Test PR-1 power oscillation period (MASSFLUX 03).

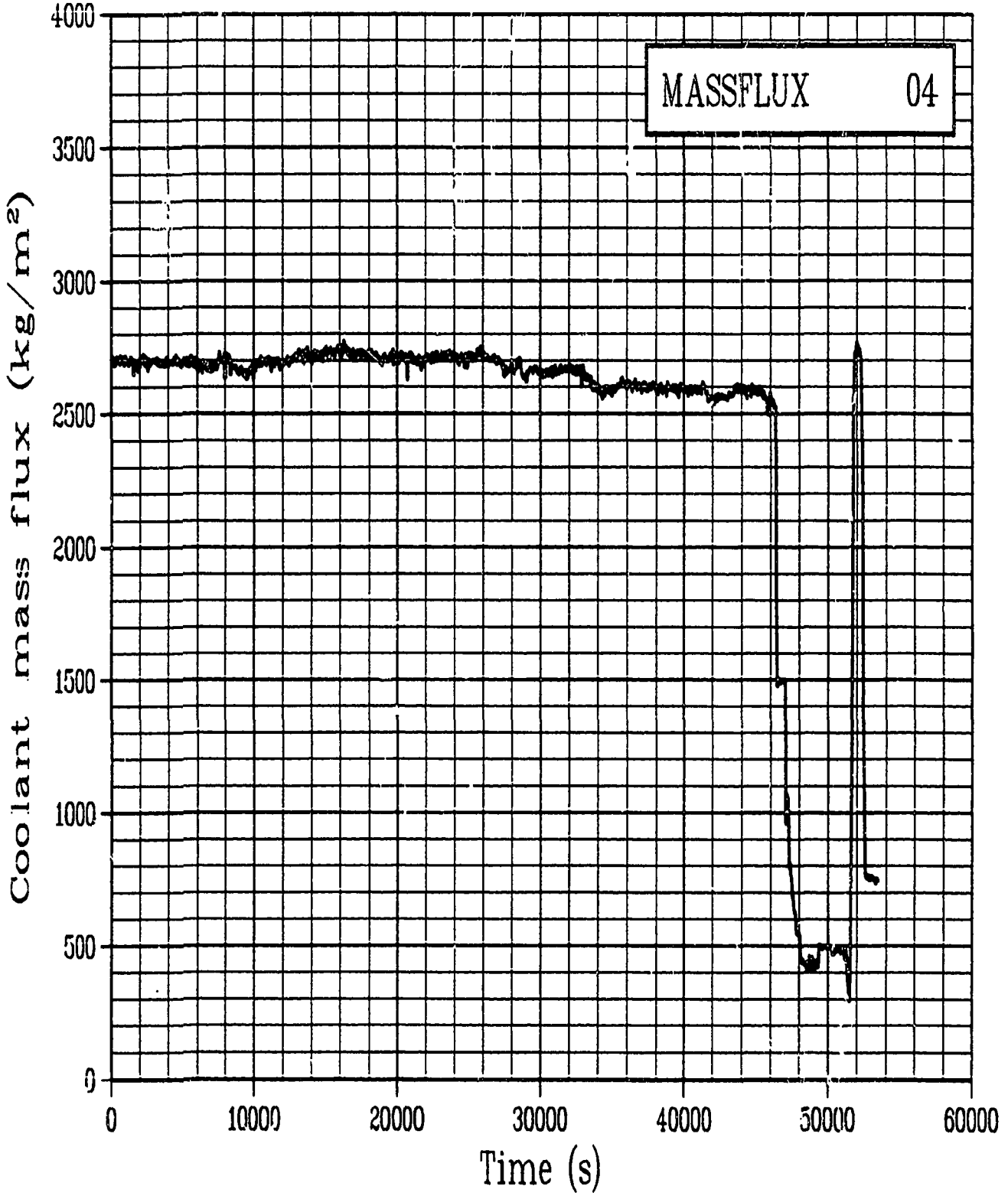

Figure C-203. Calculated coolant mass flux Rod GC 524-4 during Test PR-1 power oscillation period (MASSFLUX 04).